UILU-ENG-89-2007

CIVIL ENGINEERING STUDIES
Structural Research Series No. 548

ISSN: 0069-4274

EXPERIMENTS AND ANALYSES TO STUDY THE SEISMIC RESPONSE OF REINFORCED CONCRETE FRAME-WALL STRUCTURES WITH YIELDING COLUMNS

By

Marc O. Eberhard
and
Mete A. Sozen

A Report to the
THE NATIONAL SCIENCE FOUNDATION
Research Grant NSF ECE 84-18691

DEPARTMENT OF CIVIL ENGINEERING
UNIVERSITY OF ILLINOIS AT URBANA-CHAMPAIGN
URBANA, ILLINOIS

SEPTEMBER 1989

EXPERIMENTS AND ANALYSES TO STUDY THE SEISMIC RESPONSE OF REINFORCED CONCRETE FRAME-WALL STRUCTURES WITH YIELDING COLUMNS

by

Marc O. Eberhard

and

Mete A. Sozen

A Report to the

NATIONAL SCIENCE FOUNDATION

Research Grant ECE 84-18691

University of Illinois
at Urbana-Champaign
Urbana, Illinois
September 1989

ACKNOWLEDGMENTS

Financial support for this study was provided by the National Science Foundation under grant ECE 84-18691. Analyses were performed on a DEC VAX 11/750 computer, acquired under grant CEE 84-02176.

Professor S. L. Wood contributed to every phase of this study; her suggestions and effort are greatly appreciated. Professors W. J. Hall, K. D. Hjelmstad and D.A.W. Pecknold are thanked for reviewing the manuscript.

The authors relied heavily on the labor and suggestions support of students, including J. Bonacci, J. Dragovich, M. Harris, R. Lopez, R. Stark and H. Walther. The authors' collaboration with D. Mikitka during the experimental phase of the study was particularly rewarding.

Acknowledgment is also due to the staff of the Machine Shop, under the direction of O. Ray and C. Swan. H. Dalrymple is thanked for patiently assisting with instrumentation and data acquisition. D. Bever is thanked for carefully preparing the manuscript.

This report was prepared as a doctoral dissertation by M. O. Eberhard, directed by M. A. Sozen.

TABLE OF CONTENTS

CHAPTER Page

LIST OF TABLES

LIST OF FIGURES

CHAPTER 1

INTRODUCTION

1.1 Object of Study

The object of this study was to seek an efficient structural configuration to control distortion in reinforced concrete frames located in regions of high seismicity. Specific topics studied by experiment and analysis were the effects on lateral-displacement response of:

(1) using slender walls in frames with yielding columns

(2) introducing a structural hinge at the base of the wall to reduce strength and stiffness requirements for the foundation.

To proportion slender walls to limit lateral-displacement response, it is necessary to have a pragmatic method for estimating maximum drift. Maximum displacements calculated by nonlinear response-history analysis were compared with displacements calculated by linear analysis, following a procedure suggested by Shimazaki [35, 38].

To design walls to resist shear, it is necessary to have a realistic estimate of the base shear for a building. Several simple procedures for estimating maximum base-shear response of frame-wall structures were evaluated by comparing estimates with the observed response of small-scale test structures.

The estimates of maximum displacement response and shear demand were incorporated into a design procedure. The procedure differs from current practice in that the emphasis currently placed on base-shear strength is reduced in favor of a greater emphasis on displacement response.

1.2 Reasons for the Studying Frames with Slender Walls

In selecting a lateral-force resisting system for a building in regions of high seismic risk, the designer must consider architectural and economic factors as well as the response of the building during an earthquake. As a result of different economic conditions and architectural traditions, different approaches have evolved in different professional communities with respect to the desirable combinations of building stiffness, strength and toughness.

For example, Chilean engineers have elected to build very stiff buildings [29, 47] with few details to provide toughness. These buildings behaved well during a strong earthquake in 1985 [29, 47]. However, the presence of large structural walls limits the options available to the architect.

In the United States, architects and owners prefer structures with floor spans that are more adaptable to architectural demands. As a result, they favor buildings in which the lateral resistance is provided by frames. To compensate for a relative lack of stiffness, U.S. model codes require extensive details to provide toughness [4, 7, 40, 44]. Toughness details tend to protect the structure but not the building contents. Nonstructural elements would be damaged by large displacements.

Taking functional convenience to an extreme, the beam spans can be further increased and the columns made more slender to the point that beams are stronger than the columns. Such strong-beam, weak-column frame structures can be designed to behave satisfactorily during earthquakes, but large quantities of column reinforcement are required to control interstory displacements [32].

Frame structures with slender walls were studied because they may provide a satisfactory compromise between structural performance and architectural requirements. If some of the yielding columns of a strong-beam, weak-column structure are replaced by slender walls, the structure may have enough stiffness and strength to control damaging interstory displacements. (Slender walls are defined for the purpose of this study as walls that are expected to yield in flexure; extremely slender walls are then similar to deep columns.) The walls could also reduce column reinforcing steel requirements and, more importantly, reinforcing steel congestion. Unlike larger shear walls, which may be architecturally inconvenient, slender walls of 5-8 ft can be placed conveniently in spaces surrounding stairwells, elevator shafts, or closets.

1.3 Problems with Slender Walls

Slender walls have structural problems associated with transfer of forces at the base. Under cyclic loading, a crack traversing the entire wall depth can form at the wall-foundation interface, limiting the amount of shear that can be transferred to the foundation. If the wall is assumed to be fixed at its base, linear analysis indicates that the base of the wall, and therefore, the underlying foundation, must be designed for very large moments. Unless an expensive foundation is provided at the base of the wall to accommodate the large moment, the foundation may rotate ("rock") during strong earthquakes. An economical alternative may be to limit the moment transferred to the foundation by means of a hinge detail.

Ensuring toughness in slender-wall structures is difficult because standard procedures used to obtain design shears for columns and shear walls are not

appropriate for the shear design of slender walls. An upper bound of the shear demand in a column may be obtained by assuming plastic hinges at the ends of members. This approach, however, would lead to unreasonably high base shears for a flexural wall, or even a deep column. Therefore, a study was made to develop a simple method of estimating the maximum dynamic base shear for a frame-wall structure. The total base shear for the structure is an upper bound for the shear at the base of the wall.

1.4 Scope of Study

Experiments were performed to provide experimental benchmarks against which to calibrate existing numerical models. The experimental phase of this study included the design, construction and testing of two test structures (ES1 and ES2) of identical geometry but differing column reinforcement. Structures ES1 and ES2 included two small-scale, nine-story reinforced concrete frames with three columns and a slender wall (Fig. 1.1(b)). The geometry of the test structures was selected to permit direct comparison with the observed response of frame structures with yielding columns (Fig. 1.1(a)) tested by Schultz.

In large-scale structures, a hinge detail or foundation rocking would reduce the effective flexural strength and increase the flexibility at the base of the wall. In both test structures, additional flexibility was obtained by crossing longitudinal reinforcement at the base of the wall to form an "X" (Mesnager hinge [11, 22], Fig. A.5 and 2.11).

Each test structure was subjected to three simulations of the N-S component of ground motion measured in El Centro, California during the 1940 Imperial Valley Earthquake [9]. A sinusoidal motion with a frequency near the

fundamental frequency of the damaged structures served as a fourth base motion. Accelerations and displacements at each story were recorded, as well as rotation and slip at the base of the wall. Dynamic tests were followed by static tests during which a horizontal force was applied to the first-story mass.

The design of the test structures is discussed in Chapter 2 and the experimental program is briefly described in Chapter 3; details are provided in Appendix A. Measured response maxima and waveforms are presented in Chapter 4. In Chapter 5, the observed response is discussed and compared with the response of the frames with yielding columns (SS1 and SS2).

During the analytical phase of the study, the response of ES2 during three base motions was reproduced numerically using the nonlinear, member-by-member numerical model described in Chapter 6. A parametric study was then performed to observe the sensitivity of calculated displacement response to model parameters and to member strength and stiffness. Displacements calculated by nonlinear response-history analysis were compared with displacements calculated by linear analysis.

In Chapter 7, the strength of small-scale frames and frame components, measured during static and dynamic tests, is compared with calculated strengths. The tests considered in Chapter 7 are described in greater detail in Appendix B. In Chapter 8, the maximum base shear observed for frame-wall structures is compared with that estimated by several methods.

A summary of this study and the resulting conclusions are given in Chapter 9. The final chapter includes recommendations for proportioning slender walls and for estimating the maximum dynamic shear at the base of a frame-wall structure.

CHAPTER 2

DESIGN OF THE TEST STRUCTURES

This chapter discusses the design of the two small-scale test structures, ES1 and ES2. The selection of test configuration, story masses, base motions and analytical model are described in Section 2.1. Section 2.2 discusses the proportioning of the reinforced concrete frames and selection of reinforcement. Details of the test structures, including construction and erection procedures, are given in Appendix A.

The nominal dimensions of structure ES1 and ES2 were identical. Wall and beam reinforcement was also the same for both structures. Structure ES2, however, had less column reinforcement than Structure ES1.

2.1 Experimental Design

2.1.1 Configuration

Test structures were designed to study the in-plane behavior during earthquakes of reinforced concrete frames that contain a slender wall. Each test structure consisted of a pair of nine-story, three-bay, reinforced concrete frames, supporting a mass at each story (Fig. 2.1). Story masses, base motions and geometry of the test structures were selected to permit direct comparison with "strong-beam, weak-column" frame structures SS1 and SS2, tested by Schultz [32]. The geometry of structures ES1 and ES2, described in this report, differed from those tested by Schultz only in that a slender wall was substituted in place of an interior column (Fig. 1.1 and 2.2).

2.1.2 Story Masses

Nine 1100-lb masses, one at each story, generated both gravitational and inertial forces (Fig. A.2). Masses were designed such that calculated gravity-load stresses in first-story columns corresponded approximately to 10% of the assumed concrete compressive strength. Gravity loads were distributed equally to each wall and column. Compressive stresses in the first story due to the masses were 550 psi for columns and 180 psi for walls.

2.1.3 Base Motion

The design base motion was modelled after the NS component of the 1940 El Centro record with a maximum acceleration of 0.35 g. The earthquake simulator reproduced only one horizontal component of ground motion. Additional filtering or truncation of the recorded motion beyond that performed at the California Institute of Technology [9] was not required. The time interval between measured accelerations was compressed by a factor of 2.5 in order to obtain a satisfactory relationship between the frequency of the test structure and the frequency content of the base motion.

Conservative design response spectra for damping ratios of 2 and 10% are presented in Fig. 2.3. Periods refer to scaled time.

2.1.4 Analytical Model

Reinforced concrete frames, oriented parallel to the direction of simulator motion, carried all vertical and lateral loads. Because the frames were forced to displace equally at each story and out-of plane displacements were restrained (Section A.1.4), only in-plane displacements were considered in the design of the test structure.

The test structure was modelled as a planar frame (Fig. 2.4) using the program SARSAN [30]. The linear model included flexural and shear flexibility in all members but considered axial deformations only in columns and walls. Masses were lumped at each story. Joints were assumed to be rigid.

Because a large base girder was cast monolithically with each frame, columns were assumed fixed at the base. Support rotation at the base of the wall was controlled by means of a rotational spring (Fig. 2.4).

2.1.5 Estimation of Maximum Displacement Response

Maximum displacement response was estimated using a linear model based on suggestions by Shimazaki [35, 38]. Shimazaki found that an upper bound on the nonlinear, inelastic displacement response of a single-degree-of-freedom oscillator can be satisfactorily estimated by linear analysis provided the system has an acceptable combination of strength and initial period.
In particular, Shimazaki observed that response displacement could be estimated by linear analysis (assuming 2% damping and assuming one half the stiffness corresponding to gross-section properties) provided that:

$$TR + SR \geq 1.0 \qquad (2.1)$$

where,

$$SR = \frac{\text{Base-shear strength}}{\text{Base shear calculated for linear response (damping factor = 2\%)}}$$

$$TR = \frac{\text{Calculated initial period} * \sqrt{2}}{\text{Characteristic period for the ground motion } (T_g)}$$

The characteristic period for the base motion (T_g) is defined to be that period at which energy response ceases to increase with increase in period.

The maximum drift of multi-degree-of-freedom systems can also be estimated by linear analysis if the periods of the modes contributing significantly to displacement response satisfy Eq. 2.1. For design, a linear model was judged to be sufficiently accurate if the period of the first mode of the characteristic structure satisfied Eq. 2.1. The linear model was used to investigate the sensitivity of maximum displacement response to wall length and base fixity.

2.2 Design of the Reinforced Concrete Frames

2.2.1 Geometry

(a) Columns and Beams

To permit direct comparison with the structures tested by Schultz [32], span lengths and cross-sectional dimensions of beams and columns were identical to those of SS1 and SS2 (Fig. 1.1, 2.2). The nine-story frames had three 24-in. bays. The first story measured 12 3/8 in.; upper stories had 9-in. story heights (centerline-to-centerline dimensions). Columns had square cross-sections (1 1/2 x 1 1/2 in.) while beams had a depth-to-width ratio of 1.5 (2 1/4 x 1 1/2 in.).

(b) Wall

The length of the wall was selected to limit overall drift to 1% of the height of the structure and to limit interstory drift to 1.5% of the story height. Calculated initial and characteristic periods for 1 1/2, 3, 4 1/2, 6, 7 1/2 and 9-in. wall depths are listed in Table 2.1. Assumed support fixity

was varied from pinned to fixed by changing the stiffness of the rotational spring at the base of the wall. Table 2.1 also lists periods for structures with a spring stiffness at the base of the wall selected to produce equal moments at the base and at the lower face of the first-story beams.

The characteristic period for the 1940 El Centro ground motion is approximately 0.55 sec. Compressed by a factor of 2.5, the test base motion had a characteristic period of 0.22 sec. In comparison, the characteristic periods (initial period times $\sqrt{2}$) of the structures considered in design ranged from 0.18 sec to 0.32 sec and the period ratio, TR, ranged from 0.80 to 1.45 (Table 2.1). For reasonable base-shear strengths, all the structures listed in Table 2.1 satisfy Eq. 2.1. Ranges of initial and characteristic periods considered in the design process are superimposed on the design spectra in Fig. 2.3.

Maximum displacement response was estimated using the design response spectrum shown in Fig. 2.3, assuming gross-section properties, one-half the expected modulus of elasticity and a damping factor of two percent, as suggested by Shimazaki. Maximum displacement was calculated using the root-sum-squared combination of the first three modes. The third mode contributed less than 1% to calculated ninth-story drift and less than 3% to drift of the first story.

Calculated drifts are presented in Table 2.2 and Fig. 2.5. Calculated first-story drift was sensitive to both wall length and support fixity. Calculated overall drift, on the other hand, was only slightly sensitive to wall length and support conditions at the base of the wall.

Displacements associated with three modes are plotted in Fig. 2.6 for structures with 1 1/2, 3, 4 1/2 and 6-in walls. Displacements are plotted for

structures with a spring stiffness that resulted in equal moments at the base of the wall and at the lower face of the first-story beams.

Using design criteria of an interstory drift ratio of 1.5% and an overall drift ratio of 1.0%, a 4 1/2-in. wall was selected. A 4 1/2-in. wall was attractive, because, depending on assumed base conditions, one might judge the wall to be acceptable (fixed-base assumption, 1.0% interstory drift ratio) or unacceptable (pinned-base assumption, 2.2% interstory drift ratio).

2.2.2 Design Forces and Drifts

A modified version of the Substitute Structure Method [34] was used to determine design forces for Structure ES1. Nonlinear behavior was approximated by a linear structure of reduced stiffness (Fig. 2.7). In applying the Substitute Structure Method, each member was assigned a "damage ratio", corresponding to the ratio of the cracked stiffness to the substitute structure stiffness. Damage ratios were increased until calculated displacements approached design drift limitations.

Displacements were calculated using the design spectra of Fig. 2.3, assuming a damping factor of 10% for all modes. Design damage ratios and corresponding moments of inertia are tabulated in Tables 2.3 and 2.4. Additional softening at the base of the 4 1/2-in. wall was represented by a rotational spring. Spring stiffness was varied until the design moment at the base of the wall was half that at the lower face of the first-story beams.

Frequencies and mode shapes for the substitute structure are given in Table 2.5. Figure 2.8 shows calculated displacements for the first three modes. Design moments, corresponding to the root-sum-squared combination of three modes, are presented in Table 2.6 and Figure 2.9. Note that calculated moments

in column-lines A and C (column lines shown in Fig. 2.2) were larger in the second story than in the first story.

The Mesnager hinge detail was conservatively designed for the wall moment at the lower face of the first-story beams (12.6 k-in.), even though the substitute structure indicated a design moment that was half that large (6.1 k-in.). This conservatism was warranted based on the observed behavior of the Mesnager hinge during static tests. During static tests of the component the measured flexural strength was only 80% of that calculated by standard flexural analysis. When subjected to several reversals of loading, the Mesnager hinge was observed decrease in stiffness much more rapidly than a detail with straight reinforcement.

2.2.3 Flexural Reinforcement Requirements

Column reinforcement was fabricated from No. 13-gage wire (0.0915-in. nominal diameter). Walls and beams were reinforced with No. 7-gage wire (0.177-in. nominal diameter). A yield stress of 56 ksi for reinforcement and a concrete compressive strength of 5500 psi were assumed for calculations.

Moment-axial force interaction diagrams are presented in Fig. 2.10. Two points are plotted for each story, corresponding to loading conditions of minimum and maximum axial force. Reinforcement for Structure ES1 was selected to resist design moments (Table 2.6) under a loading condition of minimum axial load. Design moments were defined to be the square root of the sum of the squares of the moments for the first three modes.

Column reinforcement for Structure ES2 was arbitrarily reduced to the minimum 4 bars per cross-section (2 per face) required to confine columns and

to hold shear reinforcement in-place during casting of the frame. Reinforcement schedules for structures ES1 and ES2 are given in Table 2.7.

2.2.4 Reinforcement Details

Typical reinforcement details are shown in Fig. 2.11, 2.12 and 2.13. Longitudinal reinforcement was continuous through all joints. Bar cut-offs were located at mid-story height. Bar anchorage was provided at exterior joints by extending reinforcing steel into 4-in. stubs. Anchorage at the base of the structure was provided by steel plates welded to column and wall steel (Fig. 2.11).

Transverse reinforcement consisted of continuous rectangular helices of No. 16-gage wire (0.0625-in. nominal diameter) spaced at 0.4 in. (Fig. 2.12). Calculated shear strengths, neglecting concrete resistance, exceeded design shears by a factor of four.

The detail at the base of the wall (Fig. 2.11 and A.5) was designed to control slip between the wall and base girder, and to provide a base that was neither fixed, nor pinned. All four No. 7-gage wall reinforcement bars were bent at 45^0 to intersect at the centerline of the wall. Four No. 13-gage wires were placed in the corners of the rectangular helices to hold the helices in place and to contribute to the moment capacity of the base detail. The No. 13-gage wire extended 6 in. into the base girder and 6 in. into the wall. Figure A.5 presents two photographs of the base-detail reinforcement.

CHAPTER 3

EXPERIMENTAL PROGRAM

Two small-scale reinforced concrete test structures (ES1 and ES2) were subjected to three earthquake simulations, a sinusoidal base motion and static lateral loading. This chapter describes the overall features of the experimental program. Details are provided in Appendix A.

3.1 Test Structures

Each structure consisted of a pair of reinforced concrete frames mounted in parallel on a one-dimensional earthquake simulator (Fig. 1.1(b), A.1). The nine-story, three-bay frames had three columns and a slender wall.

Frame member dimensions were approximately one-fifteenth of full scale. The first story was 12 3/8-in. high. All other stories were 9 in. in height. The wall depth (4 1/2 in.) was twice the beam depth (2 1/4 in.) and three times the depth of the columns (1 1/2 in.).

A Mesnager hinge (Fig. 2.11 and A.5) was placed at the base of the slender walls of both structures. Structures ES1 and ES2 differed only in amount of column reinforcement. Maximum column reinforcement ratios were 3.5% for ES1 and 1.2% for ES2.

Frames were constructed using small aggregate concrete and steel wire reinforcement. Mean concrete compressive strength was 4360 psi (Table A.4) for the first test structure (ES1) and 4800 psi for the second structure (ES2). Number 7-gage (0.177-in. diameter) knurled wire with a yield stress of 58.4 ksi was used for wall and beam reinforcement. Column reinforcement was fabricated

from No. 13-gage wire (0.0915-in. diameter) with a yield stress of 55.5 ksi. Number 13-gage wire was also used at the base of the wall. Rectangular helices of No. 16-gage wire (0.0625-in. diameter) served as shear reinforcement. Measured reinforcing steel properties are summarized in Table A.5.

Masses, weighing approximately 1100 lbs each, were connected to each story. The masses were part of a connection system (Fig. A.2 and A.3) that (1) transferred lateral and vertical loads to the center of frame joints (2) provided out-of-plane stability and (3) coupled the frames such that displacements of each frame at a given story would be equal. The connection system negligibly affected motion within the plane of the frames.

Frames were cast horizontally. The test structures, including frames, masses and connection hardware, were assembled on the earthquake simulator (Fig. A.9). A base girder, which had been cast monolithically with each frame, was prestressed to the simulator platform to fix the base of the structure.

3.2 Testing Procedure

3.2.1 Dynamic Tests

Test structures were subjected to three earthquake simulations modelled after the North-South component of the 1940 El Centro ground motion [9]. Effective peak accelerations of 0.35, 0.52 and 0.70 g were selected for runs 1, 2 and 3 (Table 3.1). A sinusoidal base-motion (0.2 g maximum acceleration) with a frequency near that of the damage structure (2.2 Hz) served as a fourth base motion.

Displacements of each frame relative to the simulator platform were measured by LVDTs (Fig. A.13). Additional LVDTs measured rotation at the base

of the wall and relative slip between the wall and base girder (Fig. A.14). Longitudinal accelerations were measured on the south and north faces of each mass and on the base girders. Vertical accelerations were measured at the ninth story of the south frame. Transverse accelerations were measured at opposite corners of the ninth story (Fig. A.13). Electrical signals from LVDTs and accelerometers were digitized and recorded at a rate of 200 points per second.

Before and after every dynamic test, permanent drift and crack locations were recorded, and free-vibration tests were performed. Free vibration of a test structure was induced by applying and then releasing a 100-lb horizontal force at the ninth story (Fig. A.11). Displacement of the ninth level during application of the horizontal force was measured; displacement and acceleration histories after the force was released were also recorded.

3.2.2 Static Tests

Following the dynamic tests both structures ES1 and ES2 were subjected to static lateral loading at the first story. In this test, a horizontal force was applied to the first-story mass using a 10-ton hydraulic jack. The configuration and instrumentation for static tests are shown in Fig. A.12. Applied lateral load was measured with a load cell. Displacements were measured by dial gauges and LVDTs.

CHAPTER 4

OBSERVED RESPONSE DURING DYNAMIC TESTS

This chapter presents measured response of structures ES1 and ES2 during three earthquake simulations, a sinusoidal motion and six free-vibration tests. Response during static tests of the first-story is presented Section 7.2.2. An outline of the testing program is given in Chapter 3 and details are provided in Appendix A. Location of instrumentation is shown in Fig. A.13.

Following preliminary remarks on sign conventions and terminology, separate sections are devoted to recorded base motions (Section 4.2), measured response histories of the test structures (Section 4.3), observed damage (Section 4.4) and modal frequencies (Section 4.5). Section 4.6 discusses the reliability of measured data and Section 4.7 summarizes behavior of the test structures.

A key to figures for this chapter is presented in Table 4.1. Table 4.2 summarizes response maxima recorded during the eight base motions.

4.1 Conventions

4.1.1 Sign Conventions

Displacement and in-plane acceleration towards the east were defined to be positive. The positive sense of lateral inertial force was opposite to that of positive acceleration, consistent with d'Alembert's principle. As viewed from the south, clockwise rotation at the base of the wall was positive. Using these definitions, positive displacements, negative in-plane accelerations,

positive wall rotations and positive story shears would occur simultaneously during simple harmonic motion.

Positive transverse accelerations were towards the south on the south frame and towards the north on the north frame. Vertical accelerations were positive in the upward direction.

4.1.2 Terminology

To facilitate discussion of observed response, several terms commonly used to describe linear behavior are generalized to apply to nonlinear behavior. The term "first mode" refers to response in which all levels displace in the same direction. "Second" and "third modes" refer to response in which displaced shape changes direction once and twice, respectively, over the height of the structure. All displacements are assumed to occur within a vertical plane. For a particular mode, the "nodes" are points of zero displacement. The frequency observed to be associated with a given mode is the "effective frequency."

"Interstory drift ratio" (interstory DR) is defined as the difference between the horizontal displacements at adjacent levels divided by the story height. The "mean drift ratio" (mean DR) is the mean of the interstory ratios at a given time. The mean drift ratio can be computed as the top-level displacement divided by the height of the structure.

4.2 Base Motions

Each structure was subjected to three simulations of the north-south component of the 1940 El Centro ground motion at varying intensities and, a

sinusoidal motion. The nominal peak accelerations for runs 1, 2 and 3 were 0.35, 0.52 and 0.70 g, respectively. The period of the sinusoidal motion, 0.45 sec, was near that of the damaged structure.

Displacement of the test platform was measured by an LVDT connected to the hydraulic ram. Accelerometers were mounted on the top surface of each base girder; their outputs were virtually identical. Base acceleration histories, Fourier amplitude spectra and linear response spectra were obtained from the average of accelerations measured on the north and south base girders. Measured characteristics of the base motions are reported in Table 4.3.

4.2.1 Displacements

Shapes of measured base-displacement histories, plotted in Fig. 4.1, agree well with displacements calculated at the California Institute of Technology for the 1940 El Centro ground motion [9]. Maximum base displacements measured during test runs are listed in Table 4.3.

High-frequency noise, apparent during negative ram displacement of Structure ES1 during runs 1, 2 and 3, was due to a malfunctioning buffer power supply. The faulty component affected only the buffer between the control system and the data acquisition system. Once the power supply was replaced, the high-frequency noise disappeared. Actual displacements did not include the apparent high frequency disturbance shown in Fig. 4.1. If the high-frequency component reflected the actual base-motion, the high-frequency noise would have been apparent in the acceleration histories.

4.2.2 Accelerations

Maximum base accelerations (Table 4.3) and base acceleration histories (Fig. 4.2) were similar for structures ES1 and ES2. Some attenuation of large-amplitude, high-frequency acceleration is apparent in the base-acceleration histories for run 3, as compared to runs 1 and 2. However, all earthquake simulations had base-acceleration histories similar to accelerations reported by the California Institute of Technology for the El Centro ground motion.

4.2.3 Fourier Amplitude Spectra

Fourier amplitude spectra for the base motions, shown in Fig. 4.3, were normalized to obtain a peak ordinate of one. As a result, such spectra indicate the frequency content of a motion independently of base-motion intensity.

The Fourier amplitude spectra for the six earthquake simulations are nearly identical for frequencies lower than 10 Hz. Correlation is also acceptable for frequencies higher than 10 Hz. The spectra for the sinusoidal motions (run 4) are dominated by a peak at 2.25 Hz, but minor peaks also appear at odd multiples of the dominant frequency.

4.2.4 Linear Response Spectra

Displacement and acceleration response spectra for the base motions are presented in Fig. 4.4 for damping factors of 2, 5, 10 and 20%. Displacement response spectra for ES1 and ES2 were close to identical at all three levels of base-motion intensity. Acceleration response spectra for Structure ES1 show a slightly greater response acceleration than calculated for Structure ES2 for periods less than 0.1 sec. For a damping ratio of 10%, maximum amplification

factors for the base acceleration of runs 1, 2 and 3 were 2.2, 2.3 and 2.5 for Structure ES1 and 2.3, 2.2 and 2.5 for Structure ES2.

Linear response spectra for the sinusoidal motions (run 4) are dominated by a peak at 0.45 sec. The maximum amplification of base acceleration, for 10% damping, was 3.9 for ES1 and 4.0 for ES2.

Plots of normalized response spectra further indicate the similarity in frequency content of the earthquake simulations (Fig. 4.5). The response spectra shown (2% damping) are normalized to a peak base acceleration of 1 g. The design spectra, also shown in Fig. 4.5, are reasonable approximations of the calculated acceleration and displacement response spectra between periods of 0.2 and 0.5 sec. In comparison, the fundamental period of the test structures, calculated assuming gross-section properties, was 0.18 sec (Table 2.1). The fundamental period of the substitute structure was 0.28 sec (Table 2.5).

Housner spectrum intensities for the base motions are tabulated in Table 4.3. The Housner spectrum intensity is defined as the area below the velocity response spectrum between the periods of 0.1 and 2.5 sec [16]. Because of the time compression factor of 2.5, spectrum intensities were calculated between the periods of 0.04 and 1.0 sec. Calculated spectrum intensities for ES1 are consistently 1% larger than those of ES2 for the earthquake simulations. This small difference is another indication of the similarity of the base motions experienced by ES1 and ES2.

The design response spectra (Fig. 2.3) correspond to a Housner spectrum intensity of 15.3 in. for a damping factor of 2% and 7.7 in. for 10% damping. The measured spectrum intensities were approximately 30% less than the design intensity for a damping factor of 2%. On the other hand, the measured spectrum

intensity exceeded the design intensity by 1 to 3% for a damping factor of 10%. These discrepancies indicate that the design response spectra (Fig. 2.3) varied more with the assumed damping factor than did the observed base motion. Whereas the design spectral ordinate for 2% damping was twice that assumed for 10% damping, the measured spectrum intensity for 2% damping was on average 1.5 times the intensity for 10% damping.

4.3 Response Histories

In-plane relative displacements and absolute accelerations were monitored on both frames at the centerline of each story (Fig. A.13). LVDT's also measured relative slip and rotation of the base of each wall with respect to the base girder (Fig. A.14). Accelerometers, located at the ninth-level, measured transverse and vertical accelerations.

This section presents displacements, accelerations and base-of-wall rotations measured during eight base motions. Except for vertical and transverse accelerations, all data sets describe mean response of the north and south frames.

4.3.1 Displacements

Displacement histories (Fig. 4.6(a)-4.13(a)) were similar for structures ES1 and ES2 during the first earthquake simulation. Differences in displacement response waveforms of the two test structures appeared approximately 3 sec into run 2. Whereas the displacement waveform of ES1 continued oscillating at approximately the same frequency as before, the

waveform of ES2 became erratic, indicating a change in the dynamic properties of ES2. The displacements became similar again 5 sec into run 2.

Dissimilarities in displacement waveform of the two structures appeared again in run 3 approximately 2 seconds into the motion. As would be expected in a forced-vibration tests of a moderately damped structure, the periodicity of the displacement histories during run 4 was the same as that of the base motion.

Displacement maxima, listed in Tables 4.2 and 4.4, were similar for ES1 and ES2 for the first motion. Both structures satisfied the design criteria of 1.5% interstory drift ratio and 1% mean drift ratio. During subsequent earthquake simulations, first-level displacements were consistently greater for ES2 than for ES1. Maximum top-level displacements were similar for both structures.

Displacements were significantly larger for ES1 than ES2 during run 4, the sinusoidal motion. ES1 experienced larger displacements during the sinusoidal motions than during any of the earthquake simulations (runs 1-3). In contrast, the displacement maxima of ES2 recorded during run 4 were similar to the maxima recorded during run 3.

Similarities in displacement waveforms measured over the height of the structure indicate that the test structures displaced primarily in the first mode. This observation is corroborated by plots of displaced shape near times of maximum displacement and shear, shown in Fig. 4.6(d)-4.13(d). Drift ratios were greatest in the first story and least in the top story.

Changes in displaced shape can be quantified in terms of interstory drift ratio divided by mean drift ratio. The computed ratio is a measure of the concentration of drift at a given story. Such ratios, calculated for the first

and second stories, are plotted versus mean drift ratio in Fig. 4.6(e)-4.13(e). Ratios of interstory drift ratio (interstory DR) to mean drift ratio (mean DR) were calculated at points of relative maxima at which the mean DR exceeded 0.18%.

For both structures, the ratio of maximum first-story DR to mean DR increased in successive runs (Table 4.2, and Fig. 4.6(e)-4.13(e)). During the initial simulations, the first-story DR ranged between 1.0 and 1.5 times the mean DR. In later simulations, the ratio of first-story DR to mean DR increased to 2.2 for ES1 and 2.5 for ES2. Second-story DR consistently ranged between 1.2 and 1.5 times the mean DR for both ES1 and ES2.

The observed differences between the drift concentration in the first story and the second story can be explained by considering results from linear-elastic analysis. The calculated interstory drift-mean drift ratios (for the linear gross-section model described in Chapter 2) are:

	Wall Fixed at Base	Wall Pinned at Base
First Story DR/Mean DR	1.1	2.0
Second Story DR/Mean DR	1.43	1.45

The conditions at the base of the wall have a much greater influence on calculated first-story displacement than on second-story displacement. Changes in observed mode shape can be attributed to increasing flexibility at the base of the wall.

The changes in observed mode shape can also be explained by considering the results of limit analysis. As shown in Section 7.2.1, the base-shear strength of ES1 and ES2 was limited by a first-story mechanism, so concentration of

drift in the first story would be expected. The observed changes in displaced shape can then be explained in terms of increasing flexibility at the base of the wall or in terms of a first-story collapse mechanism.

4.3.2 Accelerations

Histories of in-plane accelerations at each story are presented in Fig. 4.6(b)-4.13(b). Acceleration records contained higher frequencies than appeared in the smooth displacement waveforms, especially in lower stories. Peak accelerations (Table 4.4) in upper stories of ES1 were generally greater than in ES2, consistent with the greater strength of ES1.

Fourier amplitude spectra of the recorded accelerations (Fig. 4.6(f)-4.13(f)) provide a relative measure of the energy content of response at different frequencies. The frequency content of the response of lower stories was similar to that of the base motion. The Fourier amplitude spectra for the top story were dominated by a peak near the frequency of the first mode of the structure. For the earthquake simulations acceleration response of the sixth story contained little energy near the frequency of the second mode (8-12 Hz); the sixth story corresponds to a node in the apparent second mode.

4.3.3 Story Shears

Lateral inertial forces at each level were calculated by multiplying the acceleration measured at a story by the story mass. Story shear represents the sum of lumped inertial forces above the story considered.

Histories of story shear are reported in Fig. 4.6(c)-4.13(c). Story-shear and base-moment maxima are listed in Tables 4.2 and 4.4. A decrease in stiffness near the origin was most apparent during run 4 but also occurred in

earlier runs. Reduced stiffness for small displacements was attributed to reinforcement slip and crushing of concrete at the base of the wall.

As previously noted in Section 4.3.1, the displacement response of ES1 and ES2 were similar until 3 seconds into run 2. The difference in behavior at that time is also apparent in the plots of base shear. After the first three seconds of run 2, the base-shear response of ES2 (Fig. 4.11(c)) was much less than that observed for ES1 (Fig. 4.7(c)). This sudden decrease in base-shear response may have been due to the onset of crushing at the base of the slender wall.

Shear distributions over the height of the structure at times of maximum displacement and shear are shown in Fig. 4.6(d)-4.13(d). These plots show that the base shear measured during small displacements was greater during the first base motion than in later tests, indicating a softening of the test structure.

Measured base-shear coefficients for runs 1-4 were 0.52, 0.71, 0.75 and 0.71 for ES1 and 0.50, 0.61, 0.60 and 0.51 for ES2. A general flexural-yield mechanism probably did not form in either structure until the second simulation. As discussed in Section 7.2.2, maximum base shears and base moments were similar in the positive and negative directions. This suggests that the asymmetry of the structures did not have a large effect on the observed response.

4.3.4 Shear-Interstory Displacement Hysteresis

Hysteresis plots of story shear versus interstory displacement are shown in Fig. 4.6(g)-4.13(g). Interstory displacement is not only sensitive to the

shear at that story, but also to accumulated rotation in the wall in lower stories.

The shape of a hysteresis curve is also sensitive to small errors in synchronization between acceleration and displacement signals. To correct for time delays observed in accelerometer filters [8], a 3.5 msec delay was added to interstory displacement records before plotting. Displacements between sample times were estimated by linear interpolation between samples (spaced at 5.0 msec). Channel to channel delay on the A/D board (3.8 μsec/channel) was neglected. No filtering of records was performed.

All hysteresis plots show a reduction of stiffness for small displacements. Softening of the structures can be attributed to reinforcement slip (bond degradation) and to concrete cracking and crushing. Yielding of the first story is apparent in runs 3 and 4 of ES1 and in runs 2, 3 and 4 of ES2.

4.3.5 Base Rotation and Slip

An aluminum harness was attached to the base of each slender wall one in. above the base girder (Fig. A.14). An LVDT, mounted on the base girder, measured relative horizontal displacement between the harness and the base girder. Two LVDTs monitored vertical displacement of the harness.

Base rotation was calculated as the difference between measured vertical displacement at each end of the harness divided by the distance between the two LVDTs (10.5 in.). The horizontal displacement measured one in. above the base minus the horizontal displacement due to base rotation gives the relative slip between the wall and base girder. Measured horizontal displacement, as well as calculated base rotation and slip, are presented in Fig. 4.6(h)-4.13(h). Response maxima and permanent offset (at end of run) appear in Table 4.5.

Horizontal displacement and rotation at the base of the wall were in-phase with first-story displacement throughout all test runs. The qualitative change in behavior of Structure ES2 3 sec into run 2 (noted in Sec 4.3.1 and 4.3.3) was reflected in the base rotation record.

Flexibility at the base of the wall can be quantified in terms of the nondimensional ratio of base rotation (%) to the first-story drift ratio (%). Rigid-body rotation of the wall about its base would result in a ratio of one. The linear model discussed in Chapter 2 results in a ratio of 1.1 for the first mode for a test structure with a hinge at the base of the wall.

Such ratios are plotted in Fig. 4.14 at times of relative maxima at which the mean drift ratio (mean DR) exceeded 0.18%. The same ratios are plotted versus mean DR in Fig. 4.15. As shown in Fig. 4.15(e) the ratios of base rotation to first story drift ratio were near 0.80 for early runs and for large displacements during later runs.

Wall slip did not correlate consistently with first-story displacement. Calculated slip is sensitive to minor variations in the placement and calibration of LVDTs. Most importantly, the assumed location of the axis of rotation strongly affects calculated slip. The response maxima of Table 4.5, however, indicate that slip of the wall relative to the base girder was less than 2.0% of the maximum first-story displacement for run 1. The ratio of maximum slip to maximum first-story displacement increased in subsequent runs, reaching a maximum of 4.3% during run 3 of Structure ES1. The offset in calculated slip at the end of a run was less than 0.01 in. for all runs.

4.3.6 Vertical and Transverse Accelerations

Vertical and transverse accelerations were monitored at the ninth-story (Fig. A.13). Response histories are reported in Fig. 4.6(i)-4.13(i). Transverse and vertical accelerations contained higher frequencies than appeared in in-plane acceleration histories. Positive accelerations of the east end of the north frame toward the north coincided with positive accelerations of the west end of the south frame toward the south (sign conventions presented in Section 4.1.2). This synchronization indicates torsional movement of the frames within a horizontal plane.

Fourier amplitude spectra are plotted in Fig. 4.16 for in-plane and transverse acceleration measured at the ninth story. In-plane response was much larger than out-of-plane response for frequencies less than 10 Hz.

4.4 Observed Damage

The test structures were inspected before testing began and after each earthquake simulation. Crack locations, crack widths (for cracks with a maximum width of at least 0.004 in.) and locations of spalling of concrete, are presented in Fig. 4.17. Crack widths in small-scale test specimens cannot be extrapolated to full-size structures, however, crack widths indicate the distribution and extent of damage in a structure.

To determine crack locations, a fluorescent liquid was sprayed on each frame. Fluorescent particles, which collected in the cracks, were illuminated with a fluorescent light. Steel channels, used to connect the masses to the frames, prevented inspection of beams in exterior bays and part of wall/beam

joints. Crack locations and widths are shown in Fig. 4.17 for the smooth face (cast against steel plate) of the north frame.

The north frame of ES1 had substantially more initial cracks than were present in the south frame of ES1 or the frames of ES2. Crack patterns for ES1 and ES2 (Fig. 4.17) became increasingly similar as testing progressed.

Most of the cracks observed after run 1 were initiated by preexisting cracks. No concrete spalling was observed; one could not distinguish a crack at the base of the wall.

After run 2, minor spalling in the first-story was noted. A crack traversing the full depth of the wall was visible at the wall-base girder interface.

At the end of run 3, all frames had spalled at the base of the wall and on exterior faces of exterior columns at the first story. These faces were subjected to tension strains due to overturning of the structure and bending of first-story columns. Damage extended significantly further up the frames of Structure ES2 than Structure ES1.

In general, crack patterns were consistent with nonuniform shrinkage and flexural strains.

4.5 Modal Frequencies

Characteristic frequencies of test structures were obtained from free-vibration tests and from top-displacement response during base motions.

4.5.1 Free-Vibration Tests

Free-vibration tests, described in Section A.2.2 and Fig. A.11, were conducted before and after each base motion. Free-vibration of the test structures was induced by imposing and then releasing a 100-lb horizontal force at the ninth level. Figure 4.18 shows ninth-story acceleration response during free-vibration. Because the three earthquake simulations and run 4 were conducted on different days, separate free-vibration tests were performed immediately after run 3 and before run 4.

Modal frequencies for the small-amplitude motion were obtained from Fourier amplitude spectra of ninth-story acceleration response (Fig. 4.18). Table 4.6 lists measured natural frequencies for the first three modes. The initial frequency measured for the first mode was 5.5 Hz for ES1 and 6.2 Hz for ES2. The difference in measured frequencies is consistent with the amount of cracking in the two structures before testing began.

Assuming a Young's Modulus of $2.65 * 10^6$ psi and plain uncracked section properties, one calculates a first-mode frequency of 5.7 Hz for the test structures. A frequency of 6.8 Hz was calculated for the first mode based on transformed uncracked section properties. Structure ES2 had higher initial natural frequencies than ES1, but frequencies were similar following run 2. Final frequencies for the first three modes were approximately 40%, 50% and 60%, respectively, of the initial measured frequency.

Effective damping factors (Table 4.6) were estimated from filtered waveforms of ninth-story acceleration response (Fig. 4.18) using a logarithmic decrement procedure. Filtered response included frequencies below 10 Hz, for initial free-vibration tests, and below 5 Hz for subsequent tests. The damping

factors ranged from 4-5% before testing began to 16-18% after the fourth base motion.

4.5.2 Effective Frequency

The time interval between consecutive positive or negative maxima of top-story displacement was chosen as an effective frequency for the test structures. Figure 4.19 plots effective frequency versus time for all runs. To decrease the influence of higher modes on the calculated effective frequency, relative maxima separated by less than 0.125 sec or with top-displacements less than 0.15 in. are not plotted in Fig. 4.19. The same criteria were used to plot drift ratios in Section 4.3.1 (Fig. 4.6(e)-4.13(e)) and in Section 4.3.5 (Fig. 4.14 and 4.15).

Frequencies obtained from free-vibration tests, also shown in Fig. 4.19, tended to be higher than effective frequencies measured during the subsequent base motion. The periodicity of top-displacement response during run 4 was the same as that of the base motion, as expected. Run 4 was essentially a forced-vibration test of a moderately damped structure.

4.6 Credibility of Measured Response

Response histories presented in this chapter can be verified by comparing measured response for the north and south frames. Maximum response displacements and accelerations for the north frame exceeded those measured on the south frame. Ratios of maximum measured response of the north frame to response of the south frame are presented in Table 4.7 for all runs. Table 4.7 lists mean ratios, averaged for all levels. The maximum ratio listed in Table

4.7 is 1.21 (negative displacement, ES1-run 1) indicating the north frame displaced approximately 10% further than the center of mass.

Ninth-level displacements were measured for both frames and for the story mass (Fig. A.13). Measured displacements of the three LVDT are superimposed in Fig. 4.20. Measured response was largest for the north frame and smallest for the south frame throughout the base motions. Maximum measured displacements of the story mass can be calculated accurately by interpolating between measured response of the north and south frames (mean error = 1.3%). The good agreement between interpolated and measured displacements indicates that the larger measured response of the north frame was not due to instrument error. It also indicates that any relative movement between the ninth-story mass and frame was negligible.

Because of stiff horizontal diaphragms, in-plane displacement of one frame with respect to the other would force the story mass to rotate. The resulting torsional component of the motion was reflected in the transverse acceleration records (Section 4.3.6). The consistency between measured in-plane displacements and transverse accelerations further suggests measured response reflected experimental behavior satisfactorily.

4.7 Summary of Response

1. Base motions during earthquake simulations were nearly identical for structures ES1 and ES2. The design spectra were reasonable approximations of the calculated response spectra between the periods of 0.2 and 0.5 seconds.

2. Test structures displaced primarily in the first mode.

3. Displacement response of the two test structures was similar until 3 sec into run 2.

4. Maximum interstory drift ratio, occurring in the first story, was 1 1/2 to 2 1/2 times the mean drift ratio. Concentration of drift in the first story increased in successive runs.

5. The second-story drift ratio consistently ranged between 1.2 and 1.5 times the mean drift ratio, varying little from run to run.

6. Observations 4 and 5 are consistent with the effect of increasing flexibility at the base of the wall. They are also consistent with the formation of a first-story failure mechanism.

7. The frequency content of the acceleration response of lower stories was similar to that of the base motion. The Fourier amplitude spectra for the top story accelerations were dominated by a peak near the frequency of the first mode of the structure.

8. For cycles of loading not exceeding previous displacement maxima, the stiffness for small displacements was less than the stiffness for large displacements. This stiffness difference tended to increase in successive runs.

9. Maximum slip between the wall and base girder was less than 2% of the maximum first-story displacement during run 1 and less than 4.5% of the maximum first-story displacement in all runs.

10. Response of the test structures included a small torsional component. The ratio of the maximum displacement of the north frame to the maximum displacement of the mass center varied from 1.1 in run 1 of ES1 to 1.05 in run 4 of ES1.

11. Interstory drift ratios were largest in the first story. Concrete spalling was concentrated in the first story.

12. Final free-vibration frequencies for the first three modes were approximately 40%, 50% and 60%, respectively, of those measured during initial free-vibration tests.

CHAPTER 5

DISCUSSION OF EXPERIMENTAL RESPONSE

Experimental response of two frame-wall structures, ES1 and ES2, was presented in the previous chapter. In this chapter, the dynamic response of ES1 and ES2 is discussed and compared with the response of structures SS1 and SS2, tested by Schultz [32]. Structures SS1 and SS2 (Fig. 1.1 and 2.2) were strong-beam, weak-column frame structures. Direct comparisons of experimental responses of the four structures are useful because observations of relative response are more confidently extrapolated to actual buildings than individual observations.

Section 5.1 briefly describes structures SS1, SS2, ES1 and ES2, stressing the similarities and differences among the four structures. The structures are described in greater detail in Appendices A and B, and in Ref. 32. In Section 5.2, base motions of comparable intensity for the four structures are identified. Section 5.3 evaluates the success of each structure in limiting interstory and top-level displacements and Section 5.4 further discusses the advantages of each type of structure. The behavior of the Mesnager hinge is considered in Section 5.5. In Section 5.6, the performance of the four structures is compared with the performance of other small-scale structures tested at the University of Illinois. Finally, Section 5.7 provides a summary of this chapter.

5.1 Description of Structures SS1, SS2, ES1 and ES2

Each of the four structures had a regular profile with 3 bays and 9 stories (Fig. 2.2). The first story measured 12 3/8 in. which was 40% taller than the typical height of 9 in. (centerline dimensions). Column and beam cross-section dimensions were nominally identical. The same story masses were used for all structures. Flexural reinforcement was fabricated from the same batches of steel wire. Concrete for all the structures was made using the same mix design and the same sources of sand and cement.

The only difference in frame geometry among the four structures was the depth of one of the interior vertical members. SS1 and SS2 were supported on four 1 1/2 x 1 1/2-in. columns. In ES1 and ES2, an interior column was replaced by a 4 1/2 x 1 1/2-in. slender wall (Fig. 2.1).

Column and wall reinforcement for SS1, SS2 and ES1 were determined using the Substitute Structure Method [34]. Structure SS2 had more column reinforcement than SS1; ES1 had more column reinforcement than ES2. In Structure ES2, the column reinforcement was arbitrarily reduced to the minimum required to confine the concrete (4 bars per cross-section).

The slender walls of ES1 and ES2 included a Mesnager hinge [11, 22] at the base wall (Fig. 2.11 and A.5). The hinge was formed by crossing the longitudinal reinforcement to form an "X" at mid-depth of the wall. Additional longitudinal reinforcement (No. 13-gage wire) was placed in the corners of the spiral reinforcement to confine the concrete at the base of the wall. The walls of ES1 and ES2 had nominally identical dimensions and reinforcement.

Structures SS1 and SS2 were designed to behave as strong-beam, weak-column frame structures. Beam reinforcement was selected such that columns yielded

but beams did not. Beam reinforcement for ES1 and ES2 was identical to that used for SS2. In the slender wall structures, the flexural strength of the columns was less than the flexural strength of the beams. Beams were in turn flexurally weaker than the wall. None the less, the base-shear strength of all four structures was limited by a first-story failure mechanism.

Assuming a first-story mechanism, base-shear strength ratios for SS1, SS2, ES1 and ES2 were 0.34, 0.51, 0.75 and 0.64 respectively (Chapter 7). Structures SS1 and SS2 had failure mechanisms in upper stories with calculated base shear strengths that were only slightly higher than the strengths calculated assuming a first-story mechanism. For example, assuming a fifth-story collapse mechanism (Fig. 7.1(b)) and a linear force distribution, the base shear strength ratios of SS1, SS2, ES1 and ES2 increased by 10, 2, 90 and 100% over that calculated for a first-story mechanism. One could expect structures SS1 and SS2 to yield in upper stories; ES1 and ES2 were unlikely to form failure mechanisms in locations other than the first story.

5.2 Comparable Base Motions

Direct comparison of test structure behavior was possible because the four structures were subjected to similar base motions (scaled versions of varying intensity of the 1940 El Centro ground motion). Table 5.1 lists base-motion characteristics for test runs of similar intensity for the four structures. Measured base accelerations and linear response spectra (2% damping) for three base-motion intensities (design, 1.5 times design, 2.0 times design) are given in Fig 5.1(a,b), Fig 5.2(a,b) and Fig 5.3(a,b). The designation of runs as design, 1.5 times design and 2 times design are based on spectrum intensity

rather than on peak acceleration. For this reason, the designations in Table 5.1 do not agree in all cases with those reported by Schultz [32]. Run 2 of SS1 and runs 2 and 3 for SS2 do not appear in Table 5.1 because they were repetitions of the first base motion. Structure SS1 was not subjected to a base motion corresponding to approximately twice the initial base-motion intensity.

For each run, Table 5.1 lists peak acceleration, Housner spectrum intensity [16] and a spectrum intensity targeted to periods of interest. The Housner spectrum intensity (in scaled time) corresponds to the area below the velocity response spectrum between the periods of 0.04 sec and 1.0 sec, assuming a damping ratio of 10%. The modified spectrum intensity given in Table 5.1 was calculated between the periods of 0.15 sec and 0.5 sec. The smaller period corresponds approximately to first-mode periods measured during initial free-vibration tests. The larger period is near the effective period observed during the third earthquake simulations of ES1 and ES2 (Fig. 4.19).

As seen from the response spectra and the spectrum intensities, the three sets of base motions would have similar effects on linear structures with periods exceeding 0.2 sec. The greatest difference in intensity occurred during the simulations at twice the design intensity. Even in this case, however, the targeted spectrum intensity of SS2 exceeded that of ES2 by only 17%. Differences in peak acceleration, apparent in Fig. 5.1(a)-5.3(a) and Table 5.1, would not affect significantly the displacement response of the test structures. Because the response histories are similar within the range of frequencies of interest, the test runs identified in Table 5.1 can be used to compare directly the displacement response of the four structures.

5.3 Displacement Response of SS1, SS2, ES1 and ES2

Measured first-story and top-story displacements for the three levels of base-motion intensity are presented in Fig. 5.1(c,d) - 5.3(c,d). In Fig. 5.4, maximum overall drift ratio and maximum interstory drift ratio are plotted versus Housner spectrum intensity (Table 5.1).

For the design motion, maximum overall drift ratios were approximately 30% less in ES1 and ES2 than in SS1 and SS2. In subsequent runs, the maximum overall drift ratio increased approximately linearly with spectrum intensity (Fig. 5.4). This variation was independent of base shear strength and type of structure.

Similar maximum interstory drifts were experienced by SS2, ES1 and ES2 during the three runs. Maximum interstory drifts experienced by ES1 were slightly lower than the drifts experienced by ES2 and SS2. During the design run, SS1 experienced a maximum interstory drift ratio of 3.1%, more than twice that experienced by the other structures and more than twice that anticipated during design of SS1 [32].

Figure 5.5 shows envelopes of maximum interstory drift ratios for the three intensities of base motion. Structure SS1 experienced large drifts in the first story during all runs. For the design run, distributions of maximum drift over the height of the structure were similar for SS2, ES1 and ES2. In these structures, maximum interstory drift ratios were approximately equal in the lower six stories. In subsequent runs, SS2 experienced large drifts in stories 5 to 9 whereas ES1 and ES2 experienced large drifts only in the first story.

Based on a criteria of limiting interstory displacements to 1.5%, SS1 performed unacceptably. Structures SS2, ES1 and ES2 were equally successful in limiting the maximum interstory drift though maximum interstory displacements did not occur in the same story for each structure.

5.4 Economic Considerations

Drift control during earthquakes, discussed in the previous section, is only one consideration affecting the selection of a structural system. Architectural considerations, constructibility and the cost of construction also affect the selection of a structure.

A benefit of using a structural system with long beam spans is the flexibility in the use of floor space. Structures SS1 and SS2 best meet this criterion. Slender-wall frames could still include beams with long spans, but these frames would be less architecturally flexible than frames such as SS1 and SS2. Slender-wall frames with 5-7 ft walls might still be preferable to frames with relatively short spans that limit yielding to beams. Frames with slender walls would certainly be more acceptable than the combination of frames and shear walls.

A disadvantage of frames with yielding columns is the large amount of reinforcement required in the columns. As shown in Table 5.2, SS2 had a maximum reinforcement ratio of 4.7% in the first story columns, compared to a maximum of 1.5% for ES2. Even Structure SS1, which behaved poorly, had a maximum column reinforcement ratio of 2.9%.

The slender-wall frames had a 50% larger support area than SS1 and SS2, increasing concrete and formwork requirements. On the other hand, ES2 used

less reinforcing steel in the first story than either SS1 or SS2 (Table 5.2). Total steel requirements for ES1 and ES2 could have been further reduced by decreasing wall reinforcement in the upper stories.

In summary, the use of frames with slender walls rather than frames with yielding columns reduces column reinforcement congestion at the cost of reduced architectural flexibility and increased concrete requirements. Of course observations about architectural flexibility and cost of framing schemes must be confirmed by considering large-scale structures.

5.5 Performance of the Mesnager Hinge

The behavior of the Mesnager hinge (Fig. 2.11 and A.5) is also important in evaluating the slender-wall frames. In practice, a Mesnager hinge could be used to limit the moment transferred to the foundation. In the test structure, the Mesnager hinge was intended to provide a base that was rotationally flexible but limited relative displacement between the base of the wall and the foundation. Both of these goals were satisfied.

Relative displacement between the base of the wall and the foundation was approximately 2% of the first-story displacement during the initial base motion for both structures. The relative displacement was less than 4.5% of the first-story displacement for all runs. Maximum rotations at the base of the wall varied from 1% during the initial base motion to 4% during the sinusoidal motion (run 4). The Mesnager hinge underwent large rotations without permitting large amounts of relative displacement between the wall and the foundation.

The wall showed no damage after the design run. After the second simulation, the wall showed only minor damage. Though the base of the wall was severely damaged during the third base motion, repair of a damaged slender wall would be much less expensive than repair of the underlying foundation. Performance of the detail at the base of the wall could have been improved by adding additional confinement. Reinforcing details, however, are better studied in larger specimens.

5.6 Other Small-Scale Structures

The behavior of SS1, SS2, ES1 and ES2 can also be compared with that of frames with yielding beams [15, 23, 24], frame-wall structures [2, 24] and soft-story structures of irregular profile [46]. Of the 21 test structures described in Appendix B, only 17 are considered in this section. The structures tested by Gulkan [14] are not considered because the structures had only one story.

Figure 5.6 shows that the overall drift ratio was not very sensitive to the type of framing system for the range of stiffness and strength considered in these tests. Differences between the behavior of the framing systems becomes apparent when maximum interstory drift ratio is plotted versus spectrum intensity (Fig. 5.7). During the design run, ES1 and ES2 performed as well as any of the test structures in controlling overall and maximum interstory displacement. In subsequent simulations, ES1 and ES2 behaved similarly to the other soft-story structures, experiencing large interstory drift.

The large interstory displacements of the soft-story structures during runs of high intensity cannot be attributed to differences in base shear strength

alone. In fact, the base-shear strength of SS1 exceeded that of most of the frames with yielding beams and even some of the frame-wall structures (Tables 7.9, 7.10, 7.11). Considering two frames with yielding beams, Structures FNW [24] and MF1 [15], one notes that both the area of vertical steel in the first story and the total column steel used were less in these structures than in the soft-story structures (Table 5.2). The differences in behavior must then be attributed differences in geometry and distribution of strength over the height of the structures.

5.7 Summary

1. The test runs listed in Table 5.1 can be used to compare directly the behavior of structures SS1, SS2 (strong-beam, weak-column frames), ES1 and ES2 (slender-wall structures).

2. Maximum overall drift increased nearly linearly with spectrum intensity, independent of the differences in geometry, strength and stiffness among the four structures.

3. Maximum interstory drift was sensitive to geometry and distribution of strength of the test structures, as well as to intensity of base-motion.

4. Structure SS1 performed unacceptably because it experienced large displacements in the first story. Maximum interstory drifts in structures SS2, ES1, and ES2 were nearly equal. During base motions with an intensity exceeding that considered in design, SS2 experienced large drift in stories 5 to 9, whereas ES1 and ES2 experienced large drifts only in the first story.

5. As compared with frames with yielding columns, frames with slender walls reduce flexural steel requirements at the cost of increased concrete and formwork requirements and some reduction of architectural flexibility.

6. The Mesnager hinge at the base of the wall underwent rotations of up to 4% without permitting significant displacement between the base of the wall and the foundation.

7. Frames with yielding beams require less column steel than soft-story structures. If the design earthquake is exceeded, frames with yielding beams experience smaller interstory drifts than soft-story structures.

CHAPTER 6

DISPLACEMENT RESPONSE OF FRAMES WITH SLENDER WALLS

A numerical model of ES2 was developed using the program LARZWD, a program written by Saiidi [30, 31] and modified by Lopez [20]. In Section 6.1, the model is described and calculated response is compared with the observed response of Structure ES2. Having satisfactorily reproduced the observed response of ES2 for three base motions, the model is then used to investigate the sensitivity of calculated displacement response to two groups of parameters.

The first group, considered in Section 6.2, are parameters that are difficult to estimate from first principles. There are reasonable grounds for assuming values that are appreciably different for parameters such as the slope of the unloading portion of the hysteresis curve, the amount of viscous damping and the bond stress. These parameters were varied to investigate whether different but defensible assumptions of their values would have led to different conclusions about displacement response.

The second group consists of several parameters which can be estimated reliably, such as member strength and wall depth. The purpose of these studies was to observe the influence of variations in structural properties on the calculated response of frames similar to those studied experimentally.

The results of both sets of parametric studies are discussed in Section 6.4. In Section 6.5, the displacement maxima calculated by nonlinear response-history analysis are compared with the displacement maxima calculated from linear response-spectrum analysis. If story mechanisms are avoided, linear

analysis is found to provide a conservative estimate of maximum interstory displacement.

The conclusions, summarized in Section 6.6, apply to reinforced concrete frames with slender walls in which the beams are flexurally stronger than the columns but weaker than the walls. The studies considered only the in-plane response of nine-story, three-bay frames subjected to the N-S component of the 1940 El Centro record. Except for the first-story, story heights were uniform; masses were equal at each story.

6.1 Numerical Modelling of Observed Behavior

The program LARZWD requires that the user specify inertial masses at each story, structural geometry, base motion and moment-curvature relationships for each member. The output of the program includes response histories of displacement and acceleration at each story as well as joint rotations and element forces.

A summary of some of the attributes of the program is given in reference 20. The summary is repeated here.

1. It is assumed that the structure, loads and response can be defined in one vertical plane.
2. The ground motion is assumed to be horizontal.
3. The foundation is assumed to move only in the direction of the ground motion with a single translational degree of freedom.
4. Each story has a single degree of freedom in the horizontal direction.
5. Story mass is defined in relation to the horizontal degree of freedom.
6. Axial deformation is restrained.

7. Joint cores are rigid.
8. Nonlinear response of members is in flexure only.
9. Member hysteresis is defined by Takeda rules [41].
10. Slip of reinforcement is considered at beam-column joints.
11. Effect of gravity loads on element moments can be included in the calculation.
12. The program integrates the equations of motion using the constant-average-acceleration method [26].

Moment-curvature relationships for each member were calculated using the measured material and geometric properties reported in Appendix A. Calculations were performed assuming (1) a modulus of concrete of 2800 ksi (2) a shear modulus of concrete of 1400 ksi (3) stiffness proportional damping of 0.5% (4) an unloading slope exponent of 0.4 (Section 6.2.2) (5) a bond strength of 150 psi (Section 6.2.4) (6) a modulus of rupture of 800 psi and (7) a post-yield slope of 0.25% of the slope before yield. Table 6.1 lists the flexural properties used to model the response of Structure ES2. The stiffness matrix was updated and numerical integration was performed at 0.001 second intervals.

The yield moment listed in Table 6.1 for the Mesnager hinge corresponds to 80% of that calculated by standard flexural analysis assuming that only the vertical component of the reinforcing bar force was effective. The yield curvature at the base of the wall for the numerical model was twice that calculated by standard analysis. These modifications were supported by the observed response of the Mesnager hinge detail during a static test of the component.

Calculated and measured responses of ES2 for the first and second base motions are plotted in Fig. 6.1 and 6.2. The waveforms for overall drift ratio (mean drift ratio), first-story drift ratio and base shear are well reproduced for the first motion, particularly for large displacements. For the second motion agreement between calculated and measured response waveforms is less impressive, particularly for small displacements. The change in character of the observed response 3 seconds into the second base motion was not reproduced by the numerical model (Fig. 6.2). This abrupt change in response was attributed to the onset of crushing at the base of the wall. Even though the calculated and observed waveforms did not match well at the end of the second base motion, the periodicity and magnitude of the calculated response was still similar to that observed during tests.

For the first motion (design intensity), computed response maxima exceeded the observed top-level displacement, first-story displacement and base shear by 11%, 18% and 1%, respectively (Table 6.2). Calculated top-level displacement, first-story displacement and base-shear maxima differed from observed maxima by 2%, 5% and 11% for the second motion (1.5 times design intensity) and by 4%, 11% and 13% for the third motion (2 times design intensity). The satisfactory agreement between measured and calculated response at three earthquake intensities justified the use of the numerical model to study the displacement response of frames with slender walls.

6.2 Influence of Unloading Slope, Damping and Bond Stress

Nonlinear analysis programs such as LARZ, which model structures member by member, are attractive analytical tools because the sensitivity of computed

response to member properties can be studied explicitly. To the extent that the calculated response is sensitive to model parameters that cannot be estimated confidently, the model is an inappropriate predictive tool. The unloading slope exponent of the Takeda hysteresis model [41], the amount of viscous damping and the assumed bond stress were selected for study because they are difficult to estimate from first principles. The value of each of these parameters is usually left to the judgment of the analyst.

The best fit of experimental response for run 1 of ES2 was obtained assuming an unloading slope exponent of 0.4, stiffness proportional damping of 0.5% (β = 0.000215) and a bond stress of 150 psi. In the following sections each of these parameters is varied individually while maintaining the other parameters constant. Sensitivity of displacement waveform is evaluated in terms of a goodness-of-fit index [20]. Sensitivity of computed displacement maxima is measured in terms of maximum overall and first-story drift ratios.

6.2.1 Goodness-of-Fit Index

The sensitivity of displacement waveform to changes in model parameters can be quantified in terms of a goodness-of-fit (GOF) index developed by Lopez [20]. The GOF index is a measure of the discrepancy between the Fourier amplitude spectrum of calculated and measured responses. The GOF index is defined by:

$$\text{GOF Index} = \sqrt{\sum\left(\frac{FAS_c - FAS_m}{Max(FAS_m)}\right)^2} \qquad (6.1)$$

where,

FAS_c = Calculated Fourier amplitude spectral ordinate

FAS_m = Measured Fourier amplitude spectral ordinate

The sum is taken over the range of frequencies of interest. In this study, indices were calculated for a range of 0 to 30 Hz for 12 seconds of motion. Because of the time compression factor of 2.5 used in the small-scale tests, 12 seconds of simulator motion corresponds to 30 seconds of recorded ground acceleration.

The convenience of the index lies in the fact that the discrepancy between waveforms is represented by a single number. An index of 0 would indicate perfect reproduction of observed responses; large indices indicate less satisfactory reproduction of the observed response. Three examples of calculated and measured response histories corresponding to GOF indices of 0.88, 1.13 and 1.43 are presented in Fig. 6.3.

For the design motion the GOF indices corresponding to the best match of ES2 response were 0.88 for top-level displacement and 0.94 for first-story displacement. If a model parameter is varied individually while maintaining constant the other parameters, the influence of that parameter on displacement waveform can be studied by monitoring changes in the GOF index.

6.2.2 Unloading Slope

The first parameter selected for study was the exponent α that defines the slope of the unloading portion of the Takeda hysteresis rules [41]. For deformation exceeding the yield point, the unloading slope (Fig. 6.4) is given by:

$$K' = S_{yc} \left(\frac{D_y}{D_{max}}\right)^{\alpha} \tag{6.2}$$

where,

S_{yc} = slope of a line joining the yield point in one direction with the cracking point in the other direction

D_y = yield deformation

D_{max} = maximum deformation attained in the direction of loading

α = coefficient between 0 and 1 [41].

Because $D_y/D_{max} \leq 1$, the unloading slope increases with decreasing α. As a result, the energy dissipated during one cycle of deformation also increases with decreasing α. Takeda suggested a value of α of 0.4 [41]. Lopez [20] studied the influence of using $\alpha = 0.5$ and $\alpha = 0.75$. In this study, α was varied from 0.1 to 0.9 in increments of 0.1.

The effect on displacement response of varying α is shown in Fig. 6.5 and reported in Table 6.3. Doubling α from 0.4 to 0.8 increased the GOF index by 6% for the top story and by 18% for the first story. Maximum top-level displacement remained unchanged while first-story drift increased by 5%. Halving α to 0.2 decreased the first-story GOF index by 3% but the top-level GOF index and displacement maxima did not change significantly.

6.2.3 Damping

The influence of proportional damping on computed displacement was also investigated. Some viscous damping is usually included in dynamic analysis models to provide numerical stability. If the damping is assumed to be

proportional to the mass and stiffness matrices then the damping matrix can be expressed as:

$$[C] = \alpha\,[M] + \beta\,[K] \tag{6.3}$$

where,

[M] is the mass matrix

[K] is the current stiffness matrix

and α, β are constants.

α and β can be related to the modal damping, ζ, and the modal circular frequency, ω [43].

For mode 1 $$2\zeta_1\,\omega_1 = \alpha + \beta\omega_1^2 \tag{6.4}$$

For mode 2 $$2\zeta_2\,\omega_2 = \alpha + \beta\omega_2^2 \tag{6.5}$$

If one assumes Rayleigh damping, the two above equations must be solved simultaneously to obtain α and β for given modal frequencies and damping. If the damping is assumed to be proportional to the stiffness matrix, then:

$$\alpha = 0 \tag{6.6}$$

$$\beta = \frac{2\zeta_1}{\omega_1} \tag{6.7}$$

If the damping is assumed to be proportional to the mass matrix, then:

$$\alpha = 2\zeta_1\,\omega_1 \tag{6.8}$$

$$\beta = 0 \tag{6.9}$$

The influence of varying the amount of damping is shown in Fig. 6.6 (combined mass and stiffness proportional damping), in Fig. 6.7 (stiffness proportional damping) and in Fig. 6.8 (mass proportional damping). Table 6.3 lists GOF indices and displacement response maxima for damping ratios of 0.1%, 0.5% and 2%.

Mass proportional damping affected computed displacement response more than Rayleigh damping and stiffness proportional damping. This was expected because stiffness proportional damping decreases as structural members yield whereas the mass matrix remains unchanged. A reduction in stiffness proportional damping from 0.5% to 0.1% had almost no effect on calculated response. An increase in damping from 0.5% (stiffness proportional) to 2% (mass proportional) increased the top-level and first-story GOF indices by 20% and 10%, respectively. Top-level and first-story maxima decreased by 12% and 11%, respectively.

6.2.4 Bond Stress

The third parameter studied was the assumed bond stress. LARZ allows for increase in member flexibility to compensate for slip between the concrete and reinforcement. A simple model used to calculate the additional flexibility is shown in Fig. 6.9 [30, 20]. Bond stress is assumed to be constant along the embedment length. The cross section is assumed to rotate about the center of the compression reinforcement.

The additional rotation due to reinforcement slip can be expressed as:

$$R_s = \frac{d_b f_y^2}{8E_s u(d-d')} \left(\frac{M}{M_y}\right)^2 \qquad (6.10)$$

where,

d_b = reinforcement diameter

f_y = reinforcement tensile yield stress

E_s = elastic modulus of the reinforcement

u = assumed bond stress

d = effective depth of tensile reinforcement

d' = effective depth of compressive reinforcement

M = applied moment

M_y = yield moment

Of the terms required to calculate R_s, the bond stress, u, is the most difficult to estimate. During reinforcement pullout tests of wire reinforcement [12], bond strengths varying from 200 to 400 psi were measured for 6-in. embedment lengths. Because the tests did not include reversals of loading, appropriate bond stresses for use in LARZWD, are uncertain.

Figure 6.10 and Table 6.3 document the influence of variations in assumed bond stress on displacement waveform and maxima. Doubling the assumed stress from 150 psi to 300 psi had a large effect on top-level waveform (61%) and first-story waveform (62%). Top-level and first-story maxima were less affected. For comparison, a summary of response for the assumption of infinite bond stress is also included in Table 6.3. The calculated top-level displacement maximum was 25% less than that calculated assuming a bond stress of 150 psi. Though reasonable variations in assumed bond stress do not have a large effect on response maxima, additional flexibility in small-scale reinforced concrete structures cannot be neglected.

Of the three model parameters studied in this section (unloading slope exponent α, damping and bond stress), the assumed bond stress had the largest influence on the calculated waveform. Response maxima were not strongly affected by any of the model parameters varied in this study.

6.3 Influence of Member Strengths and Yield Curvatures

In the previous section it was determined that the selected model parameters strongly affected the calculated displacement waveform but did not have a strong effect on computed displacement response maxima (for the 1940 N-S El Centro record). This section examines the influence on displacement response of (1) column strength, (2) beam strength, (3) wall strength, (4) yield moment and curvature at the base of the wall and (5) wall depth. The sensitivity of displacement response to each property was studied by calculating the response of structures similar to ES2 in which one of the structural properties was changed but the other properties were kept the same. The influence of varying structural properties on displacement response was obtained from calculated results presented in Fig. 6.11-6.21 and in Tables 6.4-6.6. The discussion will focus on response maxima.

6.3.1 Column Strength

First-story displacement maxima were more sensitive than top-level displacement maxima to changes in column strength, but the effect of column strength on drift maxima was not large (Fig. 6.11, Table 6.4). Doubling the column strength reduced the maximum first-story displacement by 10% and reduced the maximum top-level displacement by only 3%. Though beam properties were

kept constant, the beam flexural strength was never less than twice the column strength.

6.3.2 Beam Strength

Increasing the beam flexural strength from that used in Structure ES2 improved top-level response but resulted in less satisfactory first-story displacement response (Fig. 6.12, Table 6.4). Doubling the beam strength reduced the top-level displacement by 14%, but, increased first-story maximum drift response by 14%. Maximum top-level displacement response increased by 14% and first-story maximum displacement increased by only 1% when the beam strength was reduced to 50% of that of ES2.

6.3.3 Wall Strength

Wall strength had little influence on calculated top-level displacement maxima, but, increasing the wall strength decreased maximum first-story response significantly (Fig. 6.13, Table 6.4). In calculating the results presented in Fig. 6.13, yield moments and curvatures were varied so that the stiffness before yielding remained unchanged. Flexural properties at the base of the wall were assumed to be the same as those assumed in modelling ES2 (yield moment = 10.2 k-in., yield curvature = 0.0042). Assuming a wall yield moment twice as large as that of Structure ES2 resulted in an increase in maximum top-level drift of 2% and a decrease in first-story drift of 10%. Halving the strength of the wall reduced the maximum top-level displacement by 2% and increased the first-story displacement by 17%.

6.3.4 Yield Moment and Curvature at Base of Wall

Calculated top-level displacement maxima were insensitive to the assumed yield moment (Fig. 6.14, Table 6.4) and yield curvature (Fig. 6.15, Table 6.4) at the base of the wall. Calculated top-level response, assuming either half or double the yield moment or yield curvature at the base of the wall, changed the computed maximum top-level displacement of ES2 by less than 2%. The relative insensitivity of calculated top-level maxima was observed not only for the design intensity but also for motions of higher intensity (Fig. 6.16). This insensitivity was also observed for the linear model (Section 2.2.1).

First-story displacement maxima were influenced strongly by the assumed yield moment at the base of the wall but were less influenced by changes in the assumed yield curvature. Increasing the yield moment at the base of the wall to twice that of ES2 decreased the calculated first-story maximum by 17% while halving the yield moment increased the first-story drift by 24%. The strong influence of the yield moment at the base of the wall on first-story drift was also observed for motions corresponding to 1.5 times and 2 times the El Centro record (Fig. 6.16).

6.3.5 Wall Depth

The most straightforward means of increasing wall strength and stiffness is to increase the depth of the wall. Response maxima for three intensities of the 1940 El Centro record were calculated for wall depths one to six times the column depth (Fig. 6.17, 6.18 and Table 6.5). Structure ES2 had a 4 1/2-in. wall, corresponding to a ratio of wall-to-column depth of 3. The width of the wall (1-1/2 in.) and size of the columns (1-1/2 by 1-1/2 in.) were not varied. A wall reinforcement ratio of 1.5% was assumed for all cases (Fig. 2.13).

Both the strength and yield curvature of the wall were changed when the wall depth was changed. To prevent unrealistic increases in member strength, the post-yield slope of the moment-curvature relationship was reduced to 0.025% of the slope before yield.

In a first series of calculations the yield moment at the base of the wall was limited to that of the Mesnager hinge used in ES2 (yield moment = 10.2 k-in., yield curvature = 0.0042). For this case, the maximum top-level displacement was relatively insensitive (Fig. 6.17, Table 6.5) to changes in wall depth at all 3 earthquake intensities (El Centro, 1.5 times El Centro, 2 times El Centro). Calculated maximum interstory drift was much more sensitive than overall drift to changes in wall depth. Interstory drift decreased by 38%, 55% and 52% for the 3 earthquake intensities when the wall depth was doubled. The maximum interstory drift ratio occurred in the first story for all wall depths (Fig. 6.17, Table 6.5).

In a second series of calculations (Fig. 6.18, "fixed base"), it was assumed that the base moment could reach the flexural capacity of the wall. For this assumption both top-level and interstory displacement maxima were calculated to be sensitive to wall depth. For earthquake intensities corresponding to the El Centro record, 1.5 times El Centro and 2 times El Centro, the maximum overall drift ratio for a structure with double the wall depth of ES2 was 33%, 32% and 8% less than the overall drift ratio for ES2. Doubling the wall depth decreased maximum interstory drift ratios by 52%, 65% and 58%. For this series of calculations, the maximum interstory drift ratio occurred in the first story for walls with a ratio of wall to column depth of 3 or less; maximum interstory drift occurred in the second, third and fourth

stories for deeper walls. Table 6.5 lists maximum overall and interstory drift ratios for both series of calculations.

6.4 Discussion of Displacement Response

This section discusses the effect of variations in model parameters on calculated displacement waveforms, maximum displacement response and concentration of drift along the height of the structure. The section also includes a discussion of the selection of wall depth.

6.4.1 Displacement Waveforms

Of the parameters selected for study in Section 6.2 (slope of unloading portion of hysteresis curve, viscous damping and bond stress), bond stress had the greatest influence on top-level and first-story displacement waveforms. The influence on calculated displacement waveforms of doubling selected model parameters are summarized in the first two columns of Table 6.6. Variations in Goodness-of-Fit (GOF) indices are expressed as a percentage of the GOF indices calculated for Structure ES2.

As shown in Table 6.6, the effect on top-level waveform of doubling the assumed bond stress is nearly as much as the effect of doubling the beam strength. Unlike the flexural strength of a member, the appropriate value of bond stress is difficult to estimate under monotonically increasing load. The problems associated with estimating the bond stress increase if the loading is dynamic and cyclical. Since the appropriate bond stress is not known before an experiment, one should not expect the analytical model to predict accurately the observed displacement waveform.

6.4.2 Maximum Displacement Response

Fortunately, variations of the parameters of Section 6.2 do not affect greatly displacement maxima (Table 6.6).

Maximum overall drift ratio (mean drift ratio) and maximum interstory drift ratio were used in this study as indicators of expected damage. Overall drift ratio is a measure of the mean distortion of the building. Maximum interstory drift ratio indicates the extent of local damage expected in a given story. Alternatively, expected damage could be related to the tangential deviation of the wall. The use of tangential deviation as an indicator of damage, however, would be less appropriate to indicate distortion of the columns, beams and nonstructural elements away from the wall.

The analytical results summarized in the third and fourth columns of Table 6.6 indicate that doubling the strength of the columns, beams, wall or the base of wall decreased the displacement maxima by less than 20%. To obtain additional increases in strength and stiffness, the geometry of the frame must be modified. An obvious means of increasing the strength and stiffness of the structure is to increase the wall depth.

The influence of wall depth and of the Mesnager hinge are shown in Fig. 6.19 for maximum overall drift ratio and in Fig. 6.20 for maximum interstory drift ratio (the data plotted in Fig. 6.19 and 6.20 are the same as those plotted in Fig. 6.17 and 6.18). Maximum drift ratios are plotted for response to the El Centro record for peak accelerations of 0.35g (El Centro), 0.53g (1.5 times El Centro) and 0.70g (2 times El Centro).

Increases in wall depth had little beneficial effect on maximum top-level response when the properties at the base of the structure remained the same (Fig. 6.19, "Mesnager hinge"). The maximum top-level drift decreased with wall

depth only when the base of the wall was able to develop the full wall strength (Fig. 6.19, "fixed base"). Wall flexural stiffness and strength increase rapidly with wall depth if the reinforcement ratio remains the same. If the strength at the base of the wall remains the same ("Mesnager hinge"), the difference between the flexural strength of the wall and the moment that can be developed at the hinge increases with wall depth. For the deeper walls, the wall behaves almost as if it were simply-supported at the base.

Maximum interstory drift ratio was sensitive to both the wall depth and to the flexural strength of the base of the wall (Fig. 6.20). The reduction in maximum response obtained by fixing the base of the wall is reported in Table 6.5. The reduction in first-story response caused by fixing the base of the wall increased with wall depth. For a ratio of wall depth to column depth of 3, the decrease in first-story response varied from 19% to 32%, depending on the earthquake intensity. At a ratio of wall to column depth of 6, the reduction in response obtained by fixing the base varied from 35% to 47% for the three intensities of ground motion (Table 6.5).

6.4.3 Concentration of Drift Along Height of Structure

The concentration of drift at a given story can be quantified by comparing the maximum interstory drift ratio with the overall drift ratio. Figure 6.21 shows that the concentration of drift at a given story was insensitive to the intensity of ground motion for structures with walls at least 4 times as deep as the column. For the "fixed base" assumption, the concentration of drift was approximately constant with wall depth for ratios of wall to column depth greater than 3. Further reductions in interstory displacement were caused,

therefore, by a decrease in overall structure displacement rather than a reduction in concentration of drift at a story.

For the assumption of a Mesnager hinge at the base of the wall, the concentration of drift at a given story decreased steadily with increasing wall depth (Fig. 6.21). However, for a ratio of wall to column depth of 6, the maximum interstory drift ratio was only 1.2 times the overall drift ratio for all three earthquake intensities, indicating that the displaced shape of the structure was quite uniform.

6.4.4 Selection of Wall Depth

The appropriate choice of wall depth is a compromise between engineering performance criteria and economic/architectural considerations. To limit displacement response, it is obviously preferable that all structural walls be deep and that all foundations be designed for the full flexural strength of the wall. Unfortunately, deep walls may not be convenient and strong foundations can be expensive. The extent and nature of the compromise depends on the amount and distribution of damage that is acceptable.

If overall drift (an indication of the mean distortion in the building) is the only performance criterion and drift ratios of 1-2% are acceptable, then the choice of wall depth is unimportant for the range of structures considered in this study (Fig. 6.19). The overall drift ratio was calculated to be less than 1% for all wall depths for the El Centro record (peak acceleration = 0.35 g). The maximum overall drift ratio was less than 1.5% for the El Centro record with a peak acceleration of 0.53g and less than 2% for the El Centro record with a peak acceleration of 0.70g.

If limiting interstory drift is also a design goal, then there is continuous improvement in response as the wall depth and foundation strength are increased. Interstory drifts are clearly unacceptable for ratios of wall to column depths less than three (Fig. 6.20). As was discussed in Chapter 5, frames with these proportions require large amounts of column reinforcement to prevent large drifts in the first story. For larger walls, the choice of wall depth and foundation strength depends on the extent of damage that will be tolerated in a given story.

Another criterion for acceptance of a structure could be to limit the maximum interstory drift ratio to 1.5 times the overall (mean) drift ratio, regardless of the ground motion intensity. Using this criterion, the minimum wall depth to column depth ratio would be 4 if the foundation were designed for the full wall flexural strength (Fig. 6.21). The wall depth would have to increase if the foundation were not designed for the full wall strength. The appropriate depth would depend on the flexural strength at the base of the wall.

6.5 Comparison of Results from Linear and Nonlinear Analyses

During design, maximum top-level and interstory displacements were calculated by linear response-spectrum analysis following a procedure proposed by Shimazaki [35, 38] (Sections 2.1.5 and 2.2.1). The displacement maxima calculated by linear analysis (Table 2.2) can be compared to the displacement maxima calculated by nonlinear analysis (Table 6.5).

Consider top-level displacement maxima (Fig. 6.22). When the base of the wall was assumed fixed, linear analysis was conservative for structures in

which the base of the wall was able to develop the full wall flexural strength (Fig. 6.22(a)). When the base of the wall was assumed pinned, linear analysis was conservative for all the structures, including the structures with a Mesnager hinge at the base of the wall (Fig. 6.22(b)). (Results plotted in Fig. 6.22 were normalized by dividing computed displacements (Table 6.5) by 1.0, 1.5 or 2.0, depending on ground-motion intensity.)

Consider interstory displacement maxima (Fig. 6.23). For structures with walls less than four times as deep as the columns, maximum interstory displacements calculated by nonlinear analysis often exceeded maximum interstory displacements calculated by linear analysis. For structures with walls less than four times as deep as the columns, the base-shear strength was limited by a first-story mechanism. As a result, drift was concentrated in the first story. If a first-story mechanism was avoided, as in the structures with a wall-to-depth ratio greater than four, linear analysis provided a conservative estimate of maximum interstory displacement.

A parameter was developed to indicate whether a structure was likely to form a first-story mechanism. The parameter selected was the ratio of the base shear for a two-story collapse mechanism (Fig. 6.24) to the base shear calculated for a first-story collapse mechanism (Fig. 7.1(a)). If the parameter (V2/V1) is less than 1.0, the structure is unlikely to form a first-story collapse mechanism and linear analysis is likely to be conservative. If the parameter exceeds 1.0, the structure may form a first-story collapse mechanism and linear analysis may be unconservative for estimating maximum displacement.

For a first-story collapse mechanism (Fig.7.1(a)), the base shear strength is independent of the assumed force distirbution. The base-shear strength is:

$$Vl = \frac{M_{wall} + M_{base} + 2\sum_{j=1}^{m} M_{cj}}{h_{ln}} \qquad (6.11)$$

where,

Vl = base-shear strength calculated assuming a first-story collapse mechanism.

M_{wall} = flexural strength of the wall

M_{base} = moment that can be developed at the base of the wall

M_{cj} = flexural strength of column j

m = number of columns

h_{ln} = clear height of the first story

The base-shear strength for the two-story mechanism shown in Fig. 6.24 can be calculated by limit analysis using the principle of virtual work. In the following derivation it is assumed that beam spans are equal, columns have the same flexural strength in the first and second stories, and the force distribution varies linearly over the height of the structure. The external work, W_{ext}, is:

$$W_{ext} = F_1 * \left(\frac{h_1 * 1}{h_1 + h_2}\right) + \sum_{j=2}^{N} F_j * 1 \qquad (6.12)$$

where,

F_j = inertial force at level j

h_1 = height of the first story

h_2 = height of the second story

N = number of stories

For the nine-story structures considered in this study and with the assumption of an inverted triangular load distribution, Eq. 6.12 becomes:

$$W_{ext} = 0.988 * V2 \tag{6.13}$$

where V2 is the base-shear strength calculated assuming the collapse mechanism shown in Fig. 6.24.

The internal work, W_{int} is:

$$\begin{aligned} W_{int} = {} & 2 * \sum_{j=1}^{m} M_{cj} \left\{\frac{h_1 * 1}{h_1 + h_2}\right\} \left(\frac{1}{h_{1n}}\right) \\ & + 2 * \sum_{j=1}^{m} M_{cj} \left\{\frac{h_2 * 1}{h_1 + h_2}\right\} \left(\frac{1}{h_{2n}}\right) \\ & + \left(\frac{M_{wall} + M_{base}}{h_1 + h_{2n}}\right) * 1 \\ & + 2 M_b \left(\frac{1}{h_1 + h_2}\right) \left(\frac{L}{L - d/2}\right) \end{aligned} \tag{6.14}$$

where,

h_{2n} = clear height of second story

M_b = flexural strength of the beams

L = beam span

d = depth of the wall

m = number of columns

Setting the external work (Eq. 6.13) equal to the internal work (Eq. 6.14), the base shear for the two-story mechanism can expressed as:

$$V2 = 1.012 * W_{int} \tag{6.15}$$

V2/V1 can be computed using Eq. 6.11, 6.14 and 6.15.

Regardless of the value of V2/V1, estimates by linear analysis of overall drift were conservative with respect to results from nonlinear analysis (Fig. 6.25(a)). (Estimates of drift for the structures with a Mesnager hinge were computed assuming the base of the wall to be pinned.) Estimates by linear analysis of interstory drift were conservative for V2/V1 less than 0.95. Estimates by linear analysis of interstory drift often were unconservative for V2/V1 exceeding 0.95 (6.25(b)).

The parameter V2/V1 becomes more convenient if a few simplifications are made. In particular, Eq. 6.13 can be approximated by:

$$W_{ext} = V2 \tag{6.16}$$

Eq. 6.14 is simplified if one assumes:

$$\begin{aligned} h_{1n} &= h_1 \\ h_{2n} &= h_2 \\ L - d/2 &= L \end{aligned} \tag{6.17}$$

The approximate expression for V2/V1, derived for a specific structural configuration, is then:

$$\frac{V2}{V1} = \frac{M_{wall} + M_{base} + 2M_b + \sum_{j=1}^{m} M_{cj}}{M_{wall} + M_{base} + 2\sum_{j=1}^{m} M_{cj}} \left(\frac{h_1}{h_1 + h_2} \right) \qquad (6.18)$$

Using the approximate expression for V2/V1, results from nonlinear and linear analysis are compared again in Fig. 6.26. Linear analysis resulted in a conservative estimate of maximum interstory displacement for structures in which the approximate expression for V2/V1 was less than 0.90. Because member strength and inertial force distribution cannot be calculated accurately, the deviation of the limiting parameter away from 1.0 is not a serious limitation. For structures similar to those considered in this study, the simple expression for V2/V1 can be used to identify structures in which linear analysis is likely to result in an unconservative estimate of maximum interstory displacement.

6.6 Summary

The results of the parametric studies presented in this chapter are relevant to the seismic response of frames with slender walls in which the beams are flexurally stronger than the columns. The structures considered in these studies included three columns and a slender wall. Conclusions were drawn from the calculated response of small-scale reinforced concrete structures subjected to the N-S component of the 1940 El Centro record. The frames were of relatively uniform interstory height and mass distribution, except for a tall first story (40% increase in story height). Only in-plane response of the frames was considered.

1. The observed waveforms of top-level displacement, first-story displacement and base shear were reproduced well by a nonlinear model (LARZ) for the first base motion of ES2 (Fig. 6.1). Response maxima were reproduced well for two subsequent runs of higher intensity (Table 6.2).

2. Calculated first-story and top-level displacement waveforms and displacement maxima were insensitive to reasonable variations of viscous damping and to variations of the unloading slope of the Takeda hysteresis rules [41] (Figures 6.5-6.8 and Table 6.6).

3. The assumed bond stress had a strong influence on calculated displacement waveforms (Fig. 6.10 and Table 6.6). Because the appropriate value of bond stress is difficult to estimate correctly, the numerical model should not be expected to lead to accurate predictions of displacement waveforms.

4. The assumed bond stress had little influence on calculated displacement maxima (Fig. 6.10 and Table 6.6). The model can be used to estimate displacement maxima.

5. Increases in wall depth had little beneficial effect on maximum top-level response if the properties at the base of the wall remained the same (Fig. 6.19, "Mesnager hinge").

6. Top-level drift was reduced significantly by increases in wall depth if the base of the wall was assumed to be able to develop the flexural strength of the wall (Fig. 6.19, "Fixed Base").

7. If overall drift is the only performance criterion, and if drift ratios of 1-2% are acceptable, then the choice of wall depth and foundation strength was not crucial for the range of structures considered (Fig. 6.19).

8. As the wall depth and the flexural strength at the base of the wall were increased, there was a continuous decrease in the maximum interstory displacement (Fig. 6.20).

9. The depth of the wall had to be at least four times the column depth and the foundation had to be able to resist the full wall flexural strength to limit the maximum interstory drift to 1.5 times the maximum overall drift ratio.

10. If the base of the wall was assumed fixed, linear analysis provided a conservative estimate of top-level displacement for structures in which the base of the wall could develop the wall flexural strength.

11. If the base of the wall was assumed pinned, linear analysis provided a conservative estimate of top-level displacement for all the structures, including structures with a Mesnager hinge at the base of the wall.

12. Linear analysis provided a conservative estimate of maximum interstory displacement for structures that did not form a first-story collapse mechanism. A convenient expression for identifying slender-wall frames in which first-story mechanisms may form is:

$$\frac{V2}{V1} = \frac{M_{wall} + M_{base} + 2M_b + \sum_{j=1}^{m} M_{cj}}{M_{wall} + M_{base} + 2\sum_{j=1}^{m} M_{cj}} \left(\frac{h_1}{h_1 + h_2} \right) \qquad (6.18)$$

If V2/V1 exceeds 0.9, displacements calculated by nonlinear analysis may exceed displacements calculated by linear analysis.

CHAPTER 7

STRENGTH OF SMALL-SCALE REINFORCED CONCRETE STRUCTURES

This chapter compares calculated strengths of test structures with those measured during static and dynamic tests. After an introductory section which discusses limit analysis, the lateral strength of structures SS1, SS2 [32], ES1 and ES2 are considered in Section 7.2. A method of computing a reasonable upper bound for the flexural strength of columns, beams and walls is introduced in Section 7.3. Section 7.4 discusses the measured and calculated flexural strength of 40 small-scale frame components. Section 7.5 compares measured and calculated base-shear and base-moment strengths of 21 small-scale structures subjected to strong base motions. The observations made in this chapter are summarized in Section 7.6.

7.1 Limit Analysis

For given member flexural strength, structural geometry and lateral load distribution, the lateral load capacity of a structure can be estimated by limit analysis using the principle of virtual work. External work by lateral loads during a virtual displacement of the structure is set equal to the internal work by structural members. The calculated base shear or base moment capacity is the smallest of the base shears or base moments calculated for all kinematically admissible failure mechanisms.

Several admissible failure mechanisms, assuming hinges form at joint faces, are shown in Fig. 7.1. Story mechanisms (Fig. 7.1(a, b)) assume yielding of all columns and walls of a single story. Beam mechanisms (Fig. 7.1(c, d))

assume yielding of vertical members at the base and at an upper story as well as yielding of beams at intermediate stories.

For convenience, story mechanisms are designated by an "S" combined with an integer specifying the story at which plastic hinges are assumed to occur. Beam mechanisms are identified by a "B" and an integer specifying the highest story of plastic hinging. Note that mechanism types S1 (Fig. 7.1(a)) and B1 are identical. The designation BN is ambiguous in that yielding at the top of the structure may occur either in the beams (Fig. 7.1(d)) or in the columns.

The inertial force at a story can be computed as the product of horizontal acceleration and mass at the story. Base shear, V, corresponds to the sum of these inertial forces at a given time. The measured base moment, M, is the sum for all stories of the product of inertial force and story elevation (Fig. 7.2). An additional component of base moment may be computed as the sum of story mass times lateral displacement (P - Δ effect).

In general, the calculated base-shear or base-moment capacity varies with the assumed lateral force distribution. As shown in Appendix C, there are two notable exceptions to this dependence on assumed load distribution.

1. If the base-shear strength is limited by a first-story failure mechanism (Fig. 7.1(a)), calculated base-shear strength is independent of assumed lateral force distribution.

2. If the base-moment strength is limited by a beam mechanism involving yielding at all stories (Fig. 7.1(d)), calculated base-moment strength is independent of assumed lateral force distribution.

7.2 Structures SS1, SS2, ES1 and ES2

7.2.1 Calculated Base-Shear Strength

The base-shear capacities of SS1, SS2, ES1 and ES2 were estimated by limit analysis procedures. Flexural capacities were calculated assuming:

(1) Average measured member cross-sectional dimensions and effective depths (Tables A.1 and A.2)

(2) Measured material properties (Tables A.4 and A.5)

(3) Stress-strain relations for concrete and steel shown in Fig. 7.3.

(4) No tensile strength of concrete.

(5) Linear strain distribution over the depth of the section.

(6) Axial load in members due to dead load.

Variations in axial load associated with overturning of a structure were not considered in the analysis. Though the flexural strength of some of the columns would be expected to increase due to additional compression, this increase would be compensated by a decrease in the flexural strength of other columns in which the axial load is reduced due to overturning. For reinforced concrete members subjected to small axial loads, the moment-thrust interaction diagram is nearly linear.

The calculated base-shear capacities of all four structures were limited by first-story mechanisms. Table 7.1 summarizes calculations of the flexural capacity of first-story vertical members. The flexural strength of the Mesnager hinge detail (Fig. 2.11 and A.5) was calculated assuming that only the vertical component of the steel force contributed to the strength of the section.

Because of variations in assumed concrete ultimate strain and tensile strength, and because of differences in steel properties reported by Schultz [32] and this writer, calculated moment capacities could reasonably change by up to 3%. The uncertainty associated with calculating the strength of the Mesnager hinge [11, 22], however, may be greater than 3% because of reorientation of the inclined bars.

Column (1) of Table 7.2 lists base-shear capacities calculated using moment capacities of Table 7.1. Calculations indicate that the wall provided approximately 64% of the lateral resistance of ES1 and 74% of the lateral resistance of ES2.

7.2.2 Measured Base-Shear Strengths

Table 7.2 lists maximum recorded dynamic base-shears in column (3). Base shears recorded during earthquake simulations exceeded calculated capacities by 12%, 10%, 8% and 1% for structures SS1, SS2, ES1 and ES2. Static tests (Fig. 7.4 and A.12), performed after the base motions, indicated the base-shear strengths of ES1 and ES2 were reduced to 90% and 91% of those computed by standard flexural analysis assuming strain compatibility (Table 7.2). The reduction in strength was attributed to damage that occurred during the four preceding ground motions.

The eccentric location of the wall with respect to the center of the structure did not appear to affect maximum base-shear and base moment-response. Maximum recorded positive and negative base-shears and base moments (excluding P-Δ effect) for each base motion are reported in Table 7.3 for ES1 and ES2. Despite the asymmetry of the structures and the ground motions, maximum base

shears and moments were similar during positive displacements (to the east) and negative displacements (to the west).

7.3 Upper-Bound Flexural Strength

Discrepancies between measured and calculated strengths led to development of a procedure to estimate a reasonable upper bound to the flexural strength of small-scale reinforced concrete members. The upper bound procedure assumes:

(1) Measured member cross-sectional dimensions and effective depths (Tables A.1 and A.2).

(2) Ultimate stress in tension steel.

(3) Stress of 0.85 f_c' in concrete.

(4) Axial load in members due to dead load.

(5) Stress of compression steel is independent of strain compatibility and may vary from $-f_{su}$ to $+f_{su}$, where f_{su} is the strength of the steel.

The upper-bound procedure, illustrated in Fig. 7.5, differs from standard analysis in the omission of compatibility requirements. Relaxation of compatibility requirements is justified by observations that loss of bond during cyclic loading may lead to differences between strain in reinforcing steel and strain in concrete at the same level [19]. Furthermore, strain distributions in hinging regions can be highly nonlinear [42] and measured ultimate concrete strains may exceed 0.006 [21].

Base-shear strengths computed using the upper-bound flexural strength procedure are reported in column (2) of Table 7.2. The upper-bound base-shear strengths of structures SS1, SS2, ES1 and ES2 exceeded the standard base-shear strengths by 4%, 6%, 4% and 5%, respectively. Much greater increases in upper-

bound capacity would be expected for structures built with standard reinforcing bars. Whereas the strength of reinforcing bars is approximately 50% greater than the yield stress, the strength and yield stress of model reinforcement differed by approximately 10%.

The measured base-shear strengths of SS1, SS2 and ES1 exceeded the upper-bound strength by 8%, 5% and 2%. The measured base-shear strength of ES2 was 4% less than the upper-bound strength.

7.4 Tests of Small-Scale Frame and Wall Components

Results from 40 tests of small-scale frame components were used to evaluate the upper-bound strength calculation procedure described in Section 7.3. Twenty-eight of the specimens were proportioned to permit direct comparison with similar assemblies in small-scale, ten-story frames that were subjected to strong base motions (Fig. 7.6). Twelve cantilever beams, tested at Stanford University, were proportioned to model a large-size prototype [25].

7.4.1 Description of Tests

Schipper [19] tested eight interior beam-column assemblies (Fig. 7.6) with beam cross-sections of 1.5 x 1.5 in. and a beam reinforcement ratio of 0.71%. Kreger and Abrams tested four interior joints and four exterior joints (Fig. 7.6) with beam reinforcement ratios of 0.71% and 1.06%. Columns were designed so that they would not yield. Measured cross-sectional properties, effective depths and material strengths are listed in Table 7.4. Figure 7.7 shows the test set up for the Schipper and Kreger-Abrams tests. All specimens underwent

several displacement reversals before being loaded to measure the flexural capacity of the beams.

Gilbertsen and Moehle [13] tested eight 2.0 x 1.5 in. specimens representative of interior and exterior first-story columns. Four columns had reinforcement ratios of 0.88% and four had reinforcement ratios of 1.75%. Table 7.5 gives measured cross-sectional properties and material strengths as well as nominal effective depths. The test apparatus for the Gilbertsen-Moehle tests is described by Fig. 7.8. All specimens were subjected to displacement reversals. In four of the tests, the axial load remained constant, whereas in four other tests, the axial load increased in proportion to the applied horizontal load.

Four nominally identical wall specimens were tested by Moehle [24]. The 1.5 x 8 in. walls had a ratio of total reinforcement to cross-sectional area of 1.79%. Nominal properties are summarized in Table 7.5. Each wall was loaded at a different elevation using the setup shown in Fig. 7.9. The walls were tested with zero axial load.

Moncarz and Krawinkler [25] tested cantilever beams with cross-sections of 2.0 x 1.0 in. and a beam reinforcement ratio of 1.65%. Specimens were loaded cyclically by applying a concentrated force 12.08 in. from the cantilever support. Of the 12 beams tested, 4 were tested at a cycling frequency of 0.0025 Hz, effectively a static test. Four beams were tested at frequencies of 2 Hz and four were tested at 10 Hz. Properties of the specimens are given in Table 7.6.

7.4.2 Observed and Upper-Bound Strengths

Measured and upper-bound flexural strengths are given in Table 7.4, 7.5 and 7.6. Table 7.7 lists mean values of the ratio of measured to upper-bound strength for each series of tests. Ratios are listed in the first row of Table 7.7 as option #1. Observed strengths of beams and columns exceeded calculated strengths by 2 to 22%. The amount of overstrength did not vary significantly with reinforcement ratio, axial load, or between exterior and interior joints. Beams tested at a frequency of 10 Hz were approximately 5% stronger than beams tested statically.

Reported strengths of the walls are 5 to 7% less than the upper-bound strengths. Relative displacement ("slip") between the base of the walls and the base girder may have reduced the flexural strength of the walls.

7.4.3 Sources of Additional Strength

Discrepancies between observed and calculated flexural strengths are significant only if the discrepancies cannot be attributed to experimental error or uncertainty. In this section, several possible of sources of error or uncertainty are briefly discussed.

(a) Underestimation of Material Strength

The upper-bound strength calculation is based on the assumption that materials develop their strength (Section 7.3). Any other assumption for ultimate strains, stress-strain curves, compatibility and bond would decrease calculated strength.

Discrepancies between measured and calculated strengths can be resolved by assuming a compressive stress of $2 * f'_c$ in the concrete (option 4 in

Table 7.7). This assumption represents an unlikely increase of 135% in compressive strength. Because the compression steel is allowed to develop its strength in compression, almost all of the concrete compression block lies outside the spiral. Less drastic increases in compressive strength, represented by options 2 and 3 in Table 7.7, lessen, but do not eliminate, the apparent overstrength.

Steel strength has a more direct influence on flexural capacity than does concrete strength. But even arbitrary increases of steel strength of 5% (option 5) and 10% (option 6) do not fully account for observed strengths.

(b) Resistance Provided by Test Setup

At large displacements, the testing apparatus would be expected to provide some resistance to the applied force. However, reactions were provided by long pinned rods during beam tests (Fig. 7.7 and 7.8). As the rods rotate, a component of their axial load may introduce a very small tensile force into the beam which would tend to reduce the flexural strength. The effect of limiting drift ratios to 3.5% is shown in Table 7.7 as option 7. The 3.5% limit resolves differences between the Schipper and the Kreger-Abrams tests but, a 10% discrepancy between measured and calculated strengths remains unaccounted for.

(c) Contribution of Spiral Reinforcement

Continuous spiral reinforcement would contribute to flexural strength if the spiral spanned across a crack. However, this effect should be negligible because a crack can form in a region where the spiral is not present on the tension face of the member.

(d) Error in Measurement of Applied Load

Errors in alignment or calibration of the load cell also might result in overestimation of the applied load. A 5^{o} error in alignment of the applied load reduces the component of force in the direction of interest by 0.4%. This effect is not sufficient to explain the observed discrepancies. Calibration errors would be as likely to underestimate as overestimate the applied load.

None of these of these explanations of the apparent flexural overstrength of small-scale reinforced concrete components is convincing. A 10% discrepancy between measured and upper-bound strengths remains largely unaccounted for.

7.5 Dynamic Tests of Small-Scale Structures

The upper-bound procedure was also used to estimate the strength of 21 reinforced concrete test structures. Estimates of base-shear and base-moment strengths calculated by limit analysis are compared with base shears and base moments observed during 67 dynamic tests.

7.5.1 Description of Tests

Fifteen frame structures and six frame-wall structures were considered in this study. Details of the tests are provided in Appendix B. Frame structures consisted of two parallel frames linked together at each story. Frame-wall structures included a wall placed between two frames. Masses positioned at each story generated lateral inertial forces and subjected columns to axial dead load. Walls did not carry axial load.

Ten structures tested on the University of Illinois earthquake simulator were designed to concentrate yielding in columns (Fig. B.2 and B.3). Schultz

[32] tested two 9-story frames of regular profile. Wood [46] investigated the behavior of setback frames. This report describes tests of structures ES1 and ES2. Four one-story frames were tested by Gulkan [14].

Healey [15], Moehle [23, 24] and Cecen [10] tested five nine-story and ten-story frames in which beams were expected to yield (Fig. B.4). Six frame-wall structures were subjected to strong base motions by Moehle [24] and Abrams [2] (Fig. B.5).

A scaled version of 1940 El Centro ground motion was used as the base motion for all but four test structures. Base motions for structures FW3 and FW4, tested by Abrams, were based on the 1952 Taft earthquake record. Gulkan subjected structures HD1 and HD2 to sinusoidal base motions.

7.5.2 Observed and Upper-Bound Lateral Strengths

Maximum measured base-shears, base moments and drifts are given in Tables 7.9, 7.10 and 7.11. The tables summarize response for test runs in which a structure exceeded previous displacement maxima. Base moments are listed as reported by each investigator. Base-shear and base-moment strengths were calculated by limit analysis (Section 7.1). Member flexural strengths (Table 7.8) were computed following the upper-bound strength procedure described in Section 7.3, assuming dead load axial forces to act in columns.

Lateral strengths were calculated for both linear and uniform force distributions. When considering a "linear" force distribution, the magnitude of inertial force at a story was assumed to be proportional to the product of story mass and story elevation. The term "uniform" load distribution refers to the assumption that inertial force at a story is proportional to story mass.

The assumed load distribution is rarely truly "linear" or "uniform," except for structures of uniform interstory height and mass.

Calculated base-shear and base-moment capacities as well as controlling failure mechanisms are reported in Tables 7.9, 7.10 and 7.11. Figures 7.10 and 7.11 plot ratios of observed to upper-bound base-shear strengths versus maximum overall (mean) drift for 60 tests. Similar plots for base moment are presented in Fig. 7.12 and 7.13.

Test structures were divided into four families according to limiting failure mechanism. Multi-story structures whose base-shear capacity was controlled by story mechanisms were classified as soft-story structures. One-story frames tested by Gulkan were grouped into a second category. A third group of structures consisted of frames with yielding beams but no walls (mechanism types B3-B7). Frame-wall structures were grouped separately because their base-shear strengths were limited by mechanisms involving yielding of beams at all stories (mechanisms B9, B10).

There are large discrepancies between the observed and estimated base-shears (Fig. 7.10 and 7.11) and base moments (Fig. 7.12 and 7.13). Above drift ratios of 1.5%, the observed strength of frames with yielding beams and frame-wall structures greatly exceeds the calculated capacity, even when a uniform loading distribution is assumed. In contrast, soft-story structures do not display the same gain in base-shear strength. The mean value of the ratio of observed strength to upper-bound strength is reported in Table 7.12 for each family of structures.

7.5.3 Discussion of Observed and Upper-Bound Lateral Strengths

The discrepancies between observed and estimated base-shear and base moment noted in the previous sub-section are due in part to uncertainties in force distribution over the height of the structure. Preferably, limit analysis calculations should be based on actual distributions of lateral inertial force. Unfortunately, the inertial force distribution at times of maximum base-shear and base moment is rarely reported.

Linear and uniform force distributions are idealizations of observed distributions. As would be expected, the assumption that forces are distributed uniformly tends to result in a higher calculated base-shear strength. Linear distribution of forces leads to a higher calculated base-moment strength. Neither force distribution represents a bound on possible behavior.

As shown in Appendix C, calculated base-shear capacity is independent of assumed lateral force distribution if the base-shear capacity is limited by a first-story mechanism (type S1). To eliminate the effect of the assumed force distribution, the strength of the soft-story structures should be evaluated in terms of base-shear. Considering Fig. 7.10, 7.11 and Table 7.12, structures with story yielding appear to have a base-shear overstrength of 5-7%.

Calculated base-moment capacity is independent of assumed lateral force distribution if the base-moment capacity is limited by a beam mechanism involving yielding at all stories (type B9, B10). To eliminate the effect of uncertainty in inertial load distribution, the lateral strength of the frame-wall structures (B9 and B10 mechanisms) should be evaluated in terms of base moment. As shown in Fig. 7.12, 7.13 and Table 7.12, the measured base-moment

strength of frame-wall structures exceeded calculated strengths by approximately 25%.

For structures whose base-shear and base-moment strengths are limited by mechanisms other than S1 or BN, strength cannot be evaluated independently of force distribution. As shown in Table 7.10, the limiting failure mechanism of frames with yielding beams but no walls varies with the assumed inertial force distribution. Assuming the uniform and linear force distributions are reasonable, frame structures with yielding beams but no walls appear to have an overstrength in the range of 20-40%.

Of the four figures, the plot showing ratios of measured to calculated base-shear strength for a uniform load distribution (Fig. 7.11), shows the least overstrength. Comparing measured and calculated base-shear strengths of structures with mechanisms other than S1, however, is not appropriate unless the actual force distribution is used.

7.5.4 Sources of Apparent Overstrength

Some overstrength of test structures is expected based on measured strengths of components during static tests (Section 7.4). Additional overstrength in test structures can be attributed to rapid loading rates. High strain-rates are known to increase the yield stress of model reinforcement [39] and concrete compressive strength [25, 28]. Moncarz and Krawinkler [25] tested small-scale, reinforced concrete cantilevers at frequencies ranging from 0.0025 Hz to 10 Hz. The 5% increase in flexural strength they report, however, is not sufficient to account for the observed lateral strengths of the frame-wall structures and the frames with yielding beams.

The difference in overstrength between the two types of structures is better rationalized in terms of restraint provided by experimental apparatus. At large displacements, steel channels used to support story masses (Fig. A.3) may put beams into compression [24]. The resulting increase in beam flexural strength would increase the strength of structures in which large inelastic rotations occurred in beams but should not affect the strength of structures with story mechanisms. This explanation of the overstrength is consistent with the observed behavior of the small-scale test structures.

7.6 Summary of Strength Study

1. The observed base-shear strengths of structures SS1, SS2, ES1 and ES2 were consistent with calculated capacities.

2. A reasonable upper-bound flexural strength for small-scale reinforced concrete members can be computed by assuming that tensile reinforcement and compressed concrete develop their strengths. The compressive steel is assigned a stress (not exceeding its strength) to maximize section capacity.

3. Observed flexural strengths of small-scale frame components were approximately 8-12% more than computed upper-bound upper-bound strengths.

4. Resolving discrepancies between observed and calculated static flexural strengths of small-scale components required the assumption of a 135% increase in concrete strength or a 10% increase in reinforcement strength.

5. Base-shear strength is a convenient measure of the lateral strength of structures in which a first-story failure mechanism (type S1) is expected to form.

6. Observed base-shear strengths of structures with story mechanisms were approximately 5-7% more than computed upper-bound strengths. This discrepancy is similar to that observed during tests of components.

7. Base-moment strength is a convenient measure of the lateral strength of structures in which beams are expected to yield at all stories (mechanism types B9, B10).

8. Observed base-moment strengths of frame-wall structures (mechanism types B9, B10) exceeded calculated upper-bound strengths by approximately 25%.

9. Observed lateral strengths of frames with yielding beams but no walls were approximately 20-40% greater than computed upper-bound strengths.

10. The discrepancies between observed and calculated lateral strengths of test structures at large drifts can be attributed to restraint provided by experimental hardware.

CHAPTER 8

BASE-SHEAR RESPONSE OF FRAME-WALL STRUCTURES

Three methods of estimating the maximum dynamic base shear in a frame-wall structure are discussed in this chapter: limit analysis (Section 8.2), an approach developed by Kabeyasawa and Aoyama [6] (Section 8.3) and a procedure developed during the course of this study that combines results from limit analysis with results from response spectrum analysis (Section 8.4). Estimates from the three methods are compared with base shears measured during earthquake simulations of small-scale, frame-wall structures. The Kabeyasawa and response spectrum procedures are evaluated in Section 8.5 and the procedures are generalized to consider frame structures in Section 8.6. The chapter is summarized in Section 8.7.

8.1 Introduction

In existing model codes [4, 7, 40, 44] it is recommended that design forces for columns and beams be calculated by assuming plastic hinges at the ends of each member [ACI 318-83, Section A.7.1.1]. This approach is inappropriate for the design of slender walls because the resulting design shears are unrealistically high. If the wall is deep enough to prevent formation of a first-story failure mechanism, plastic hinges will form only at the base, and not at the first story.

Design forces for walls are calculated from elastic analysis using design lateral forces [ACI 318-83, Section A.7.1.3]. If this procedure is followed, the calculated design shear will be independent of the strength of the

structure. This independence is inconsistent with the observed response of small-scale structures and with results from nonlinear response-history analysis.

An alternative method of estimating the maximum dynamic shear at the base of a wall is first to estimate the total base shear for the structure and then to assign a portion of the total base shear to the wall. This chapter addresses the problem of estimating the total base shear of a frame-wall structure subjected to an earthquake.

8.2 Limit Analysis

In Chapter 7, the maximum base shear of 21 small-scale reinforced concrete structures subjected to earthquake simulations was estimated by limit analysis. Base-shear strength was calculated assuming that plastic hinges formed at the face of members and that the plastic moment for each member was the upper-bound flexural strength, calculated following the procedure developed in Section 7.3. As shown in Fig. 7.10 and 7.11, the observed base shear often exceeded the base shear calculated by limit analysis. The results shown in Fig. 7.10 were calculated assuming the inertial force at each story was proportional to the product of the story mass and the height of the mass above the base ("linear force distribution"). In Fig. 7.11, the ratios of measured to calculated base shear are plotted for the assumption that story forces were proportional to the story mass ("uniform force distribution"). Neither assumption led to acceptable estimates of maximum measured base shear.

As observed in the Chapter 7, the discrepancy between calculated and measured strengths depended on the failure mechanism for each structure. For

structures ES1 and ES2 the minimum base-shear strength was calculated for a first-story failure mechanism. Because the calculated base shear strength was independent of the assumed load distribution in this case, limit analysis calculations resulted in excellent estimates of the maximum base shear. The ratio of maximum observed base shear to that calculated by limit analysis was 1.02 for ES1 and 0.96 for ES2.

Results were much less satisfactory for frame-wall structures whose base-shear strength was not governed by a first-story mechanism. Measured and calculated base shears are listed in Table 8.1 for structures FHW, FFW (tested by Moehle [24]), FW1, FW2, FW3 and FW4 (tested by Abrams [2]). The characteristics of the 16 base motions experienced by these structures are summarized in Table 8.2. The structures tested by Moehle and Abrams had walls which were almost twice as deep as the walls of ES1 and ES2. The beams were less than half as deep as those of structures ES1 and ES2. As a result, the first-story mechanism was not the critical failure mechanism for any of the Moehle or Abrams structures. Instead, except for FHW, whose critical failure mechanism involved yielding at only 5 stories, all these structures had limiting mechanisms that involved yielding of the beams at all stories.

As noted previously, measured base shears consistently exceeded those calculated by limit analysis when the inertial forces were assumed to vary linearly over the height of the structure (Fig. 8.1 and Table 8.1). The maximum ratio of measured to calculated base shear was 1.92 for Structures FW1. The maximum ratio of measured to calculated base shear decreased to 1.51 when the force distribution was assumed to be uniform (Fig. 8.2). However, both sets of calculations resulted in large discrepancies between observed and calculated response. Most importantly, limit analysis calculations did not

reproduce the trend of increasing base shear with base-motion intensity apparent in Fig. 8.1 and 8.2.

The effect of force distribution can be taken into account by comparing maximum base moment instead of base shear (Fig. 8.3). The variation in the ratio of observed to calculated base moment was less than that calculated for base shear. Furthermore, the maximum base moment for the second and third motions was approximately equal, confirming that an upper bound on base moment was reached. Unfortunately, a reliable estimate of base moment is not useful in obtaining a design shear at the base of a wall.

Unless the force distribution is known, limit analysis does not give a satisfactory estimate of maximum dynamic base shear for structures whose failure mechanism is not a first-story mechanism. The methods presented in the following two sections attempt to account for changes in the shape of the inertial force distribution without requiring experiments or nonlinear response-history analysis.

8.3 Kabeyasawa and Aoyama Approach

Kabeyasawa and Aoyama [18, 6] proposed a procedure for estimating the maximum base shear for frame-wall structures based on results of an analytical study of a large-scale reinforced concrete structure. The structure was tested as part of the US-Japan Cooperative Program in Earthquake Engineering [45, 17]. The model used by Kabeyasawa reproduced well the observed displacement and base-shear behavior of the large-scale structure during static tests. Because an inverted triangular force distribution was imposed on the test structure during testing (effectively forcing the structure to respond as

a single degree of freedom system), the effect of changes in shape of the force distribution could not be measured during the test. The procedure developed by Kabeyasawa was motivated by the observation that the numerical model gave higher base shears when the model was permitted to respond as a multi-degree-of-freedom structure than when the structure was constrained to displace as a system with a single degree of freedom.

Kabeyasawa decomposed the horizontal force distribution into mutually orthogonal shapes. The force distribution at a given time is then:

$$\{f\}_{total} = \{f\}_1 + \{f\}_2 + \ldots \{f\}_j \ldots + \ldots \{f\}_N \qquad (8.1)$$

where $\{f\}_j$ is a vector containing the jth component of the force distribution and N is the number of stories in the structure. The first shape was assumed be an inverted triangle ("linear component"). In the Kabeyasawa study, the shape of other components ("higher modes") were obtained from simple polynomials. "The second mode shape is assumed to be a cubic corrected to be orthogonal to the inverted triangular first mode [18]." In this study, the shape of each higher mode was chosen as the mode shape of the initial structure, orthogonalized with respect to the linear component and the other higher modes by a Gram-Schmidt process [5]. Table 8.3 lists the modified modal properties for the FW structures.

Kabeyasawa observed that the higher-mode components of inertial force varied in-phase with the ground motion, a condition that would be approached for a very stiff structure. The inertial forces due to the higher modes are equal to the inertial force distribution minus the linear component. The inertial forces due to the higher modes can be expressed as:

$$\{f(t)\}_{\text{higher modes}} = - [m] \sum_{j=2}^{N} \beta_j * \{u\}_j * (1 + \Delta w_j) \; a_g(t) \qquad (8.2)$$

where,

$\{f(t)\}_{\text{higher modes}}$ = vector containing the contribution of higher modes to the inertial force at each story

$[m]$ = mass matrix

β_j = participation factor

$$= \frac{\{u\}_j^t [m] \{e\}}{\{u\}_j^t [m] \{u\}_j}$$

$\{u\}_j$ = vector containing the jth mode shape

$(1+\Delta w_j)$ = amplification factor

$a_g(t)$ = base acceleration at time t

$\{e\}$ = unit vector

Based on results from nonlinear response history analysis, Kabeyasawa estimated the amplification factor, $(1+\Delta w_j)$, to be approximately 1.7 for the second mode and 1.0 for modes of higher order.

By summing the forces over the height of the structure the total base shear can be expressed as the sum of base shears associated with each component of the force distribution.

$$V_{\text{total}} = V_1 + V_2 + V_3 + \ldots + V_j + \ldots V_N \qquad (8.3)$$

where,

V_{total} = total base shear

V_1 = base shear due to the linear component of the force distribution

$V_j(t) = (1 + \Delta w_j) * W_j * a_g(t)$

W_j = effective weight of the shape

$$= \frac{[\{e\}_j^t [m] \{u\}_j]^2}{\{u\}_j^t [m] \{u\}_j}$$

Kabeyasawa assumed that the linear component could be estimated by limit analysis assuming an inverted triangular load distribution ($V_1 = V_{limit}$). Recognizing that the base acceleration is a common factor in the expressions for each component of base shear, the estimate of the maximum base shear can be expressed as:

$$V_{total\ max} = V_{limit} + \sum_{j=2}^{N} (1+\Delta w_j) * W_j * a_{g_{max}} \tag{8.4}$$

$$V_{total\ max} = V_{limit} + D_m * W * a_{g_{max}} \tag{8.5}$$

where,

$V_{total\ max}$ = estimate of maximum dynamic base shear

V_{limit} = base shear calculated from limit analysis assuming an inverted triangular load distribution

$$D_m * W = \sum_{j=2}^{N} (1 + \Delta w_j) * W_j$$

W = total weight of the structure

$a_{g_{max}}$ = peak ground acceleration

This formulation implicitly assumes that the linear component and higher-mode components reach their maxima at the same time. The procedure is quite easy to use because D_m is approximately 0.3 for a wide range of buildings heights. The most time consuming step in the procedure is the limit analysis calculation.

To provide experimental checks of the Kabeyasawa procedure, which was based on analytical results, the procedure was used to estimate the maximum base shear for the six frame-wall structures listed in Table 8.1. As shown in Fig. 8.4 and Table 8.1, the procedure gave a reasonable upper bound to the measured base shear for the 16 tests of the frame-wall structures. The most attractive aspect of the Kabeyasawa and Aoyama approach is that it gave good results without being complex. The least desirable aspect of this procedure is its reliance on amplification factors for the higher modes that are not explicitly related to properties of the structure or to the design ground motion.

8.4 Response Spectrum Approach

An alternative to assuming that the higher modes fluctuate in phase with the base acceleration is to assume linear-elastic behavior for the higher modes. This assumption eliminates the need for assigned amplification factors. Instead, the higher-mode maxima are estimated from a response spectrum, making the procedure sensitive both to dominant frequencies of the structure and to ground-motion characteristics. As in the Kabeyasawa approach, the base shear

due to the linear component of the force distribution is calculated by limit analysis.

Replacing the amplification factors of Eq. 8.4 with response spectrum ordinates, the estimate of the maximum base shear becomes:

$$V_{\text{total max}} = V_{\text{limit}} + \sum_{j=2}^{N} (W_j * Sa_j) \qquad (8.6)$$

where,

$V_{\text{total max}}$ = estimate of maximum dynamic base shear

V_{limit} = base shear calculated by limit analysis, assuming an inverted triangular inertial force distribution.

N = number of stories in the structure.

W_j = effective weight of jth mode.

Sa_j = spectral acceleration for response at the frequency and damping corresponding to the jth mode.

To simplify the procedure, the spectral accelerations for the fourth mode and higher were assumed to be the same as for the third mode.

To implement this approach, it was necessary to determine appropriate values of effective weight, frequency and amount of viscous damping for each of the higher modes. To be consistent with linear analysis, the effective weights were calculated from the mode shapes in the same manner as they would be calculated if the shapes were eigenvectors of a stiffness matrix.

Estimates of frequencies and damping factors were necessary to compute a response-spectrum ordinate for each mode (Eq. 8.6). The frequencies and damping factors for the higher modes of the FW structures were estimated by comparing the measured response history of each higher-mode component of base shear with the response histories of linear, single-degree-of-freedom oscillators. The measured higher-mode components of base shear at a given time were calculated for each test by computing the component of the measured inertial force distribution along each of the mode shapes. The history of each measured component of base shear was then compared for each run to histories of linear response for frequencies ranging from 6 to 32 Hz and for damping ratios of 5, 10, 15 and 20%.

The goodness-of-fit index (GOF), developed by Lopez [20] (Section 6.2.2), was used to measure the extent to which linear response histories were similar to the measured histories of the higher-mode components of base shear. Low values of the index indicate that the response is well reproduced; an index of 0 would indicate perfect reproduction of observed response. The GOF indices for runs 1, 2 and 3 of structures FW1, FW2 and FW4 are plotted in Fig. 8.5 for the second mode and in Fig. 8.6 for the third mode. GOF indices are listed in Table 8.4 for frequencies and damping ratios corresponding to the best fit of observed response.

For all nine runs, the goodness-of-fit index calculated for linear response was less than that calculated for the assumption that the higher-modes varied in-phase with the base acceleration (Table 8.4). The frequency corresponding to the best fit of observed response decreased slightly from one motion to another. However, a good fit was obtained assuming a damping factor of 10% and a frequency of approximately 1/2 the frequency calculated assuming

gross-section properties (10 Hz for the second mode and 24 Hz for the third mode).

Assuming a damping factor of 10%, a second-mode frequency of 10 Hz and a frequency of 24 Hz for modes of higher order, the dynamic base shear were estimated using Eq. 8.6. These estimates are compared with measured dynamic base shears in Fig. 8.7 and Table 8.1. The results are comparable to those obtained following the Kabeyasawa procedure.

8.5 Evaluation of Approaches

The accuracy of the Kabeyasawa and response-spectrum procedures depends on (1) the limit-analysis estimate of the first-mode component, (2) the estimate of the base shear due to the higher modes and (3) the method used to combine first-mode and higher-mode components.

One assumption common to both procedures is that the first-mode component of base shear can be estimated by limit analysis. This assumption is verified by the results shown in Fig. 8.8 and Table 8.5. The average ratio of observed to computed base shear for runs 1, 2 and 3 were 0.95, 1.19 and 1.20, respectively. The 20% discrepancy in first-mode component is consistent with the 25% discrepancy in base moment apparent in Fig. 8.3.

In Fig. 8.9, histories of total base shear and of first-mode base shear are plotted for run 2 of FW2. The total base shear is the sum over the height of the structure of the inertial forces (mass times acceleration). The first-mode component of base shear is the portion of the total base shear due to the linear component of force distribution. (The linear component can be calculated by taking the dot product between a vector containing the inertial

force at a given time and a unit vector containing the first-mode shape.) Though the total base shear maxima varied in successive excursions, the first-mode component reached the same maximum several times, suggesting that there is a limit to the magnitude of the first-mode component. The existence of an upper bound on the first-mode component is also suggested by Fig. 8.8. Fig. 8.8 shows that the maximum measured first-mode base shears were approximately the same for runs 2 and 3, though the runs had different maximum base accelerations (Table 8.2).

The Kabeyasawa and response-spectrum procedures differ only in the way higher-mode maxima are estimated. Whereas the Kabeyasawa procedure assumes that the higher modes vary in-phase with the base acceleration, the response-spectrum procedure assumes linear response for the higher modes. The waveforms estimated following both approaches are compared with the observed higher-mode response in Fig. 8.10. The assumption of linear behavior resulted in a better fit of the observed higher-mode base-shear waveform than resulted from the assumption that the higher modes fluctuated in phase with the base acceleration.

Measured and calculated higher-mode maxima are compared in Fig. 8.11 and Table 8.5 for structures FW1, FW2 and FW4. In Fig. 8.11, the estimated and observed higher-mode base shears have been normalized with respect to the first-mode base shear. The three sets of bars to the left of Fig. 8.11 correspond to initial simulations. The Kabeyasawa procedures gives better results for these runs but, in these cases, the higher-mode base shear corresponds to only approximately 30% of the first-mode base shear. For runs of higher intensity (the six sets of bars to the right), the response-spectrum procedure results in better estimates. For some of these higher intensity

runs, the higher-mode component of base shear was as large as the first-mode component and should not be neglected.

Both procedures combine modal maxima directly, implicitly assuming the maxima may occur simultaneously. This approach is defensible because large first-mode base shears occurred several times during each motion. A more complicated scheme of modal combination is not warranted given the approximate nature of the base-shear estimate.

The advantage of the Kabeyasawa procedure is its simplicity. The advantage of the response-spectrum approach is its sensitivity to the dominant frequencies of the structure and to ground-motion characteristics.

The two procedures can be shown to give similar results for structures with fewer than 15 stories. Consider the expression used to estimate the maximum base shear for the response-spectrum procedure (Eq. 8.6). If the response spectrum is similar to that assumed for design of the test structures (Fig. 2.3), the higher modes of structures with fewer than 15 stories are likely to fall in the constant acceleration range of the linear response spectrum. For the response spectrum shown in Fig. 2.3, the maximum acceleration amplification is 0.656/0.35 = 1.87. Substituting this spectral amplification factor into Eq. 8.6, the base-shear estimate becomes:

$$V_{\text{total max}} = V_{\text{limit}} + 1.87 * a_{g_{\max}} \sum_{j=2}^{N} W_j \qquad (8.7)$$

For the FW structures tested by Abrams, the first-mode effective weight is 88% of the total weight of the structures (Table 8.3). The sum of the effective

weights of the higher modes is then 0.22W. Substituting 0.22W into Eq. 8.7, the estimate of maximum base-shear can be written as:

$$V_{total\ max} = V_{limit} + 1.87 * a_{g_{max}} * 0.22\ W \tag{8.8}$$

$$V_{total\ max} = V_{limit} + 0.41 * W * a_{g_{max}} \tag{8.9}$$

The only difference between Eq. 8.8 and the expression used to estimate base-shear in the Kabeyasawa procedure (Eq. 8.5) is the multipier of $W * a_{g_{max}}$. Instead of the factor of 0.41 that appears in Eq. 8.8, D_m in Eq. 8.5 is approximately 0.3.

8.6 Frame Structures

The Kabeyasawa and response-spectrum procedures can be modified to apply to frame structures. As noted in Section 8.2, the base-shear maxima of structures with first-story failure mechanisms can be estimated by limit analysis alone. On the other hand, additional components of base shear must be considered if the limiting mechanism is not a first-story mechanism. The modified procedures assume the contribution of higher-mode shear is related to the ratio of the minimum base-shear strength calculated for all failure mechanisms to the base-shear strength calculated assuming a first-story mechanism.

For the Kabeyasawa procedure (Eq. 8.5), the modified estimate is:

$$V_{total} = V_{limit} + \left(1 - \frac{V_{limit}}{V_1}\right) D_m * W * a_{g_{max}} \tag{8.7}$$

where V_1 is the base shear strength calculated assuming a first-story collapse mechanism.

The measured and calculated base shears are compared in Fig. 8.12 for the 21 small-scale structures described in Appendix B. The modified Kabeyasawa procedure gives a conservative estimate of the observed dynamic base shear for soft-story structures, frame structures and frame-wall structures.

The equivalent formulation for the response-spectrum procedure is:

$$V_{total} = V_{limit} + \left\{\left[1 - \frac{V_{limit}}{V_1}\right] \sum_{j=2}^{N} (W_j * Sa_j)\right\} \qquad (8.8)$$

8.7 Summary

1. Limit-analysis calculations do not estimate satisfactorily the maximum dynamic base shear experienced by frame-wall structures.

2. The observed high base shears can be rationalized by considering the contribution of higher modes to response.

3. Observations made by Kabeyasawa and Aoyama [6, 18], based on analytical studies of the U.S.-Japan reinforced concrete structure, are corroborated by the observed response of small-scale structures.

4. Higher-mode response in frame-wall structures can be conveniently approximated by assuming linear behavior for the higher modes. The maximum base shear for the structure, V_{total}, can then be estimated from the following expression:

$$V_{total\ max} = V_{limit} + \sum_{j=2}^{N} (W_j * Sa_j) \qquad (8.6)$$

where,

$V_{total\ max}$ = estimate of maximum dynamic base shear

V_{limit} = base shear calculated by limit analysis, assuming an inverted triangular inertial force distribution.

N = number of stories in the structure.

W_j = effective weight of jth mode.

Sa_j = spectral acceleration for response at the frequency and damping corresponding to the jth mode.

In computing the spectral acceleration for each mode, each mode should be assumed to have a damping factor of 10% and a frequency of one-half that calculated assuming gross-section properties.

5. The combination of limit analysis and response-spectrum analysis can also be used to estimate the maximum base shear in frame structures without walls. The estimate of the maximum base shear is:

$$V_{total} = V_{limit} + \left\{\left[1 - \frac{V_{limit}}{V_1}\right] \sum_{j=2}^{N} (W_j * Sa_j)\right\} \qquad (8.8)$$

where V_1 is the base-shear strength calculated assuming a first-story collapse mechanism.

CHAPTER 9

SUMMARY AND CONCLUSIONS

The goal of this study was to seek an efficient structural configuration to control distortion in reinforced concrete frames. Using experiments and analyses, the effect on lateral-displacement response of two factors were considered. These were the effects on drift response of:

(1) using slender walls in frames with yielding columns, and

(2) placing a structural hinge at the base of slender walls to reduce strength and stiffness requirements for the foundation.

Frame structures with slender walls were studied because they may provide a satisfactory compromise between structural performance and architectural requirements. If no walls are included in a frame with long spans, beams are likely to be flexurally stronger than columns. Such strong-beam weak-column frames are architecturally convenient but tend to experience unacceptable interstory displacements unless the columns are heavily reinforced [32].

If large walls are included in the lateral-force-resisting-system, the structure will be sufficiently stiff to prevent objectionable interstory displacements [29, 47]. Such structures, however, may be uneconomical and architecturally undesirable. Slender-wall frames may be stiff enough to limit interstory displacements and slender enough to be compatible with the functional requirements.

To make recommendations about the proportioning of slender walls, it was necessary to have a pragmatic method for estimating maximum lateral-displacement response. Maximum drifts calculated by nonlinear response-

history analysis were compared with maximum drifts calculated by linear response-spectrum analysis.

To make recommendations about the design of walls to resist shear, it was necessary to have a realistic estimate of the base shear for a structure. Several pragmatic procedures for estimating maximum base-shear response of frame-wall structures were evaluated by comparing estimates with the observed response of test structures.

9.1 Outline of Experimental Work

Experiments were performed to provide benchmarks against which to calibrate existing numerical models. The experimental phase of this study included the design, construction and testing of two small-scale structures (ES1 and ES2) of identical dimensions but differing column reinforcement (Fig. 1.1(b)). The lateral-load resistance of the structures was provided by a pair of nine-story, reinforced concrete frames with three columns and a slender wall (Fig. 2.1). The wall depth (4 1/2 in.) was twice the depth of the beams (2 1/4 in.) and three times the depth of the columns (1 1/2 in.).

The observed response of two reinforced concrete frames with yielding columns was compared with the response of the slender-wall frames (Schultz, [32]). Additional test results were available from many other investigators. Measured strengths of small-scale components are reported in references 13, 19, 24 and 25. Displacement and base-shear response of small-scale test structures are reported in references 2, 10, 14, 15, 23, 24, 32 and 46.

9.1.1 Design of Test Structures

Story masses, base motions and geometry of test structures ES1 and ES2 were selected to permit direct comparison with strong-beam, weak-column frame structures SS1 and SS2 (Fig. 1.1(a)), tested by Schultz [32]. The wall depth was selected such that maximum first-story displacement response was sensitive to the strength and stiffness at the base of the wall.

Maximum displacement response was estimated by linear response-spectrum analysis. According to Shimazaki [35, 38], linear analysis provides a conservative estimate of maximum displacement response for structures that have an acceptable combination of strength and initial period (Section 2.1.5, Eq. 2.1). Since ES1 and ES2 satisfied this criterion, maximum displacements were estimated assuming gross-section properties, one half the expected modulus of elasticity and a damping factor of 2%, as specified by Shimazaki.

The estimated top-level displacement was insensitive to the stiffness assumed at the base of the wall. Top-level displacement varied from 1% to 1.1% of the height of the structure depending on whether the wall was assumed fixed or pinned at the base. In contrast, estimated first-level displacement was sensitive to the assumed stiffness at the base of the wall. Assuming the base of the wall to be fixed, the estimated first-story displacement was 1.0% of the first-story height. Assuming the base of the wall to be pinned, the calculated first-story drift ratio increased to 2.2% of the first-story height.

A modified version of the Substitute Structure Method [34] was used to determine design forces for Structure ES1. Nonlinear behavior was approximated by a linear structure of reduced stiffness (Fig. 2.7). Displacements were calculated using the design spectrum of Fig. 2.3, assuming a damping factor of 10%. Beam reinforcement in structures ES1 and ES2 was identical to that used

in Structure SS2. Wall reinforcement was also the same for ES1 as for ES2. Column reinforcement for ES1 was selected to satisfy the design forces calculated using the Substitute Structure Method. In Structure ES2, column reinforcement ES2 was arbitrarily reduced to 4 bars per cross-section (2 per face).

9.1.2 Construction of Test Structures

Frames were cast horizontally. The test structures, including frames (Fig. A.6), masses (Fig. A.2) and connection hardware (Fig. A.3) were assembled on the earthquake simulator (Fig. A.9). A stiff base-girder, which had been cast monolithically with each frame, was prestressed to the simulator platform.

Longitudinal reinforcement at the base of the wall formed an "X" (Mesnager hinge [11, 22], Fig. A.5 and 2.11). The Mesnager hinge increased flexibility of the base of the wall and limited slip between the wall and base girder.

Flexural reinforcement was fabricated from No. 13-gage wire (yield stress = 55 ksi) and No. 7-gage wire (yield stress = 58 ksi). Mean concrete compressive strengths were 4360 psi for Structure ES1 and 4800 psi for Structure ES2 (4 x 8-in. cylinders).

9.1.3 Testing Procedure

Both structures ES1 and ES2 were subjected to three base motions modelled after the N-S component of the 1940 El Centro ground motion [9]. A sinusoidal motion with a frequency near the fundamental frequency of the damaged structures served as a fourth base motion.

Response of the test structures was observed by monitoring:

(1) Base acceleration and base displacement

(2) In-plane displacement of frames at each level

(3) In-plane acceleration of each story mass

(4) Rotation of the base of the wall with respect to the base girder

(5) Slip between the wall and base girder

(6) Transverse and vertical accelerations of the ninth-level mass

(7) Crack locations, crack widths and crushing of concrete

Free-vibration tests were performed before and after each dynamic test to determine modal frequencies for low-amplitude response. After the dynamic tests, a static test was performed of each structure to determine residual base-shear strength.

9.2 Observed Response of Test Structures

9.2.1 Response of Structures ES1 and ES2

Base motions were almost identical for both structures, particularly at frequencies dominating displacement response. The similarity was apparent in base-acceleration histories, base-displacement histories, linear response spectra and Fourier amplitude spectra of the base acceleration records.

The displacement-response histories of both structures were similar for the first base motion (peak acceleration = 0.35 and 0.36 g). During subsequent motions of higher intensity, the displacement-response histories of ES1 and ES2 differed noticeably.

Though displacement response was primarily in the first mode, the shape of the first mode changed. Maximum first-story drift ratio varied from approximately 1 1/2 times the overall drift ratio during the first runs to 2

1/2 times the overall drift ratio in final runs. The drift concentration was slightly less severe for Structure ES1 (maximum column reinforcement ratio = 3.5%) than for Structure ES2 (column reinforcement ratio = 1.2%). These changes in mode shape were consistent with an increase in flexibility at the base of the wall and with the formation of a first-story collapse mechanism.

Compared with displacement response, acceleration response was more influenced by higher modes, particularly in the lower levels of the structures. The frequency content of acceleration response in the lower levels was similar to that of the ground motion.

The Mesnager hinge performed as intended, providing a flexible detail without permitting significant slip between the base of the wall and the base girder. The hinge detail underwent rotations of up to 4% while limiting displacement between the base of the wall and the base girder to 2% of the first-story displacement during the initial motion and 4.5% of the first-story displacement during all runs.

9.2.2 Displacement Response of Test Structures with and without Walls

Displacement response of the two frames with slender walls (ES1 and ES2, Fig. 1.1(b)) were compared with the displacement response of the two frames without walls (SS1 and SS2, Fig. 1.1(a)). Maximum overall drift for all four structures varied linearly with intensity of ground motion. In contrast, maximum interstory drift was sensitive to distribution of strength and stiffness of the four structures.

During the design base motion, Structure SS1 (maximum column reinforcement ratio = 2.9%) experienced a drift ratio of 3.1% in the first-story. This drift

ratio was more than twice that experienced by structures SS2, ES1 and ES2 during motions of similar intensity.

Maximum interstory drifts for the heavily-reinforced frame SS2, (maximum column reinforcing ratio = 4.7%) were similar to maximum interstory drifts experienced by the slender-wall structures. Maximum interstory drift, however, did not occur at the same level in each structure. The slender-wall structures (ES1 and ES2) experienced maximum interstory drifts in the first story; Structure SS2 experienced large drifts in stories 5 through 9.

As compared with frames without walls, the frames with walls required less flexural reinforcement and much lower reinforcement ratios to achieve a similar level of drift control. Frames with slender walls, however, would require more concrete and formwork and would occupy more floor space than columns.

9.3 Calculated Displacement Response

In order to study displacement response of frames with slender walls, the response of ES2 was reproduced analytically using the program LARZWD, written by Saiidi [30, 31] and modified by Lopez [20]. The numerical model was then used to observe the sensitivity of calculated displacement response to two groups of parameters.

The first group included parameters that are difficult to estimate. These parameters were: (1) the slope of the unloading portion of the hysteresis curve, (2) the amount of viscous damping and (3) the bond stress. Because the assumed bond stress had a strong influence on calculated displacement waveform (Fig. 6.10), it was concluded that the numerical model should not be expected to lead to accurate predictions of displacement waveform. Calculated

displacement maxima were found to be insensitive to reasonable variations in values of unloading slope exponent, viscous damping and bond stress. Thus, the model was judged to be reliable for estimating displacement maxima.

The second group consisted of parameters that are easier to estimate, such as member strength and stiffness. For Structure ES2 subjected to the El Centro motion, a 100% increase in column strength, beam strength, wall strength, strength at the base of the wall or yield curvature at the base of the wall, changed first-story and top-level maxima by less than 20%.

The effect on displacement response of changes in wall depth was studied analytically for three intensities of the El Centro motion with a time scale of 2.5 [9] (El Centro, 1.5 times El Centro, 2 times El Centro). As the wall depth was varied the reinforcement ratio was kept constant at 1.5%. Accordingly, both strength and stiffness increased as the wall depth was increased.

Increases in wall depth had little influence on maximum top-level drift if the properties at the base of the wall remained the same (Fig. 6.19, "Mesnager hinge"). Maximum top-level drift decreased with increasing wall depth only when the base of the wall was able to develop the flexural strength of the wall (Fig. 6.19, "fixed base"). Maximum top-level drift calculated by nonlinear response-history analysis (LARZ) was estimated conservatively using the linear model used for design (Fig. 6.22). Maximum response of the structures with a Mesnager hinge were estimated conservatively assuming the base of the wall to be pinned.

Calculated maximum interstory displacement was sensitive to wall depth and to the placement of a hinge at the base of the wall (Fig. 6.20). Maximum interstory drift response calculated by nonlinear analysis was estimated

conservatively by linear analysis for structures that did not form a first-story mechanism. For structures whose base-shear strength was governed by a first-story collapse mechanism, linear analysis often resulted in unconservative estimates of first-story displacements (Fig. 6.23 and 6.25(b)).

Using limit analysis, a simple expression was developed to indicate whether a first-story mechanism was likely to form in a frame-wall structure with yielding columns (Eq. 6.18).

9.4 Strength of Small-Scale Structures

In order to evaluate procedures for estimating base shear, it was necessary to be able to estimate strengths of small-scale reinforced concrete test structures. First, the measured flexural strengths of simple small-scale components were compared with estimated strengths. Second, the lateral strength of the multi-story test structures during earthquake simulations was considered.

The measured strengths of small-scale reinforced concrete frame components were compared with strengths calculated by an "upper-bound" procedure. The procedure differs from standard analysis in that compatibility requirements are omitted from the procedure. Tensile reinforcement and compressed concrete are assumed to develop their strengths; compressive steel is assigned a stress (not exceeding its strength) to maximize section capacity (Fig. 7.5).

Flexural strengths measured for the components exceeded "upper-bound" strengths by approximately 10% (Table 7.7, option #1). Resolving this discrepancy required either a 135% increase in the assumed concrete compressive strength (Table 7.7, option #4) or a 10% increase in the assumed reinforcement

strength (Table 7.7, option #6). Because such increases in material strength were thought to be unlikely, the discrepancy between measured and calculated strengths remained unresolved.

The upper-bound procedure was also used to estimate the strength of reinforced concrete test structures. Estimates of base-shear and base-moment strengths were compared with base shears and base moments observed during dynamic tests. The discrepancy between measured and calculated strength was observed to vary according to the governing collapse mechanism.

If lateral strength was governed by a first-story mechanism (Fig. 7.1a) measured base shears exceeded calculated base shears by 5 to 7% (Table 7.12 and Fig. 7.10). This discrepancy was consistent with results from tests of components.

If lateral strength was governed by a mechanism involving beam yielding at all stories, measured base moments exceeded calculated base moments by approximately 25%. This discrepancy was larger than the discrepancy observed during tests of components.

9.5 Maximum Base-Shear Response

Obtaining reasonable estimates of maximum base-shear response for frame-wall structures is of practical interest because the total base shear for the structure represents a reasonable upper-bound for the design shear at the base of the wall. Three methods of estimating maximum base-shear response in frame-wall structures were considered in this study: limit analysis (Section 8.2), an approach developed by Kabeyasawa [6.18] (Section 8.3) and a procedure that combines results from limit analysis with results from linear response-spectrum

analysis (Section 8.4). Estimates from each method were compared with base shears measured during earthquake simulations of small-scale, frame-wall structures [2, 24].

The maximum base-shear response of six frame-wall structures was estimated by limit analysis for two assumptions of inertial-force distribution. In one set of calculations, inertial forces were assumed to vary linearly over the height of the structure. In a second set of calculations, inertial forces were assumed to be uniform over the height of the structure. Neither assumption was found to be satisfactory (Fig. 8.1 and 8.2) because the appropriate force distribution varies with the intensity of ground motion and the strength of the structure.

Kabeyasawa and Aoyama [6, 18] proposed a procedure to estimate maximum base-shear response (Section 8.3). Their estimate of maximum base shear is:

$$V_{\text{total max}} = V_{\text{limit}} + D_m * W * A_{g_{max}} \tag{8.5}$$

where,

$V_{\text{total max}}$ = estimate of maximum base-shear response

V_{limit} = base shear calculated by limit analysis assuming an inverted triangular inertial force distribution

W = total weight of the structure

$A_{g_{max}}$ = peak ground acceleration

D_m = approximately 0.3 (Section 8.3)

The procedure was found to lead to conservative estimates of maximum base shear for the small-scale frame-wall structures.

An alternate procedure was developed that combines limit analysis and linear response-spectrum analysis. The alternate estimate of base shear is:

$$V_{total\ max} = V_{limit} + \sum_{j=2}^{N} (W_j * Sa_j) \qquad (8.6)$$

where,

$V_{total\ max}$ = estimate of maximum base-shear response

V_{limit} = base shear calculated by limit analysis, assuming an inverted triangular inertial force distribution.

N = number of stories in the structure

W_j = effective weight of jth mode (Eq. 8.3)

S_{aj} = spectral acceleration (damping factor = 0.1) for response at half the initial frequency corresponding to the jth mode.

The response-spectrum procedure also resulted in a conservative estimate of the maximum base-shear response of the small-scale structures. The advantage of the Kabeyasawa procedure is its simplicity. The advantage of the response-spectrum procedure is its sensitivity to dominant frequencies of the structure and to ground-motion characteristics. If the design response spectrum resembles the response spectrum used for design of the test structures (Fig. 2.3), results of the Kabeyasawa and response-spectrum procedures are nearly identical.

9.6 Conclusions

The conclusions made in this study are relevant to the seismic response of frames with slender walls in which beams are stronger flexurally than columns.

Conclusions were drawn from the observed and calculated response of small-scale reinforced concrete structures subjected to N-S component of the 1940 El Centro record. Except for a tall first story, the frames were of relatively uniform interstory height and mass distribution. The study considered only in-plane response of the frames.

Principal conclusions of the study were:

(1) Slender walls provide a practical means of controlling drift in reinforced concrete frames with long spans. The experimental and analytical work presented in this study indicate that, given a design response spectrum and tolerable drift limits, linear analysis may be used to select appropriate wall dimensions. Mean drift can be estimated satisfactorily using linear response-spectrum analysis as described in Section 2.1.5. If a first-story collapse mechanism is prevented, interstory drifts may also be estimated by linear analysis.

(2) The effect on interstory drift of introducing a Mesnager hinge at the base of the wall may be estimated by linear response spectrum analysis, if a first-story mechanism is prevented.

(3) Limit analysis, assuming either an inverted triangular force distribution or a uniform force distribution, did not lead to satisfactory estimates of measured maximum base shear for test structures that did not develop a first-story collapse mechanism. The procedure proposed by Kabeyasawa [6, 18] and the response-spectrum procedure, developed in this study, resulted in improved estimates of maximum base shear.

9.7 Closing Remarks

Though only one type of structural configuration was considered in this study, the recommendations can be combined with elements of current practice to form an alternative design procedure. The procedure can be organized into six steps. These are:

1. Selection of design response spectrum. The response spectrum would be determined by building officials in consultation with seismologists and engineers. Ideally, the response spectrum would reflect the expected intensity and frequency content of ground motion at a particular site.

2. Selection of allowable drifts. Allowable drifts would depend on the fragility and value of the building contents, as well as the importance of the structure.

3. Check of drift maxima using linear analysis following the recommendations by Shimazaki [35, 38].

4. Check for story-collapse mechanisms. If story-collapse mechanisms form, linear analysis may be unconservative.

5. Design of members to resist shear. Columns and beams could be designed by assuming plastic hinges at the face of members. Wall shears could be calculated by following either the Kabeyasawa procedure [6, 18] or the response-spectrum procedure.

6. Design of reinforcement details. Detail requirements would be prescribed to provide structures with a minimum level of toughness. Ideally, the detailing requirements would be related to the maximum drift response expected for the structure.

The alternative procedure differs from current practice in four ways. Currently, the minimum stiffness of a structure is determined by comparing nominal drifts calculated for nominal forces with nominal allowable drifts. In the alternate procedure, an effort is made to estimate realistic levels of maximum drift response (Step 3).

The proposed procedure also departs from current practice by reducing the emphasis placed on base-shear strength. Rather than making base-shear strength the centerpiece of the design procedure, the alternative procedure relegates base-shear strength to a minor role. The minimum base-shear strength appears only indirectly in the new procedure (Eq. 2.1) (Step 3).

A third difference is that the alternate procedure explicitly requires limit-analysis calculations to check for story-collapse mechanisms (Step 4). Current practice requires only that the relative flexural strength of beams and columns at a joint be considered.

Finally, a fourth difference between current practice and the proposed procedure is the method used to estimate the maximum base shear in a wall (Step 5). In the proposed procedure the maximum base shear in the wall depends both on the strength of the structure and the intensity of ground motion.

TABLES

Table 2.1 Initial and Characteristic Periods

Length of Wall	Assumed Base Condition	Initial[a] Period (sec)	Characteristic[b] Period (sec)	Period[f] Ratio
1 1/2"	pinned	0.22	0.32	1.45
	fixed	0.21	0.30	1.36
3"	pinned	0.20	0.29	1.32
	equal end moments[c]	0.19	0.27	1.23
	fixed	0.18	0.26	1.18
4 1/2"	pinned	0.19	0.27	1.23
	equal end moments[d]	0.18	0.25	1.14
	fixed	0.16	0.23	1.05
6"	pinned	0.18	0.25	1.16
	equal end moments[e]	0.18	0.24	1.09
	fixed	0.15	0.21	0.95
7 1/2"	pinned	0.17	0.24	1.10
	fixed	0.14	0.19	0.88
9"	pinned	0.16	0.23	1.04
	fixed	0.13	0.18	0.80

[a]Modulus of elasticity = 3.0×10^6 psi
Gross-section properties

[b]Modulus of elasticity = 1.5×10^6 psi
Gross-section properties

[c]Spring stiffness = 1.0×10^6 k-in./rad

[d]Spring stiffness = 1.3×10^6 k-in./rad

[e]Spring stiffness = 1.5×10^6 k-in./rad

[f]Ratio of structure characteristic period to base-motion characteristic period

Table 2.2 Calculated Drifts for Characteristic Structure[a]

Length of Wall	Assumed Base-Condition	1-Story Drift (in.)	1-Story Drift (%)	Maximum Interstory Drift Ratio Story	Maximum Interstory Drift Ratio (%)	Overall Drift (in.)	Overall Drift (%)
1 1/2"	pinned	0.360	2.9	1	2.9	1.094	1.3
	fixed	0.298	2.4	1	2.4	1.051	1.2
3"	pinned	0.313	2.5	1	2.5	0.986	1.2
	equal end-moments[b]	0.243	2.0			0.943	1.1
	fixed	0.187	1.5	1	1.5	0.904	1.1
4 1/2"	pinned	0.267	2.2	1	2.2	0.937	1.1
	equal end-moments[c]	0.206	1.7			0.887	1.1
	fixed	0.126	1.0	2	1.3	0.830	1.0
6"	pinned	0.230	1.9	1	1.9	0.893	1.1
	equal end-moments[d]	0.187	1.5			0.855	1.0
	fixed	0.091	0.7	3	1.2	0.760	0.9
7 1/2"	pinned	0.203	1.6	1	1.6	0.861	1.02
	fixed	0.065	0.5	4	1.0	0.645	0.76
9"	pinned	0.182	1.5	1	1.5	0.831	0.98
	fixed	0.048	0.4	4	0.8	0.548	0.65

[a]RSS of first 3 modes
modulus of elasticity = $1.50 * 10^6$ psi
gross-section properties
El Centro response spectrum, 2% damping

[b]Spring stiffness = $1.0 * 10^6$ k-in./rad

[c]Spring stiffness = $1.3 * 10^6$ k-in./rad

[d]Spring stiffness = $1.5 * 10^6$ k-in./rad

Table 2.3 Substitute-Structure Damage Ratios

Story	Damage Ratio		
	Wall	Columns	Beams
1	2.0[a]	3.0	1.0
2,3	1.0	4.0	1.0
4-9	1.0	3.0	1.0

[a]Spring stiffness at Base = $5.0 * 10^6$ k-in./rad

Table 2.4 Moments of Inertia for Substitute Structure[a]

Story	Moment of Inertia, $in.^4$		
	Wall	Columns	Beams
1	2.567	0.0833[b]	1.021
2,3	5.134	0.0625[b]	1.021
4-9	5.134	0.0666[c]	0.792

[a]Calculated assuming a modulus of elasticity of 3,000,000 psi.

[b]Calculated for 6 No. 13 g. wires per face.

[c]Calculated for 4 No. 13 g. wires per face.

Table 2.5 Frequencies and Mode Shapes of Substitute Structure

	First Mode	Second Mode	Third Mode
Frequency, Hz	3.55	11.4	22.0
Mode Shape			
Level			
9	1.000	1.000	1.000
8	0.965	0.718	0.261
7	0.915	0.352	-0.477
6	0.847	-0.065	-0.920
5	0.789	-0.462	-0.856
4	0.663	-0.768	-0.330
3	0.553	-0.922	0.360
2	0.432	-0.897	0.855
1	0.291	-0.690	0.912

Table 2.6 Design Moments for Members

Story	Design Moments[a], k-in				
	Column A[b]	Wall[b]	Column C[b]	Column D[b]	Girder[c]
9	0.47/0.42	1.83/1.0	0.63/0.60	0.35/0.32	0.95
8	0.58/0.57	3.90/0.77	0.81/0.80	0.44/0.41	1.47
7	0.83/0.82	4.74/0.86	1.10/1.09	0.60/0.56	2.12
6	1.05/1.04	5.26/1.57	1.37/1.36	0.73/0.70	2.80
5	1.23/1.21	5.52/2.61	1.59/1.58	0.84/0.81	3.41
4	1.44/1.49	5.38/3.59	1.81/1.84	0.95/0.96	3.94
3	1.64/1.63	6.70/3.25	1.97/1.97	1.04/1.06	5.12
2	2.01/2.04	8.41/1.20	2.38/2.42	1.20/1.13	5.88
1	2.04/1.74	12.64/6.12	2.20/1.82	1.60/1.53	7.02

[a]RSS combination of first three modal moments at joint face.

[b]Top end-moment/bottom end-moment.

[c]Maximum end-moment for story.

Table 2.7 Reinforcement Schedule

Test Structure	Story	Columns A,C		Wall		Column D		Girder	
		Reinforcement Ratio[a] (%)	Bars per Face	Reinforcement Ratio[a] (%)	Bars per Face	Reinforcement Ratio[a] (%)	Bars per Face	Reinforcement Ratio[b] (%)	Bars per Face
ES1	9	1.17	2	1.46	2	1.17	2	1.76	2
	8	1.17	2	1.46	2	1.17	2	1.76	2
	7	1.17	2	1.46	2	1.17	2	1.76	2
	6	2.34	4	1.46	2	1.17	2	1.76	2
	5	2.34	4	1.46	2	1.17	2	1.76	2
	4	2.34	4	1.46	2	1.17	2	1.76	2
	3	2.34	4	1.46	2	1.17	2	2.64	3
	2	3.51	6	1.46	2	1.75	3	2.64	3
	1	3.51	6	1.46	2	1.75	3	2.64	3
ES2	4-9	1.17	2	1.46	2	1.17	2	1.76	2
	1-3	1.17	2	1.46	2	1.17	2	2.64	3

[a]Based on gross sections.
[b]Based on effective depth.

Table 3.1 Schedule of Earthquake Simulations

Run	Base-Motion	Nominal Effective Peak Acceleration
1	Simulated El Centro	0.35 g
2	1.5 * Simulated El Centro[a]	0.52 g
3	2.0 * Simulated El Centro	0.70 g
4	Sinusoidal Motion	0.20 g

[a]Magnification factor based on effective peak base acceleration.

Table 4.1 Key to Figures of Chapter 4

	All Runs	ES1				ES2			
		Run 1	Run 2	Run 3	Run 4	Run 1	Run 2	Run 3	Run 4
Ground Motions:									
Displacement Histories	4.1								
Acceleration Histories	4.2								
Fourier Amplitude Spectra	4.3								
Linear Response Spectra		4.4(a)	4.4(b)	4.4(c)	4.4(d)	4.4(e)	4.4(f)	4.4(g)	4.4(h)
Normalized Response Spectra	4.5								
Structural Response:									
Displacement Histories		4.6(a)	4.7(a)	4.8(a)	4.9(a)	4.10(a)	4.11(a)	4.12(a)	4.13(a)
Acceleration Histories		4.6(b)	4.7(b)	4.8(b)	4.9(b)	4.10(b)	4.11(b)	4.12(b)	4.13(b)
Story-Shear Histories		4.6(c)	4.7(c)	4.8(c)	4.9(c)	4.10(c)	4.11(c)	4.12(c)	4.13(c)
Displacement and Shear Distributions		4.6(d)	4.7(d)	4.8(d)	4.9(d)	4.10(d)	4.11(d)	4.12(d)	4.13(d)
Ratio of Interstory to Mean Drift		4.6(e)	4.7(e)	4.8(e)	4.9(e)	4.10(e)	4.11(e)	4.12(e)	4.13(e)
Fourier Amplitude Spectra		4.6(f)	4.7(f)	4.8(f)	4.9(f)	4.10(f)	4.11(f)	4.12(f)	4.13(f)
Hysteretic Response		4.6(g)	4.7(g)	4.8(g)	4.9(g)	4.10(g)	4.11(g)	4.12(g)	4.13(g)
Rotation and Slip at Base of Wall		4.6(h)	4.7(h)	4.8(h)	4.9(h)	4.10(h)	4.11(h)	4.12(h)	4.13(h)
Vertical and Transverse Accelerations		4.6(i)	4.7(i)	4.8(i)	4.9(i)	4.10(i)	4.11(i)	4.12(i)	4.13(i)
Base Rotation/1st-Story Drift Ratio	4.14, 4.15								
Fourier Amplitude Spectra of Ninth-Level Accelerations	4.16								
Crack Patterns	4.17								
Free-Vibration Tests	4.18								
Variation of Apparent Frequency	4.19								
North and South Top-Level Displ.	4.20								
Tables:									
Spectrum Intensities	4.3								
Summary of Response	4.2								
Response Maxima		4.4(a)	4.4(b)	4.4(c)	4.4(d)	4.4(e)	4.4(f)	4.4(g)	4.4(h)
Frequencies and Damping Ratios in Free-Vibration Tests	4.5								

Table 4.2 Summary of Measured Maxima

	Structure ES1				Structure ES2			
	Run 1	Run 2	Run 3	Run 4 (Sinusoidal)	Run 1	Run 2	Run 3	Run 4 (Sinusoidal)
Acceleration (g)								
Base-Level	0.36	0.52	0.62	0.26	0.35	0.52	0.61	0.25
Top-Level	0.98	1.42	1.57	1.23	0.82	1.21	1.25	0.82
Amplification Factor	2.7	2.7	2.5	4.8	2.3	2.3	2.0	3.2
Displacement (in.)								
First-Story	0.15	0.29	0.49	0.66	0.16	0.38	0.57	0.53
Top-Story	0.72	1.22	1.70	2.03	0.65	1.27	1.63	1.60
Drift Ratio (%)								
First-Story	1.2	2.3	4.0	5.3	1.3	3.1	4.6	4.3
Mean (Overall)	0.8	1.4	2.0	2.4	0.8	1.5	1.9	1.9
Ratio of 1st-Story to Mean	1.4	1.6	2.0	2.2	1.7	2.0	2.4	2.3
Base Shear (kips)	5.41	7.33	7.79	7.39	5.14	6.36	6.23	5.29
Base Shear Coefficient	0.52	0.71	0.75	0.71	0.50	0.61	0.60	0.51
Base Moment (kip-in.)	333	416	454	443	305	366	373	309

Table 4.3 Measured Characteristics of Base Motions

Structure	Run	Peak Displacement (in.)	Peak Acceleration (g)	Spectrum Intensities[a] Damping Ratio 2%	5%	10%	20%
ES1	1	-0.91	-0.36	12.0	9.6	7.9	6.2
	2	-1.32	-0.52	18.0	14.3	11.7	9.1
	3	-1.74	-0.62	23.8	18.9	15.4	12.0
	4	0.39	-0.26	14.4	11.3	8.9	6.8
ES2	1	-1.02	-0.35	11.9	9.5	7.7	6.1
	2	-1.24	-0.52	17.8	14.1	11.6	9.0
	3	-1.64	-0.61	23.5	18.6	15.2	11.8
	4	-0.47	-0.25	13.8	10.8	8.6	6.6

[a]Area below velocity response spectrum between periods of 0.04 and 1.0 sec. Units are in. [16]

Table 4.4 Measured Response Maxima
(a) ES1 - Run 1

Story/Level	Average Displacement (in.)	Interstory Drift Ratio (%)	Average Acceleration (g)	Story Shear (kips)
9	0.72 at 1.805 sec -0.68 at 1.970 sec	0.4 at 1.815 sec -0.4 at 1.960 sec	0.97 at 1.950 sec -0.98 at 1.815 sec	1.12 at 1.815 sec -1.11 at 1.950 sec
8	0.69 at 1.805 sec -0.65 at 1.970 sec	0.5 at 1.820 sec -0.5 at 3.040 sec	0.83 at 1.960 sec -0.90 at 1.815 sec	2.16 at 1.815 sec -2.05 at 1.955 sec
7	0.64 at 1.805 sec -0.61 at 1.975 sec	0.7 at 1.815 sec -0.6 at 1.965 sec	0.74 at 1.970 sec -0.80 at 1.805 sec	3.06 at 1.815 sec -2.81 at 1.960 sec
6	0.58 at 1.805 sec -0.56 at 1.975 sec	0.9 at 1.810 sec -0.9 at 1.970 sec	0.69 at 1.975 sec -0.70 at 1.805 sec	3.83 at 1.810 sec -3.44 at 1.965 sec
5	0.50 at 3.220 sec -0.49 at 1.975 sec	0.9 at 1.805 sec -0.9 at 1.965 sec	0.56 at 1.920 sec -0.59 at 1.790 sec	4.46 at 1.810 sec -3.99 at 1.970 sec
4	0.42 at 3.220 sec -0.41 at 1.980 sec	0.9 at 1.810 sec -1.0 at 1.970 sec	0.55 at 1.920 sec -0.55 at 1.780 sec	4.85 at 1.810 sec -4.41 at 1.970 sec
3	0.34 at 3.225 sec -0.33 at 1.985 sec	1.1 at 3.225 sec -1.0 at 1.975 sec	0.54 at 1.995 sec -0.47 at 1.780 sec	5.11 at 1.805 sec -4.70 at 1.975 sec
2	0.24 at 3.225 sec -0.24 at 1.985 sec	1.1 at 3.225 sec -1.0 at 1.985 sec	0.50 at 1.995 sec -0.38 at 1.770 sec	5.30 at 1.795 sec -5.05 at 1.985 sec
1	0.15 at 3.225 sec -0.15 at 1.990 sec	1.2 at 3.225 sec -1.2 at 1.990 sec	0.37 at 1.995 sec -0.31 at 1.750 sec	5.41 at 1.795 sec -5.39 at 1.990 sec

Table 4.4 (cont.) Measured Response Maxima
(b) ES1 - Run 2

Story/Level	Average Displacement (in.)	Interstory Drift Ratio (%)	Average Acceleration (g)	Story Shear (kips)
9	1.10 at 2.610 sec -1.22 at 2.815 sec	0.6 at 1.845 sec -0.7 at 2.805 sec	1.31 at 2.800 sec -1.42 at 1.835 sec	1.63 at 1.835 sec -1.50 at 2.800 sec
8	1.05 at 2.615 sec -1.16 at 2.815 sec	0.9 at 1.835 sec -0.9 at 2.810 sec	1.20 at 2.805 sec -1.23 at 1.845 sec	2.98 at 1.835 sec -2.88 at 2.805 sec
7	0.99 at 2.615 sec -1.08 at 2.815 sec	1.0 at 1.845 sec -1.1 at 2.805 sec	1.03 at 2.010 sec -1.05 at 1.845 sec	4.13 at 1.840 sec -3.97 at 2.805 sec
6	0.91 at 2.615 sec -0.98 at 2.035 sec	1.3 at 1.845 sec -1.4 at 2.805 sec	0.89 at 2.020 sec -0.89 at 2.595 sec	4.99 at 1.845 sec -4.78 at 2.810 sec
5	0.80 at 2.615 sec -0.88 at 2.035 sec	1.2 at 1.840 sec -1.6 at 2.815 sec	0.82 at 2.025 sec -0.85 at 2.600 sec	5.55 at 1.845 sec -5.33 at 2.015 sec
4	0.70 at 2.615 sec -0.74 at 2.035 sec	1.3 at 2.600 sec -1.6 at 2.820 sec	0.78 at 2.035 sec -0.77 at 2.605 sec	5.80 at 1.845 sec -5.97 at 2.020 sec
3	0.58 at 2.620 sec -0.61 at 2.040 sec	1.6 at 2.605 sec -1.7 at 2.030 sec	0.71 at 2.045 sec -0.77 at 1.885 sec	6.16 at 2.600 sec -6.53 at 2.025 sec
2	0.44 at 2.620 sec -0.45 at 2.040 sec	1.8 at 2.625 sec -1.8 at 2.040 sec	0.68 at 2.045 sec -0.73 at 1.880 sec	6.63 at 2.605 sec -6.96 at 2.030 sec
1	0.28 at 2.620 sec -0.29 at 2.040 sec	2.3 at 2.620 sec -2.3 at 2.040 sec	0.46 at 2.045 sec -0.72 at 2.620 sec	7.23 at 2.615 sec -7.33 at 2.040 sec

Table 4.4 (cont.) Measured Response Maxima
(c) ES1 - Run 3

Story/Level	Average Displacement (in.)	Interstory Drift Ratio (%)	Average Acceleration (g)	Story Shear (kips)
9	1.64 at 2.725 sec -1.70 at 2.085 sec	0.8 at 2.725 sec -0.8 at 2.075 sec	1.33 at 1.715 sec -1.57 at 1.860 sec	1.80 at 1.860 sec -1.53 at 1.715 sec
8	1.57 at 2.725 sec -1.64 at 2.085 sec	0.8 at 1.865 sec -0.8 at 2.045 sec	1.13 at 1.725 sec -1.24 at 1.865 sec	3.18 at 1.860 sec -2.65 at 1.720 sec
7	1.49 at 2.725 sec -1.57 at 2.085 sec	1.5 at 2.715 sec -1.3 at 2.065 sec	1.08 at 2.055 sec -1.09 at 2.705 sec	4.17 at 1.865 sec -3.68 at 2.050 sec
6	1.36 at 2.725 sec -1.45 at 2.090 sec	1.6 at 2.720 sec -1.4 at 2.070 sec	1.04 at 2.060 sec -1.01 at 2.290 sec	4.77 at 2.060 sec -5.07 at 2.715 sec
5	1.22 at 2.725 sec -1.34 at 2.090 sec	1.8 at 2.725 sec -2.1 at 2.070 sec	0.89 at 2.070 sec -0.94 at 2.285 sec	5.70 at 2.065 sec -5.80 at 2.715 sec
4	1.06 at 2.720 sec -1.16 at 2.095 sec	2.1 at 2.720 sec -2.2 at 2.065 sec	0.77 at 2.110 sec -0.86 at 1.915 sec	6.55 at 2.065 sec -6.31 at 2.720 sec
3	0.87 at 2.725 sec -0.97 at 2.095 sec	2.4 at 2.725 sec -2.4 at 2.085 sec	0.73 at 2.100 sec -0.90 at 1.900 sec	7.11 at 2.065 sec -6.56 at 2.720 sec
2	0.66 at 2.730 sec -0.75 at 2.095 sec	2.7 at 2.730 sec -2.9 at 2.095 sec	0.68 at 2.100 sec -0.95 at 1.905 sec	7.42 at 2.060 sec -7.70 at 1.895 sec
1	0.41 at 2.725 sec -0.49 at 2.095 sec	3.4 at 2.725 sec -4.0 at 2.095 sec	0.60 at 2.945 sec -0.77 at 1.905 sec	7.70 at 2.085 sec -7.79 at 1.900 sec

Table 4.4 (cont.) Measured Response Maxima
(d) ES1 - Run 4

Story/Level	Average Displacement (in.)	Interstory Drift Ratio (%)	Average Acceleration (g)	Story Shear (kips)
9	2.03 at 3.230 sec -2.04 at 2.990 sec	0.7 at 2.740 sec -0.7 at 2.510 sec	1.18 at 2.515 sec -1.23 at 2.740 sec	1.42 at 2.740 sec -1.34 at 2.515 sec
8	1.97 at 3.225 sec -1.98 at 2.990 sec	1.0 at 2.735 sec -1.0 at 2.495 sec	1.08 at 2.510 sec -1.06 at 2.735 sec	2.57 at 2.740 sec -2.59 at 2.515 sec
7	1.88 at 3.230 sec -1.92 at 2.990 sec	1.1 at 2.750 sec -1.4 at 2.990 sec	1.05 at 2.490 sec -0.99 at 2.725 sec	3.58 at 2.735 sec -3.70 at 2.510 sec
6	1.79 at 3.230 sec -1.80 at 2.990 sec	1.9 at 2.740 sec -1.7 at 2.510 sec	1.04 at 2.495 sec -1.04 at 2.715 sec	4.44 at 2.735 sec -4.66 at 2.510 sec
5	1.63 at 3.230 sec -1.66 at 2.990 sec	1.9 at 2.755 sec -2.4 at 2.990 sec	0.87 at 2.500 sec -0.94 at 2.715 sec	5.29 at 2.725 sec -5.58 at 2.500 sec
4	1.47 at 3.225 sec -1.45 at 2.990 sec	2.2 at 2.735 sec -2.3 at 2.510 sec	0.77 at 2.960 sec -0.75 at 2.710 sec	6.07 at 2.720 sec -6.34 at 2.500 sec
3	1.28 at 3.230 sec -1.26 at 2.985 sec	3.3 at 3.230 sec -3.3 at 2.990 sec	0.67 at 2.960 sec -0.62 at 2.765 sec	6.71 at 2.725 sec -6.85 at 2.505 sec
2	0.98 at 3.235 sec -0.96 at 2.985 sec	3.7 at 3.210 sec -3.9 at 3.005 sec	0.64 at 2.465 sec -0.55 at 2.695 sec	7.16 at 2.730 sec -7.09 at 2.505 sec
1	0.66 at 3.230 sec -0.62 at 2.985 sec	5.3 at 3.230 sec -5.0 at 2.985 sec	0.50 at 2.465 sec -0.46 at 2.695 sec	7.39 at 2.725 sec -7.24 at 2.515 sec

Table 4.4 (cont.) Measured Response Maxima
(e) ES2 - Run 1

Story/Level	Average Displacement (in.)	Interstory Drift Ratio (%)	Average Acceleration (g)	Story Shear (kips)
9	0.65 at 1.810 sec -0.57 at 1.975 sec	0.2 at 3.225 sec -0.2 at 1.955 sec	0.78 at 1.950 sec -0.82 at 1.810 sec	0.94 at 1.810 sec -0.90 at 1.950 sec
8	0.64 at 1.810 sec -0.55 at 1.975 sec	0.4 at 3.230 sec -0.4 at 1.960 sec	0.71 at 1.955 sec -0.78 at 1.815 sec	1.81 at 1.810 sec -1.70 at 1.950 sec
7	0.60 at 1.810 sec -0.52 at 1.975 sec	0.6 at 1.810 sec -0.4 at 5.830 sec	0.65 at 1.960 sec -0.73 at 1.820 sec	2.62 at 1.815 sec -2.41 at 1.955 sec
6	0.55 at 1.805 sec -0.49 at 1.975 sec	0.7 at 1.815 sec -0.7 at 1.965 sec	0.59 at 1.970 sec -0.66 at 1.810 sec	3.35 at 1.815 sec -3.00 at 1.955 sec
5	0.49 at 1.805 sec -0.43 at 1.975 sec	0.8 at 1.815 sec -0.7 at 1.960 sec	0.53 at 1.975 sec -0.59 at 1.785 sec	3.96 at 1.815 sec -3.50 at 1.960 sec
4	0.43 at 1.805 sec -0.37 at 1.980 sec	0.8 at 1.810 sec -0.8 at 1.970 sec	0.52 at 1.995 sec -0.52 at 1.775 sec	4.43 at 1.810 sec -3.93 at 1.970 sec
3	0.35 at 1.805 sec -0.30 at 1.980 sec	1.1 at 1.805 sec -0.9 at 1.970 sec	0.54 at 3.070 sec -0.49 at 1.780 sec	4.73 at 1.810 sec -4.29 at 1.970 sec
2	0.25 at 1.800 sec -0.23 at 1.985 sec	1.1 at 1.800 sec -0.9 at 1.985 sec	0.51 at 1.990 sec -0.41 at 1.770 sec	5.00 at 1.800 sec -4.60 at 1.985 sec
1	0.16 at 1.805 sec -0.15 at 1.990 sec	1.3 at 1.805 sec -1.2 at 1.990 sec	0.41 at 1.990 sec -0.39 at 1.765 sec	5.14 at 1.795 sec -5.03 at 1.985 sec

Table 4.4 (cont.) Measured Response Maxima
(f) ES2 - Run 2

Story/Level	Average Displacement (in.)	Interstory Drift Ratio (%)	Average Acceleration (g)	Story Shear (kips)
9	1.27 at 2.675 sec -1.15 at 2.045 sec	0.3 at 2.660 sec -0.4 at 2.025 sec	1.01 at 2.815 sec -1.21 at 1.825 sec	1.39 at 1.825 sec -1.16 at 2.815 sec
8	1.24 at 2.670 sec -1.12 at 2.045 sec	0.6 at 1.830 sec -0.6 at 2.045 sec	0.82 at 2.030 sec -1.08 at 1.830 sec	2.58 at 1.830 sec -1.98 at 2.820 sec
7	1.18 at 2.675 sec -1.06 at 2.050 sec	0.9 at 2.670 sec -0.7 at 2.030 sec	0.78 at 2.050 sec -0.97 at 1.840 sec	3.58 at 1.830 sec -2.77 at 2.025 sec
6	1.11 at 2.675 sec -1.00 at 2.045 sec	1.3 at 2.665 sec -1.1 at 2.045 sec	0.75 at 2.040 sec -0.80 at 1.845 sec	4.37 at 1.835 sec -3.59 at 2.025 sec
5	0.99 at 2.675 sec -0.90 at 2.050 sec	1.1 at 2.675 sec -1.2 at 2.040 sec	0.76 at 2.845 sec -0.72 at 2.625 sec	4.93 at 1.835 sec -4.39 at 2.040 sec
4	0.89 at 2.675 sec -0.79 at 2.050 sec	1.5 at 2.670 sec -1.4 at 2.045 sec	0.77 at 2.845 sec -0.72 at 2.630 sec	5.26 at 1.840 sec -5.07 at 2.035 sec
3	0.75 at 2.675 sec -0.67 at 2.050 sec	2.0 at 2.675 sec -1.8 at 2.040 sec	0.58 at 2.845 sec -0.73 at 1.880 sec	5.42 at 1.845 sec -5.68 at 2.030 sec
2	0.57 at 2.675 sec -0.50 at 2.050 sec	2.1 at 2.675 sec -1.9 at 2.050 sec	0.51 at 2.465 sec -0.70 at 1.870 sec	5.64 at 2.670 sec -6.12 at 2.025 sec
1	0.38 at 2.680 sec -0.34 at 2.055 sec	3.1 at 2.680 sec -2.7 at 2.055 sec	0.44 at 2.915 sec -0.63 at 1.870 sec	6.12 at 1.870 sec -6.36 at 2.020 sec

Table 4.4 (cont.) Measured Response Maxima
(g) ES2 - Run 3

Story/Level	Average Displacement (in.)	Interstory Drift Ratio (%)	Average Acceleration (g)	Story Shear (kips)
9	1.55 at 3.340 sec -1.63 at 2.125 sec	0.4 at 2.325 sec -0.5 at 2.125 sec	1.03 at 1.715 sec -1.25 at 1.870 sec	1.44 at 1.870 sec -1.19 at 1.715 sec
8	1.52 at 3.345 sec -1.59 at 2.130 sec	0.7 at 3.320 sec -0.8 at 2.120 sec	0.91 at 2.110 sec -1.01 at 1.875 sec	2.51 at 1.875 sec -2.16 at 2.105 sec
7	1.47 at 3.345 sec -1.52 at 2.130 sec	0.8 at 3.325 sec -0.8 at 2.110 sec	0.88 at 2.085 sec -0.75 at 1.855 sec	3.23 at 1.875 sec -3.09 at 2.105 sec
6	1.40 at 3.345 sec -1.45 at 2.135 sec	1.4 at 3.300 sec -1.4 at 2.105 sec	0.89 at 2.085 sec -0.71 at 1.905 sec	3.52 at 1.875 sec -3.90 at 2.105 sec
5	1.28 at 3.345 sec -1.33 at 2.135 sec	1.3 at 3.310 sec -1.6 at 2.115 sec	0.77 at 2.090 sec -0.82 at 1.910 sec	4.08 at 3.315 sec -4.65 at 2.095 sec
4	1.18 at 3.350 sec -1.19 at 2.130 sec	1.8 at 3.320 sec -1.8 at 2.095 sec	0.68 at 2.145 sec -0.88 at 1.905 sec	4.71 at 3.310 sec -5.36 at 2.095 sec
3	1.03 at 3.350 sec -1.04 at 2.135 sec	2.5 at 3.335 sec -2.4 at 2.120 sec	0.65 at 3.095 sec -0.86 at 1.905 sec	5.07 at 3.310 sec -5.82 at 2.095 sec
2	0.80 at 3.355 sec -0.83 at 2.140 sec	3.0 at 3.355 sec -2.9 at 2.130 sec	0.64 at 3.090 sec -0.70 at 1.915 sec	5.72 at 1.910 sec -6.00 at 2.100 sec
1	0.54 at 3.350 sec -0.57 at 2.135 sec	4.3 at 3.350 sec -4.6 at 2.135 sec	0.59 at 2.755 sec -0.63 at 1.920 sec	6.17 at 1.915 sec -6.23 at 2.120 sec

Table 4.4 (cont.) Measured Response Maxima
(h) ES2 - Run 4

Story/Level	Average Displacement (in.)	Interstory Drift Ratio (%)	Average Acceleration (g)	Story Shear (kips)
9	1.60 at 2.800 sec -1.59 at 3.030 sec	0.4 at 2.775 sec -0.5 at 3.035 sec	0.81 at 2.565 sec -0.82 at 2.745 sec	0.95 at 2.745 sec -0.93 at 2.565 sec
8	1.57 at 2.795 sec -1.55 at 3.030 sec	0.6 at 2.790 sec -0.7 at 2.570 sec	0.75 at 2.560 sec -0.73 at 2.750 sec	1.72 at 2.795 sec -1.78 at 2.560 sec
7	1.51 at 2.795 sec -1.49 at 3.025 sec	0.6 at 2.800 sec -0.5 at 2.560 sec	0.66 at 2.560 sec -0.71 at 2.775 sec	2.46 at 2.790 sec -2.54 at 2.560 sec
6	1.46 at 2.795 sec -1.45 at 3.030 sec	1.7 at 2.785 sec -1.5 at 3.025 sec	0.65 at 2.535 sec -0.71 at 2.780 sec	3.14 at 2.785 sec -3.15 at 2.560 sec
5	1.31 at 2.800 sec -1.32 at 3.030 sec	1.3 at 2.800 sec -1.5 at 3.025 sec	0.61 at 2.540 sec -0.68 at 2.770 sec	3.88 at 2.780 sec -3.65 at 3.025 sec
4	1.19 at 2.795 sec -1.18 at 3.030 sec	1.9 at 2.785 sec -1.7 at 3.005 sec	0.52 at 3.005 sec -0.60 at 2.775 sec	4.52 at 2.775 sec -4.07 at 3.020 sec
3	1.03 at 2.795 sec -1.03 at 3.030 sec	2.6 at 2.795 sec -2.5 at 3.030 sec	0.38 at 3.010 sec -0.46 at 2.355 sec	4.95 at 2.775 sec -4.48 at 3.015 sec
2	0.80 at 2.805 sec -0.81 at 3.030 sec	3.0 at 2.805 sec -3.1 at 3.030 sec	0.38 at 2.510 sec -0.46 at 2.800 sec	5.08 at 2.780 sec -4.76 at 3.020 sec
1	0.53 at 2.800 sec -0.53 at 3.030 sec	4.3 at 2.800 sec -4.3 at 3.035 sec	0.27 at 2.505 sec -0.33 at 2.805 sec	5.29 at 2.795 sec -4.94 at 3.020 sec

Table 4.5 Response at Base of Wall

		Structure ES1				Structure ES2			
		Run 1	Run 2	Run 3	Run 4	Run 1	Run 2	Run 3	Run 4
MAXIMA:									
Horizontal Displacement, in.[a]		0.009	0.017	0.035	0.052	0.013	0.032	0.046	0.041
		-0.011	-0.025	-0.053	-0.066	-0.011	-0.033	-0.054	-0.050
Rotation, rad		0.009	0.019	0.024	0.035	0.011	0.027	0.035	0.033
		-0.009	-0.018	-0.032	-0.041	-0.009	-0.024	-0.040	-0.036
Calculated Slip, in.		0.001	0.000	0.011	0.017	0.003	0.008	0.012	0.009
		-0.002	-0.008	-0.021	-0.025	-0.002	-0.009	-0.015	-0.014
PERMANENT OFFSET:									
Horizontal Displacement, in.	Dial Gauge	-0.0005	-0.0025			-0.0007	-0.0080		
	LVDT	-0.0007	-0.0017	0.0030	0.0019	0.0004	0.0060	0.0069	0.0048
Rotation, rad		0.0001	-0.0003	-0.0019	-0.0005	-0.0001	0.0001	-0.0010	-0.0008
Calculated Slip, in.		-0.0008	-0.0014	0.0049	0.0024	0.0005	0.0059	0.0079	0.0056

[a]Measured one in. above base girder

Table 4.6 Natural Frequencies and Damping Factors Measured During Free-Vibration Tests

Structure	Free-Vibration Test	Estimated Damping Factor (%)	Natural Frequencies		
			Mode 1 (hz)	Mode 2 (hz)	Mode 3 (hz)
Structure ES1					
	Before Run 1	4	5.5	17.8	31.1
	Following Run 1	12	3.3	11.1	22.0
	Following Run 2	12	2.7	9.6	19.2
	Following Run 3	15	2.2	8.6	17.6
	Before Run 4	15	2.3	8.6	17.7
	Following Run 4	18	2.1	8.5	17.3
Structure ES2					
	Before Run 1	5	6.2	19.3	33.1
	Following Run 1	13	4.0	13.3	25.6
	Following Run 2	14	2.8	10.7	21.3
	Following Run 3	15	2.3	9.5	19.8
	Before Run 4	14	2.4	9.8	19.9
	Following Run 4	16	2.3	9.5	19.9

Table 4.7 Ratios of Maximum Response of North Frame to Maximum Response of South Frame[a]

	Structure ES1				Structure ES2			
	Run 1	Run 2	Run 3	Run 4	Run 1	Run 2	Run 3	Run 4
Positive Acceleration	1.15	1.07	1.10	1.05	1.08	1.10	1.10	1.14
Negative Acceleration	1.05	1.08	1.02	1.07	1.05	1.07	1.05	1.11
Positive Displacement	1.11	1.14	1.08	1.05	1.05	1.11	1.09	1.09
Negative Displacement	1.21	1.14	1.14	1.09	1.09	1.08	1.13	1.11

[a]Mean of ratios at all levels

Table 5.1 Base-Motion Characteristics and Displacement Response Maxima

	Maximum Base Acceleration (g)	Housner Spectrum Intensity[a] (in.)	Modified Spectrum Intensity[b] (in.)	Maximum Interstory Drift Ratio (%)	Maximum Overall Drift Ratio (%)
Design Intensity Earthquake					
SS1 - Run 1	0.35	8.2	3.3	3.1	1.2
SS2 - Run 1	0.35	6.9	2.9	1.4	1.1
ES1 - Run 1	0.36	7.9	3.3	1.2	0.8
ES2 - Run 1	0.35	7.7	3.2	1.3	0.8
Mean	0.35	7.7	3.2		
1.5 * Design Intensity Earthquake					
SS1 - Run 3	0.53	11.1	4.6	4.3	1.5
SS2 - Run 4	0.66	12.1	5.0	2.9	1.8
ES1 - Run 2	0.52	11.7	4.9	2.3	1.4
ES2 - Run 2	0.52	11.6	4.8	3.1	1.5
Mean	0.56	11.6	4.8		
2.0 * Design Intensity Earthquake					
SS1 -	-	-	-	-	-
SS2 - Run 5	0.99	17.7	7.4	4.3	2.4
ES1 - Run 3	0.62	15.4	6.4	4.0	2.0
ES2 - Run 3	0.61	15.2	6.3	4.6	1.9
Mean	0.74	16.1	20.1		

[a]Area below velocity response spectrum between periods of 0.04 and 1.0 sec (10% damping)

[b]Area below velocity response spectrum between periods of 0.15 and 0.5 sec (10% damping)

Table 5.2 Properties of Frame Structures[a]

	SS1[b]	SS2[b]	ES1	ES2	FNW[c]	MF1[d]
Cross-Sectional Area of Vertical Members, $in.^2$	9.0	9.0	13.5	13.5	12.0	12.0
Maximum Column Reinforcement Ratio, %	2.9	4.7	3.5	1.5	1.8	1.3
Area of Vertical Steel in First Story, $in.^2$	0.26	0.42	0.32	0.20	0.21	0.16
Volume of Flexural Reinforcement in Vertical Members, $in.^3$	13.4	18.0	19.4	15.0	11.9	10.7

[a]Quantities given for a single frame

[b]Tested by Schultz [32]

[c]Tested by Moehle [24]

[d]Tested by Healey [15]

Table 6.1 Flexural Properties Used in Model of Structure ES2

Story/Level	Cracking Moment[1] (k-in.)	Yield Moment (k-in.)	Ultimate Moment (k-in.)	Yield Curvature (rad/in.)
Wall				
8,9	4.26	11.26	11.86	0.00071
7	4.37	11.54	12.11	0.00071
6	4.48	11.77	12.36	0.00071
5	4.59	12.01	12.61	0.00071
4	4.70	12.23	12.86	0.00072
3	4.80	12.45	13.11	0.00072
2	4.91	12.74	13.36	0.00077
1	5.02	12.95	13.61	0.00078
Base	3.00	10.20	10.37	0.0042
Columns				
9	0.49	0.88	0.99	0.0024
8	0.52	0.95	1.06	0.0024
7	0.56	1.03	1.13	0.0025
6	0.59	1.11	1.20	0.0025
5	0.63	1.18	1.27	0.0027
4	0.67	1.25	1.34	0.0027
3	0.70	1.32	1.41	0.0028
2	0.74	1.39	1.47	0.0029
1	0.77	1.46	1.54	0.0029
Beams				
4-9	1.01	4.45	4.62	0.0018
1-3	1.01	6.49	6.67	0.0019

[1]Modulus of rupture was assumed to be equal to 800 psi.

Table 6.2 Calculated and Measured Response Maxima for Structure ES2

	Maximum Overall Drift Ratio %	Maximum Interstory Drift Ratio[1] %	Maximum Base Shear Coefficient
Design Base Motion			
Calculated	0.9	1.5	0.50
Observed	0.8	1.3	0.50
1.5* Design Base Motion			
Calculated	1.3	2.9	0.63
Observed	1.5	3.1	0.61
2.0* Design Base Motion			
Calculated	1.8	4.1	0.68
Observed	1.9	4.6	0.60

[1]Maximum interstory drift ratio occurred in first story.

Table 6.3 Influence of Parameters of Section 6.2 on Computed Response

	GOF Index		Maximum Drift Ratio	
	Overall	First Story	Overall %	First-Story %
Unloading Slope Exponent, α				
0.2	0.89	0.91	0.84	1.49
0.4	0.89	0.94	0.84	1.49
0.8	0.94	1.11	0.84	1.56
Stiffness Proportional Damping, %				
0.1	0.87	0.94	0.84	1.50
0.5	0.89	0.94	0.84	1.49
1.0	0.90	0.93	0.82	1.46
2	0.93	0.93	0.80	1.41
Mass Proportional Damping, %				
0.5	0.91	0.92	0.82	1.46
2	1.11	1.06	0.73	1.30
Combined Stiffness and Mass Proportional Damping, %				
0.5	0.90	0.92	0.82	1.45
2	1.07	1.03	0.74	1.33
Bond Stress, psi				
100	0.97	1.05	0.86	1.53
150	0.89	0.94	0.84	1.49
300	1.43	1.52	0.78	1.46
infinity	1.65	1.68	0.63	1.25

Table 6.4 Influence of Member Properties on Computed Response

	GOF Index		Maximum Drift Ratio	
	Top Story	First Story	Top Story %	First Story %
Column Strength[1]				
75%	0.86	0.92	0.85	1.49
100%	0.89	0.94	0.84	1.49
200%	1.89	1.97	0.81	1.35
Beam Strength[1]				
50%	1.22	1.10	0.96	1.51
100%	0.89	0.94	0.84	1.49
200%	1.60	1.94	0.72	1.70
Wall Strength[1]				
50%	0.80	1.11	0.82	1.75
100%	0.89	0.94	0.84	1.49
200%	0.98	0.98	0.86	1.34
Strength at Base of Wall[1]				
50%	0.85	1.29	0.83	1.85
100%	0.89	0.94	0.84	1.49
200%	1.12	1.10	0.83	1.24
Yield Curvature at Base of Wall[1]				
50%	0.93	0.95	0.83	1.44
100%	0.89	0.94	0.84	1.49
200%	0.84	1.04	0.83	1.63

[1]Values expressed as percentage of strength or curvature of that of ES2

Table 6.5 Influence of Depth of Wall and Mesnager Hinge on Maximum Drift Ratios[3]

Ratio of Wall to Column Depth[1]	Maximum Overall Drift Ratio			Maximum Interstory Drift Ratio		
	Mesnager Hinge[2] (%)	Fixed Base (%)	Improvement (%)	Mesnager Hinge[2] (%)	Fixed Base (%)	Improvement (%)
Design Base Motion						
1.0		0.87			4.83	
2.0		0.82			3.00	
3.0	0.84	0.78	7	1.51	1.22	19
4.0	0.79	0.56	29	1.24	0.74	40
5.0	0.84	0.57	32	1.07	0.69	36
6.0	0.83	0.52	37	0.93	0.58	38
1.5* Design Base Motion						
1.0		1.33			7.92	
2.0		1.22			5.60	
3.0	1.42	1.30	8	3.96	2.71	32
4.0	1.34	1.21	10	2.59	1.58	39
5.0	1.43	1.11	30	2.20	1.29	41
6.0	1.46	0.88	40	1.80	0.95	47
2* Design Base Motion						
1.0		2.35			14.55	
2.0		1.67			8.25	
3.0	1.66	1.73	-4	5.50	4.07	26
4.0	1.88	1.72	8	3.58	2.53	29
5.0	2.00	1.76	12	3.04	1.98	35
6.0	2.05	1.60	22	2.62	1.71	35

[1]Column Depth was 1.5 in.
Wall reinforcement ratio was 1.5% for all wall depths.

[2]Mesnager hinge yield moment was 10.2 k-in. for all wall depths.

[3]Response calculated assuming a post-yield slope of 0.025% of the slope of the moment-curvature relationship before yield.

Table 6.6 Effect on Calculated Response of Doubling Selected Parameters

Parameter	Effect on Response of Doubling Each Parameter			
	GOF Index		Maximum Drift Ratio	
	Top Level[1]	First Story[1]	Overall[2]	First Story[2]
Parameters Considered in Section 6.2				
Unloading Slope Exponent	+6%	+18%	0%	+5%
Stiffness Proportional Damping	+1%	-1%	-2%	-2%
Bond Strength	+61%	+62%	-7%	-2%
Parameters Considered in Section 6.3				
Column Strength	+110%	+112%	-3%	-10%
Beam Strength	+80%	+106%	-14%	-14%
Wall Strength	+10%	+4%	+2%	-10%
Strength at Base of Wall	+26%	+17%	-1%	-17%
Yield Curvature at Base of Wall	-6%	+11%	-1%	+9%
Wall Depth			-1%	-38%
Wall Depth and "Fixed Base"			-38%	-61%

[1]Variation in GOF Index expressed as percentage of GOF index for Structure ES2.

[2]Variation in maximum drift ratio expressed as percentage of maximum drift ratio for Structure ES2.

Table 7.1 Standard Calculated Flexural Strengths of First-Story Members for SS1, SS2, ES1 and ES2

Location	Reinforcement per Face	Area of Steel per Face ($in.^2$)	Width b (in.)	d^a (in.)	d'^b (in.)	f_c' (psi)	f_y (ksi)	$M_o{}^c$ (k-in.)	$M_1{}^d$ (k-in.)
Structure ES1									
West and Interior Col.	6-13 g	0.0395	1.52	1.18	0.31	4350	55.0	2.20	2.75
Wall (1st-story)	2-7 g	0.0492	1.52	4.14	0.35	4350	57.6	11.53	13.76
Wall (Base)	2-13 g	0.0132	1.51	4.14	0.35	4350	55.0	10.41	12.31
	$2\sqrt{2}$-7 g	0.0696		2.25			57.6		
East Column	3-13 g	0.0197	1.52	1.21	0.28	4350	55.0	1.26	1.85
Structure ES2									
All Columns	2-13 g	0.0132	1.52	1.21	0.28	4800	55.0	0.93	1.54
Wall (1st-story)	2-7 g	0.0492	1.51	4.12	0.37	4800	57.6	11.49	13.69
Wall (Base)	2-13 g	0.0132	1.48	4.13	0.37	4800	55.0	10.50	12.48
	$2\sqrt{2}$-7 g	0.0696		2.25			57.6		
Structure SS2									
All Columns	8-13 g	0.0526	1.53	1.20	0.31	5260	55.0	2.96	3.50
Structure SS1									
All Columns	5-13 g	0.0329	1.53	1.16	0.33	5590	55.0	1.92	2.46

[a]Effective depth to bottom reinforcement
[b]Effective depth to top reinforcement
[c]Flexural strength calculated for zero axial load
[d]Flexural strength calculated for first-story axial load (1.29 k)

Table 7.2 Calculated and Measured Base-Shear Strengths for SS1, SS2, ES1 and ES2

Structure	(1) Calculated Base-Shear Strength (k)	(2) Upper Bound Base-Shear Strength (k)	(3) Maximum Measured Base-Shear During Dynamic Tests (k)	(4) Maximum Measured Base-Shear During Static Tests (k)
SS1	3.50	3.64	3.93	-
SS2	4.98	5.26	5.50	-
ES1	7.24	7.65	7.79	6.54
ES2	6.29	6.63	6.36	5.72

1: Base-shear strength calculated based on standard compatibility assumptions (Sec. 7.2.1)

2: Base-shear strength calculated following upper-bound procedure (Sec. 7.3)

3: Sum of lateral inertial forces

4: Lateral load was applied at first level

Table 7.3 Positive and Negative Measured Base Shears and Base Moments[a]

Structure	Run	Maximum Positive Base Shear (k)	Maximum Negative Base Shear (k)	$\frac{V+}{V-}$[b]	Maximum Positive Base Moment (k-in.)	Maximum Negative Base Moment (k-in.)	$\frac{M+}{M-}$[c]
ES1	1	5.41	-5.39	1.00	333	-305	1.09
	2	7.23	-7.33	0.99	398[d]	-408	0.97
	3	7.70	-7.79	0.99	431[d]	-442	0.97
	4	7.39	-7.24	1.02	421	-429	0.98
	Mean			1.00			1.01
ES2	1	5.14	-5.03	1.02	300	-268	1.12
	2	6.12	-6.36	0.96	360	-352	1.02
	3	6.17	-6.23	0.99	310[d]	-361	0.86
	4	5.29	-4.94	1.07	297	-288	1.03
	Mean			1.01			1.01

[a]Base moments do not include P-Δ effect

[b]Ratio of maximum positive base shear to maximum negative base shear

[c]Ratio of maximum positive base moment to maximum negative base moment

[d]Maximum base shear and base moment did not occur during same cycle

Table 7.4 Upper-Bound and Measured Flexural Strengths of Beams [19]

Designation	Steel Area Per Face ($in.^2$)	Beam Width b (in.)	Beam Depth h (in.)	d[a] (in.)	d'[b] (in.)	Concrete Compressive Strength (psi)	Tension Steel Stress[c] (ksi)	Compression Steel Stress[c] (ksi)	Nominal Flexural Strength (k-in.)	Measured Flexural Strength (k-in.)
Schipper - Interior Joints[d]										
2-1A	0.0132	1.54	1.41	1.21	0.26	5740	55.5	55.5	0.93	1.02
2-1	0.0132	1.50	1.45	1.15	0.25	5740	55.5	55.5	0.88	1.00
2-2	0.0132	1.51	1.44	1.07	0.19	6570	55.5	55.5	0.78	0.95
2-3	0.0132	1.48	1.42	1.18	0.24	6570	55.5	55.5	0.91	0.95
3-1A	0.0132	1.51	1.40	1.18	0.22	5740	55.5	55.5	0.88	0.95
3-1	0.0132	1.50	1.41	1.21	0.23	5740	55.5	55.5	0.91	1.05
3-2	0.0132	1.49	1.38	1.20	0.24	6570	55.5	55.5	0.89	1.03
3-3	0.0132	1.51	1.42	1.20	0.25	6570	55.5	55.5	0.95	0.99
Kreger and Abrams - Interior Joints[d]										
IJ1	0.0197	1.49	1.48	1.22	0.27	4370	55.5	20.0	1.25	1.41
IJ2	0.0132	1.50	1.51	1.21	0.26	4370	55.5	55.5	0.91	1.07
IJ3	0.0197	1.50	1.52	1.22	0.27	4370	55.5	20.0	1.25	1.47
IJ4	0.0132	1.47	1.45	1.20	0.27	4370	55.5	55.5	0.88	1.04
Kreger and Abrams - Exterior Joints										
EJ2	0.0197	1.47	1.37	1.19	0.24	3580	55.5	0.0	1.17	1.43
EJ3	0.0132	1.50	1.46	1.21	0.33	3580	55.5	55.5	0.90	1.03
EJ4	0.0132	1.49	1.49	1.21	0.32	3580	55.5	55.5	0.88	0.97
EJ5	0.0197	1.49	1.45	1.14	0.20	3580	55.5	0.0	1.12	1.33

[a]Effective depth to bottom reinforcement
[b]Effective depth to top reinforcement
[c]Tensile stress is positive
[d]Mean properties for two beams

Table 7.5 Upper-Bound and Measured Flexural Strengths of Columns and Walls

Designation	Steel Area Per Face ($in.^2$)	Section Width b (in.)	Section Height h (in.)	d[a] (in.)	d'[b] (in.)	Axial Load (k)	Concrete Compressive Strength (psi)	Tension Steel Stress[c] (ksi)	Compression Steel Stress[c] (ksi)	Nominal Flexural Strength (k-in.)	Measured Flexural Strength (k-in.)
Gilbertsen and Moehle - Columns [13]											
2A	0.0132	1.50	2.03	1.69	0.31	1.20	5110	59.9	0.0	2.26	2.30
2B	0.0132	1.51	1.99	1.69	0.31	1.20	5110	59.1	0.0	2.22	2.40
2C	0.0132	1.49	2.03	1.69	0.31	2.13	5110	60.4	-60.4	2.92	3.00
2D	0.0132	1.50	2.02	1.69	0.31	2.35	5110	62.5	-62.5	3.09	3.32
4A	0.0263	1.52	2.01	1.69	0.31	1.20	5410	60.7	-25.0	3.39	3.93
4B	0.0263	1.53	1.98	1.69	0.31	1.20	5410	59.4	-25.0	3.32	3.46
4C	0.0263	1.50	2.00	1.69	0.31	2.41	5410	61.9	-61.9	4.25	4.79
4D	0.0263	1.49	2.00	1.69	0.31	2.38	5410	59.4	-59.4	4.14	4.66
Moehle - Walls [24]											
TW1	0.1077	1.50	8.00	7.62	0.38	0.00	6235	56.8	-30.0	44.9	41.5
TW2	0.1077	1.50	8.00	7.62	0.38	0.00	6235	56.8	-30.0	44.9	41.8
TW3	0.1077	1.50	8.00	7.62	0.38	0.00	6235	56.8	-30.0	44.9	42.7
TW4	0.1077	1.50	8.00	7.62	0.38	0.00	6235	56.8	-30.0	44.9	42.3

[a]Effective depth to bottom reinforcement
[b]Effective depth to top reinforcement
[c]Tensile stress is positive

Table 7.6 Upper-Bound and Measured Flexural Strengths of Cantilever Beams [25]

Designation	Steel Area Per Face ($in.^2$)	Beam Width b (in.)	Beam Height h (in.)	d[a] (in.)	d'[b] (in.)	Axial Load (k)	Concrete Compressive Strength (psi)	Tension Steel Stress[c] (ksi)	Compression Steel Stress[c] (ksi)	Nominal Flexural Strength (k-in.)	Measured Flexural Strength (k-in.)
Static tests											
1.1.1	0.029	1.00	2.00	1.76	0.24	0.00	5500	63.7	25.0	2.97	3.25
1.1.2	0.029	1.00	2.00	1.76	0.24	0.00	5500	63.7	25.0	2.97	3.15
1.2.1	0.029	1.00	2.00	1.76	0.24	0.00	5500	63.7	25.0	2.97	3.20
1.2.2	0.029	1.00	2.00	1.76	0.24	0.00	5500	63.7	25.0	2.97	3.30
2 Hz Cycling Frequency											
2.1.1	0.029	1.00	2.00	1.76	0.24	0.00	5500	63.7	25.0	2.97	3.30
2.1.2	0.029	1.00	2.00	1.76	0.24	0.00	5500	63.7	25.0	2.97	3.26
2.2.1	0.029	1.00	2.00	1.76	0.24	0.00	5500	63.7	25.0	2.97	3.16
2.2.2	0.029	1.00	2.00	1.76	0.24	0.00	5500	63.7	25.0	2.97	3.13
10 Hz Cycling Frequency											
3.1.1	0.029	1.00	2.00	1.76	0.24	0.00	5500	63.7	25.0	2.97	3.30
3.1.2	0.029	1.00	2.00	1.76	0.24	0.00	5500	63.7	25.0	2.97	3.32
3.2.1	0.029	1.00	2.00	1.76	0.24	0.00	5500	63.7	25.0	2.97	3.33
3.2.2	0.029	1.00	2.00	1.76	0.24	0.00	5500	63.7	25.0	2.97	3.30

[a]Effective depth to bottom reinforcement
[b]Effective depth to top reinforcement
[c]Tensile stress is positive

Table 7.7 Ratios of Measured to Upper-Bound Flexural Strength for Component Tests[a]

Option	Assumed Concrete Stress[b]	Assumed Steel Stress[c]	Limit On Maximum Drift Ratio	Mean Ratio of Measured to Nominal Flexural Strength						
				Schipper [19]	Kreger Abrams [19]	Gilbertsen Moehle [13]	Moehle [24]	Moncarz and Krawinkler [25] Static	2Hz	10Hz
#1	0.85 f_c'	f_{su}	none	1.11	1.17	1.08	0.94	1.07	1.09	1.12
#2	f_c'	f_{su}	none	1.09	1.13	1.06	0.94	1.06	1.08	1.12
#3	1.2 f_c'	f_{su}	none	1.07	1.10	1.04	0.93	1.05	1.07	1.10
#4	2 f_c'	f_{su}	none	1.02	1.02	0.96	0.92	1.01	1.03	1.06
#5	0.85 f_c'	1.05 f_{su}	none	1.07	1.12	1.05	0.89	1.02	1.04	1.07
#6	0.85 f_c'	1.10 f_{su}	none	1.03	1.08	1.03	0.85	0.98	1.00	1.03
#7	0.85 f_c'	f_{su}	3.5%	1.11	1.12	1.08	0.94	1.07	1.09	1.12

[a] Ratios were computed for flexural strengths reported in Tables 7.4, 7.5 and 7.6

[b] f_c' is the measured compressive strength of 4 by 8 in. cylinders

[c] f_{su} is the ultimate steel strength in tension

Table 7.8 Upper-Bound Flexural Strengths of First-Story Members of Test Structures

Investigator	Reference[b]	Structure	Nominal Strength of First-Story Members[a]			
			Exterior Columns (k-in.)	Interior Columns (k-in.)	Wall (k-in.)	Beam (k-in.)
Schultz	32	SS1	2.56	2.56		7.32
		SS2	3.70	3.70		7.22
Wood	46	Tower	1.93	2.92		7.56
		Stepped	2.96,2.66	3.57,3.44		7.41
Eberhard		ES1	2.89,1.92	2.89	14.7[c] 13.0[d]	6.72
		ES2	1.57	1.57	14.7[c] 13.2[d]	6.90
Gulkan	14	HD1	5.28			
		HD2	5.28			
		HE1	5.28			
		HE2	5.28			
Healey	15	MF1	2.92	2.92		1.40
Moehle	23	MF2	3.31	3.31		1.35
Cecen	10	H1	5.73	5.22		
		H2	5.70	5.18		1.10
Moehle	24	FNW	3.45	3.45		1.45
		FHW	2.29	2.29	45.0	1.03
		FFW	2.29	2.29	45.0	1.04
Abrams	2	FW1	2.17	2.17	134.7	0.91
		FW2	2.75	2.24	41.9	
		FW3	2.66	2.16	41.8	
		FW4	2.18	2.18	134.8	0.91

[a]Calculated according to procedure described in Section 7.3 assuming dead load acts on section
[b]Reference numbers refer to reference list
[c]Flexural strength of wall at lower face of first-story beam
[d]Flexural strength of Mesnager hinge detail at base of wall

Table 7.9 Measured and Upper-Bound Lateral Strengths of Frames with Story Mechanisms

			Measured Response				Nominal Strength[a]					
							Linear Load Distribution			Uniform Load Distribution		
Investigator	Structure	Run	Base Shear (k)	Base Moment (k-in.)	Mean Drift Ratio (%)	Maximum Drift Ratio (%)	Base Shear (k)	Base Moment (k-in.)	Mechanism Type	Base Shear (k)	Base Moment (k-in.)	Mechanism Type
Schultz	SS1	1	3.93	240	1.19	3.09	3.64	217	S1	3.64	176	S1
		3	3.89	249	1.48	4.28						
	SS2	1	4.37	274	1.07	1.43	5.26	313	S1	5.26	255	S1
		2	5.07	307	1.33	2.22						
		4	5.25	341	1.79	2.88						
		5	4.88	325	2.36	4.25						
		6	5.50	278	4.03	10.35						
Wood	Tower	1	2.79	150	1.03	1.5	3.32	198	S4	3.45	167	S1
		2	3.61	197	1.67	2.7						
		3	3.75	190	2.01	3.0						
		4	3.63	188	2.61	4.6						
	Stepped	A	1.36	57	0.17	0.3	4.49	267	S1	4.49	217	S1
		B	4.41	216	0.98	1.7						
		1	4.32	220	1.05	1.7						
		2	4.95	268	1.43	2.8						
		3	4.79	264	1.72	4.7						
Eberhard	ES1	1	5.41	328	0.85	1.19	7.65	455	S1	7.65	370	S1
		2	7.33	408	1.44	2.33						
		3	7.79	442	2.02	3.96						
		4	7.39	443	2.42	5.30						
	ES2	1	5.14	300	0.77	1.26	6.63	395	S1	6.63	321	S1
		2	6.36	360	1.50	3.09						
		3	6.23	361	1.93	4.60						
Gulkan	HD1	1	0.88	14	0.18	0.18	1.63	25	S1	1.63	25	S1
		2	1.64	25	0.97	0.97						
		6	1.66	26	1.22	1.22						
	HD2	1	1.82	28	0.89	0.89	1.63	25	S1	1.63	25	S1
		5	1.13	18	0.90	0.90						
	HE1	1	1.49	23	0.54	0.54	1.63	25	S1	1.63	25	S1
		2	1.83	28	1.61	1.61						
	HE2	2	1.68	26	1.71	1.71	1.63	25	S1	1.63	25	S1

[a]Nominal strength of members listed in Table 7.8

Table 7.10 Measured and Upper-Bound Lateral Strengths of Frames with Yielding Beams

Investigator	Structure	Run	Measured Response				Nominal Strength[a]					
							Linear Load Distribution			Uniform Load Distribution		
			Base Shear (k)	Base Moment (k-in.)	Mean Drift Ratio (%)	Maximum Drift Ratio (%)	Base Shear (k)	Base Moment (k-in.)	Mechanism Type	Base Shear (k)	Base Moment (k-in.)	Mechanism Type
Healey	MF1	1	3.51	224	0.99	1.71	2.76	180	B5	3.10	160	B4
		2	3.71	278	2.14	3.90						
		3	3.64	266	2.85	4.26						
Moehle	MF2	1	2.88	192	1.02	2.06	2.61	169	B5	2.85	147	B4
		2	3.15	220	1.82	3.11						
		3	3.21	234	2.41	3.81						
Cecen	H1	1	2.70	180	1.0	1.7	2.80	176	B8	3.45	171	B7
		2	3.60	209	2.1	3.5						
		3	4.22	274	3.9	5.0						
	H2	1	1.57	97	0.3	0.6	2.80	176	B8	3.45	171	B7
		2	2.40	147	0.7	1.3						
		3	2.76	164	1.0	1.5						
		5	2.92	117	1.6	2.2						
		6	3.37	217	2.4	3.9						
		7	4.22	249	3.9	5.6						
Moehle	FNW	1	2.74	171	1.15	2.0	2.47	158	B5	2.64	143	B3
		2	2.83	206	1.92	3.1						
		3	(b)	(b)	3.11[c]	(b)						

[a]Nominal strength of members listed in Table 7.8

[b]Not reported

[c]Double-amplitude displ./2 (See Reference 3)

Table 7.11 Measured and Upper-Bound Lateral Strengths of Frame-Wall Structures

Investigator	Structure	Run	Measured Response				Nominal Strength[a]					
							Linear Load Distribution			Uniform Load Distribution		
			Base Shear (k)	Base Moment (k-in.)	Mean Drift Ratio (%)	Maximum Drift Ratio (%)	Base Shear (k)	Base Moment (k-in.)	Mechanism Type	Base Shear (k)	Base Moment (k-in.)	Mechanism Type
Moehle	FHW	1	2.97	201	1.01	1.4	2.78	178	B6	3.14	169	B5
		2	3.48	229	1.75	2.6						
		3	(b)	(b)	2.23[c]	(b)						
	FFW	1	3.15	211	1.14	1.4	3.09	197	B9	3.65	197	B9
		2	3.78	229	1.92	2.6						
		3	(b)	(b)	2.45[c]	(b)						
Abrams	FW1	1	4.80	301	1.23	1.7	4.89	308	B10	6.22	308	B10
		2	6.29	363	1.66	2.5						
		3	9.37	363	2.41[c]	(b)						
	FW2	1	4.04	248	1.21	1.5	3.57	225	B10	4.55	225	B10
		2	5.62	283	1.88	2.3						
		3	5.71	274	1.97[c]	(b)						
	FW3	1	3.60	204	0.74	1.2	3.41	215	B10	4.34	215	B10
		2	5.84	292	2.10	2.9						
		3	4.49	292	2.45[c]	(b)						
	FW4	1	4.77	301	0.80	1.1	4.91	309	B10	6.24	309	B10
		2	6.95	363	2.01	2.8						
		3	7.93	380	2.36[c]	(b)						

[a]Nominal strength of members listed in Table 7.8
[b]Not reported
[c]Double-amplitude displ./2 (See Reference 3)

Table 7.12 Ratios of Measured to Upper-Bound Lateral Strengths for Test Structures

	Linear Load Distribution		Uniform Load Distribution	
	Mean Ratio of Measured to Nominal Base Shear (Mean ± Std. Dev.)	Mean Ratio of Measured to Nominal Base Moment (Mean ± Std. Dev.)	Mean Ratio of Measured to Nominal Base Shear (Mean ± Std. Dev.)	Mean Ratio of Measured to Nominal Base Moment (Mean ± Std. Dev.)
Soft-Story Structures	1.06 ± 0.06	1.02 ± 0.09	1.05 ± 0.05	1.25 ± 0.10
One-Story Structures	1.07 ± 0.05	1.07 ± 0.05	1.07 ± 0.05	1.07 ± 0.05
Frames with Yielding Beams	1.35 ± 0.15	1.44 ± 0.10	1.17 ± 0.06	1.56 ± 0.11
Frame-Wall Structures	1.55 ± 0.25	1.25 ± 0.07	1.25 ± 0.16	1.26 ± 0.08

Table 8.1 Measured and Calculated Dynamic Base Shears for Frame-Wall Structures

Structure	Run	Maximum Measured Base Shear (k)	Calculated Base Shear			
			Linear Force Distribution (k)	Uniform Force Distribution (k)	Kabeyasawa Procedure (k)	Response-Spectrum Procedure (k)
FHW	1	2.97	2.78	3.14	3.83	-
	2	3.48			4.01	
FFW	1	3.15	3.09	3.65	3.91	-
	2	3.78			4.50	
FW1	1	4.80	4.89	6.22	6.35	7.24
	2	6.29			9.76	9.64
	3	9.37			11.79	11.69
FW2	1	4.04	3.57	4.55	4.95	5.20
	2	5.62			6.21	6.44
	3	5.71			6.72	7.06
FW3	1	3.60	3.41	4.34	4.61	-
	2	5.84			6.16	
	3	4.49			6.47	
FW4	1	4.77	4.91	6.24	6.25	6.20
	2	6.95			7.60	7.86
	3	7.93			8.54	8.55

Table 8.2 Base-Motion Characteristics for Frame-Wall Structures

Structure	Run	Ground Motion[a]	Peak Base Acceleration (g)	Housner Spectrum Intensity[b] (in.)	Effective Base Accleration[c] (g)
FHW	1	EC	0.41	7.6	0.33
	2	EC	0.48	12.9	0.56
FFW	1	EC	0.32	7.2	0.31
	2	EC	0.55	13.2	0.57
FW1	1	EC	0.51	9.1	0.40
	2	EC	1.70	16.9	0.74
	3	EC	2.41	19.9	0.87
FW2	1	EC	0.48	9.0	0.39
	2	EC	0.92	15.9	0.69
	3	EC	1.10	15.7	0.68
FW3	1	EC	0.42	8.6	0.37
	2	EC	0.96	19.1	0.83
	3	EC	1.07	20.5	0.89
FW4	1	T	0.47	9.7	0.42
	2	T	0.94	20.2	0.88
	3	T	1.27	22.1	0.96

[a]EC = NS component of ground motion measured in El Centro, California. (1940 Imperial Valley Earthquake)

T = N21E component of ground motion measured in Taft, California. (1952 Tehachapi Earthquake)

[b]Area below velocity response spectrum between periods of 0.04 and 1.0 sec (10% damping)

[c]Calculated from Housner Spectrum Intensity (0.0435 in./g)

Table 8.3 Modified Modal Properties for FW Structures[a]

	First Mode	Second Mode	Third Mode
Mode Shape			
Level			
10	1.000	-1.125	0.903
9	0.900	-0.562	-0.183
8	0.800	-0.020	-0.939
7	0.700	0.433	-1.037
6	0.600	0.725	-0.485
5	0.500	0.818	0.354
4	0.400	0.720	0.942
3	0.300	0.503	1.029
2	0.200	0.265	0.715
1	0.100	0.078	0.262
Participation Factor	1.429	0.481	0.274
Effective Weight, k	8.06	0.91	0.44

[a]Linear-elastic mode shapes have been orthogonalized with respect to the linear mode shape and with respect to the other modified mode shapes.

Weight per story = 1.03k

D_m = 0.28 (Defined in Eq. 8.5)

Table 8.4 Goodness-of-Fit Indices for Higher-Mode Components of Base Shear

	Kabeyasawa Approximation GOF	Linear Elastic Best Fit of Response			Approximation		
		Frequency (Hz)	Damping (%)	GOF	Frequency (Hz)	Damping (%)	GOF
Second Mode							
FW1 run 1	2.8	11	10	2.3	10	10	2.3
run 2	3.4	10	10	2.6	10	10	2.6
run 3	3.2	9	10	2.5	10	10	2.8
FW2 run 1	3.5	12	10	2.8	10	10	3.3
run 2	2.8	9	10	2.2	10	10	2.2
run 3	2.7	9	10	2.2	10	10	2.4
FW4 run 1	3.9	14	5	3.2	10	10	4.2
run 2	3.4	11	10	2.8	10	10	2.9
run 3	2.7	8	10	2.1	10	10	2.4
Third Mode							
FW1 run 1	-	24	10	3.0	24	10	3.0
run 2	-	24	20	3.9	24	10	4.2
run 3	-	19	20	3.9	24	10	5.2
FW2 run 1	-	26	10	4.2	24	10	4.4
run 2	-	24	10	3.4	24	10	3.4
run 3	-	19	10	3.4	24	10	3.7
FW4 run 1	-	32	10	2.8	24	10	3.1
run 2	-	24	10	3.3	24	10	3.3
run 3	-	21	5	3.7	24	10	3.9

Table 8.5 Measured and Calculated Components of Base Shear

Structure	Run	Maximum First-Mode Component		Maximum Higher-Mode Component		
		Measured Base Shear (k)	Calculated Base Shear (k)	Measured Base Shear (k)	Calculated Base Shear	
					Kabeyasawa[a] (k)	Linear-Elastic[b] (k)
FW1	1	4.66	4.89	1.53	1.46	2.35
	2	5.70		4.19	4.87	4.75
	3	5.67		6.04	6.90	6.80
FW2	1	3.34	3.57	1.33	1.38	1.63
	2	4.40		2.86	2.64	2.87
	3	4.28		3.85	3.15	3.49
FW3	1	4.76	4.91	1.51	1.34	1.29
	2	5.79		3.49	2.69	2.95
	3	6.03		5.73	3.63	3.64

[a]Calculated for D_m = 0.28, W = 10.3k

[b]Calculated assuming 10% damping for higher modes
Assumed 2nd-mode frequency = 10 Hz
Assumed 3rd-mode frequency = 24 Hz

FIGURES

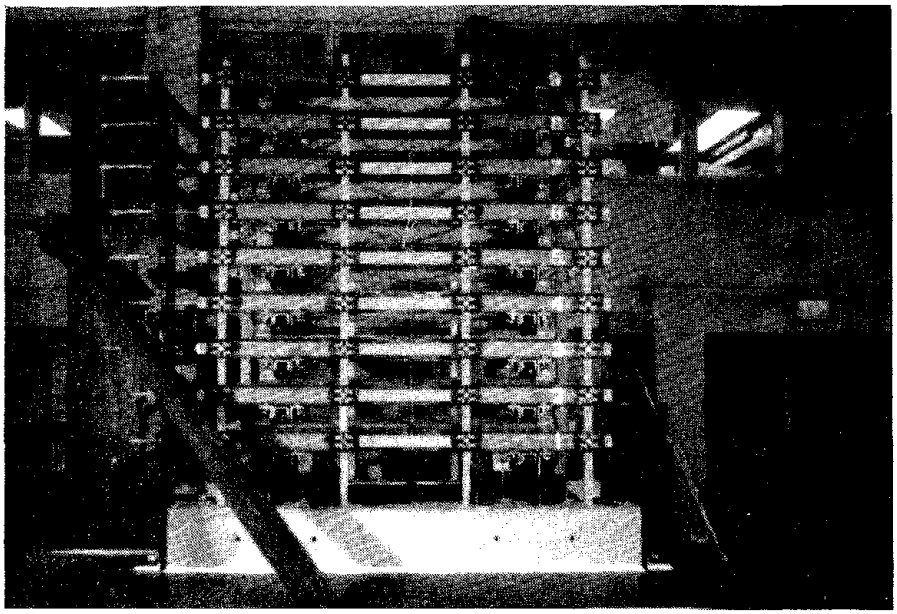

(a) Frame Structure with Yielding Columns

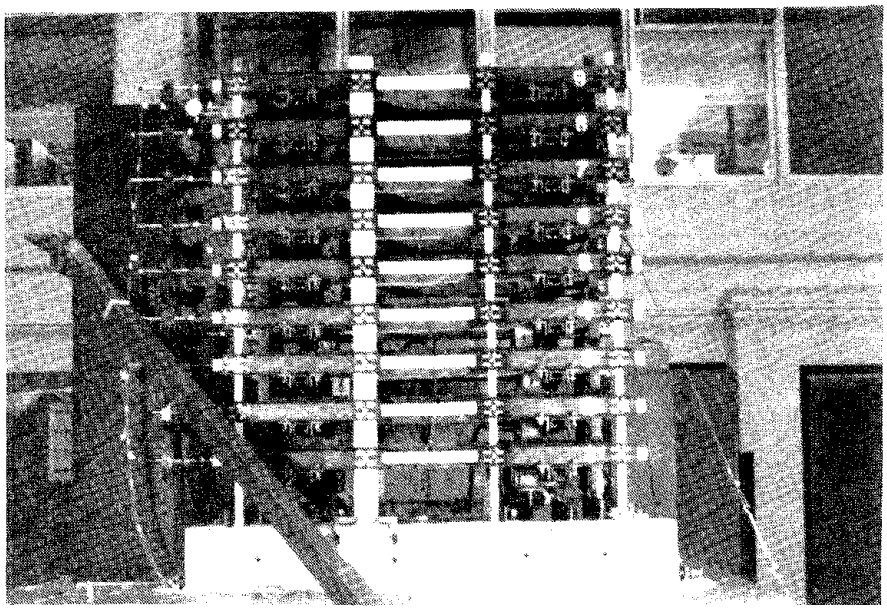

(b) Frame Structure with Slender Wall

Fig. 1.1 Photographs of the Test Structures

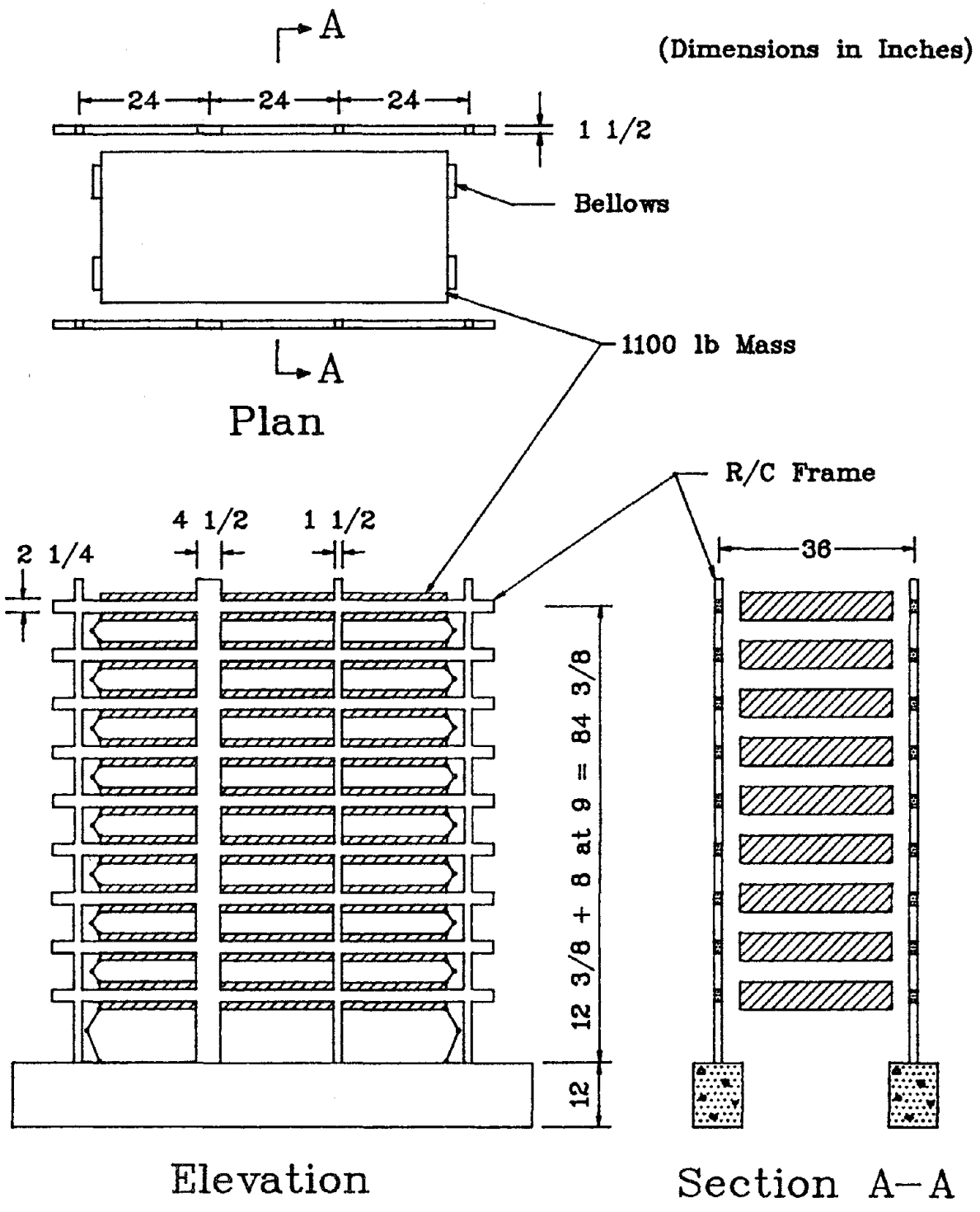

Fig. 2.1 Test Structure

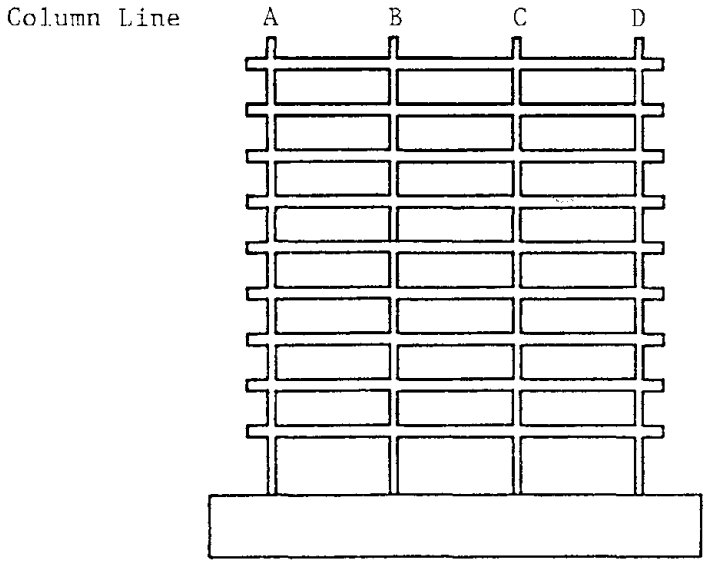

Structures SS1 and SS2

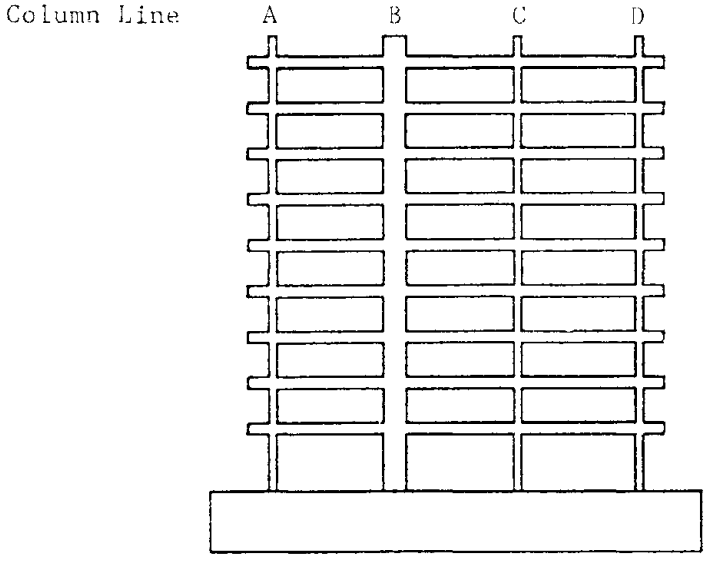

Structures ES1 and ES2

Fig. 2.2 Frame Profiles

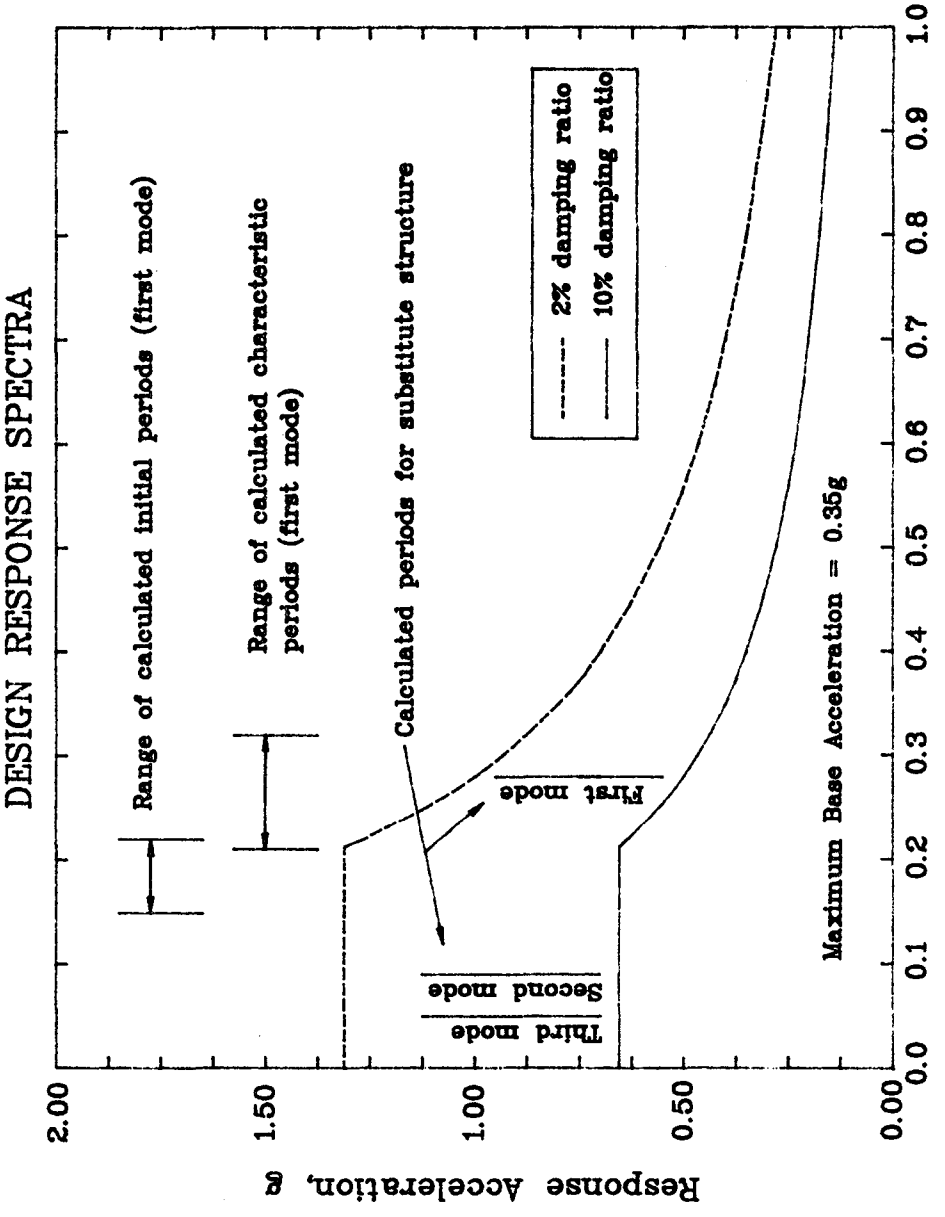

Fig. 2.3 Linear Acceleration Response Spectra Used for Design

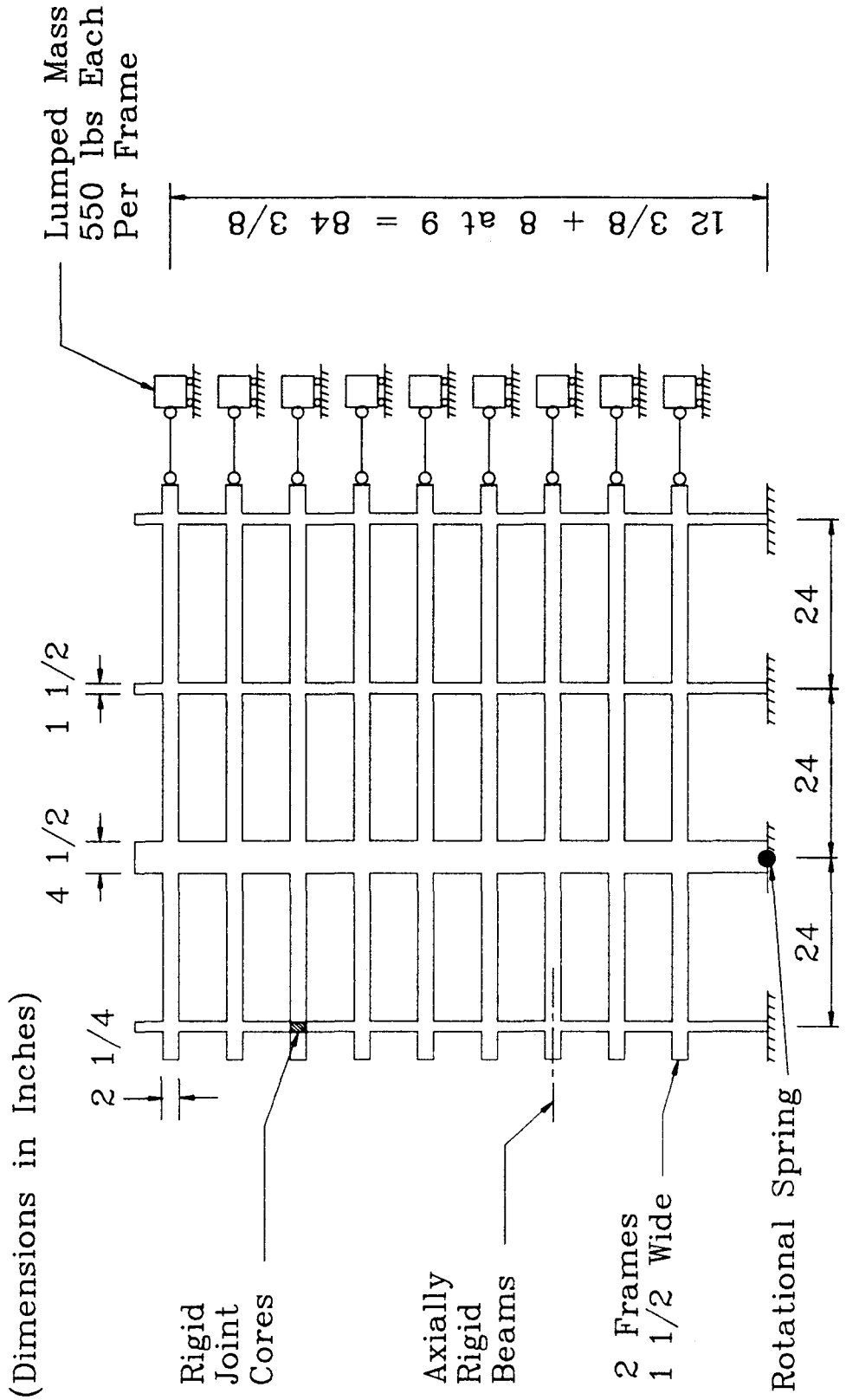

Fig. 2.4 Analytical Model Used for Design of Structure ES1

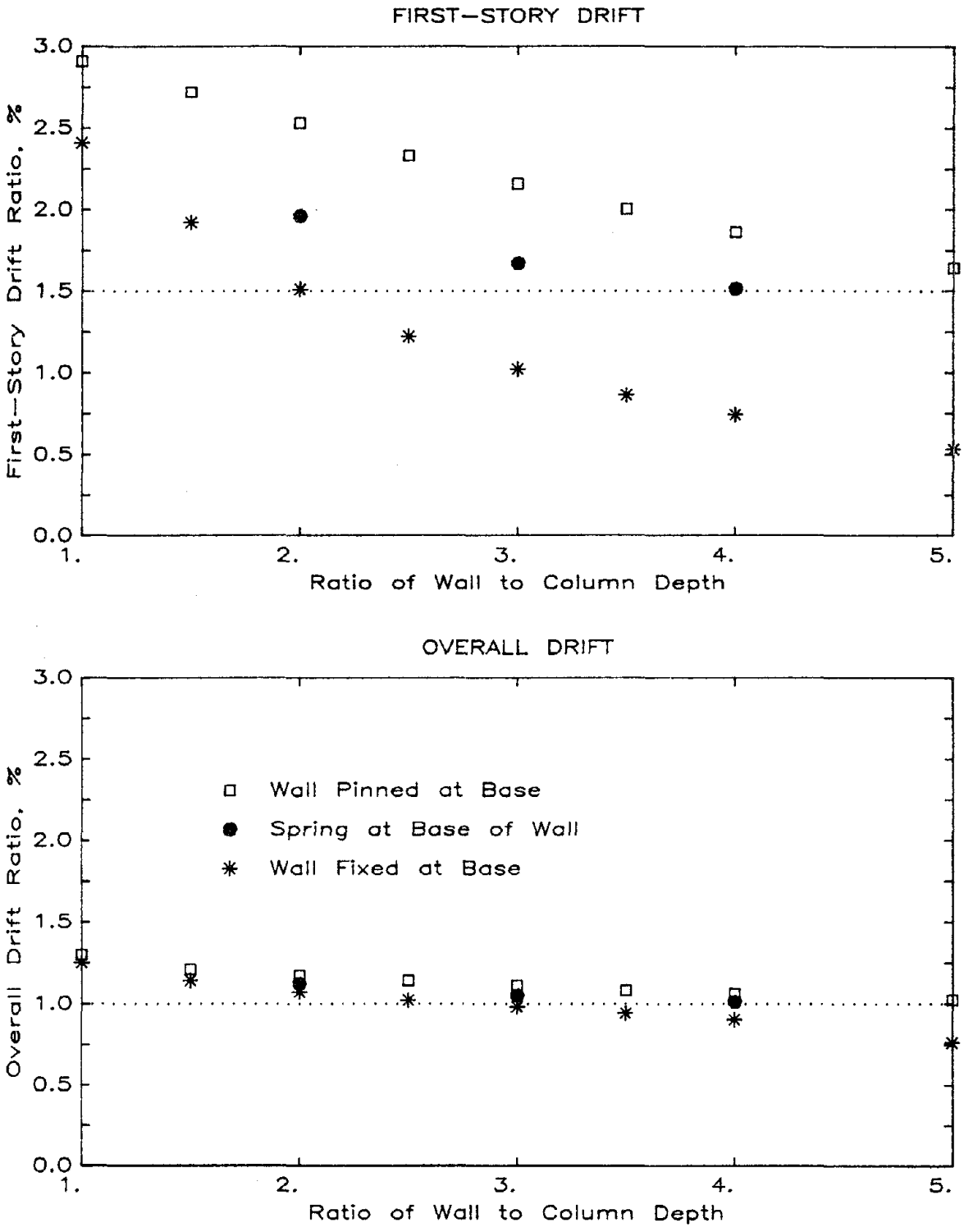

Fig. 2.5 Calculated First-Story and Overall Drift Ratios

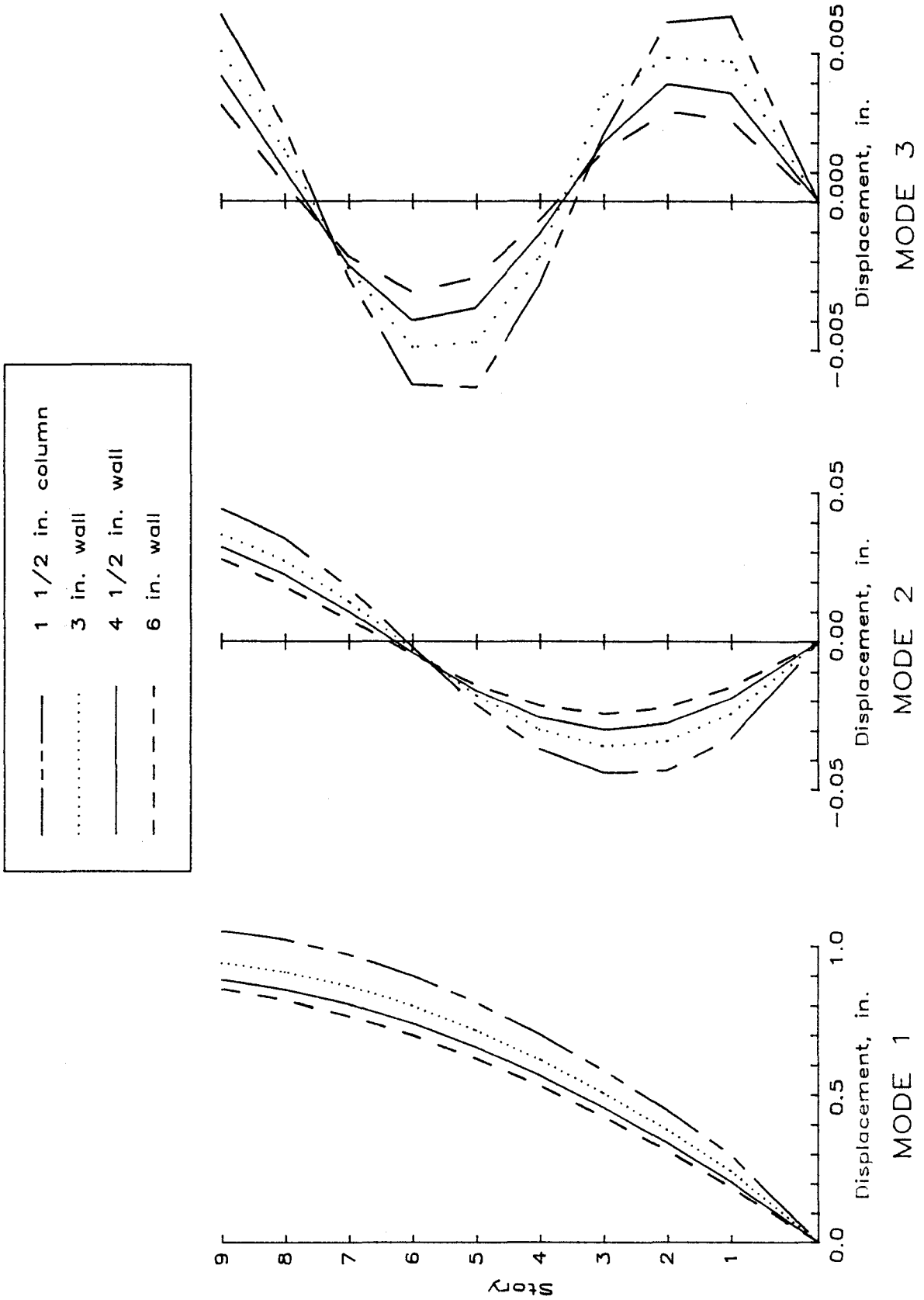

Fig. 2.6 Calculated Displacements of the Characteristic Structures for the First Three Modes

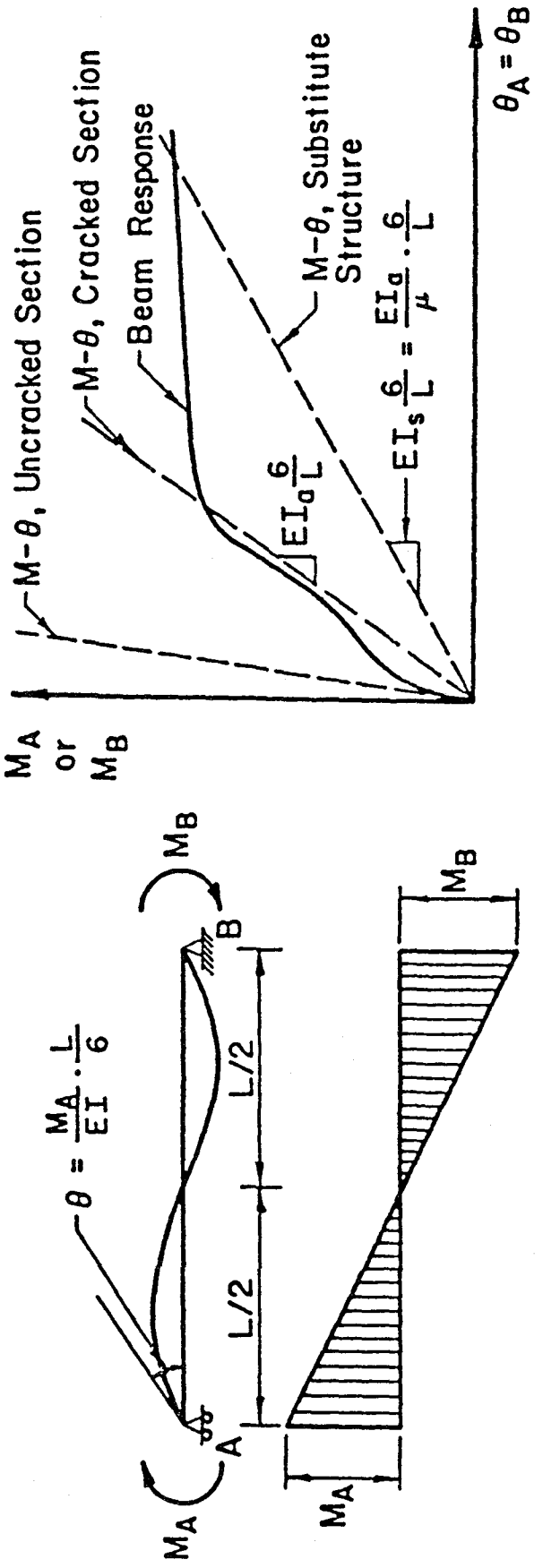

Fig. 2.7 Interpretation of Damage Ratio

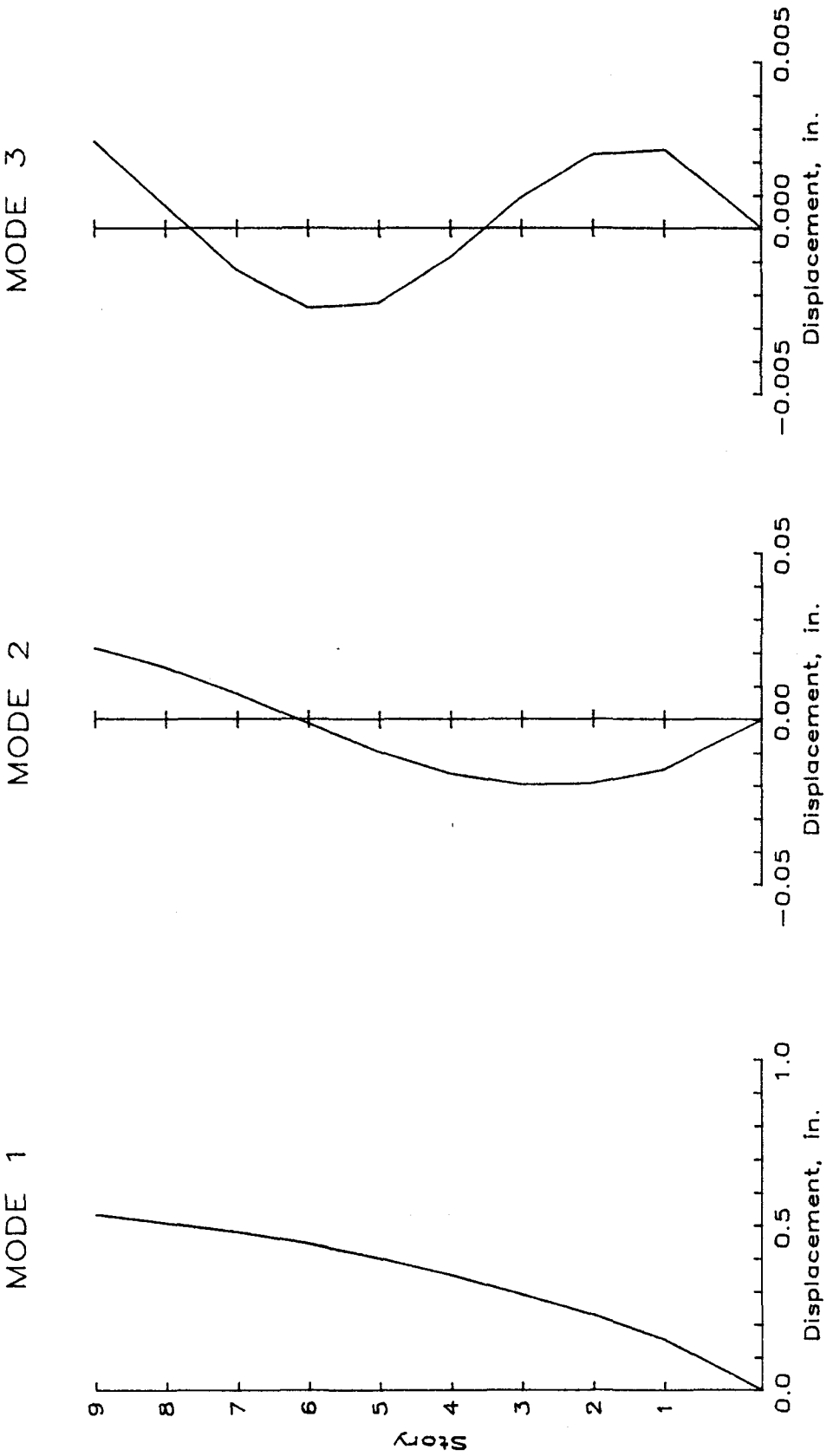

Fig. 2.8 Calculated Displacements of the Substitute Structure for the First Three Modes

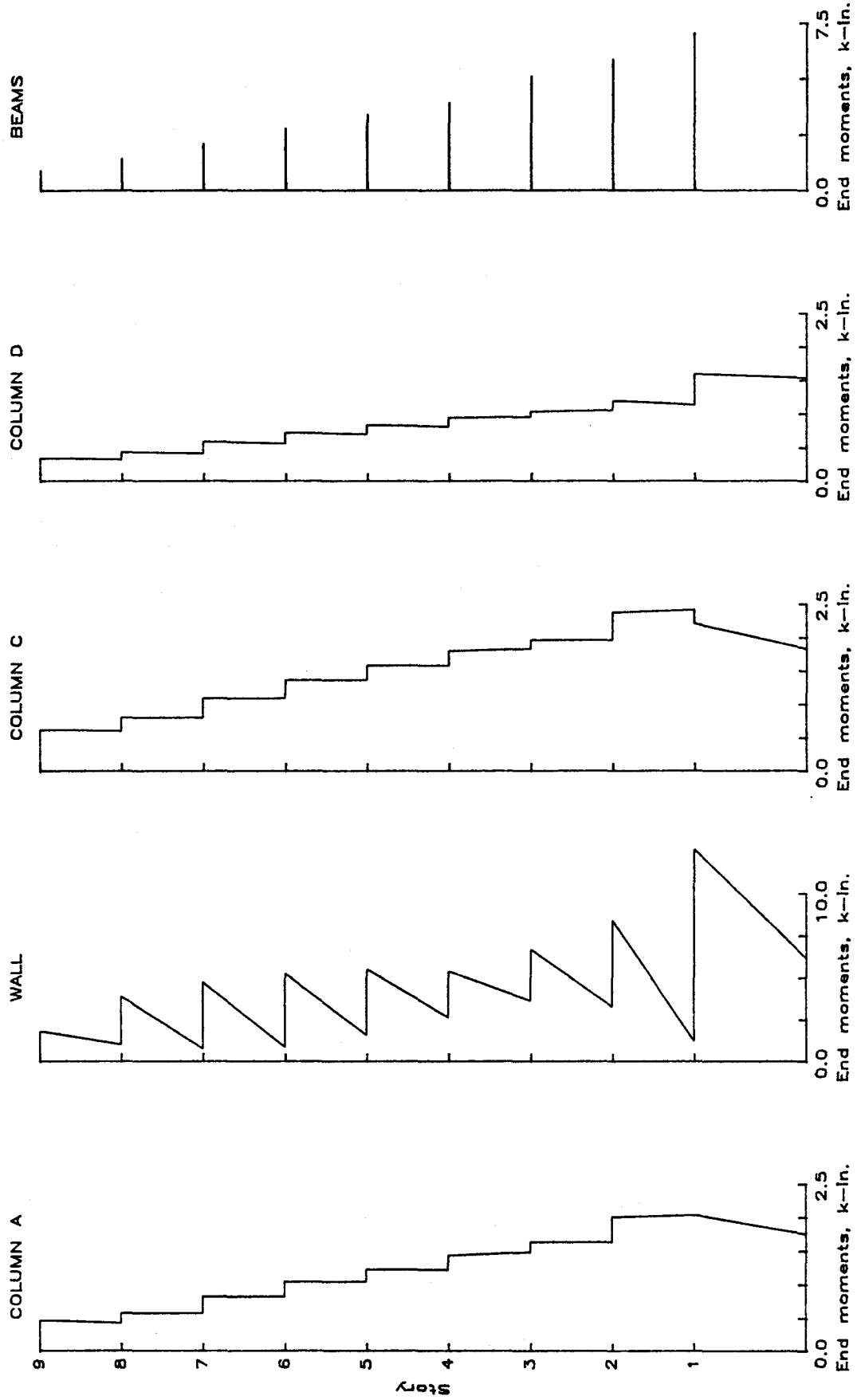

Fig. 2.9 Member Design Forces for Structure ES1

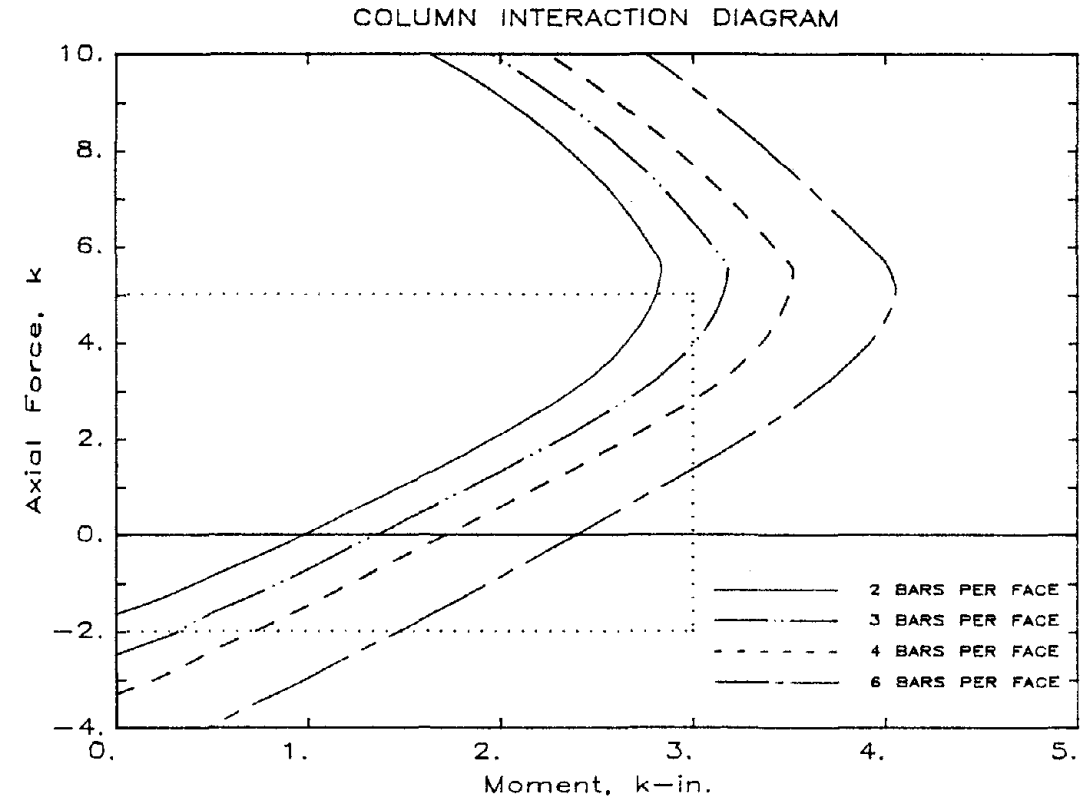

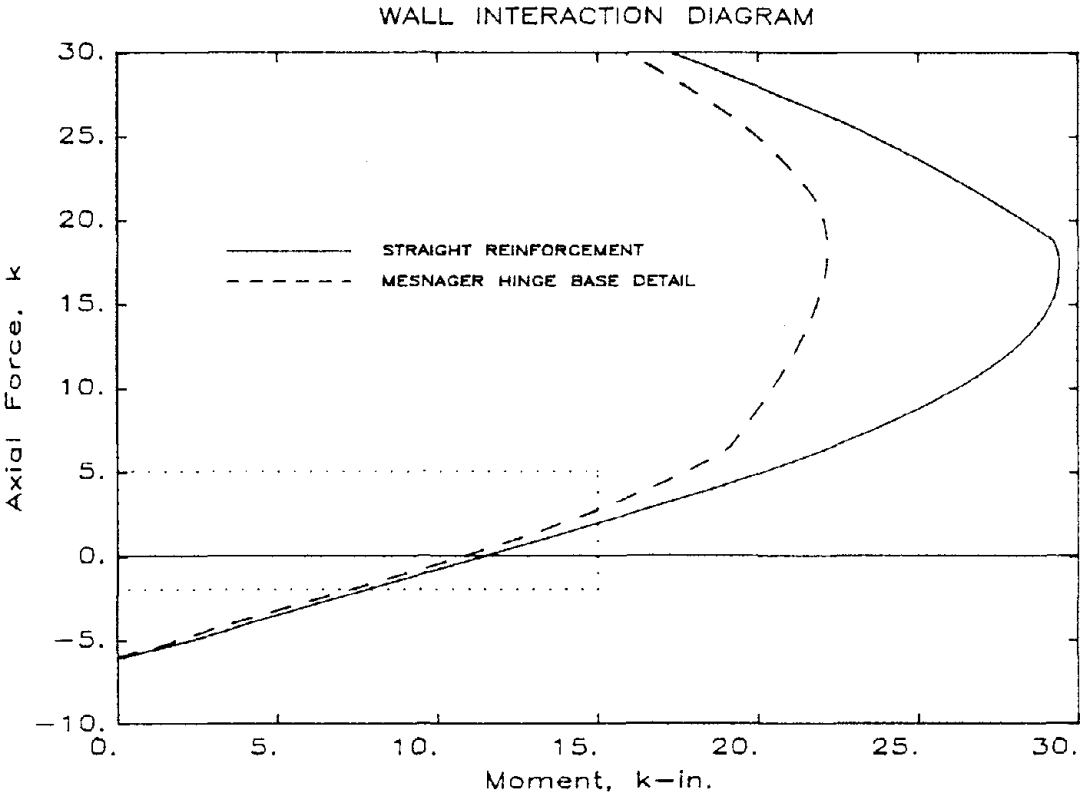

Fig. 2.10 Moment-Axial Force Interaction Diagrams

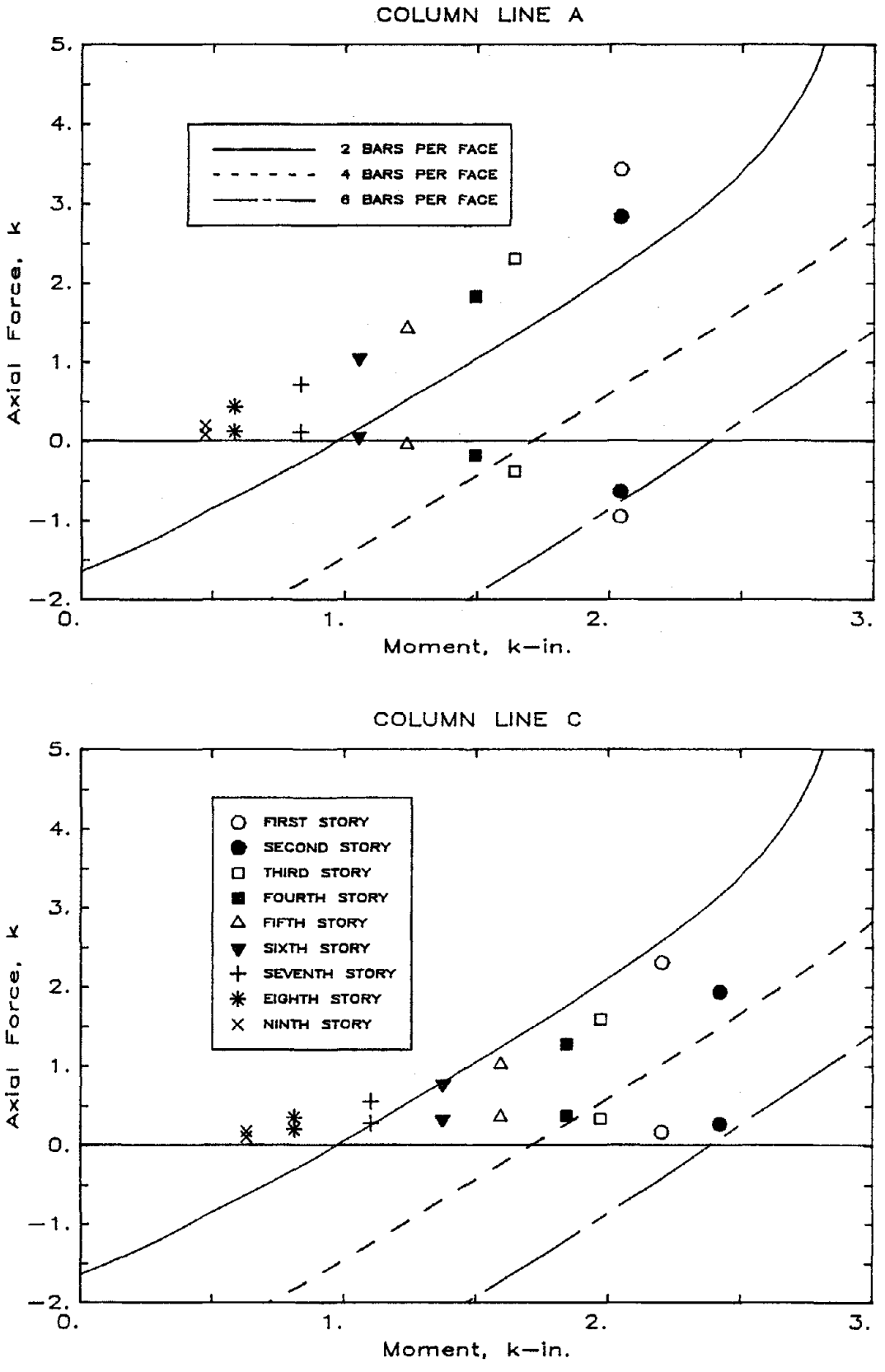

Fig. 2.10 (cont.) Moment-Axial Force Interaction Diagrams

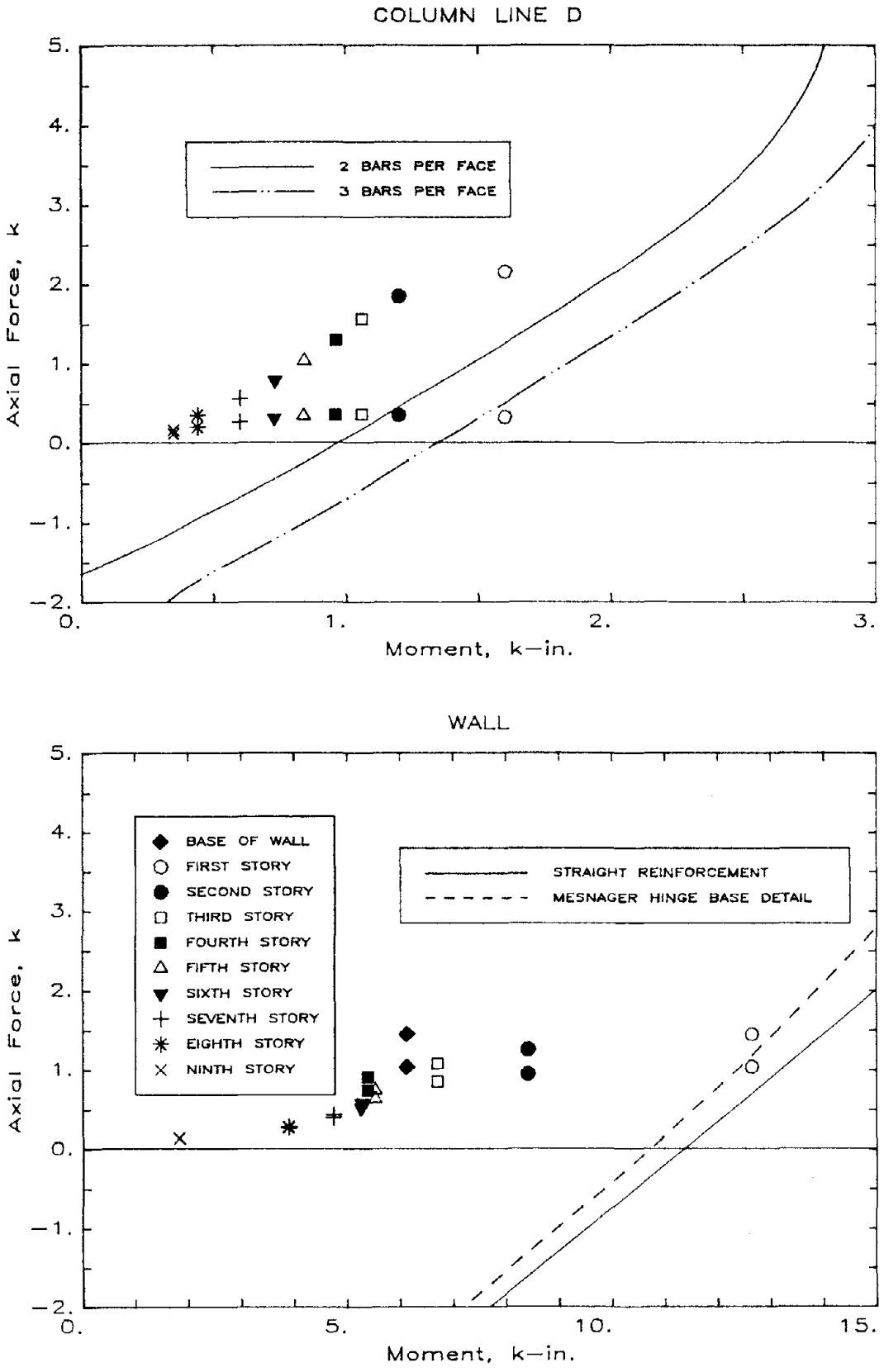

Fig. 2.10 (cont.) Moment-Axial Force Interaction Diagrams

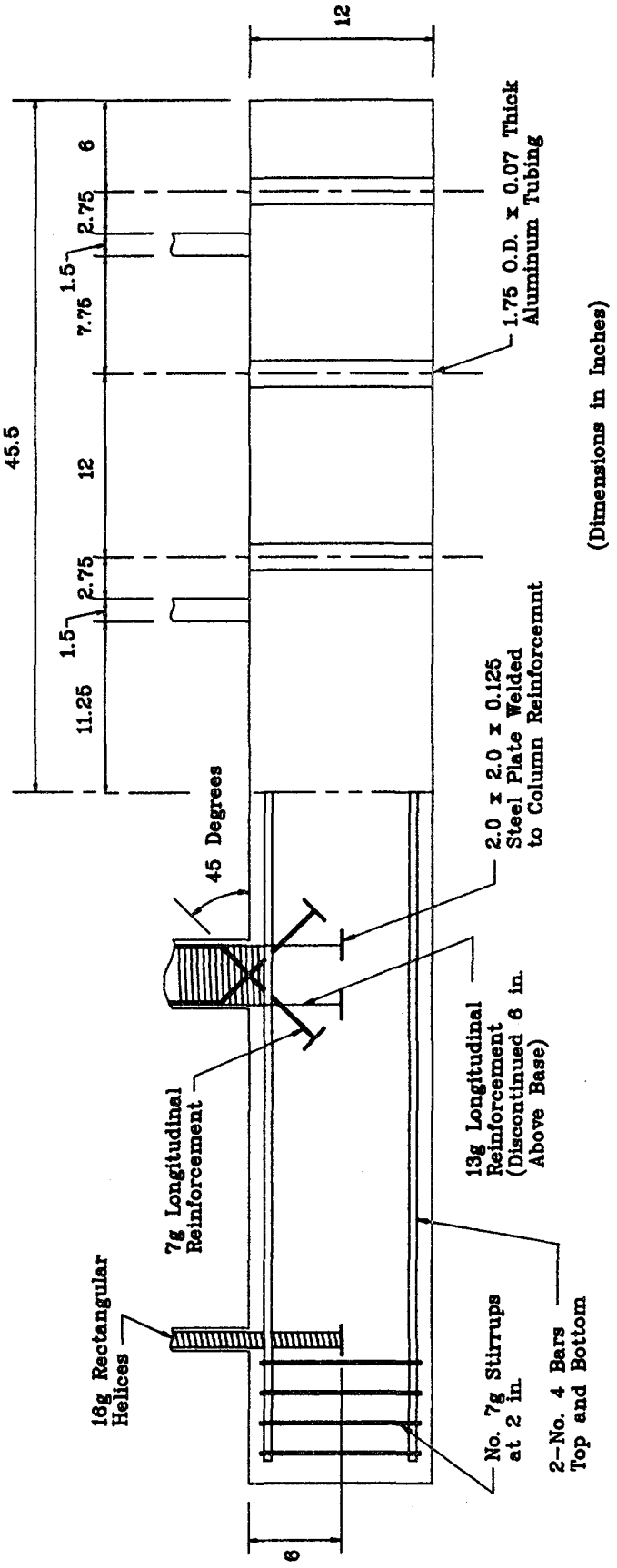

Fig. 2.11 Detail of Base of Structure

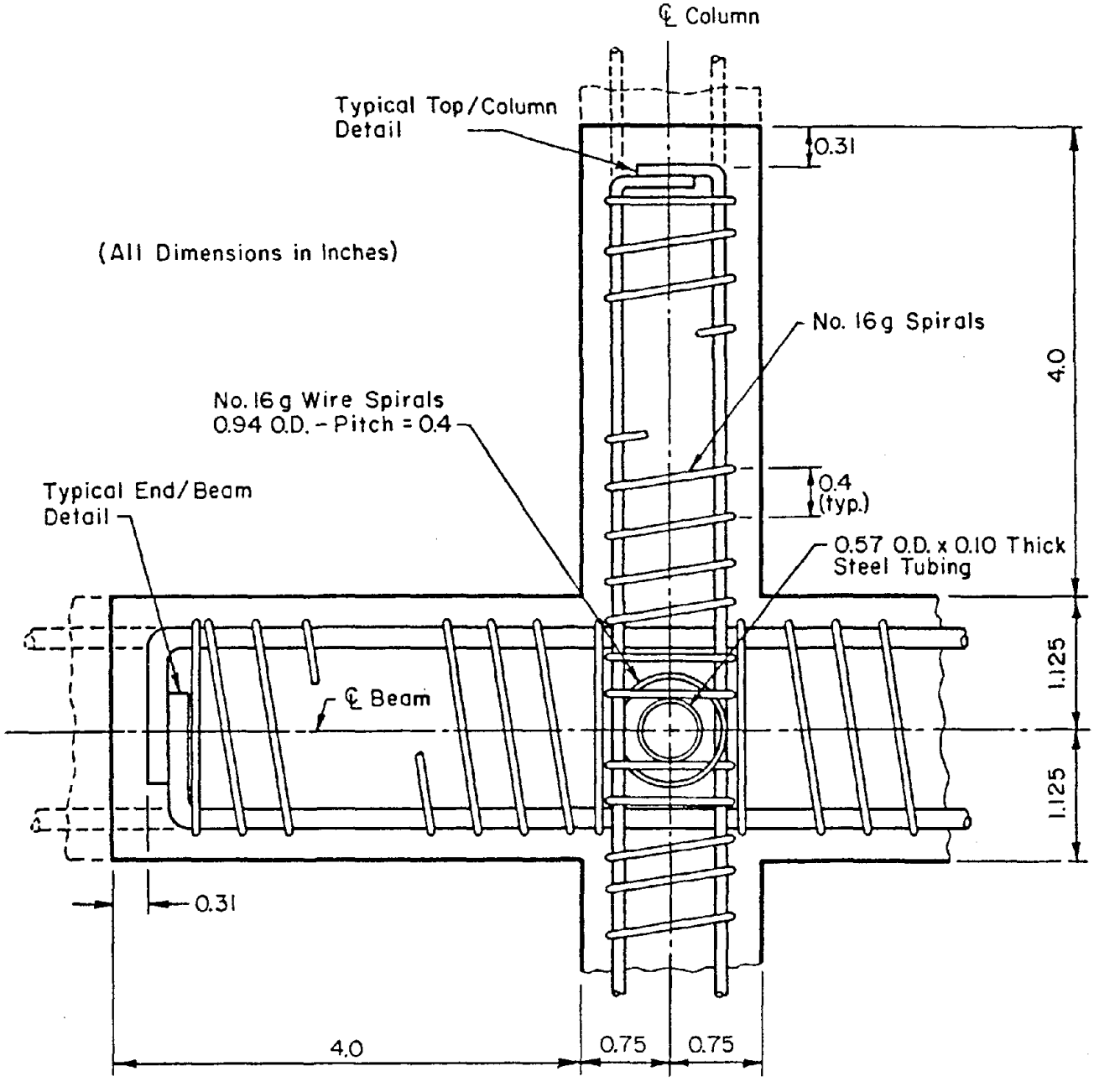

Fig. 2.12 Reinforcement Details

(All Dimensions in Inches)

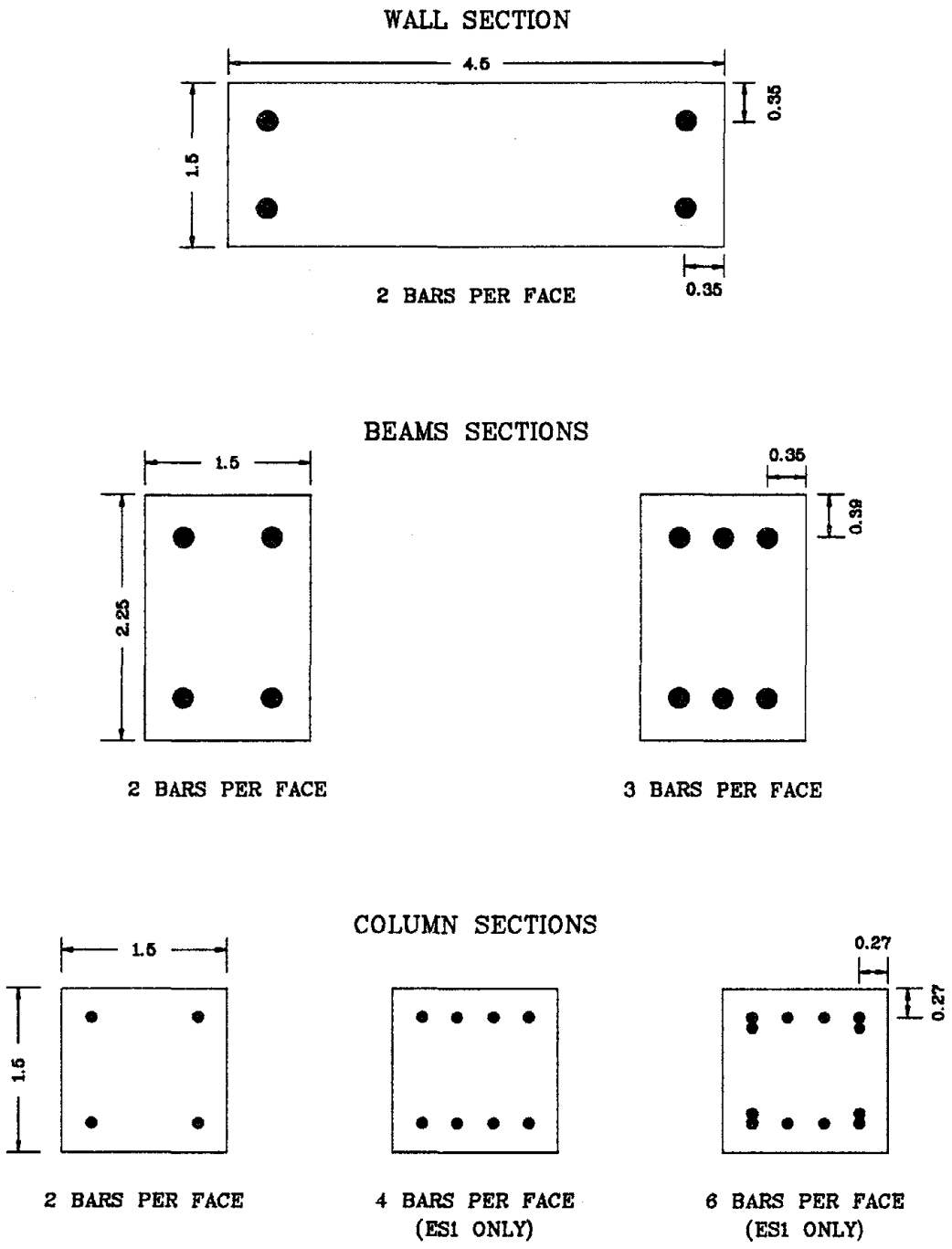

Fig. 2.13 Cross-sections of Members

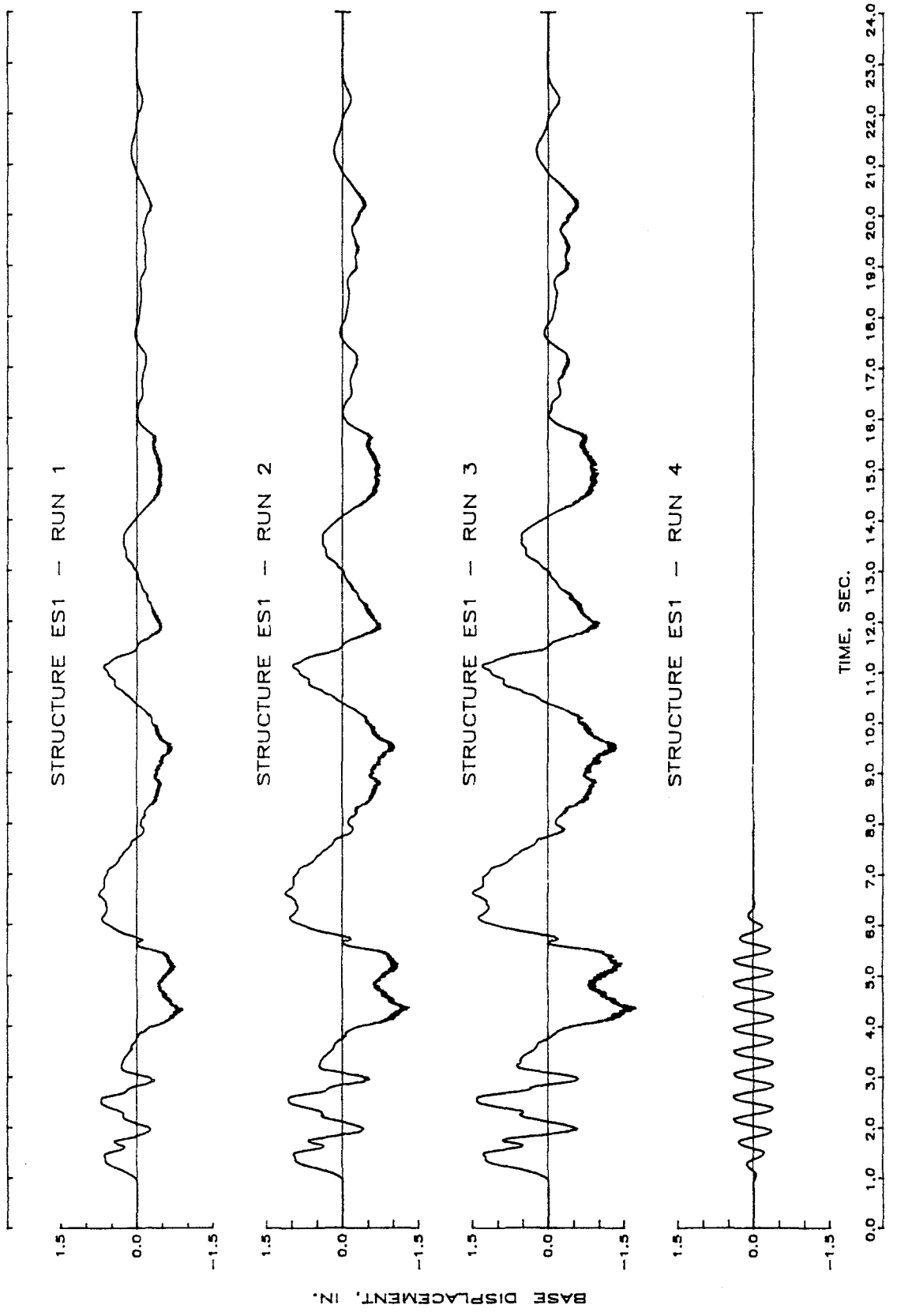

Fig. 4.1 Base Displacement Histories
(a) Structure ES1

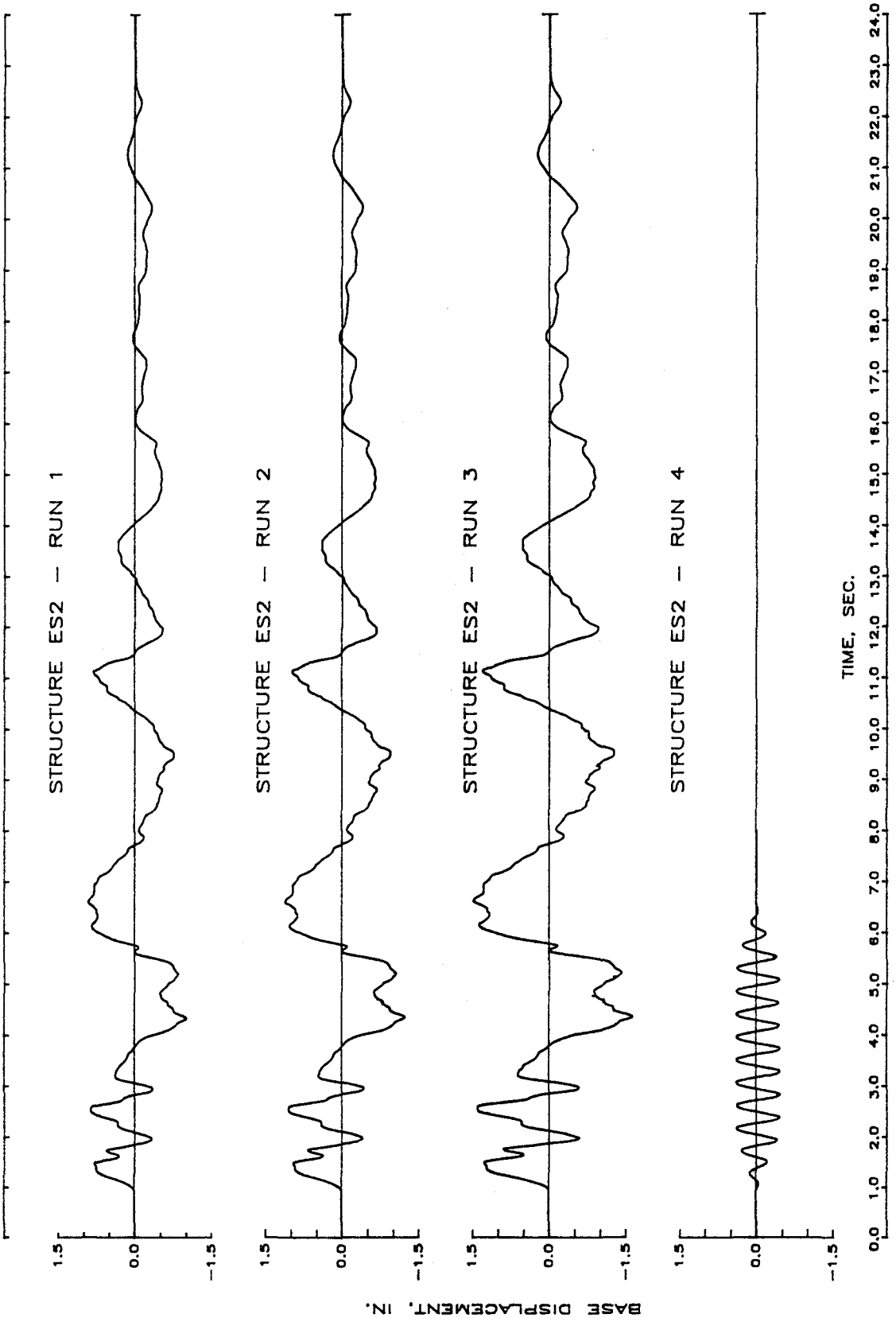

Fig. 4.1 (cont.) Base Displacement Histories
(b) Structure ES2

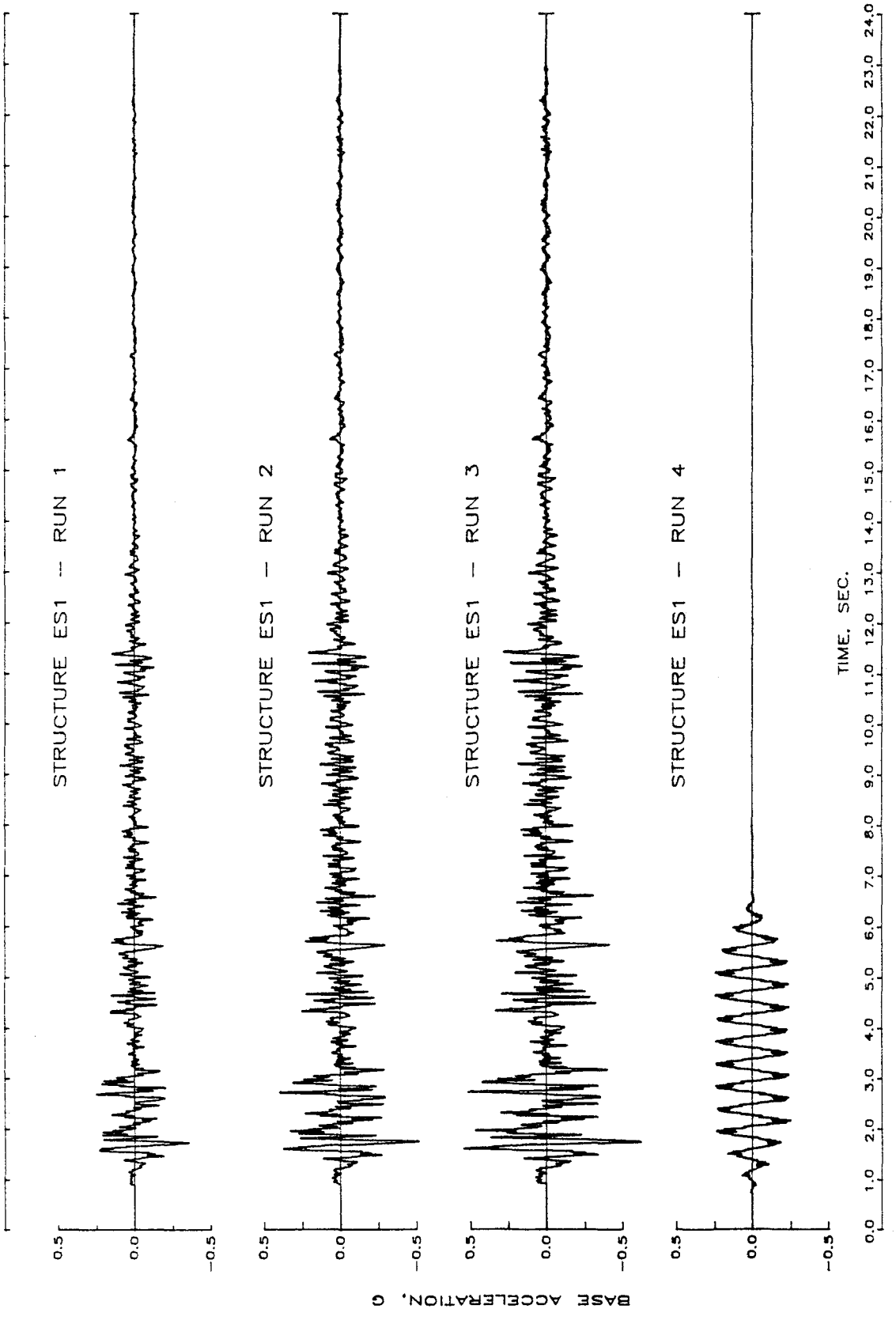

Fig. 4.2 Base Acceleration Histories
(a) Structure ES1

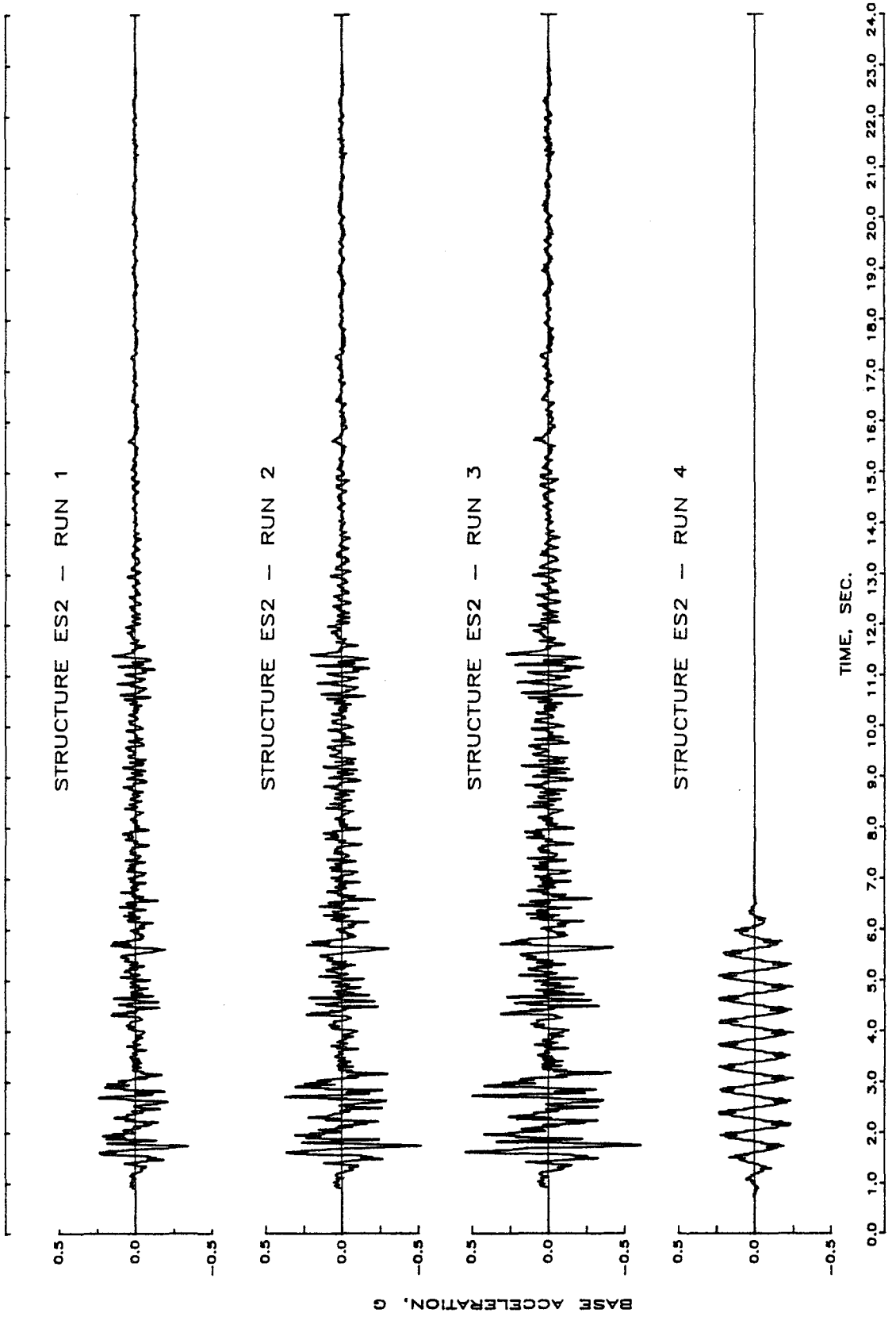

Fig. 4.2 (cont.) Base Accelerations Histories
(b) Structure ES2

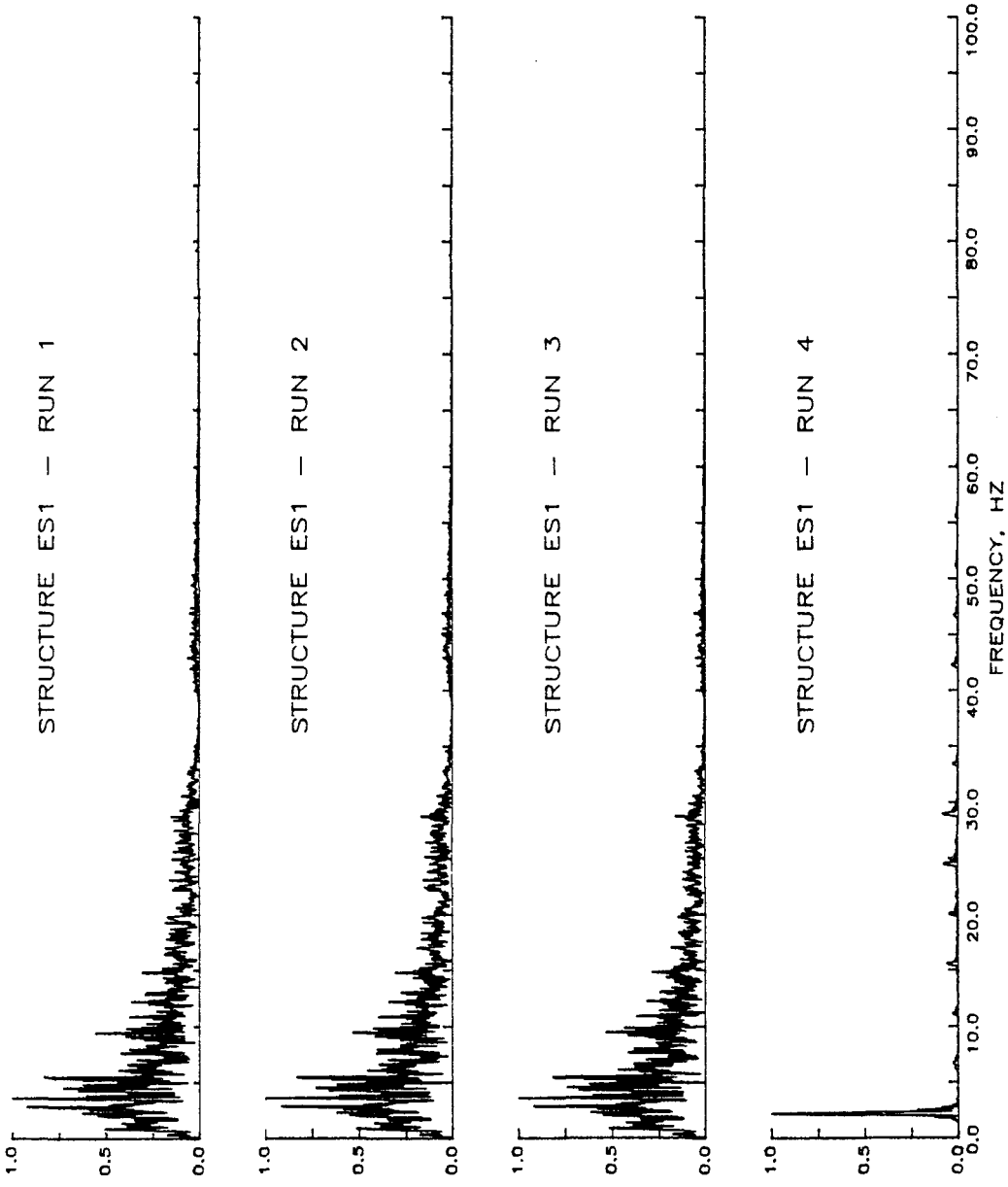

Fig. 4.3 Fourier Amplitude Spectra of Base Accelerations
(a) Structure ES1

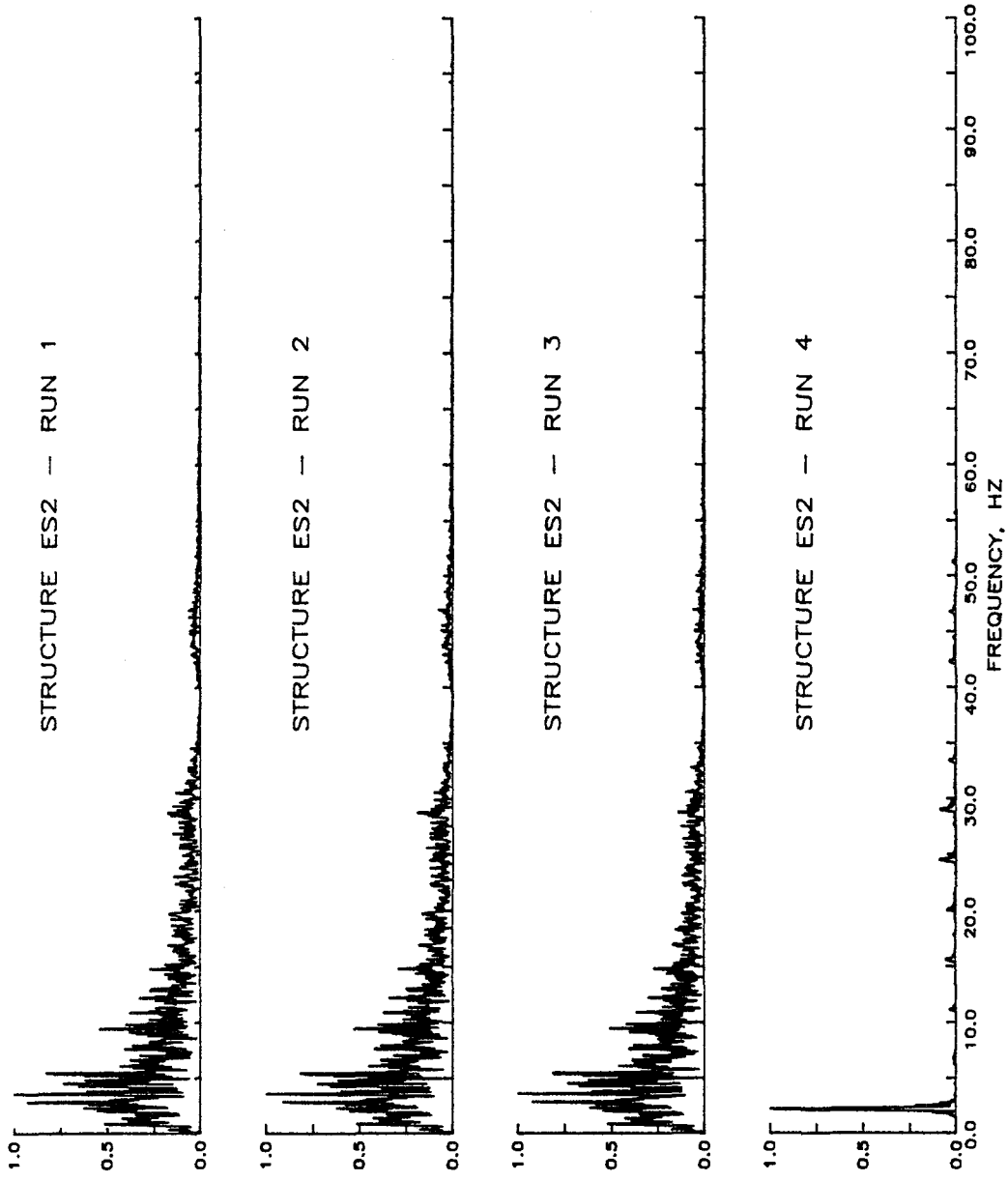

Fig. 4.3 (cont.) Fourier Amplitude Spectra of Base Accelerations
(b) Structure ES2

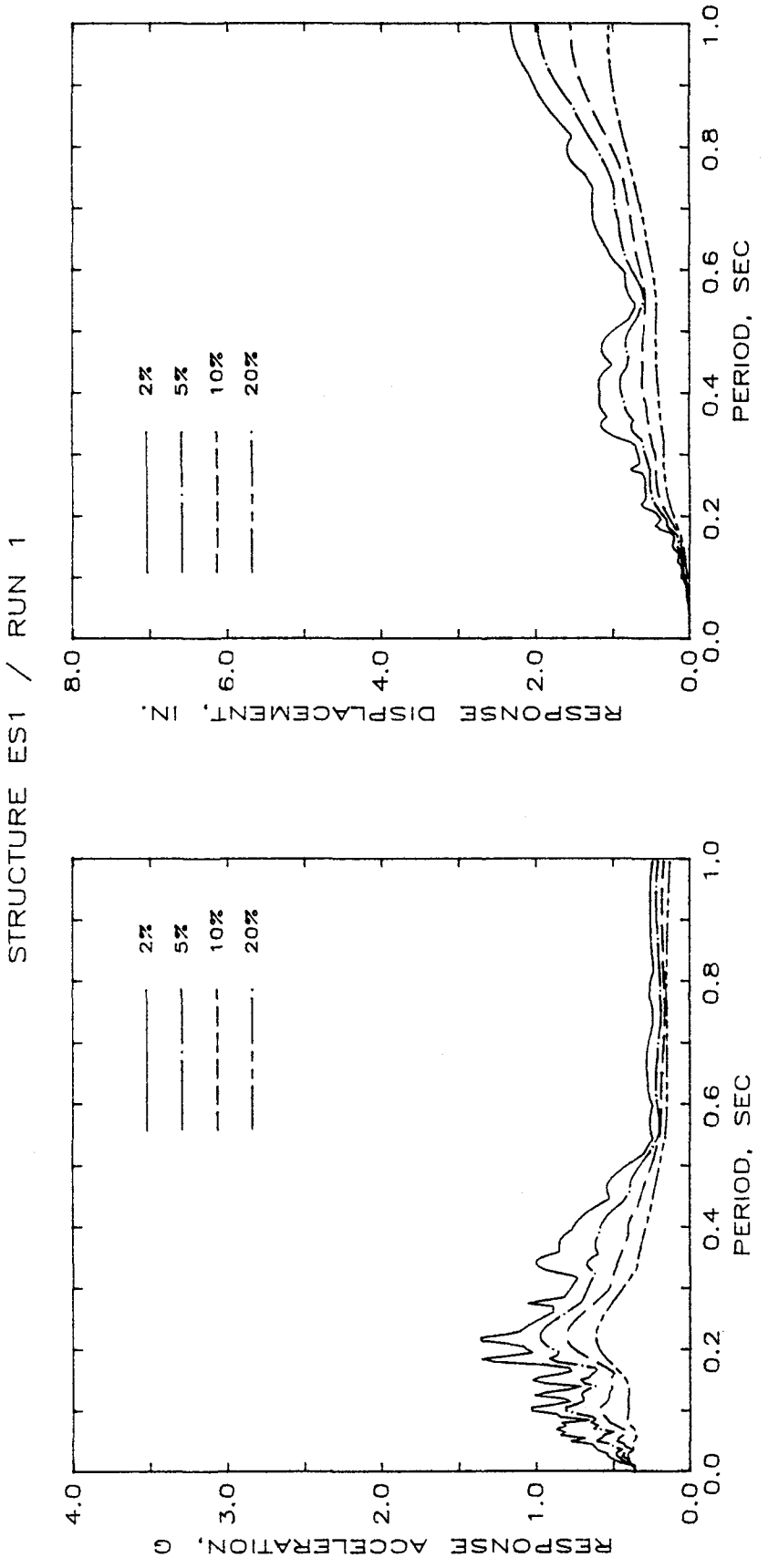

Fig. 4.4 Acceleration and Displacement Response Spectra
(a) Structure ES1 - Run 1

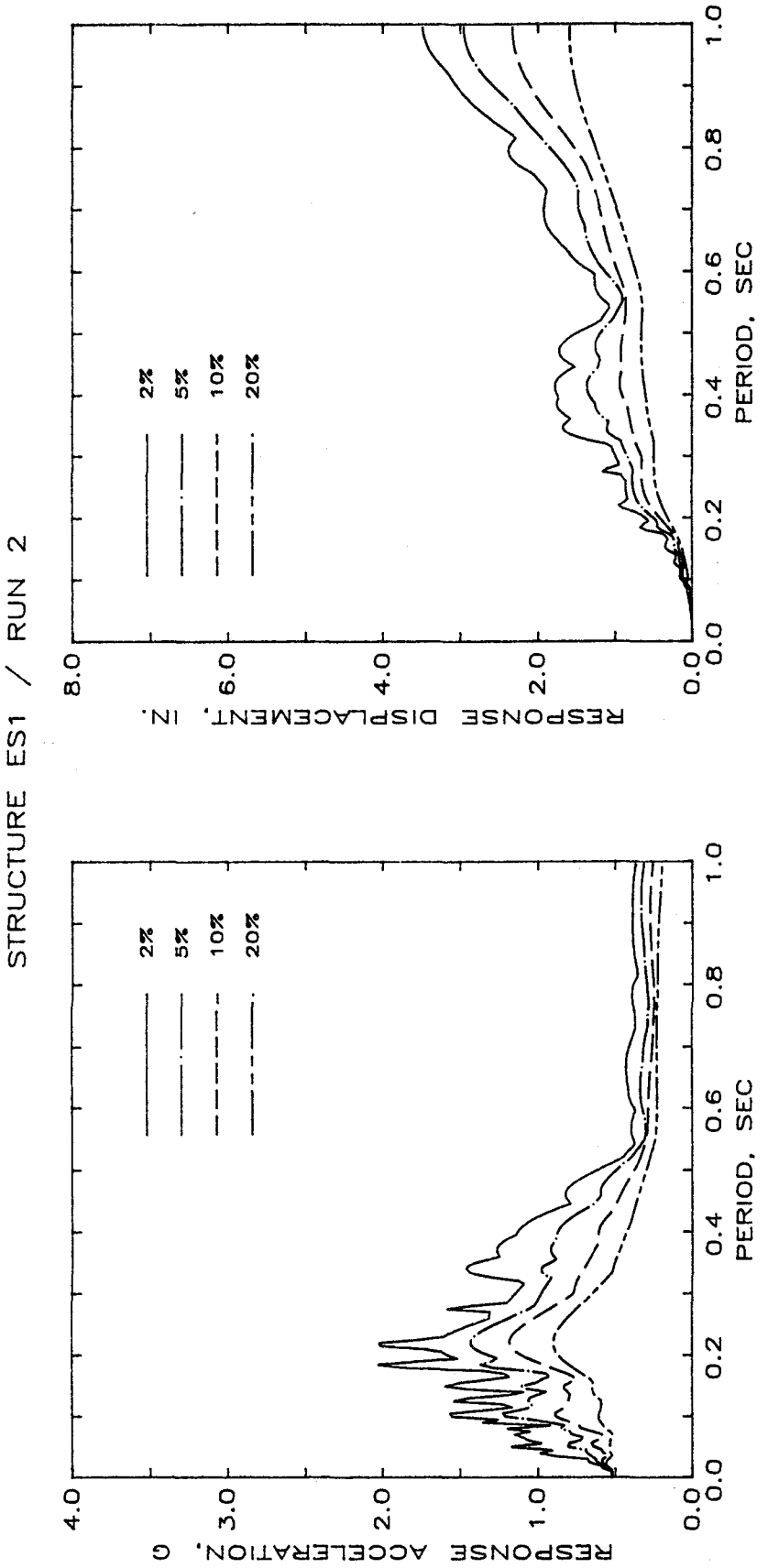

Fig. 4.4 (cont.) Acceleration and Displacement Response Spectra
(b) Structure ES1 - Run 2

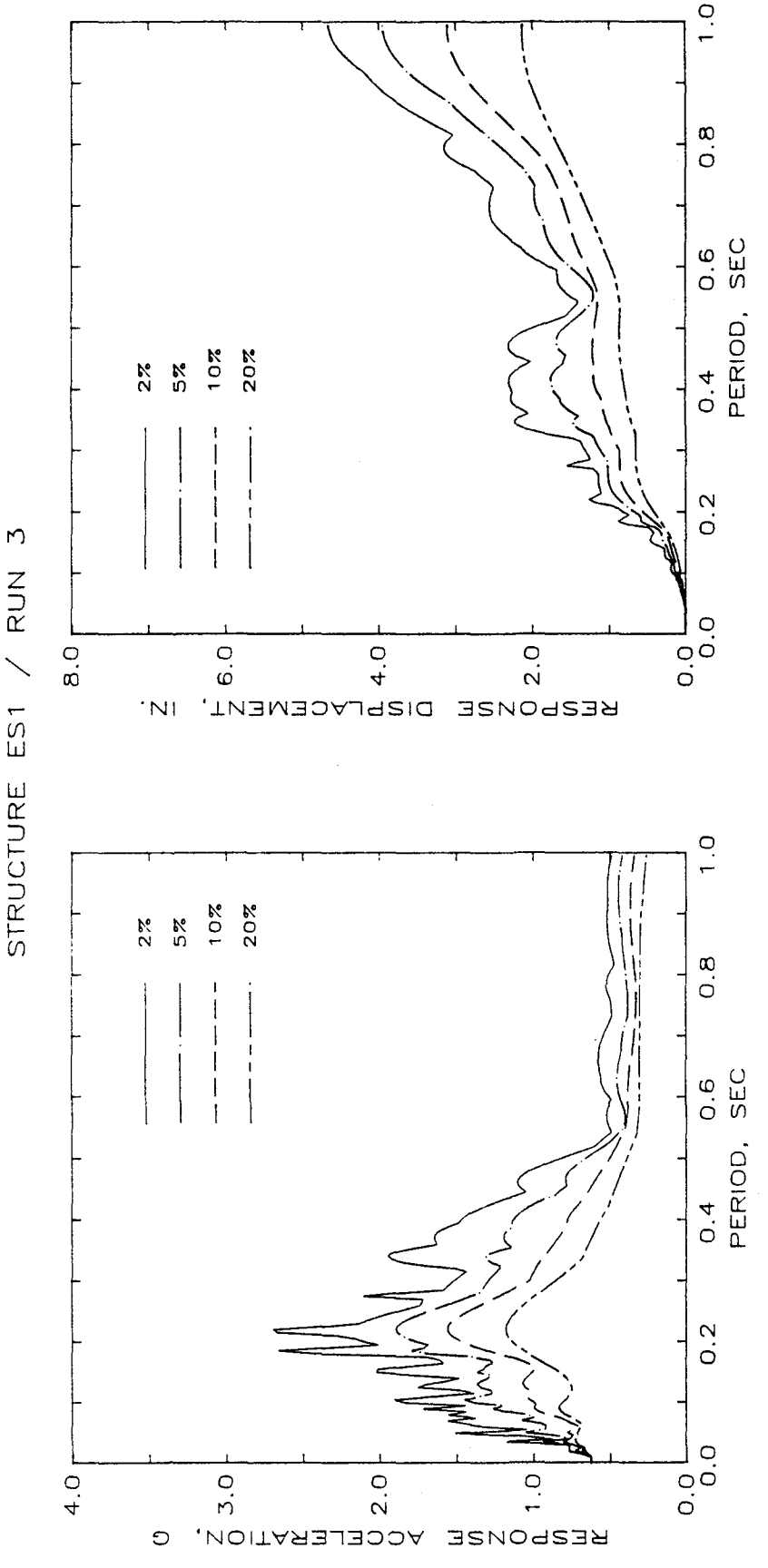

Fig. 4.4 (cont.) Acceleration and Displacement Response Spectra
(c) Structure ES1 - Run 3

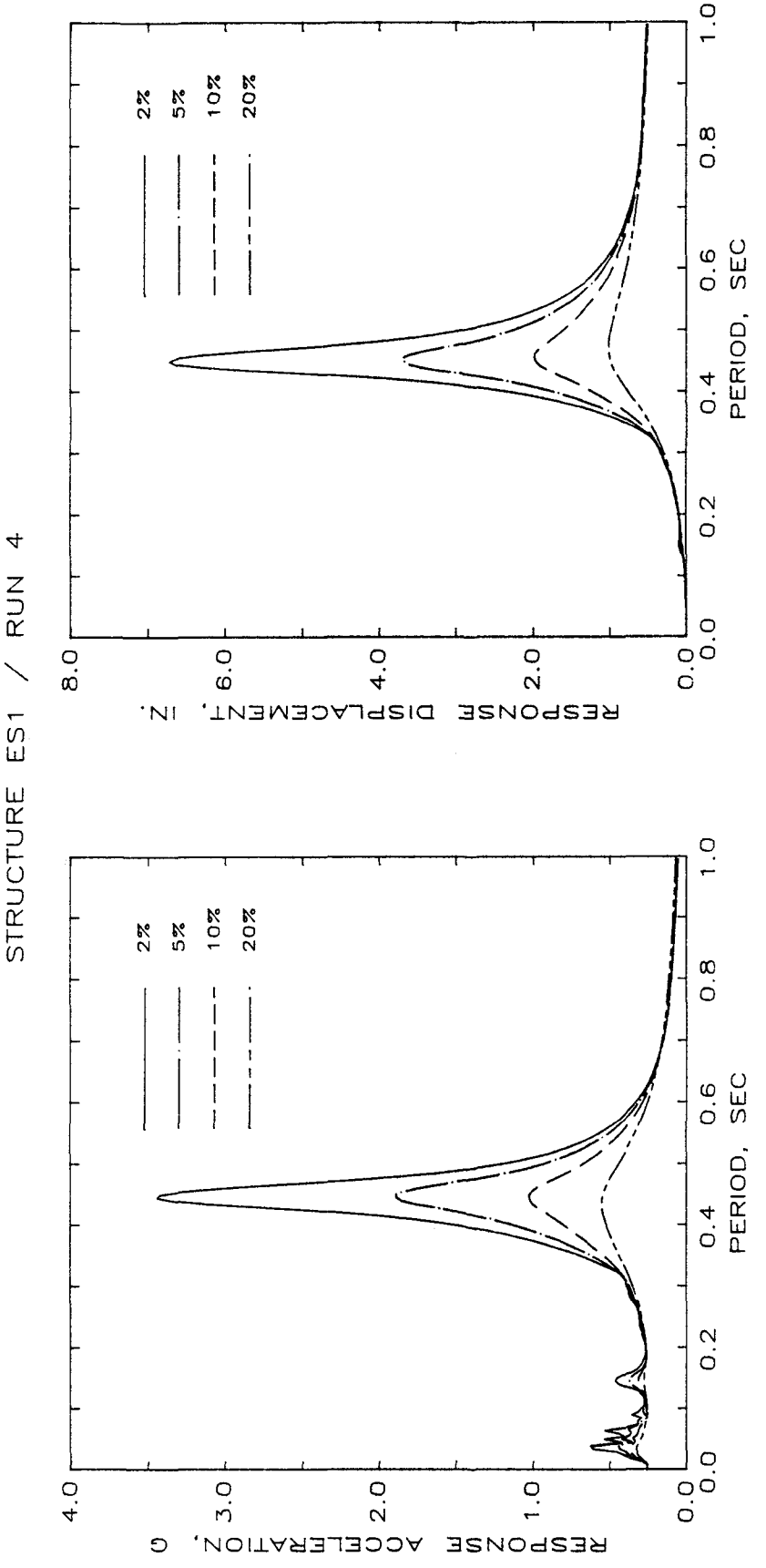

Fig. 4.4 (cont.) Acceleration and Displacement Response Spectra
(d) Structure ES1 - Run 4

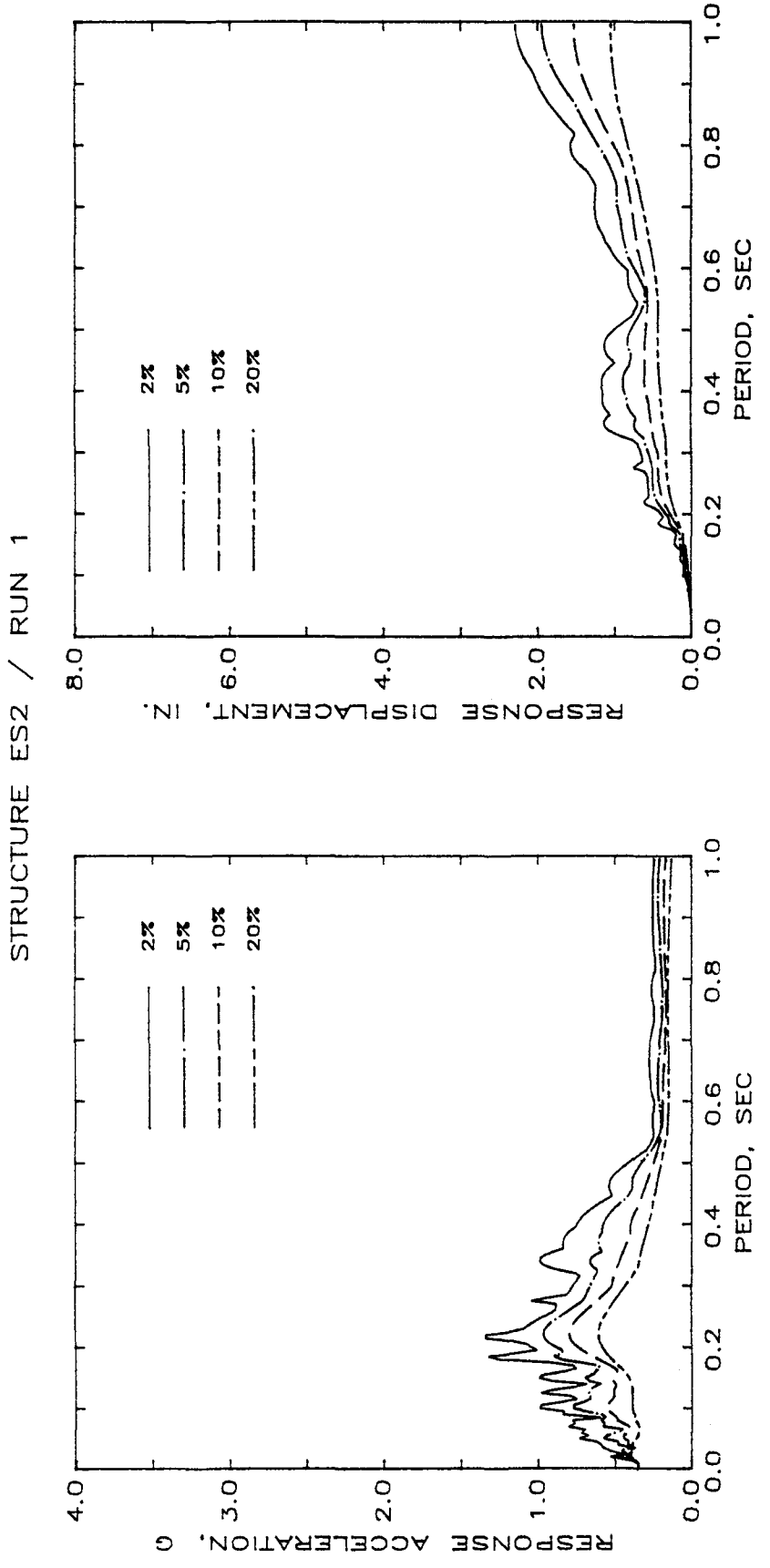

Fig. 4.4 (cont.) Acceleration and Displacement Response Spectra
(e) Structure ES2 - Run 1

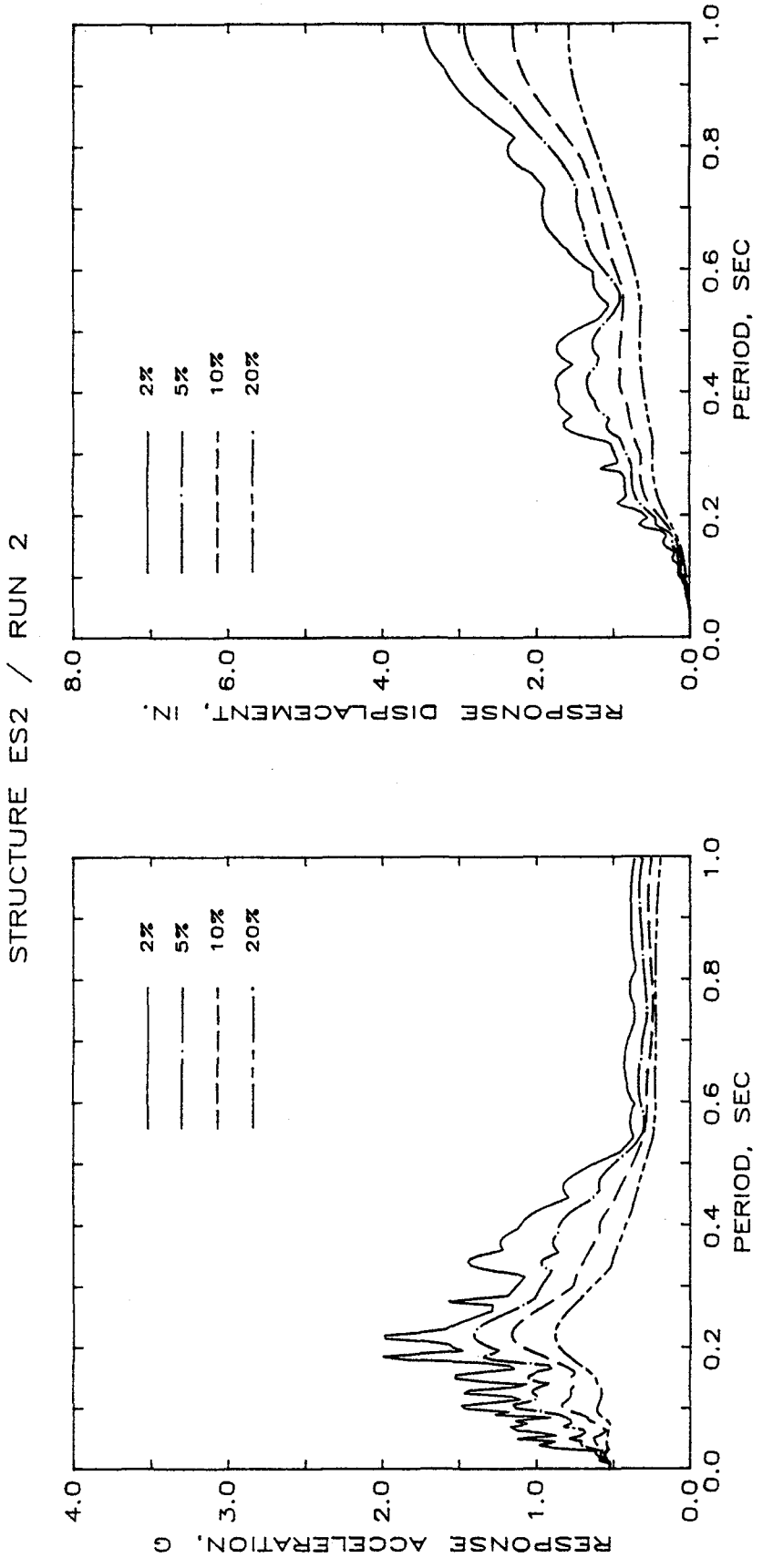

Fig. 4.4 (cont.) Acceleration and Displacement Response Spectra
(f) Structure ES2 - Run 2

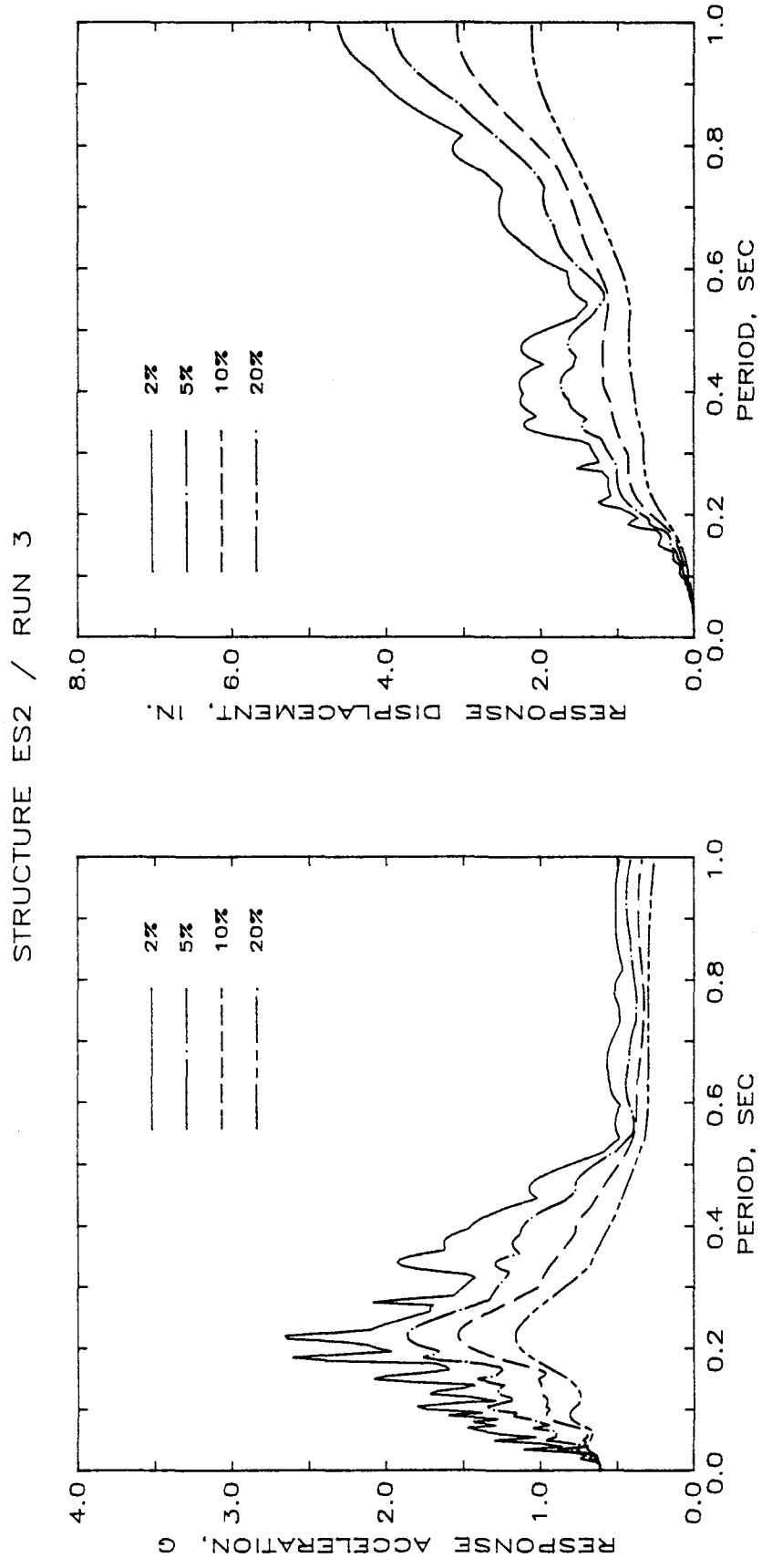

Fig. 4.4 (cont.) Acceleration and Displacement Response Spectra (g) Structure ES2 - Run 3

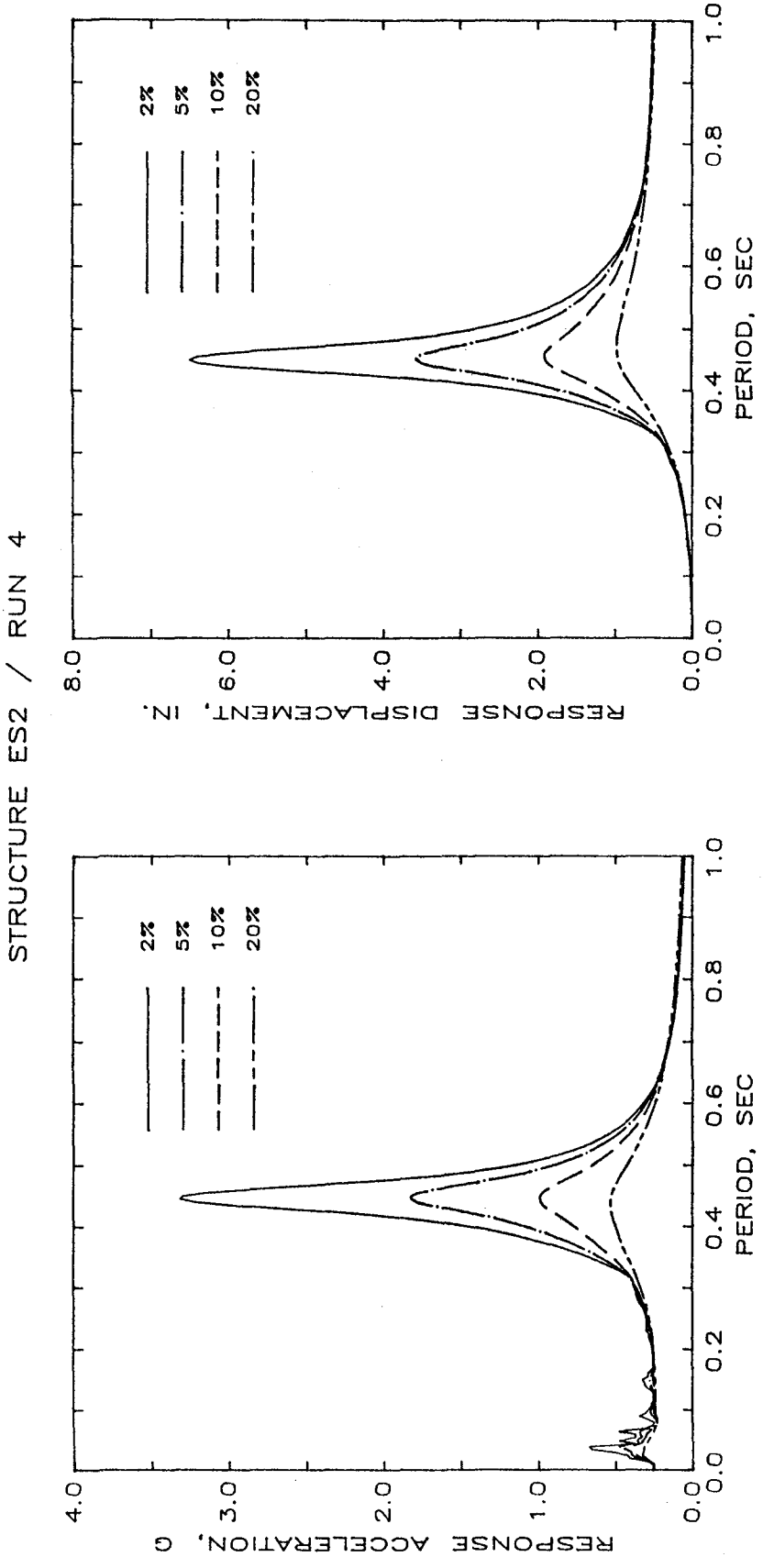

Fig. 4.4 (cont.) Acceleration and Displacement Response Spectra
(h) Structure ES2 - Run 4

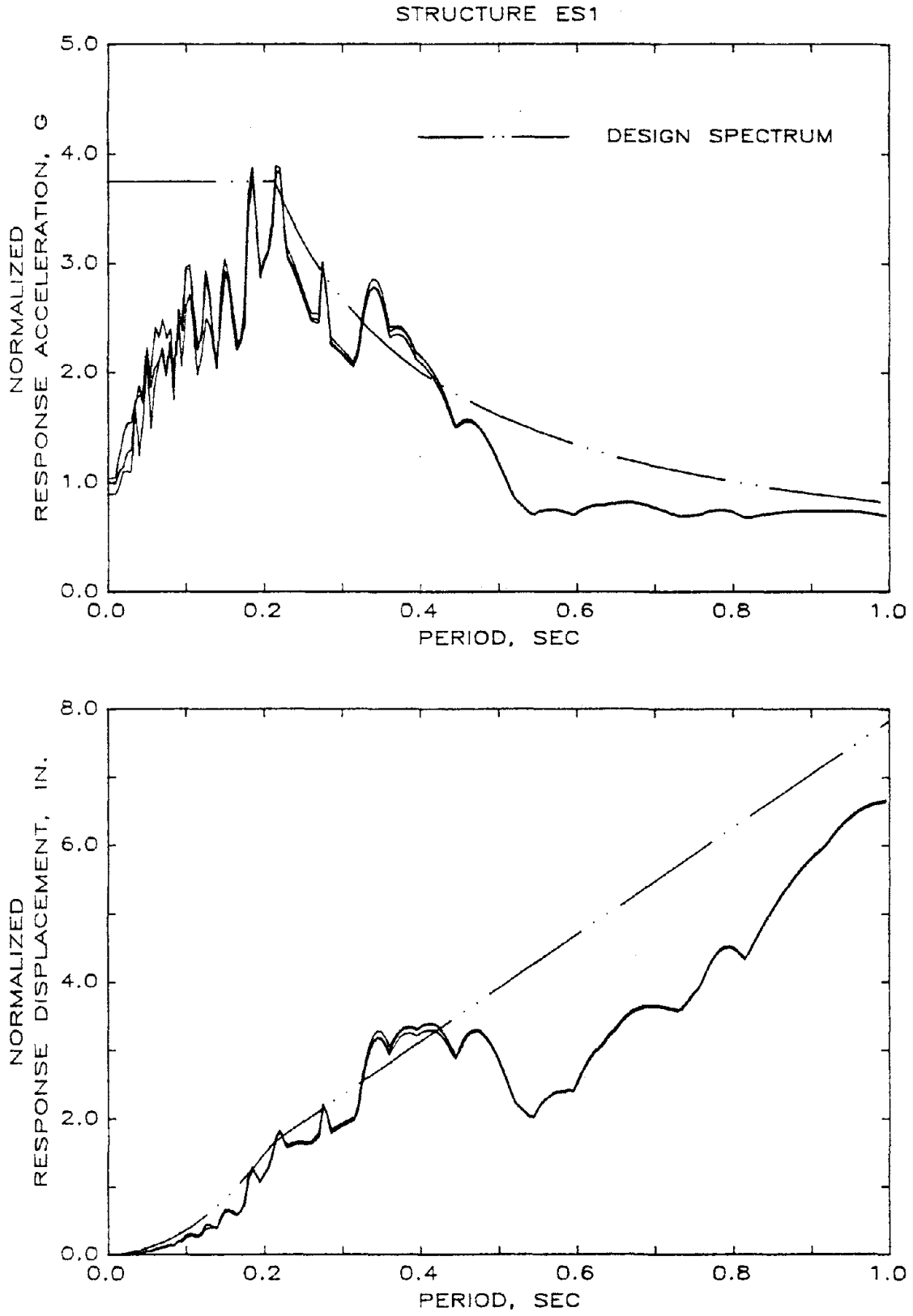

Fig. 4.5 Normalized Response Spectra (Damping Factor = 0.02)
(a) Structure ES1

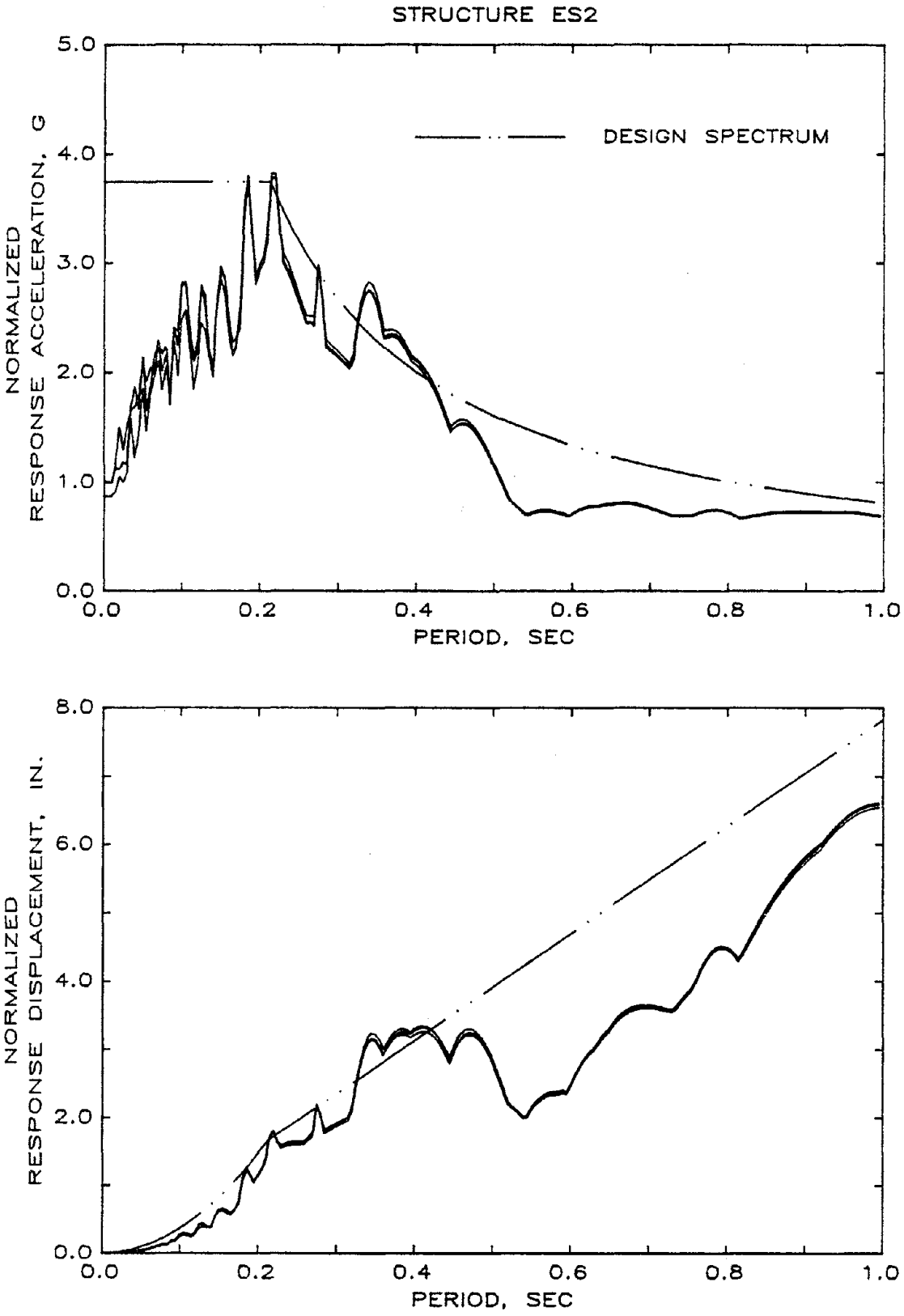

Fig. 4.5 (cont.) Normalized Response Spectra (Damping Factor = 0.02)
(b) Structure ES2

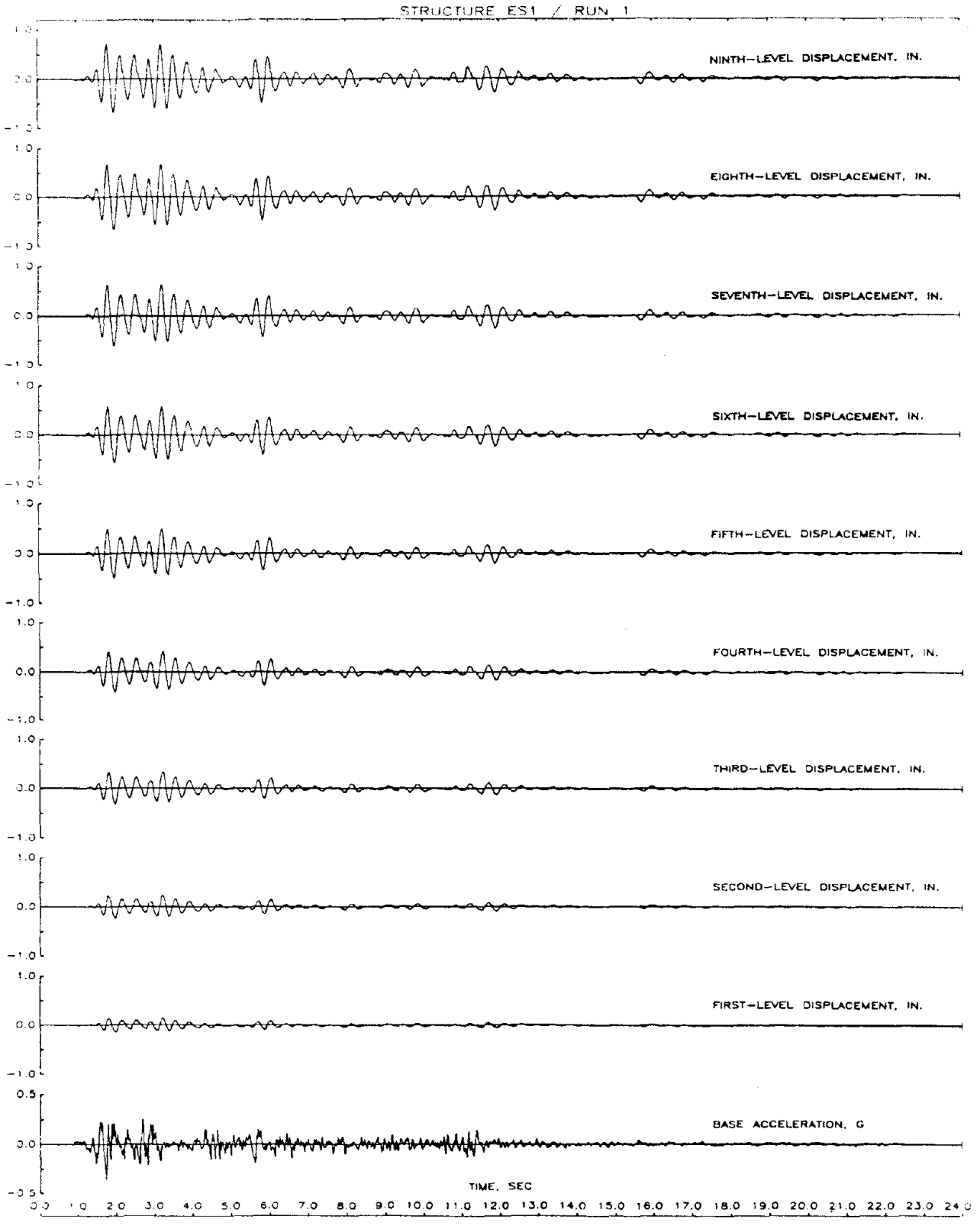

Fig. 4.6 Response of Structure ES1 During Run 1
(a) Displacement Histories

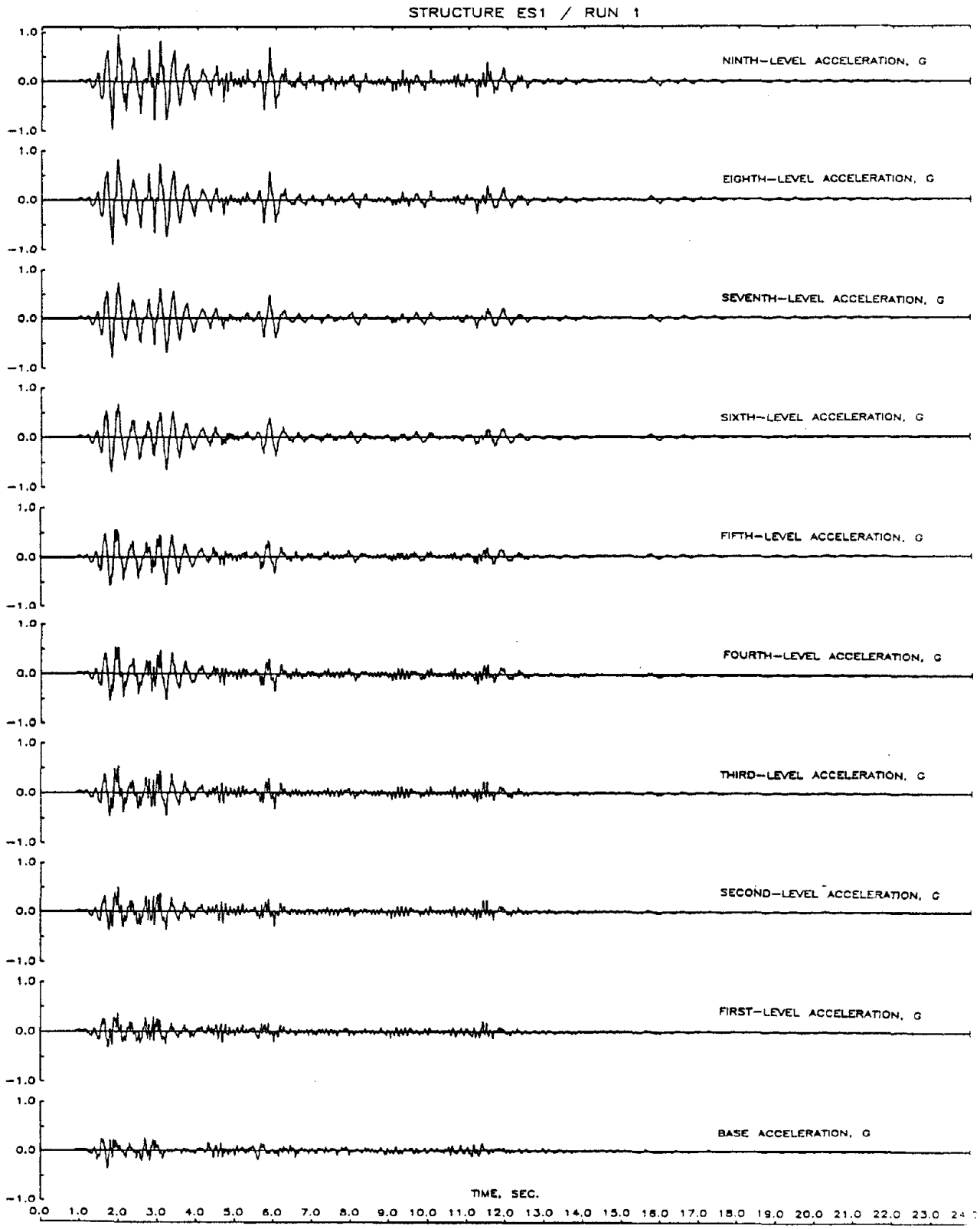

Fig. 4.6 (cont.) Response of Structure ES1 During Run 1
(b) Acceleration Histories

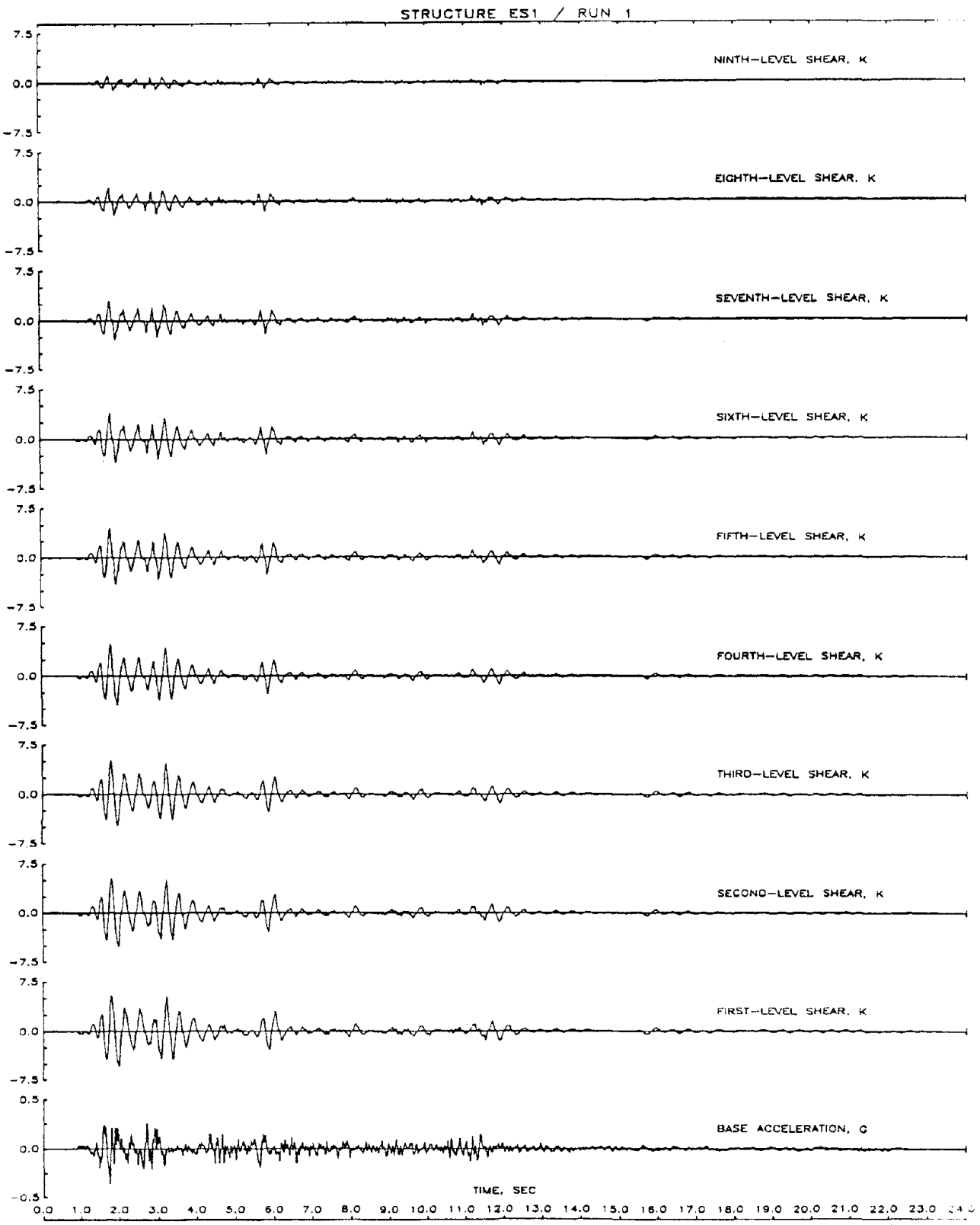

Fig. 4.6 (cont.) Response of Structure ES1 During Run 1
(c) Shear Histories

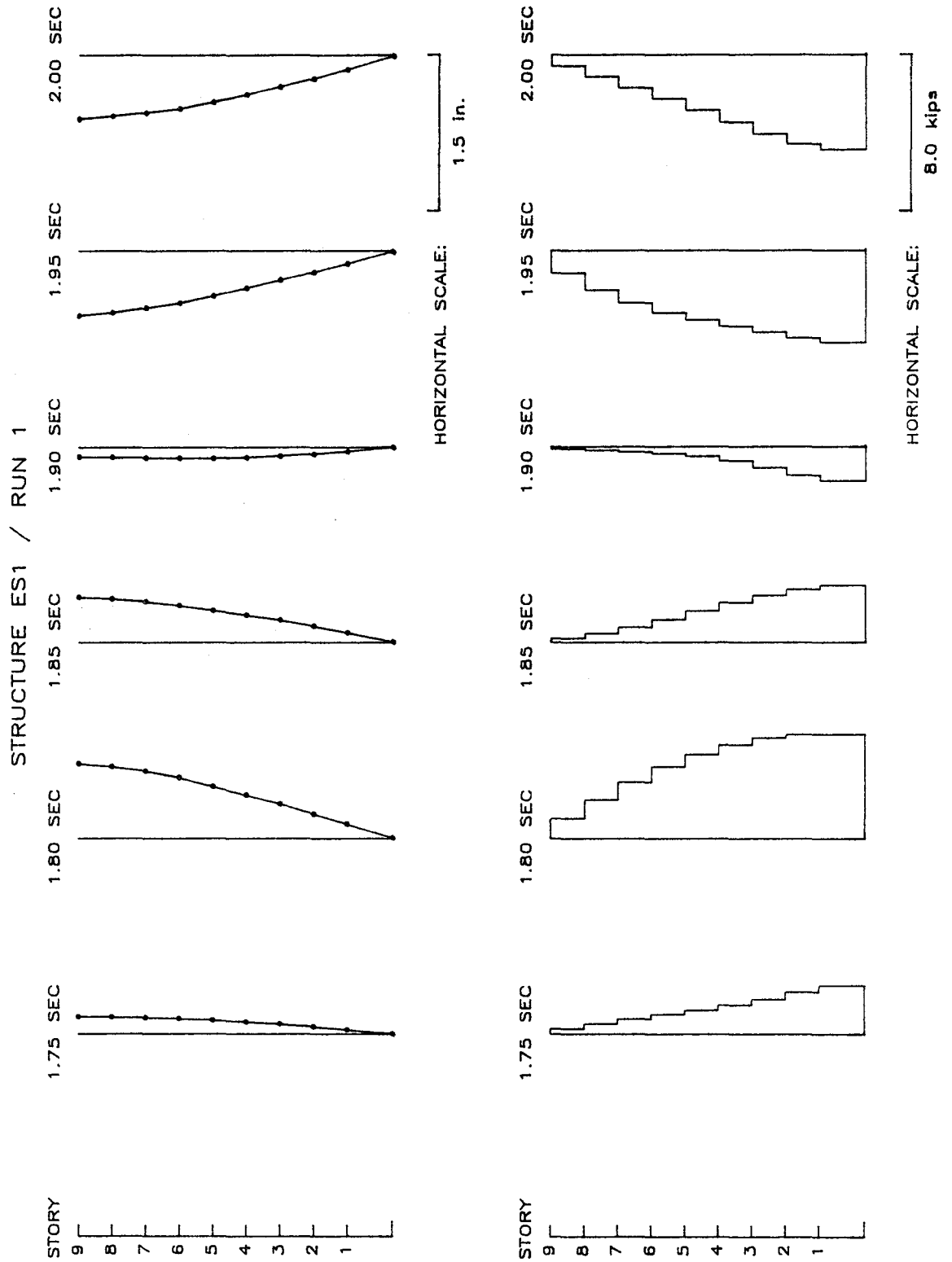

Fig. 4.6 (cont.) Response of Structure ES1 During Run 1
(d) Displacement and Shear Distributions

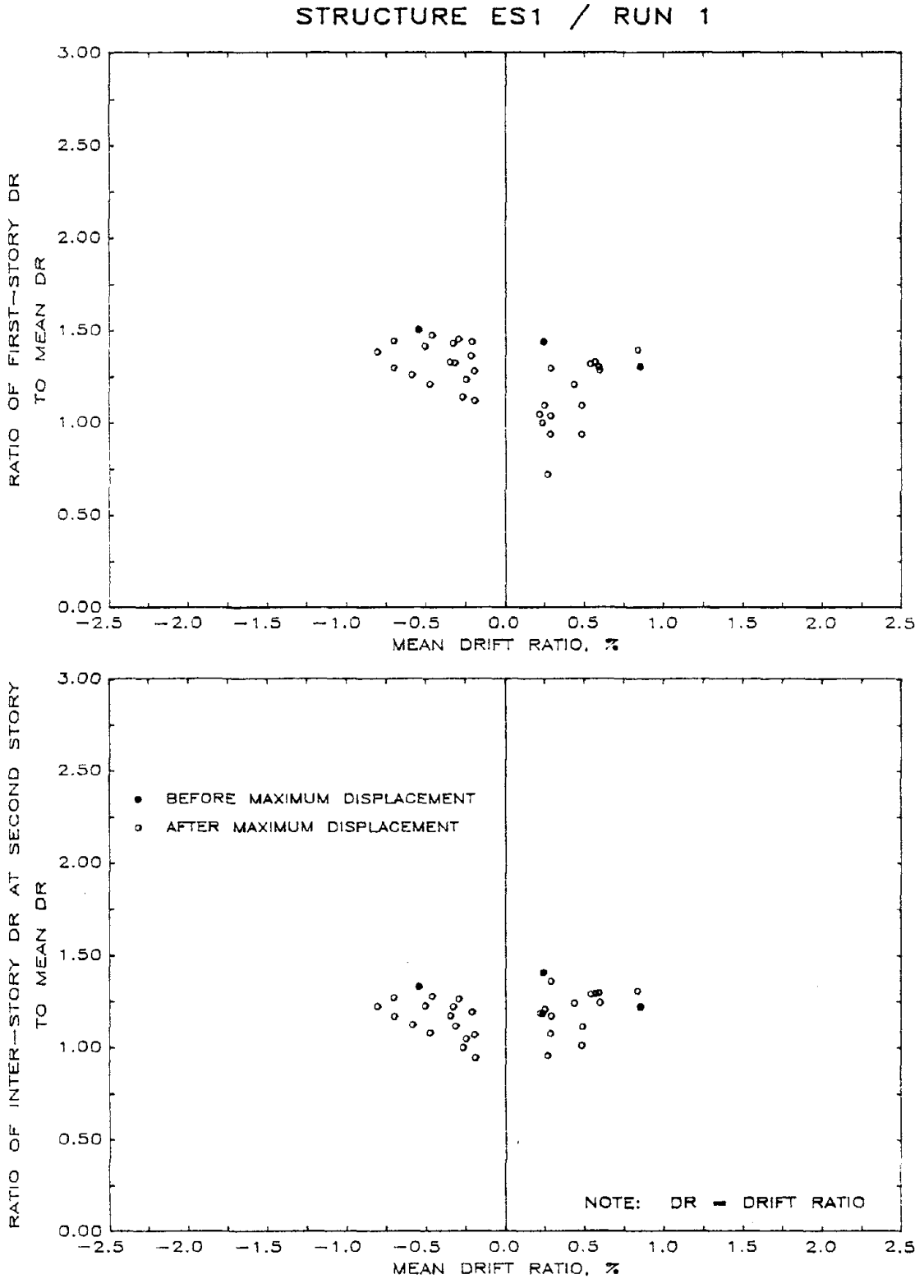

Fig. 4.6 (cont.) Response of Structure ES1 During Run 1
(e) Ratio of Interstory to Mean Drift

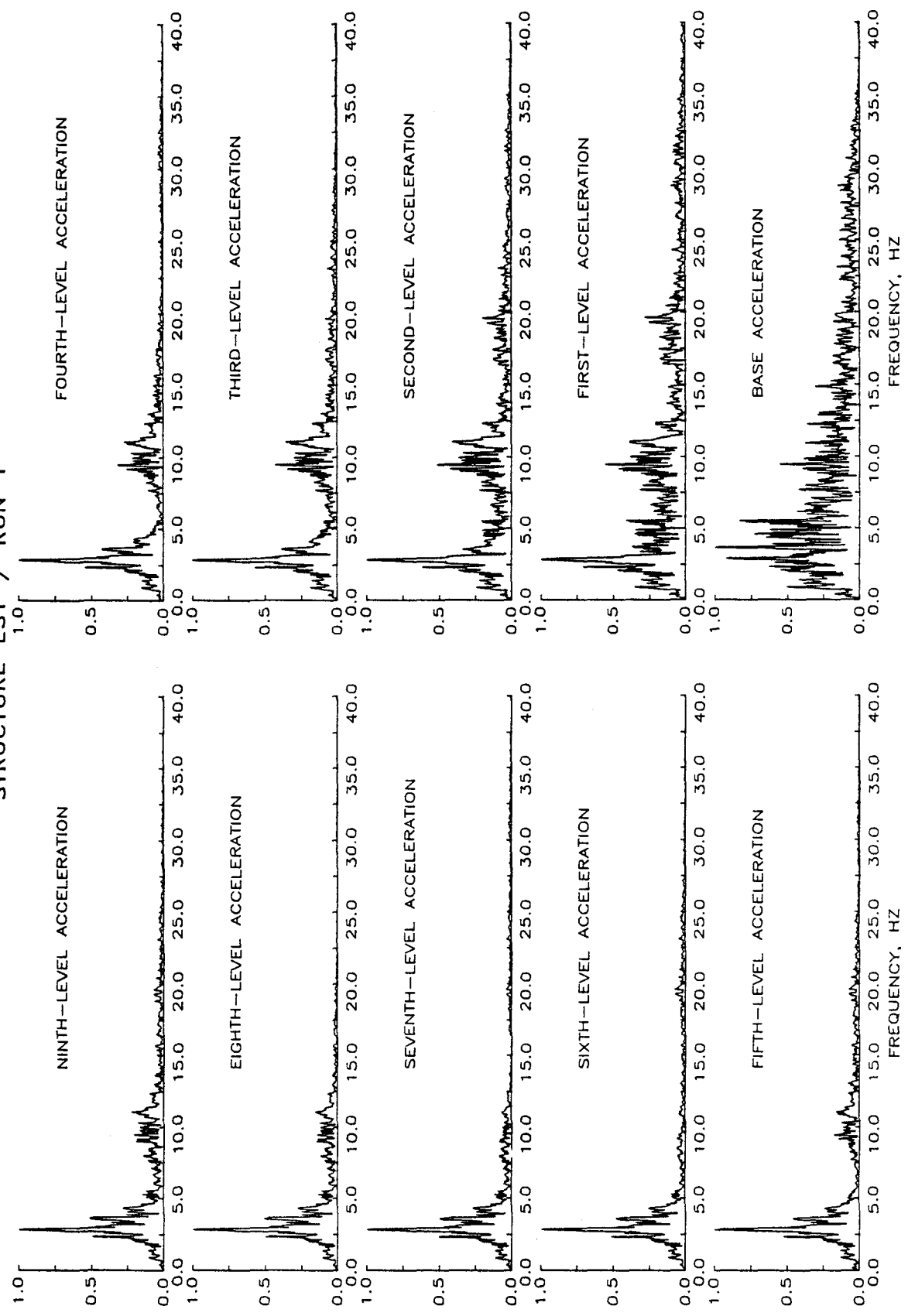

Fig. 4.6 (cont.) Response of Structure ES1 During Run 1
(f) Fourier Amplitude Spectra

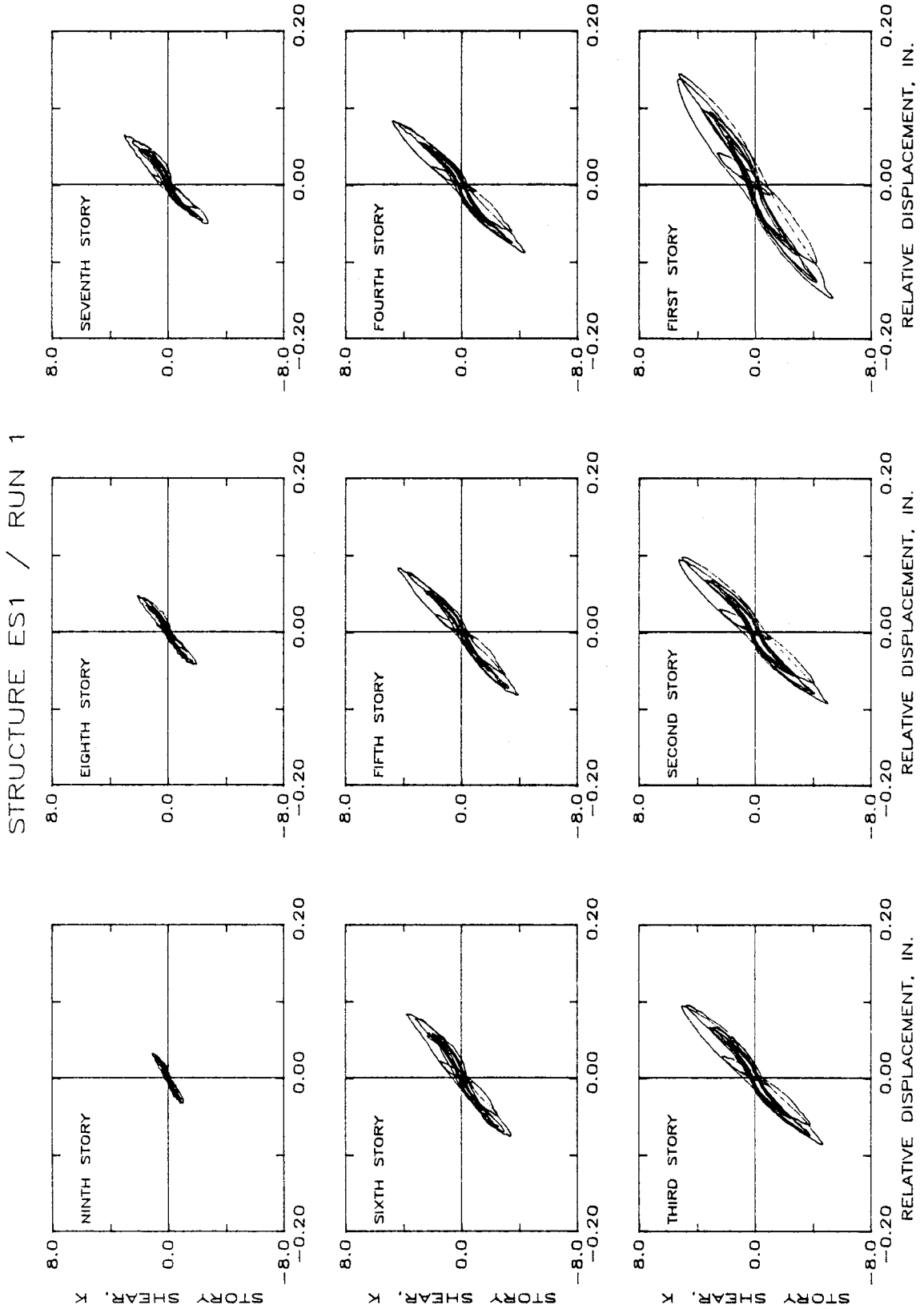

Fig. 4.6 (cont.) Response of Structure ES1 During Run 1
(g) Hysteretic Response

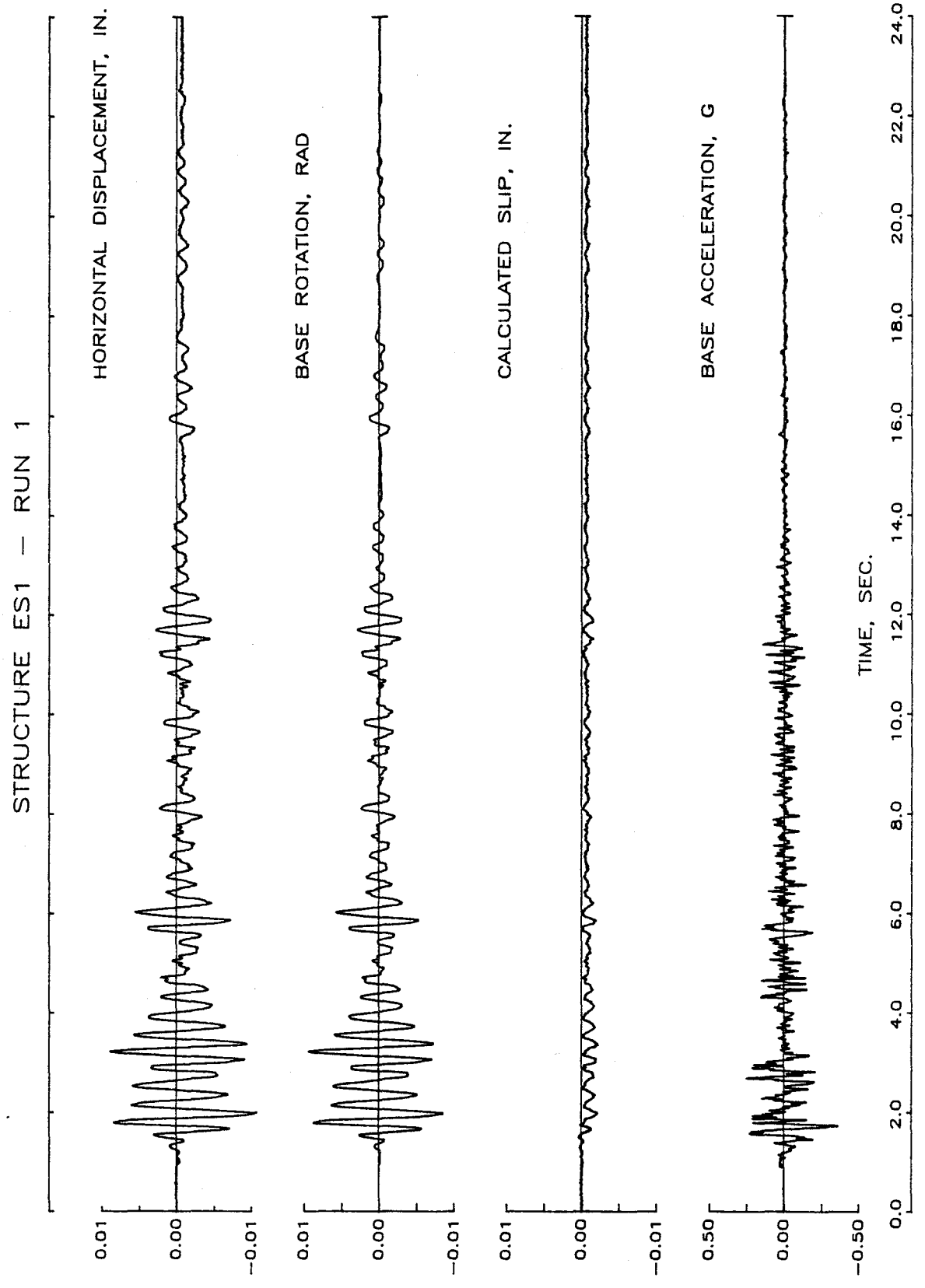

Fig. 4.6 (cont.) Response of Structure ES1 During Run 1
(h) Rotation and Slip at Base of Wall

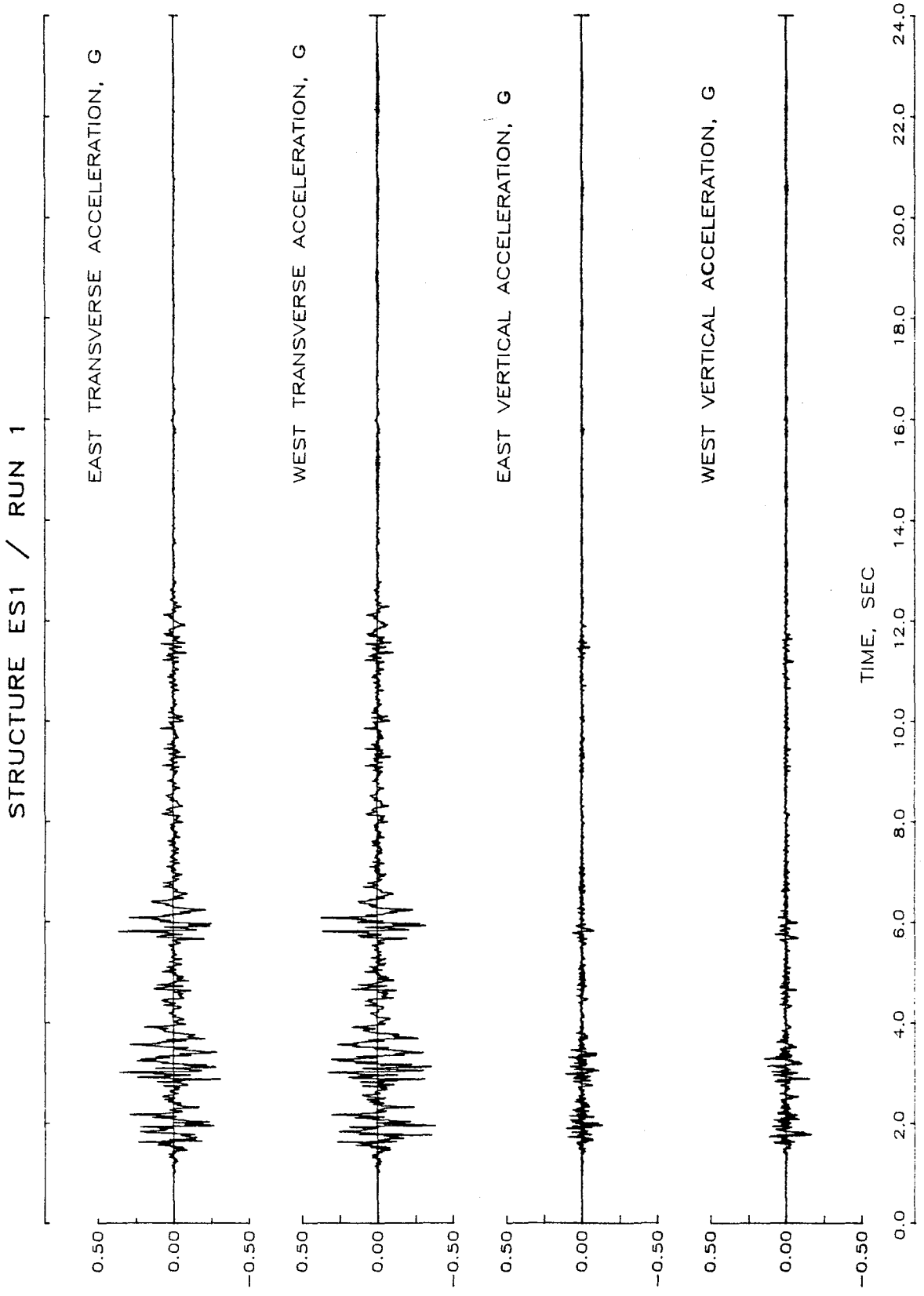

Fig. 4.6 (cont.) Response of Structure ES1 During Run 1
(i) Vertical and Transverse Accelerations

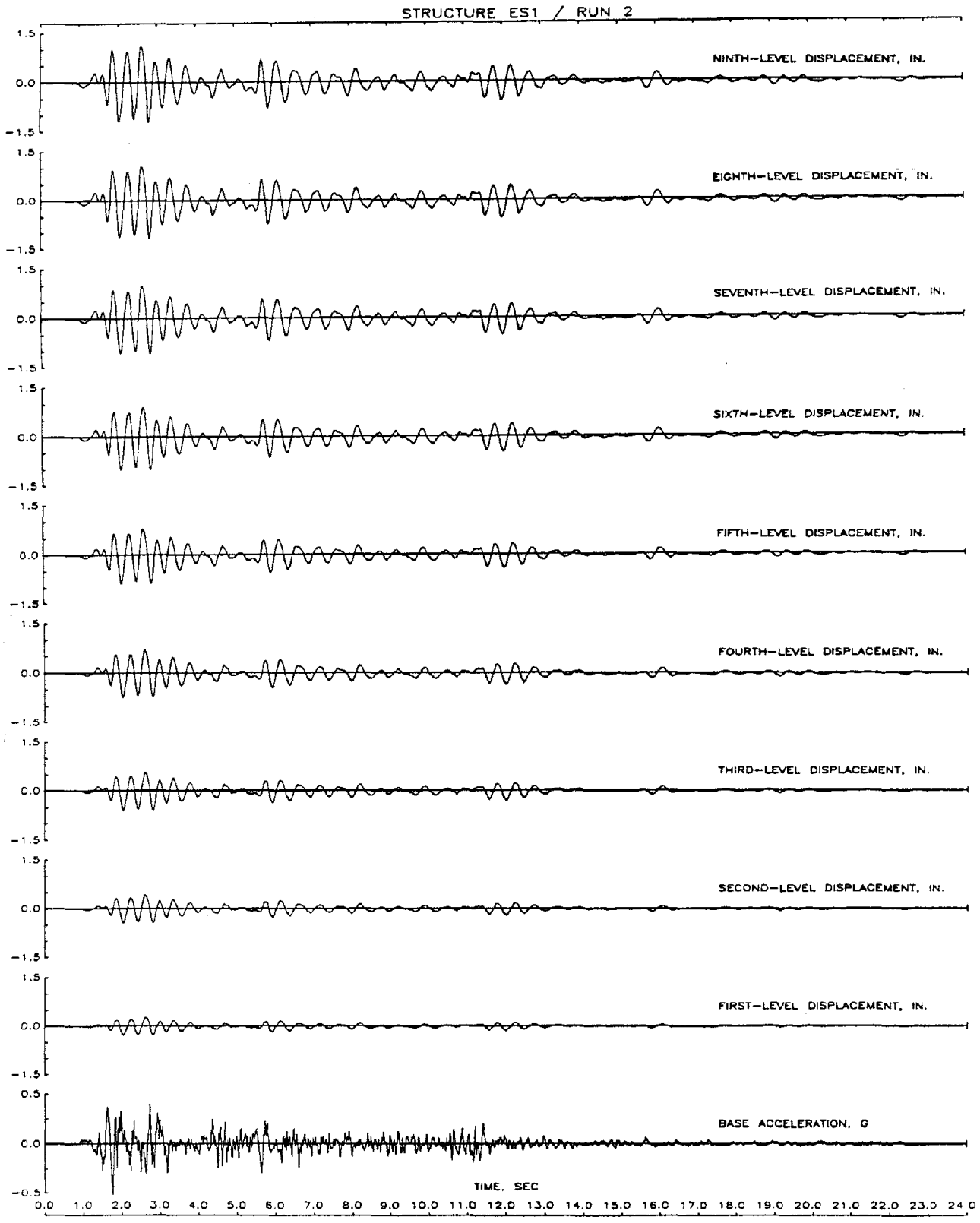

Fig. 4.7 Response of Structure ES1 During Run 2
(a) Displacement Histories

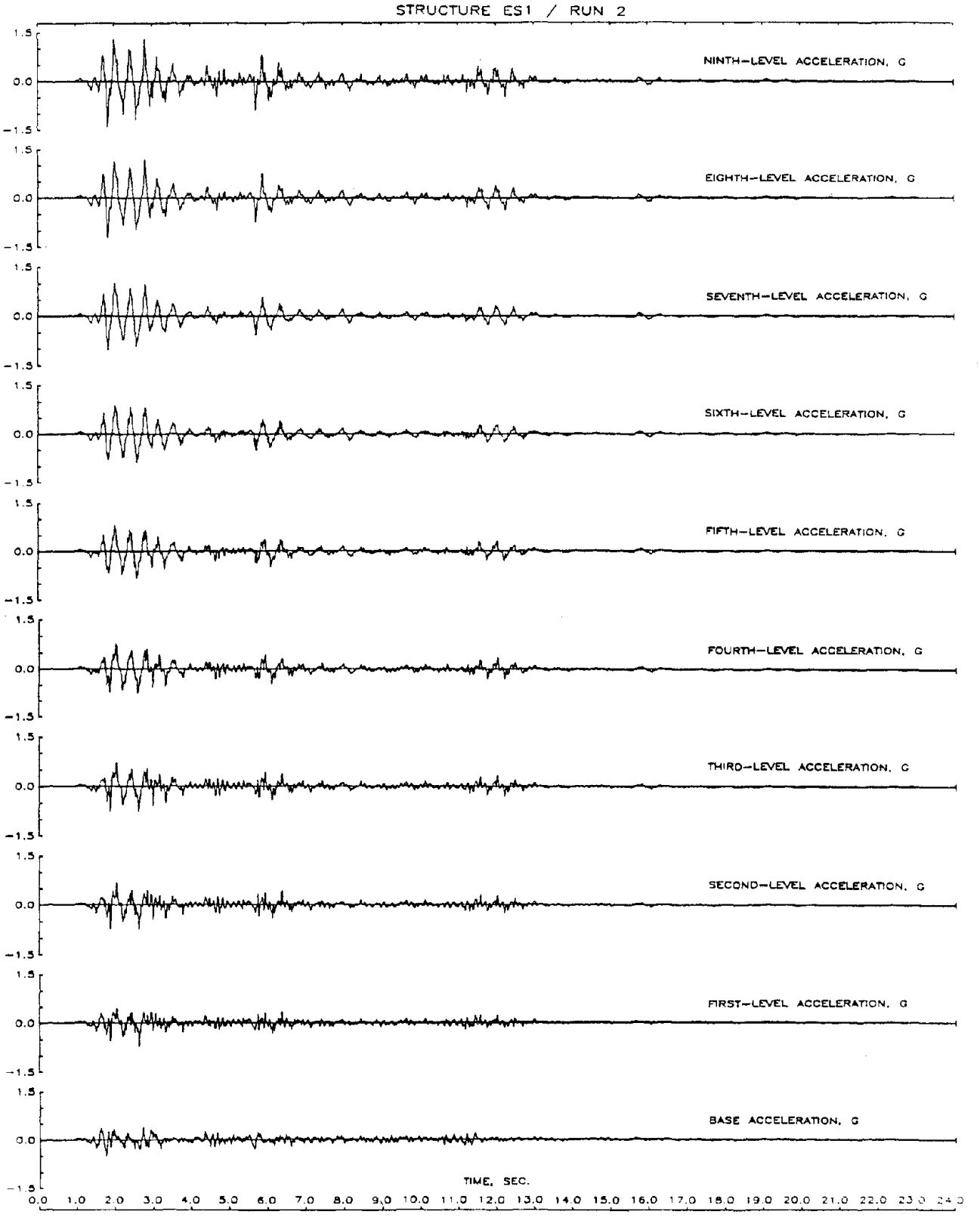

Fig. 4.7 (cont.) Response of Structure ES1 During Run 2
(b) Acceleration Histories

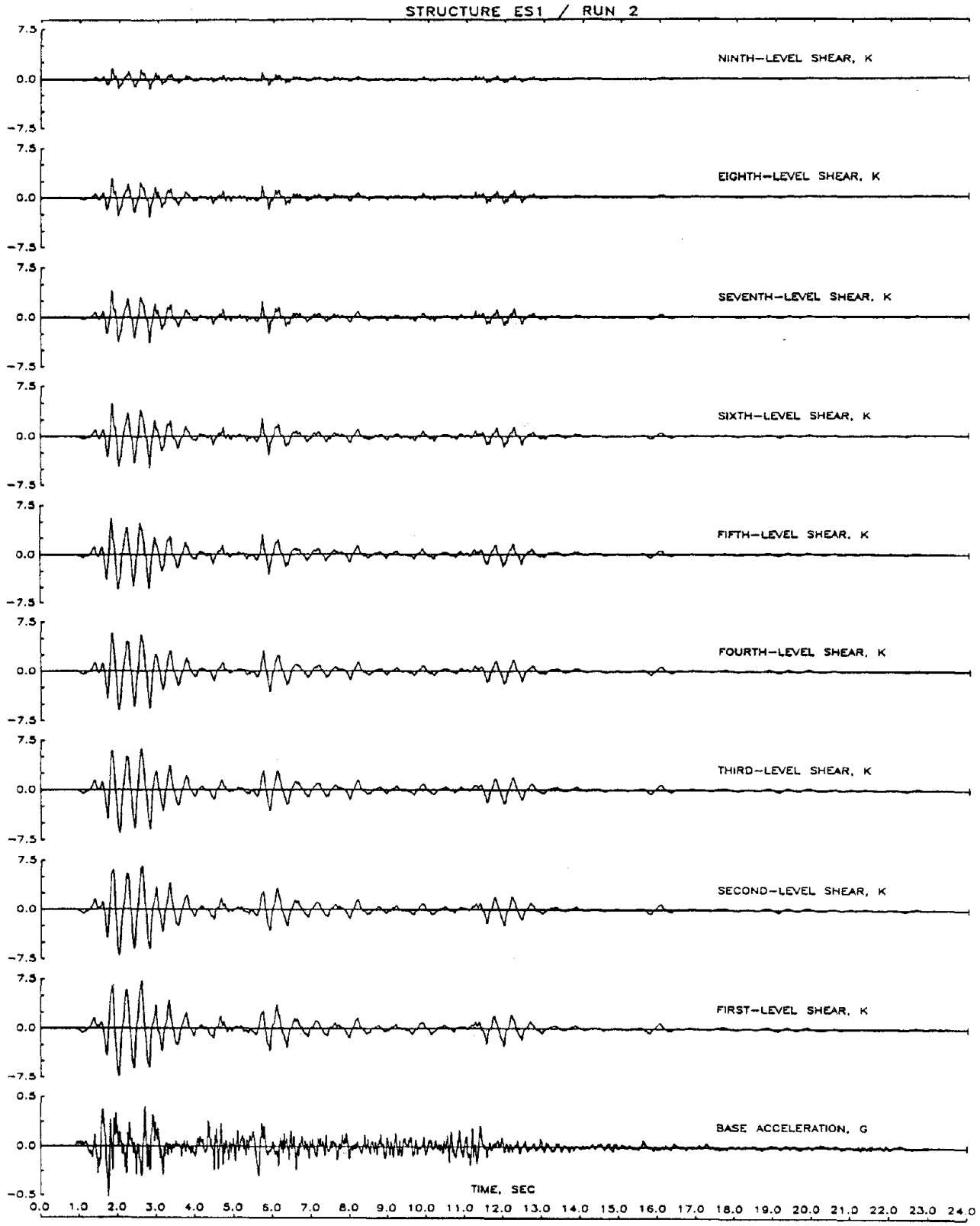

Fig. 4.7 (cont.) Response of Structure ES1 During Run 2
(c) Shear Histories

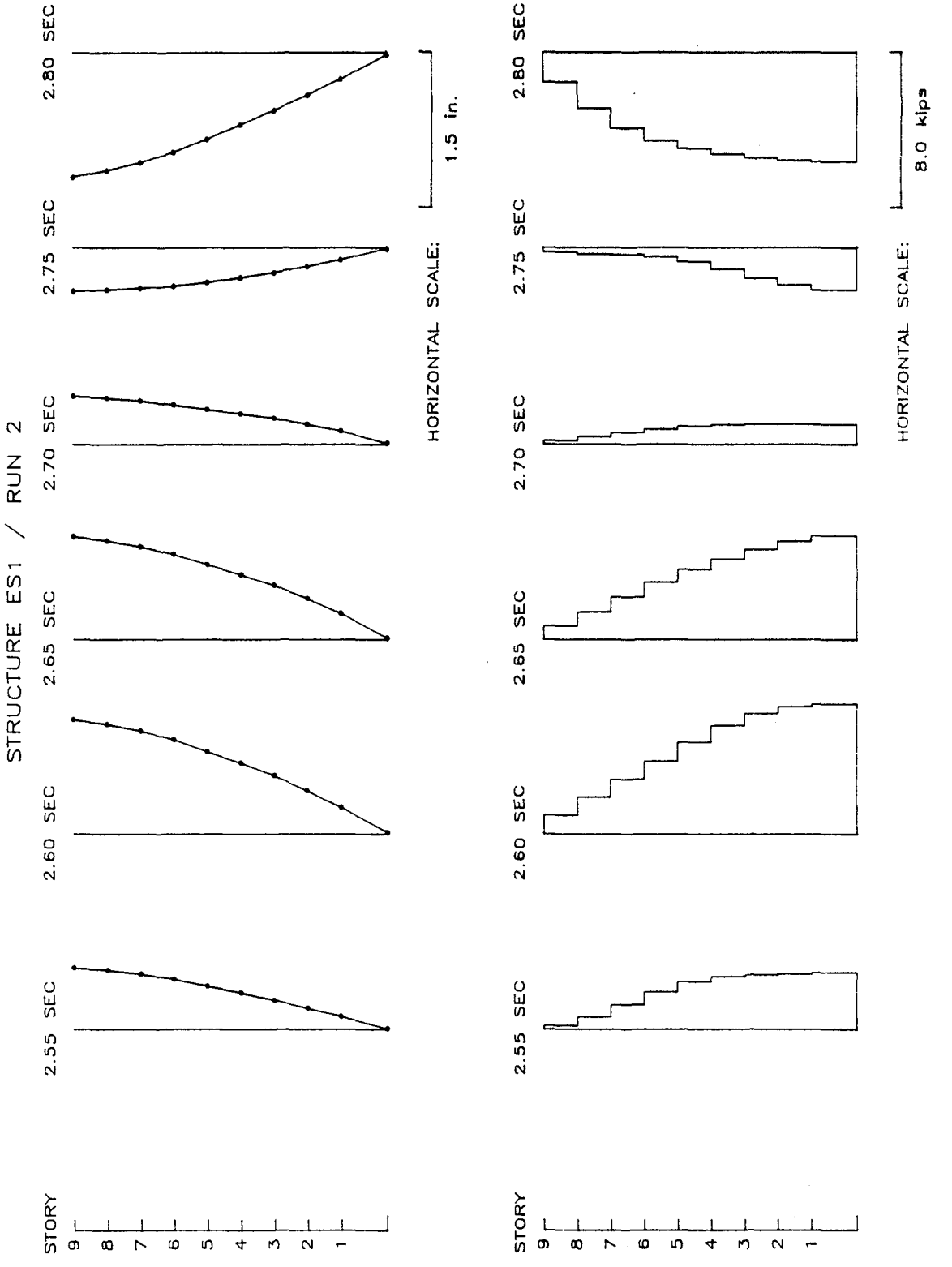

Fig. 4.7 (cont.) Response of Structure ES1 During Run 2
(d) Displacement and Shear Distributions

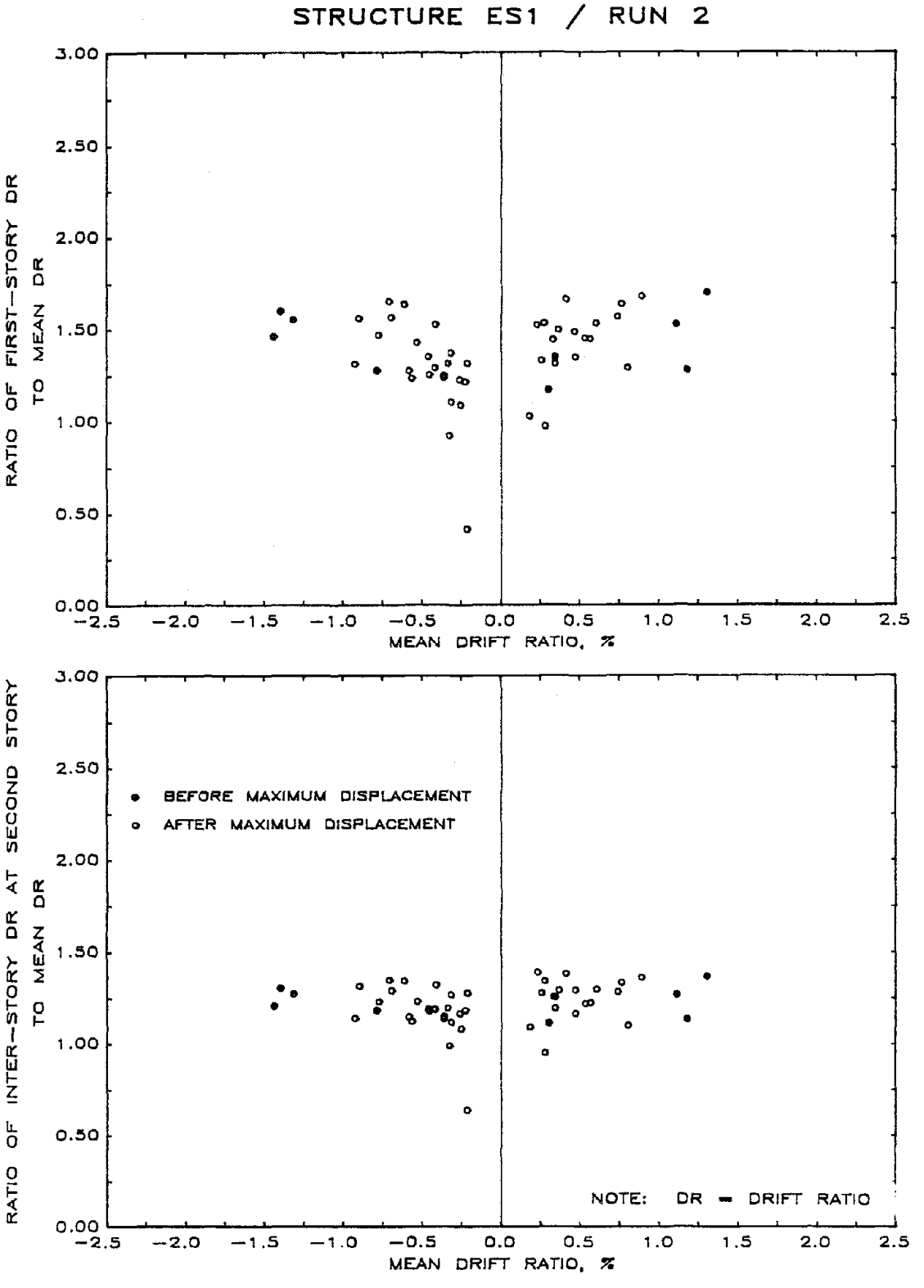

Fig. 4.7 (cont.) Response of Structure ES1 During Run 2
(e) Ratio of Interstory to Mean Drift

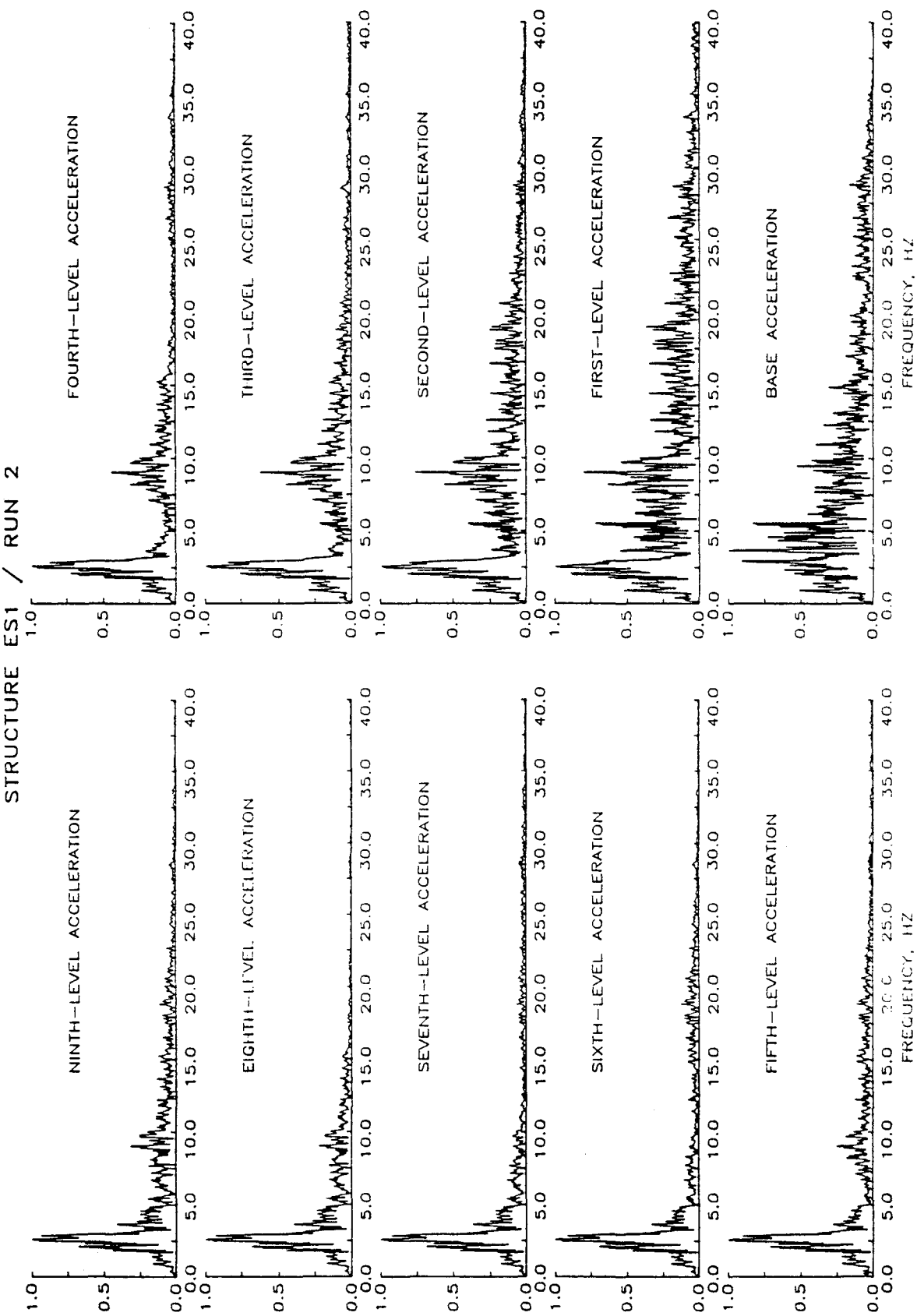

Fig. 4.7 (cont.) Response of Structure ES1 During Run 2
(f) Fourier Amplitude Spectra

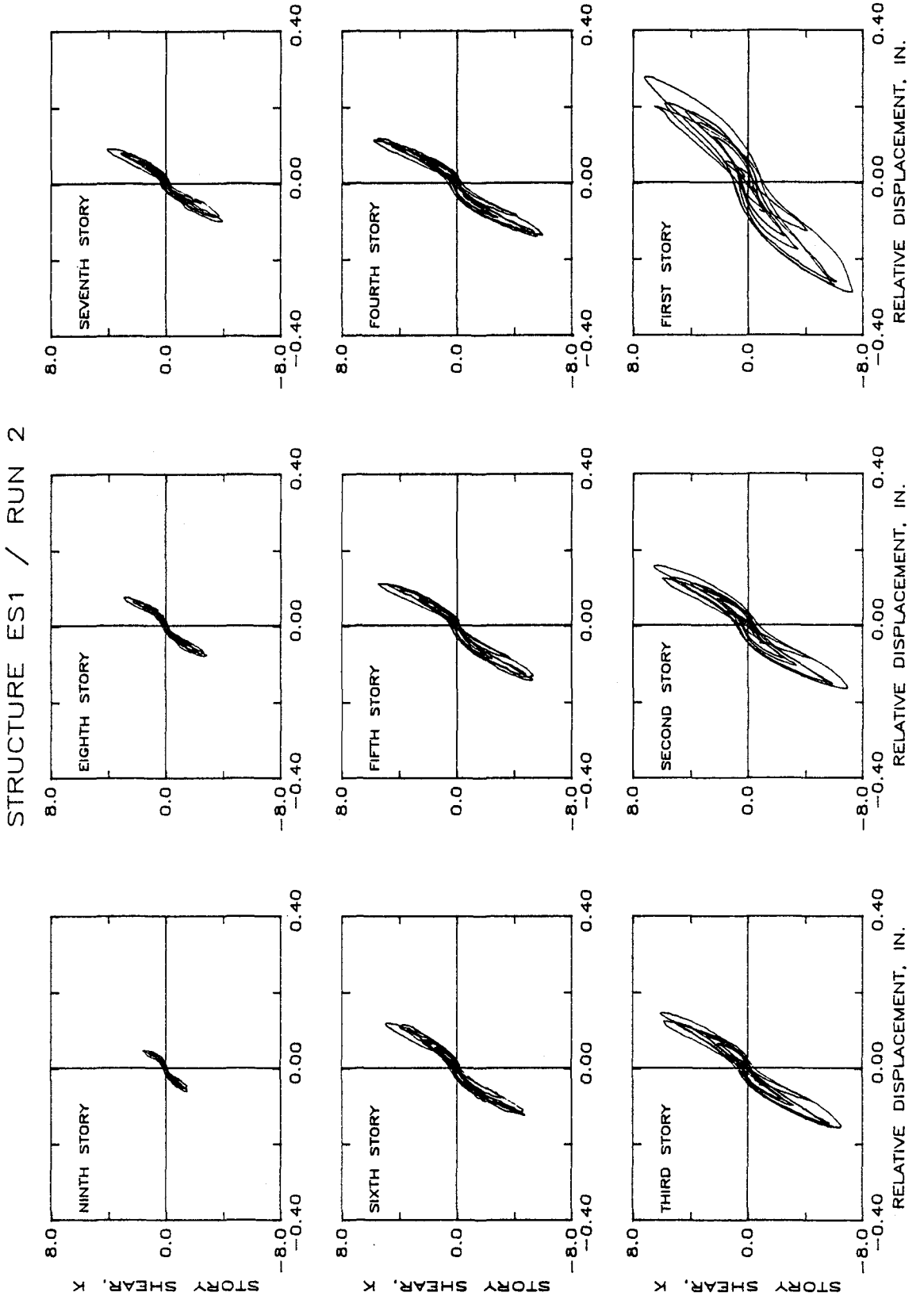

Fig. 4.7 (cont.) Response of Structure ES1 During Run 2
(g) Hysteretic Response

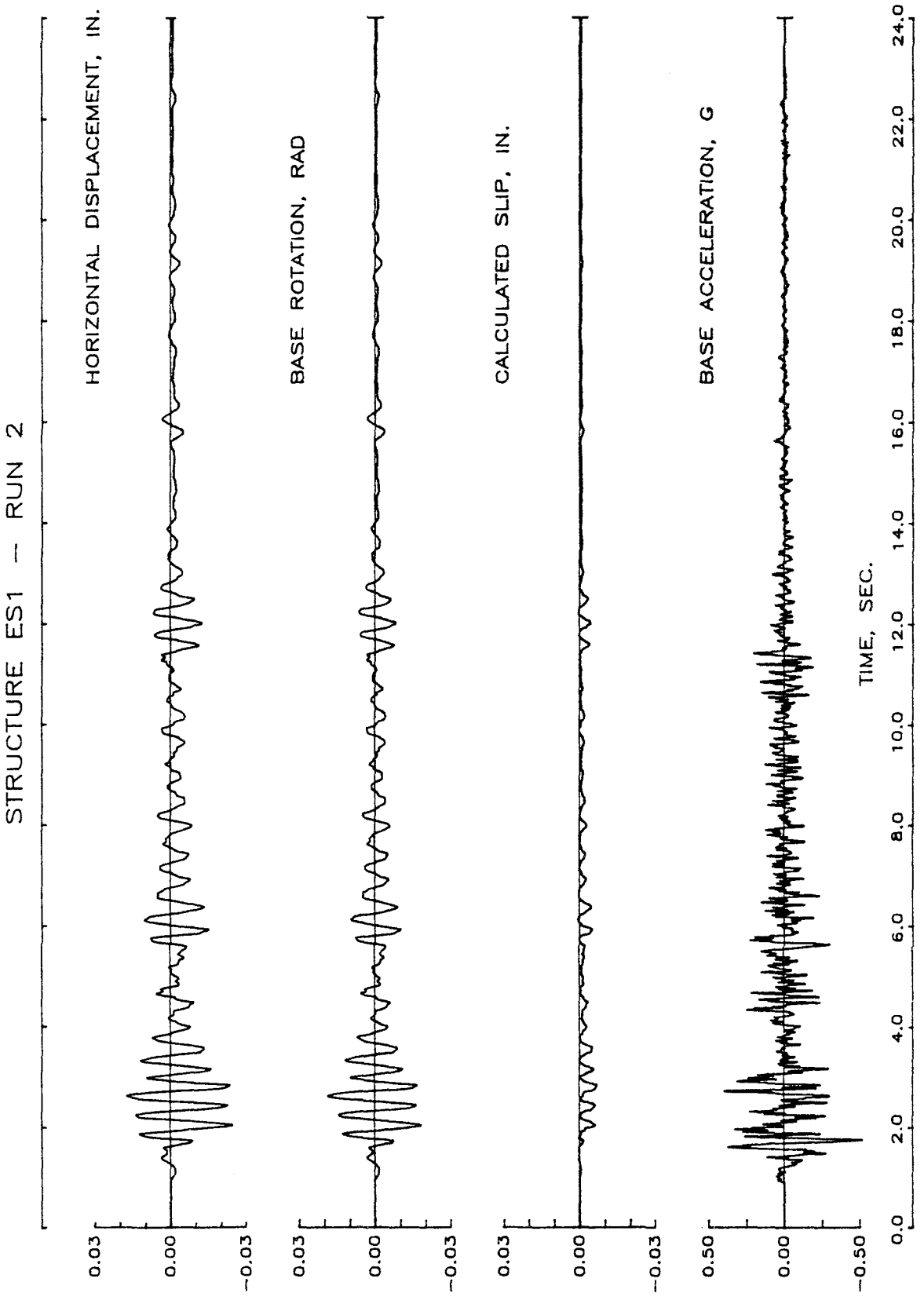

Fig. 4.7 (cont.) Response of Structure ES1 During Run 2
(h) Rotation and Slip at Base of Wall

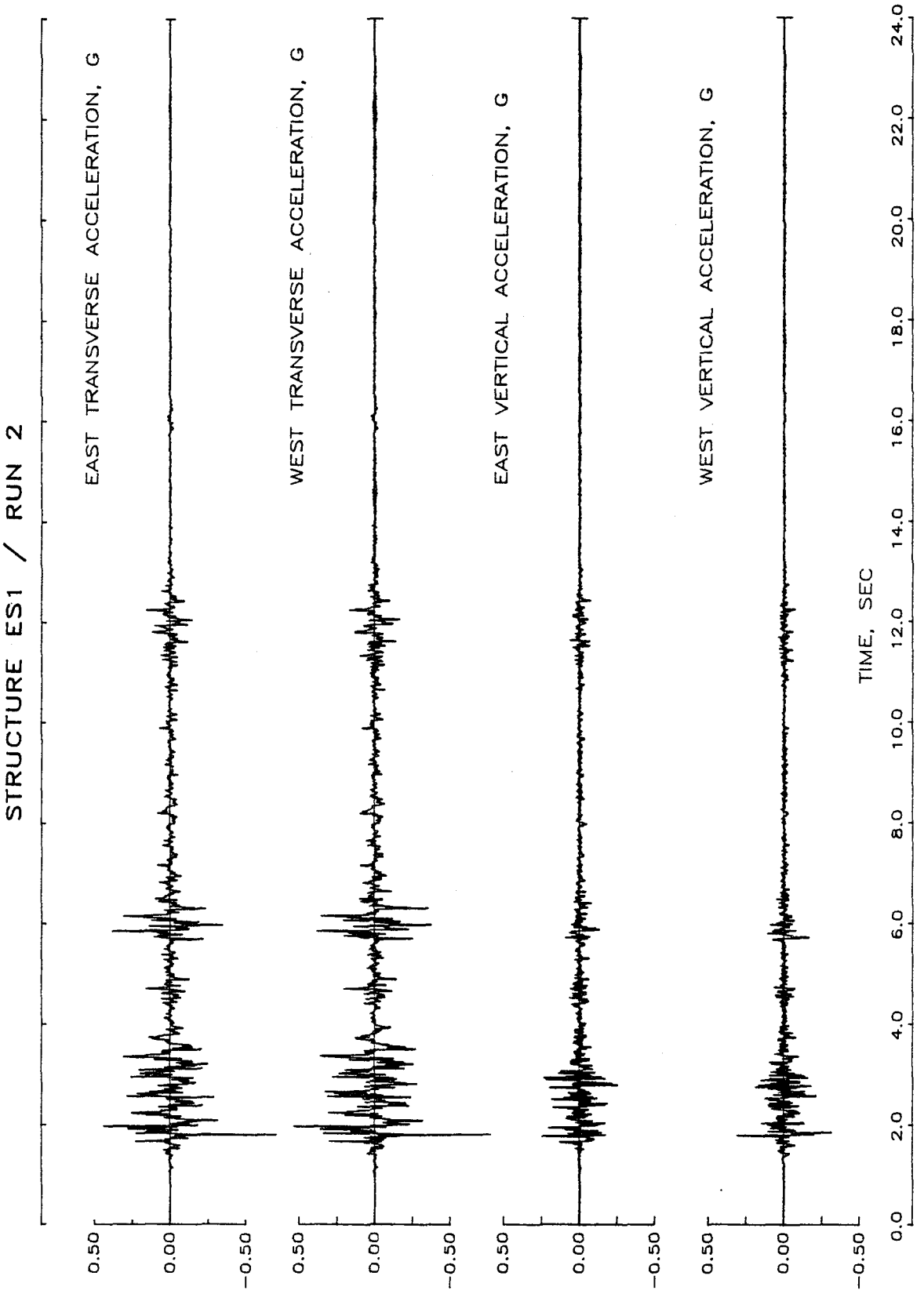

Fig. 4.7 (cont.) Response of Structure ES1 During Run 2
(i) Vertical and Transverse Accelerations

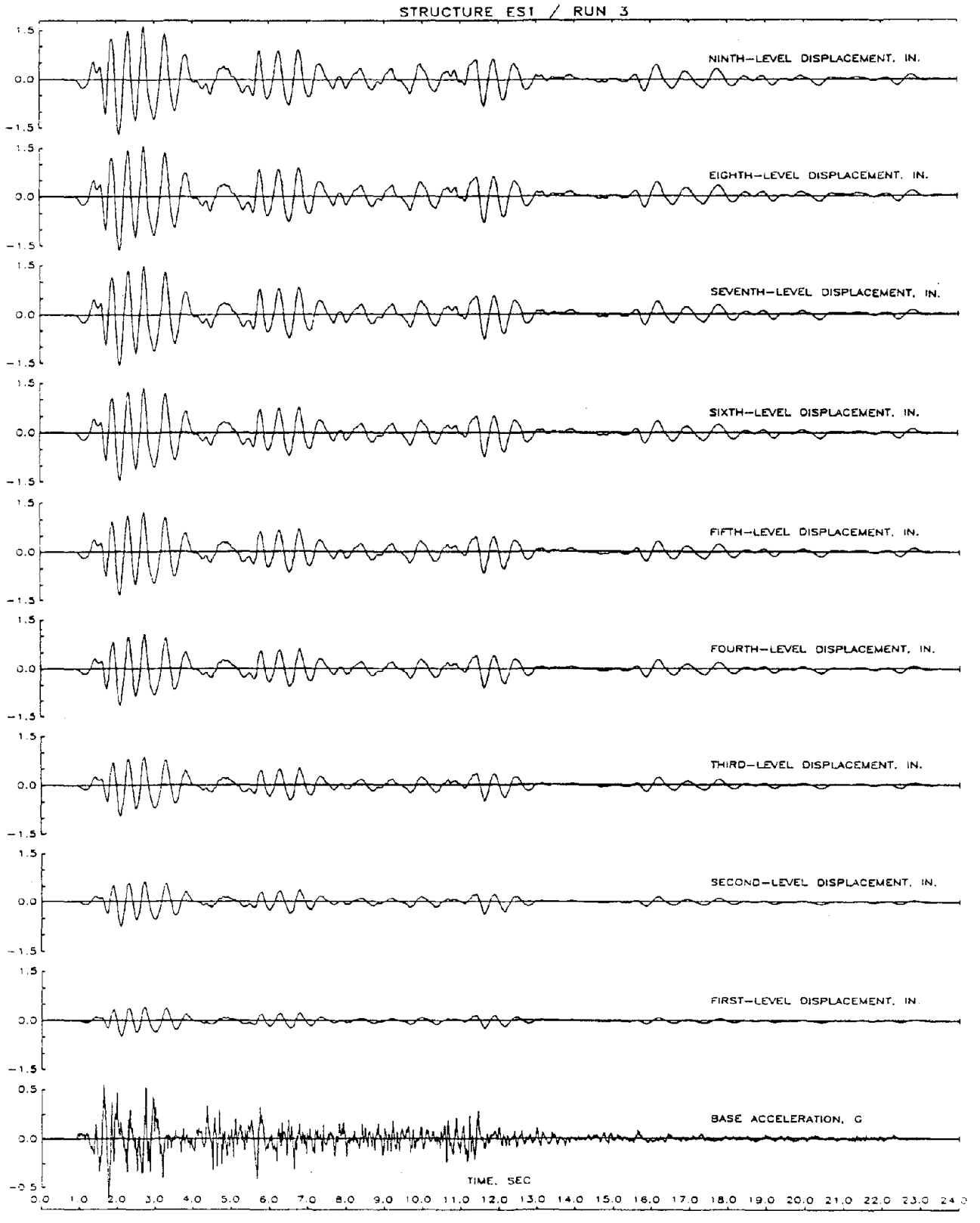

Fig. 4.8 Response of Structure ES1 During Run 3
(a) Displacement Histories

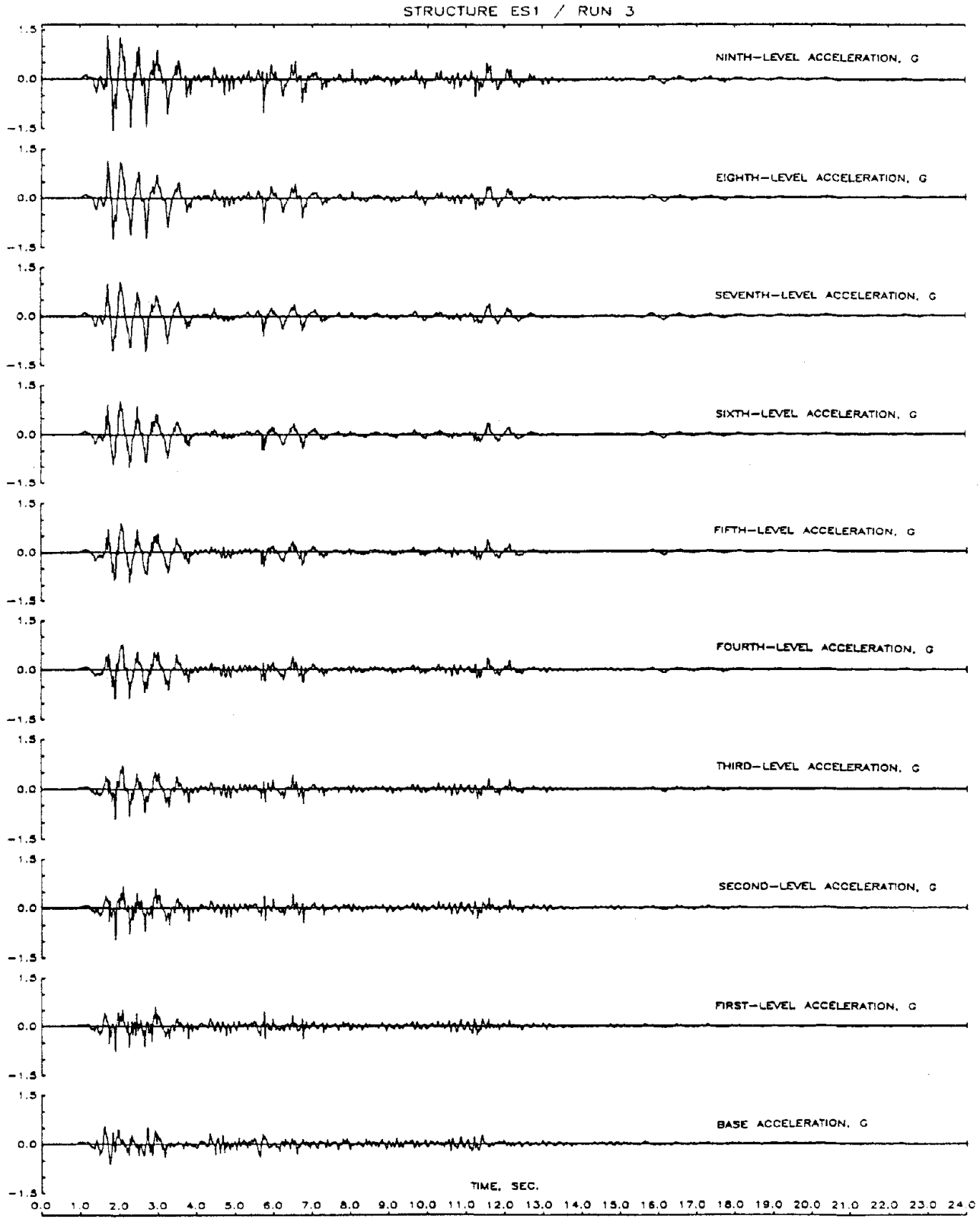

Fig. 4.8 (cont.) Response of Structure ES1 During Run 3
(b) Acceleration Histories

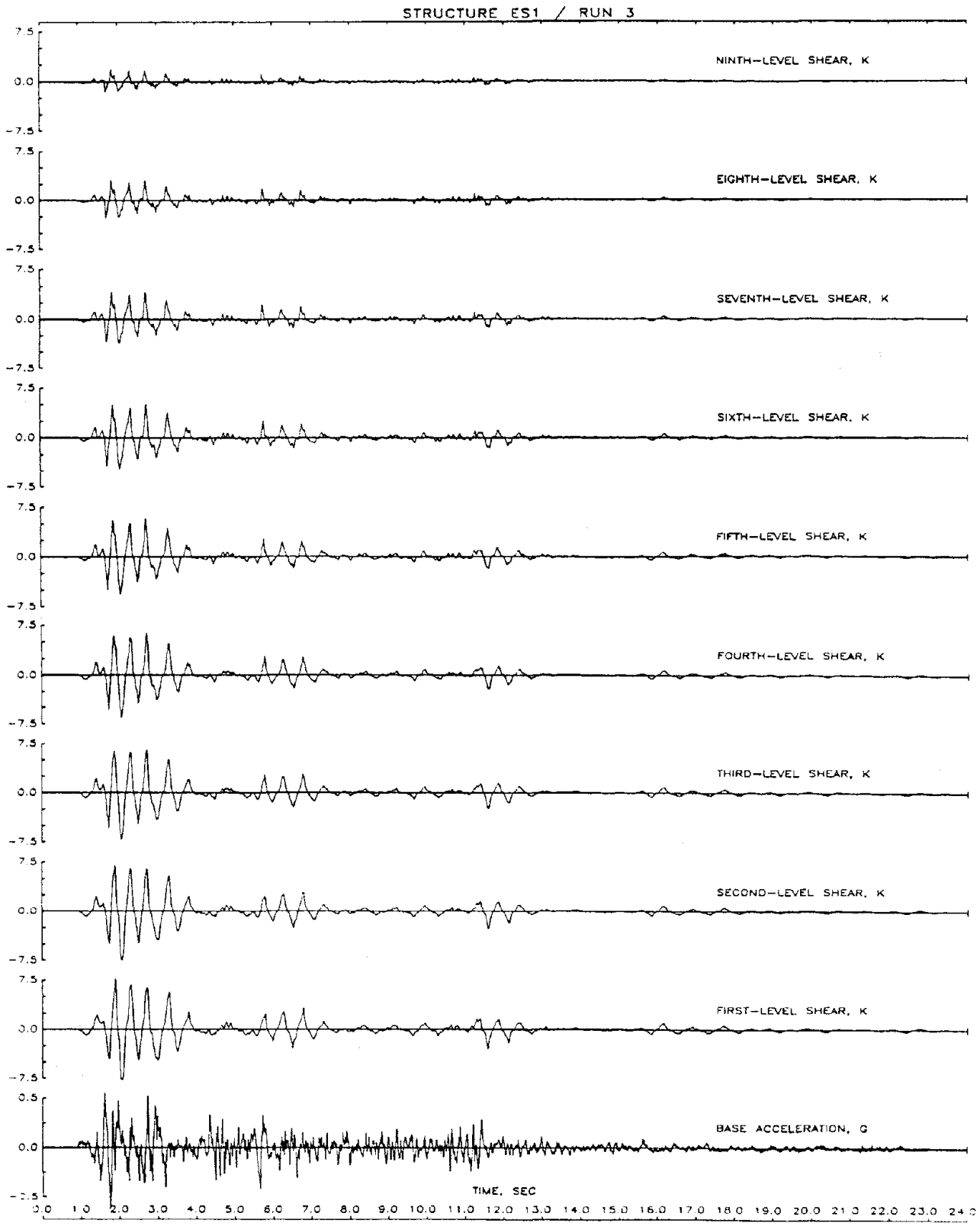

Fig. 4.8 (cont.) Response of Structure ES1 During Run 3
(c) Shear Histories

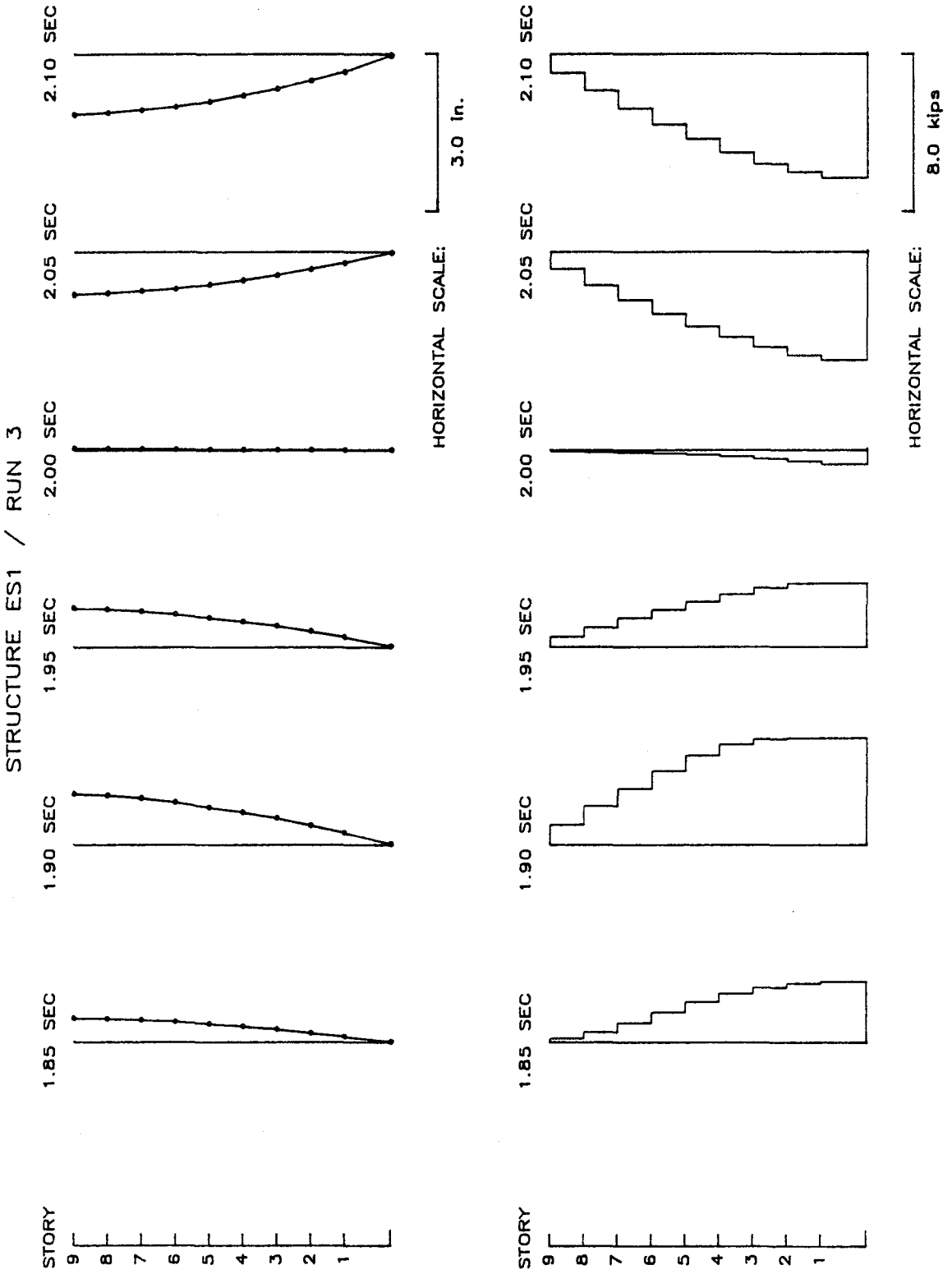

Fig. 4.8 (cont.) Response of Structure ES1 During Run 3
(d) Displacement and Shear Distributions

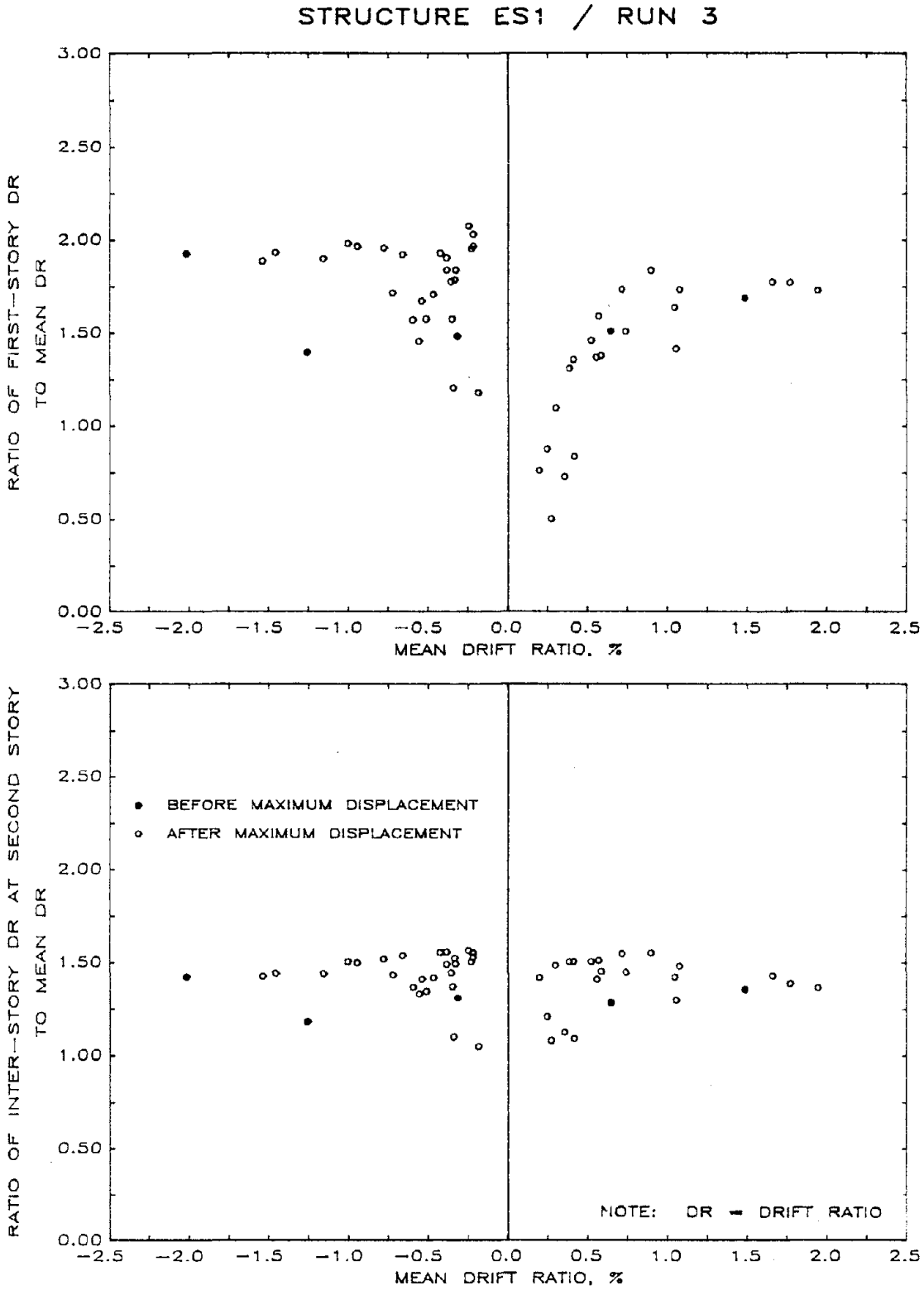

Fig. 4.8 (cont.) Response of Structure ES1 During Run 3
(e) Ratio of Interstory to Mean Drift

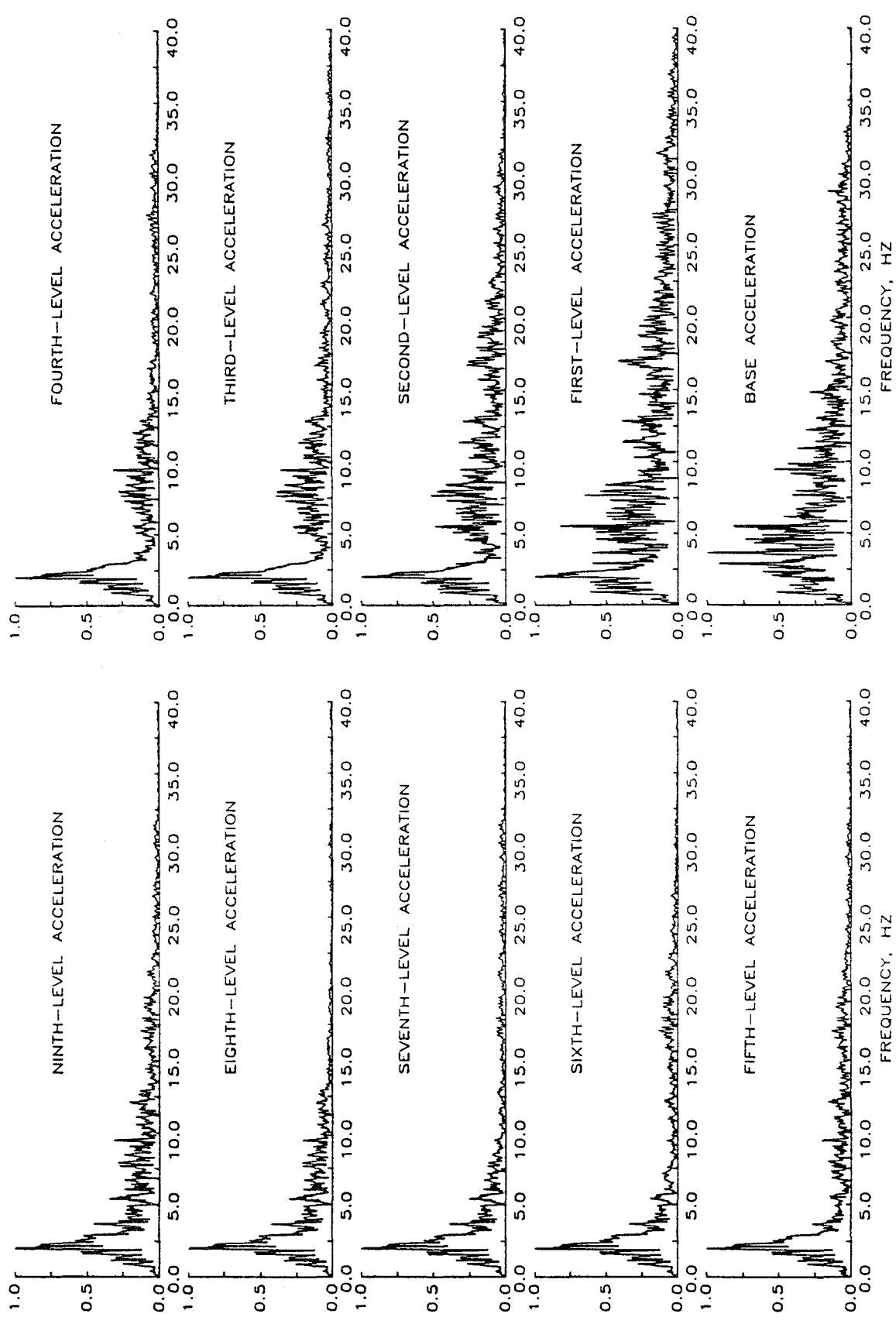

Fig. 4.8 (cont.) Response of Structure ES1 During Run 3
(f) Fourier Amplitude Spectra

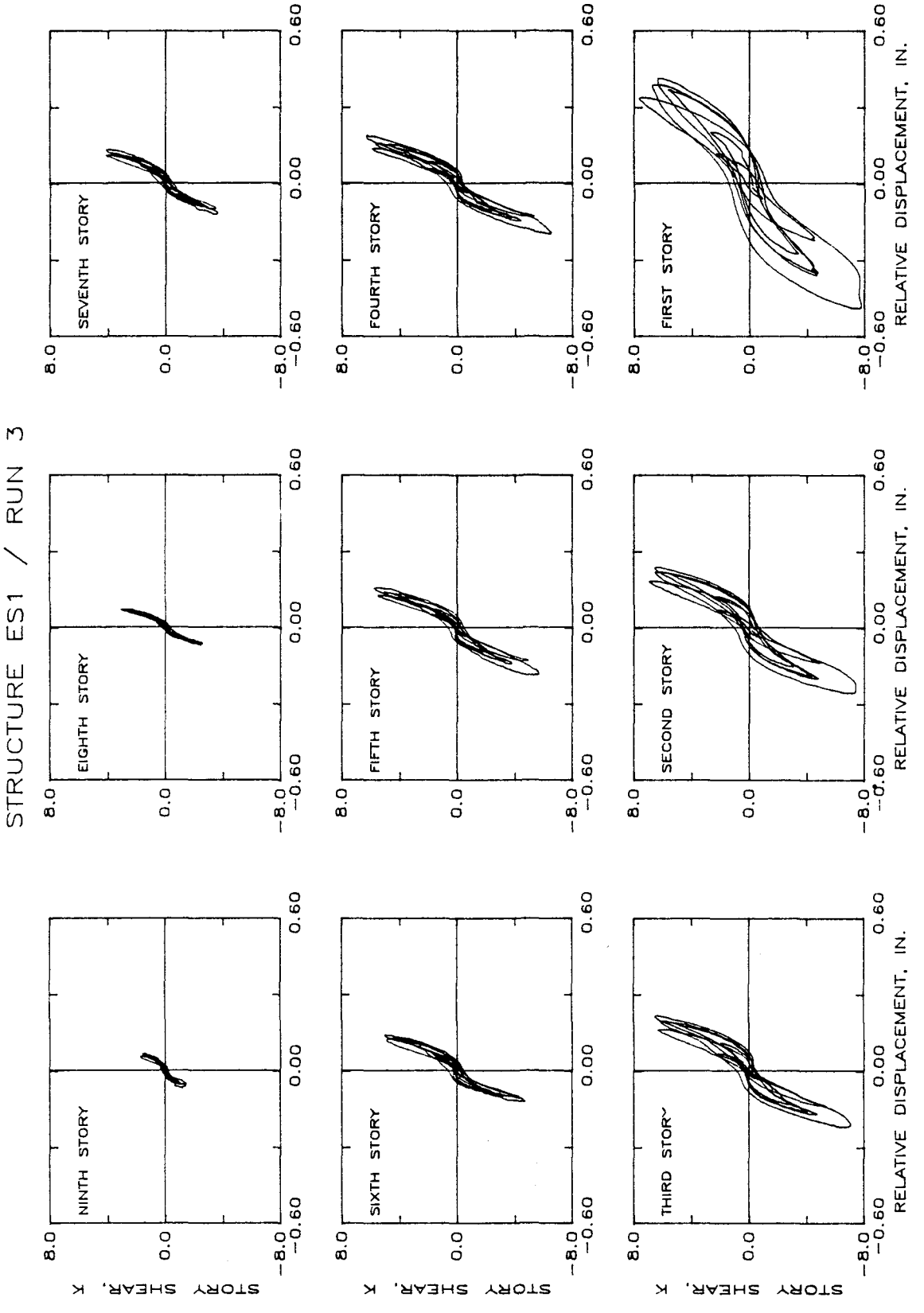

Fig. 4.8 (cont.) Response of Structure ES1 During Run 3
(g) Hysteretic Response

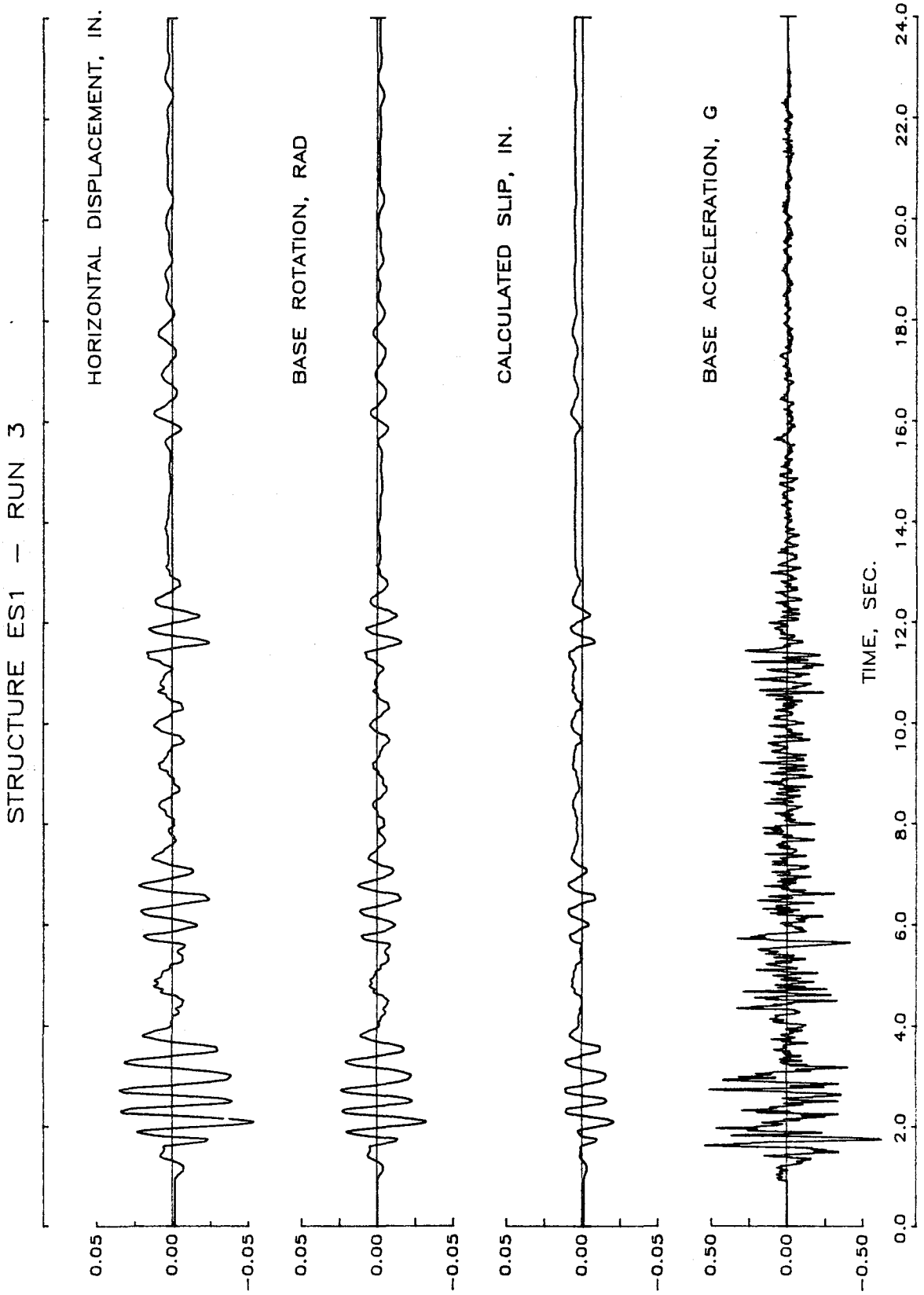

Fig. 4.8 (cont.) Response of Structure ES1 During Run 3
(h) Rotation and Slip at Base of Wall

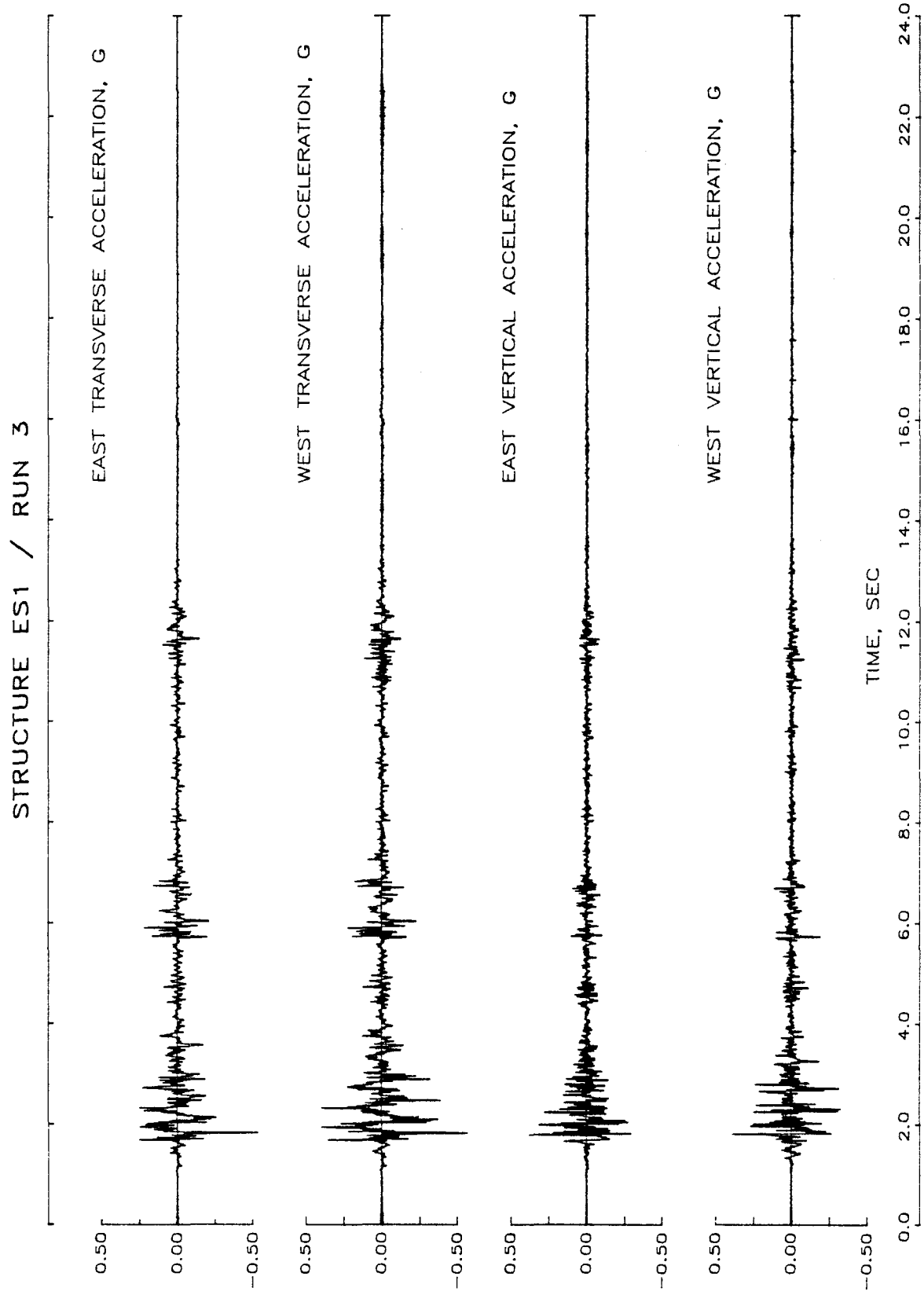

Fig. 4.8 (cont.) Response of Structure ES1 During Run 3
(i) Vertical and Transverse Accelerations

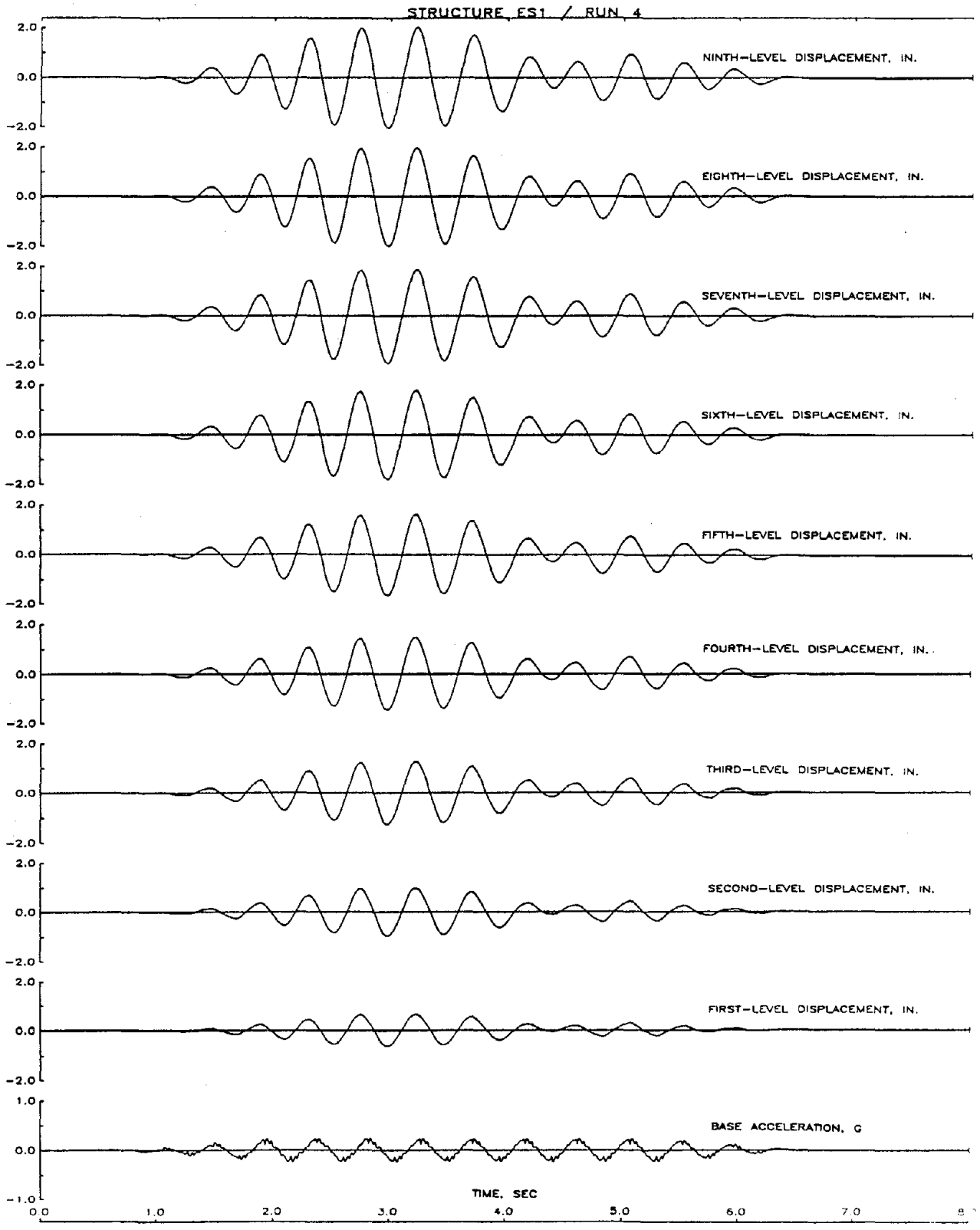

Fig. 4.9 Response of Structure ES1 During Run 4
(a) Displacement Histories

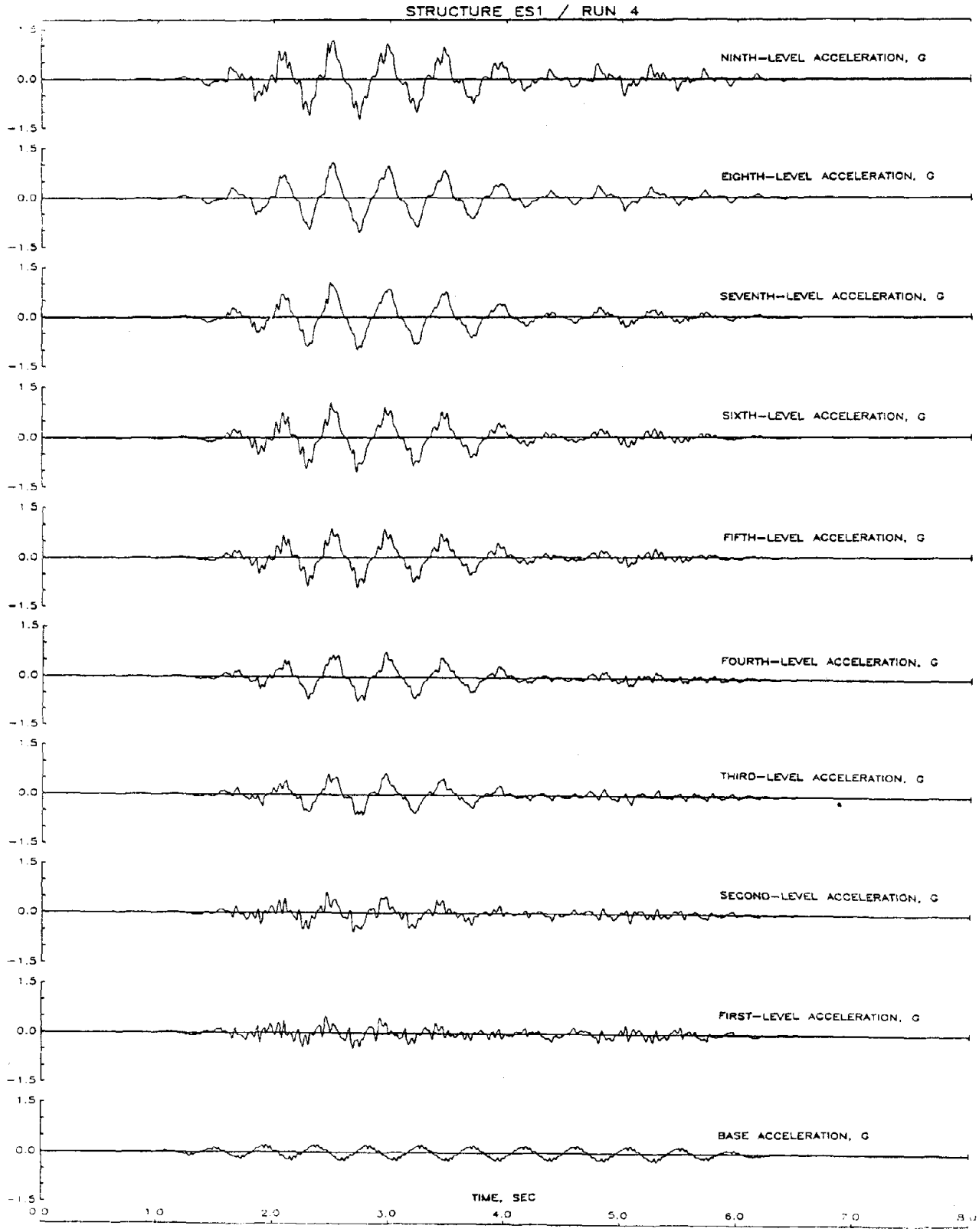

Fig. 4.9 (cont.) Response of Structure ES1 During Run 4
(b) Acceleration Histories

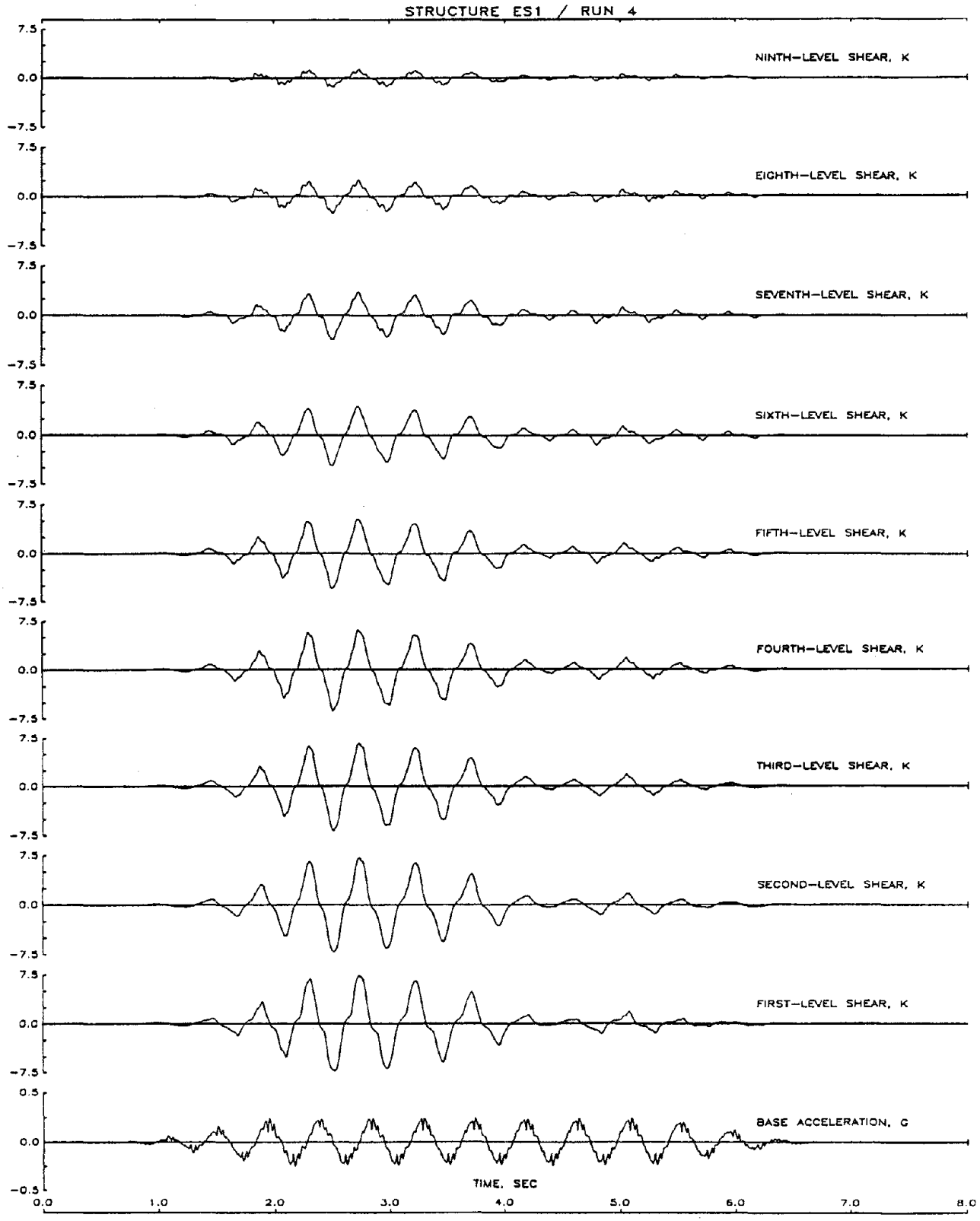

Fig. 4.9 (cont.) Response of Structure ES1 During Run 4
(c) Shear Histories

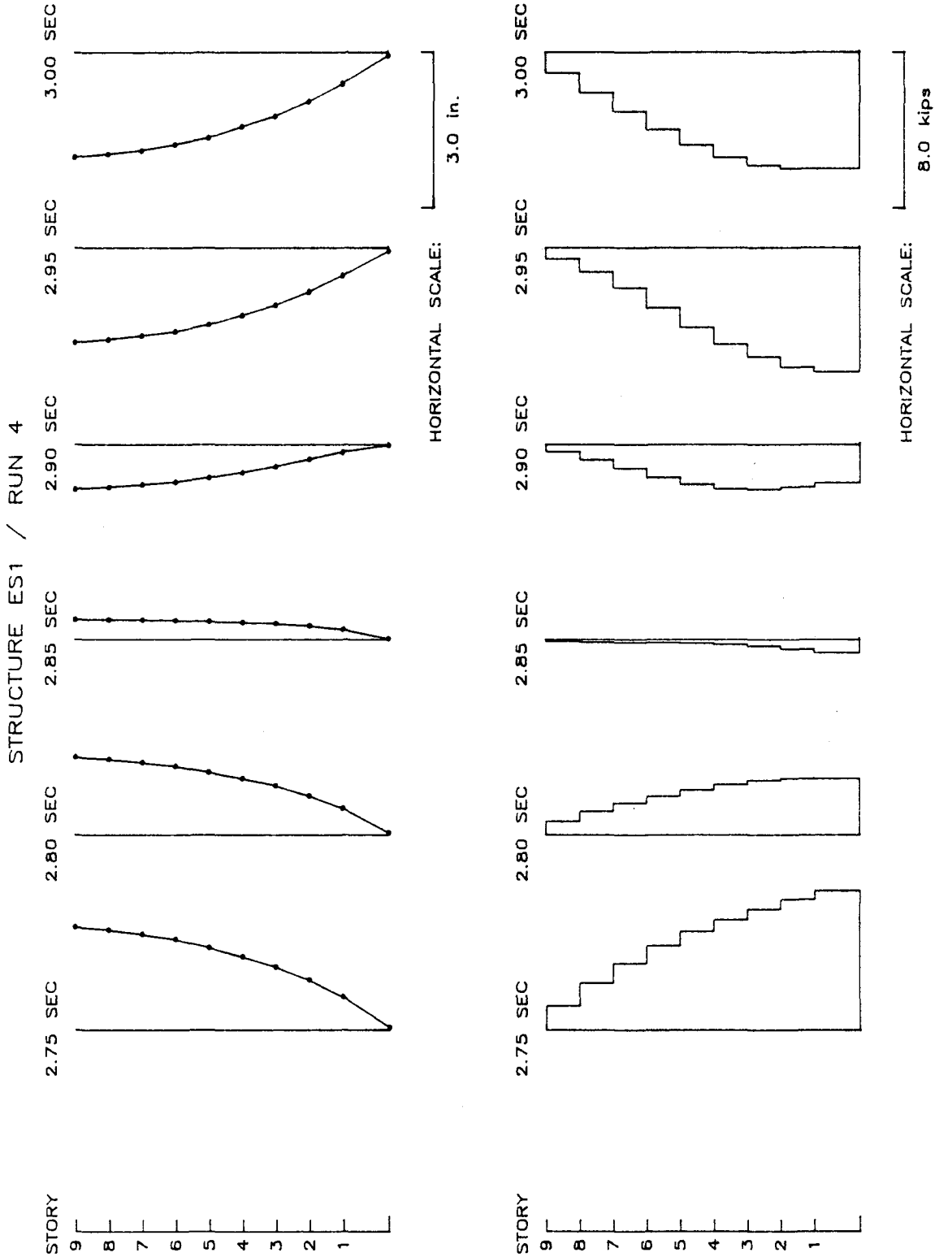

Fig. 4.9 (cont.) Response of Structure ES1 During Run 4
(d) Displacement and Shear Distributions

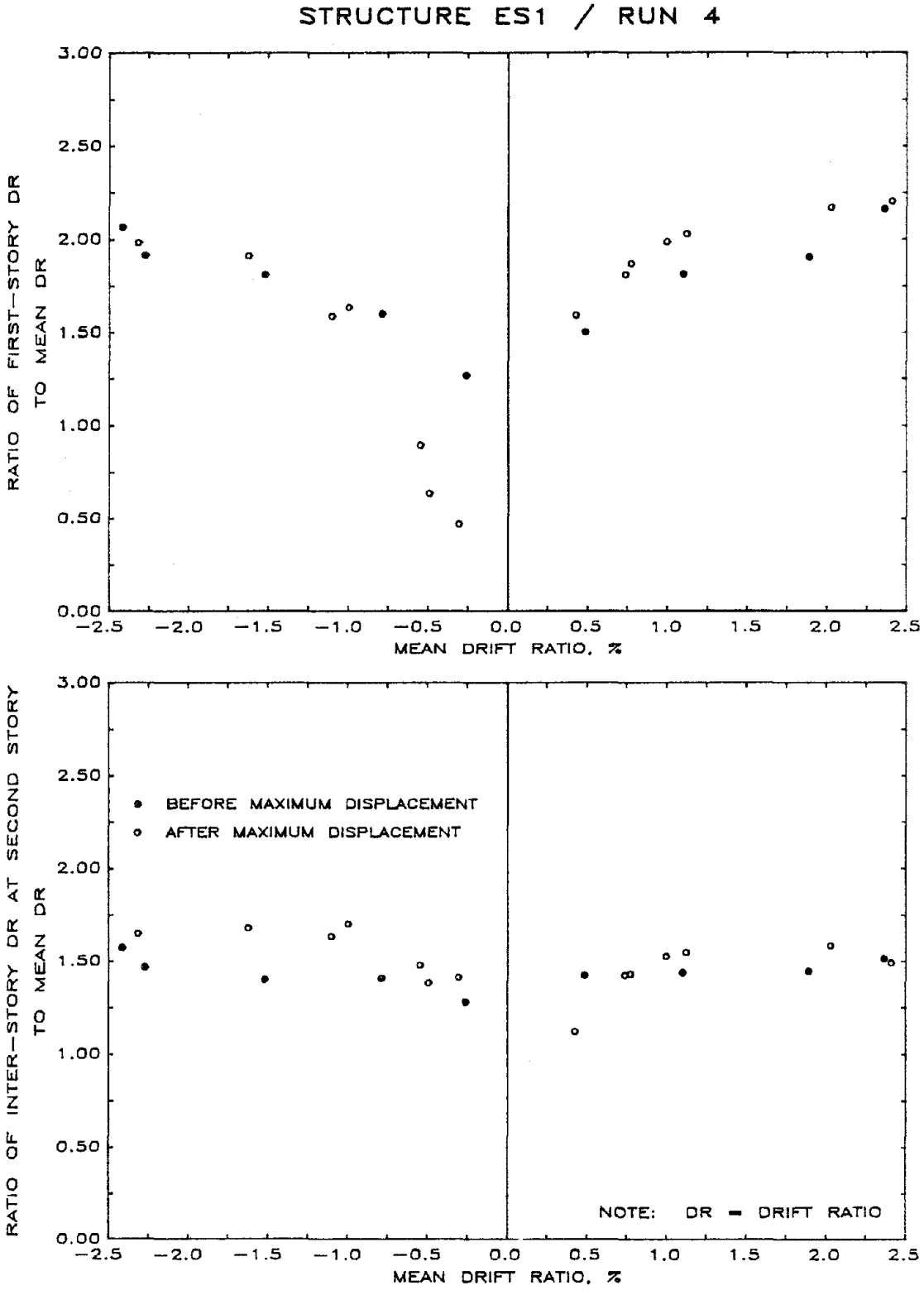

Fig. 4.9 (cont.) Response of Structure ES1 During Run 4
(e) Ratio of Interstory to Mean Drift

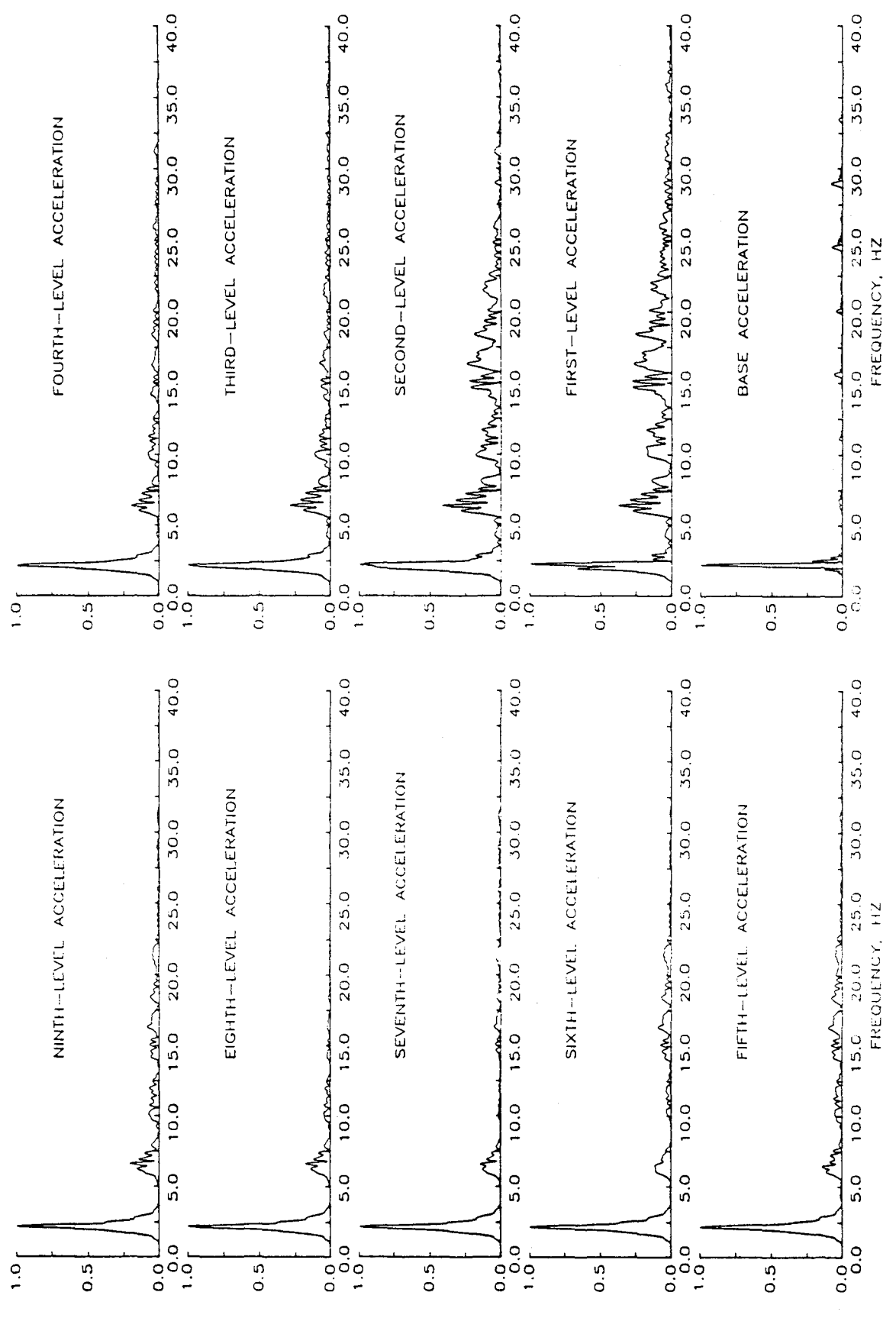

Fig. 4.9 (cont.) Response of Structure ES1 During Run 4
(f) Fourier Amplitude Spectra

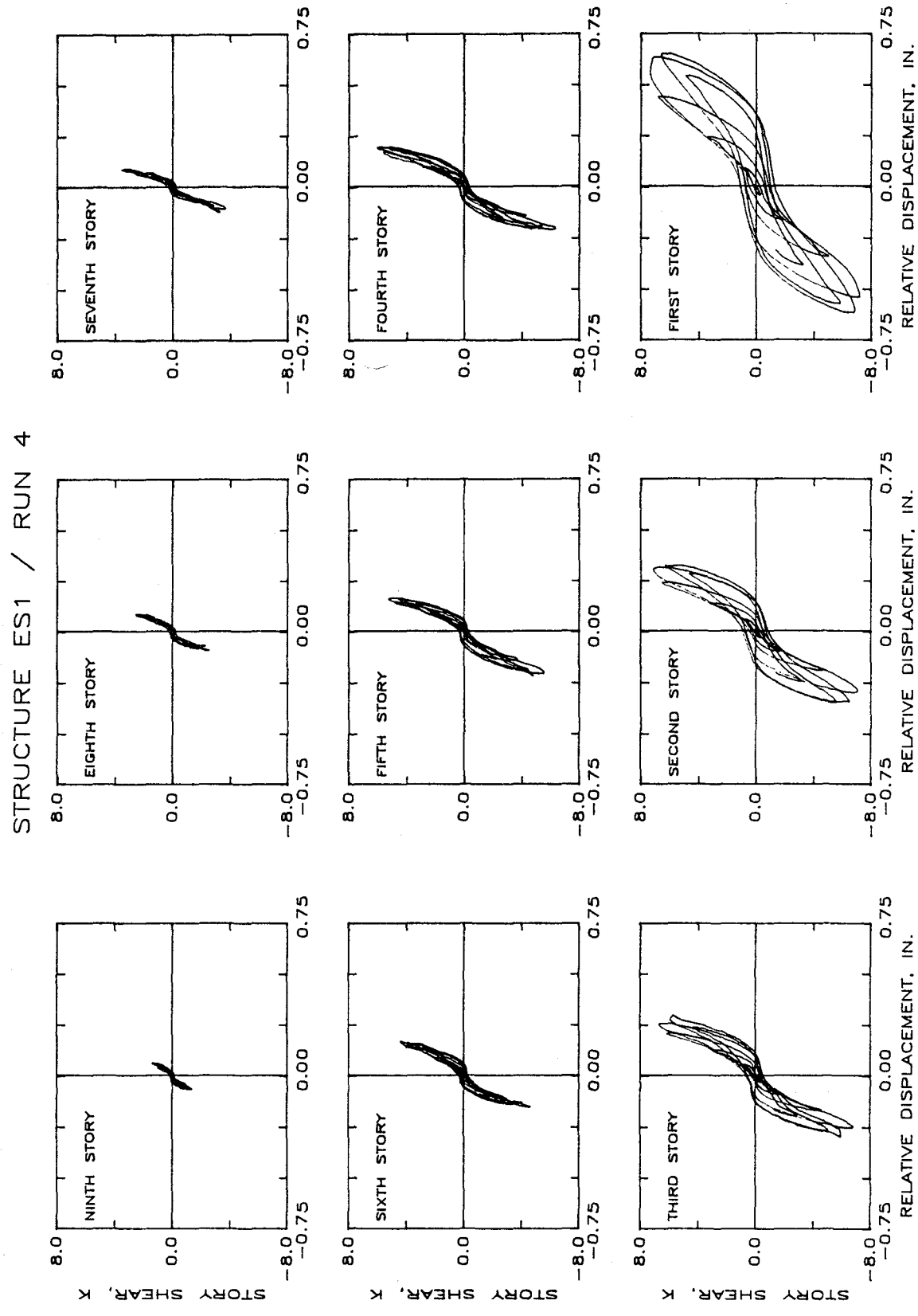

Fig. 4.9 (cont.) Response of Structure ES1 During Run 4
(g) Hysteretic Response

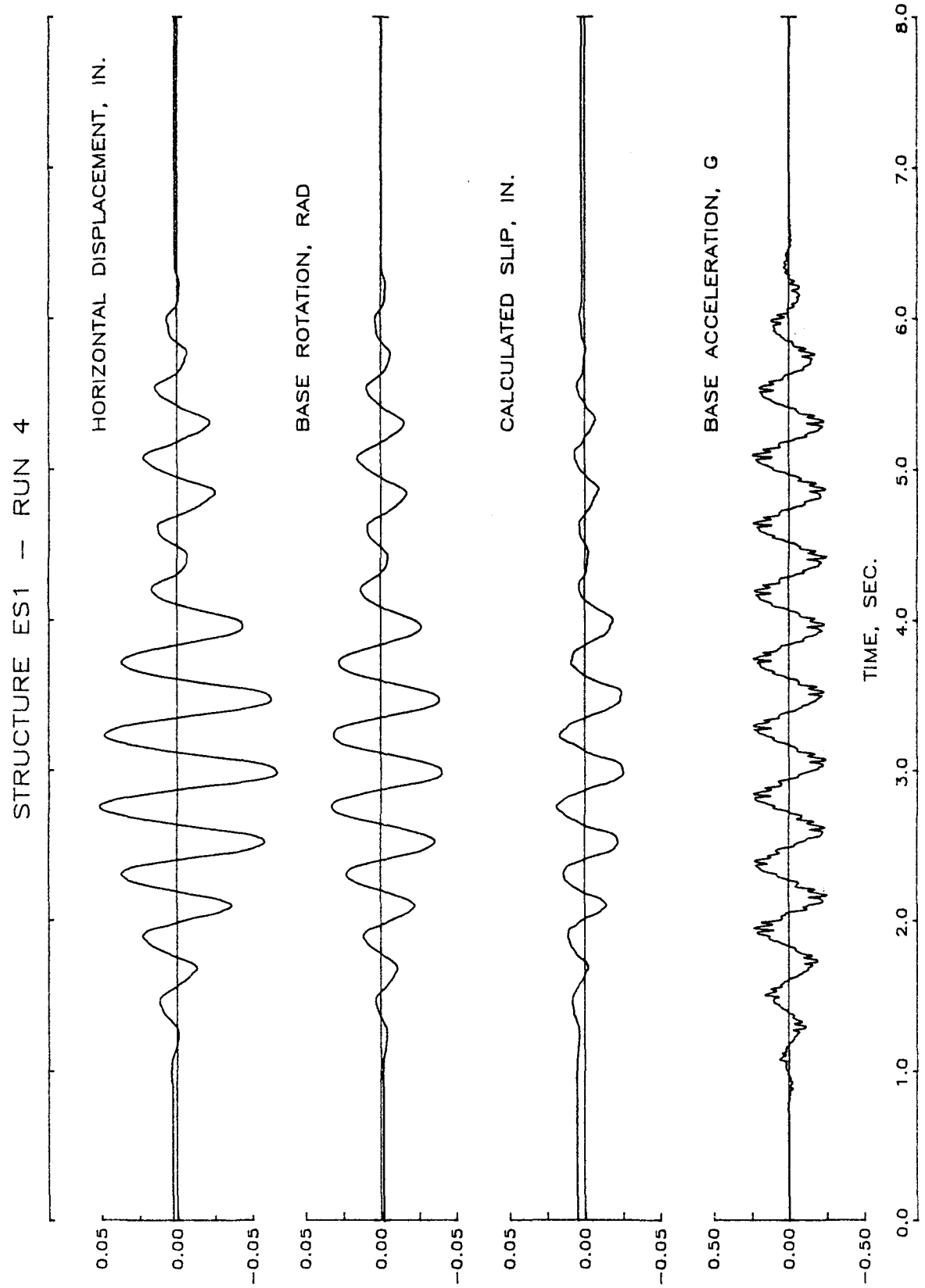

Fig. 4.9 (cont.) Response of Structure ES1 During Run 4
(h) Rotation and Slip at Base of Wall

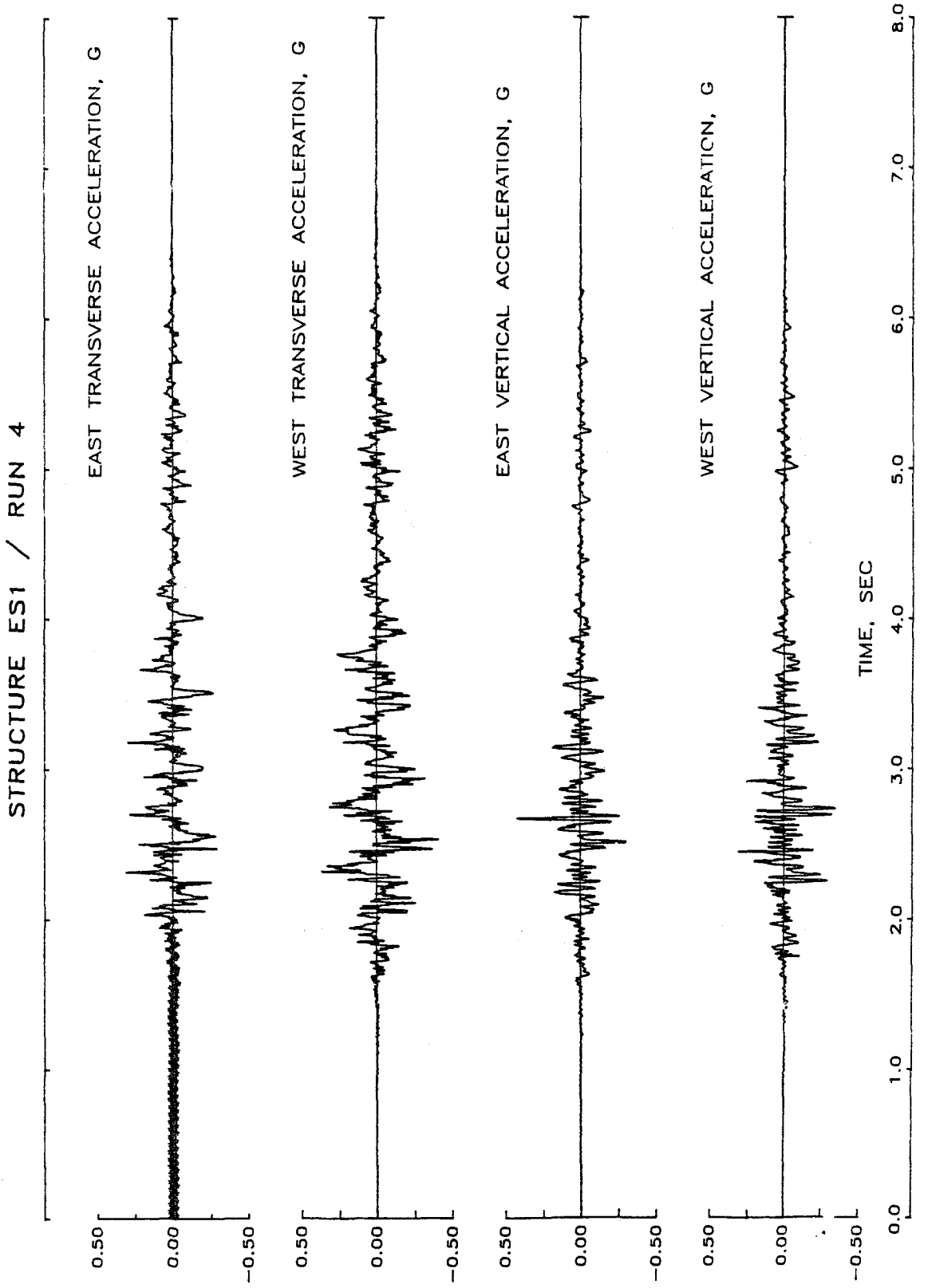

Fig. 4.9 (cont.) Response of Structure ES1 During Run 4
(i) Vertical and Transverse Accelerations

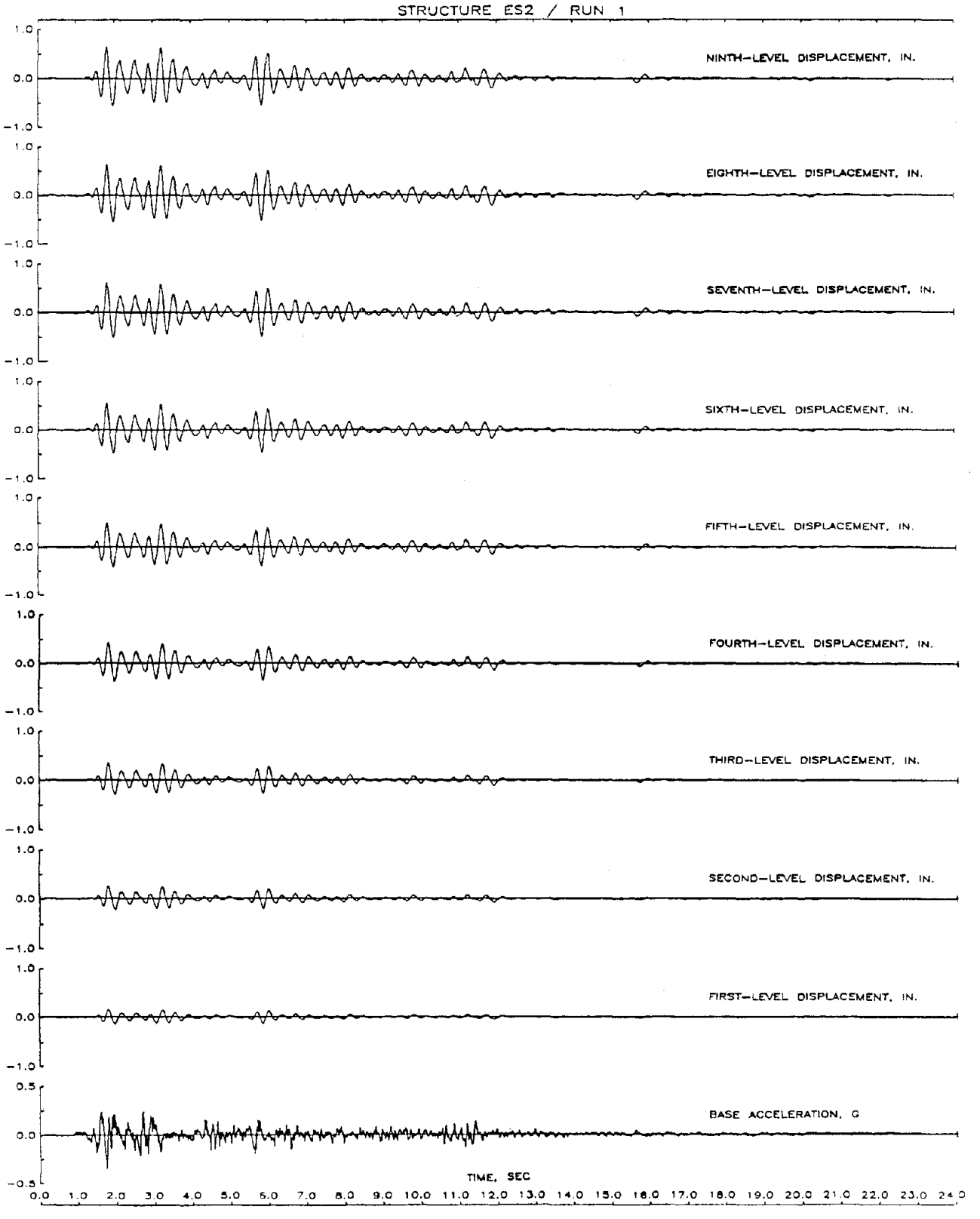

Fig. 4.10 Response of Structure ES2 During Run 1
(a) Displacement Histories

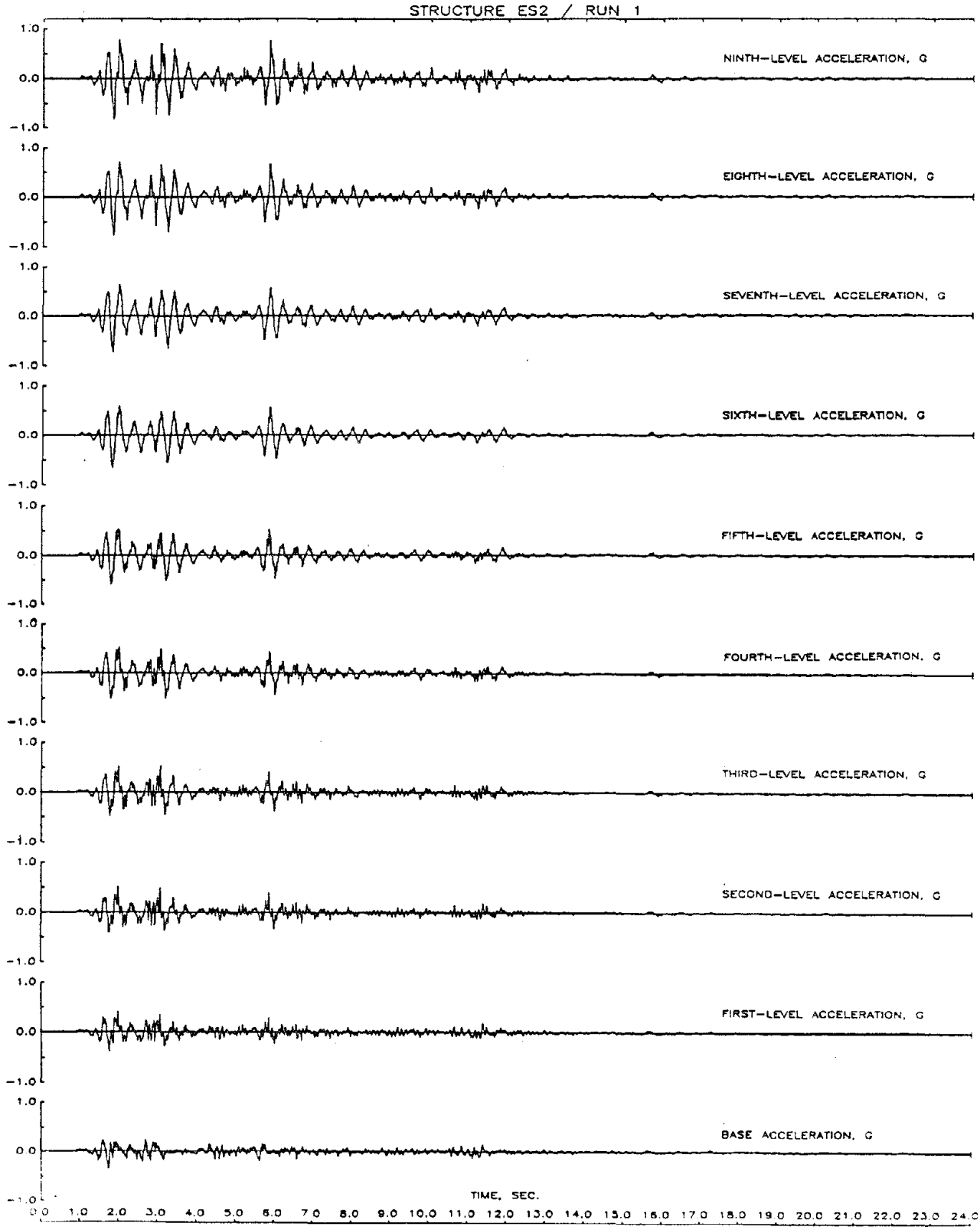

Fig. 4.10 (cont.) Response of Structure ES2 During Run 1
(b) Acceleration Histories

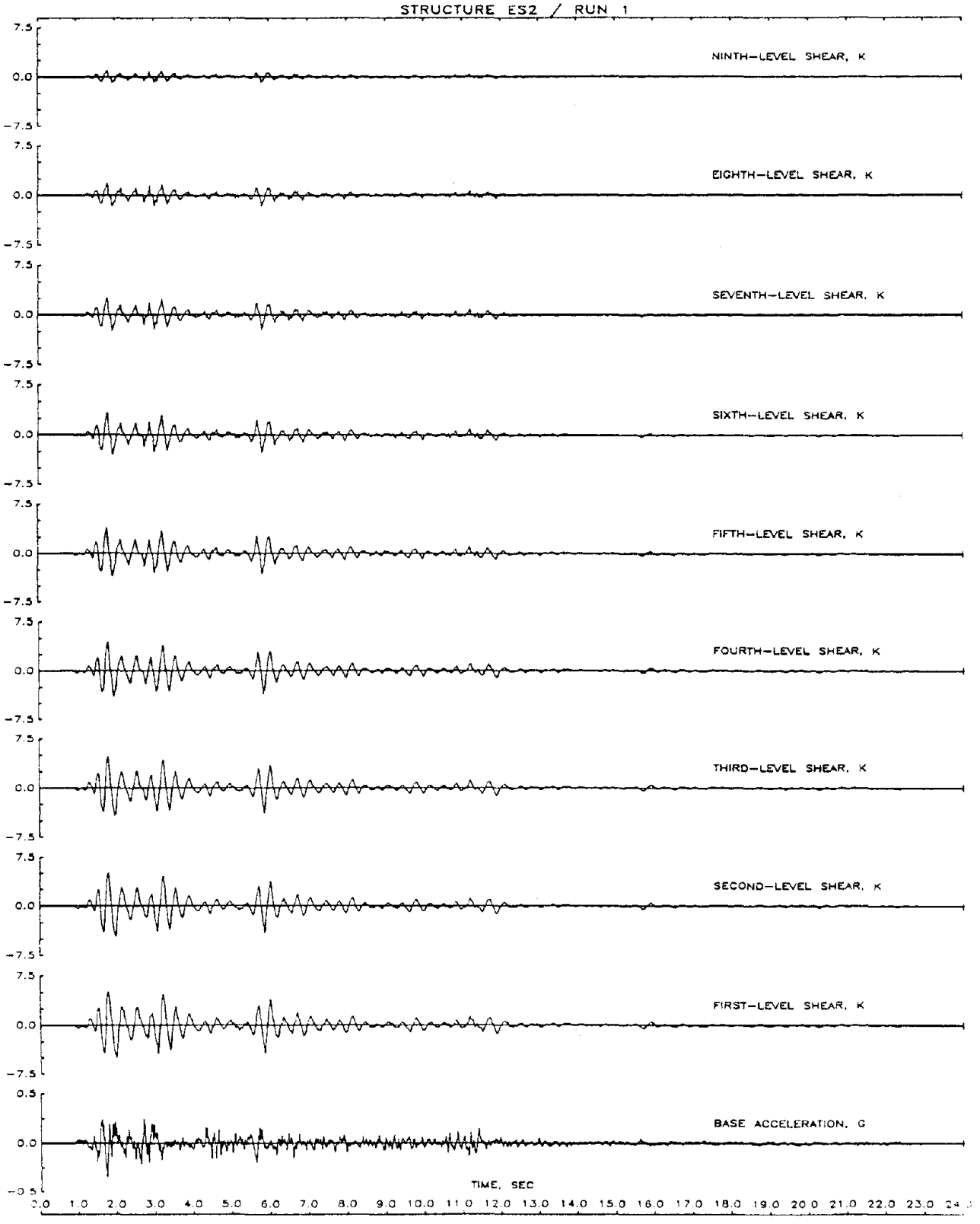

Fig. 4.10 (cont.) Response of Structure ES2 During Run 1
(c) Shear Histories

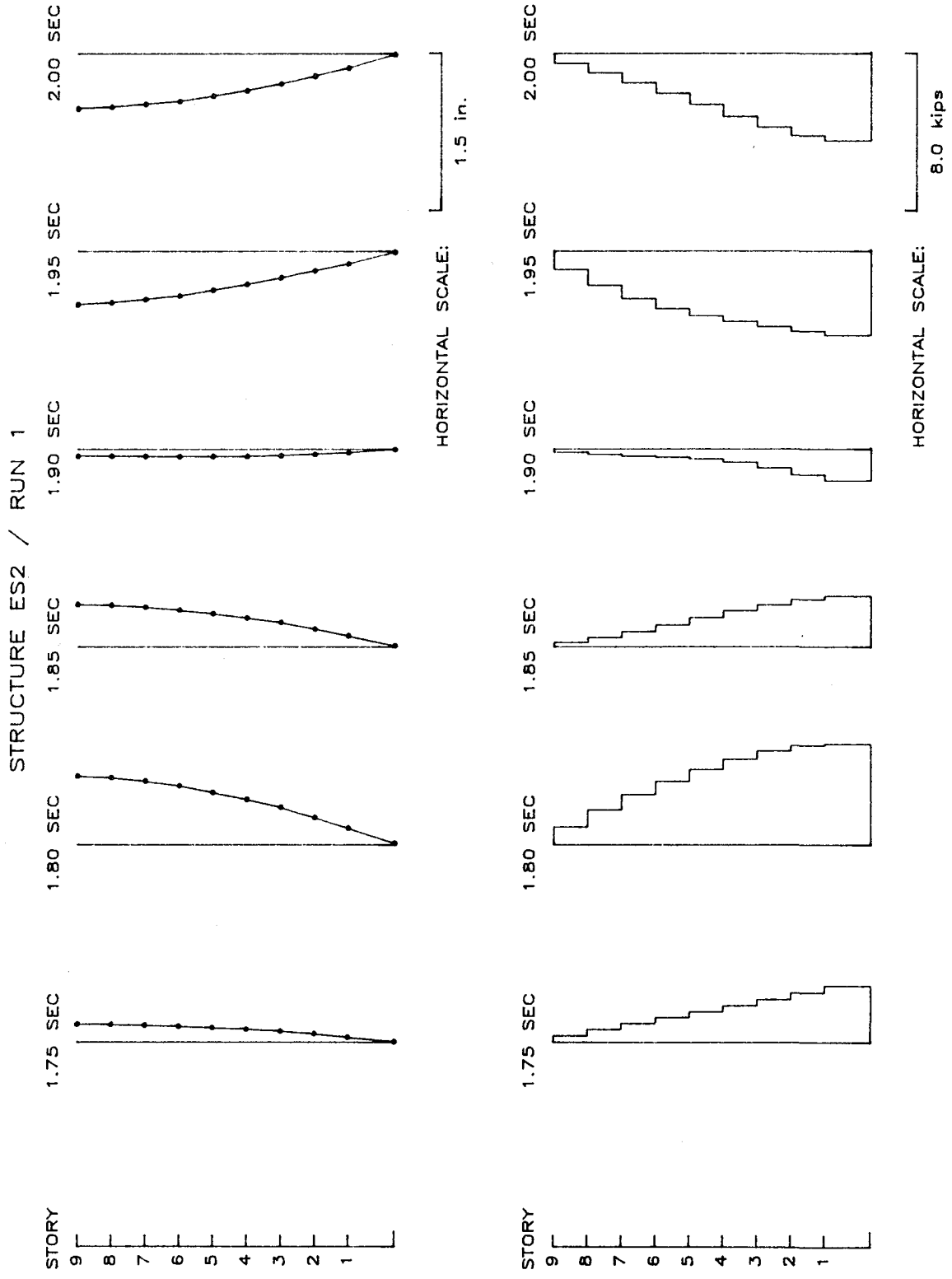

Fig. 4.10 (cont.) Response of Structure ES2 During Run 1
(d) Displacement and Shear Distributions

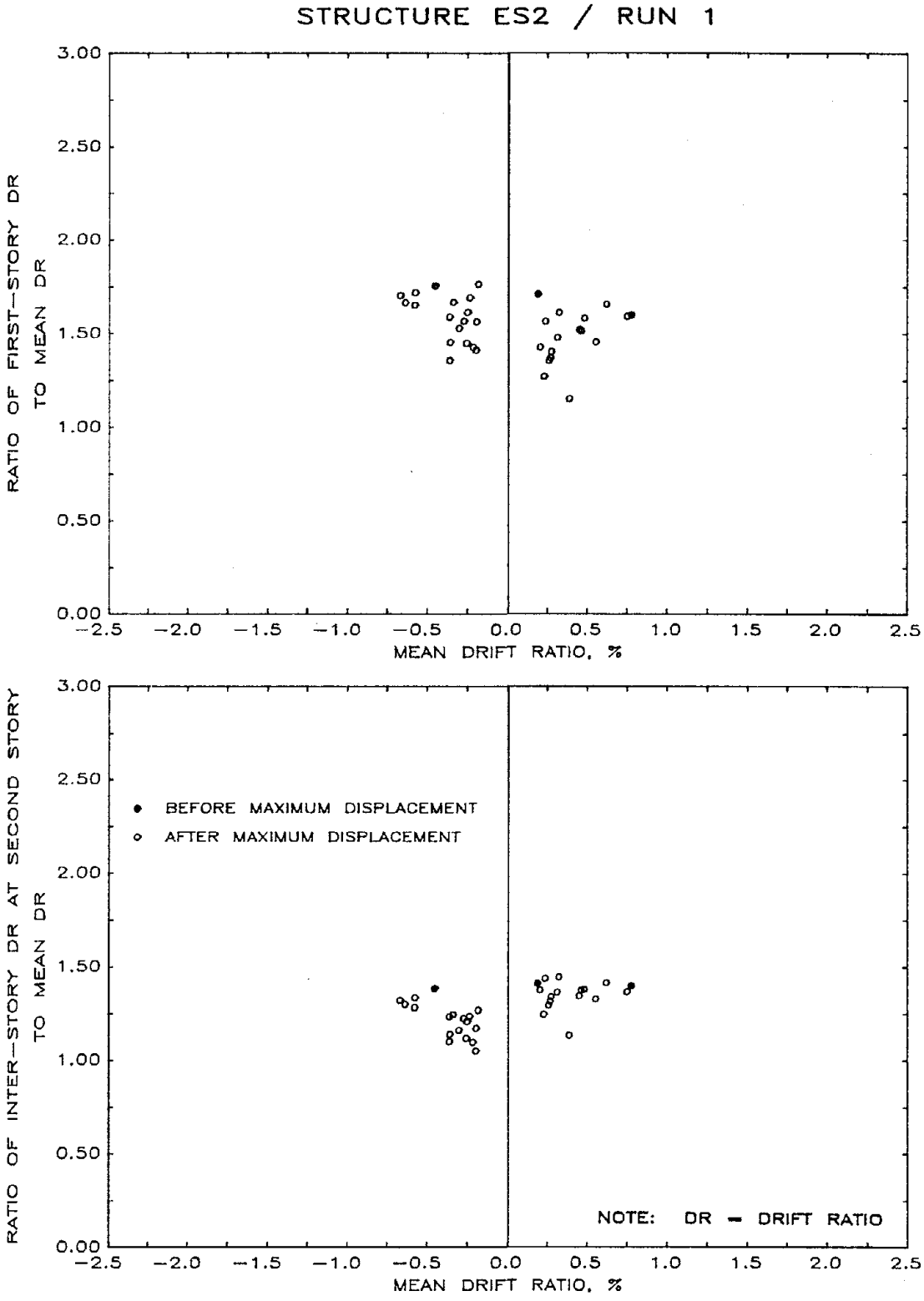

Fig. 4.10 (cont.) Response of Structure ES2 During Run 1
(e) Ratio of Interstory to Mean Drift

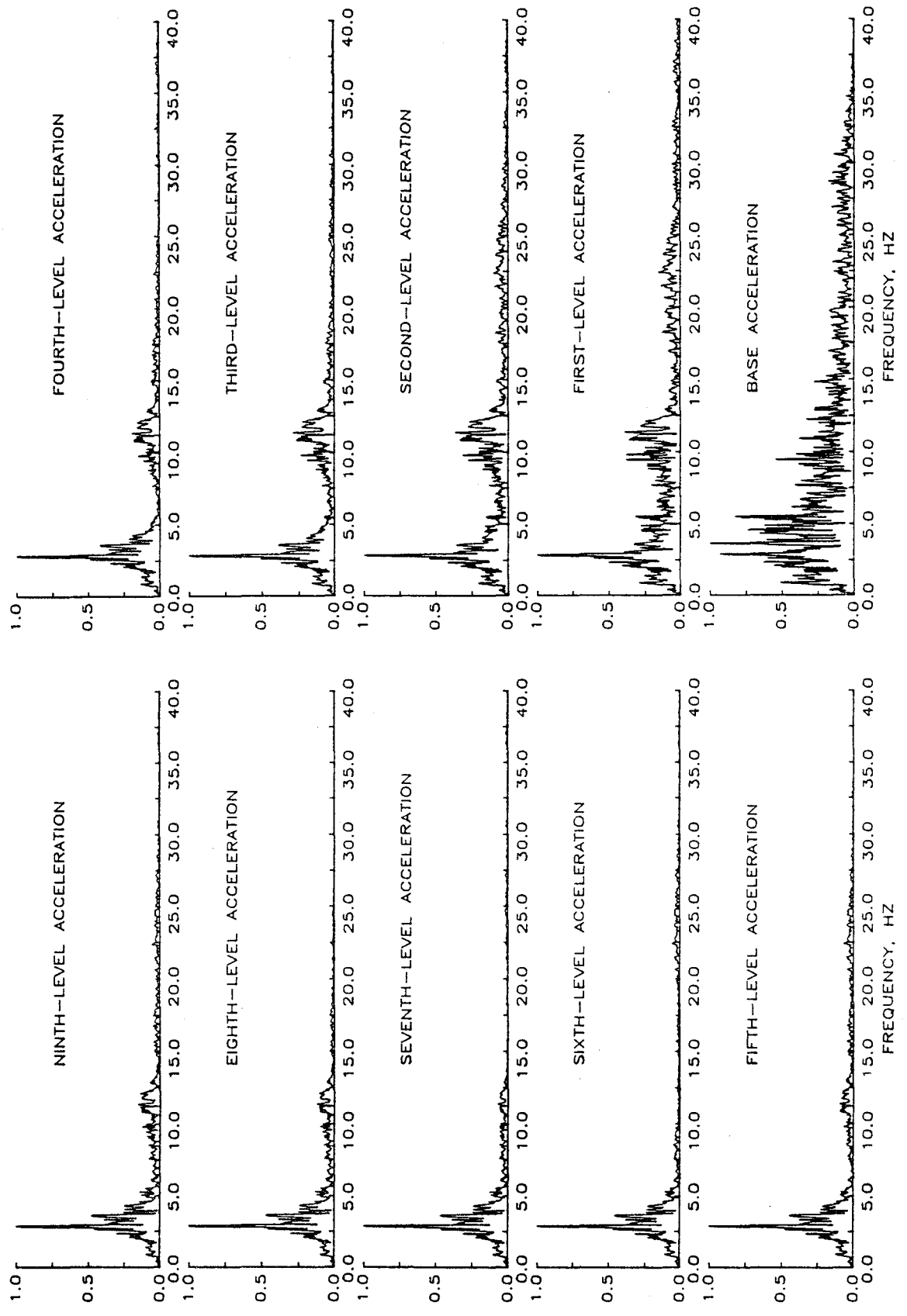

Fig. 4.10 (cont.) Response of Structure ES2 During Run 1
(f) Fourier Amplitude Spectra

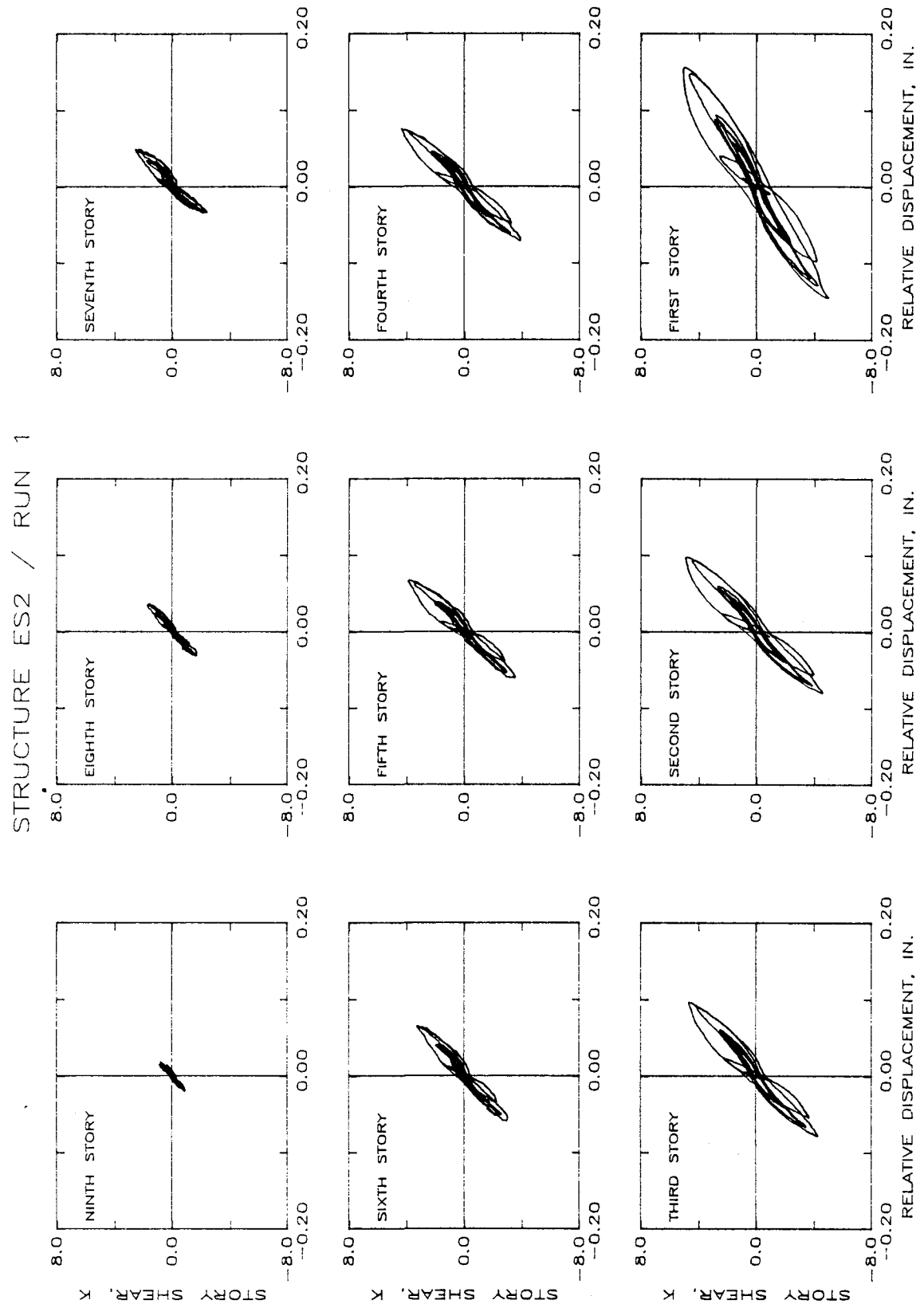

Fig. 4.10 (cont.) Response of Structure ES2 During Run 1
(g) Hysteretic Response

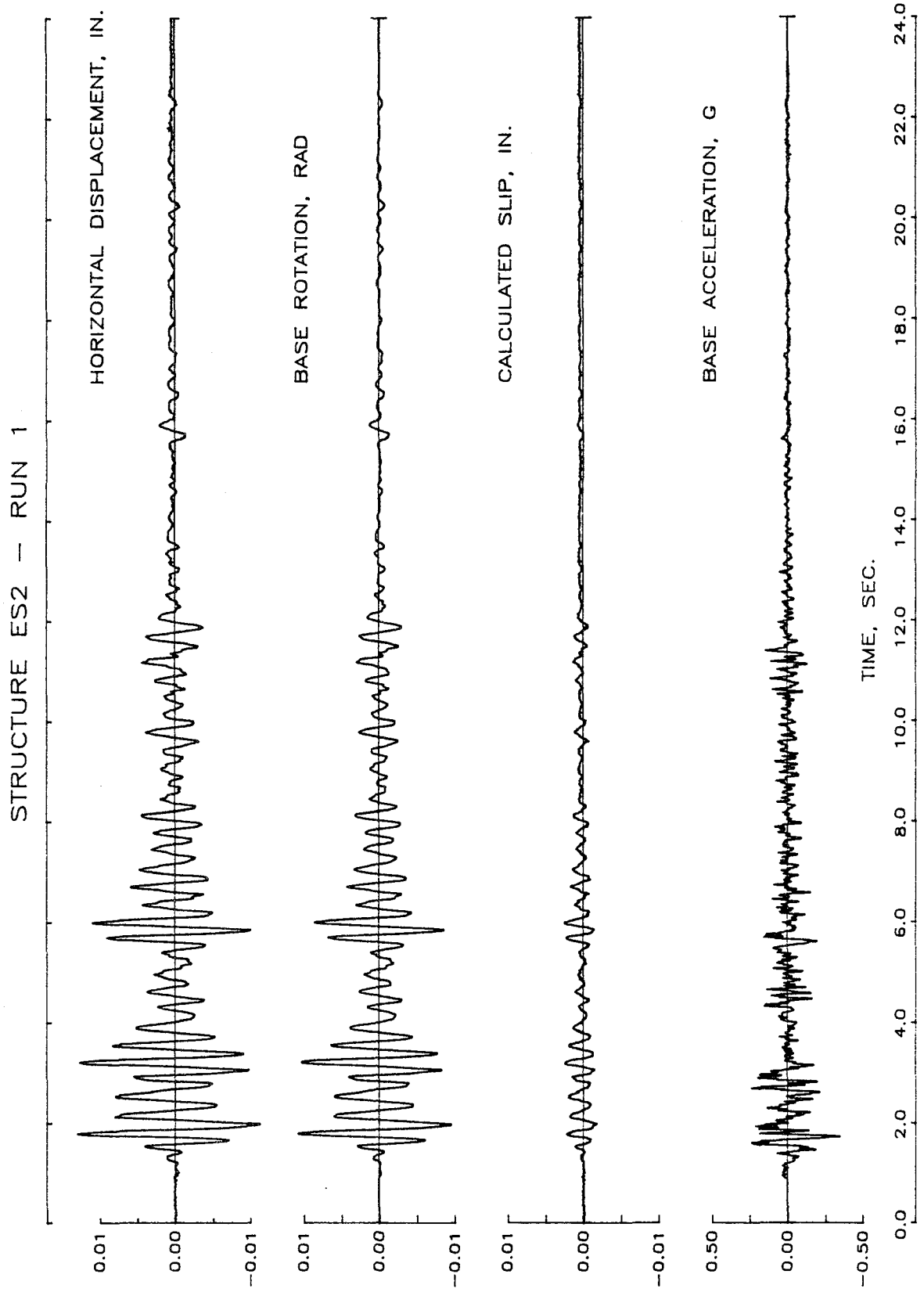

Fig. 4.10 (cont.) Response of Structure ES2 During Run 1
(h) Rotation and Slip at Base of Wall

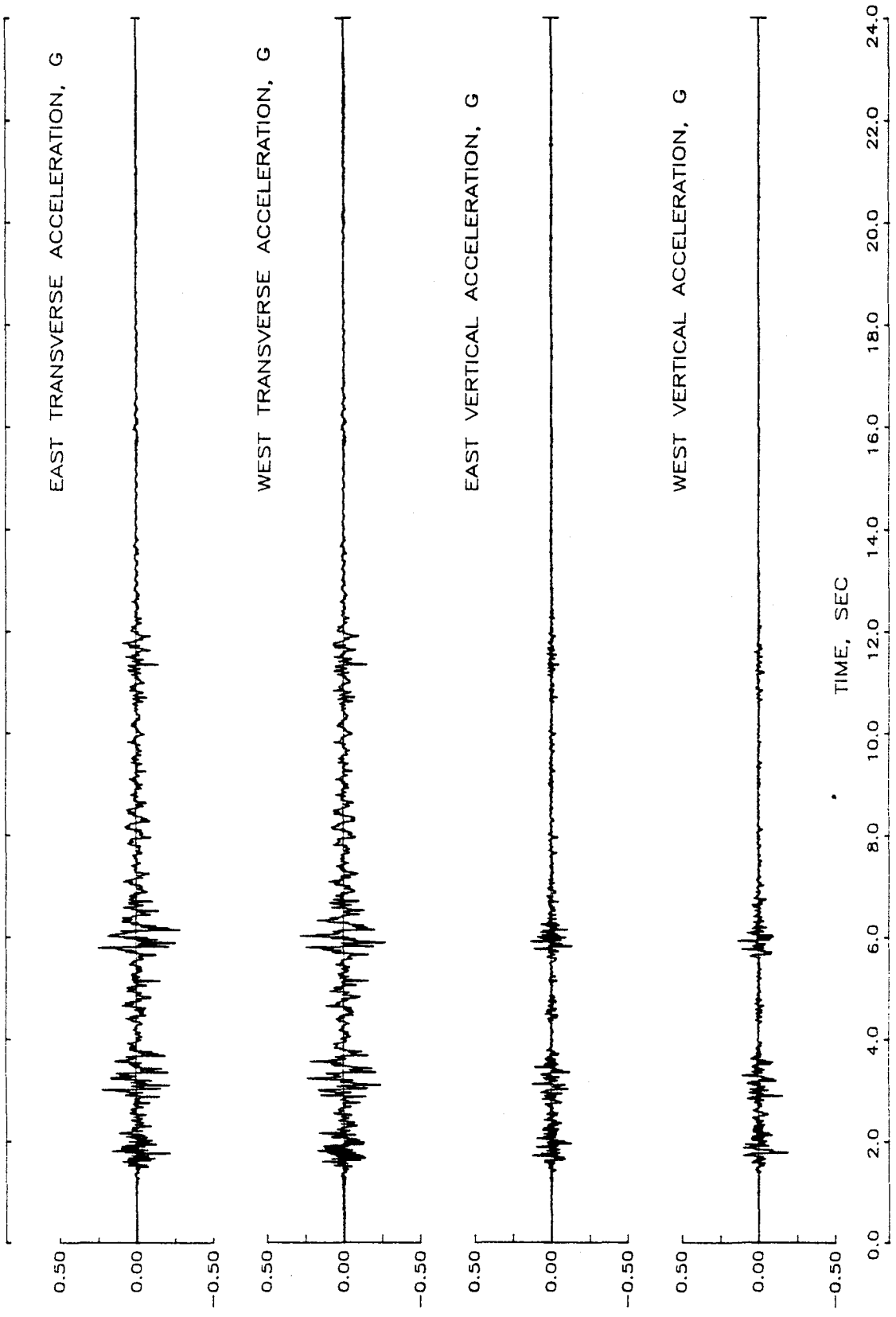

Fig. 4.10 (cont.) Response of Structure ES2 During Run 1
(i) Vertical and Transverse Accelerations

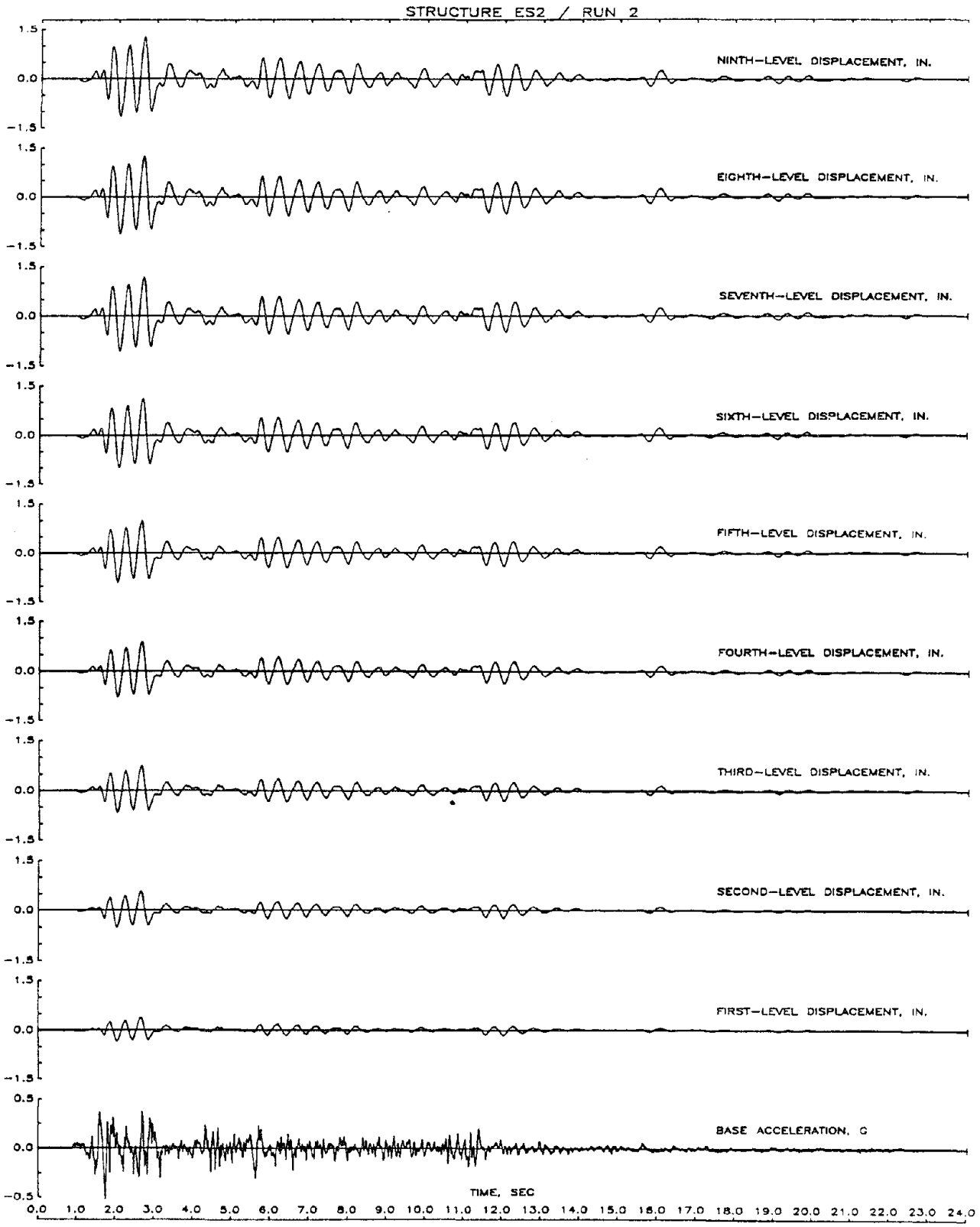

Fig. 4.11 Response of Structure ES2 During Run 2
(a) Displacement Histories

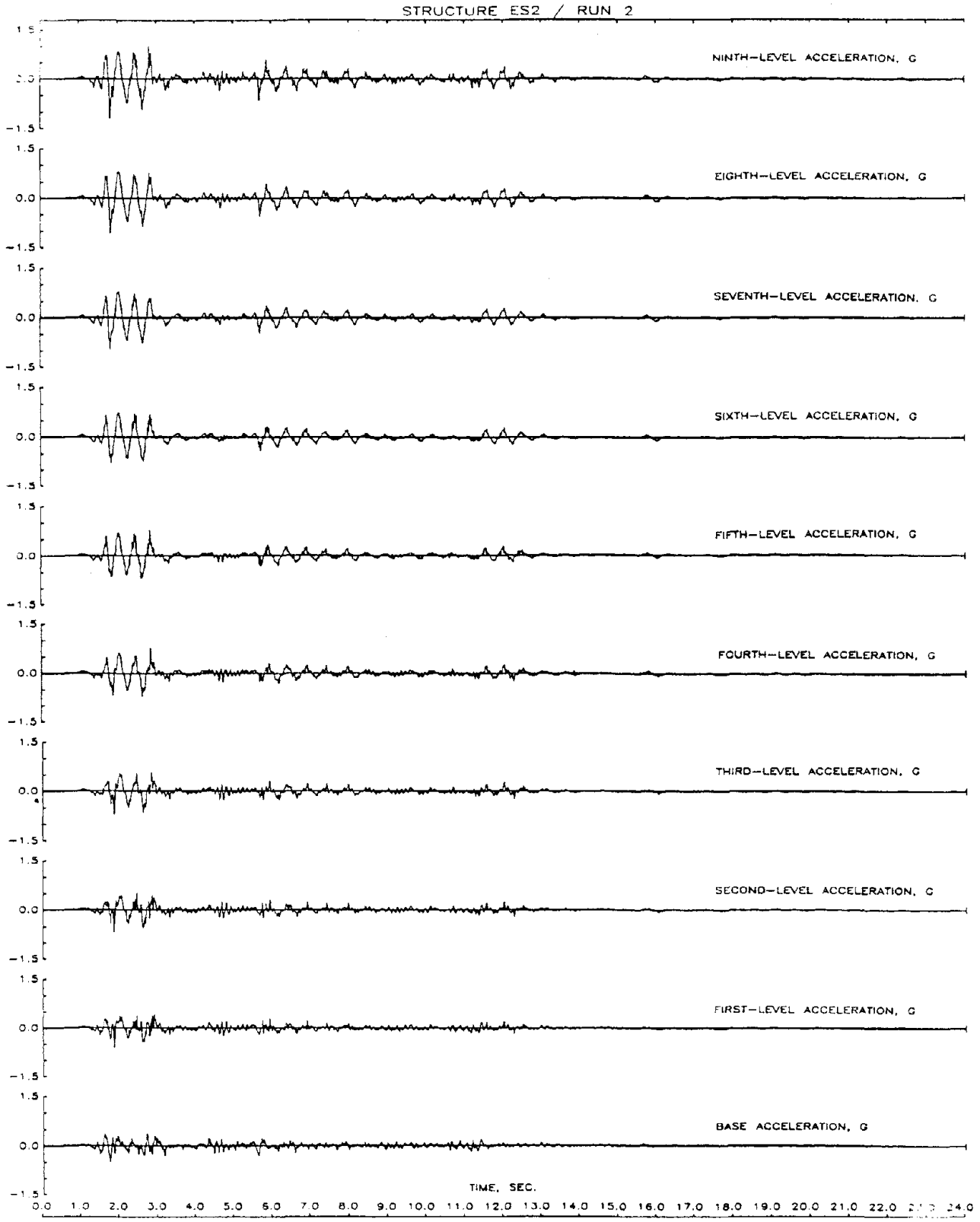

Fig. 4.11 (cont.) Response of Structure ES2 During Run 2
(b) Acceleration Histories

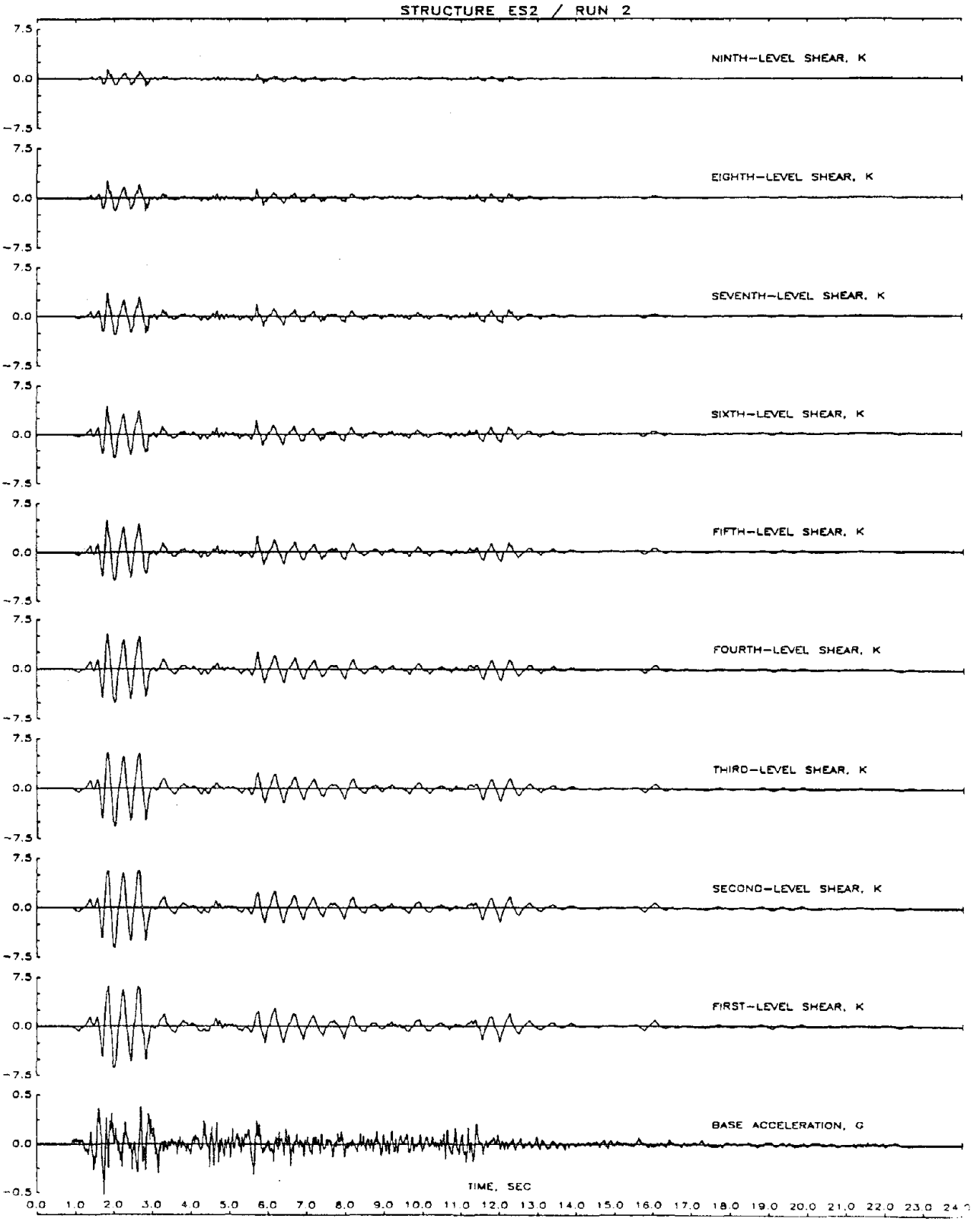

Fig. 4.11 (cont.) Response of Structure ES2 During Run 2
(c) Shear Histories

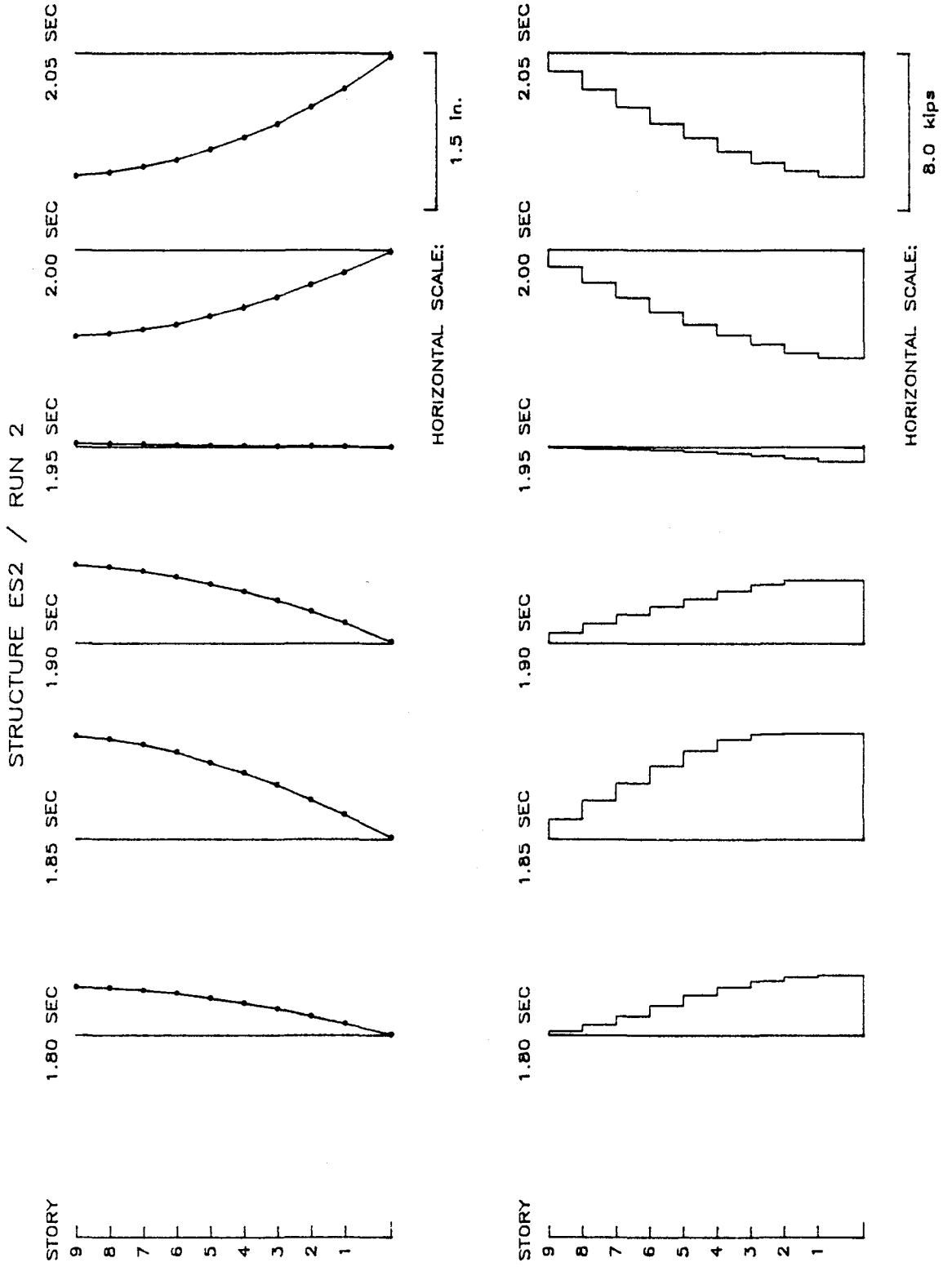

Fig. 4.11 (cont.) Response of Structure ES2 During Run 2
(d) Displacement and Shear Distributions

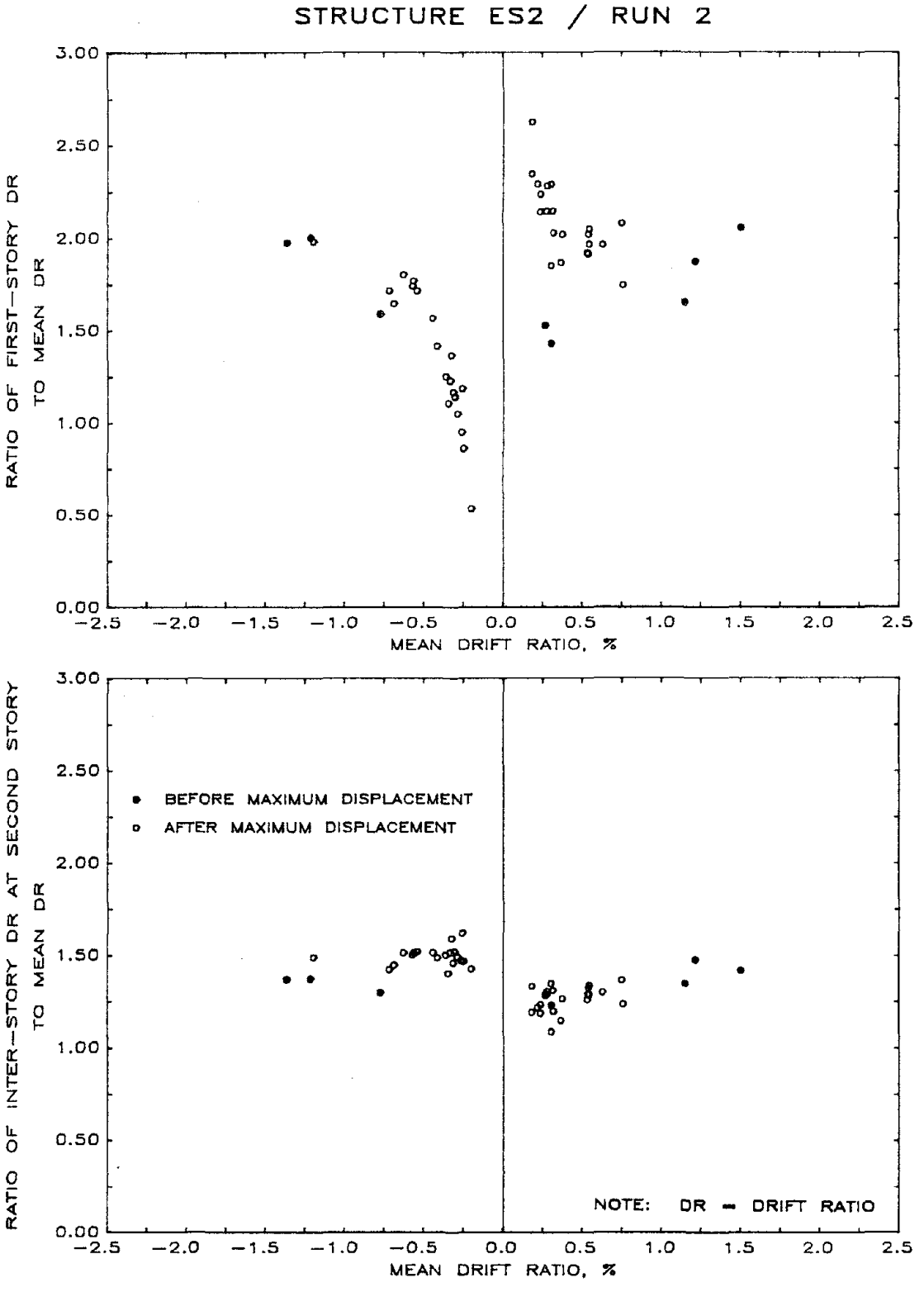

Fig. 4.11 (cont.) Response of Structure ES2 During Run 2
(e) Ratio of Interstory to Mean Drift

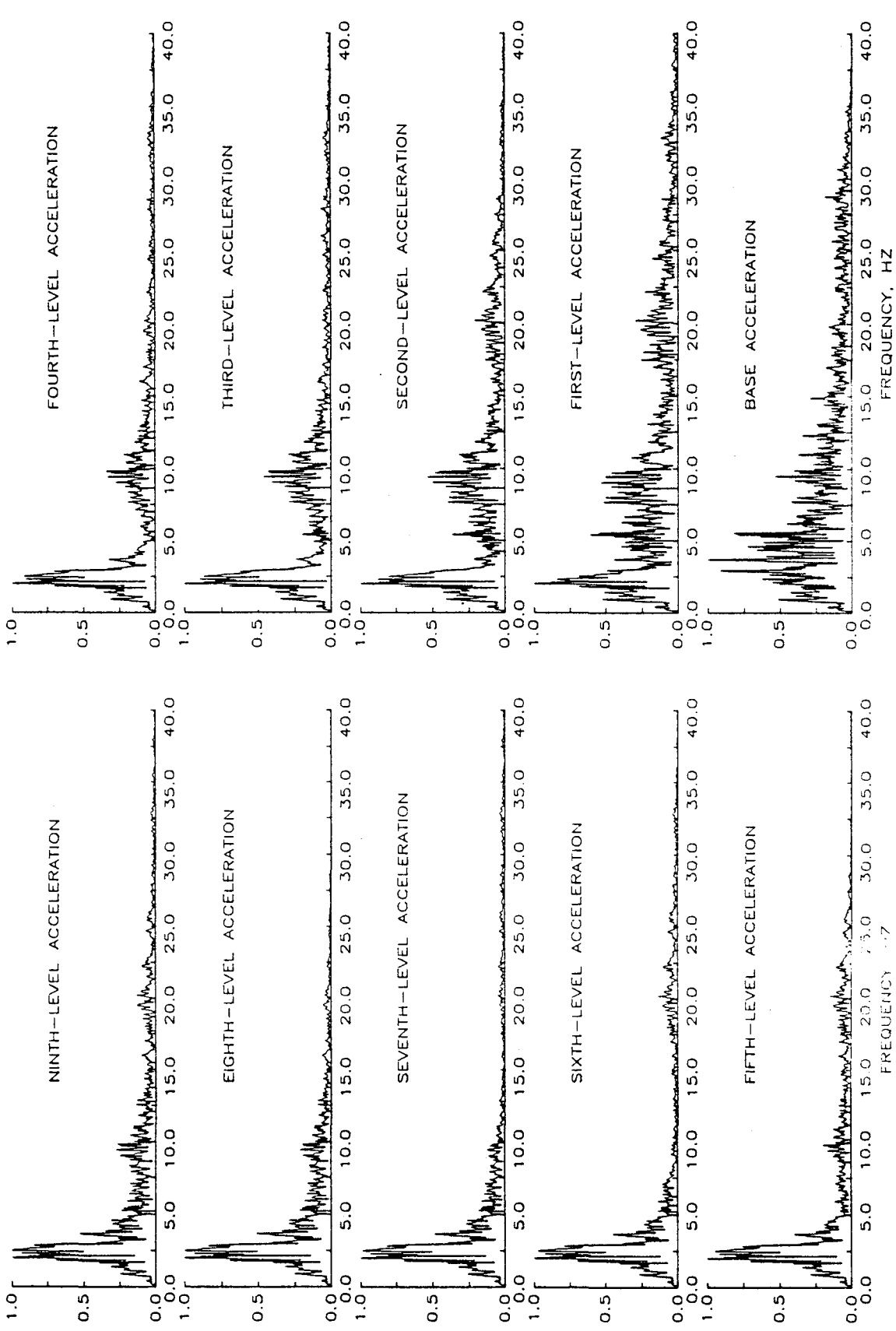

Fig. 4.11 (cont.) Response of Structure ES2 During Run 2
(f) Fourier Amplitude Spectra

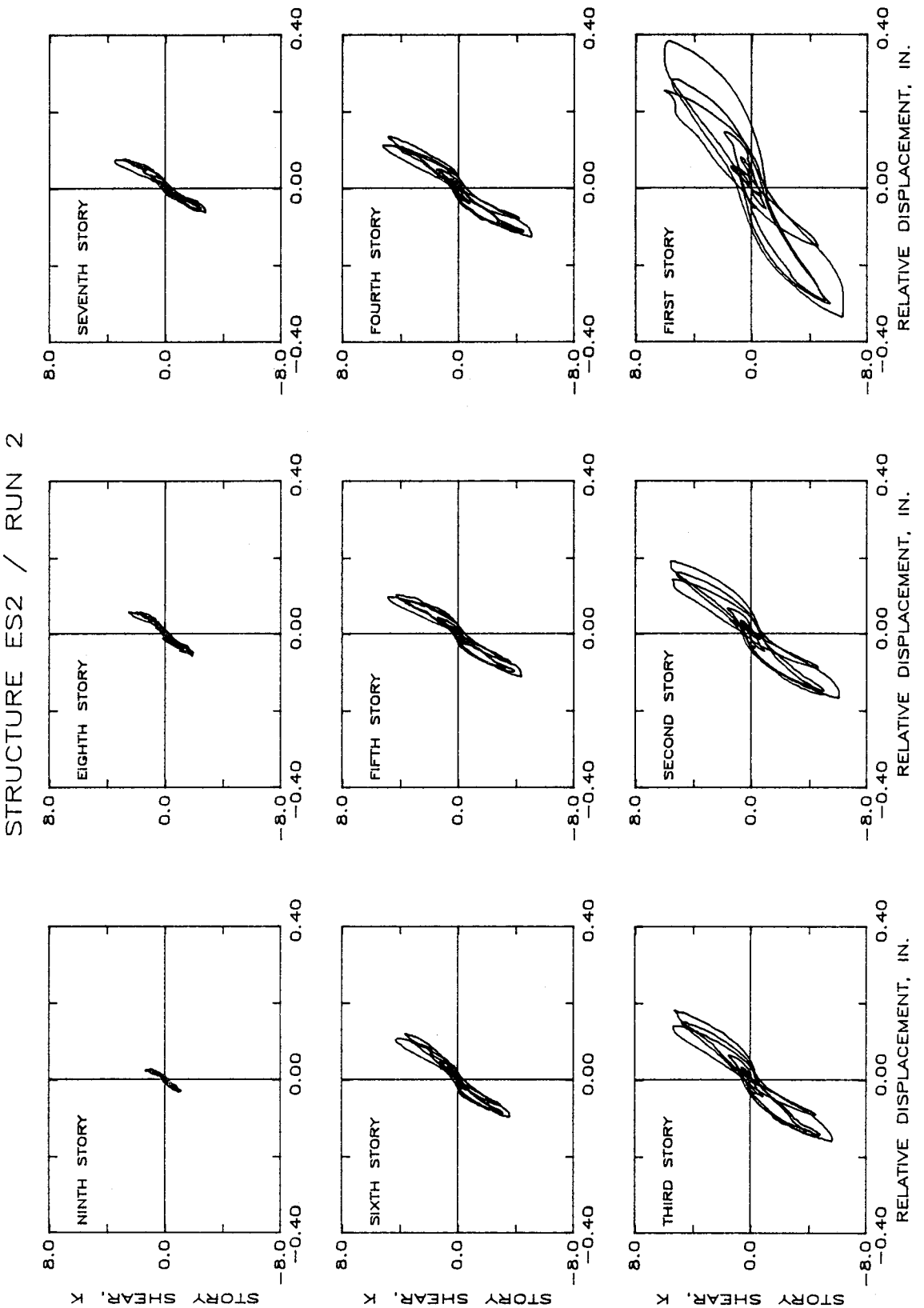

Fig. 4.11 (cont.) Response of Structure ES2 During Run 2
(g) Hysteretic Response

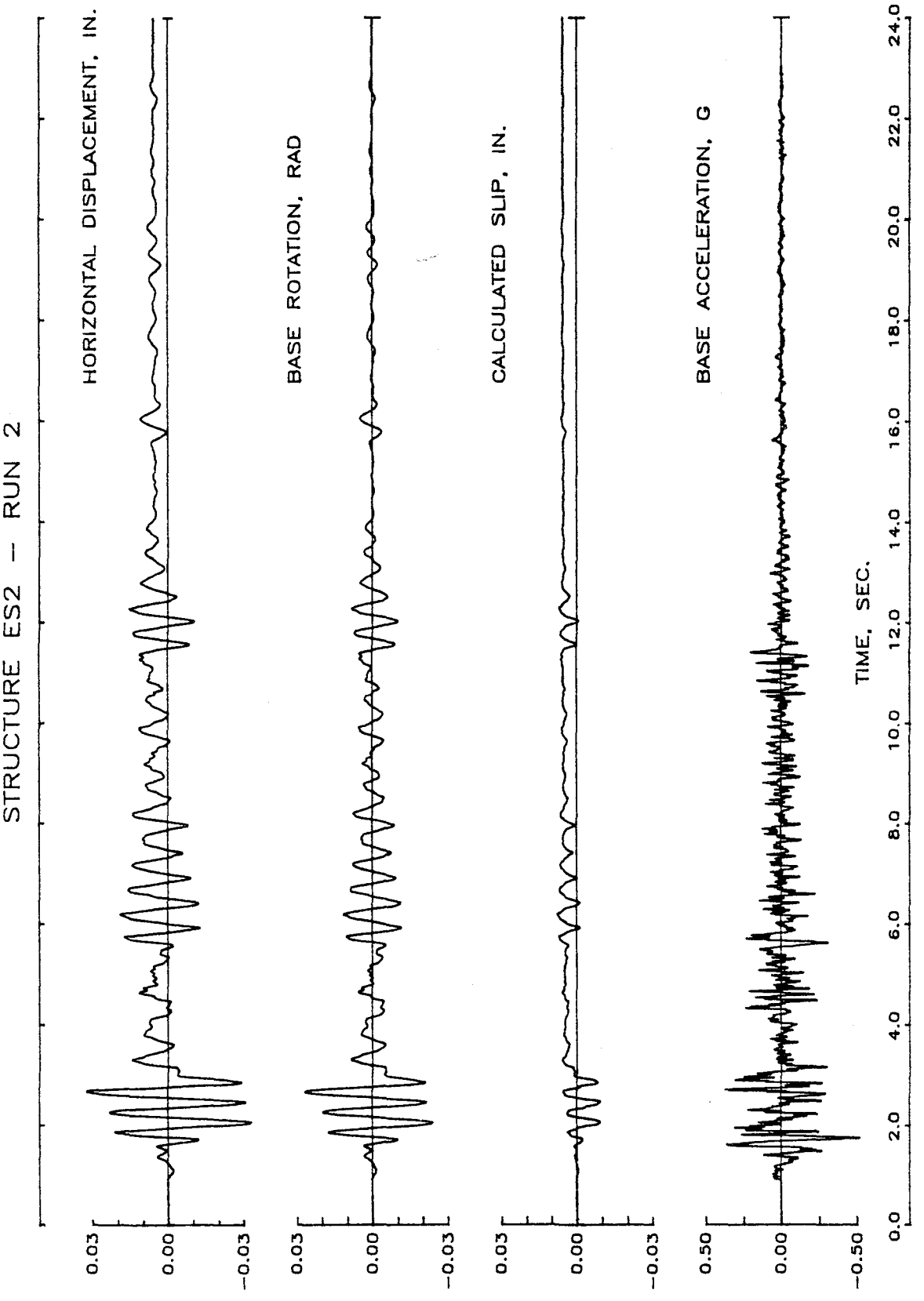

Fig. 4.11 (cont.) Response of Structure ES2 During Run 2
(h) Rotation and Slip at Base of Wall

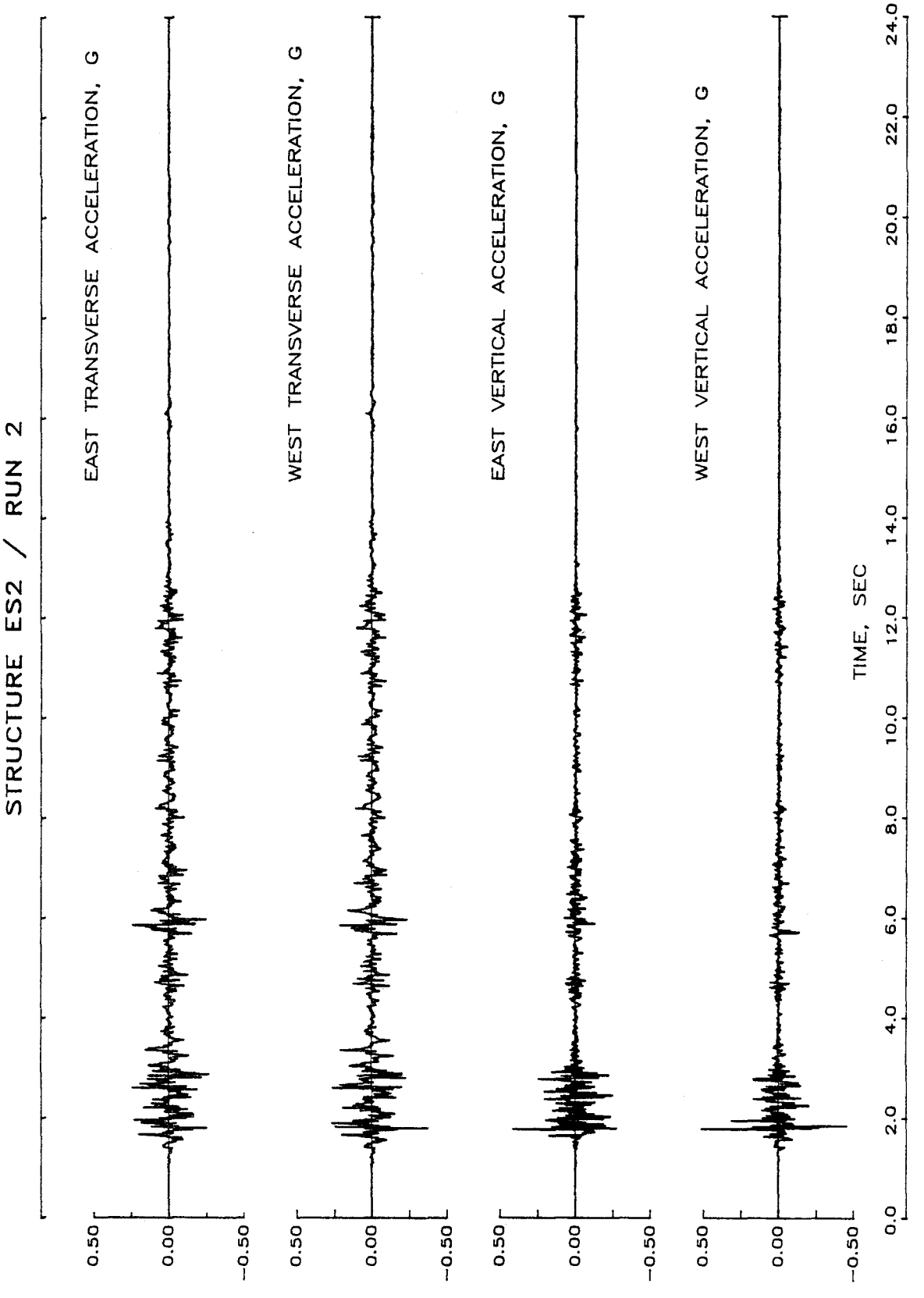

Fig. 4.11 (cont.) Response of Structure ES2 During Run 2
(i) Vertical and Transverse Accelerations

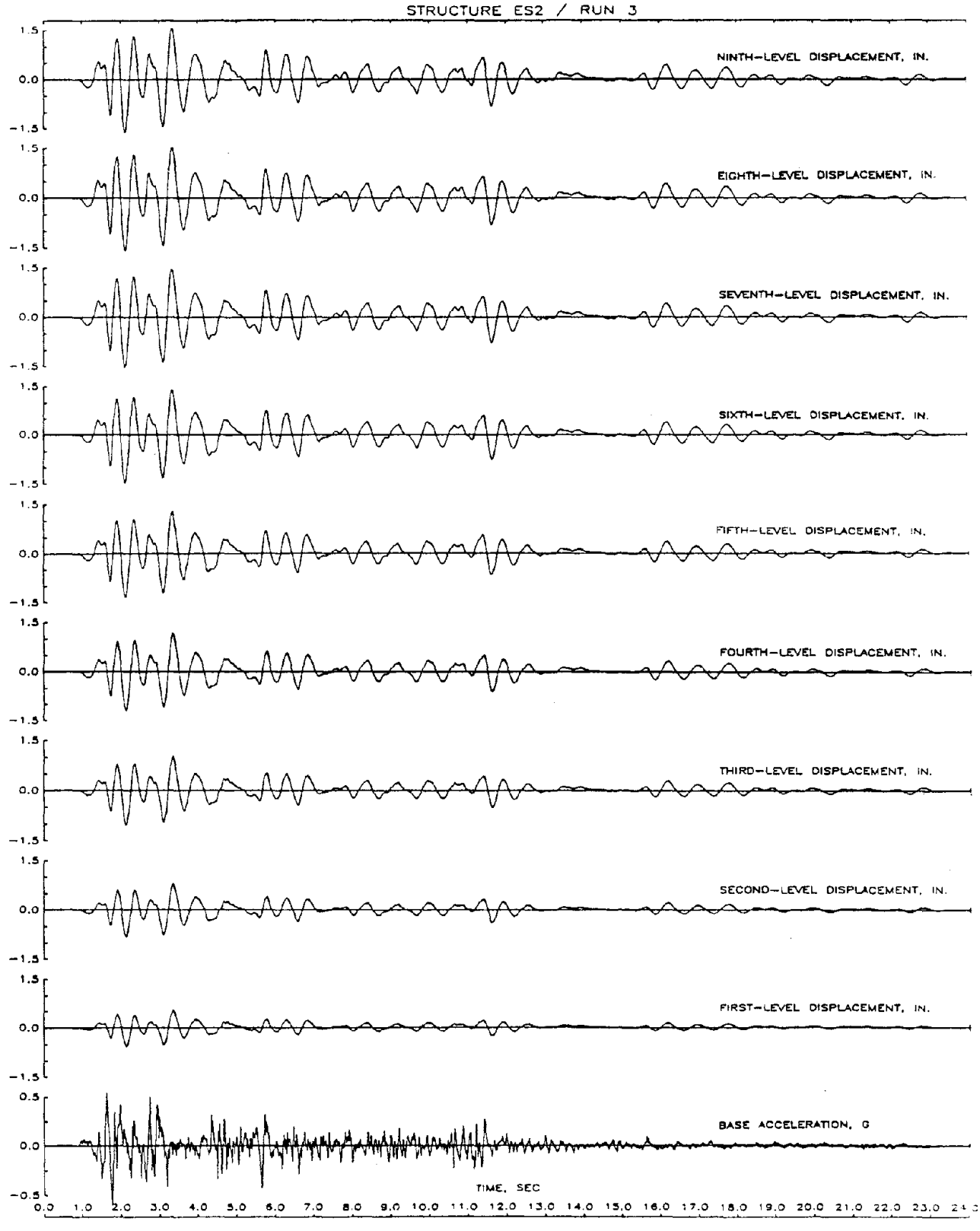

Fig. 4.12 Response of Structure ES2 During Run 3
(a) Displacement Histories

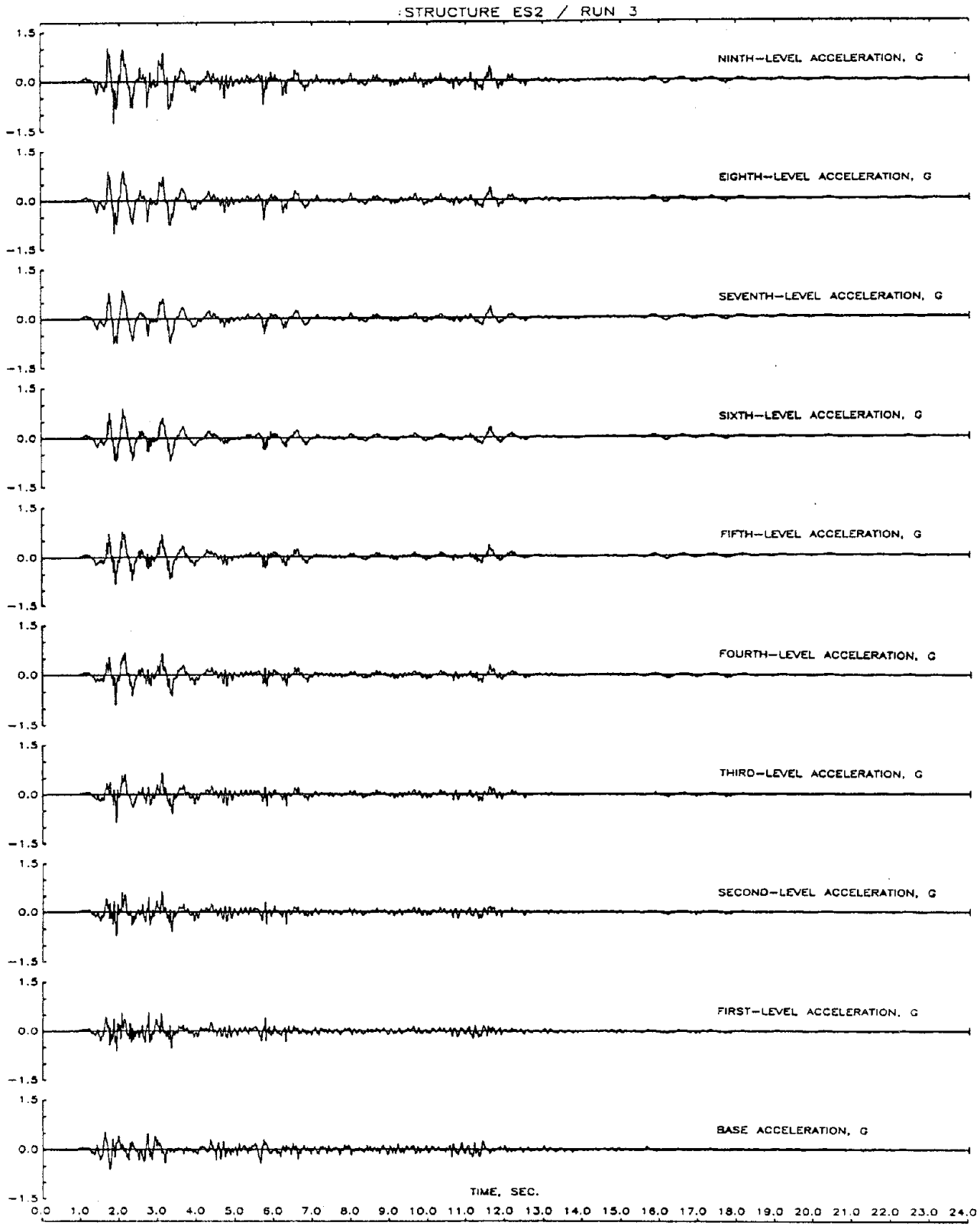

Fig. 4.12 (cont.) Response of Structure ES2 During Run 3
(b) Acceleration Histories

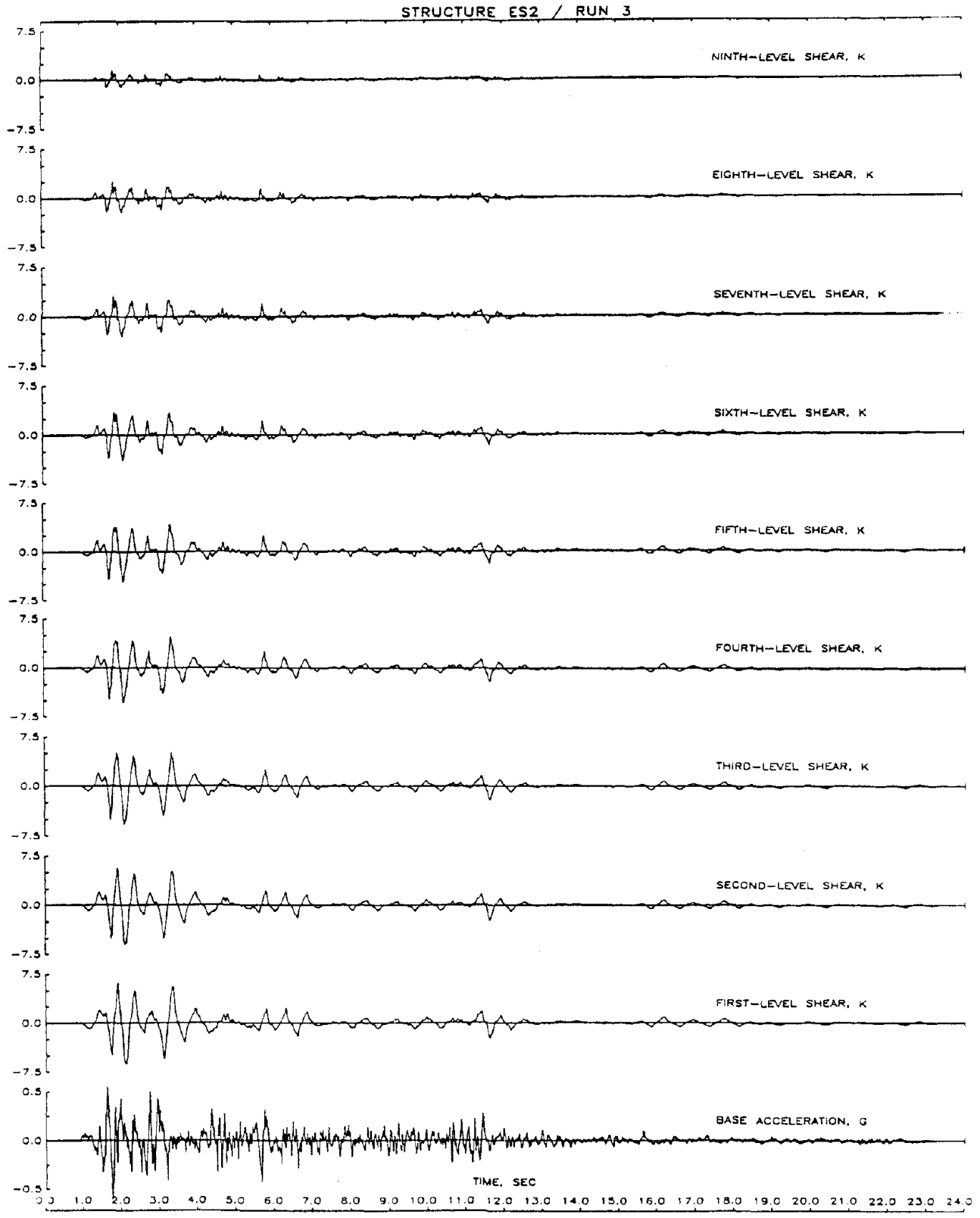

Fig. 4.12 (cont.) Response of Structure ES2 During Run 3
(c) Shear Histories

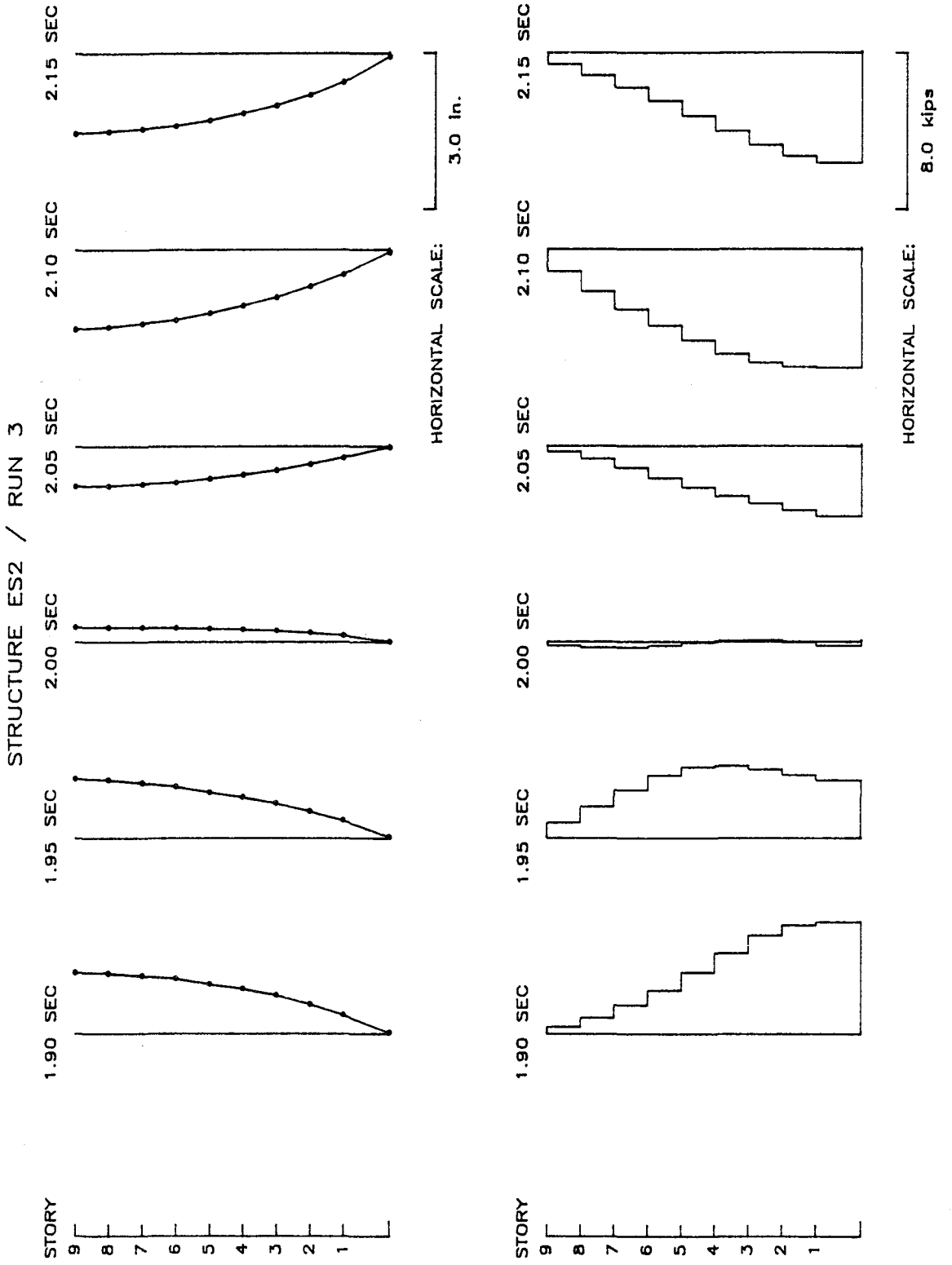

Fig. 4.12 (cont.) Response of Structure ES2 During Run 3
(d) Displacement and Shear Distributions

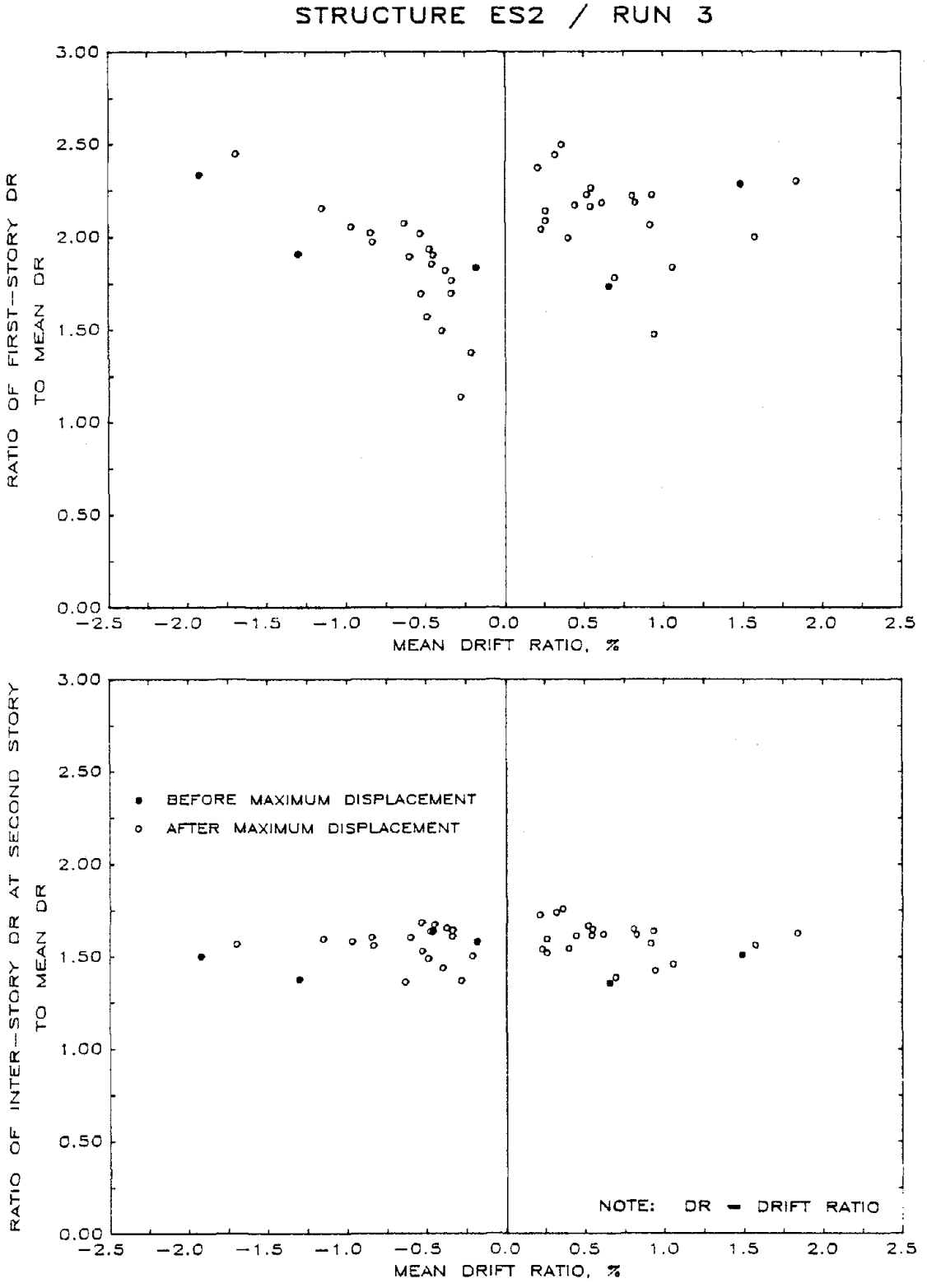

Fig. 4.12 (cont.) Response of Structure ES2 During Run 3
(e) Ratio of Interstory to Mean Drift

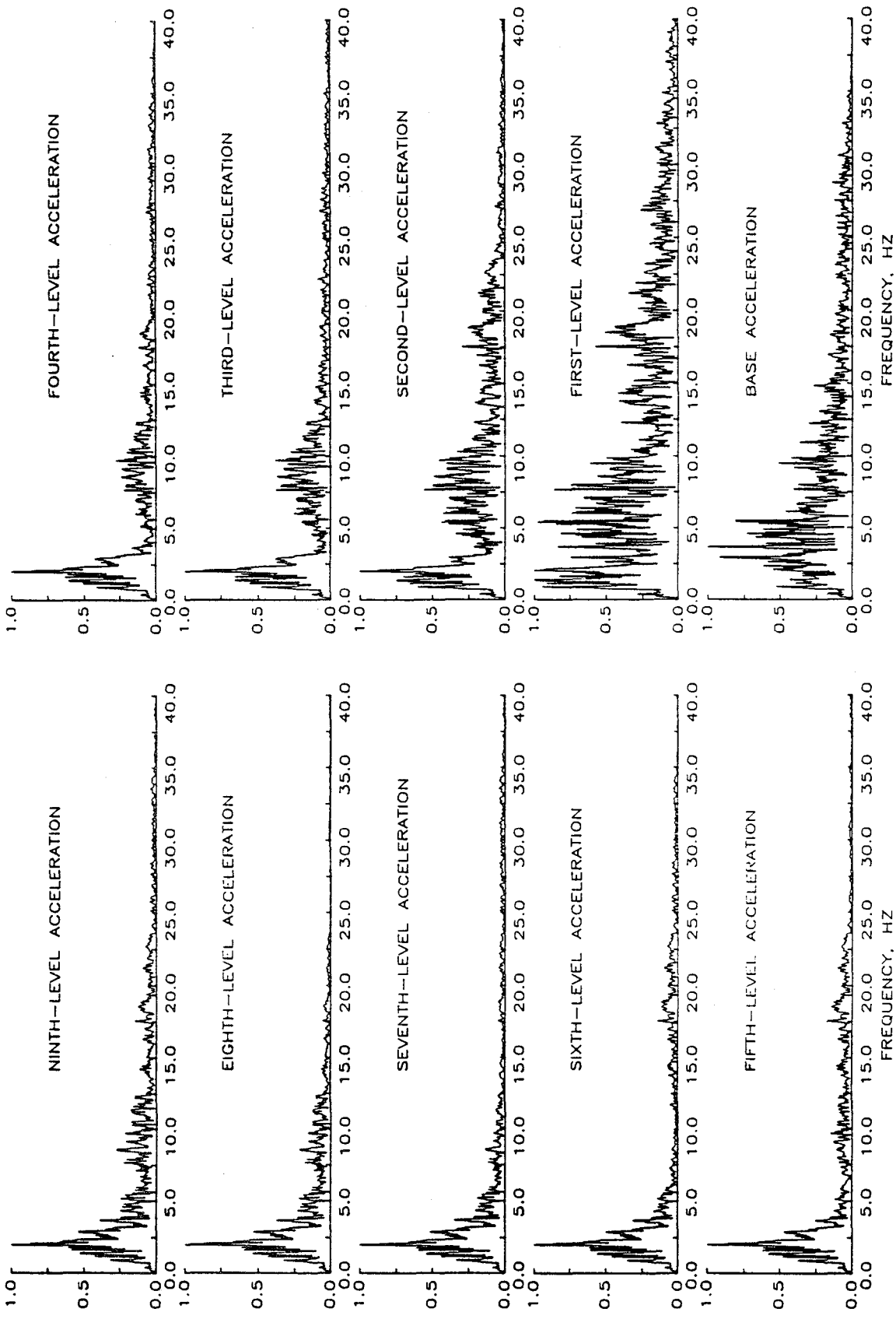

Fig. 4.12 (cont.) Response of Structure ES2 During Run 3
(f) Fourier Amplitude Spectra

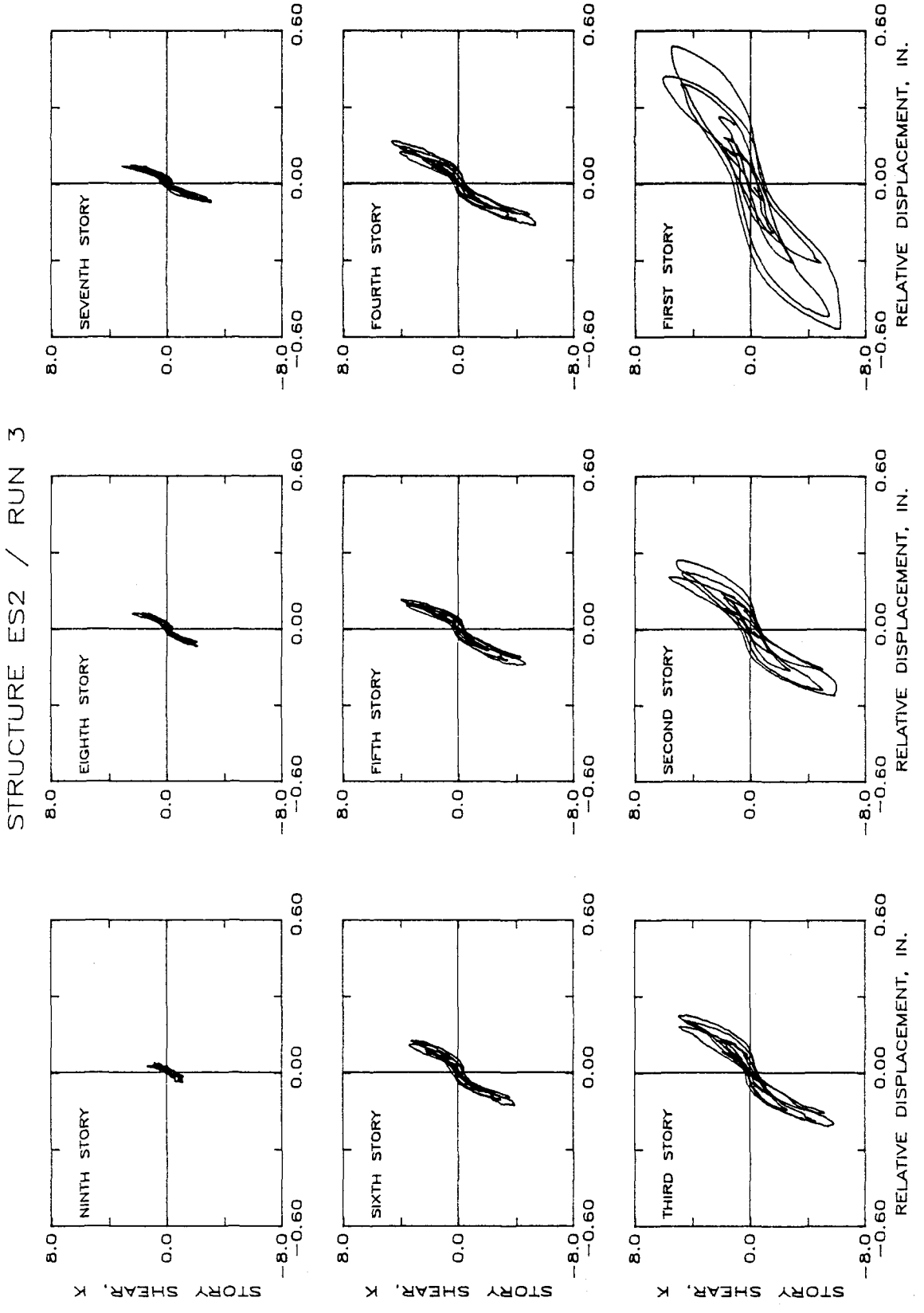

Fig. 4.12 (cont.) Response of Structure ES2 During Run 3
(g) Hysteretic Response

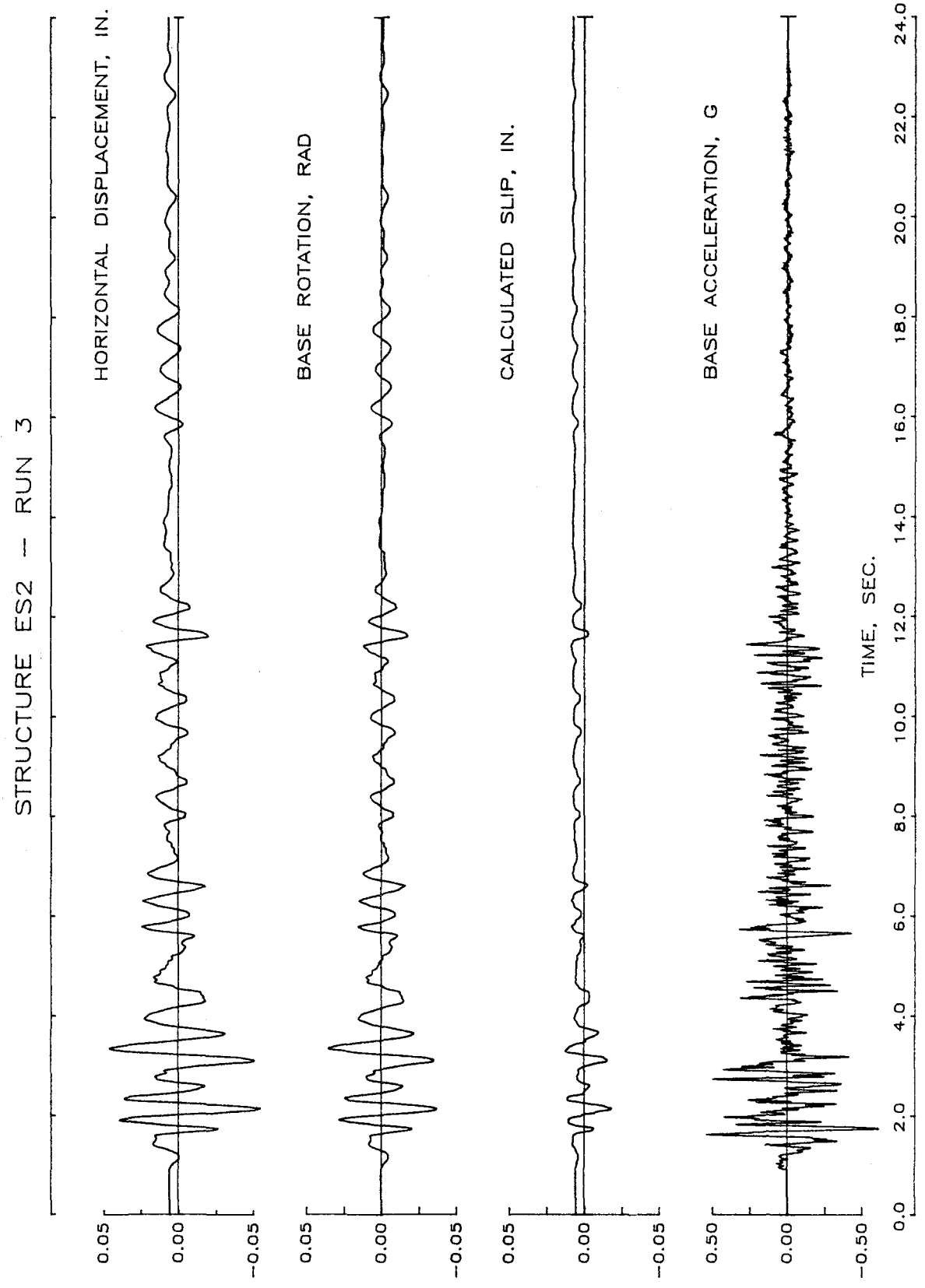

Fig. 4.12 (cont.) Response of Structure ES2 During Run 3
(h) Rotation and Slip at Base of Wall

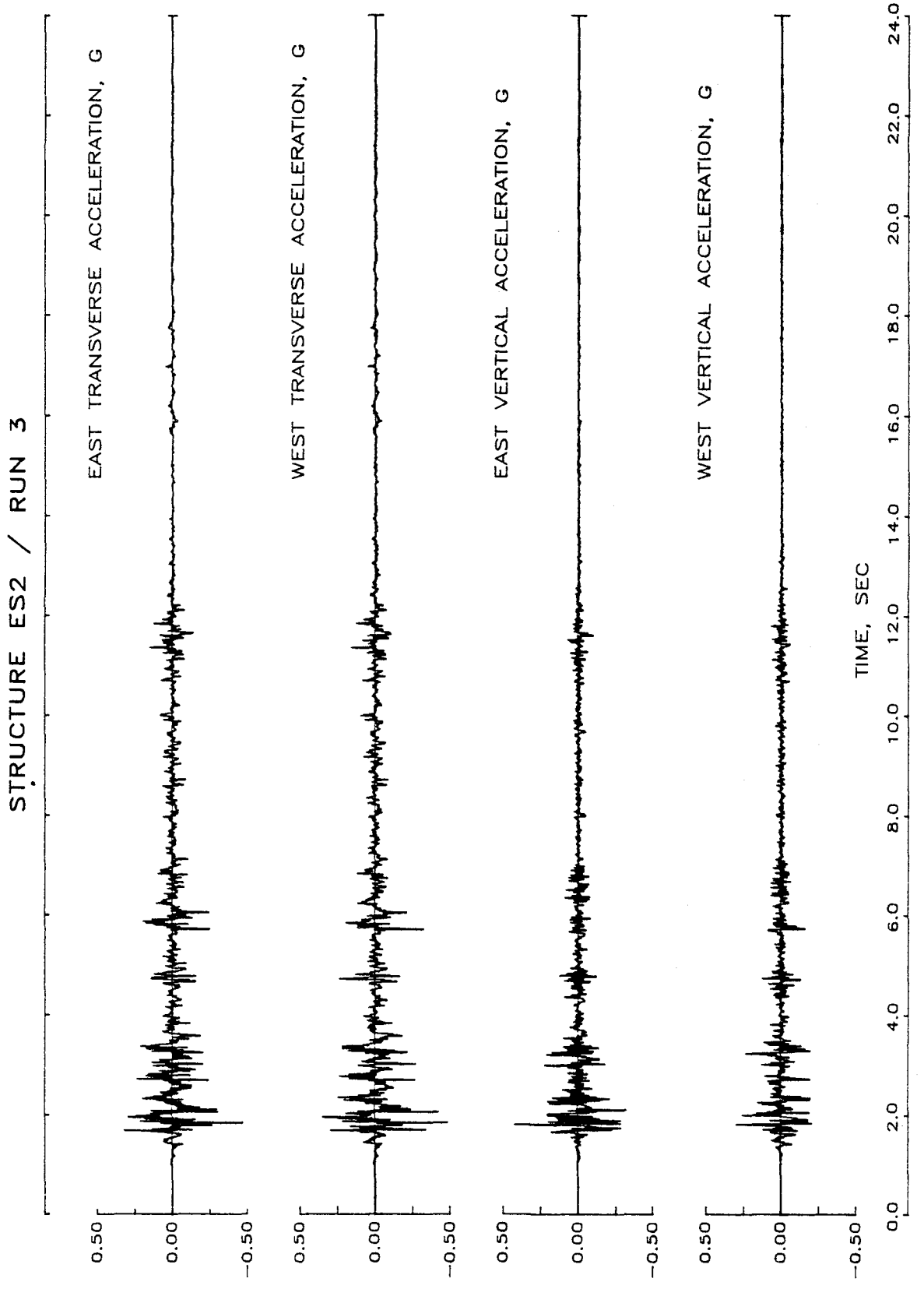

Fig. 4.12 (cont.) Response of Structure ES2 During Run 3
(i) Vertical and Transverse Accelerations

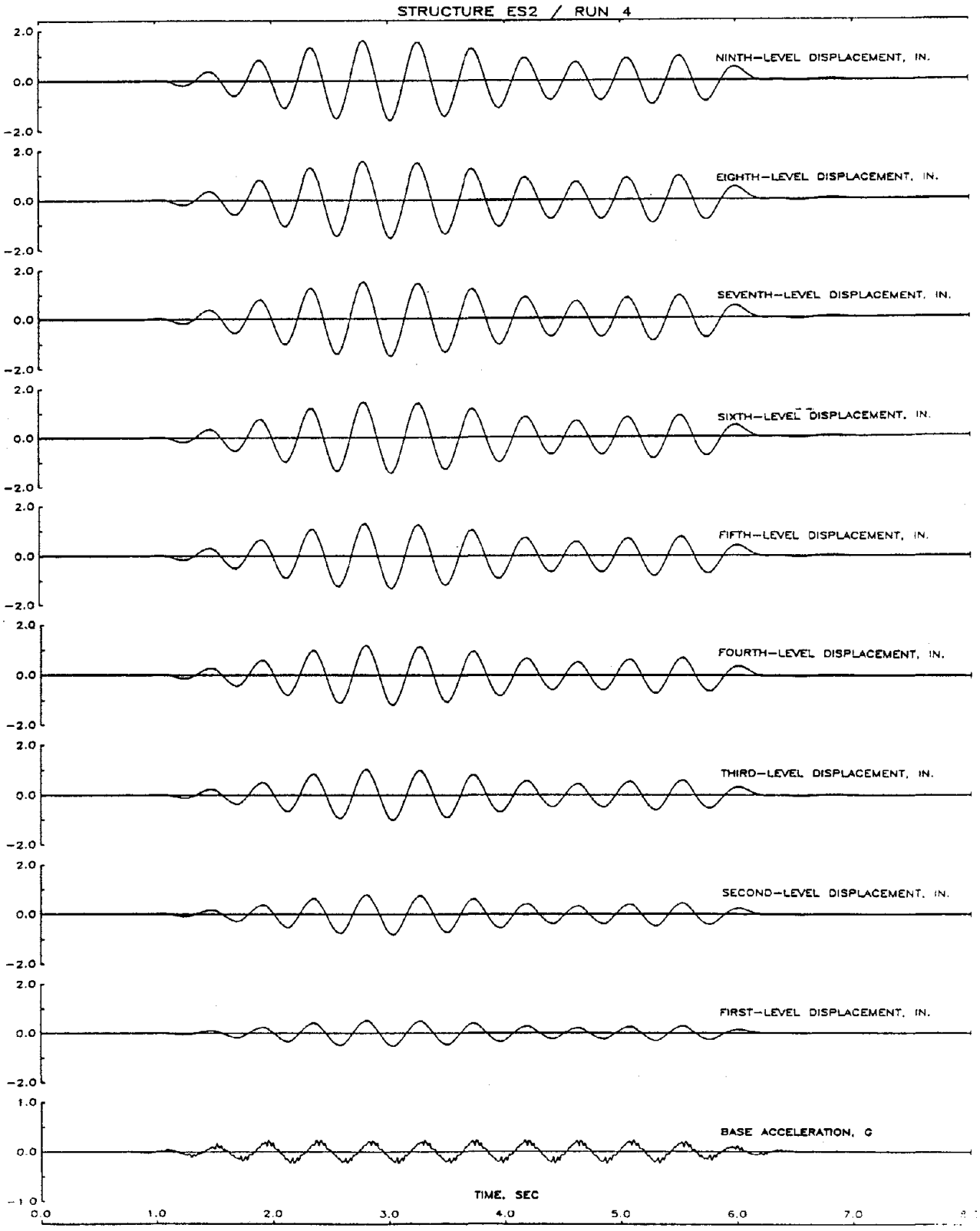

Fig. 4.13 Response of Structure ES2 During Run 4
(a) Displacement Histories

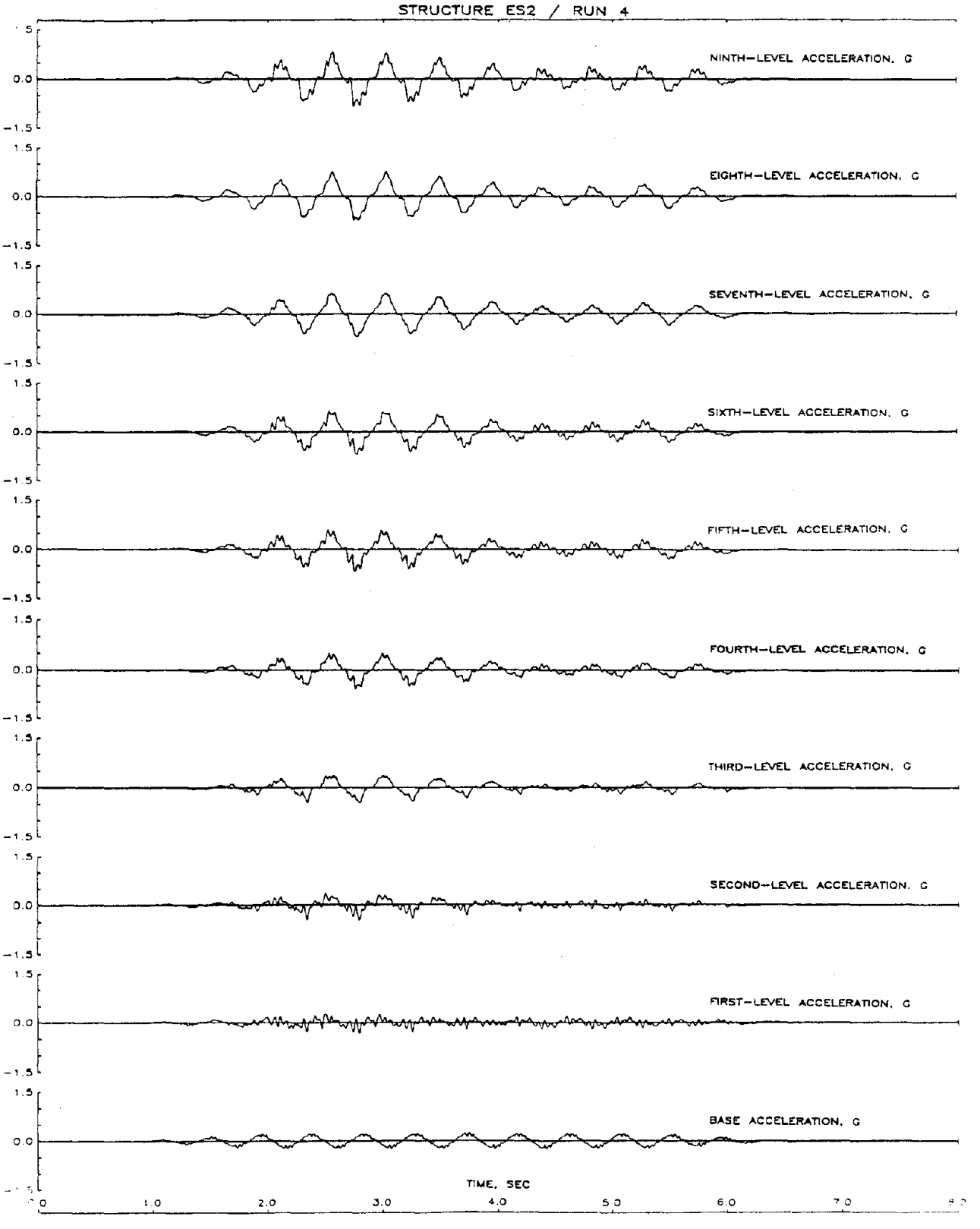

Fig. 4.13 (cont.) Response of Structure ES2 During Run 4
(b) Acceleration Histories

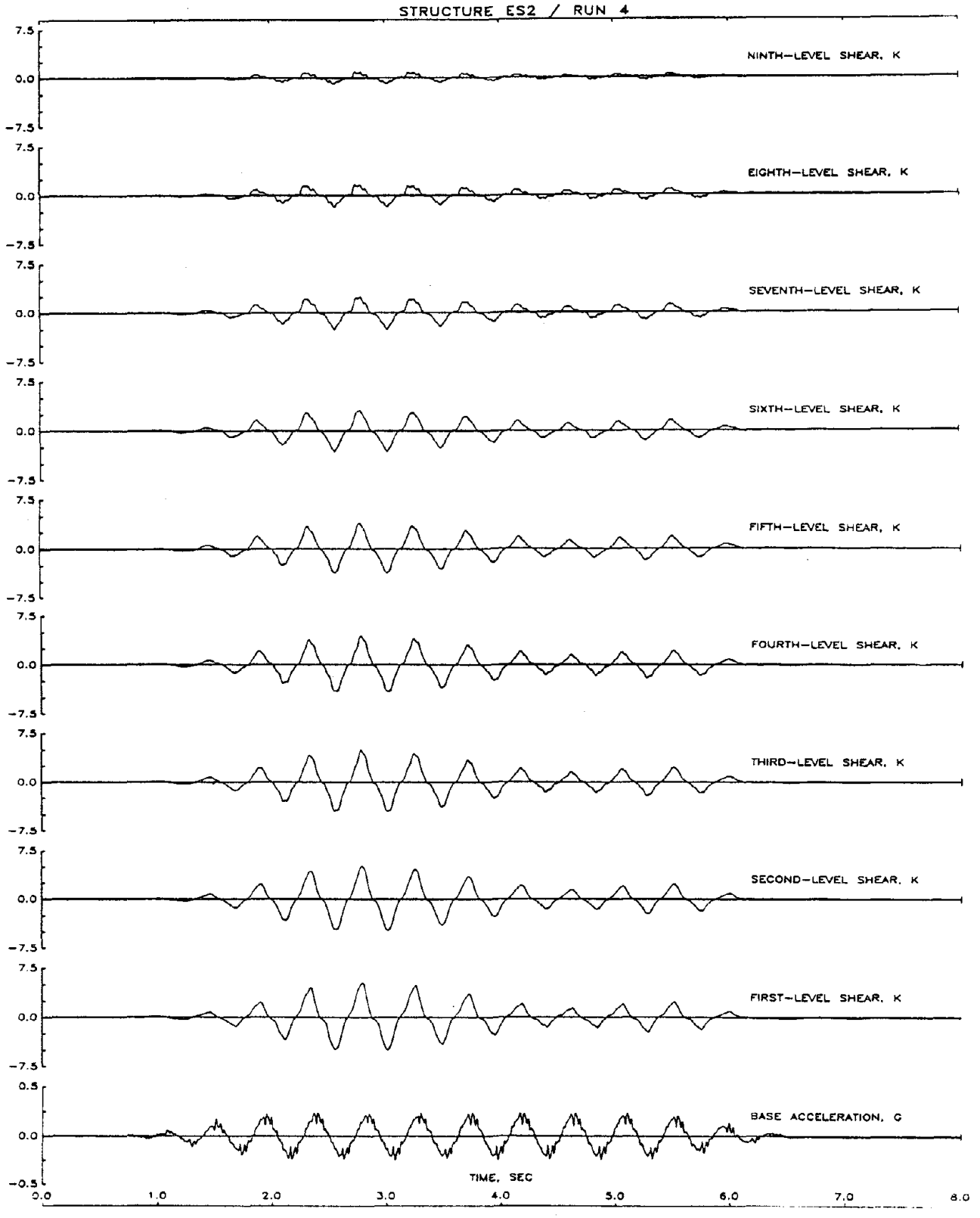

Fig. 4.13 (cont.) Response of Structure ES2 During Run 4
(c) Shear Histories

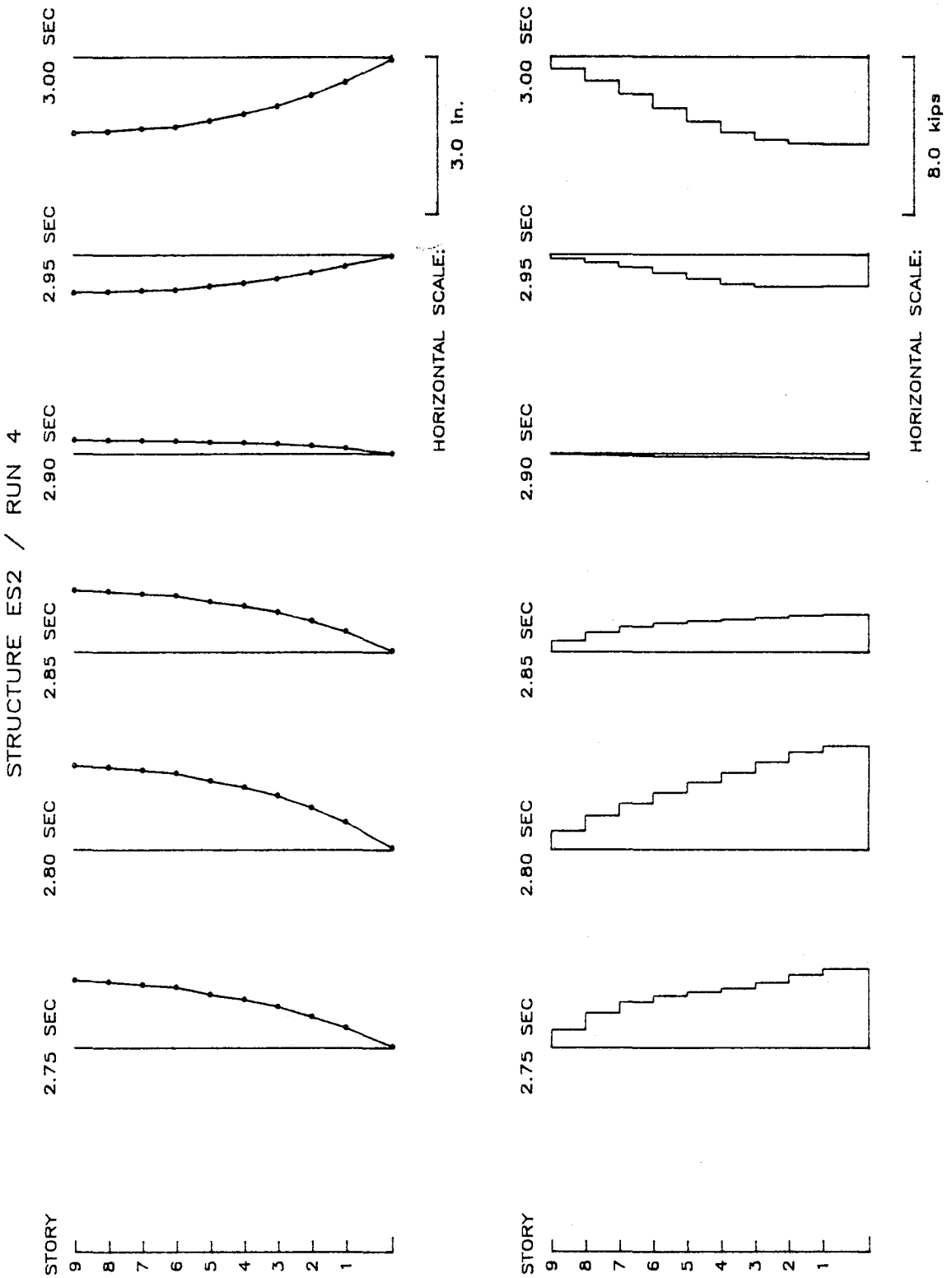

Fig. 4.13 (cont.) Response of Structure ES2 During Run 4
(d) Displacement and Shear Distributions

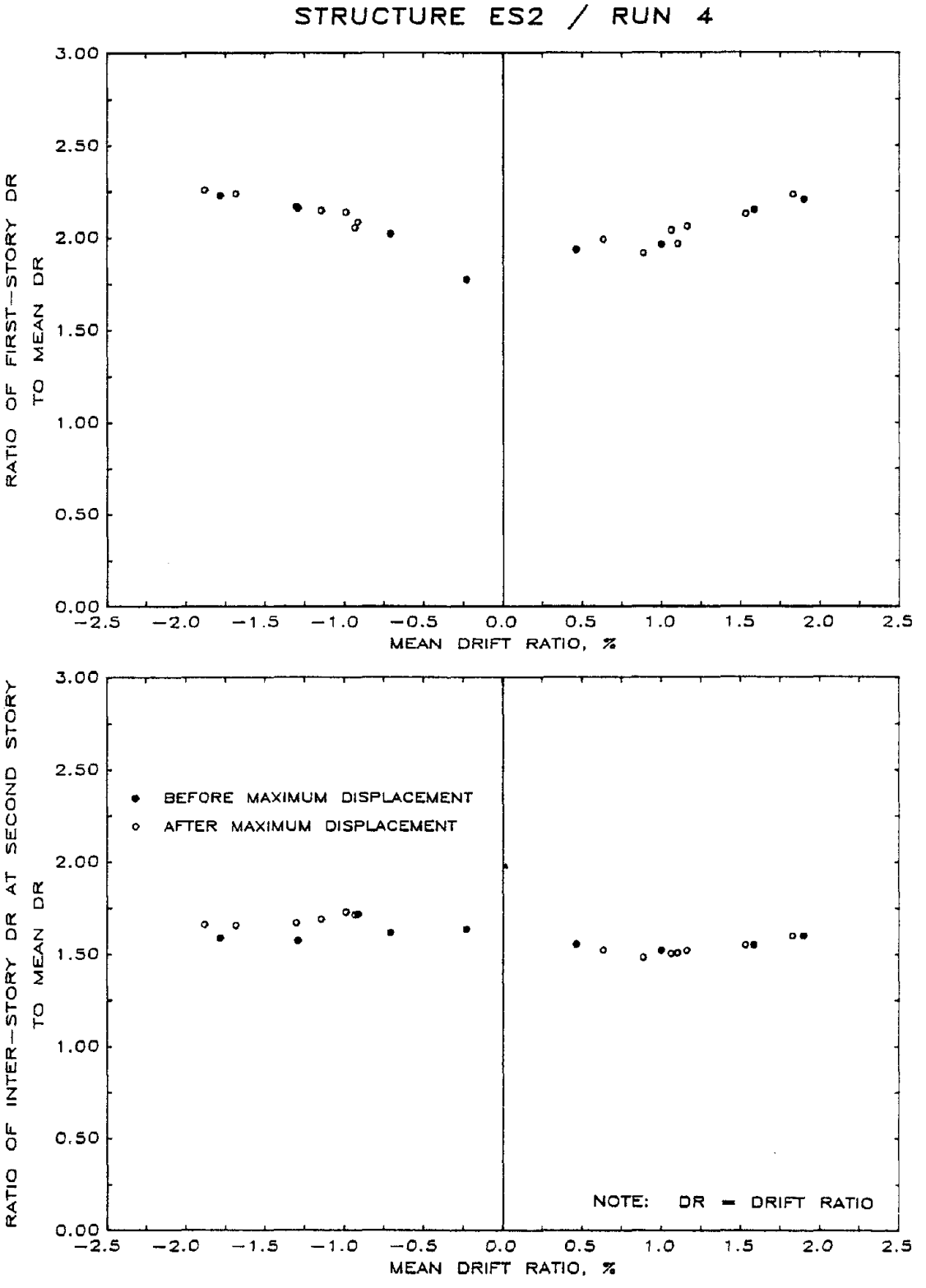

Fig. 4.13 (cont.) Response of Structure ES2 During Run 4
(e) Ratio of Interstory to Mean Drift

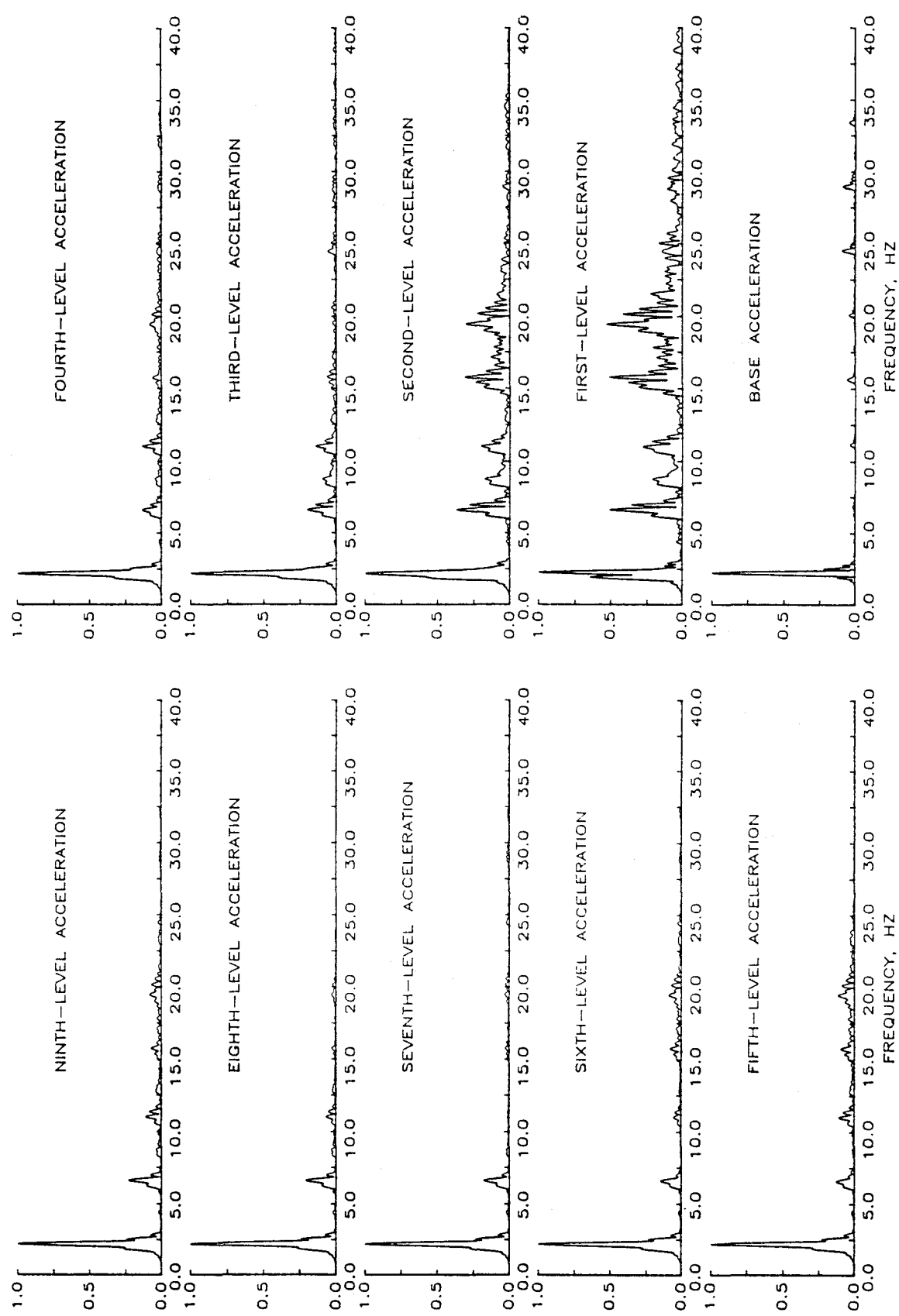

Fig. 4.13 (cont.) Response of Structure ES2 During Run 4
(f) Fourier Amplitude Spectra

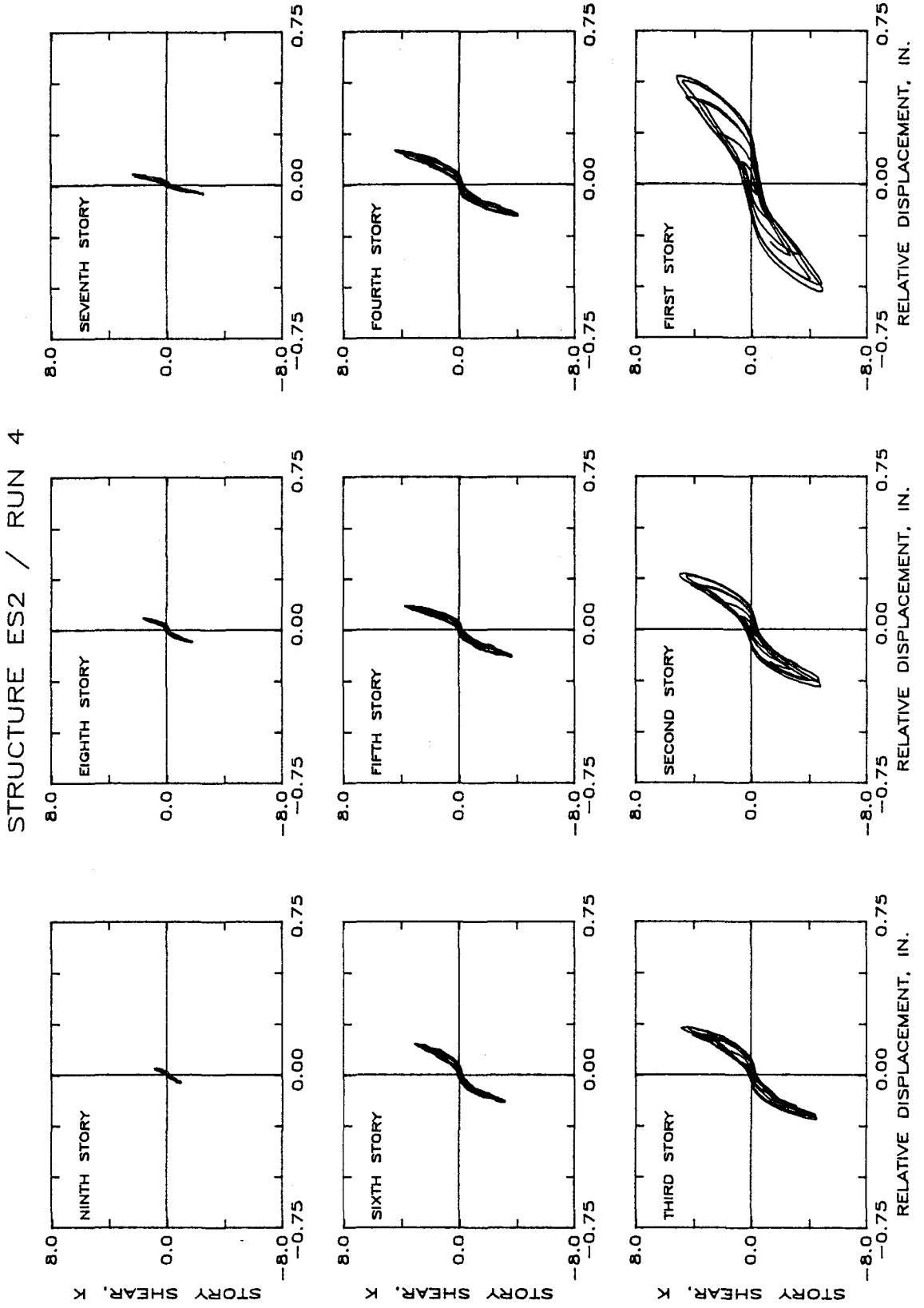

Fig. 4.13 (cont.) Response of Structure ES2 During Run 4
(g) Hysteretic Response

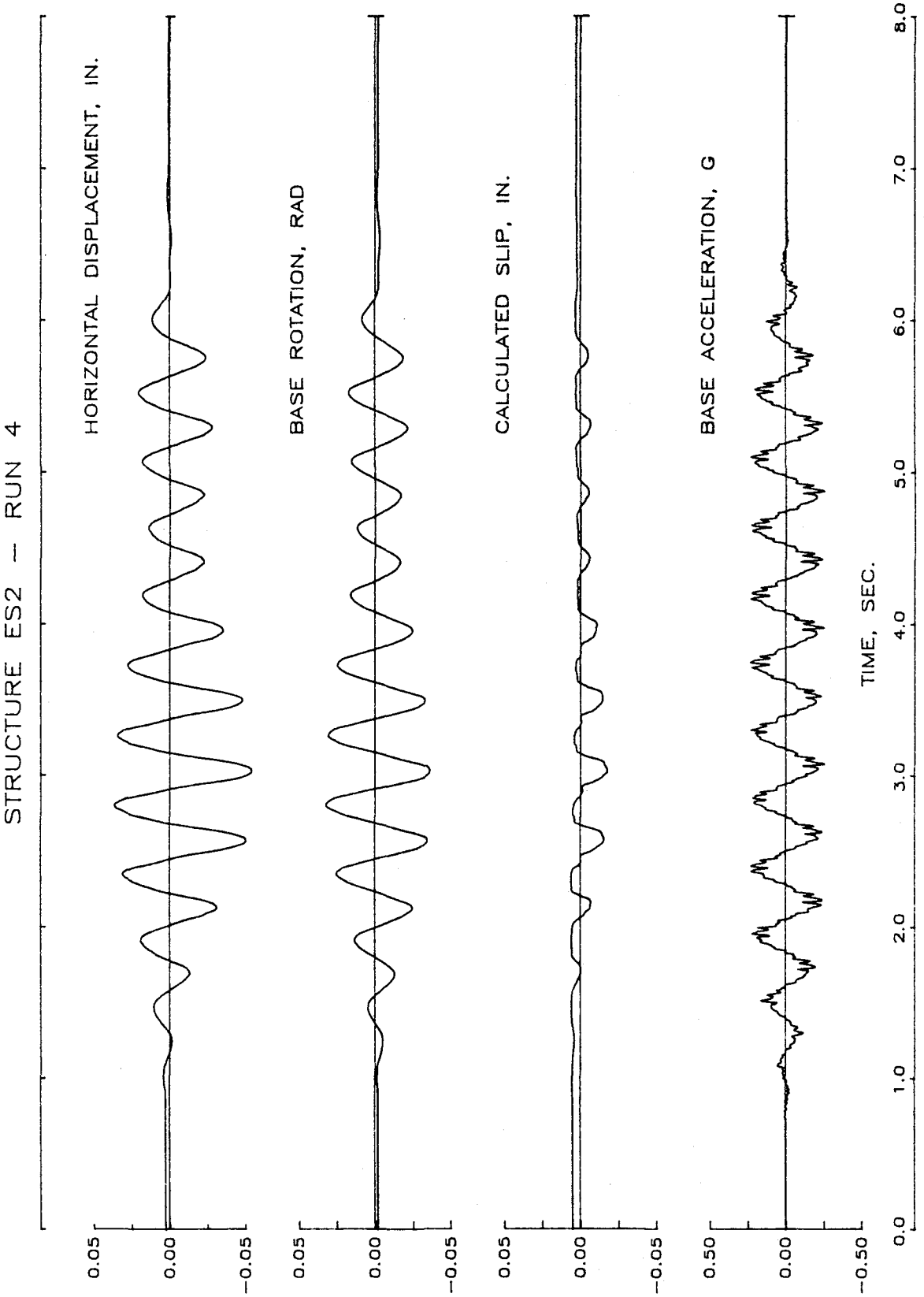

Fig. 4.13 (cont.) Response of Structure ES2 During Run 4
(h) Rotation and Slip at Base of Wall

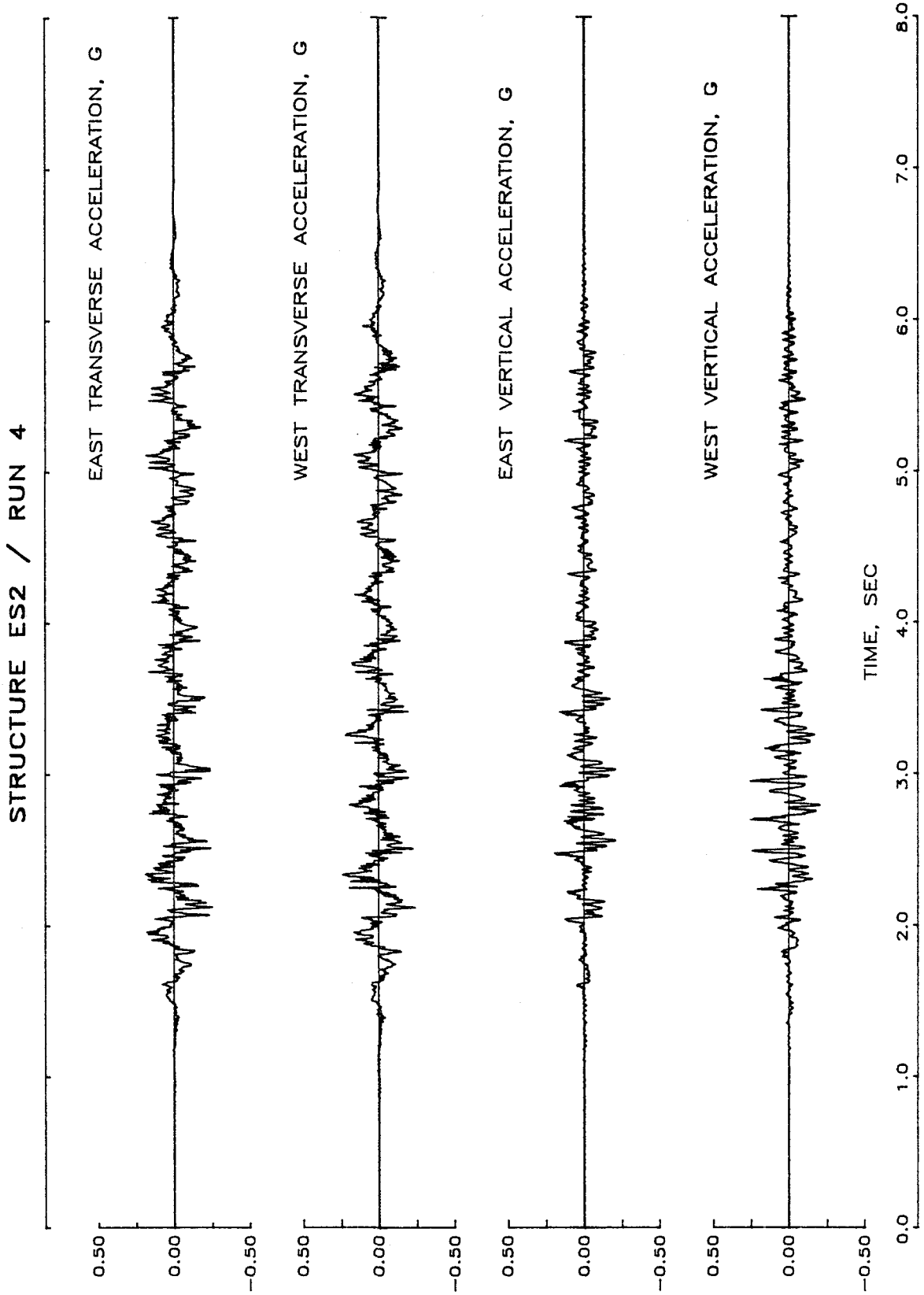

Fig. 4.13 (cont.) Response of Structure ES2 During Run 4
(i) Vertical and Transverse Accelerations

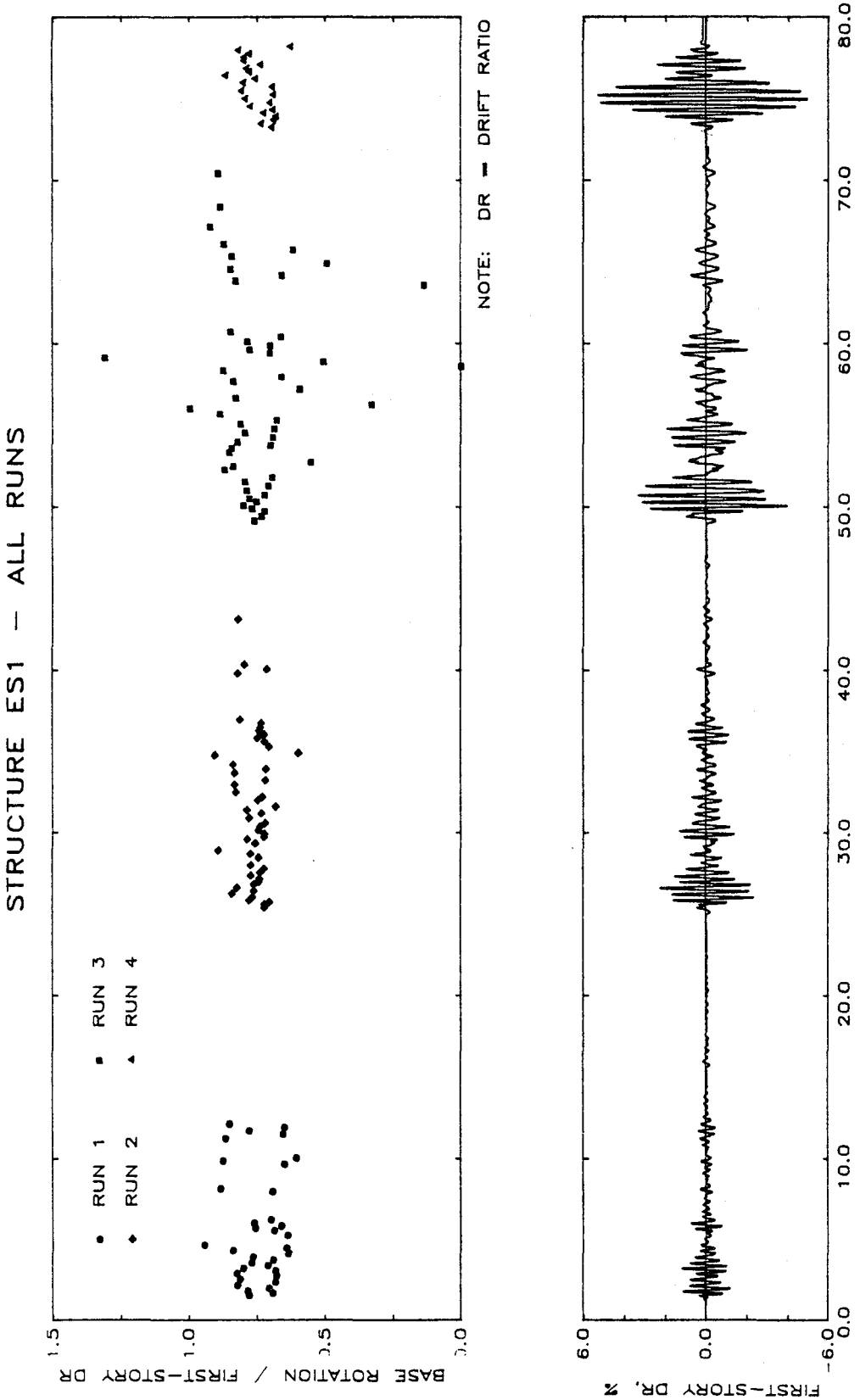

Fig. 4.14 Variation with Time of Ratio of Base Rotation to First-Story Drift Ratio
(a) Structure ES1

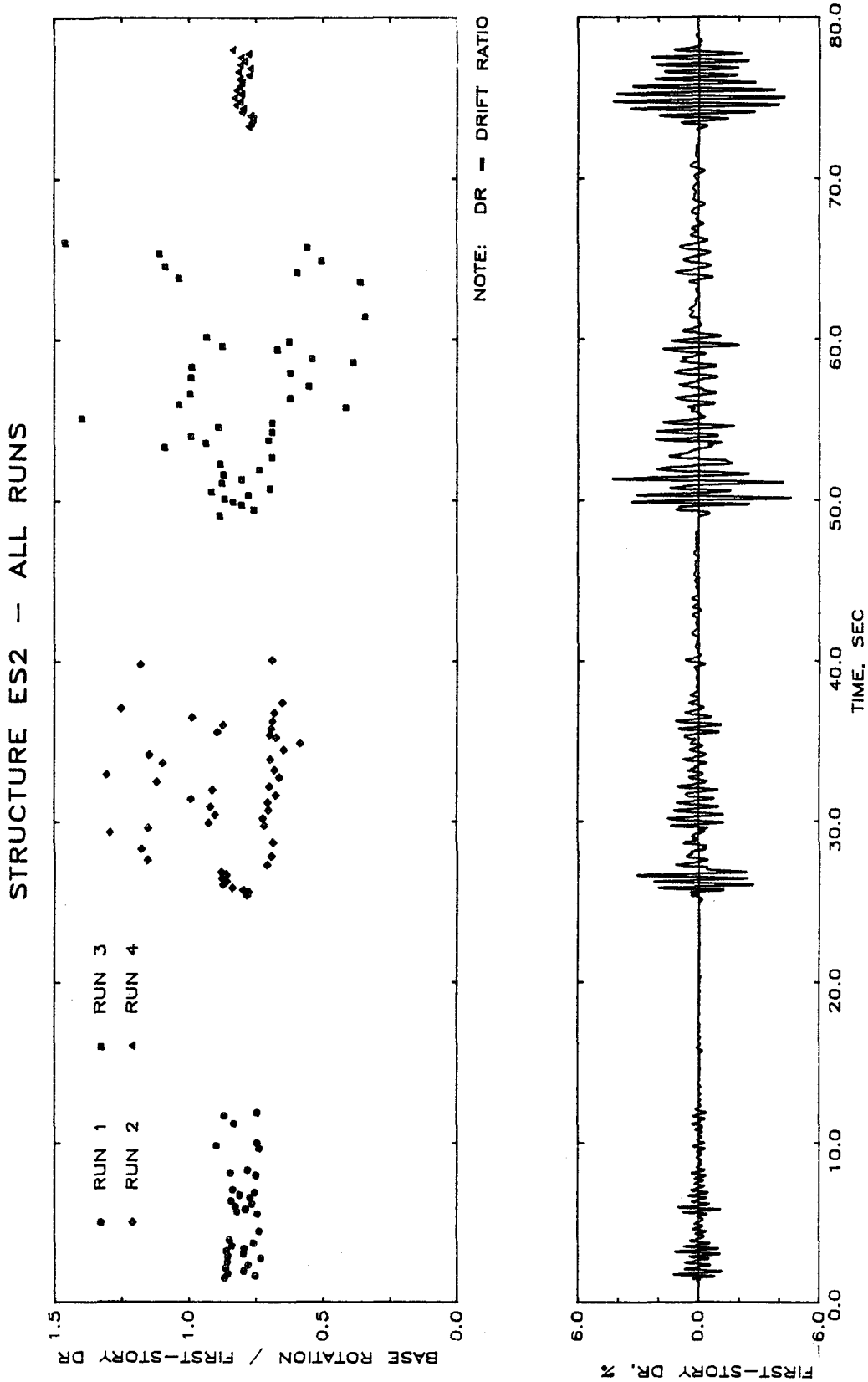

Fig. 4.14 (cont.) Variation with Time of Ratio of Base Rotation to First-Story Drift Ratio
(b) Structure ES2

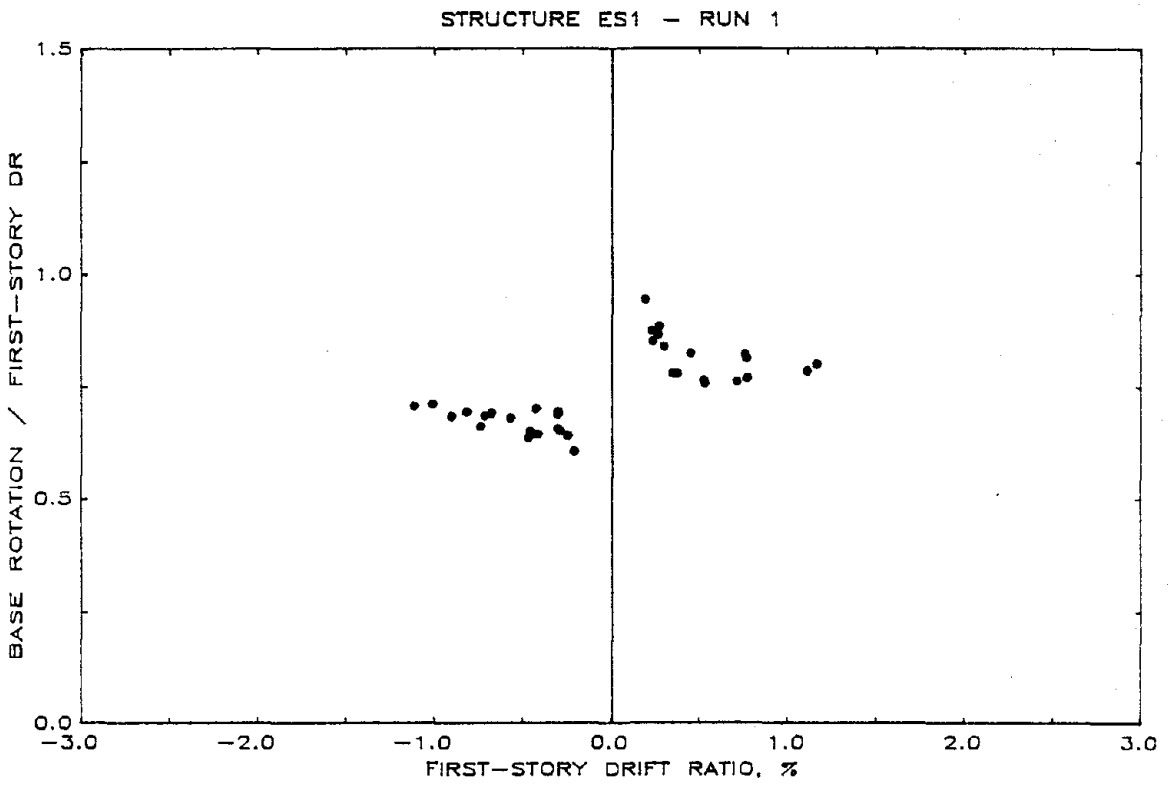

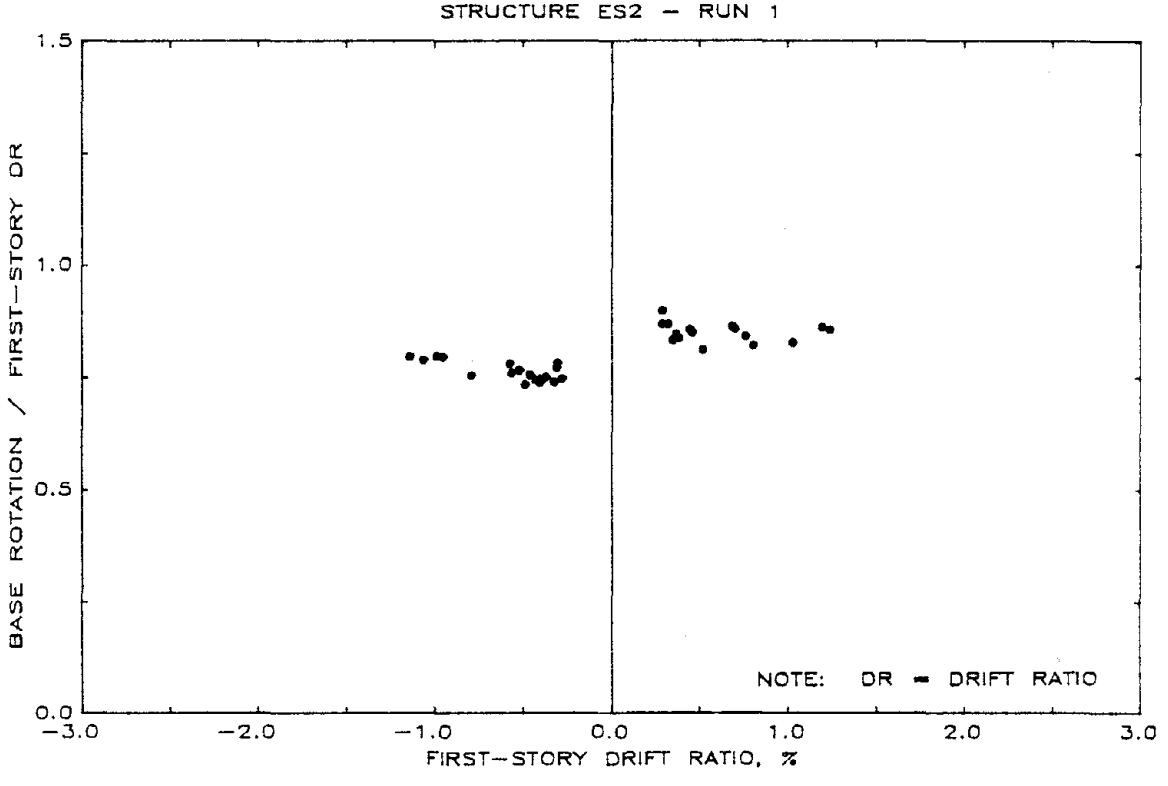

Fig. 4.15 Ratio of Base Rotation to First-Story Drift Ratio
(a) Run 1

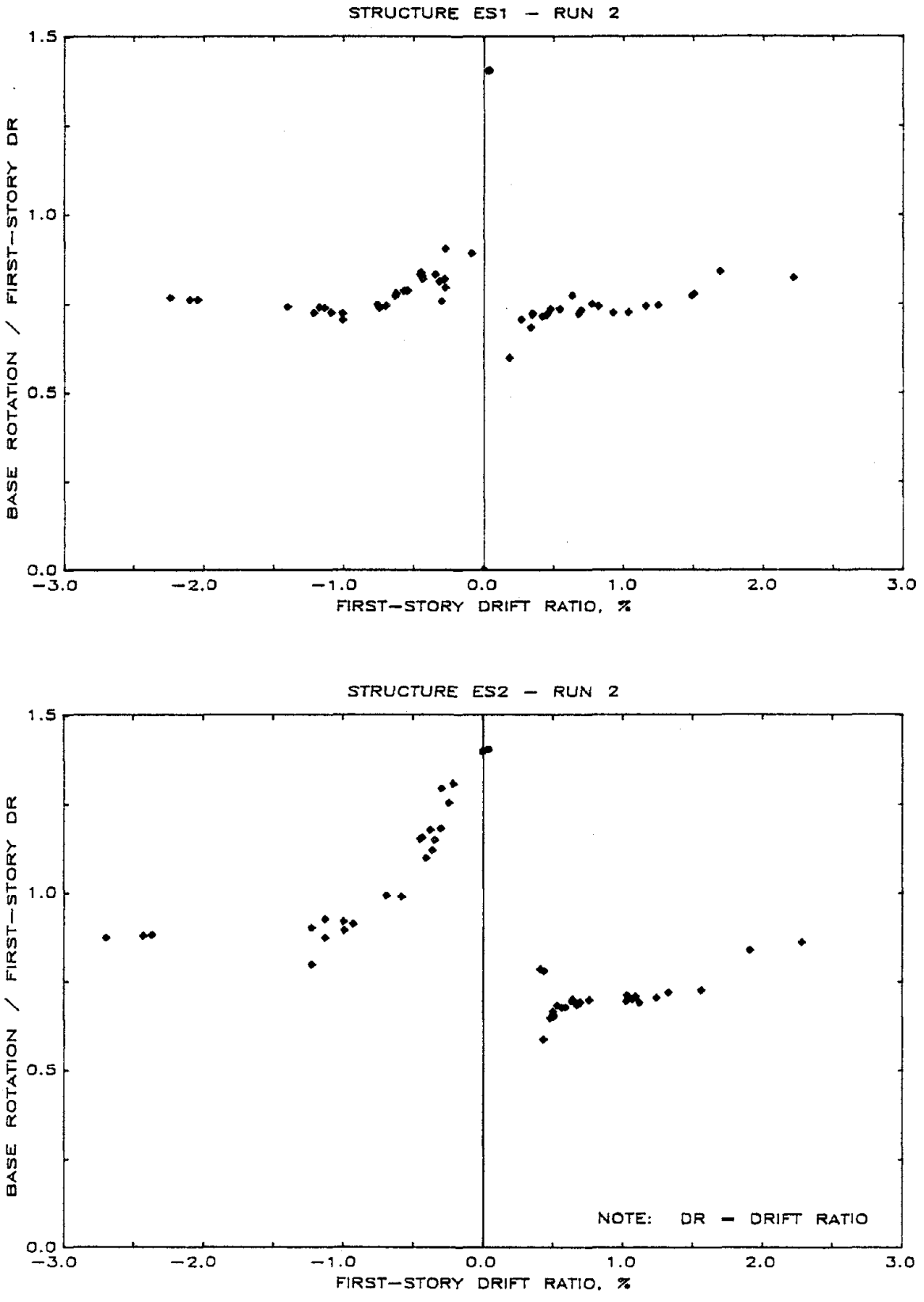

Fig. 4.15 (cont.) Ratio of Base Rotation to First-Story Drift Ratio
(b) Run 2

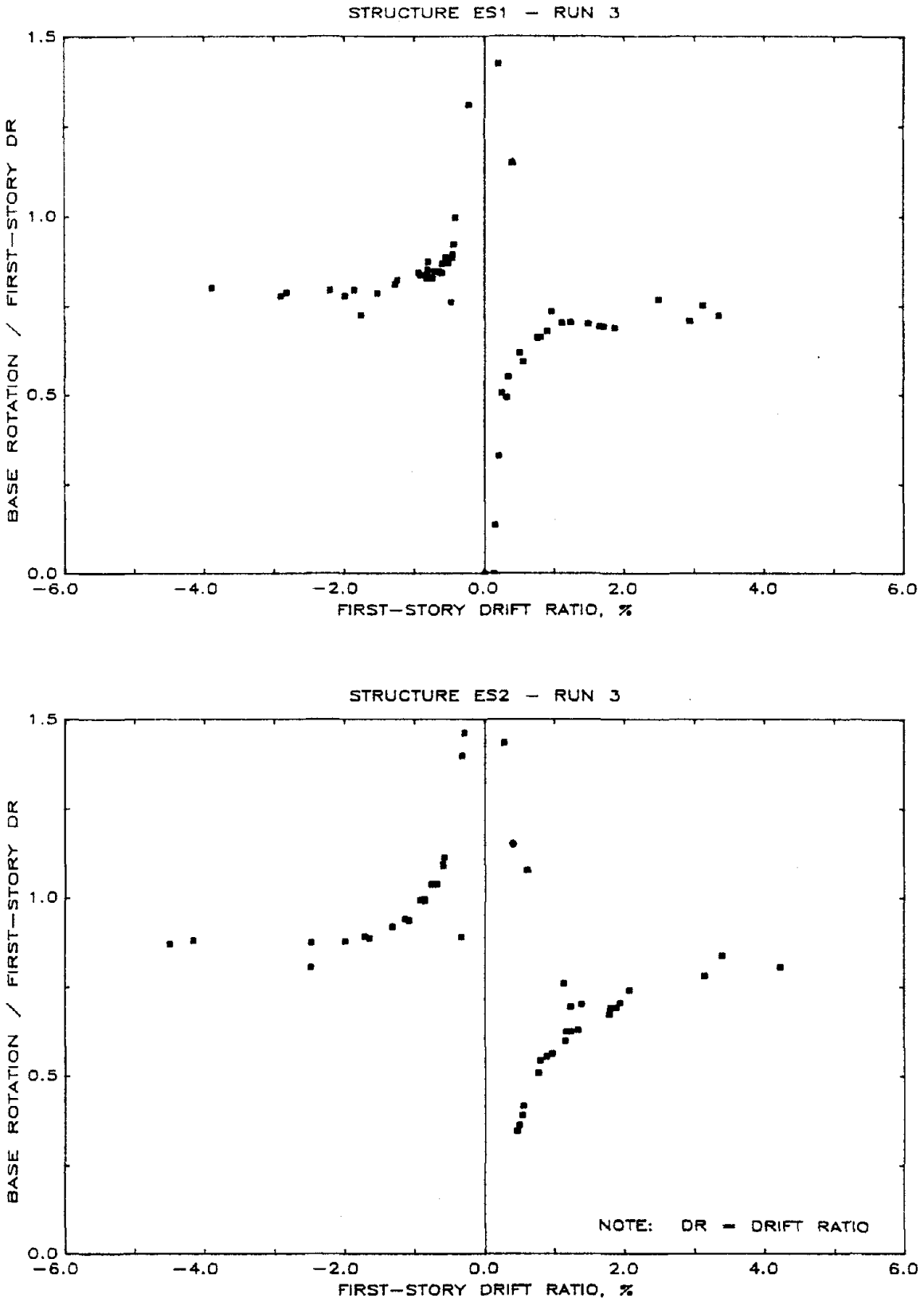

Fig. 4.15 (cont.) Ratio of Base Rotation to First-Story Drift Ratio
(c) Run 3

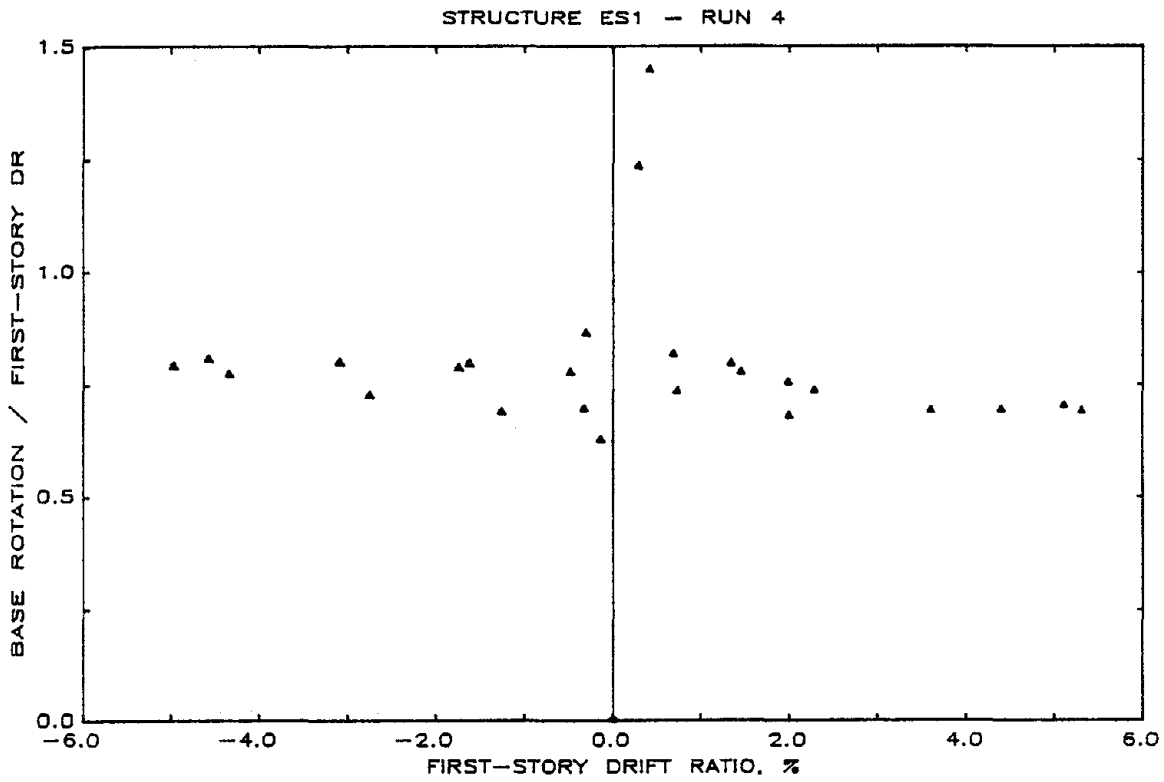

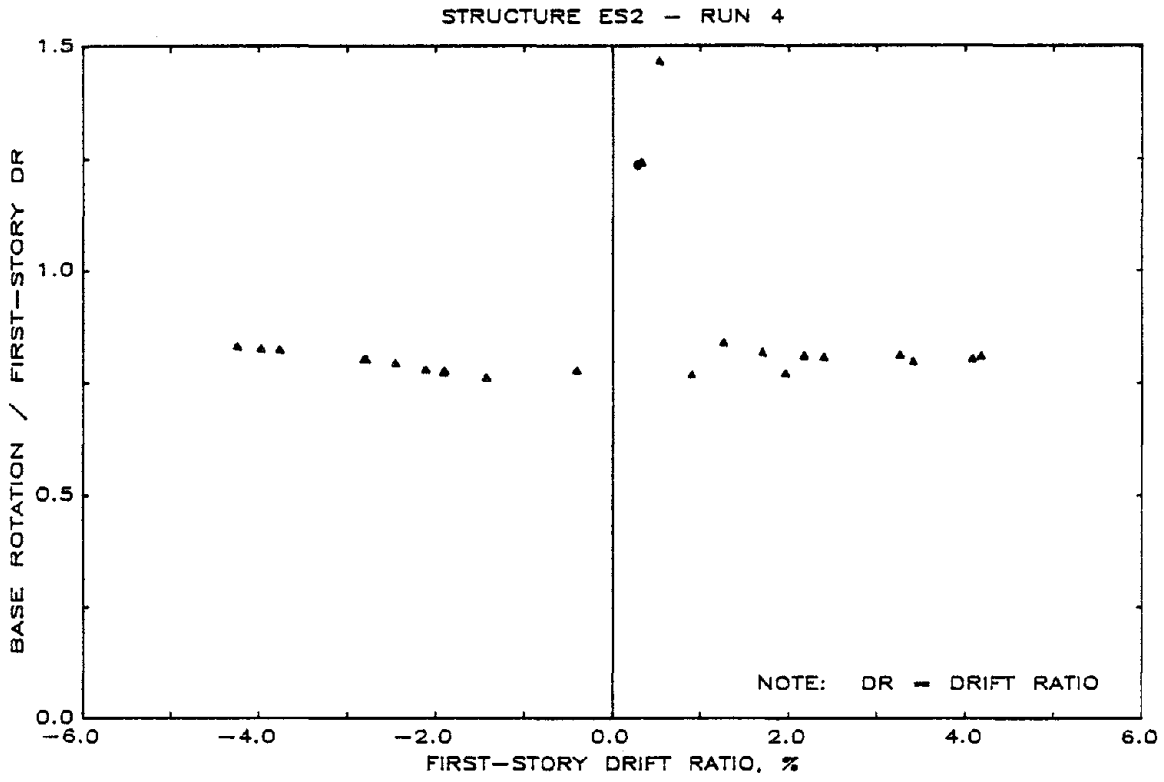

Fig. 4.15 (cont.) Ratio of Base Rotation to First-Story Drift Ratio
(d) Run 4

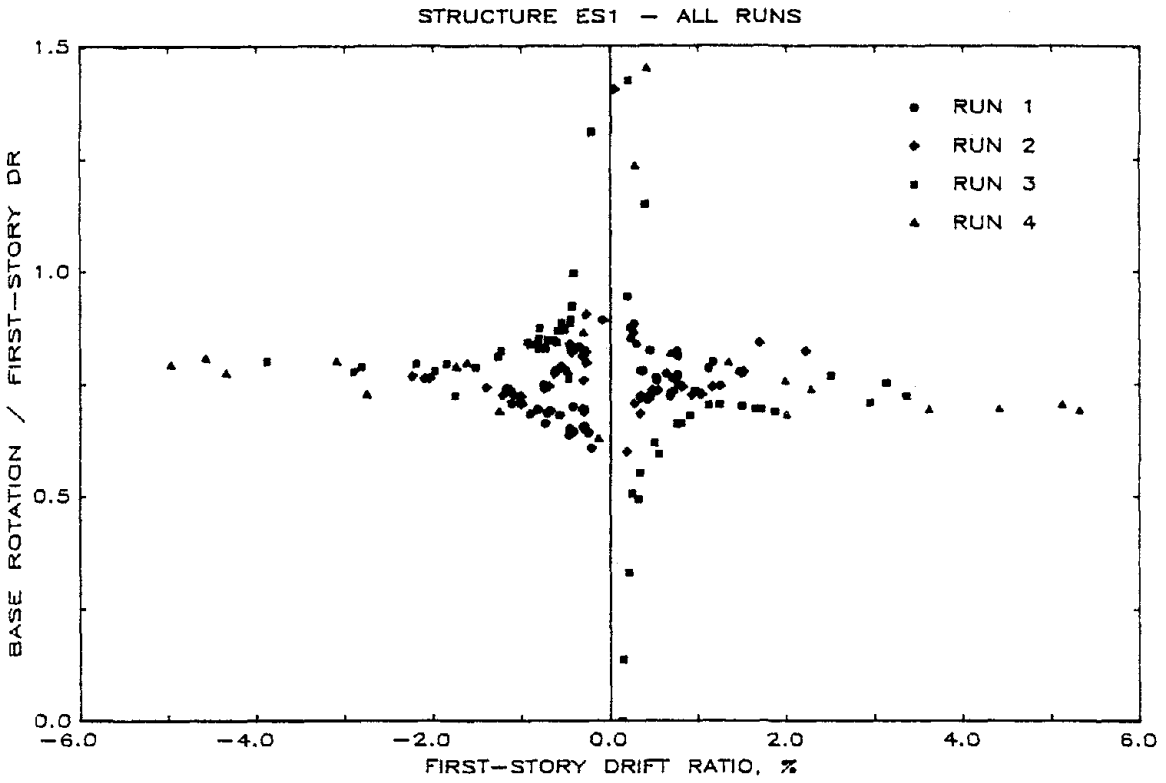

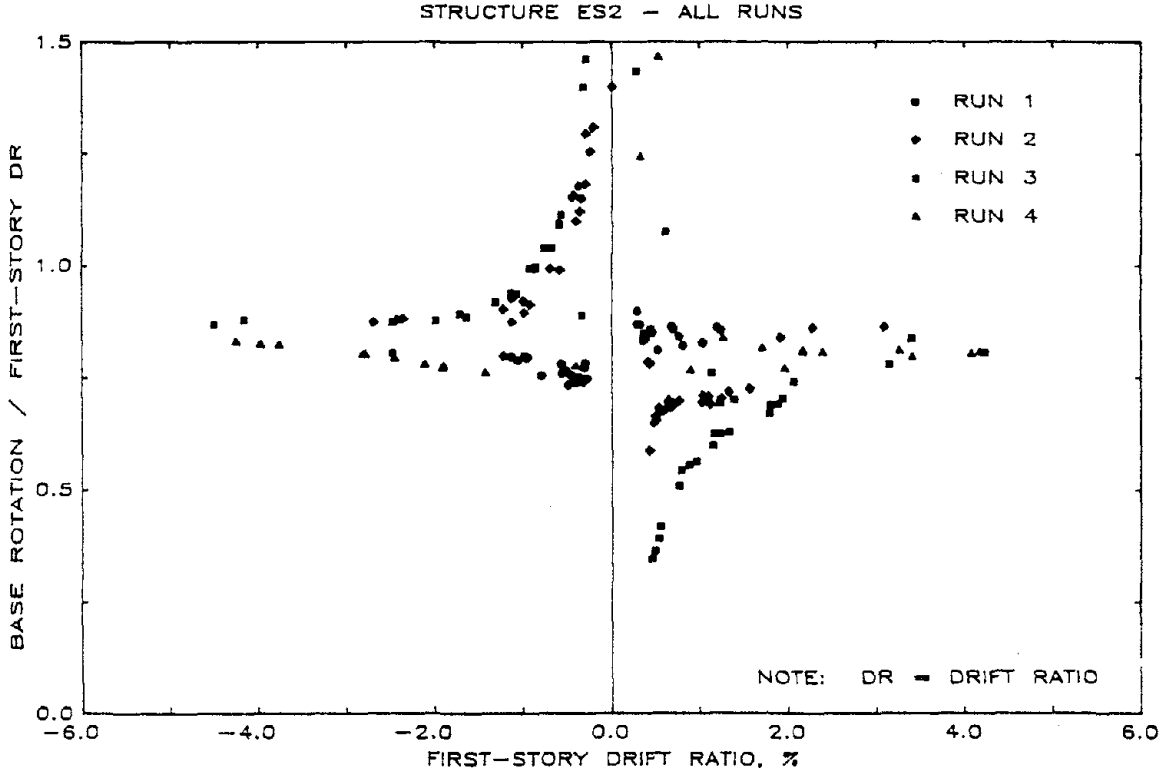

Fig. 4.15 (cont.) Ratio of Base Rotation to First-Story Drift Ratio
(e) All Runs

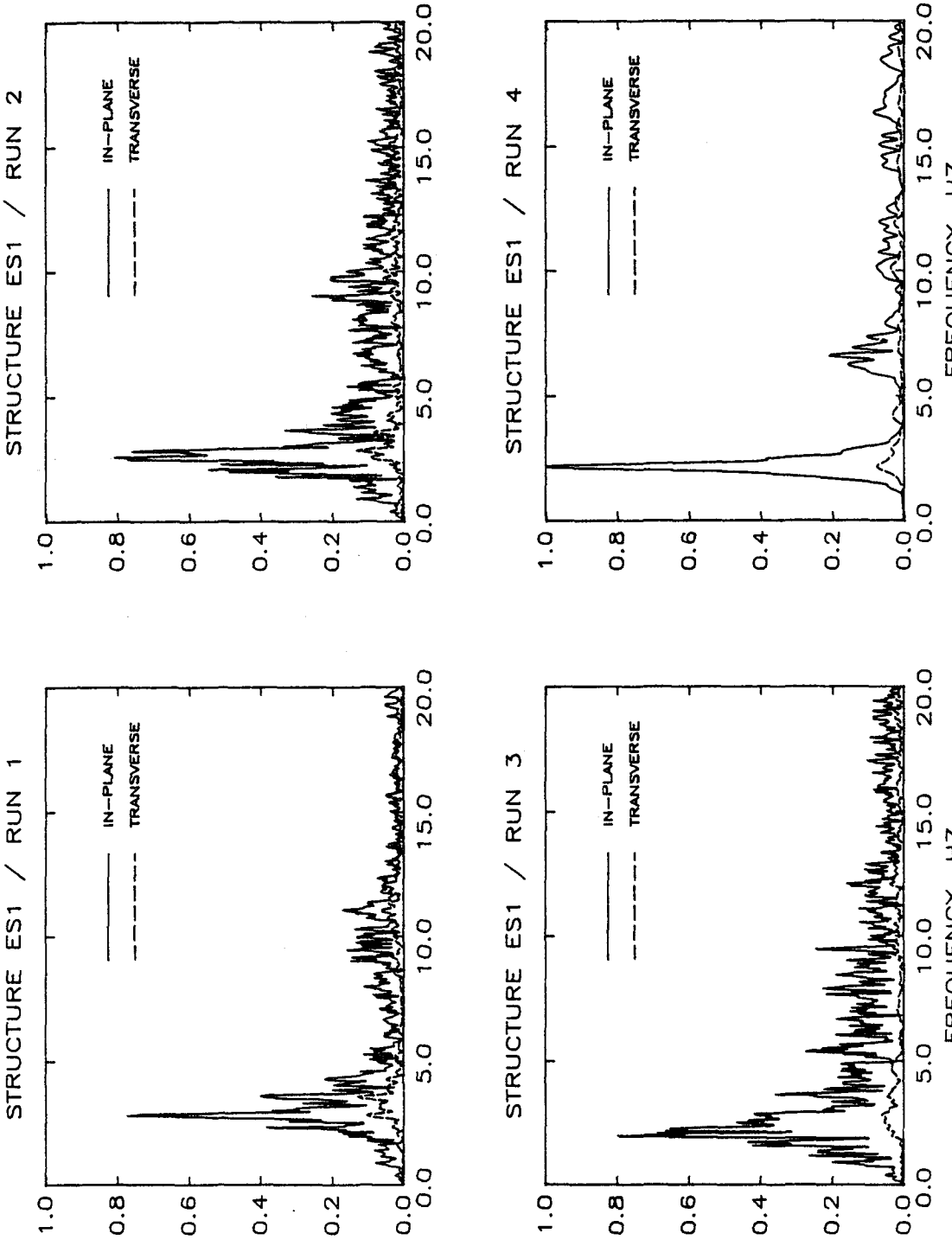

Fig. 4.16 Fourier Spectra for Ninth Level Accelerations (Damping Factor = 0.02)
(a) Structure ES1

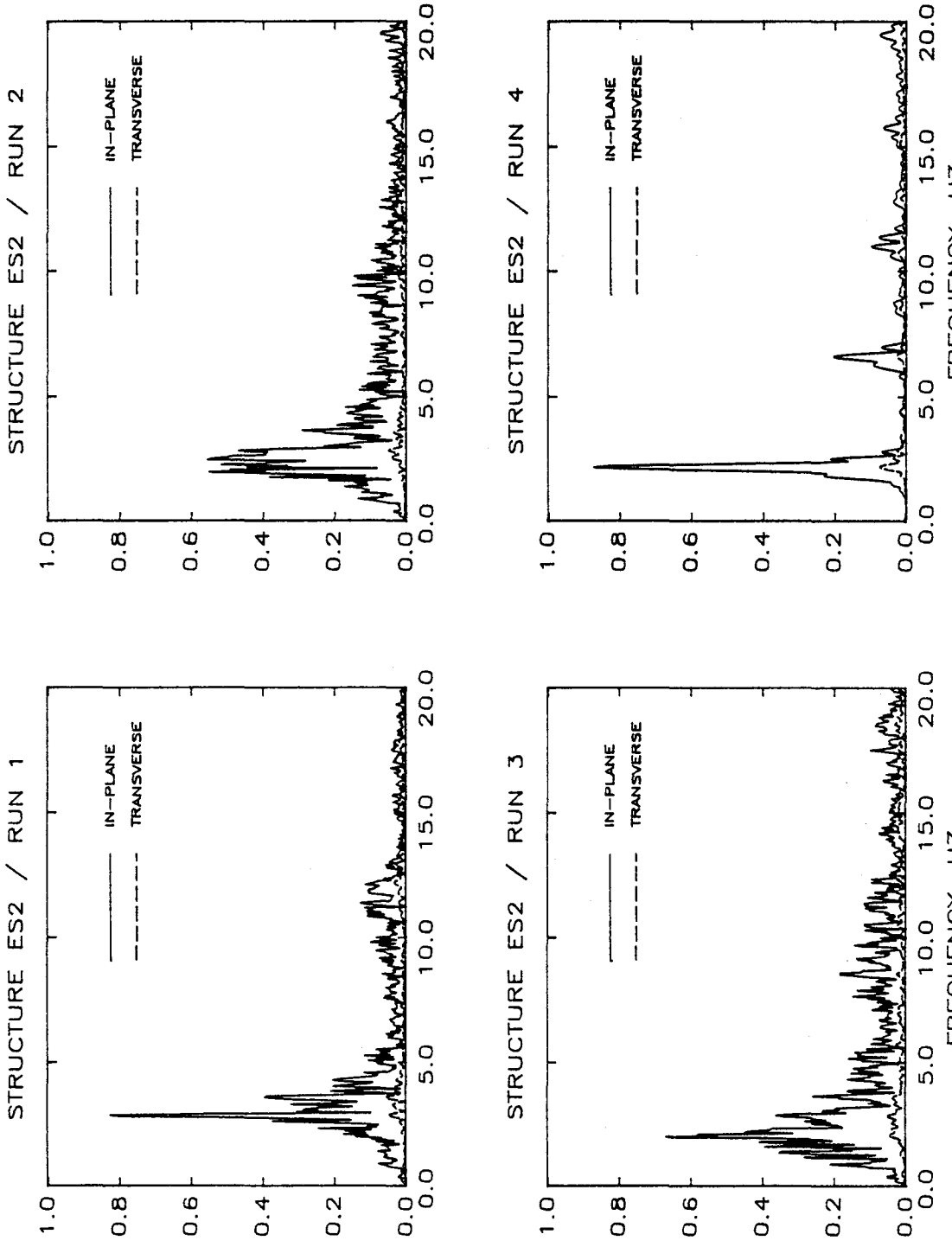

Fig. 4.16 (cont.) Fourier Spectra for Ninth Level Accelerations (Damping Factor = 0.02)
(b) Structure ES2

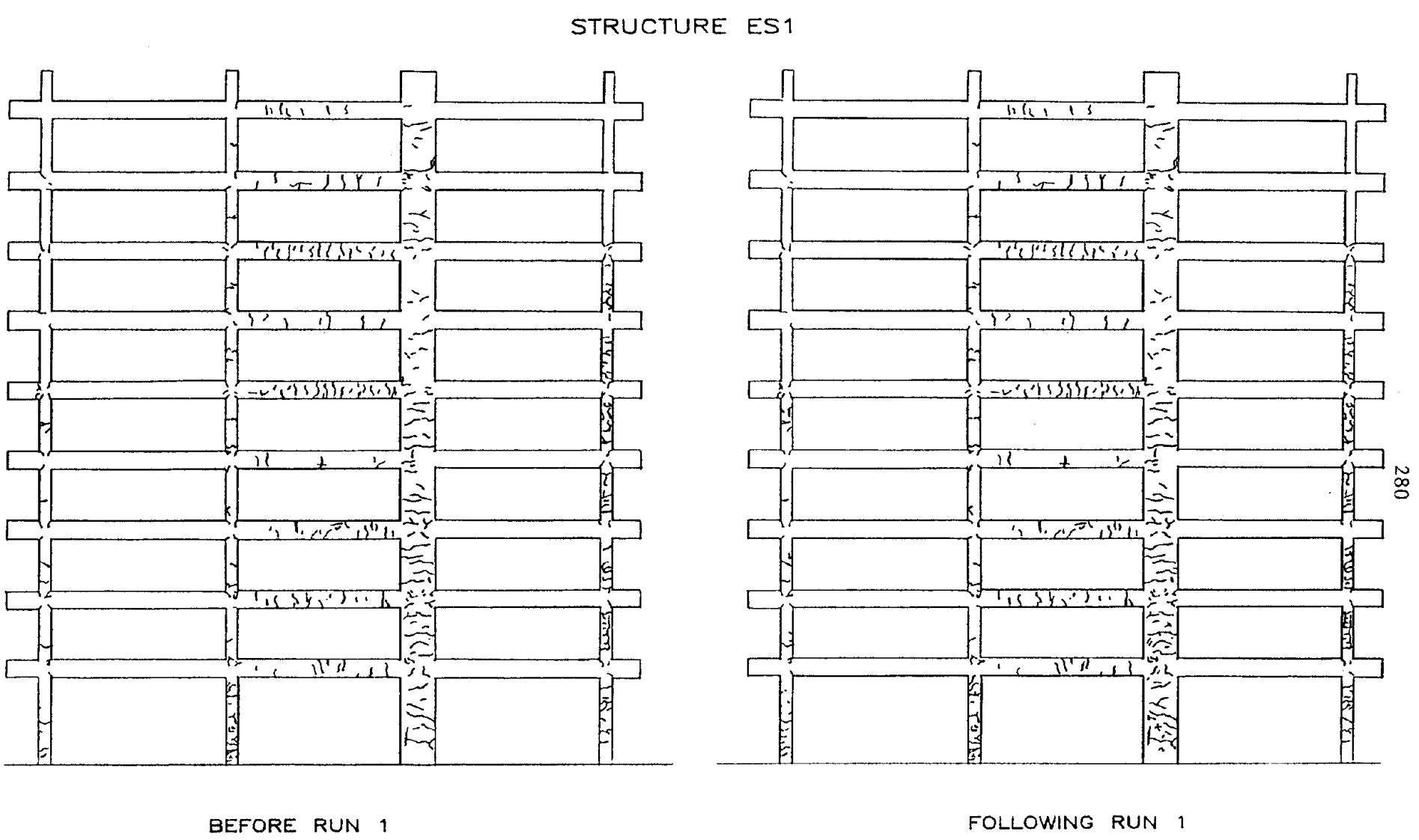

Fig. 4.17 Crack Patterns

STRUCTURE ES1

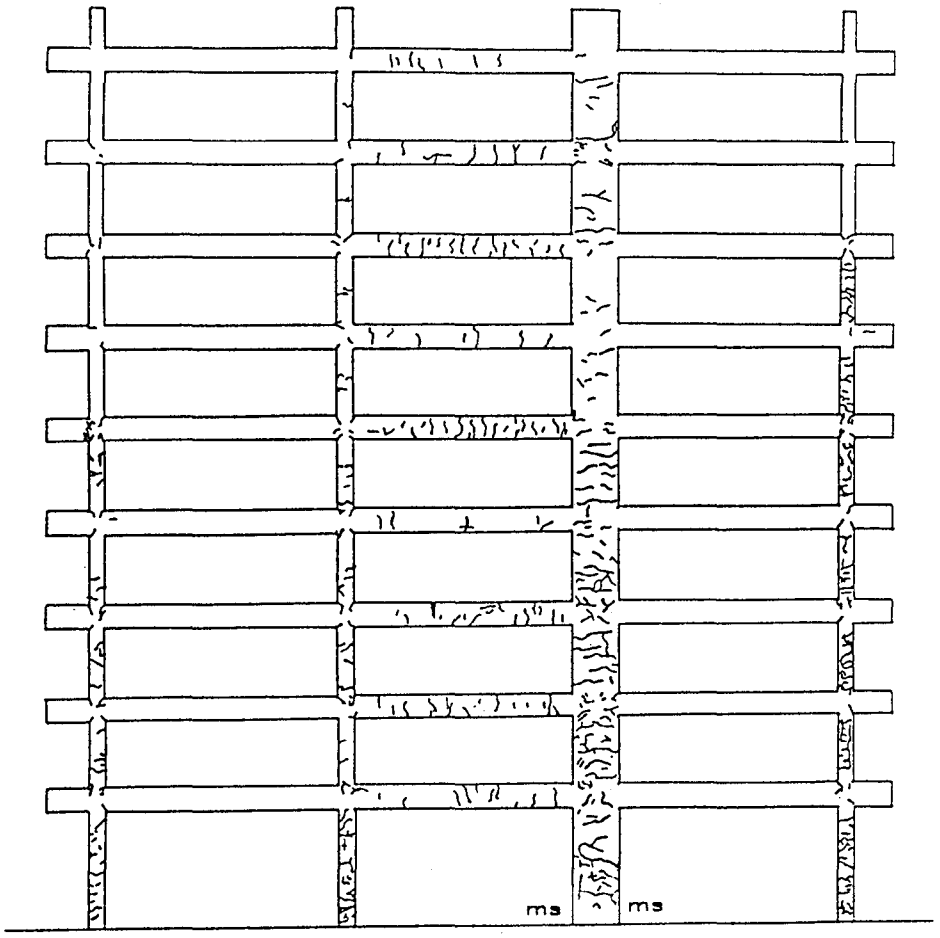

FOLLOWING RUN 2

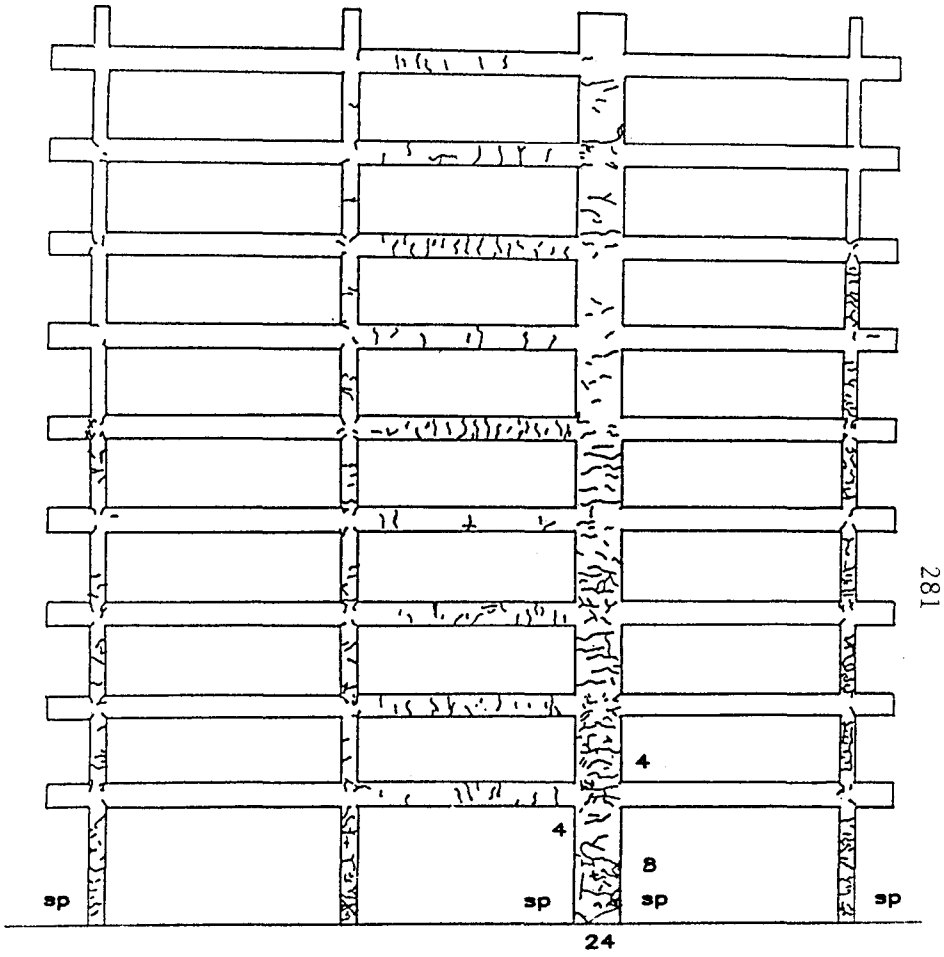

FOLLOWING RUN 3

crack widths in 1/1000 in.

ms = minor spalling of concrete

sp = spalling

Fig. 4.17 (cont.) Crack Patterns

STRUCTURE ES2

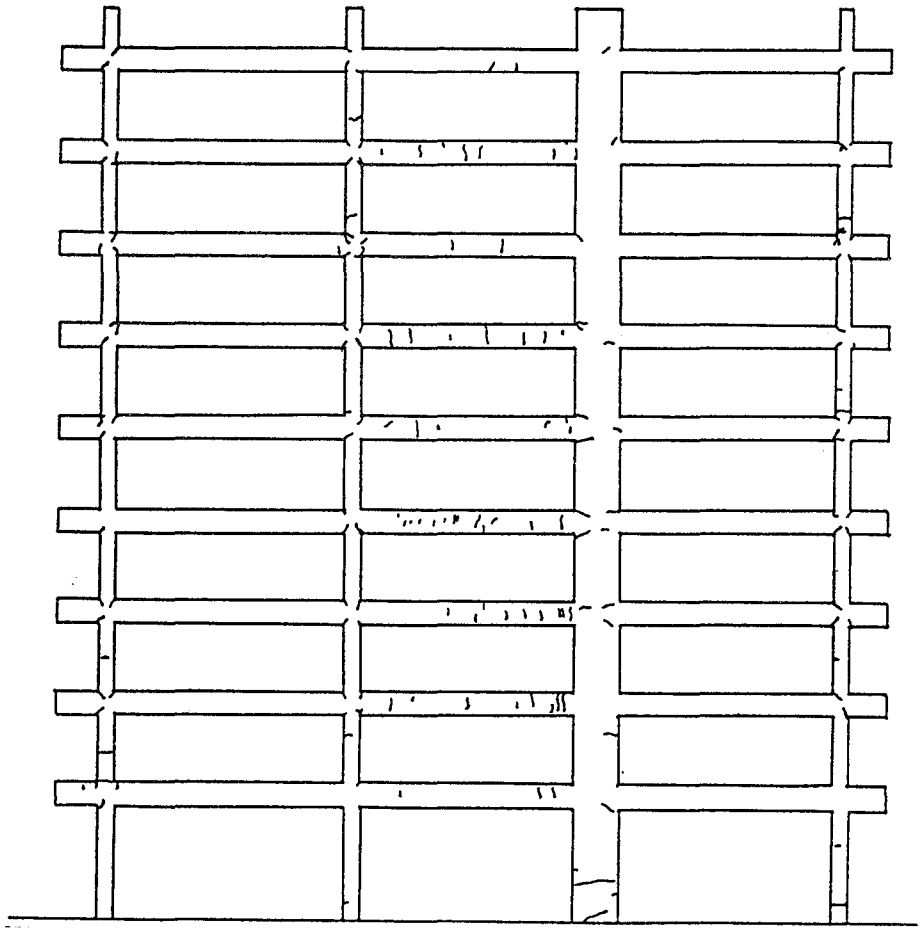

BEFORE RUN 1

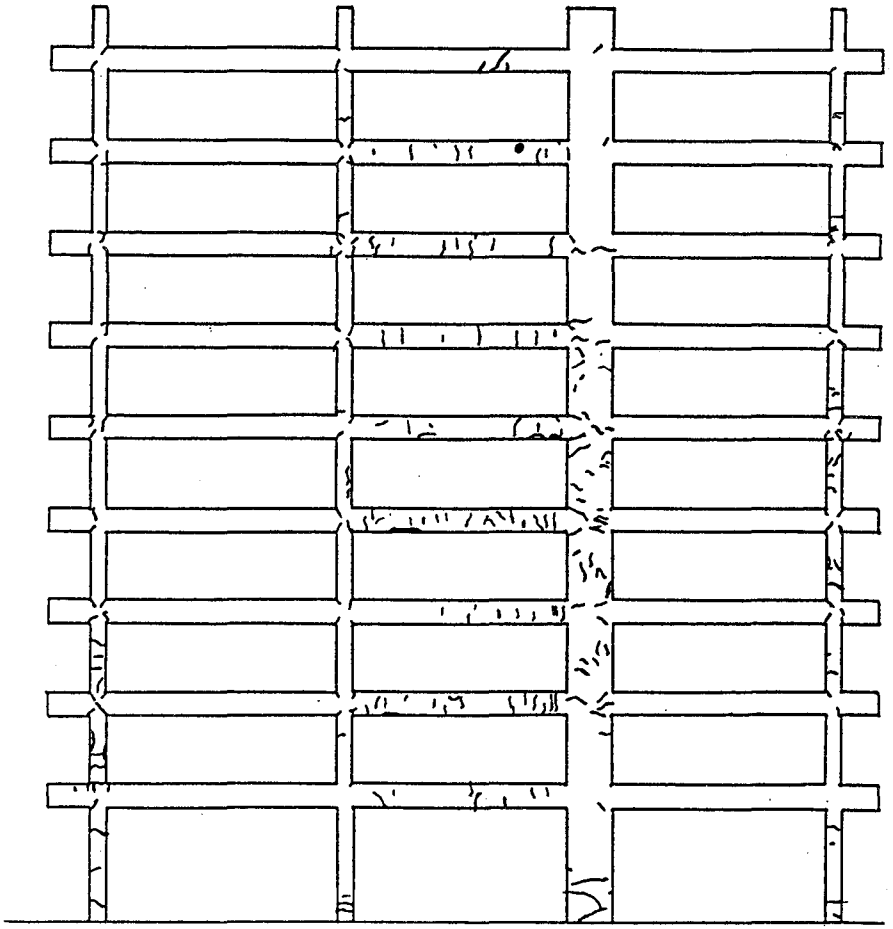

FOLLOWING RUN 1

Fig. 4.17 (cont.) Crack Patterns

STRUCTURE ES2

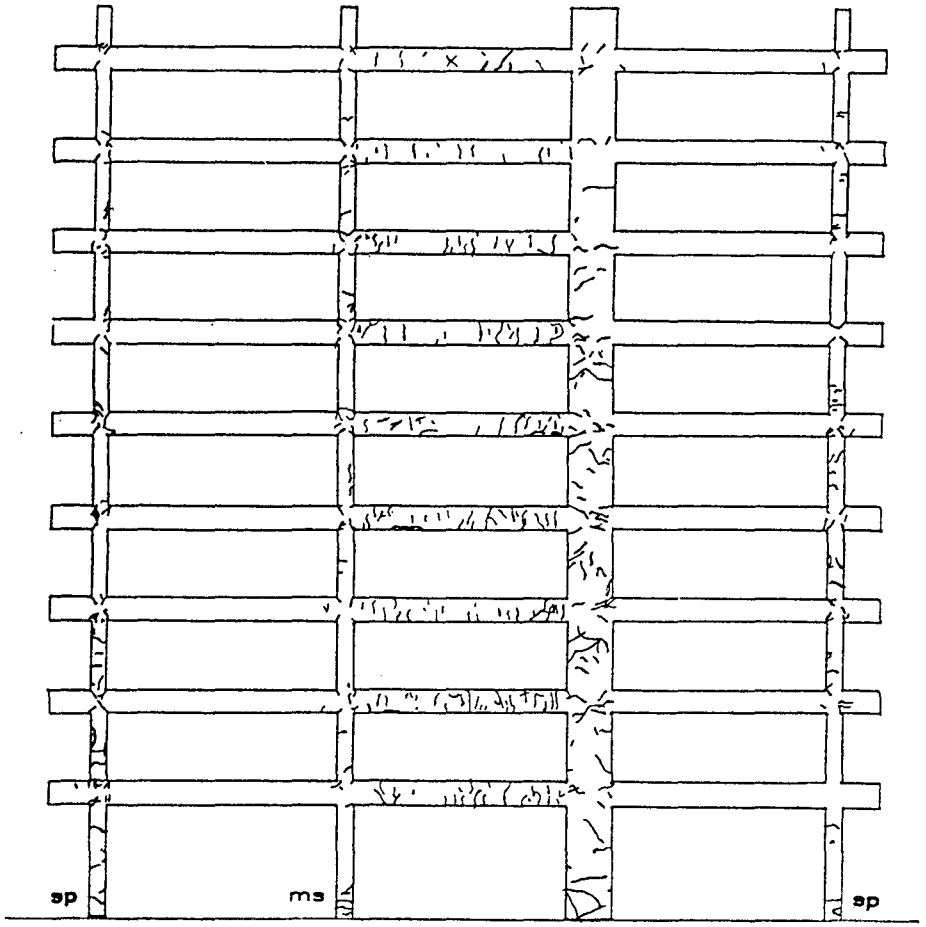

FOLLOWING RUN 2

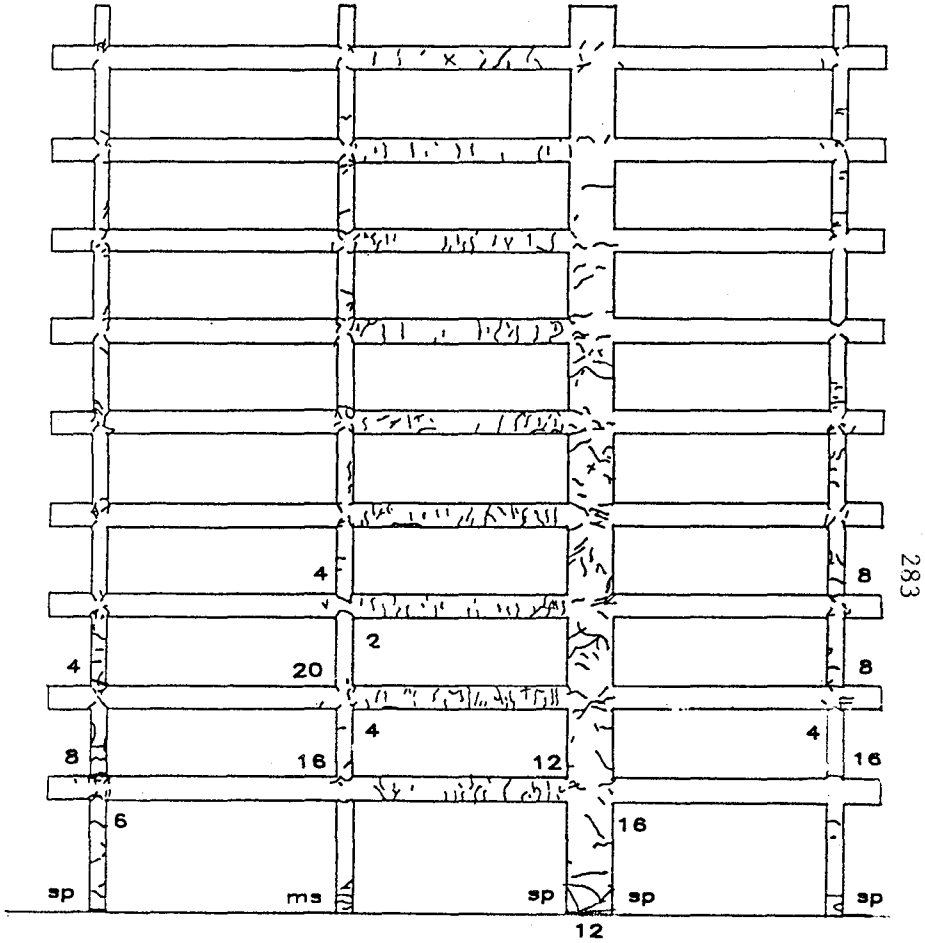

FOLLOWING RUN 3

crack widths in 1/1000 in.

ms = minor spalling of concrete

sp = spalling

Fig. 4.17 (cont.) Crack Patterns

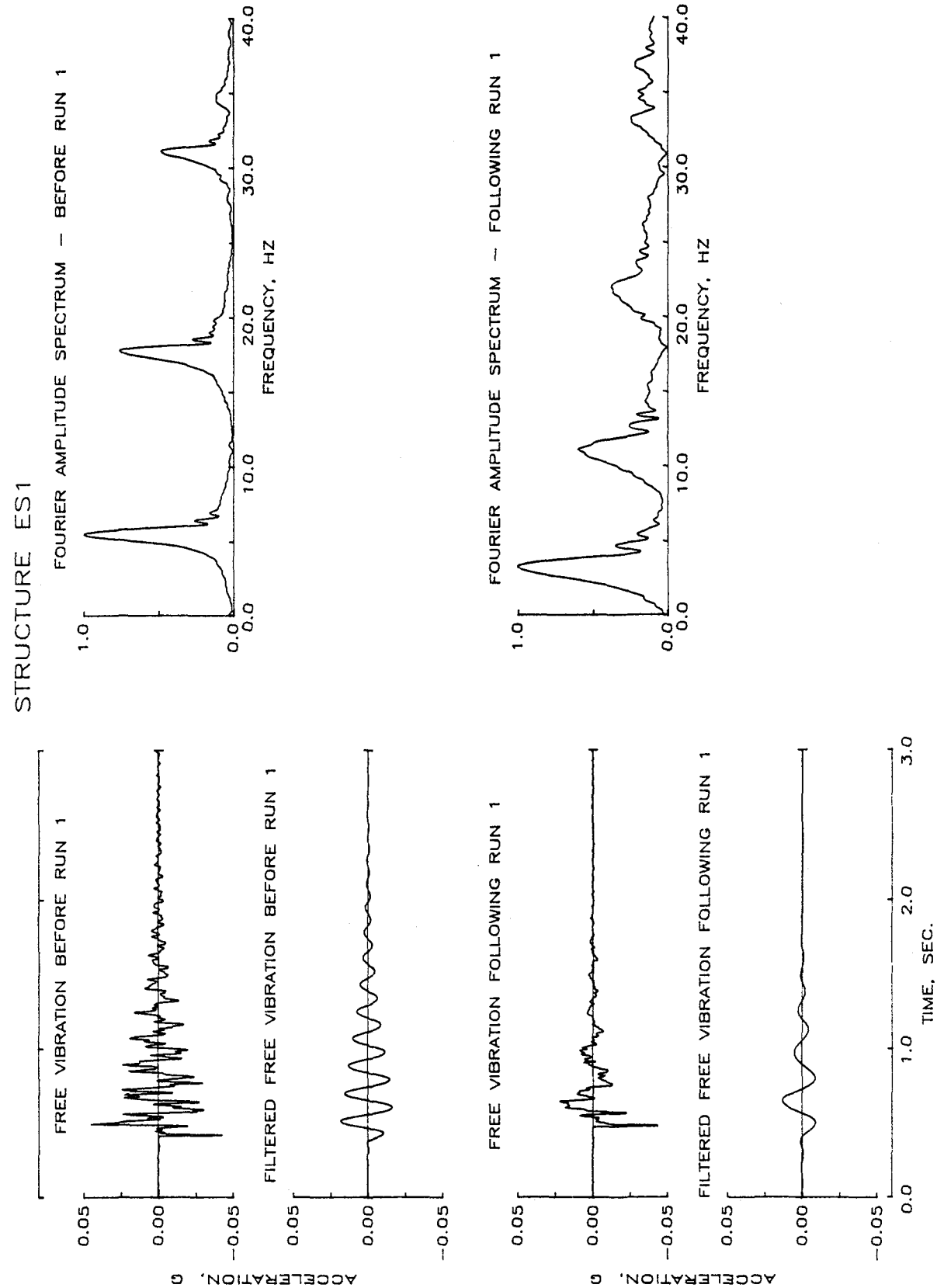

Fig. 4.18 Response During Free-Vibration Tests
(a) Structure ES1

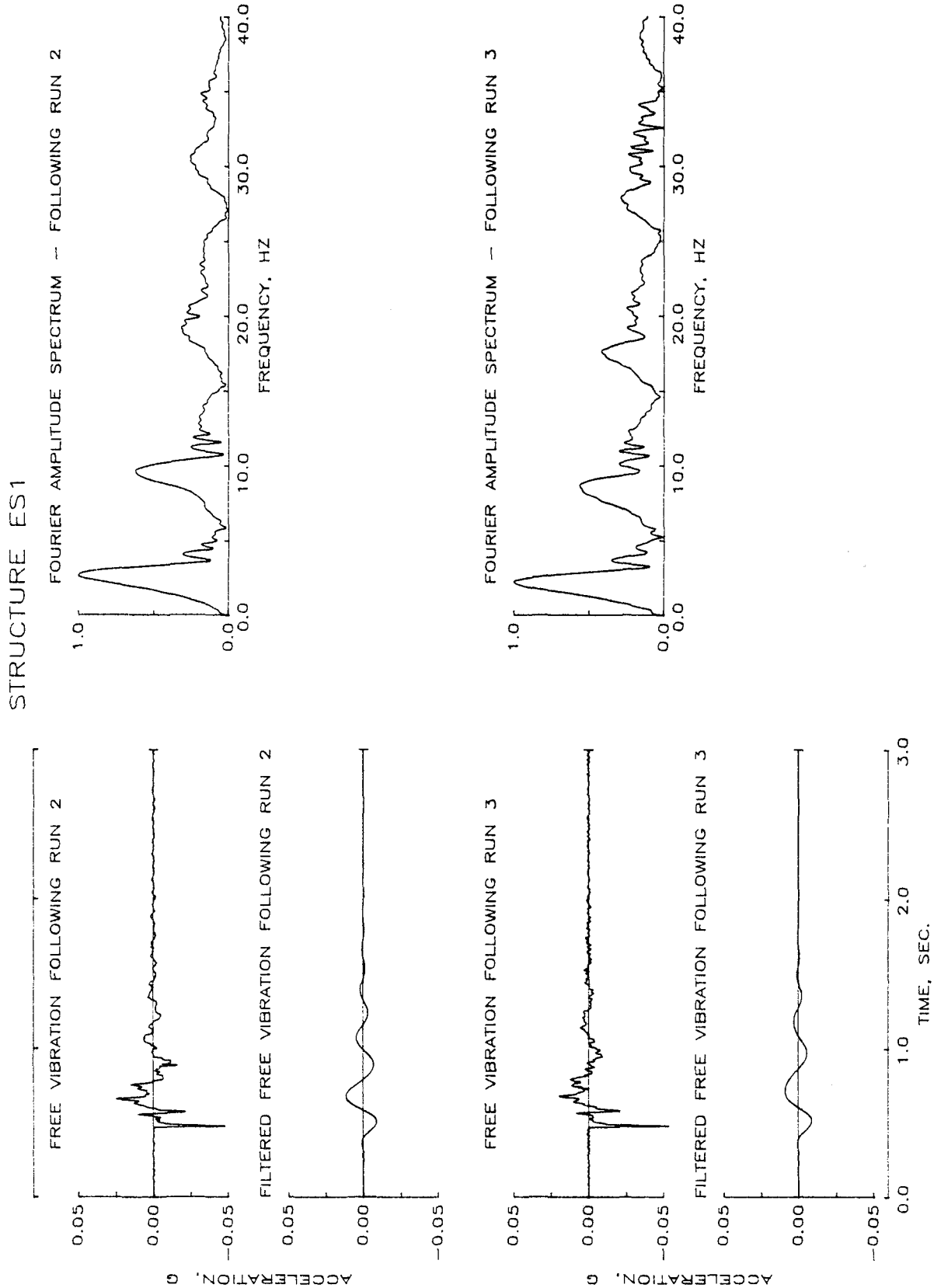

Fig. 4.18 (cont.) Response During Free-Vibration Tests
(a) (cont.) Structure ES1

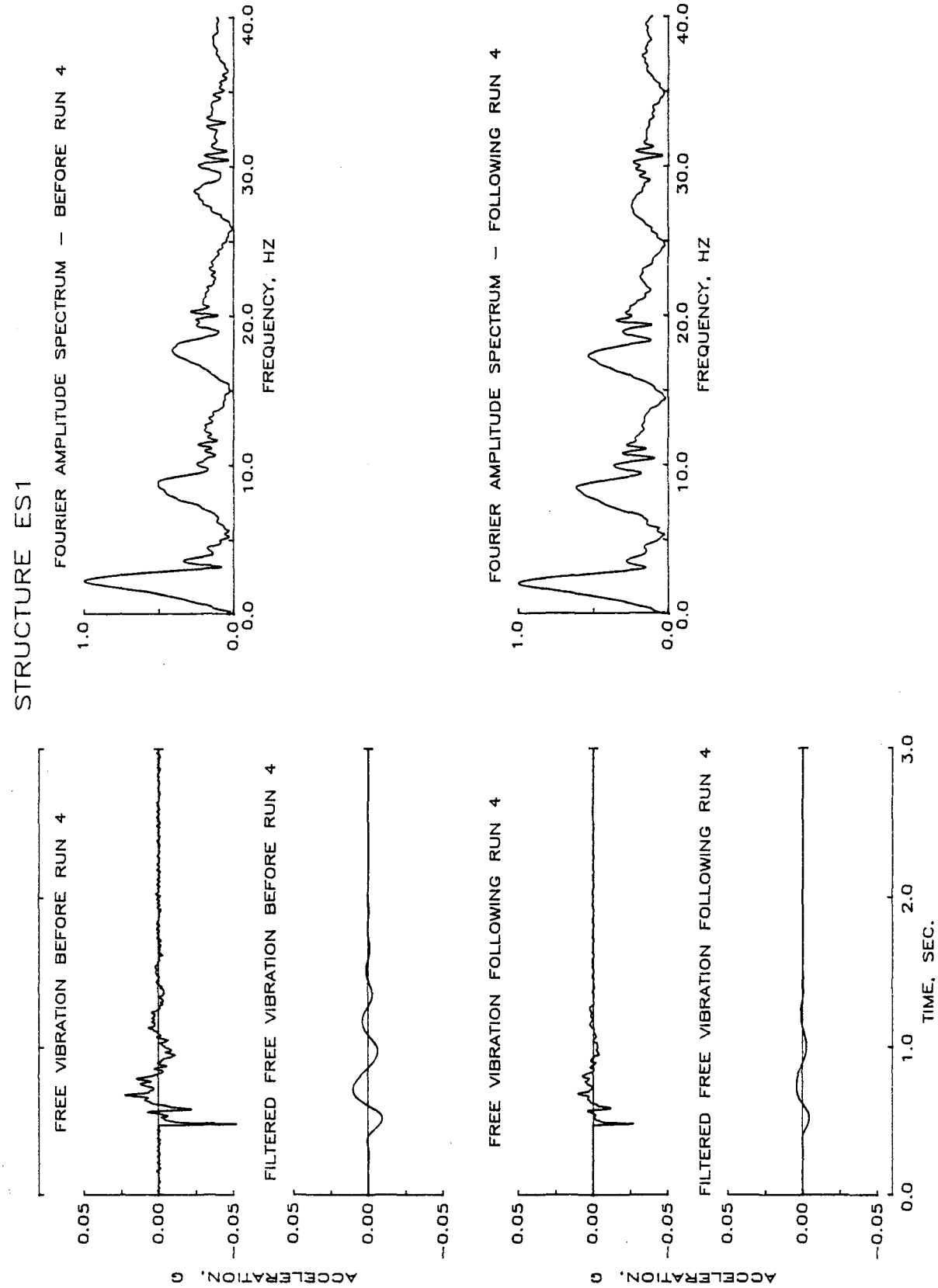

Fig. 4.18 (cont.) Response During Free-Vibration Tests
(a) (cont.) Structure ES1

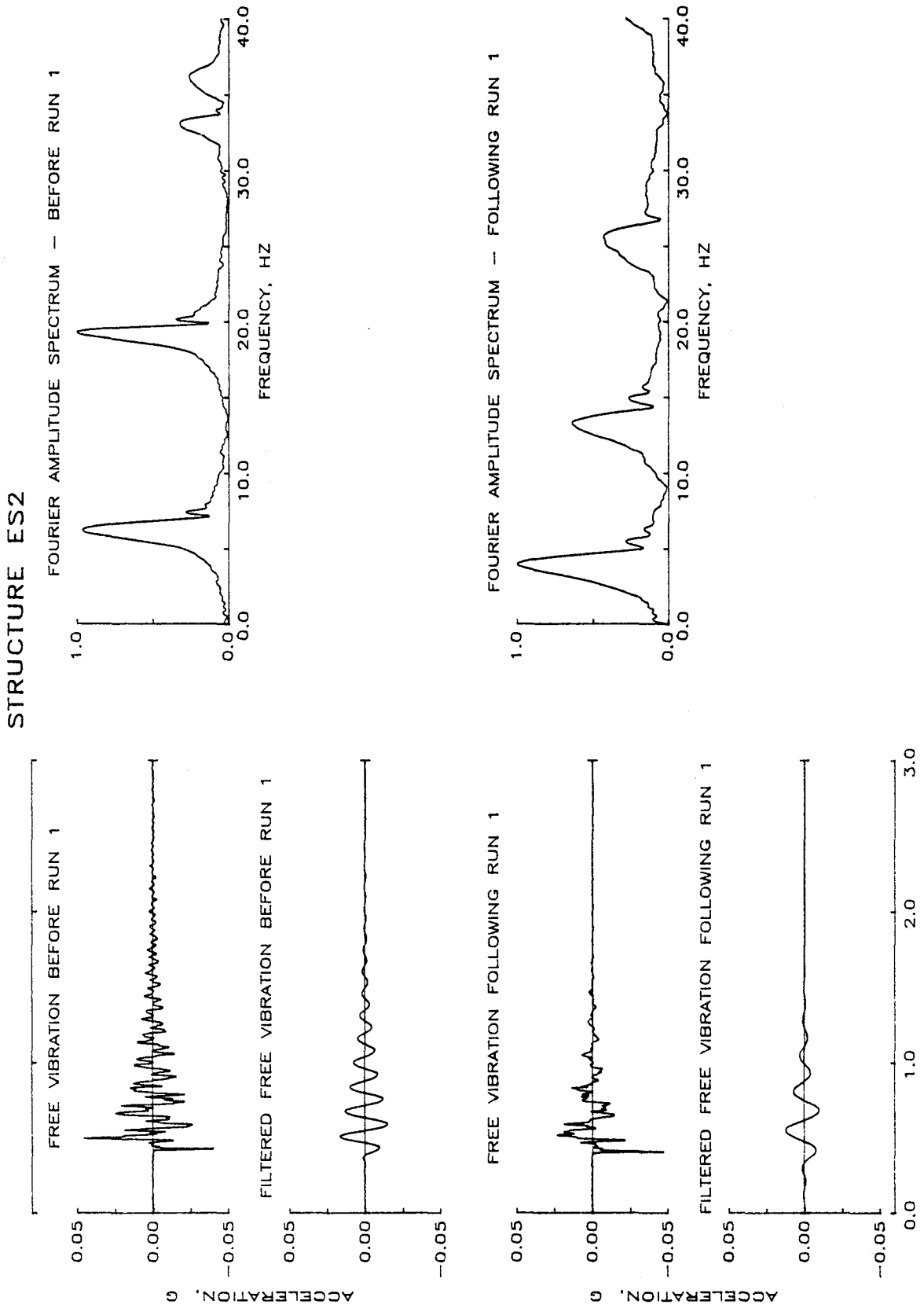

Fig. 4.18 (cont.) Response During Free-Vibration Tests
(b) Structure ES2

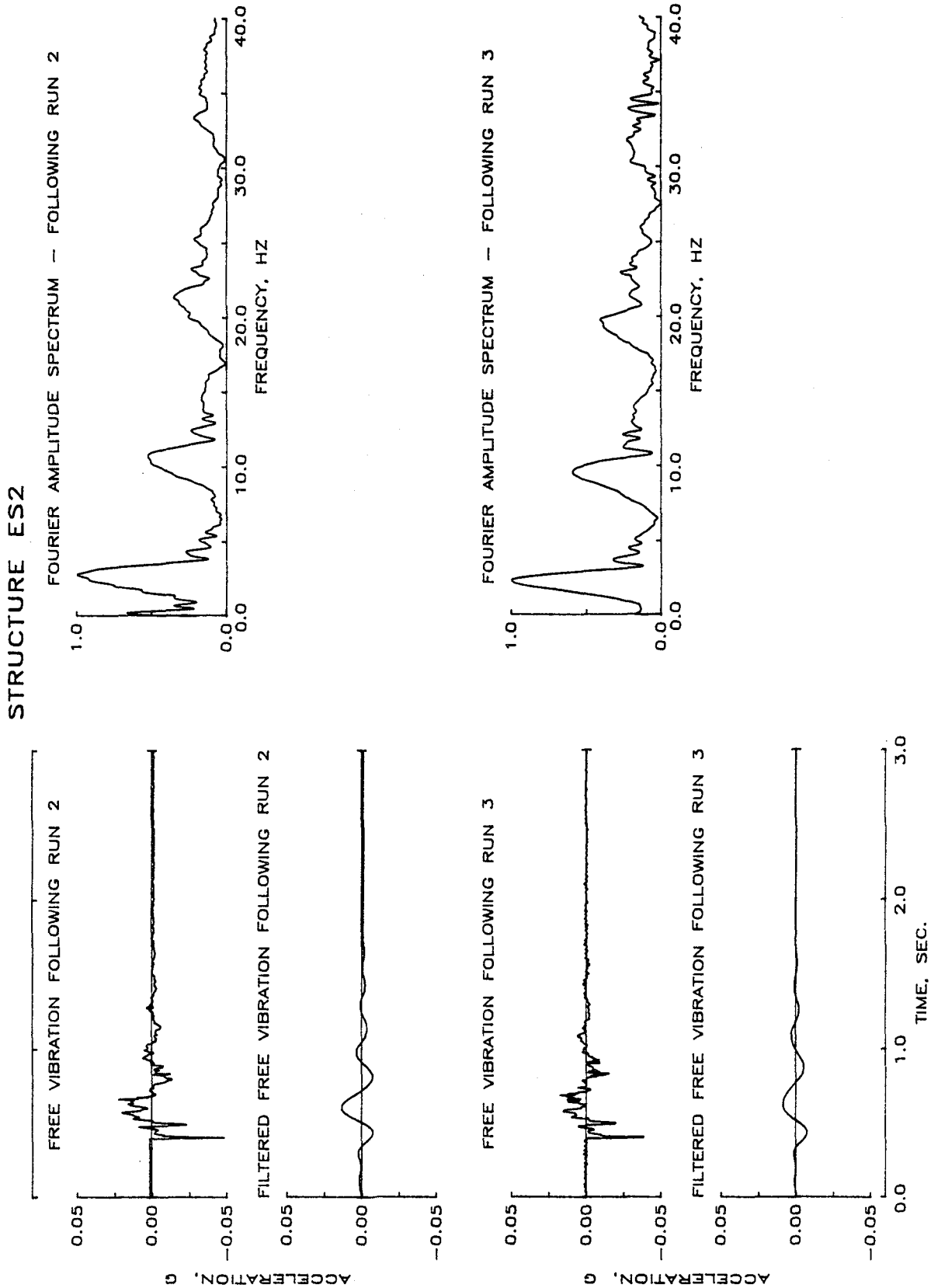

Fig. 4.18 (cont.) Response During Free-Vibration Tests
(b) (cont.) Structure ES2

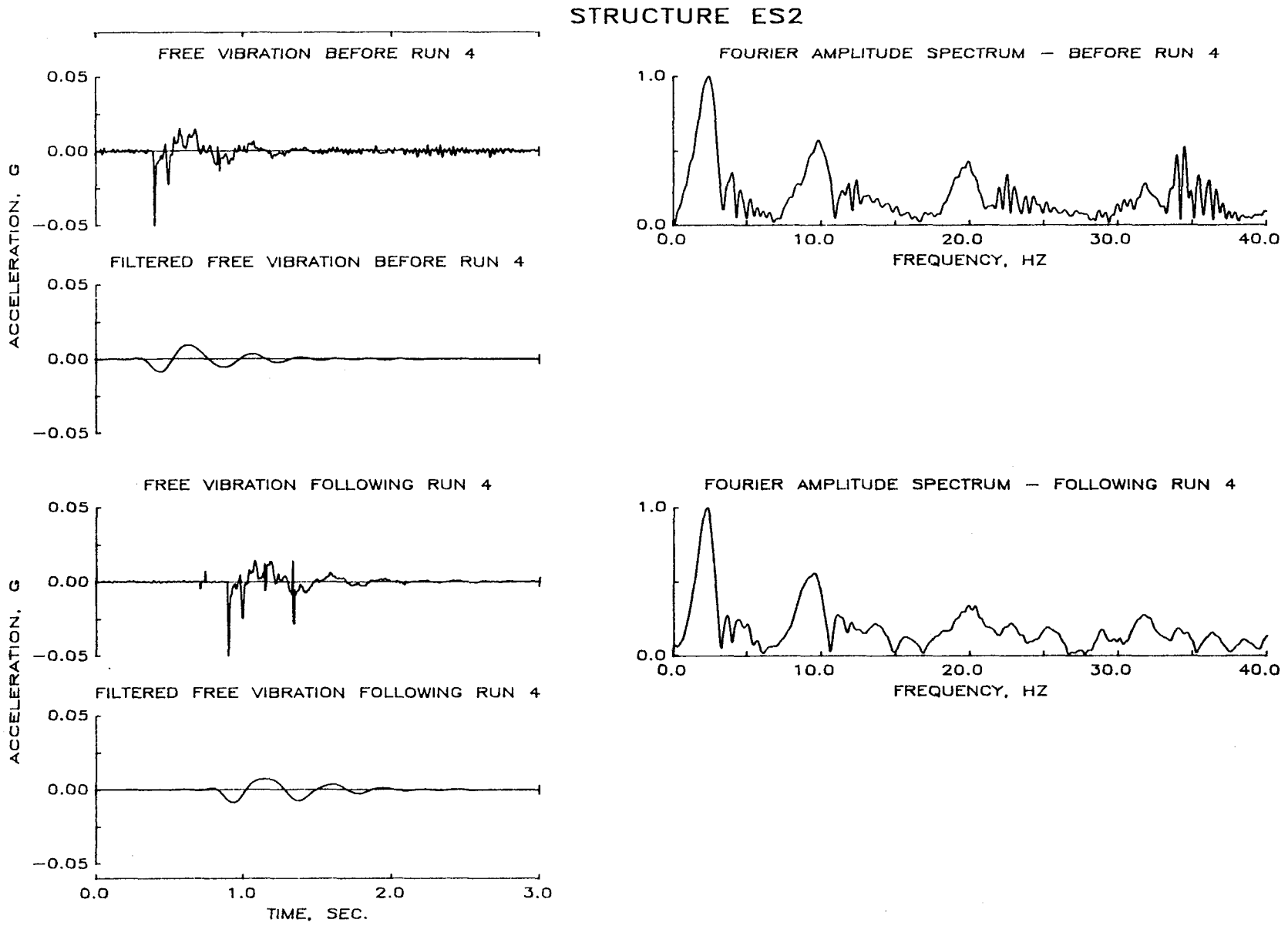

Fig. 4.18 (cont.) Response During Free-Vibration Tests
(b) (cont.) Structure ES2

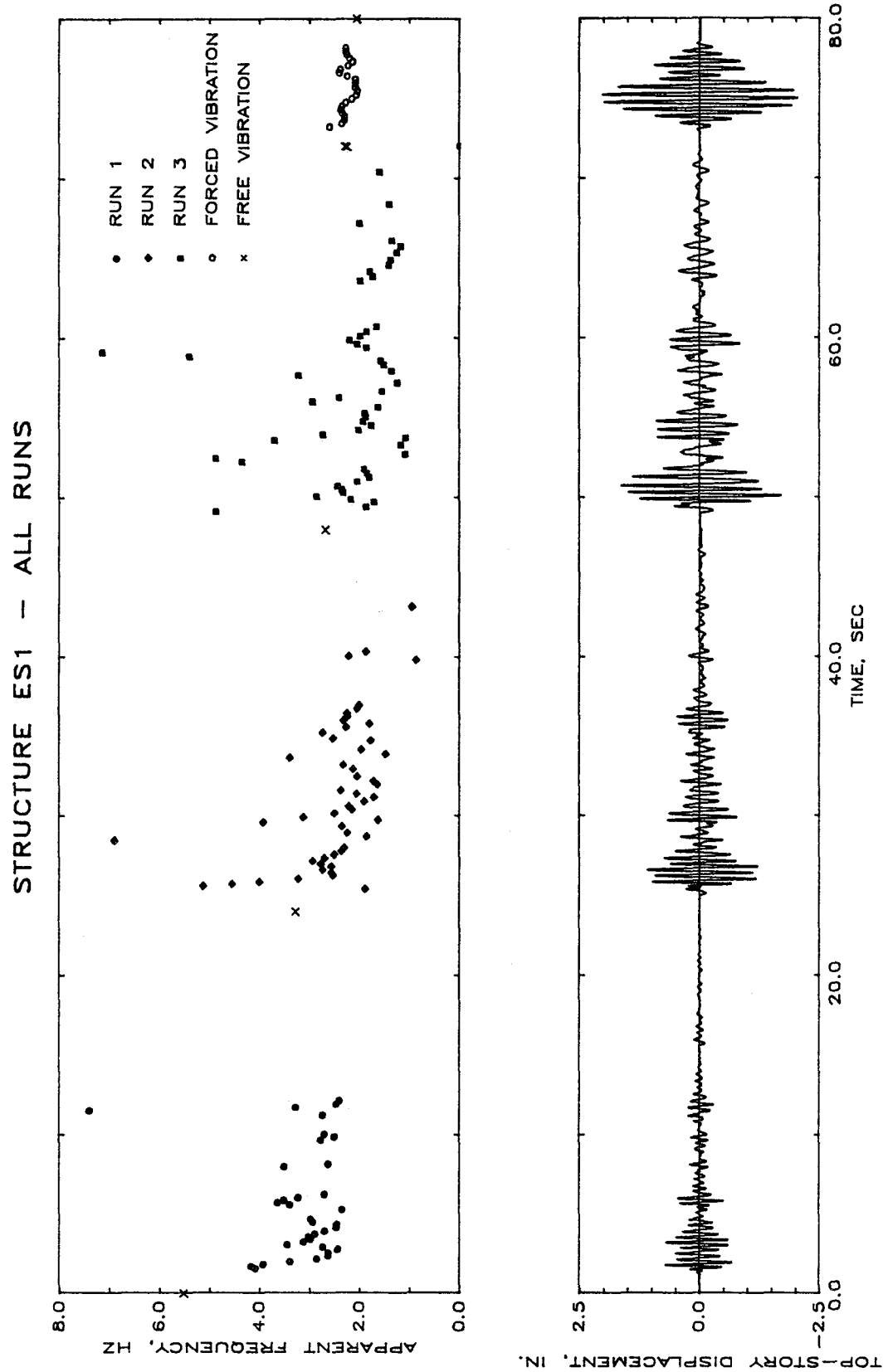

Fig. 4.19 Variation of Apparent Fundamental Frequency with Time
(a) Structure ES1

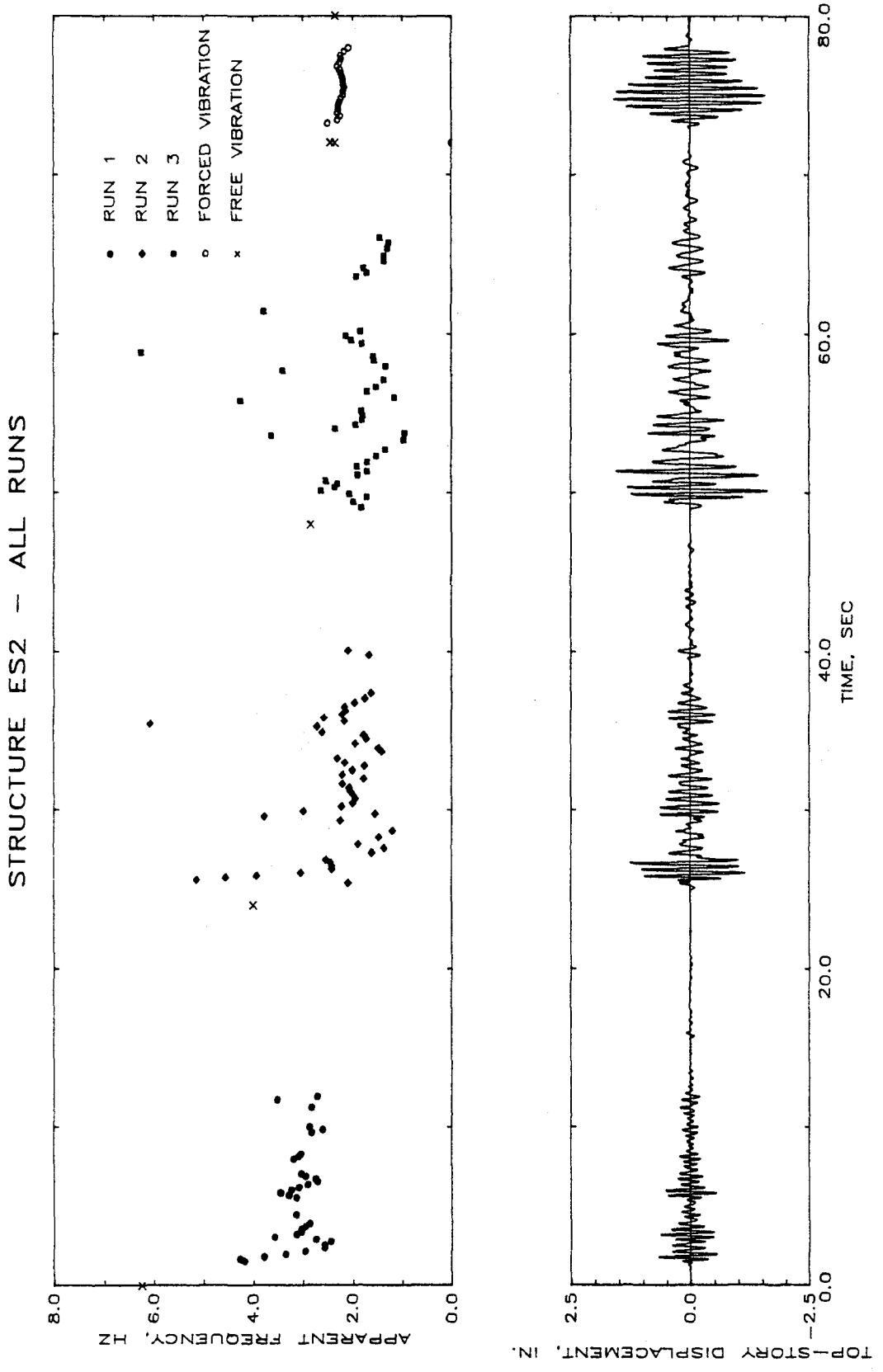

Fig. 4.19 Variation of Apparent Fundamental Frequency with Time
(b) Structure ES2

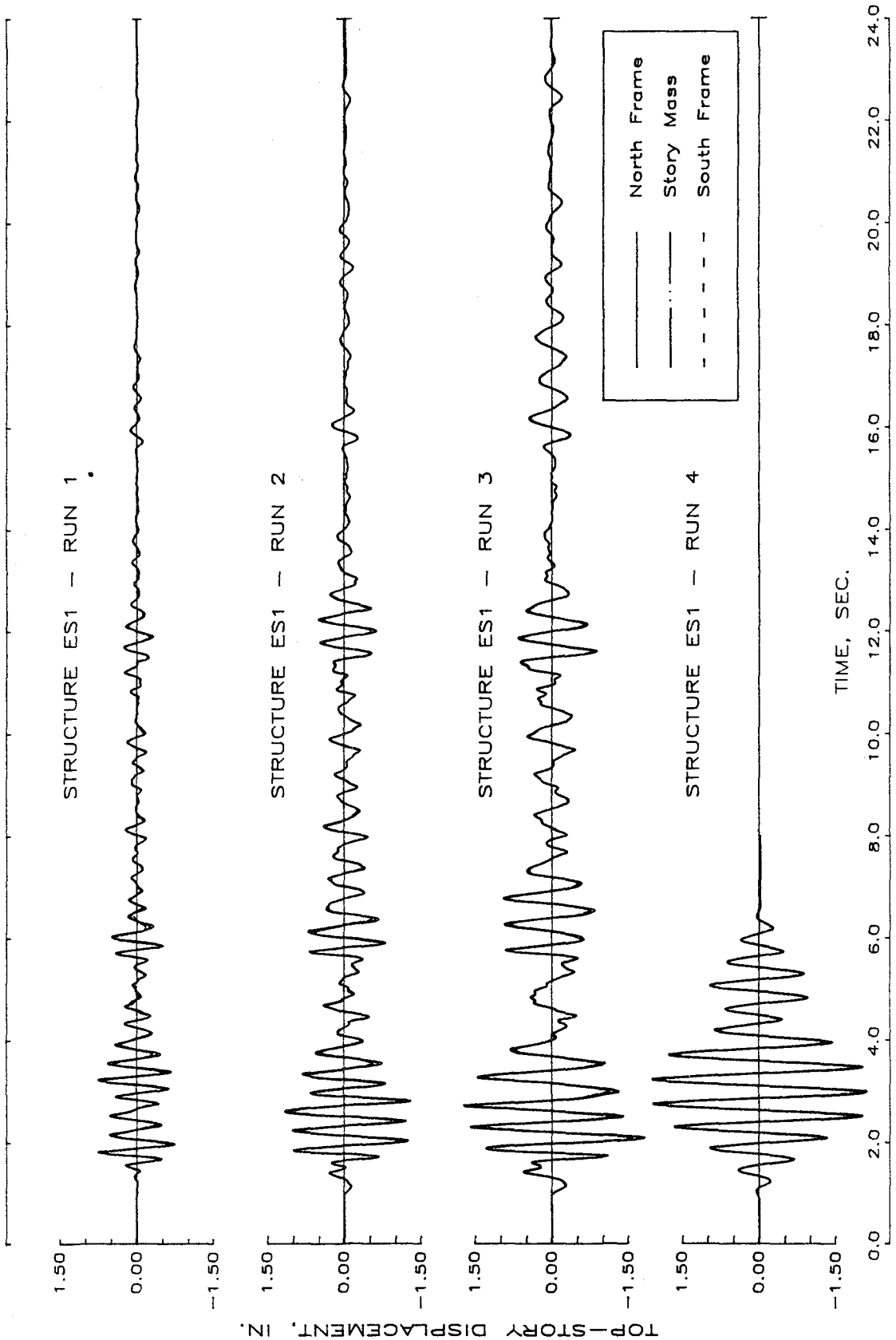

Fig. 4.20 Ninth-Level Displacement Histories
(a) Structure ES1

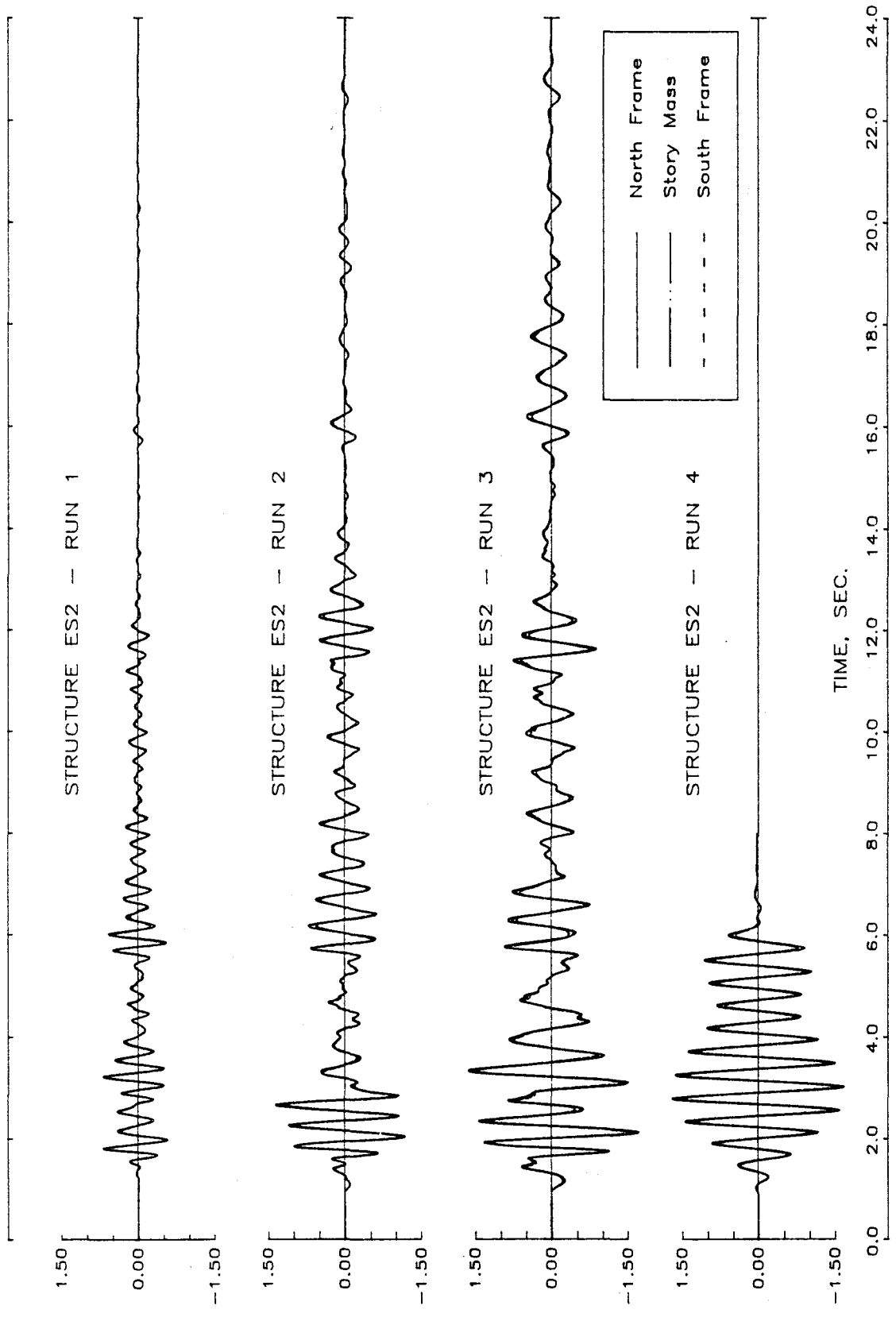

Fig. 4.20 (cont.) Ninth-Level Displacement Histories
(b) Structure ES2

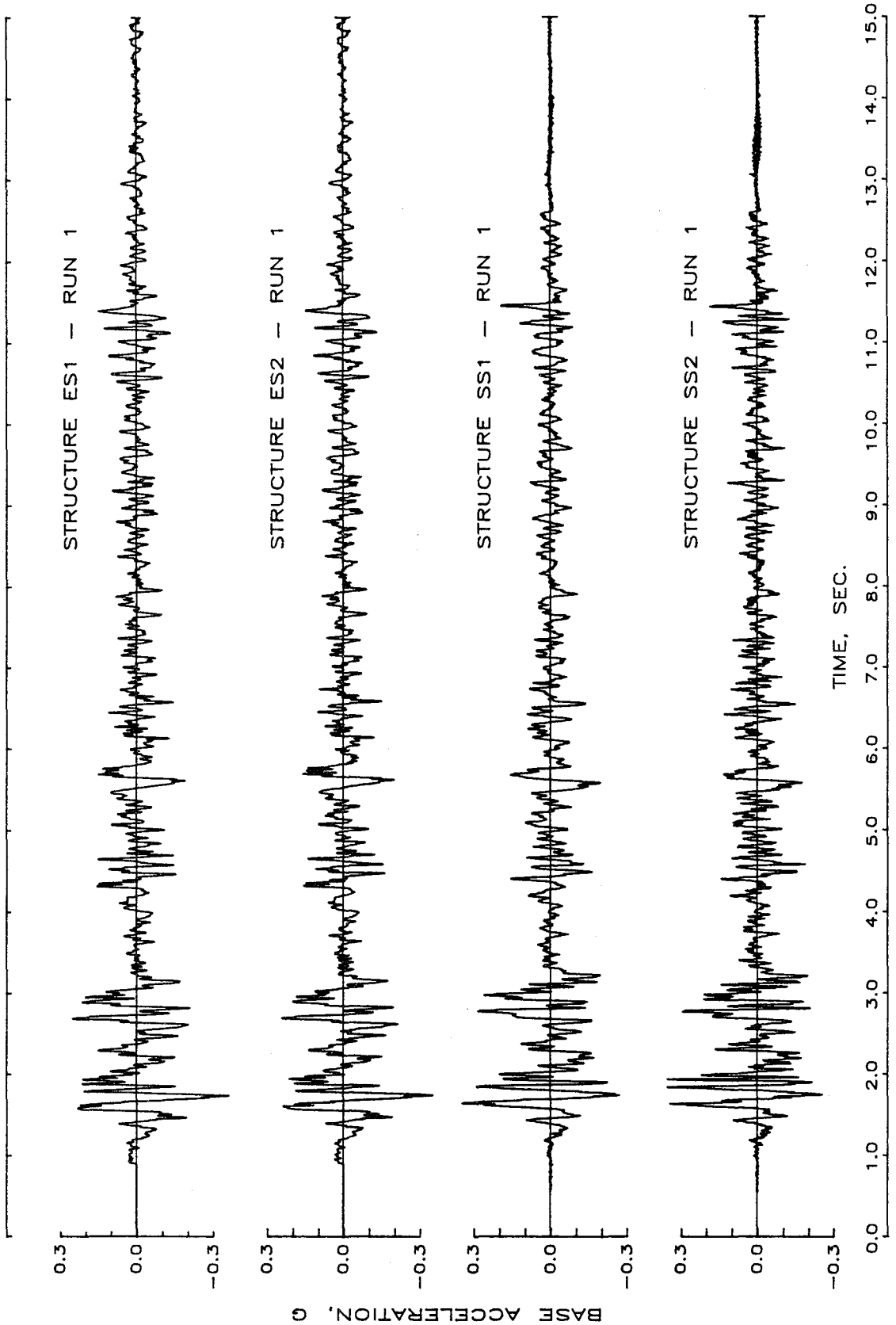

Fig. 5.1 Base Motions and Displacement Response for Design Intensity Earthquakes
(a) Base Acceleration Histories

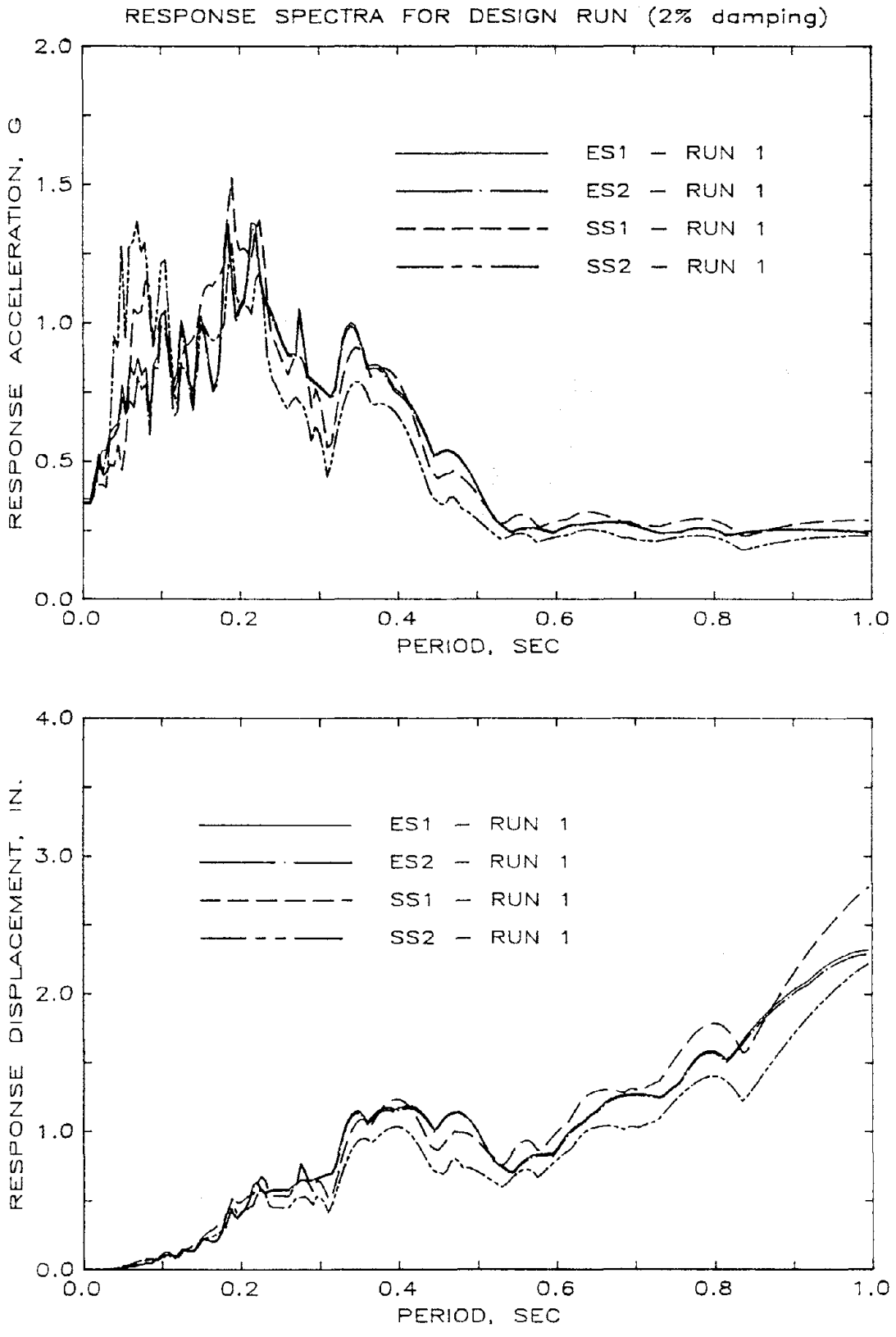

Fig. 5.1 (cont.) Base Motions and Displacement Response for Design Intensity Earthquakes
(b) Acceleration and Displacement Response Spectra

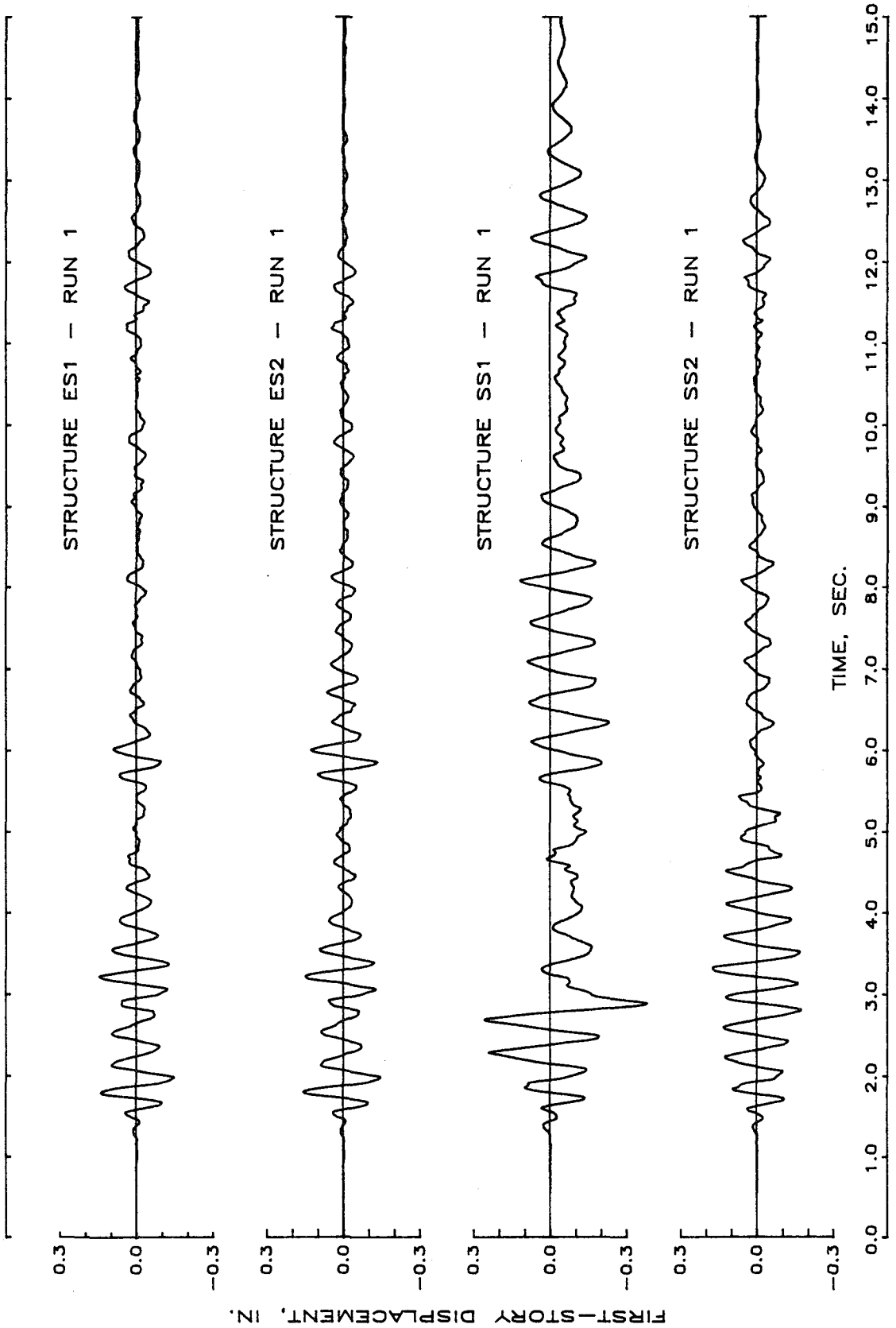

Fig. 5.1 (cont.) Base Motions and Displacement Response for Design Intensity Earthquakes

(c) First-Story Displacement Histories

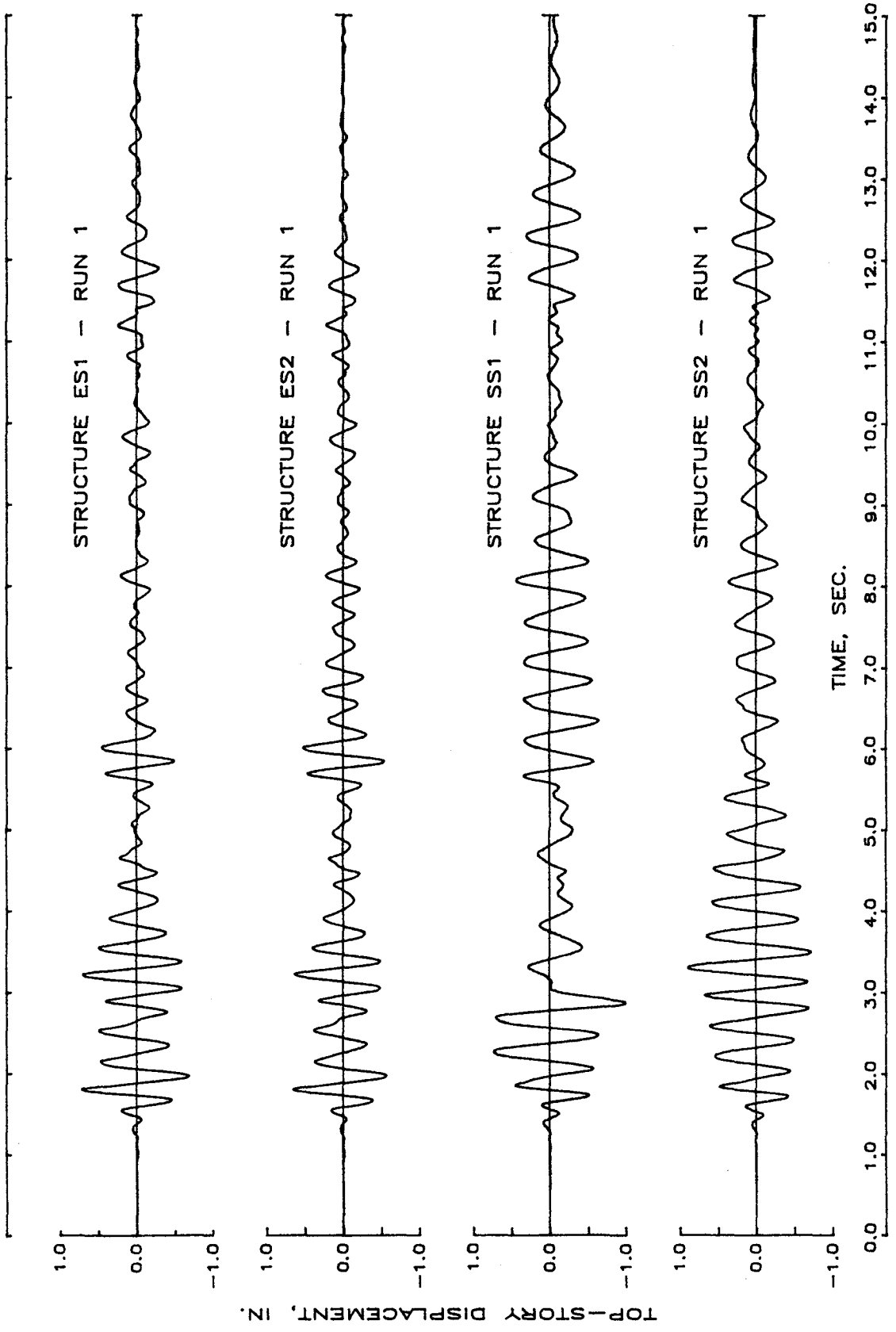

Fig. 5.1 (cont.) Base Motions and Displacement Response for Design Intensity Earthquakes
(d) Top-Level Displacement Histories

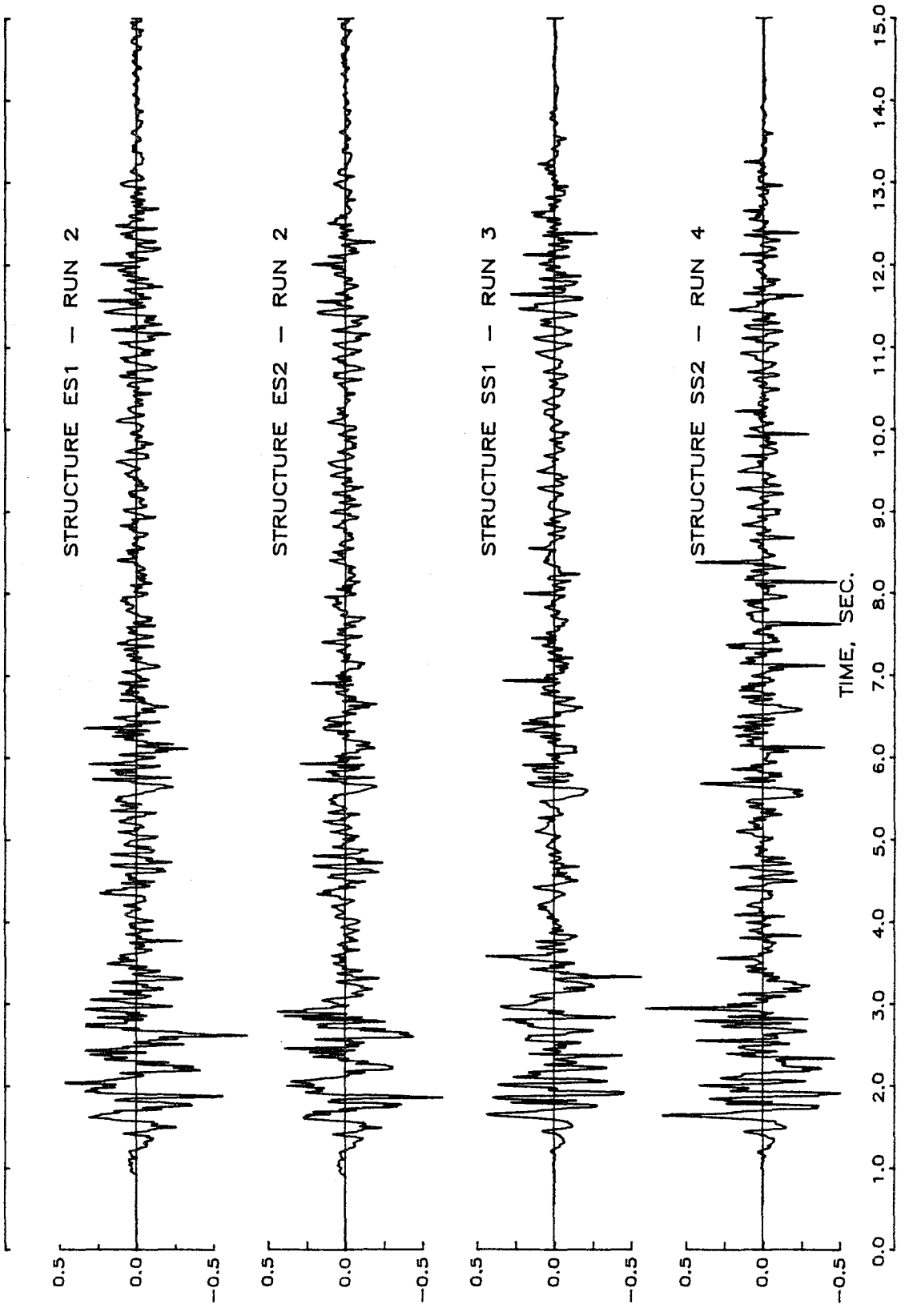

Fig. 5.2 Base Motions and Displacement Response for 1.5 Times Design Intensity Earthquakes
(a) Base Acceleration Histories

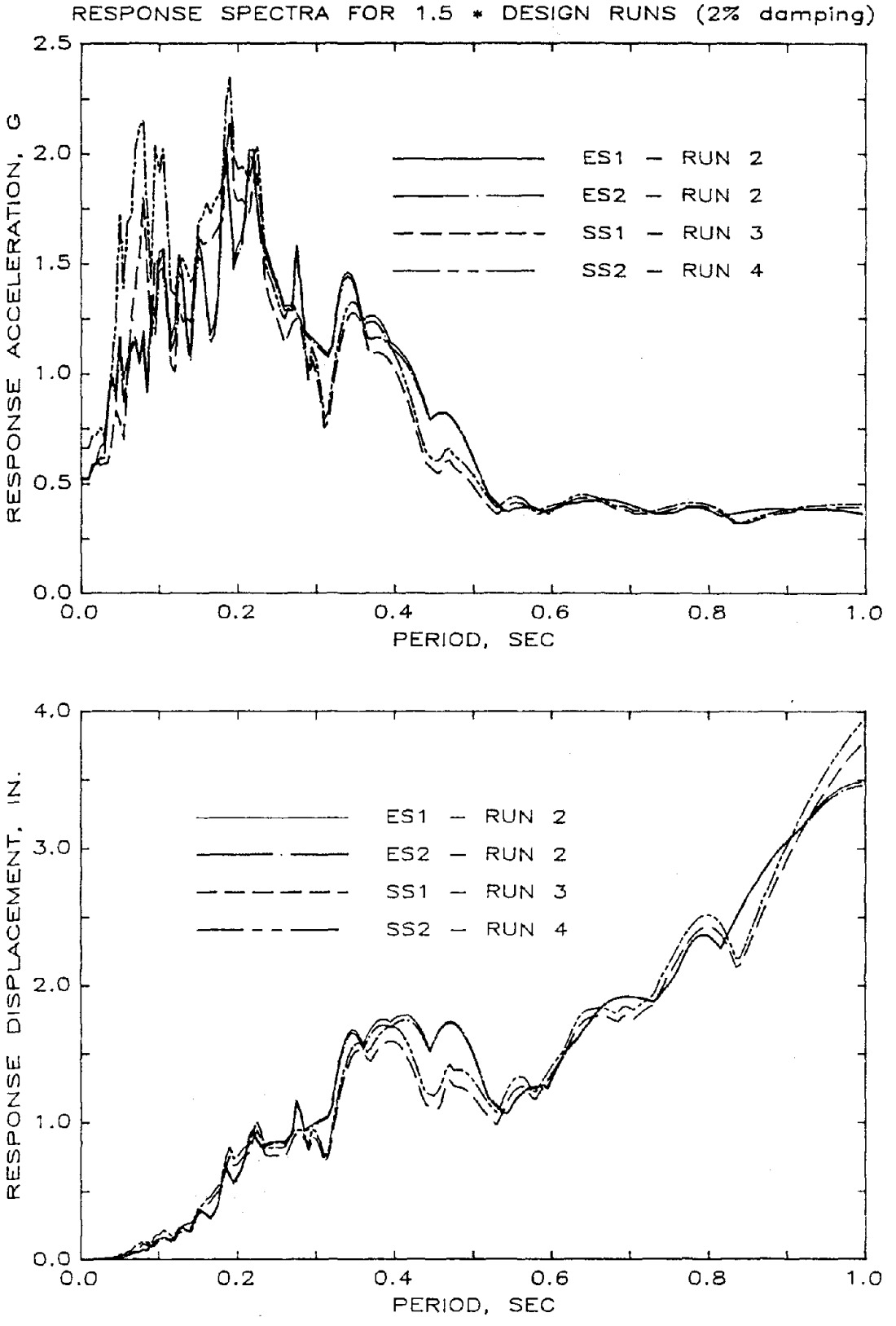

Fig. 5.2 (cont.) Base Motions and Displacement Response for 1.5 Times Design Intensity Earthquakes
(b) Acceleration and Displacement Response Spectra

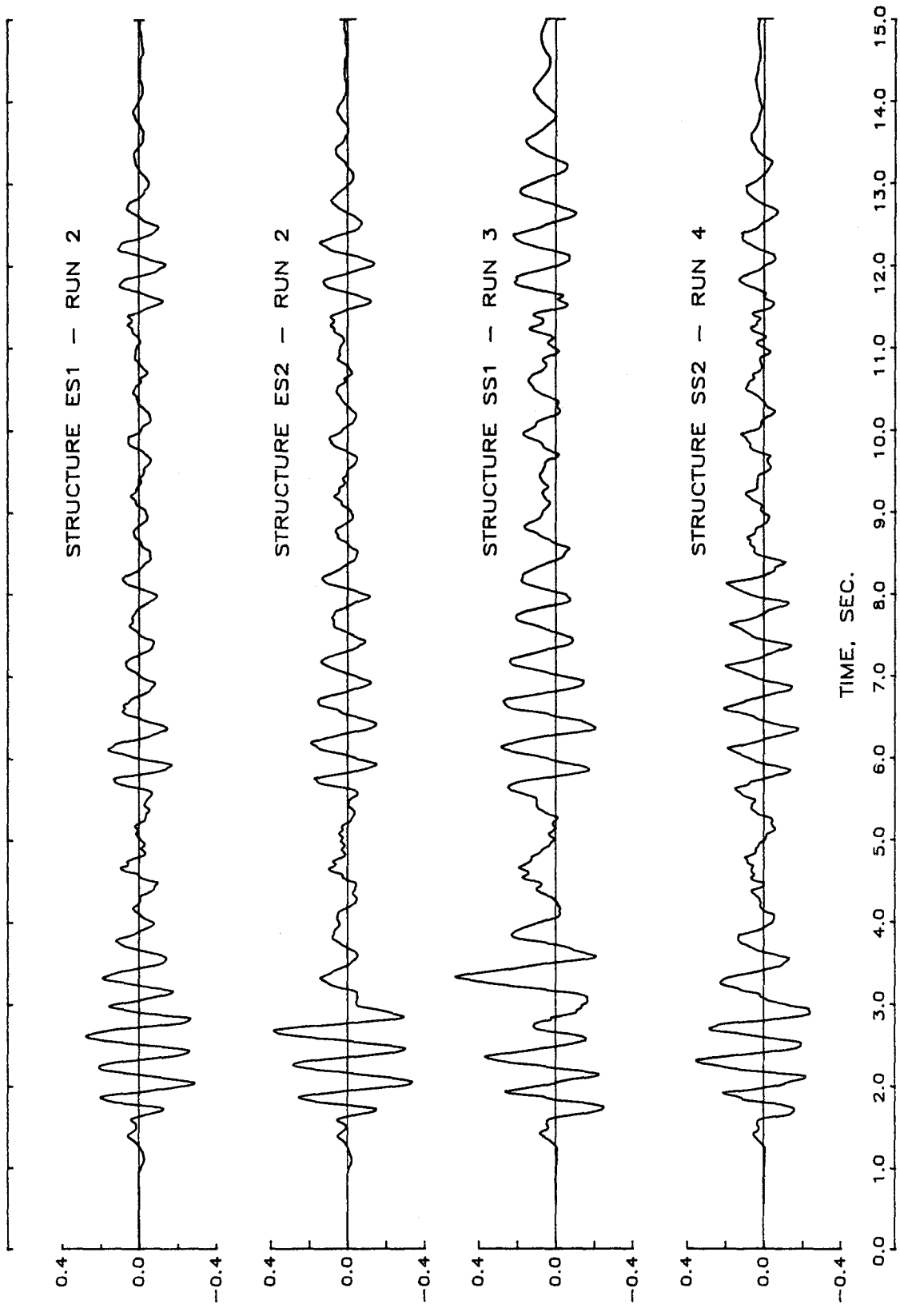

Fig. 5.2 (cont.) Base Motions and Displacement Response for 1.5 Times Design Intensity Earthquakes
(c) First-Story Displacement Histories

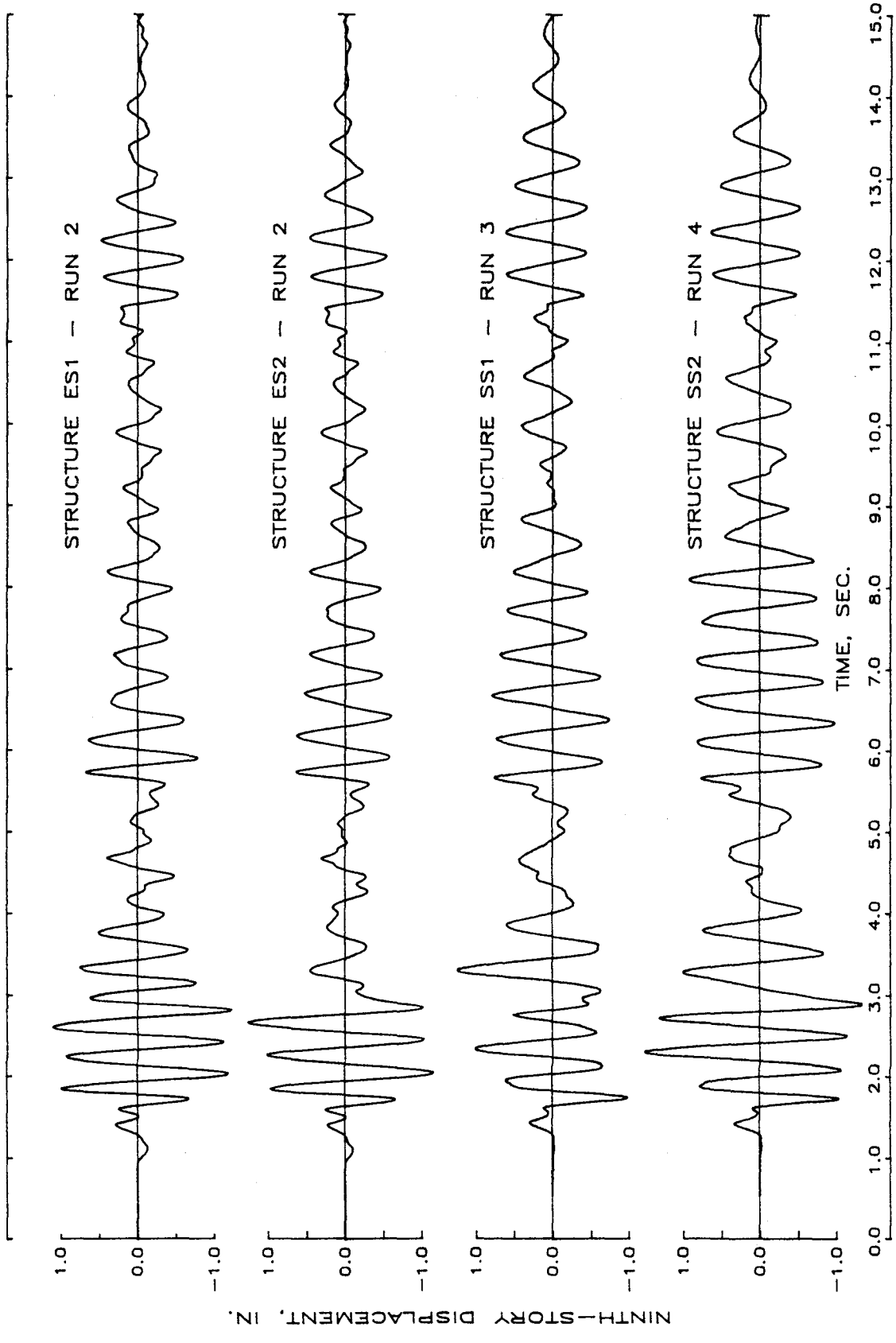

Fig. 5.2 (cont.) Base Motions and Displacement Response for 1.5 Times Design Intensity Earthquakes
(d) Top-Level Displacement Histories

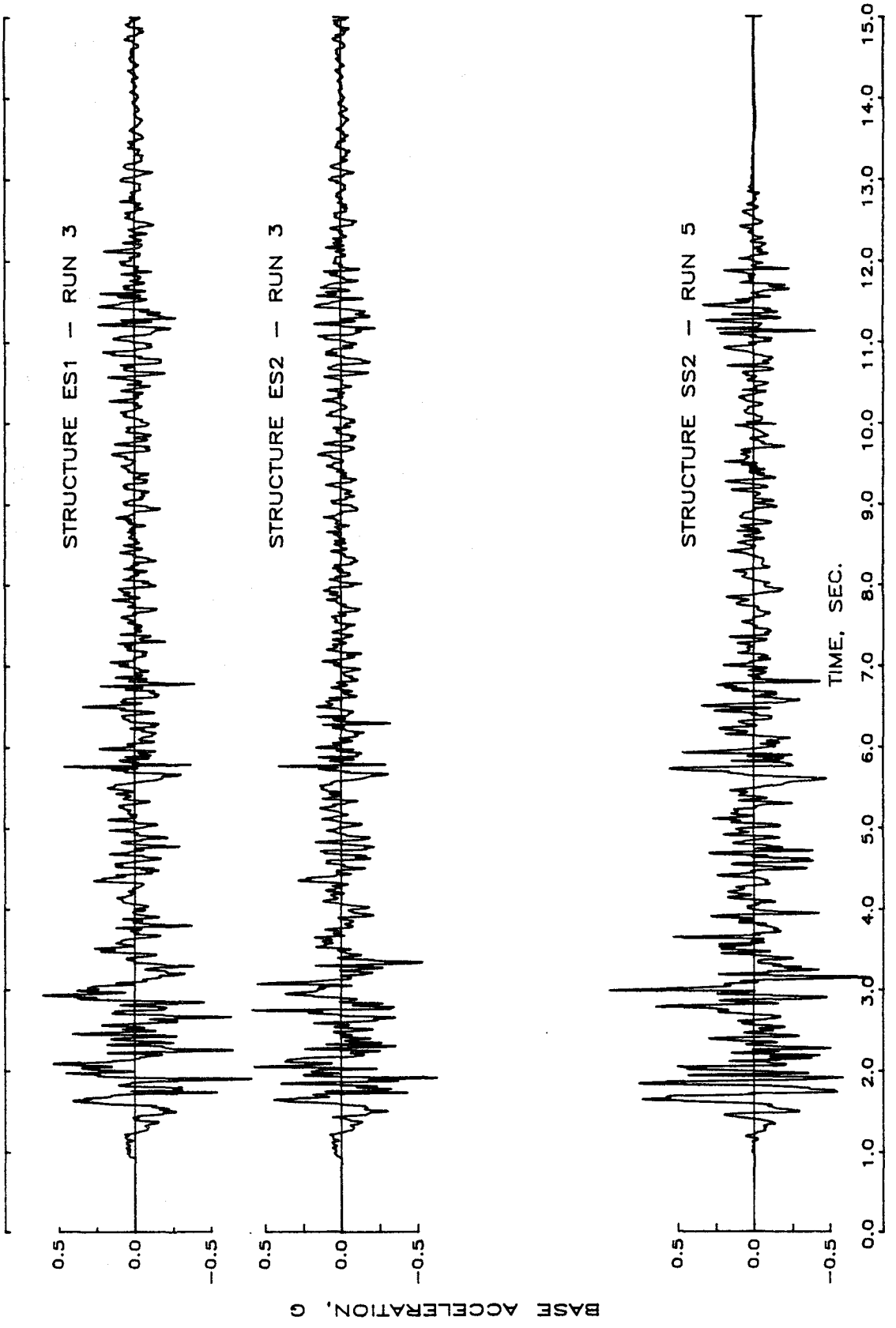

Fig. 5.3 Base Motions and Displacement Response for 2 Times Design Intensity Earthquakes
(a) Base Acceleration Histories

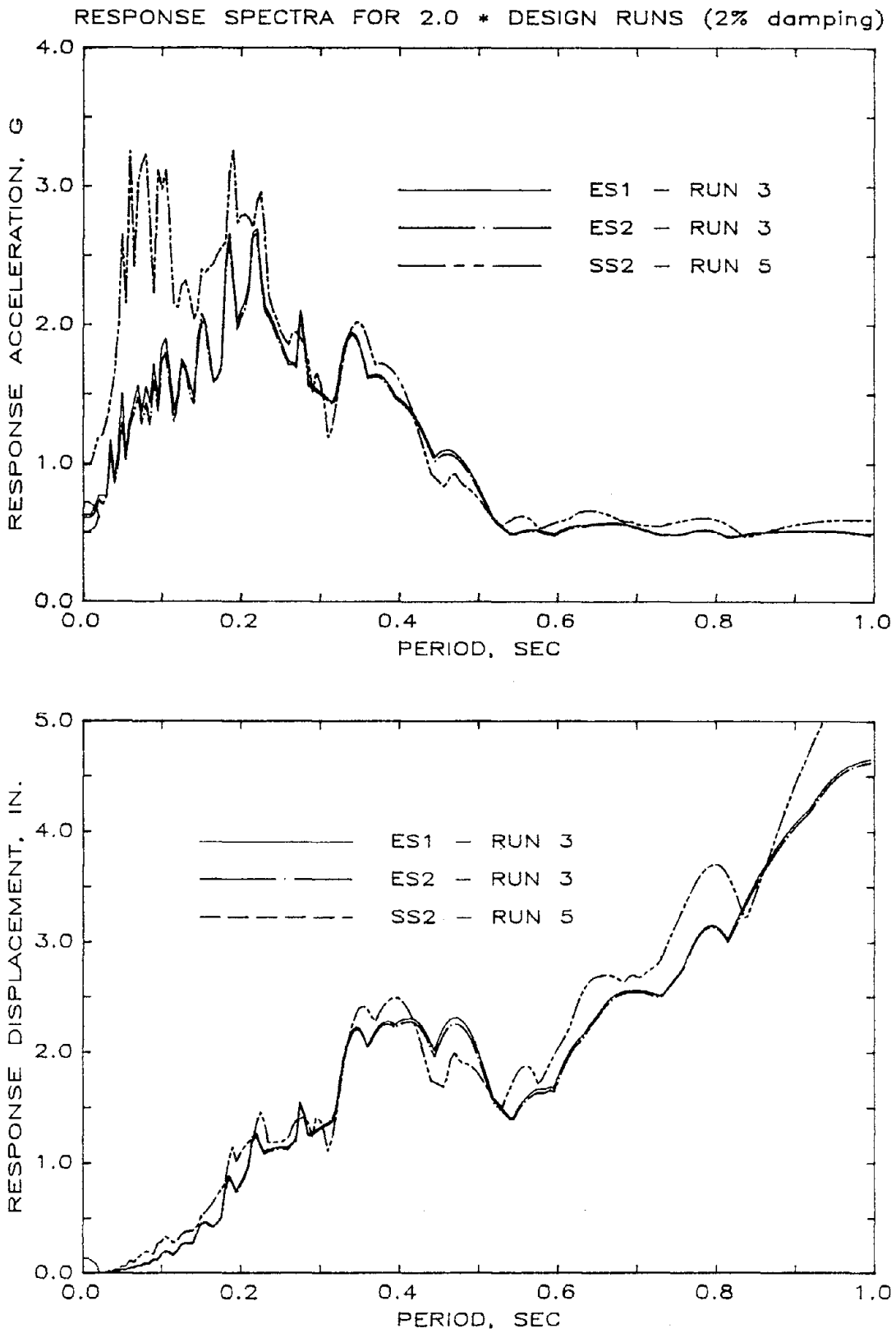

Fig. 5.3 (cont.) Base Motions and Displacement Response for 2 Times Design Intensity Earthquakes
(b) Acceleration and Displacement Response Spectra

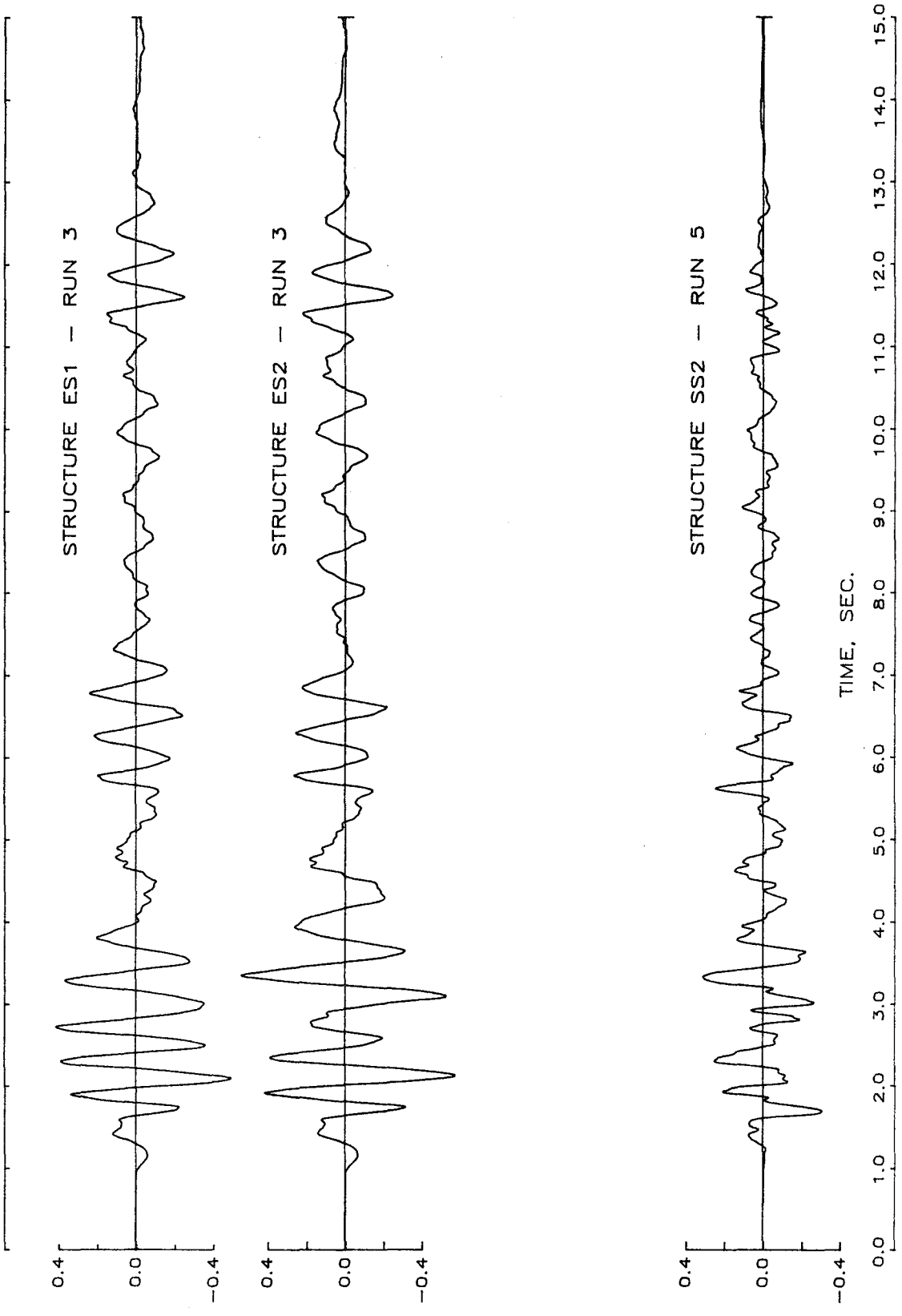

Fig. 5.3 (cont.) Base Motions and Displacement Response for 2 Times Design Intensity Earthquakes
(c) First-Story Displacement Histories

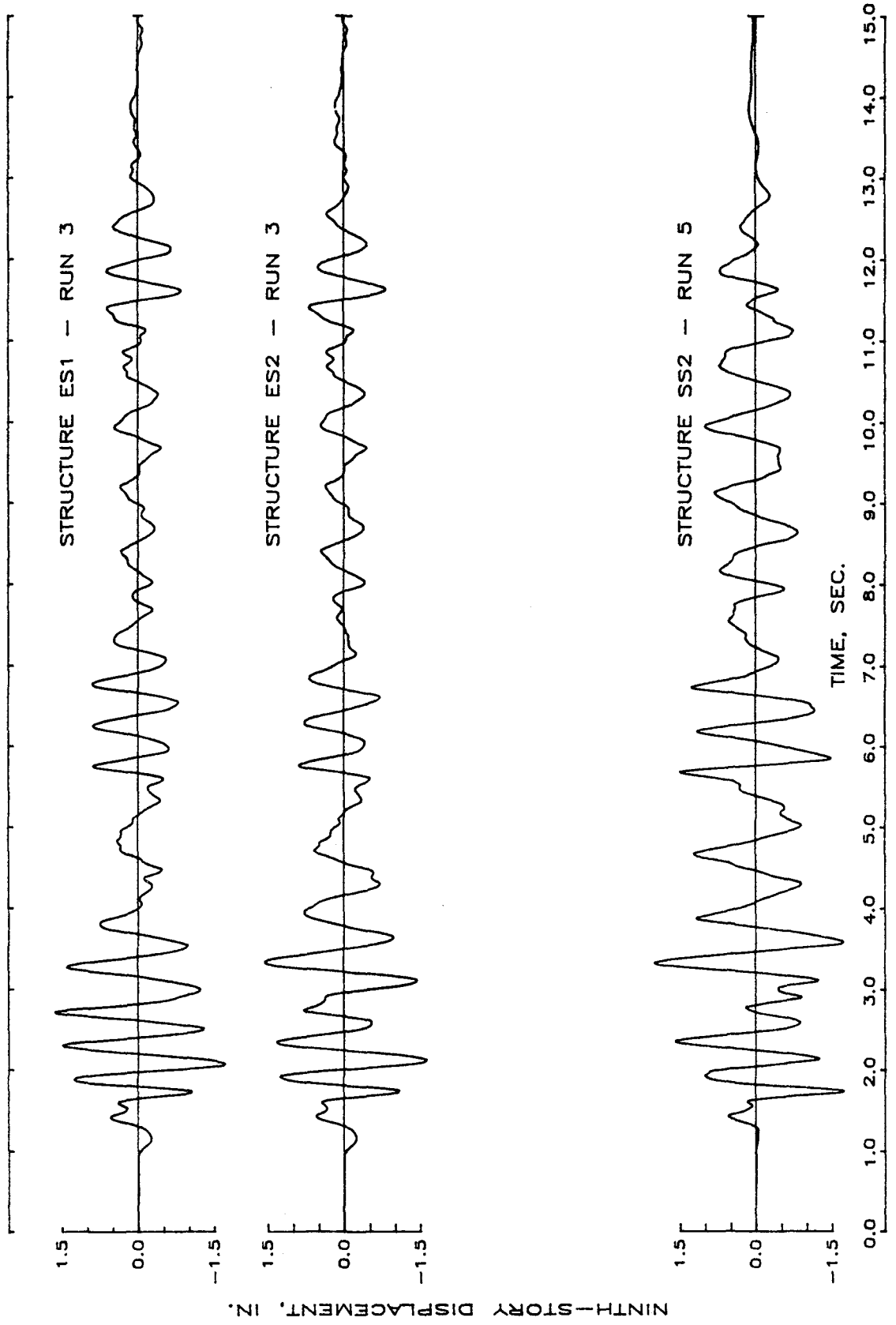

Fig. 5.3 (cont.) Base Motions and Displacement Response for 2 Times Design Intensity Earthquakes
(d) Top-Level Displacement Histories

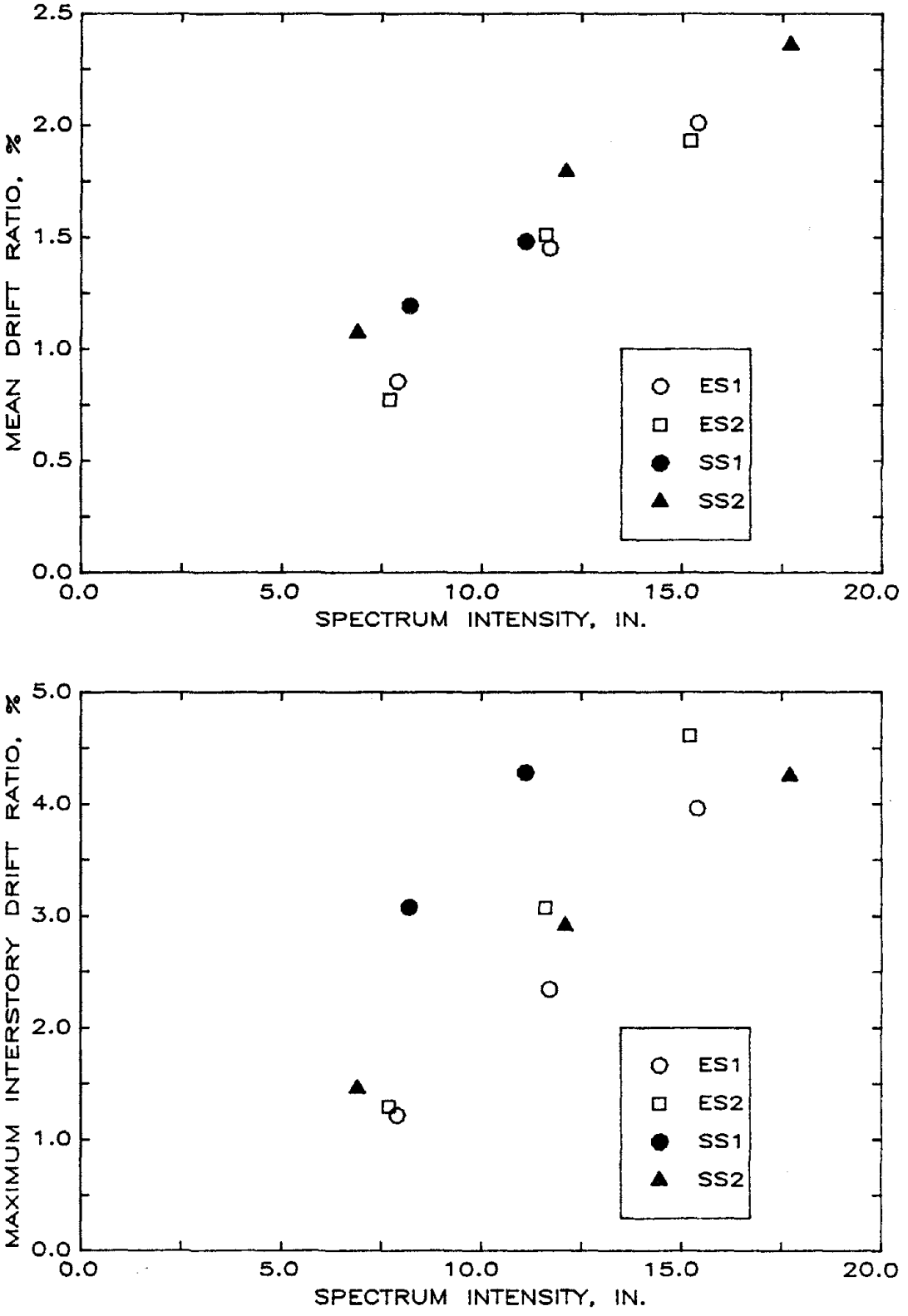

Fig. 5.4 Maximum Overall and Interstory Drift Ratios for ES1, ES2, SS1 and SS2

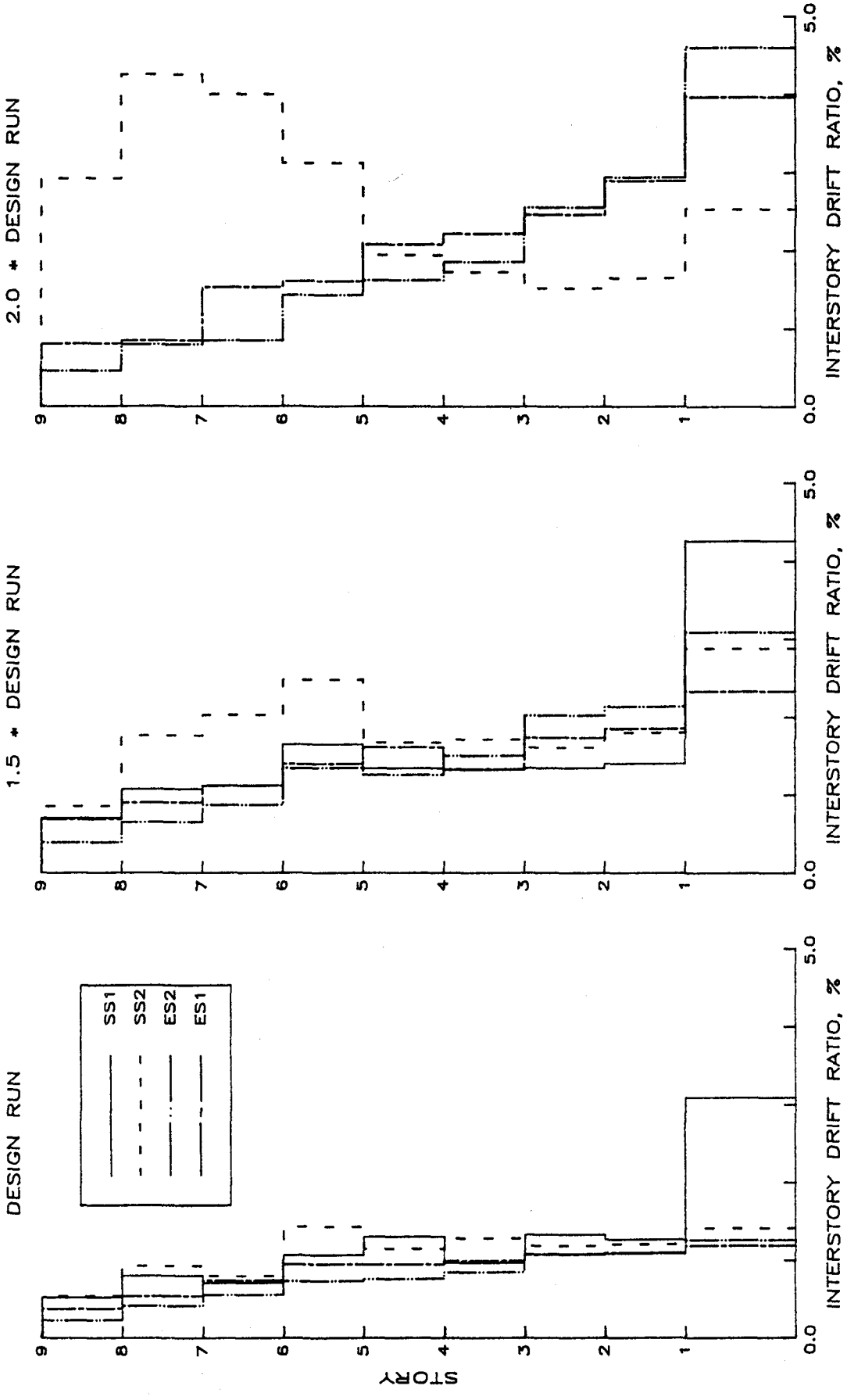

Fig. 5.5 Distributions of Interstory Drift Ratios

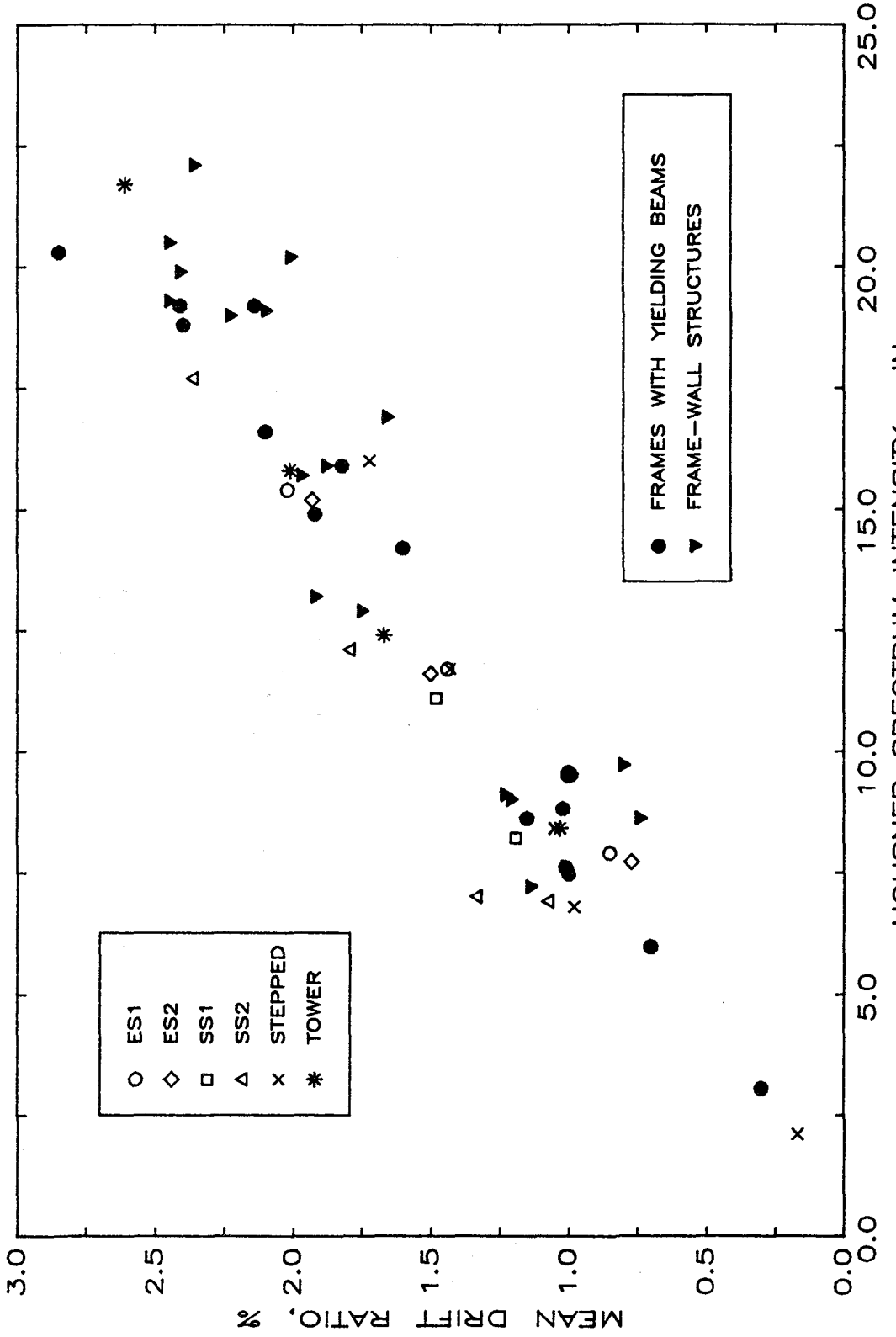

Fig. 5.6 Influence of Base-Motion Intensity on Mean Drift

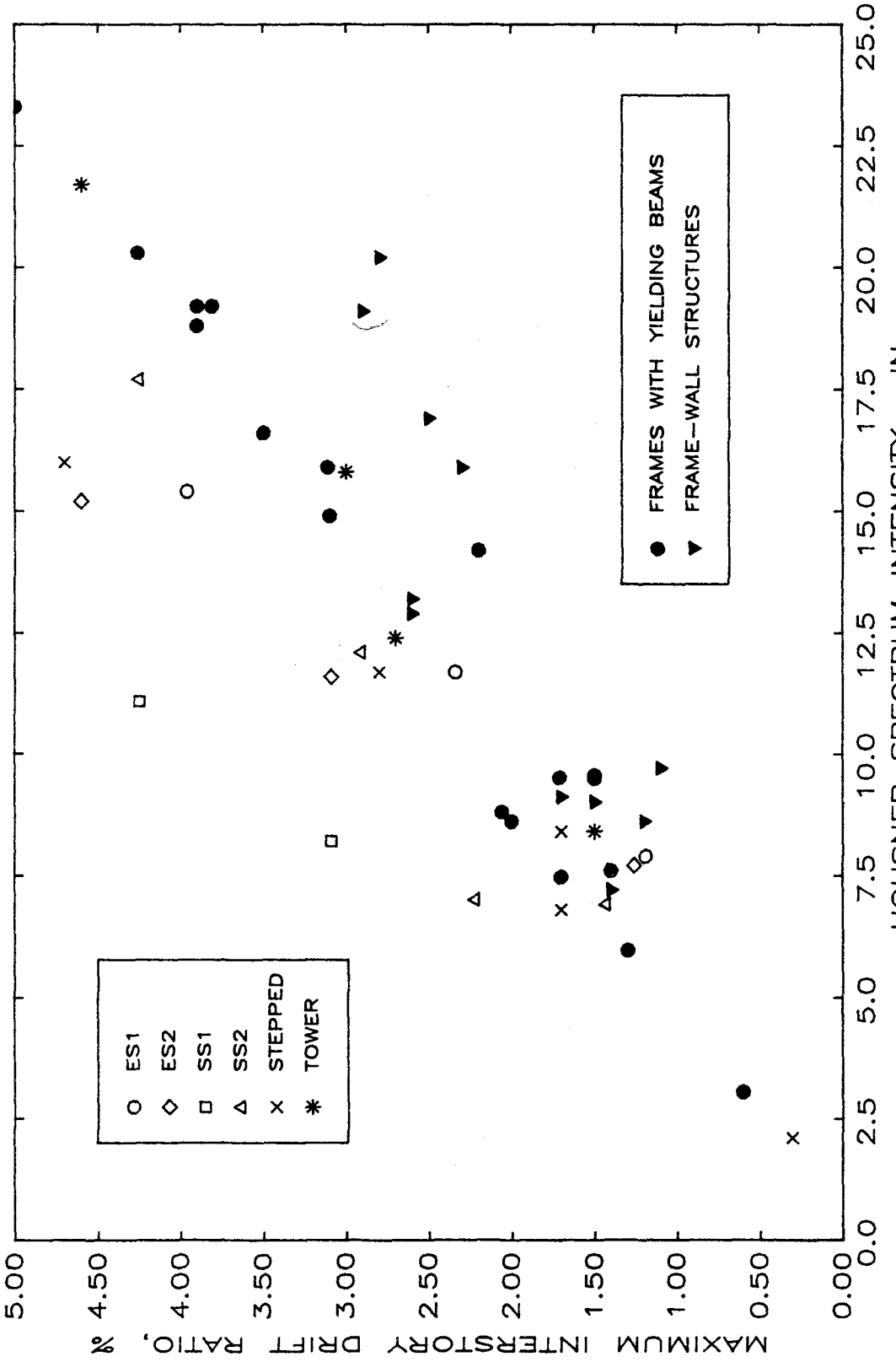

Fig. 5.7 Influence of Base-Motion Intensity on Interstory Drift

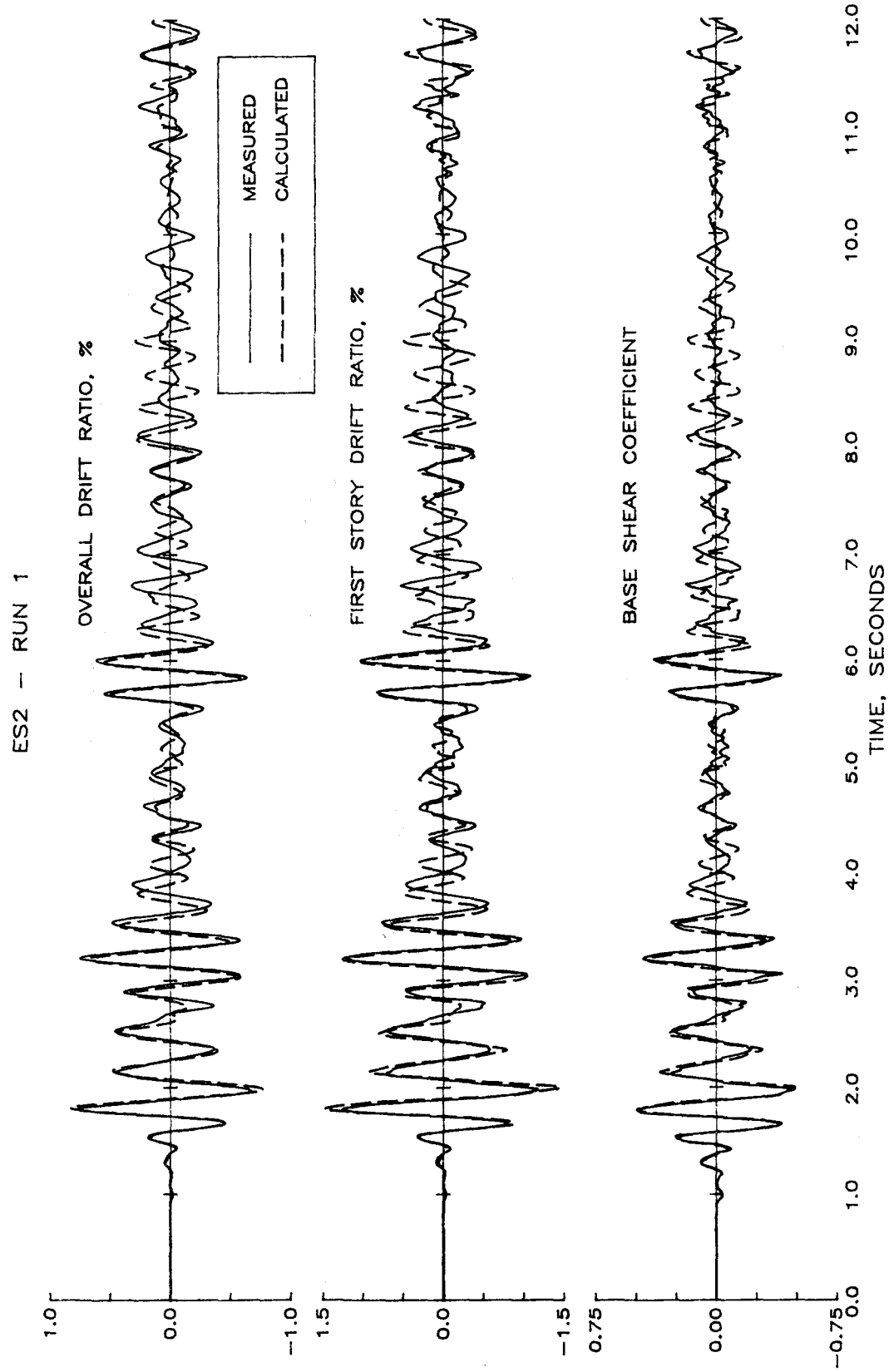

Fig. 6.1 Calculated and Measured Response Histories for Run 1 of Structure ES2

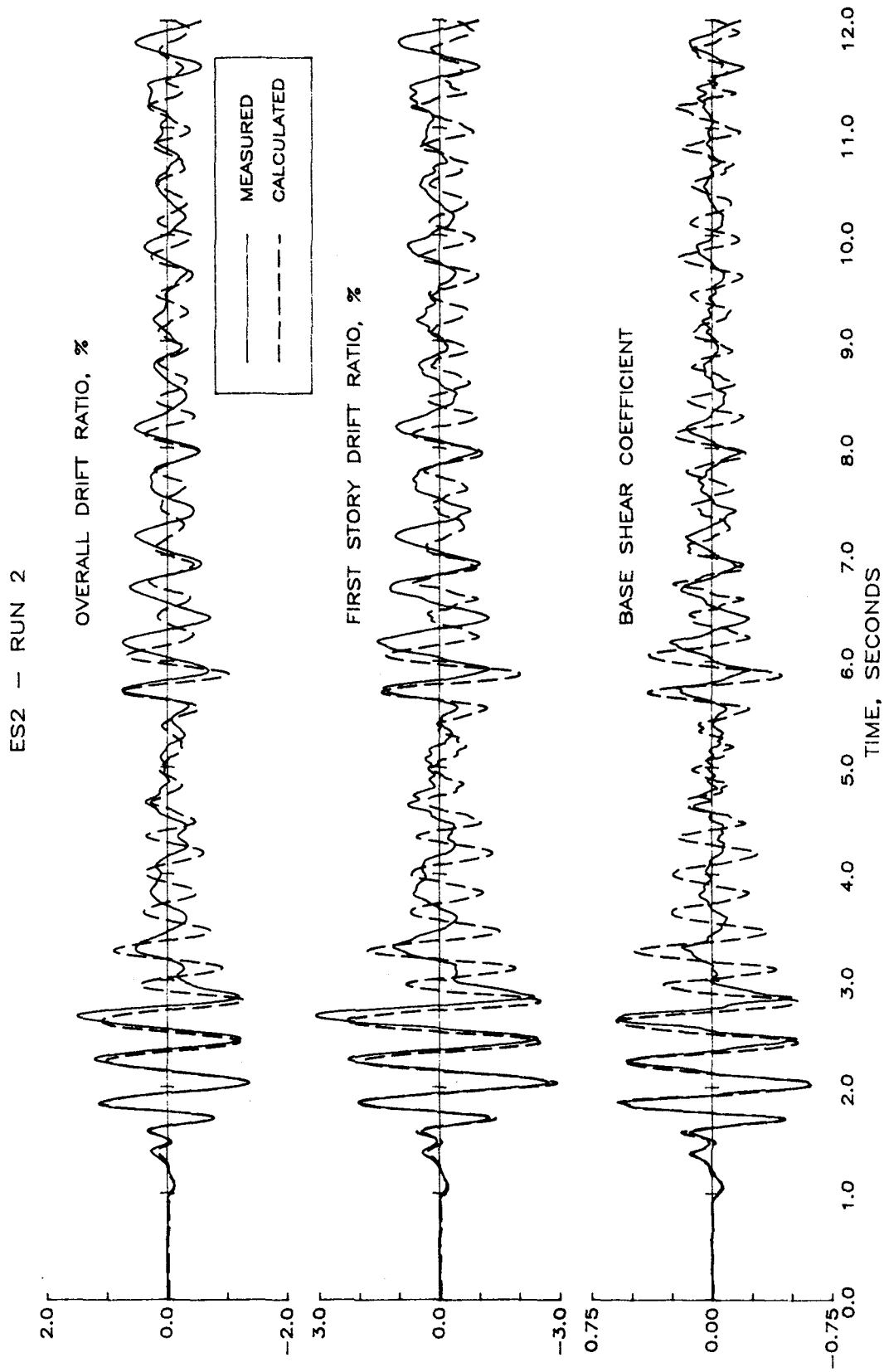

Fig. 6.2 Calculated and Measured Response Histories for Run 2 of Structure ES2

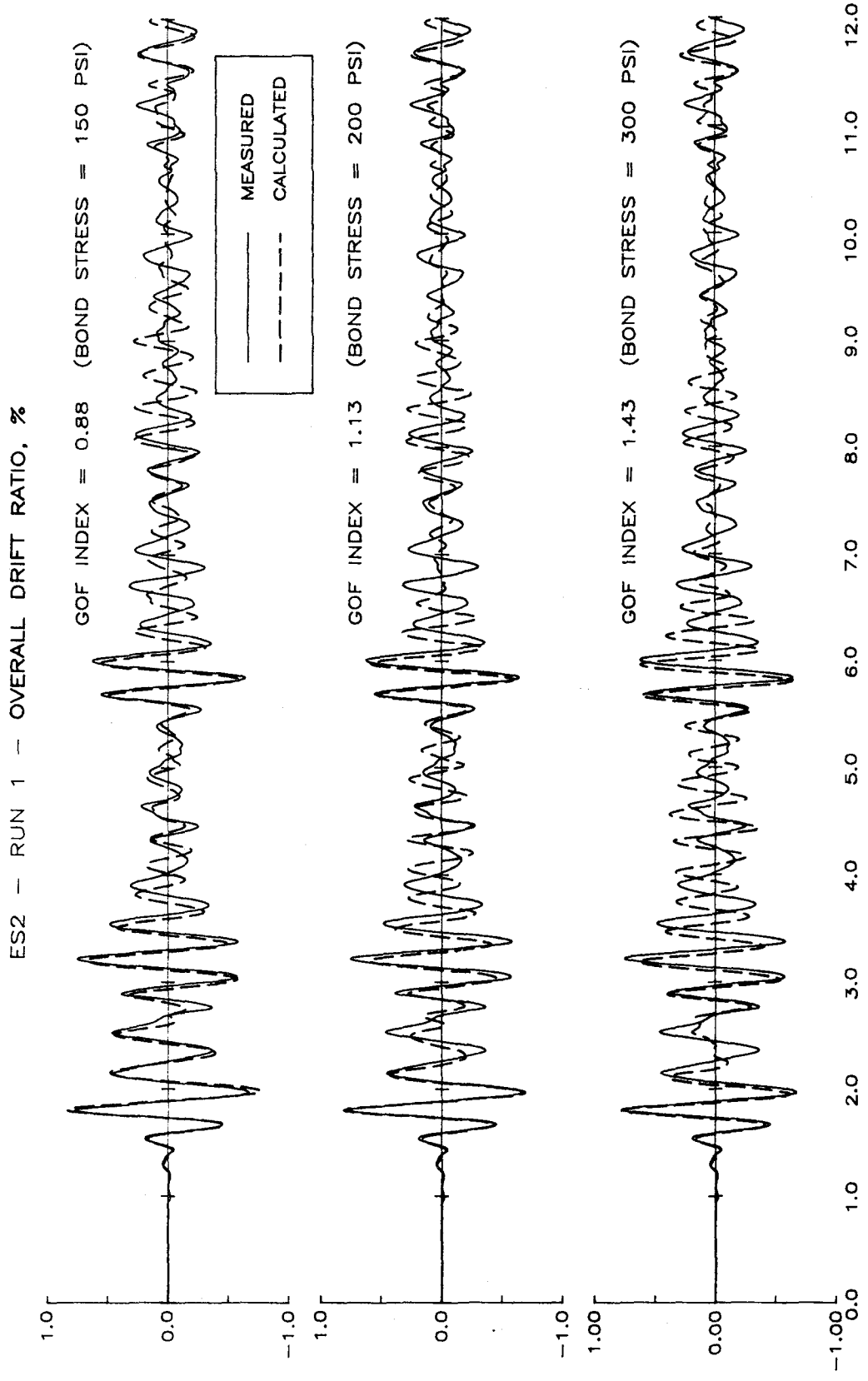

Fig. 6.3 Examples of Response Histories for Three Values of Goodness-of-Fit Index

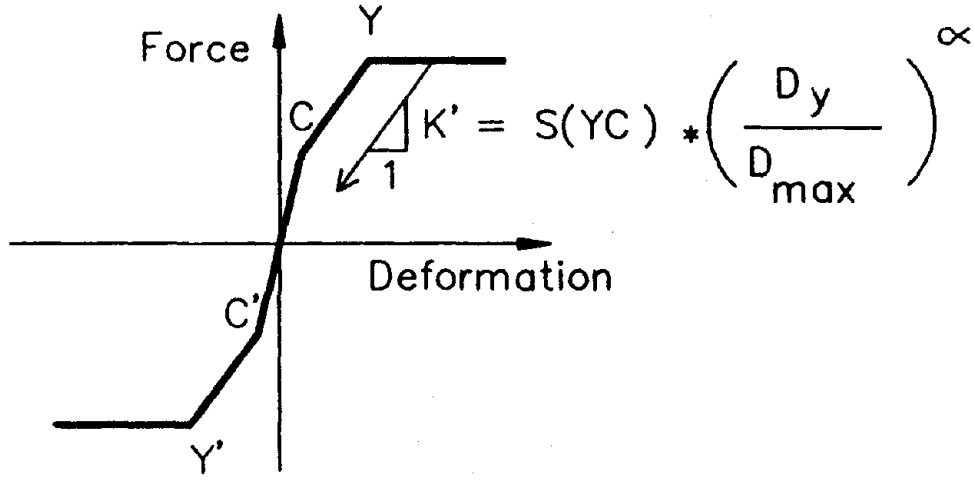

Fig. 6.4 Definition of Unloading Slope of Takeda Hysteresis Rules

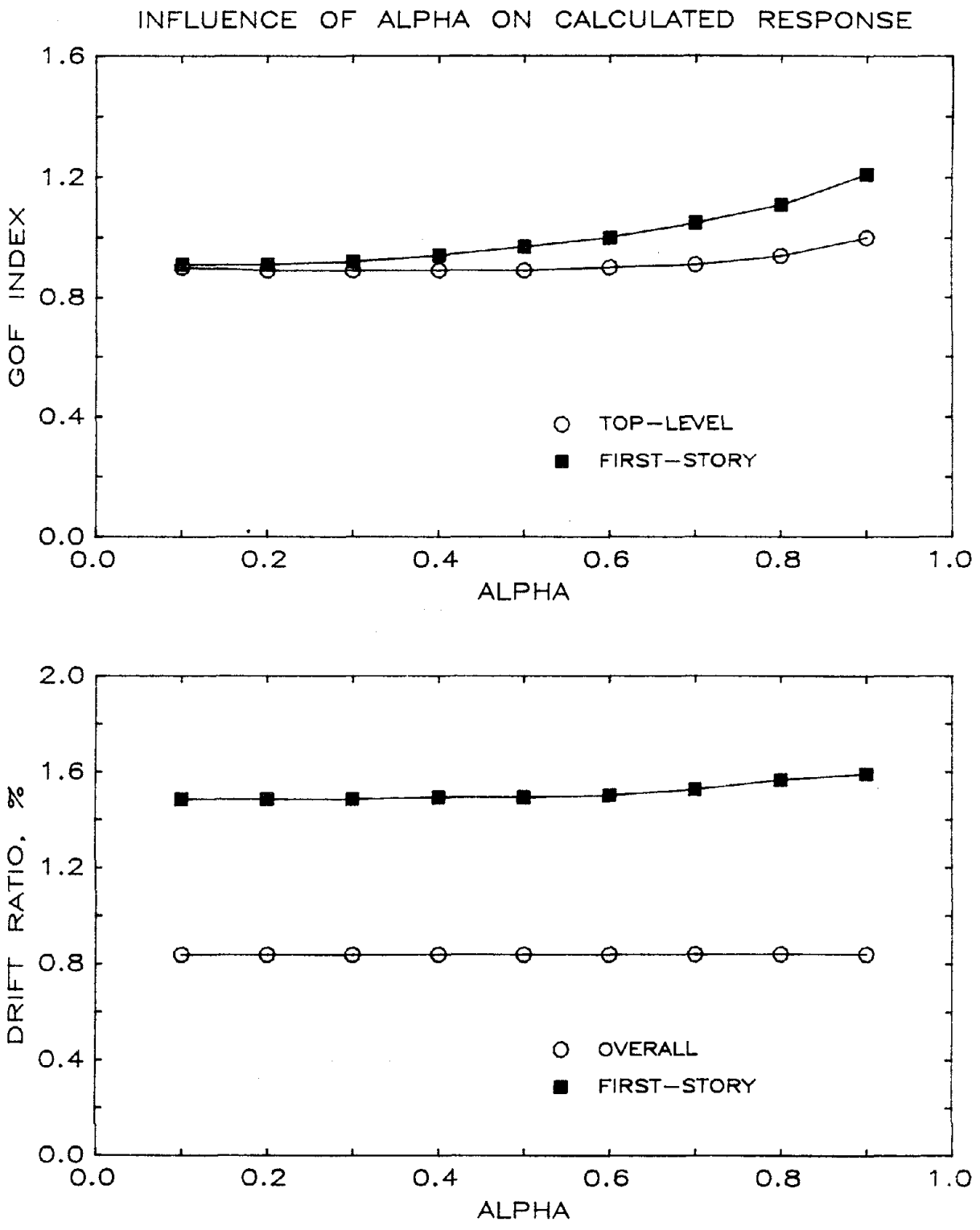

Fig. 6.5 Influence on Calculated Displacement Response of Variations in Unloading Slope Exponent

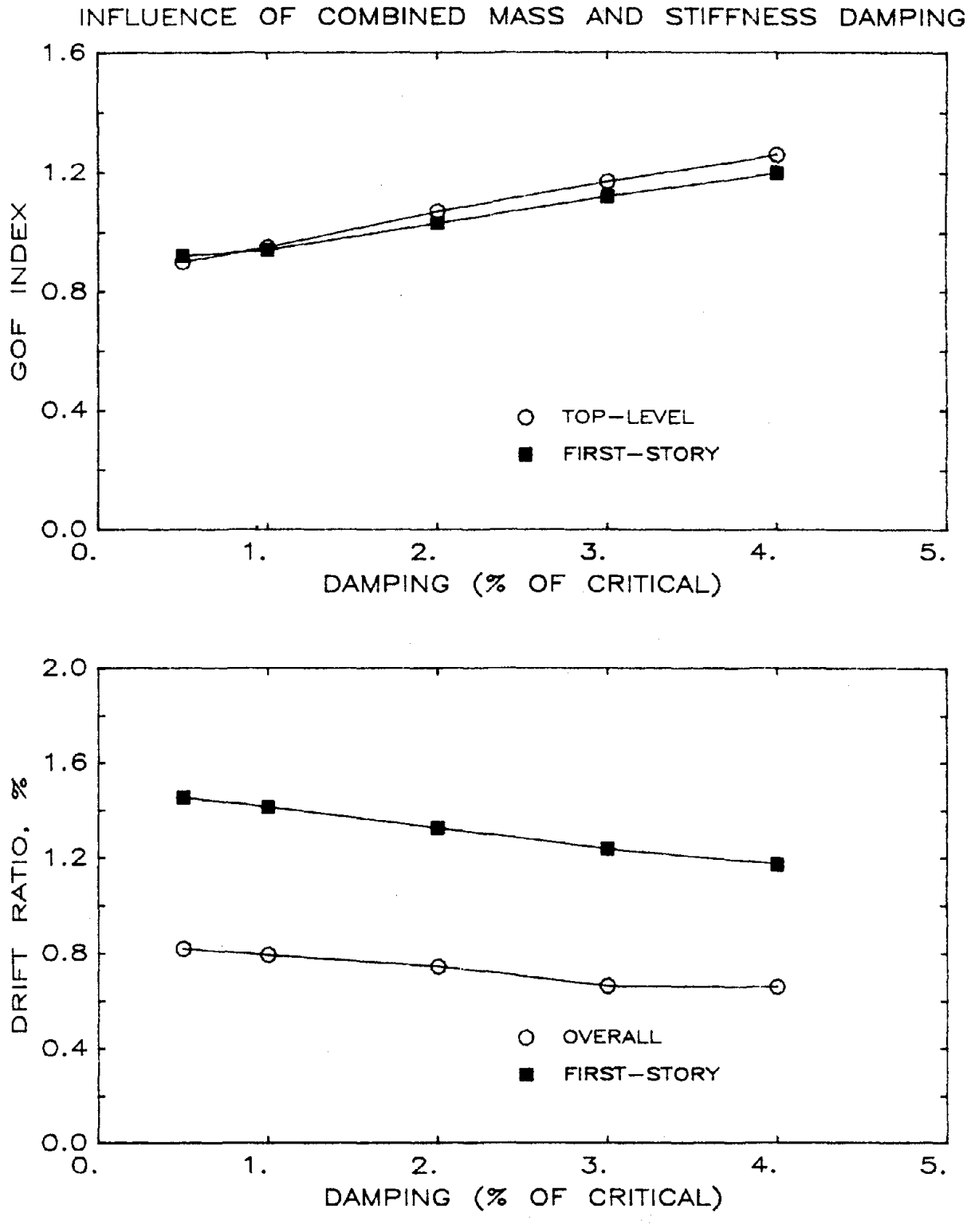

Fig. 6.6 Influence on Calculated Displacement Response of Variations in Rayleigh Damping

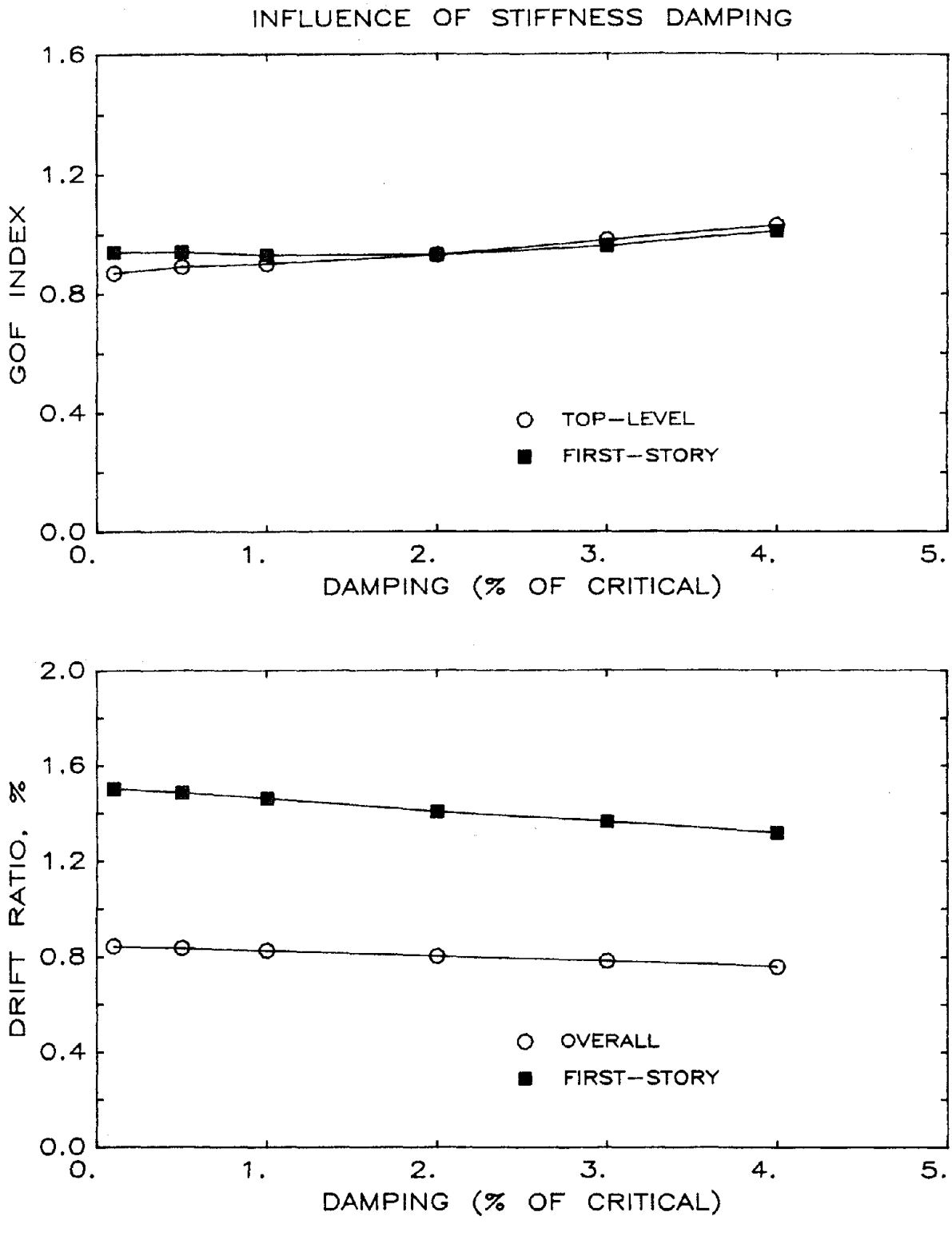

Fig. 6.7 Influence on Calculated Displacement Response of Variations in Stiffness Proportional Damping

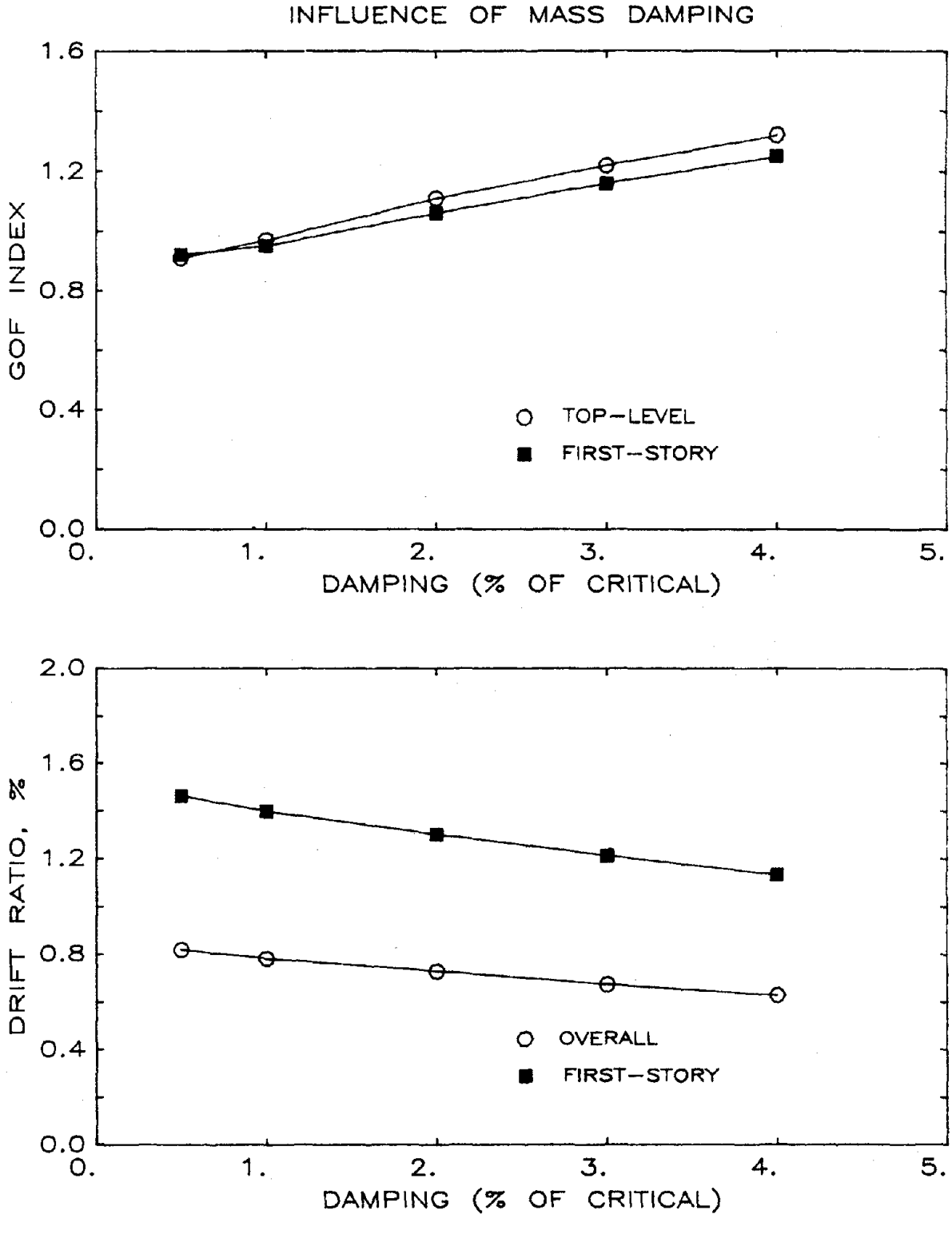

Fig. 6.8 Influence on Calculated Displacement Response of Variations in Mass Proportional Damping

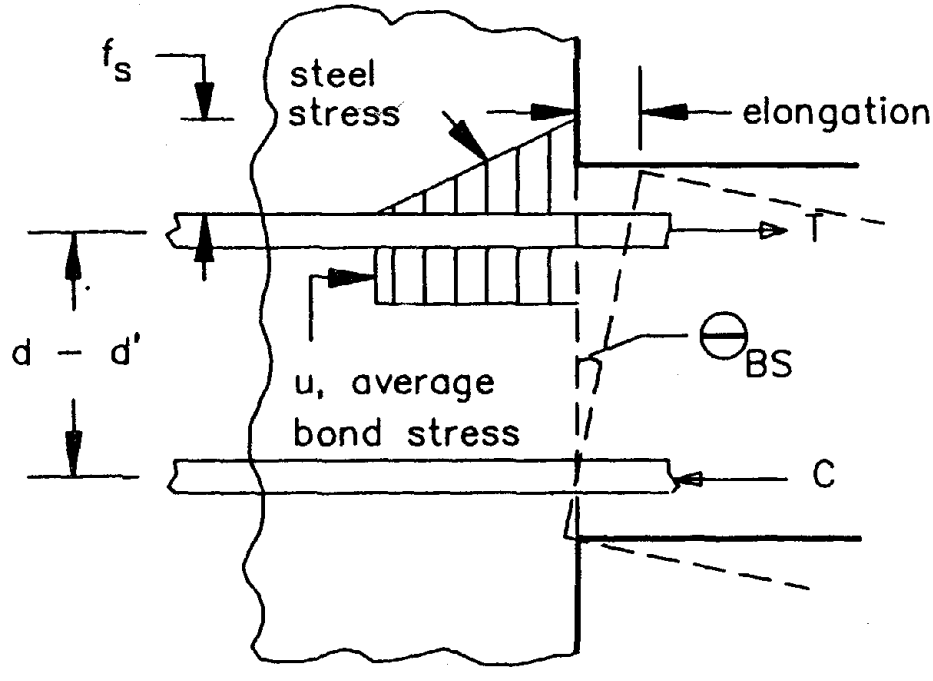

Fig. 6.9 Assumed Mechanism of Slip of Reinforcement

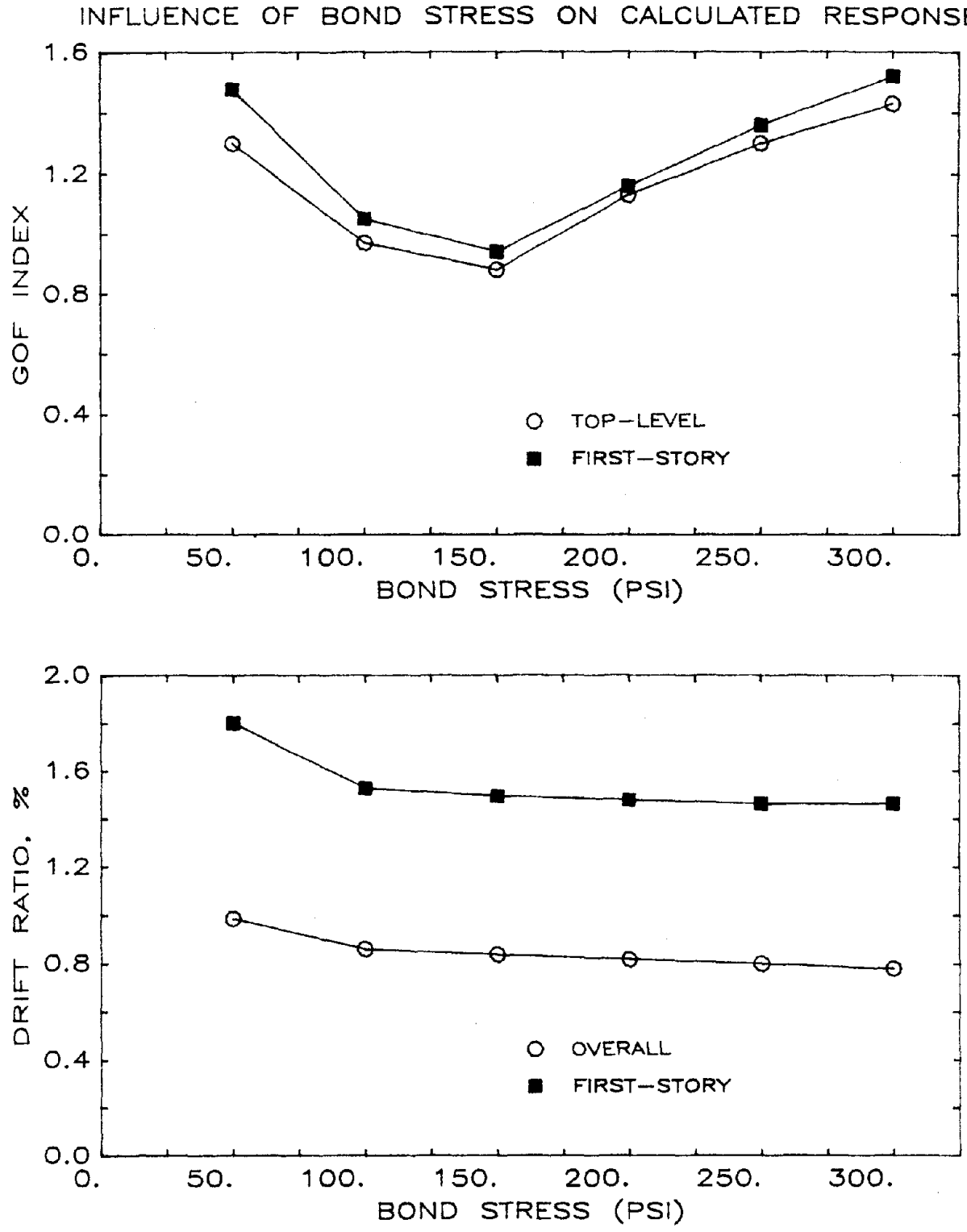

Fig. 6.10 Influence on Calculated Displacement Response of Variations in Bond Stress

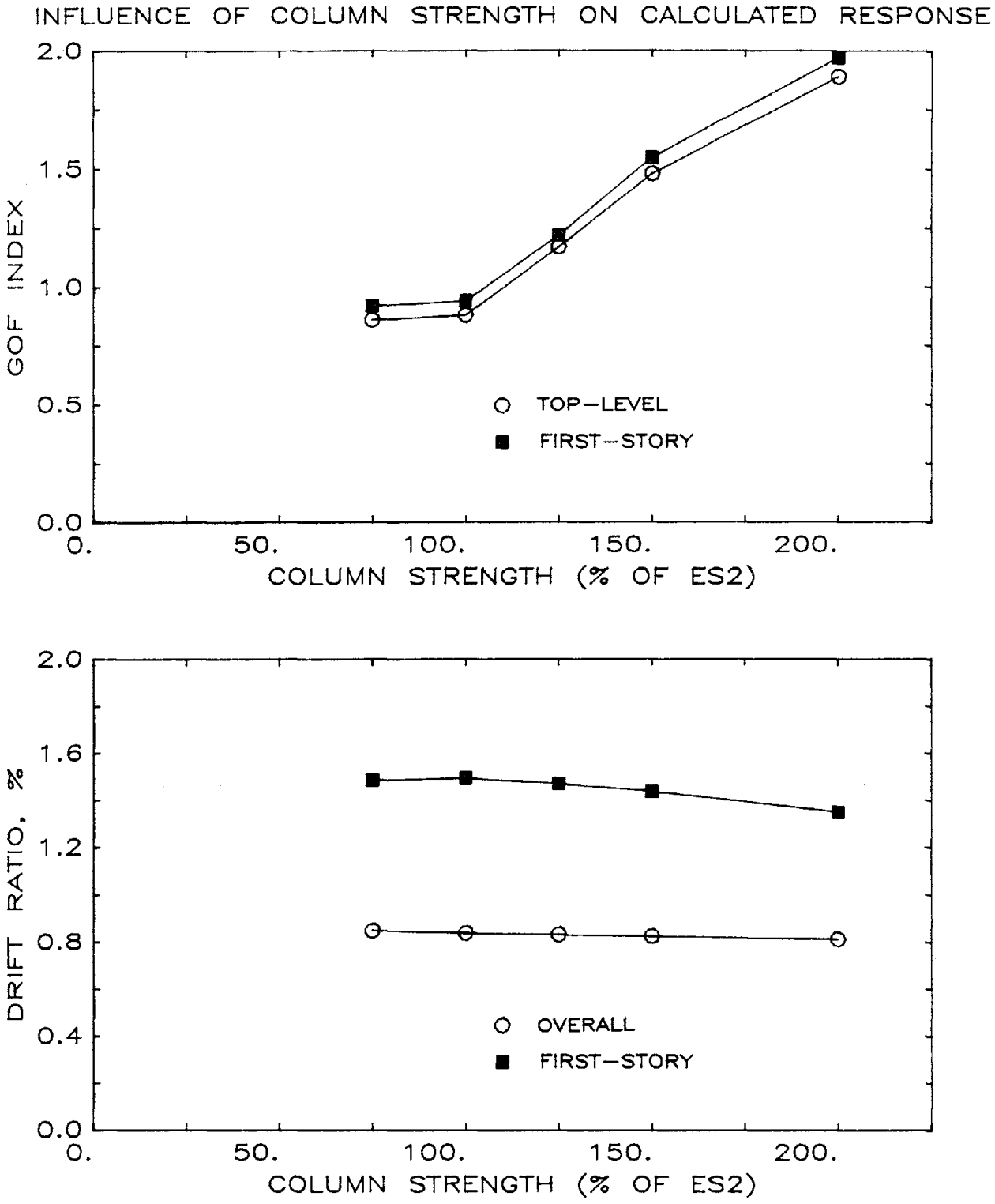

Fig. 6.11 Influence on Calculated Displacement Response of Variations in Column Flexural Strength

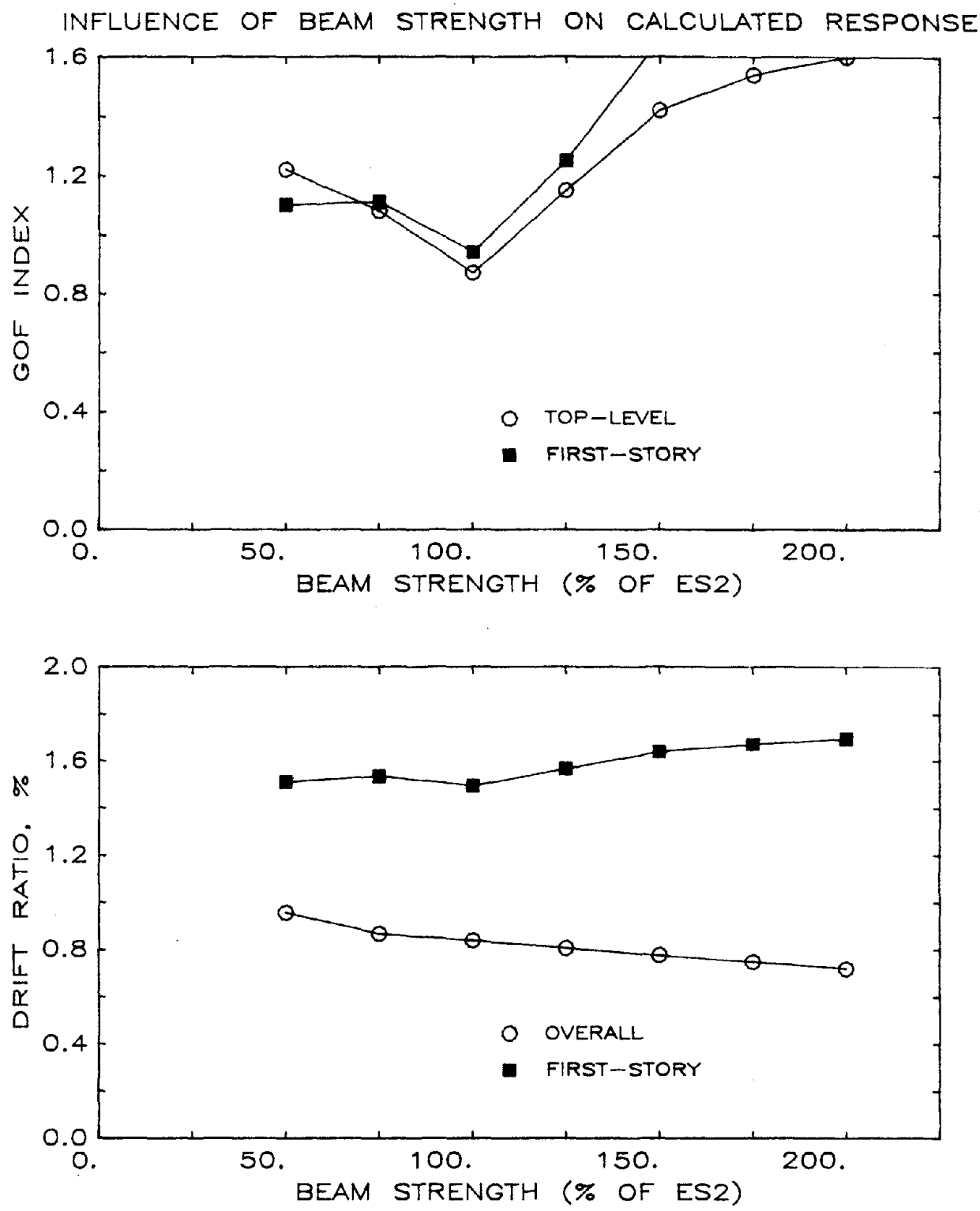

Fig. 6.12 Influence on Calculated Displacement Response of Variations in Beam Flexural Strength

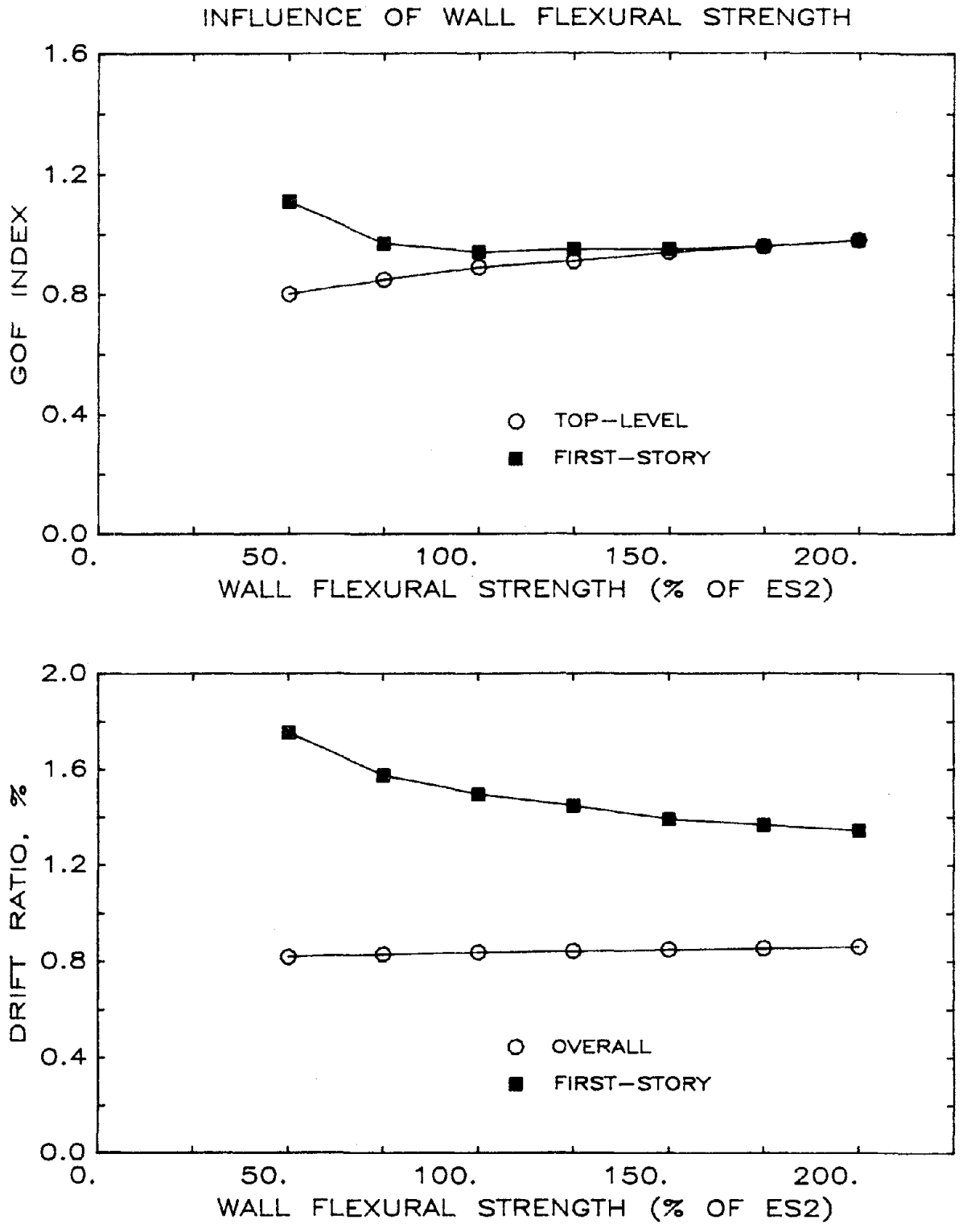

Fig. 6.13 Influence on Calculated Displacement Response of Variations in Wall Flexural Strength

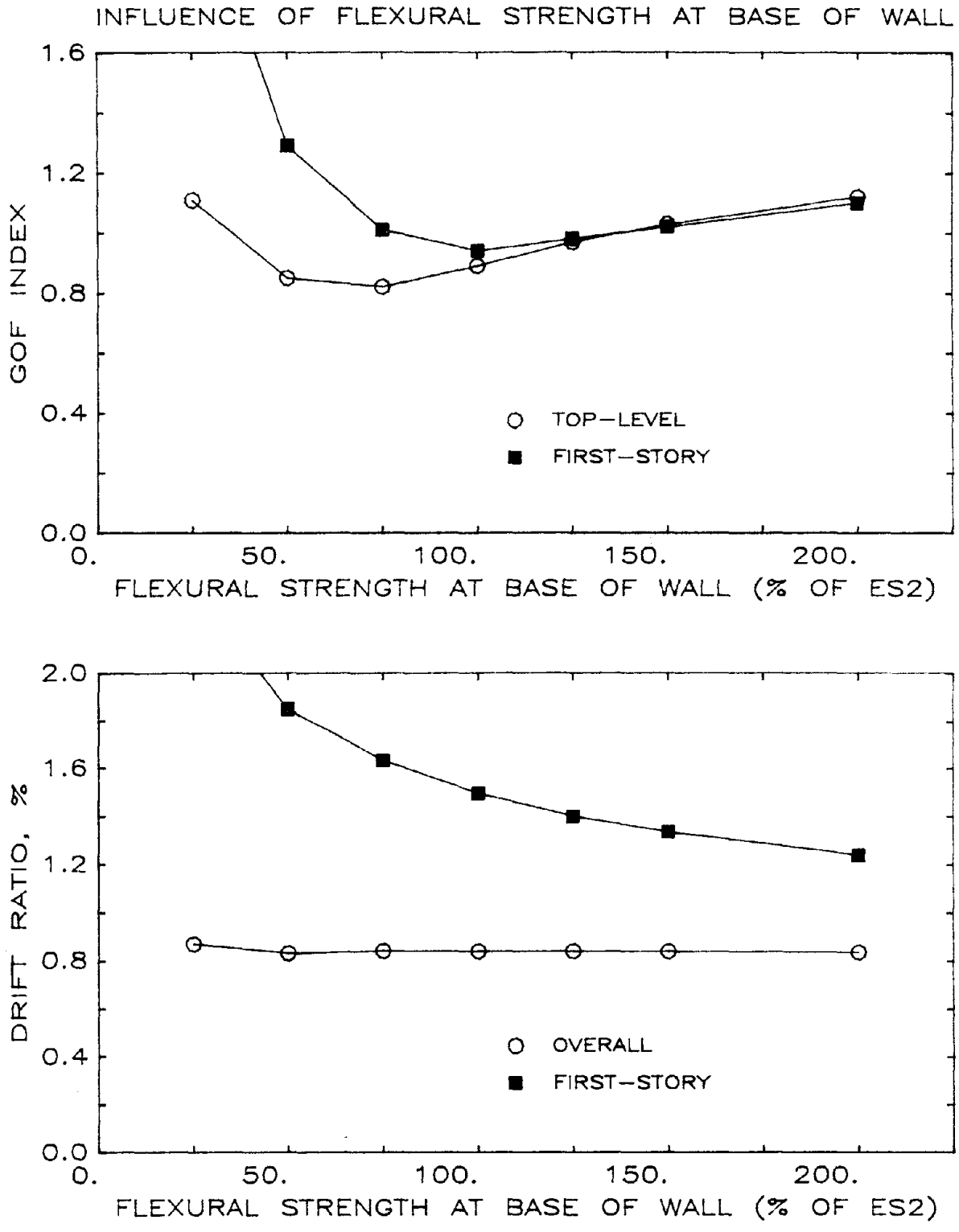

Fig. 6.14 Influence on Calculated Displacement Response of Variations in Flexural Strength at Base of Wall

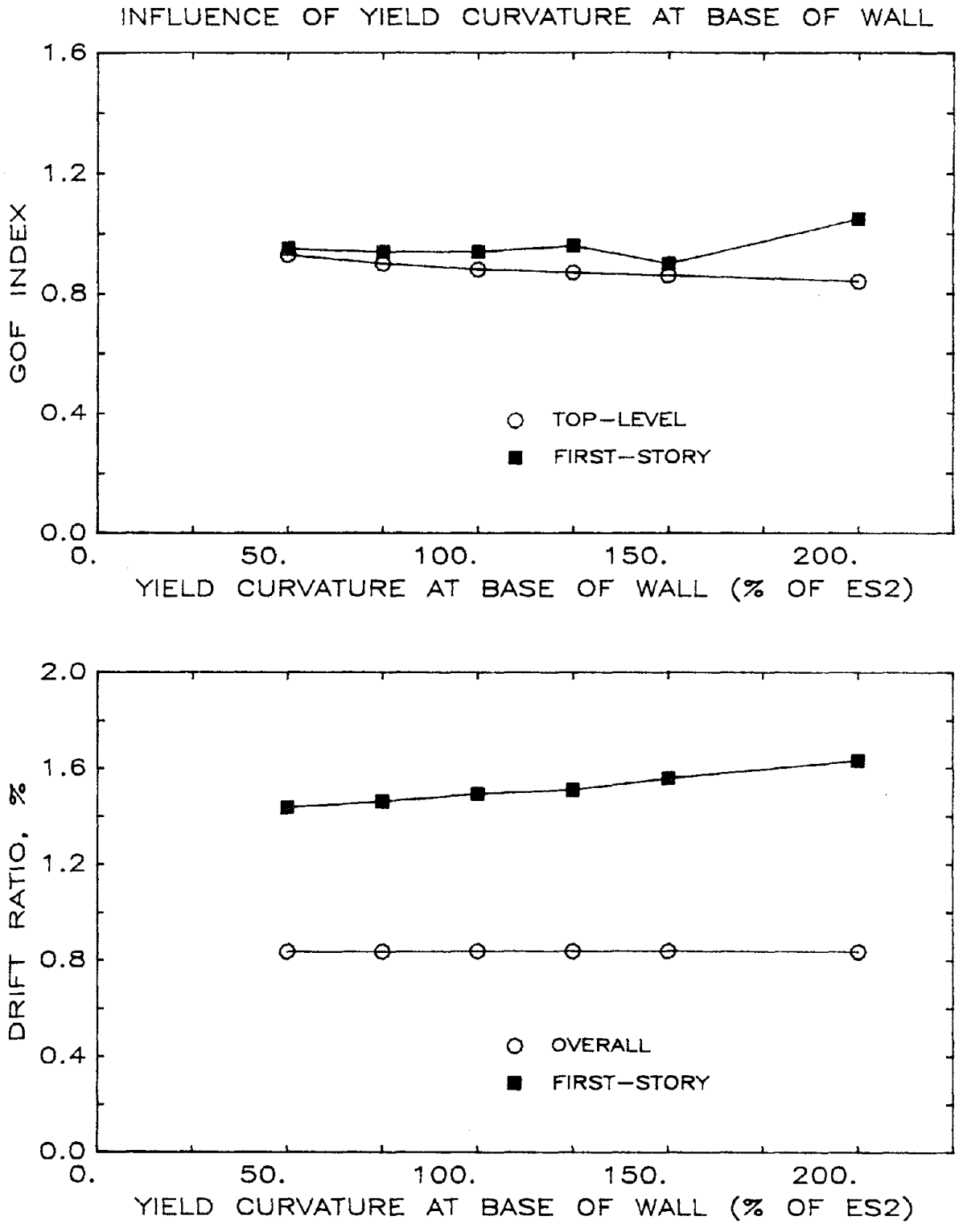

Fig. 6.15 Influence on Calculated Displacement Response of Variations in Yield Curvature at Base of Wall

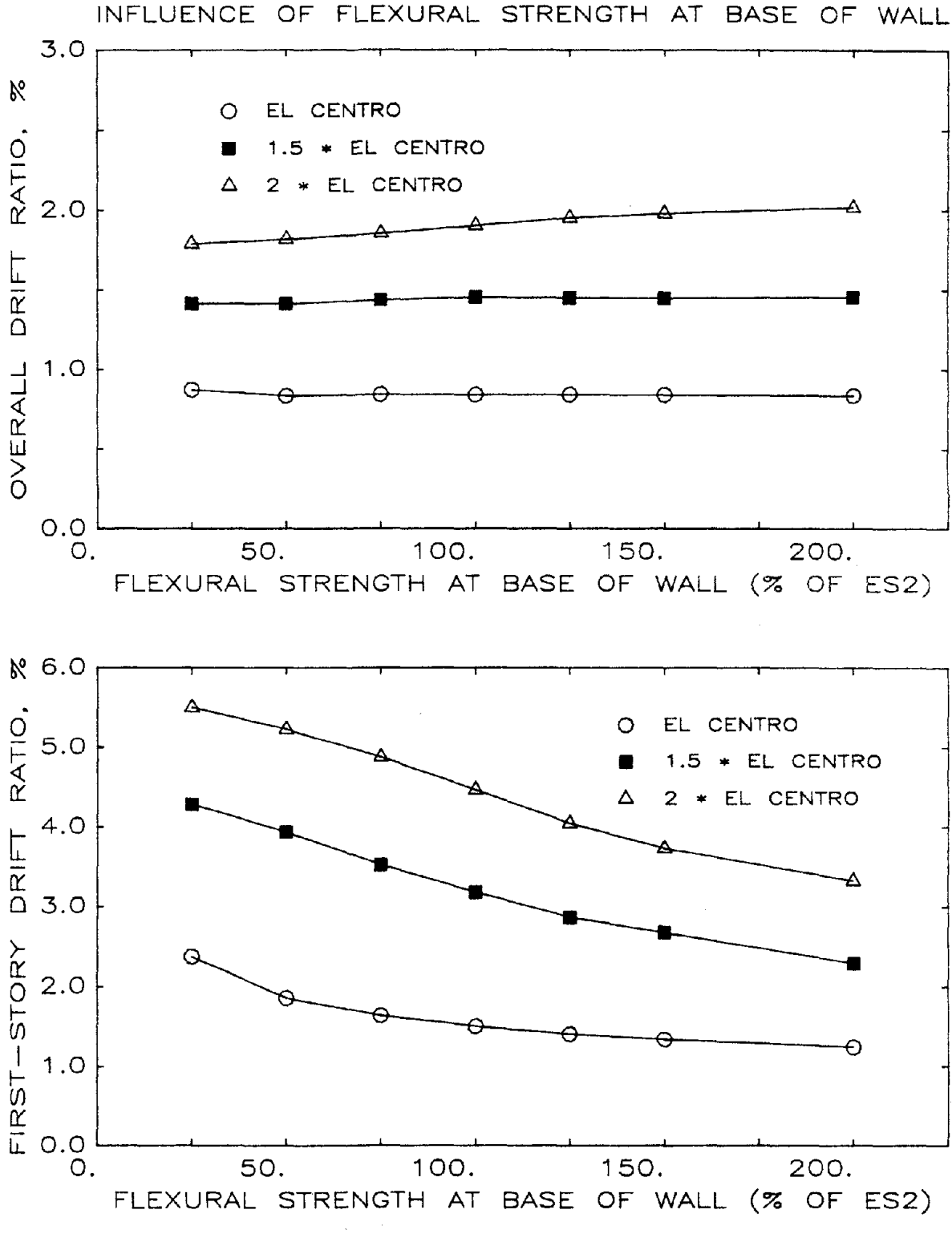

Fig. 6.16 Influence on Drift Maxima of Flexural Strength at Base of Wall

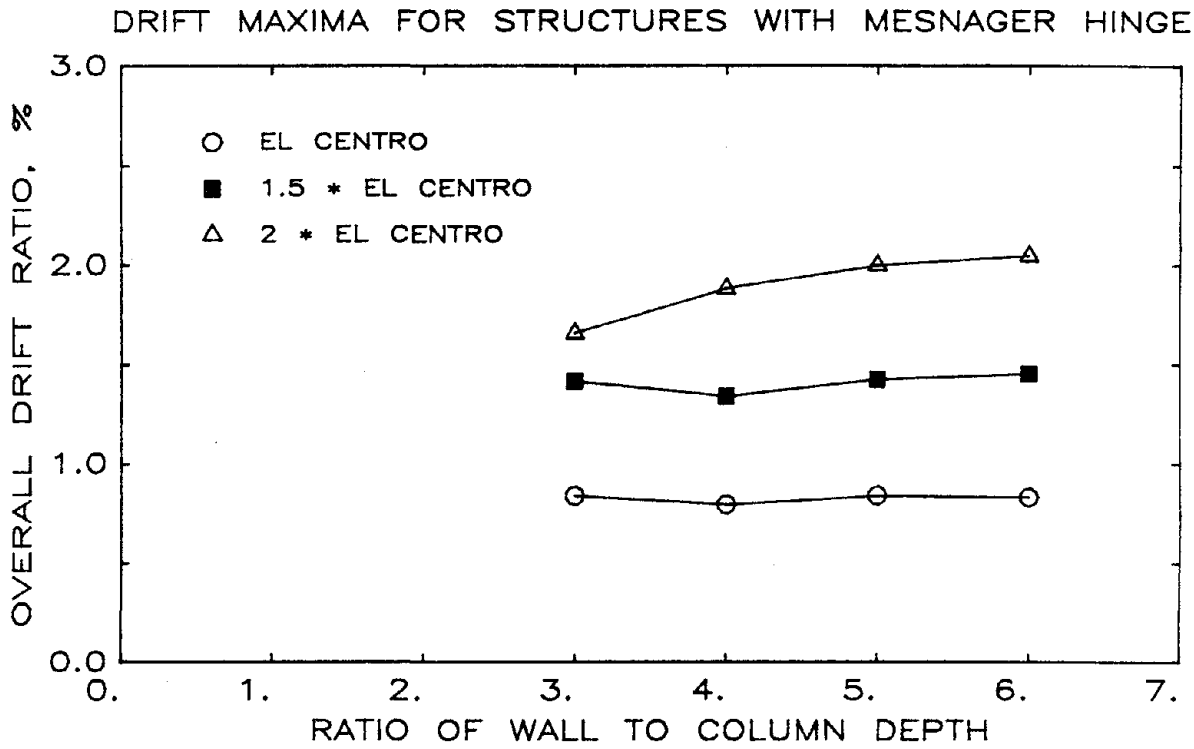

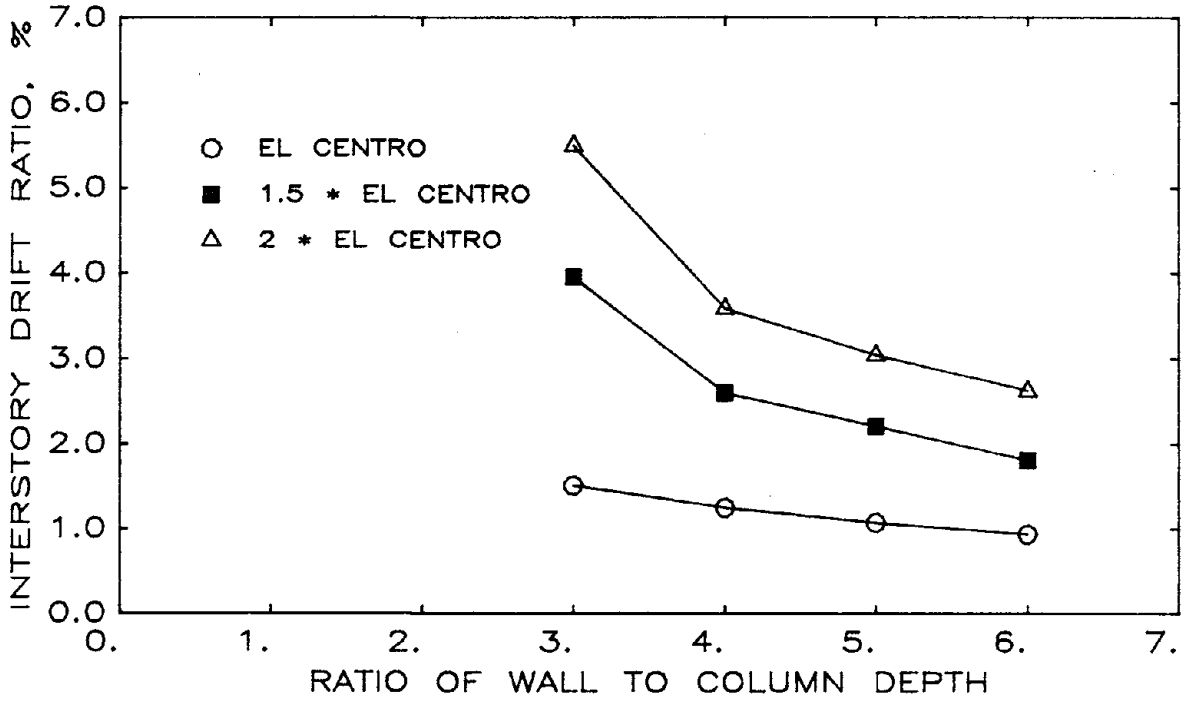

Fig. 6.17 Calculated Drift for Structures with a Mesnager Hinge

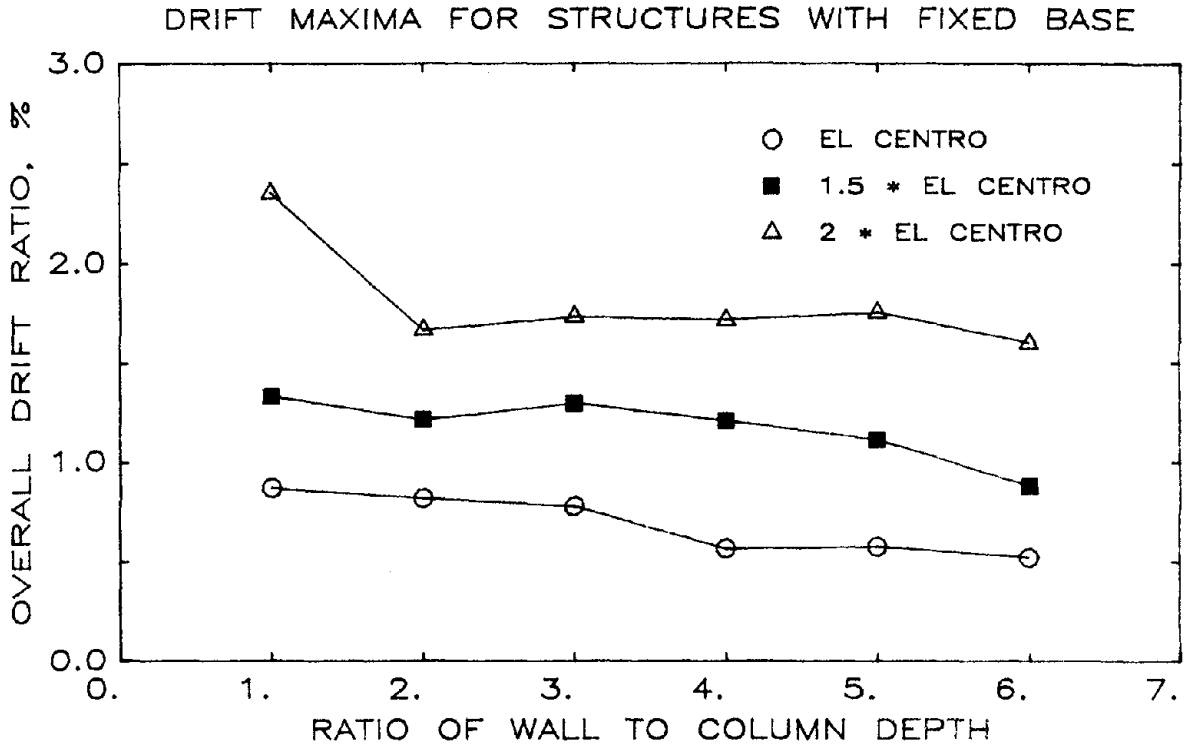

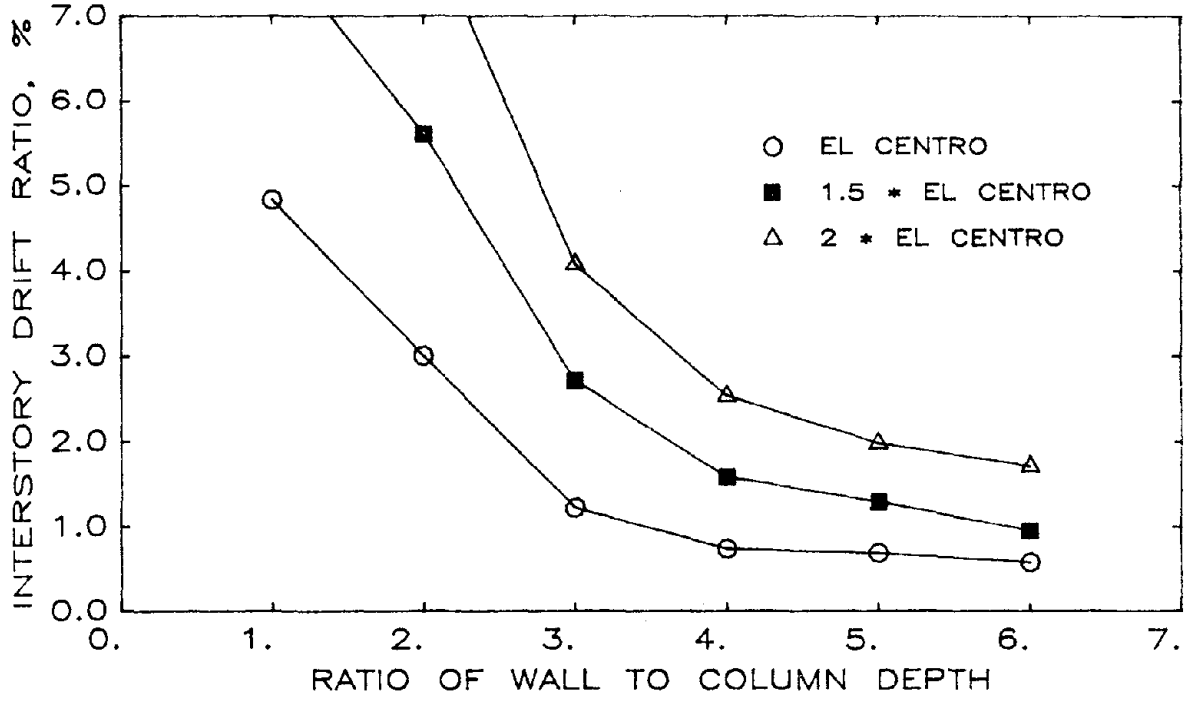

Fig. 6.18 Calculated Drift for Structures without a Mesnager Hinge

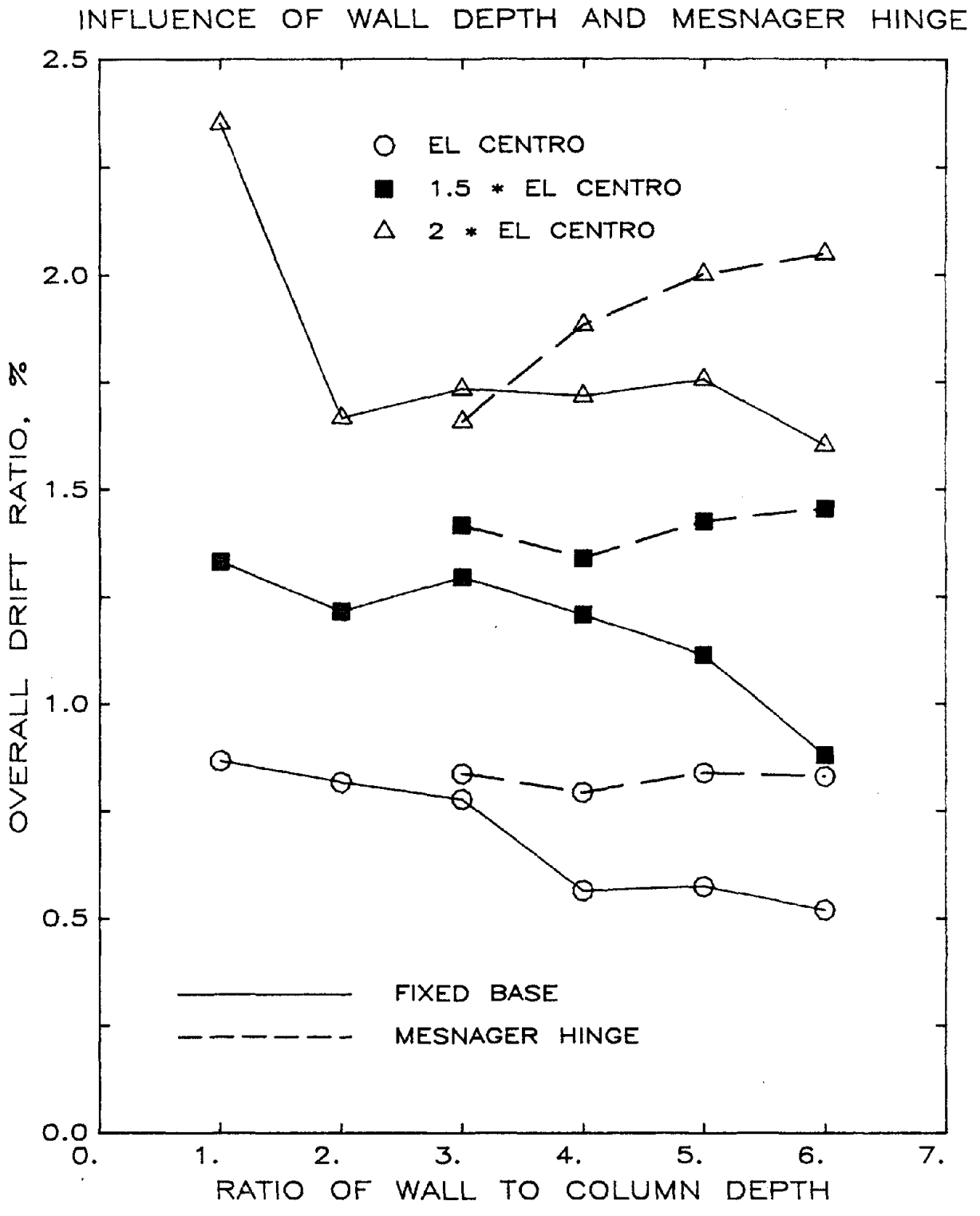

Fig. 6.19 Influence on Overall Drift Ratio of Wall Depth and Mesnager Hinge

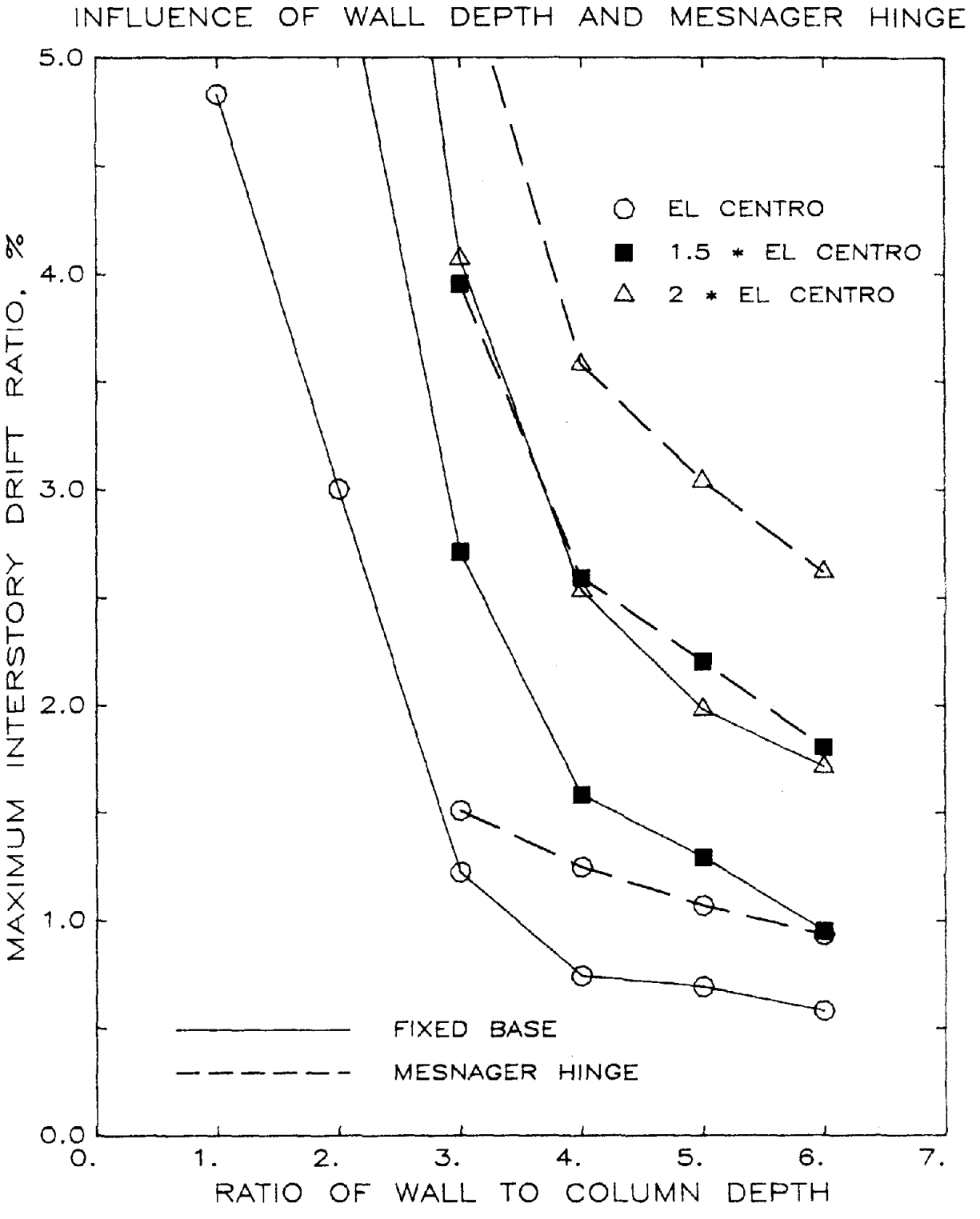

Fig. 6.20 Influence on Maximum Interstory Drift Ratio of Wall Depth and Mesnager Hinge

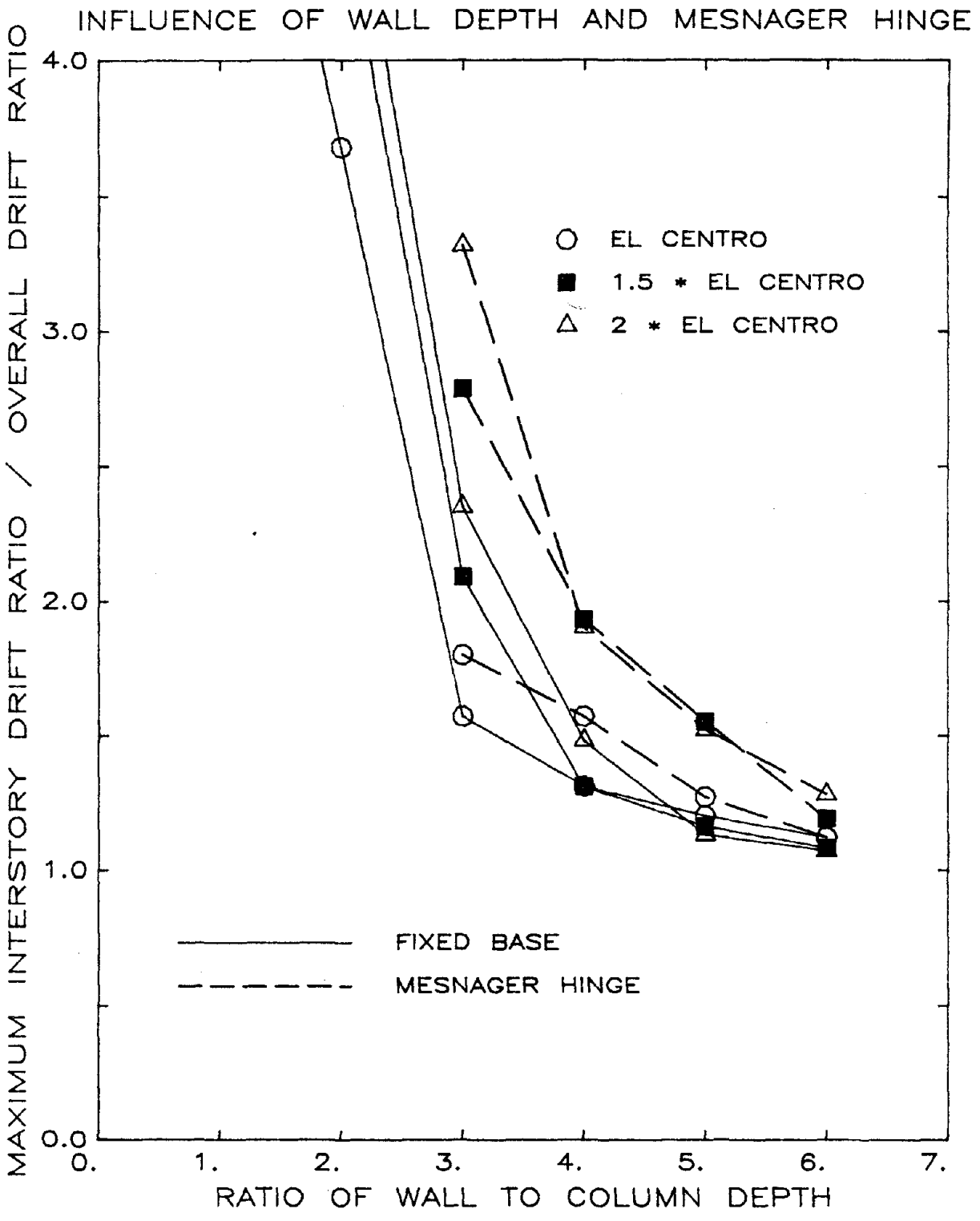

Fig. 6.21 Influence on Drift Concentration of Wall Depth and Mesnager Hinge

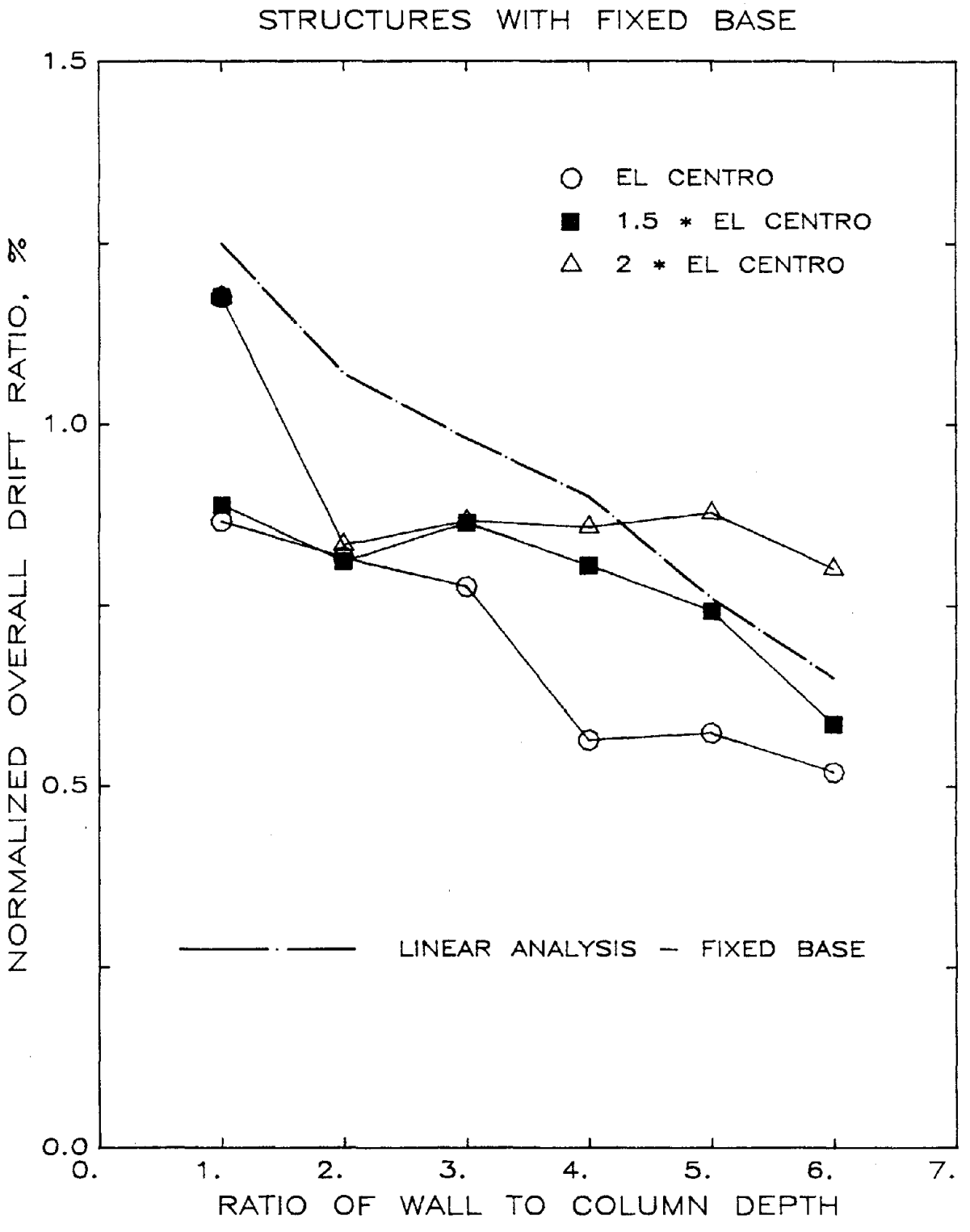

Fig. 6.22 Overall Drift Ratios Calculated by Linear and Nonlinear Analysis
(a) Structures without a Mesnager Hinge

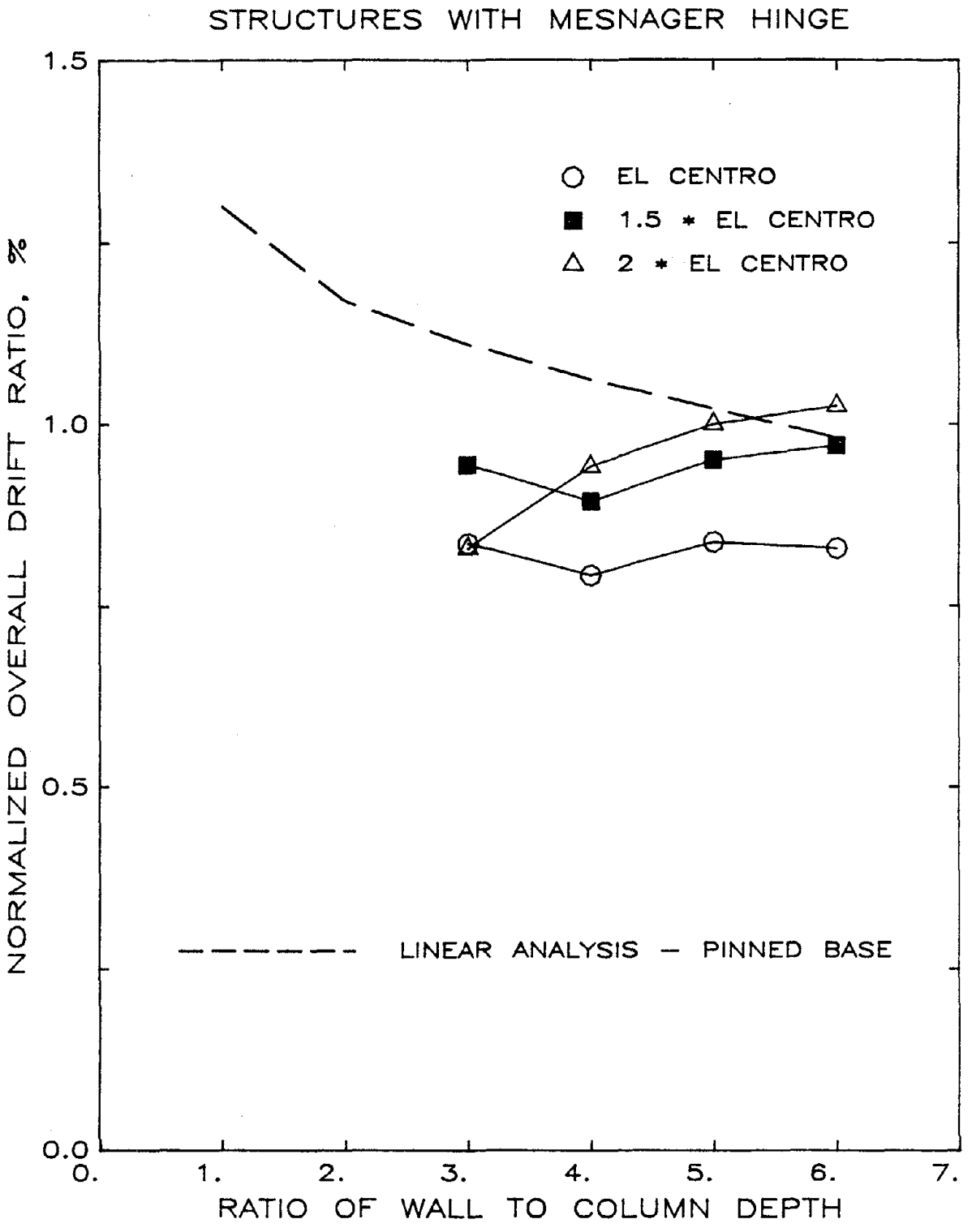

Fig. 6.22 (cont.) Overall Drift Ratios Calculated by Linear and Nonlinear Analysis
(b) Structures with a Mesnager Hinge

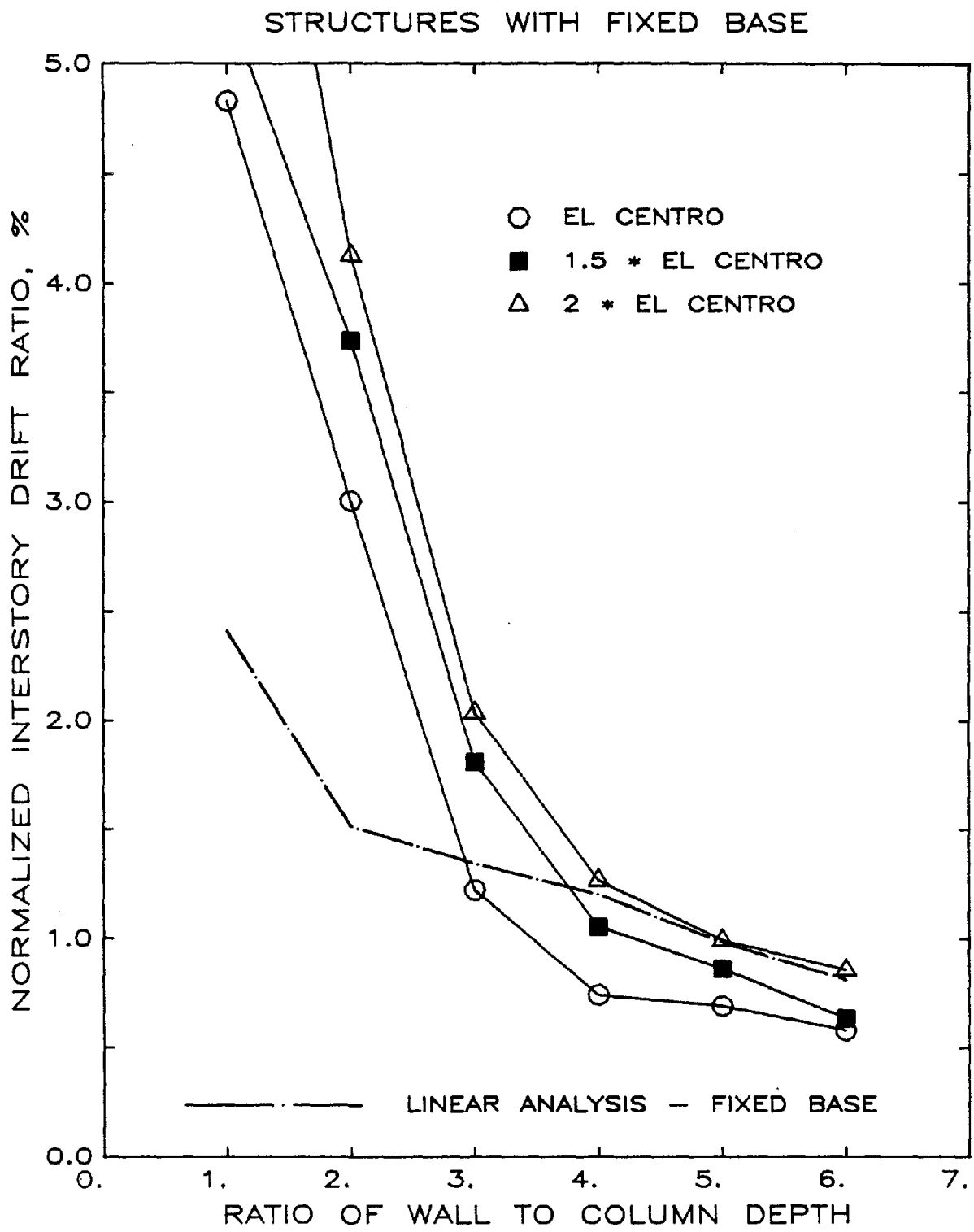

Fig. 6.23 Interstory Drift Ratios Calculated by Linear and Nonlinear Analysis
(a) Structures without a Mesnager Hinge

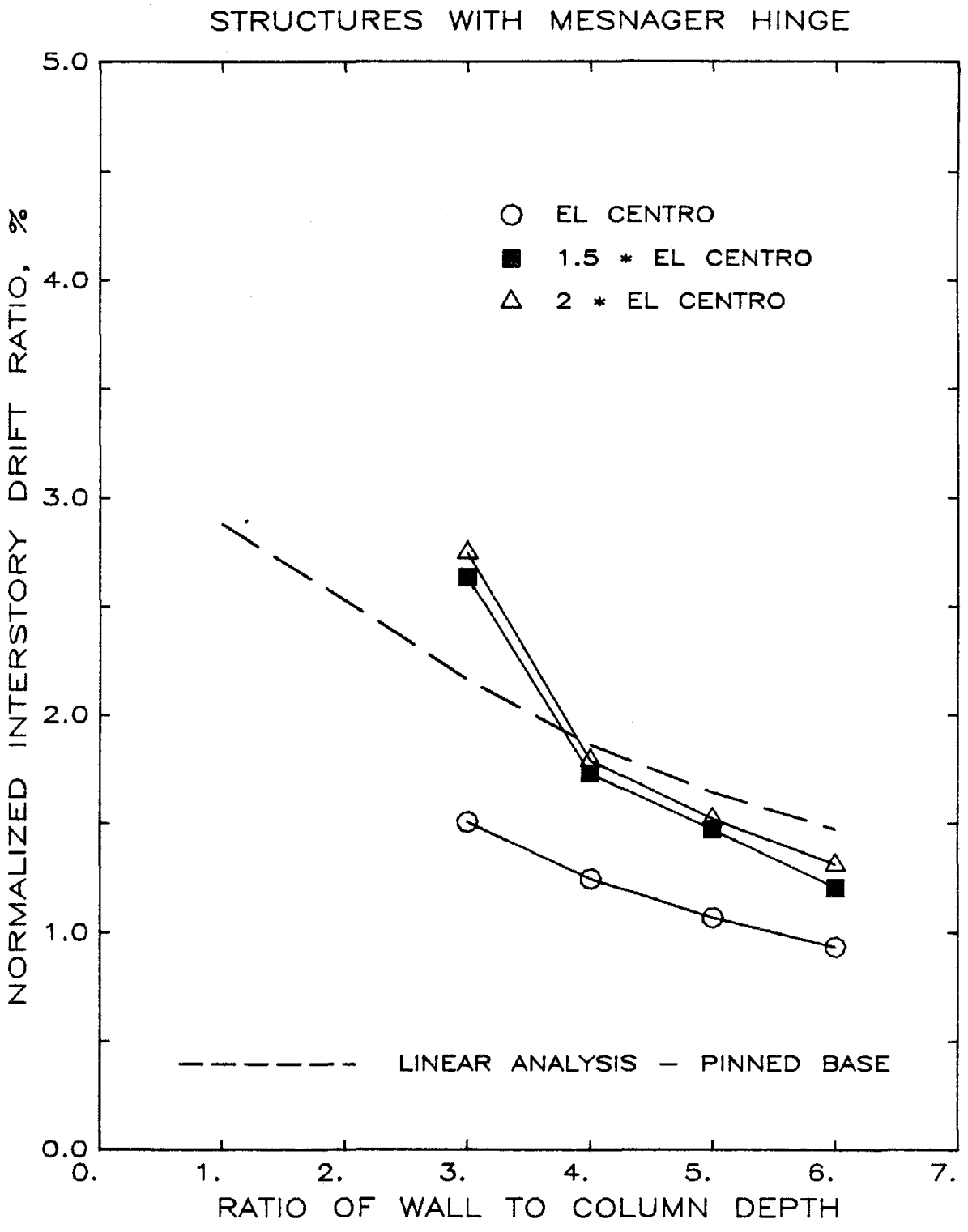

Fig. 6.23 (cont.) Interstory Drift Ratios Calculated by Linear and Nonlinear Analysis
(b) Structures with a Mesnager Hinge

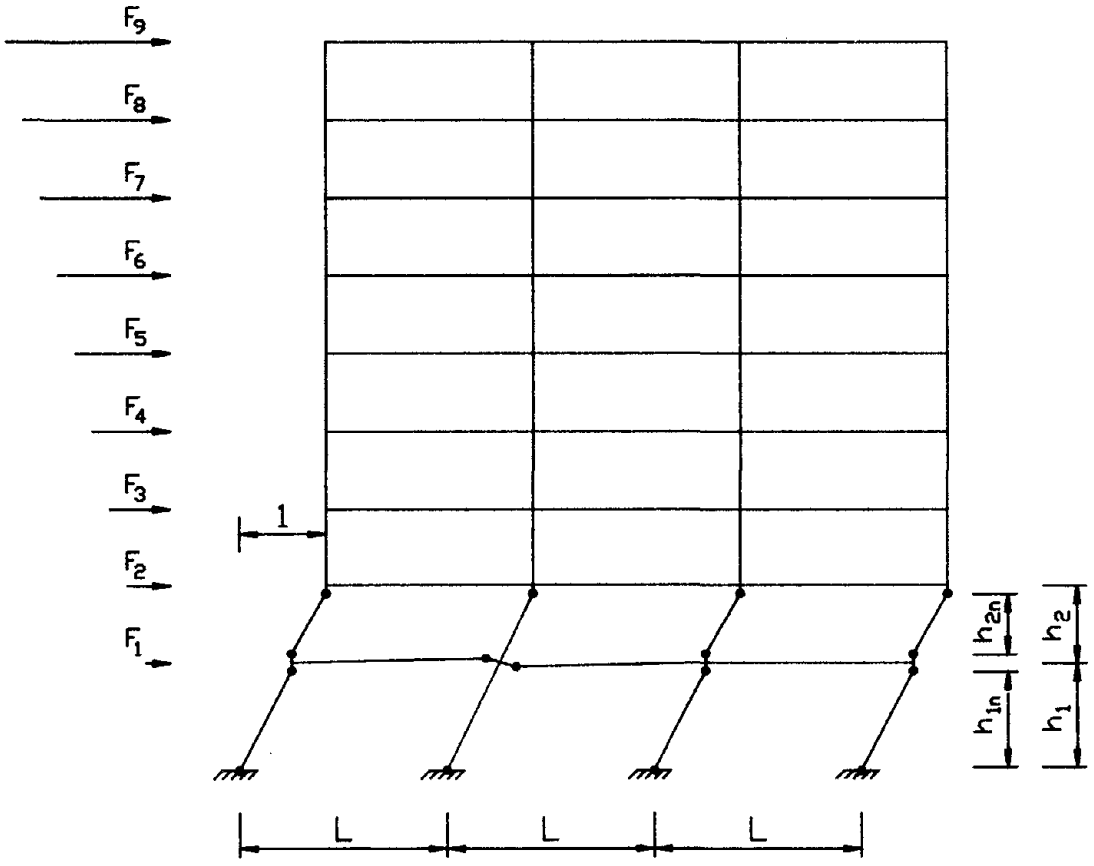

Fig. 6.24 Two-Story Collapse Mechanism for a Frame-Wall Structure with Yielding Columns

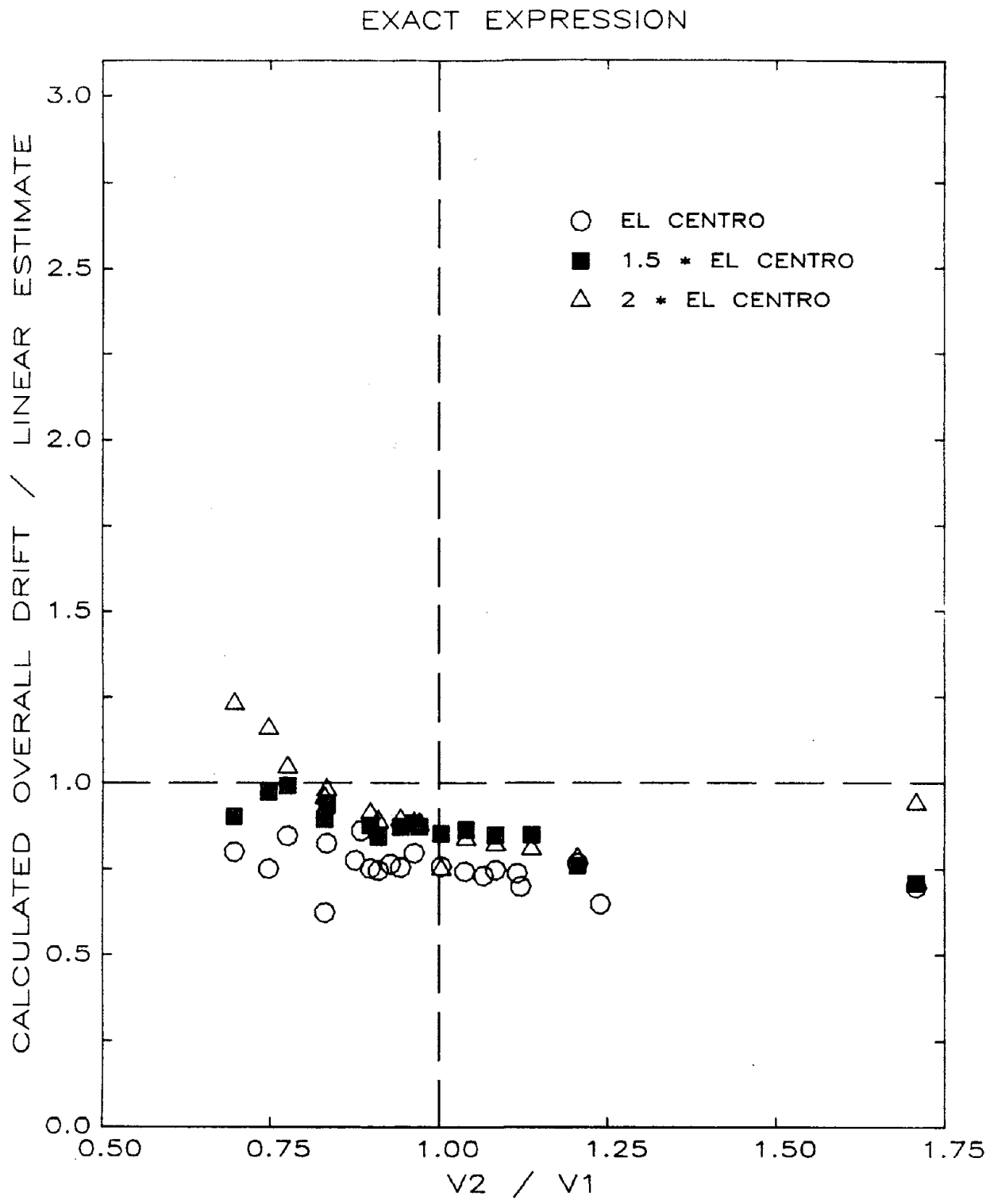

Fig. 6.25 Correlation Between the Conservatism of Drift Estimates Calculated by Linear Analysis and V2/V1 Calculated by Limit Analysis
(a) Overall Drift

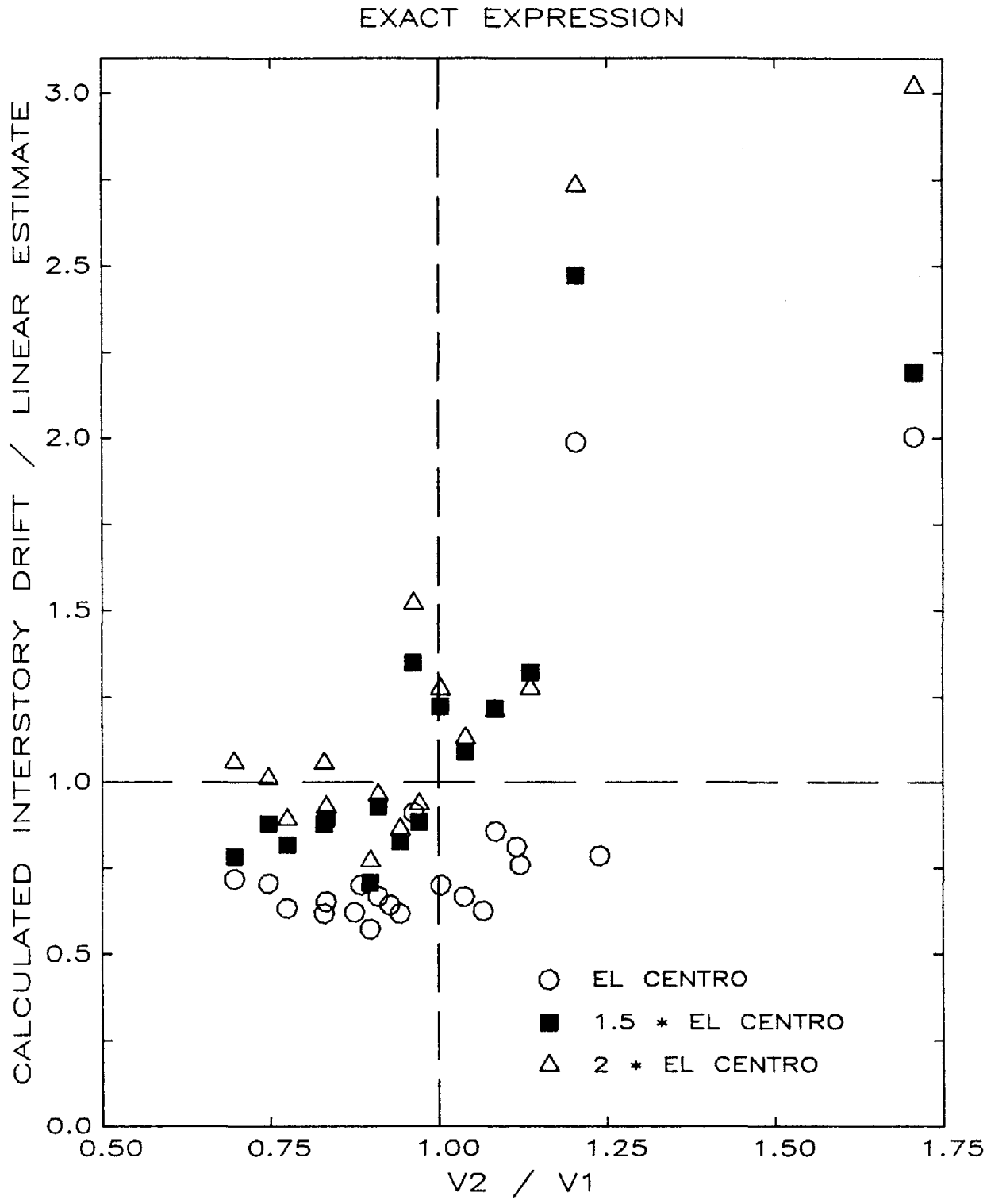

Fig. 6.25 (cont.) Correlation Between the Conservatism of Drift Estimates Calculated by Linear Analysis and V2/V1 Calculated by Limit Analysis
(b) Maximum Interstory Drift

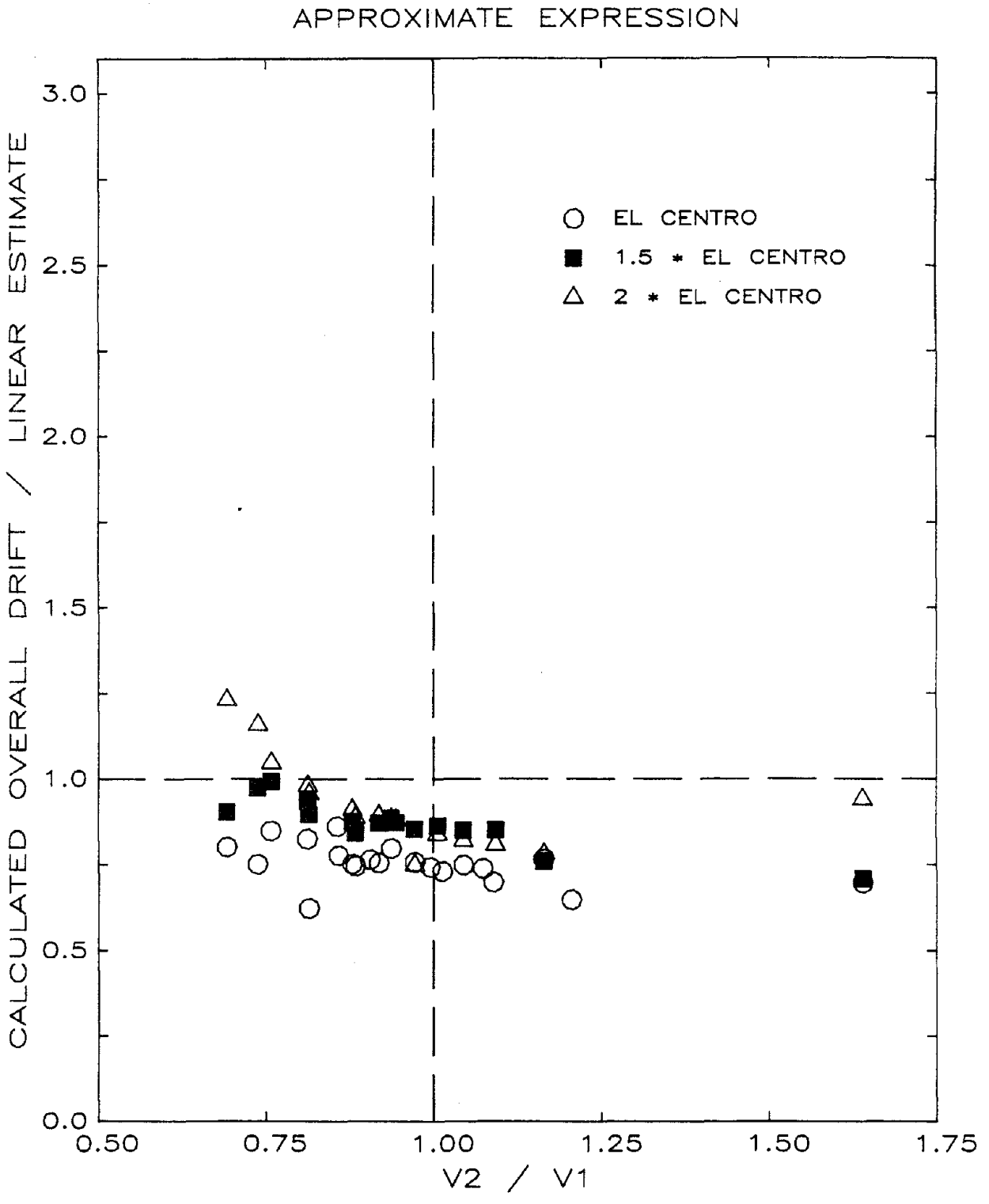

Fig. 6.26 Correlation Between the Conservatism of Drift Estimates Calculated by Linear Analysis and V2/V1 Calculated by an Approximate Expression (Eq. 6.18)
(a) Overall Drift

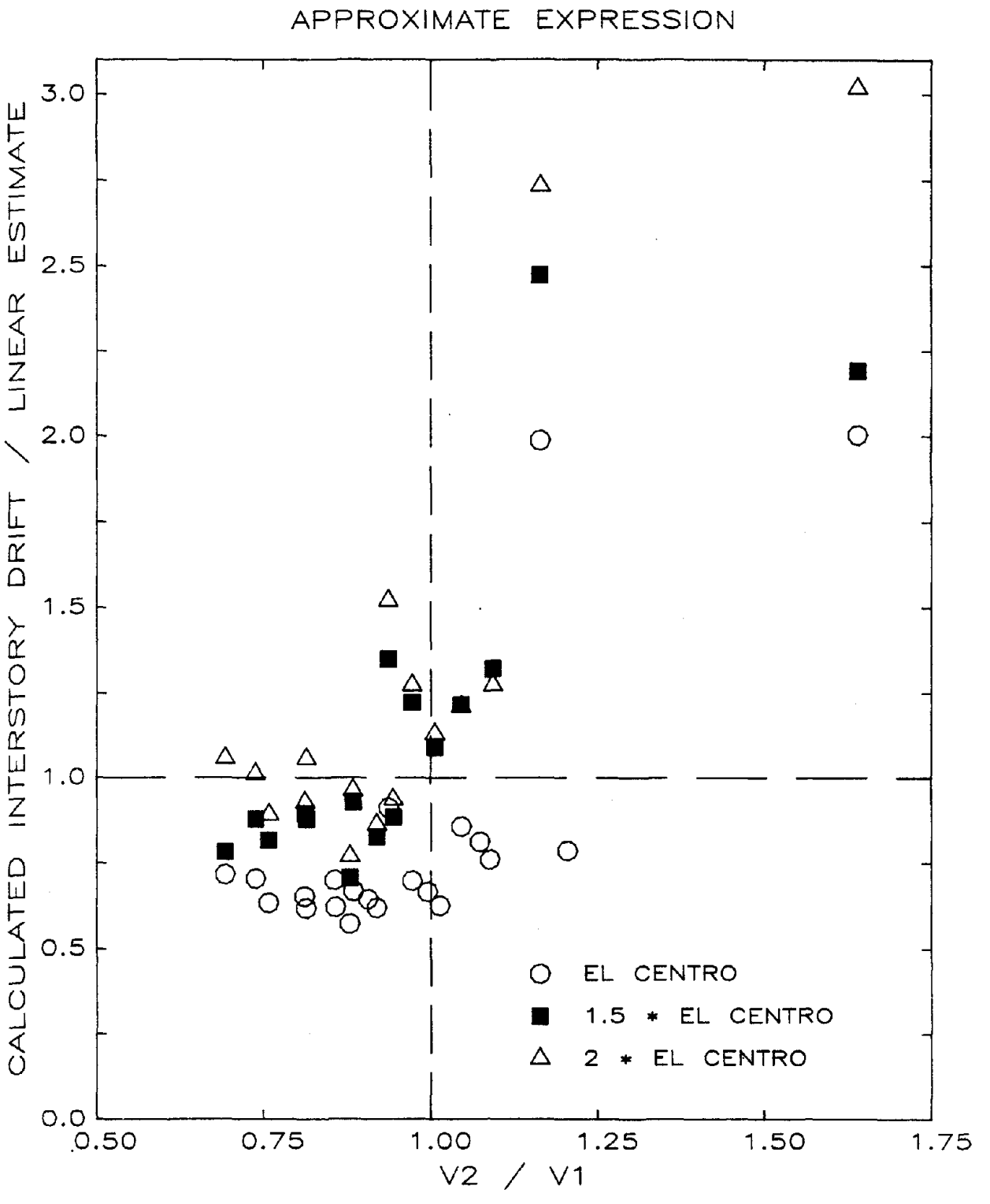

Fig. 6.26 (cont.) Correlation Between the Conservatism of Drift Estimates Calculated by Linear Analysis and V2/V1 Calculated by an Approximate Expression (Eq. 6.18)
(b) Interstory Drift

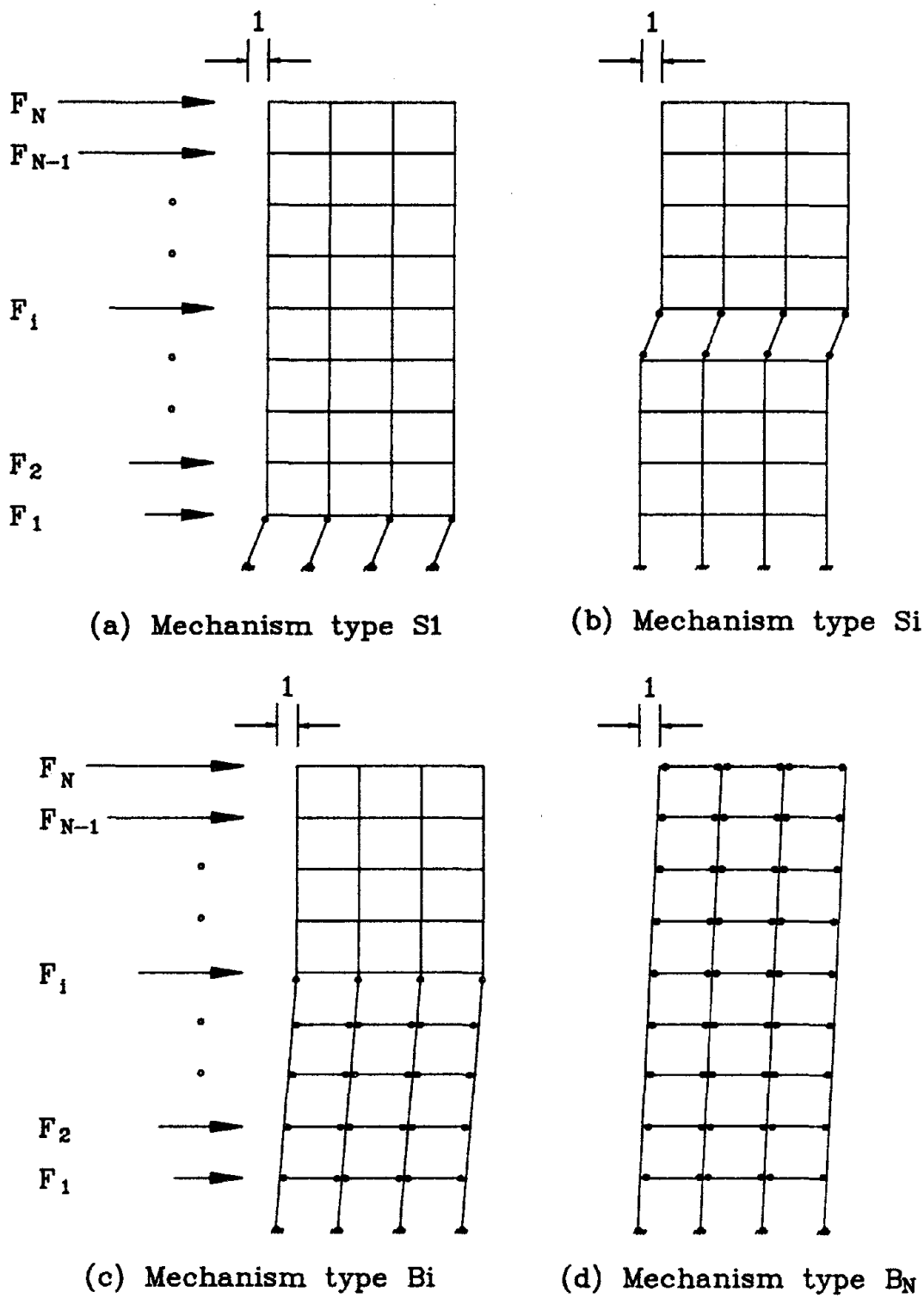

Fig. 7.1 Collapse Mechanisms

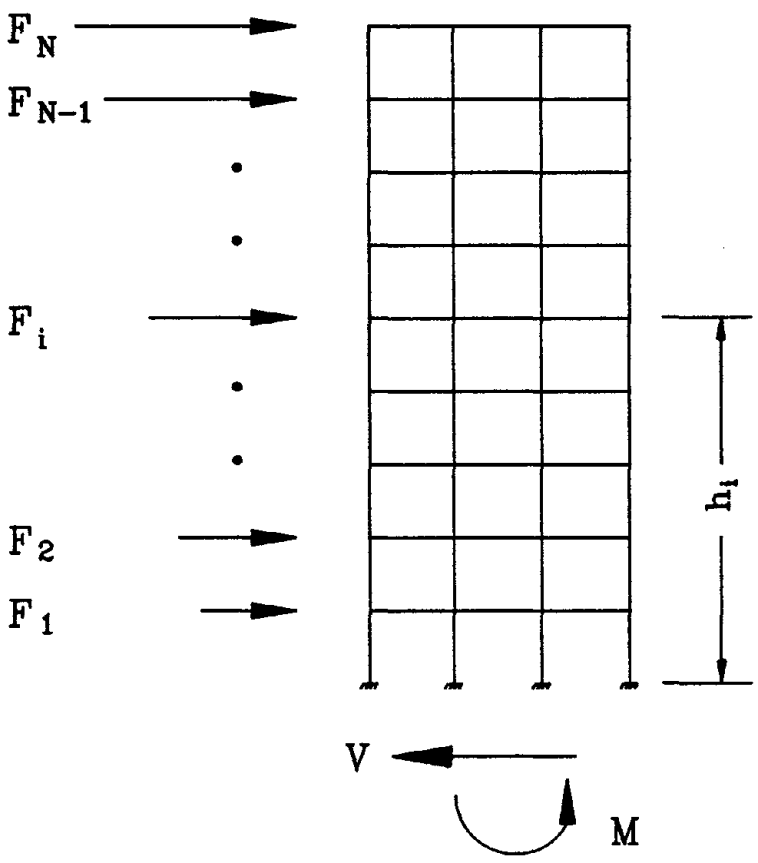

$$V = \text{Base Shear} = \sum_{i=1}^{N} F_i$$

$$M = \text{Base moment} = \sum_{i=1}^{N} F_i * h_i$$

Fig. 7.2 Definition of Base Shear and Base Moment

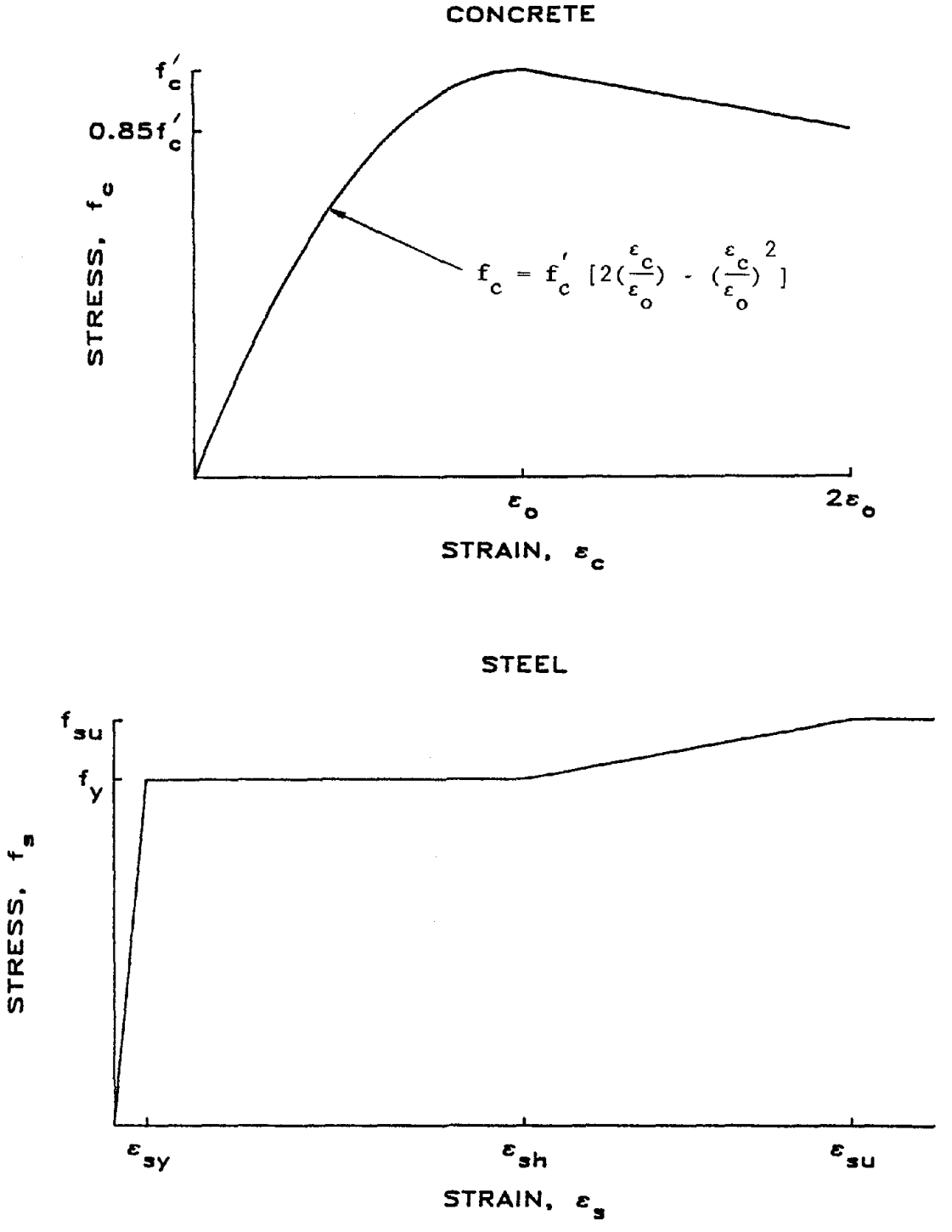

Fig. 7.3 Assumed Stress-Strain Relations for Concrete and Steel

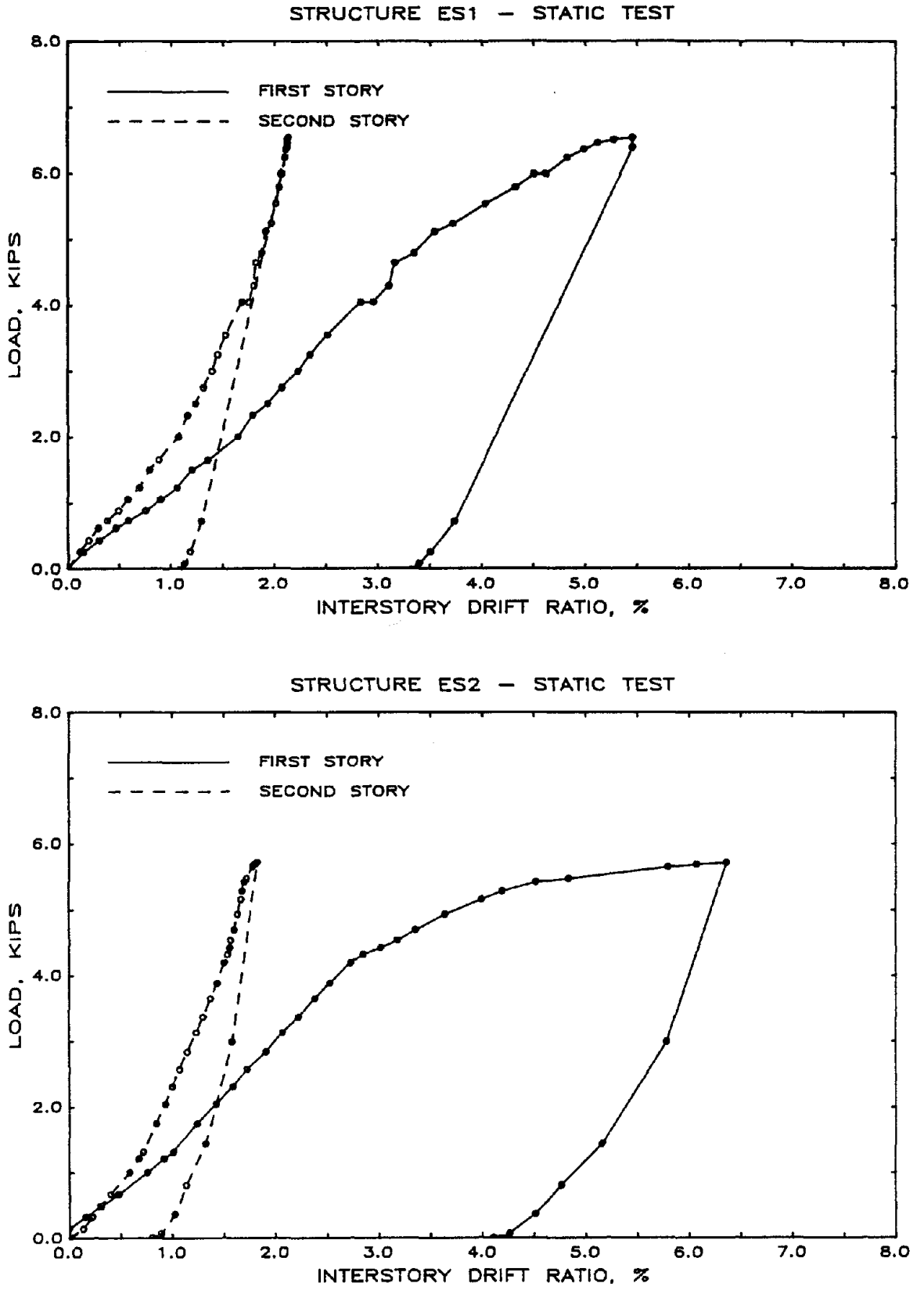

Fig. 7.4 Story Hysteresis During Static Tests

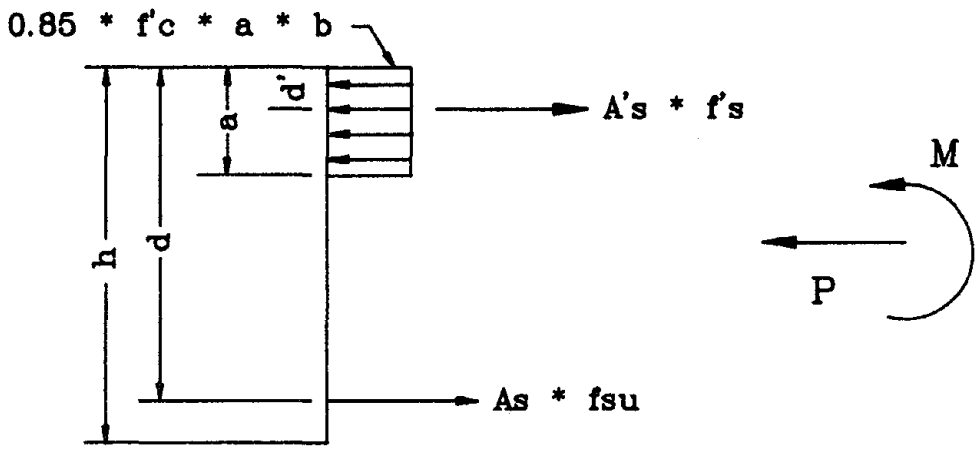

$$a = \text{Depth of compression block}$$

$$= \frac{P + As * fsu + As' * fs'}{.85 * f'c * b}$$

$$M = \text{Nominal flexural strength}$$

$$= [0.85 * f'c * a * b]\,[h/2 - a/2]$$
$$+ [As * fsu]\,[d - h/2]$$
$$- [A's * f's]\,[h/2 - d'\}$$

Fig. 7.5 Calculation of Upper-Bound Flexural Strength

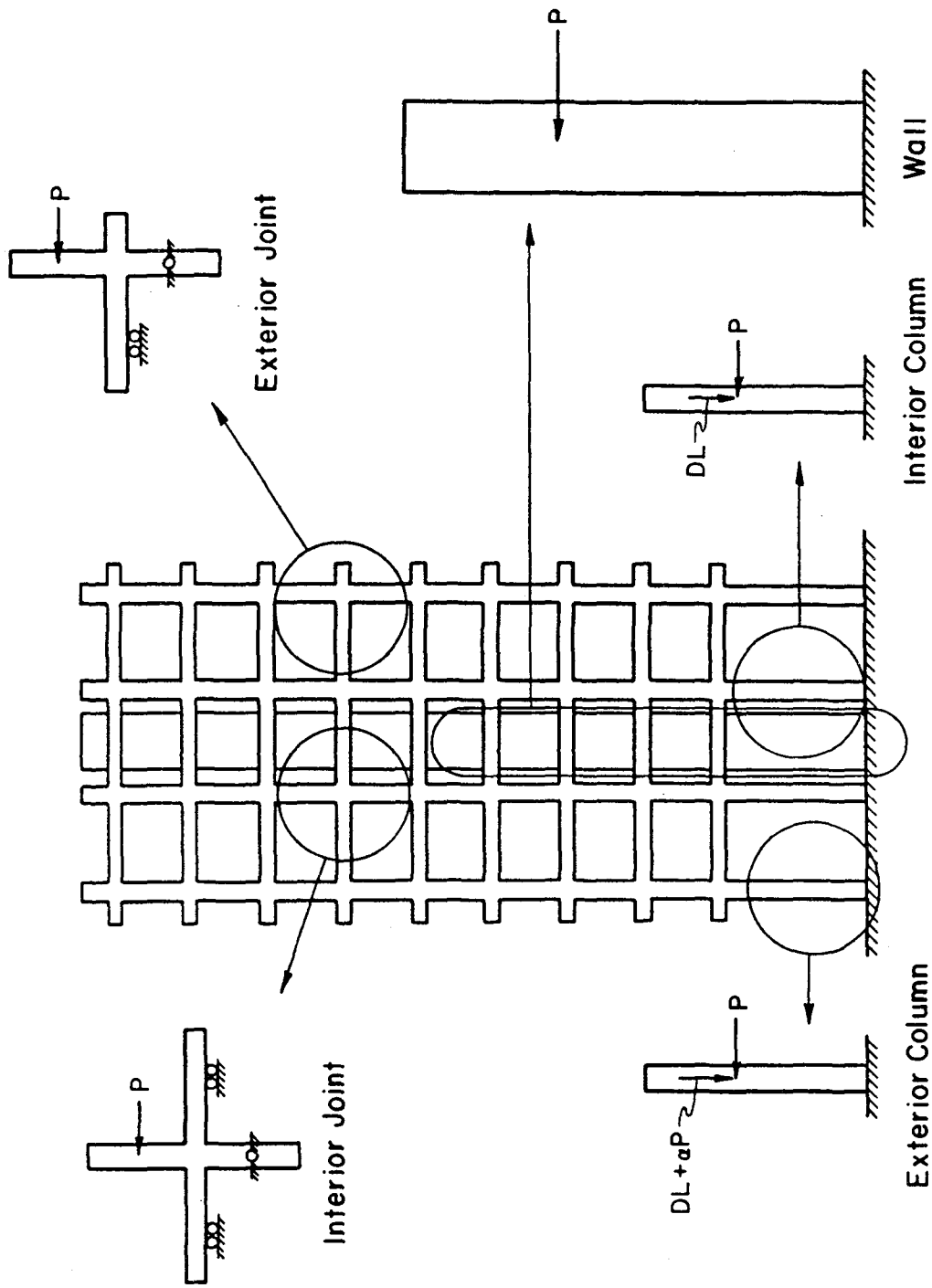

Fig. 7.6 Correspondence Between Test Structures and Components

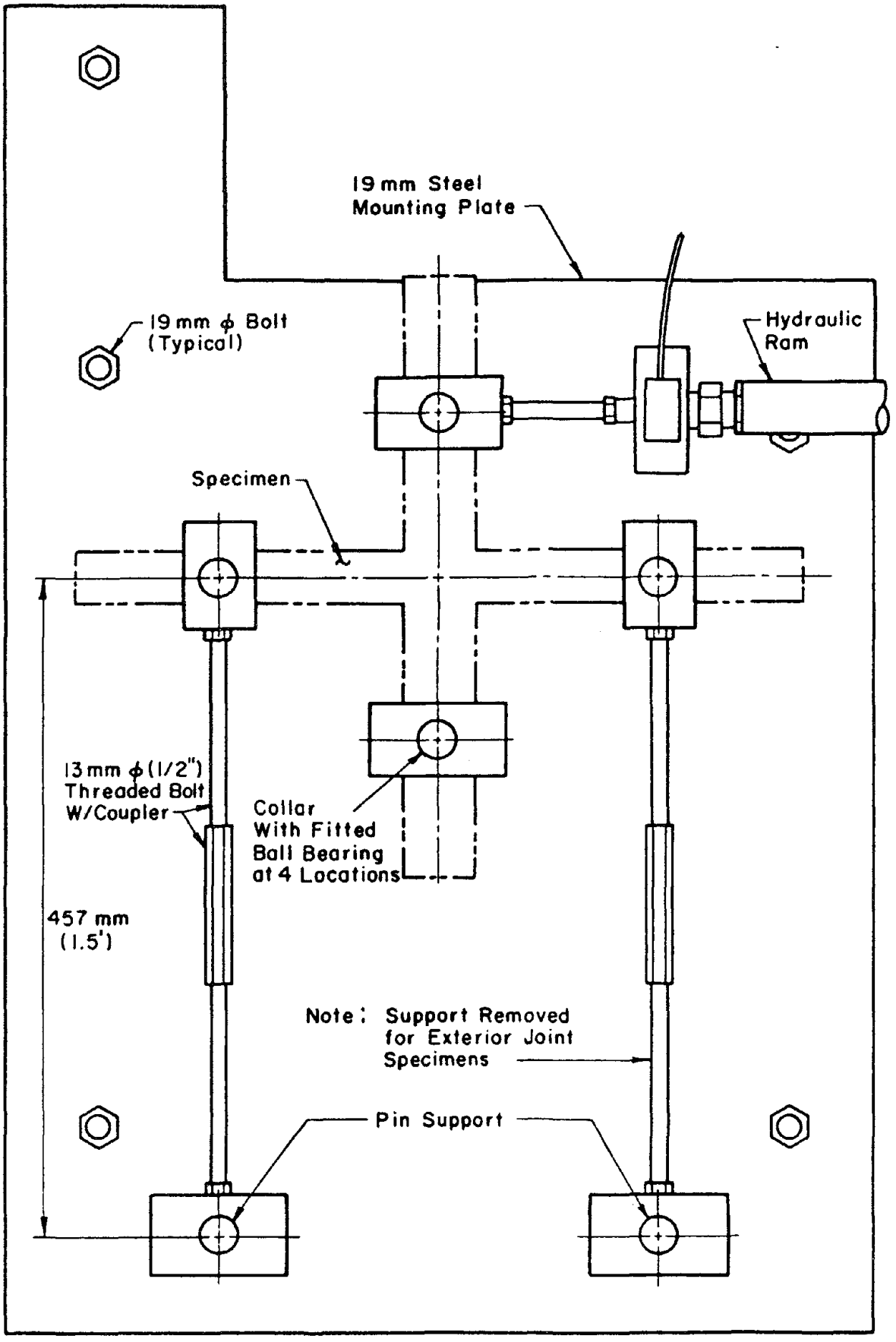

Fig. 7.7 Setup for Kreger and Abrams Tests [19]

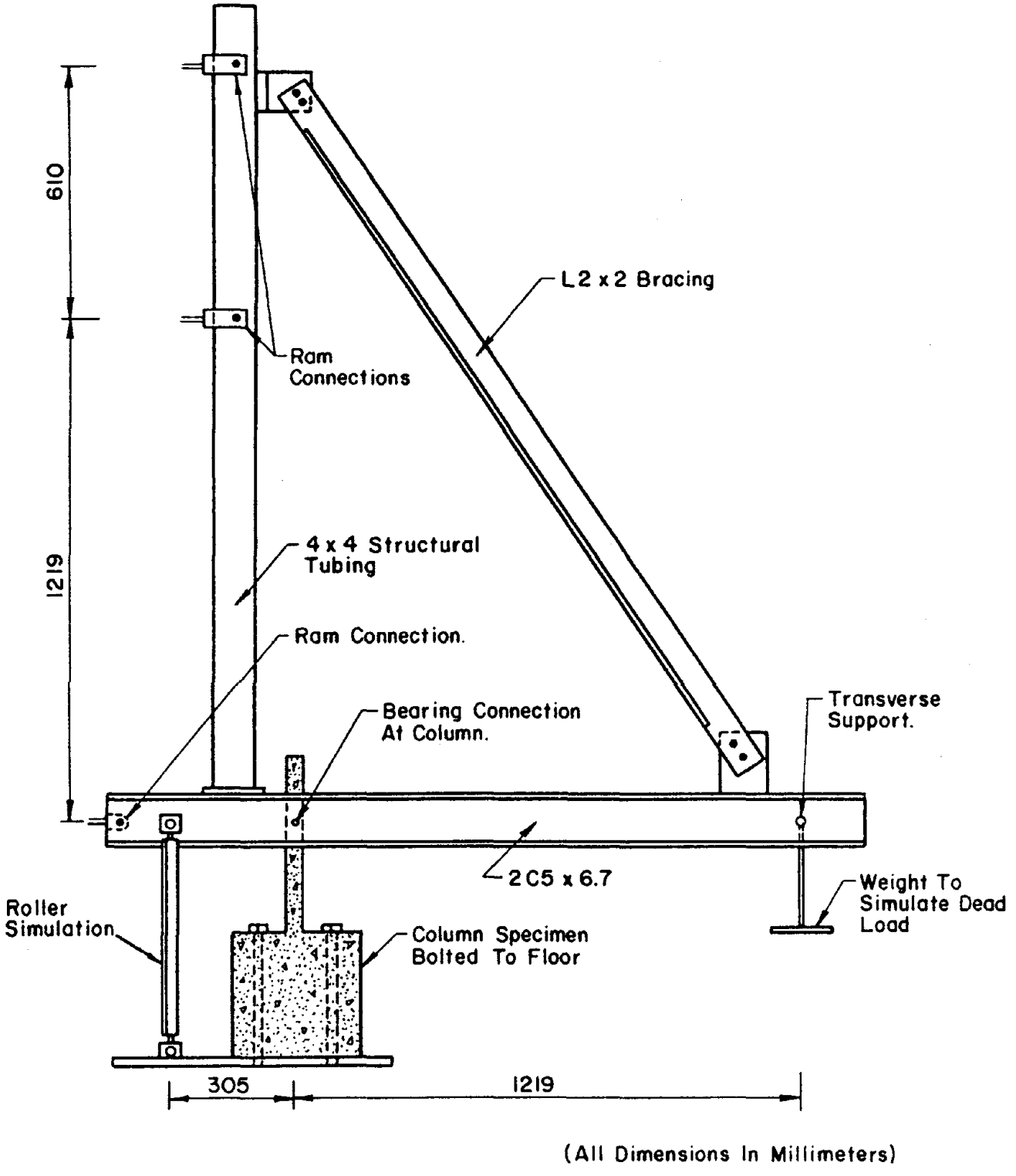

Fig. 7.8 Test Setup for Gilbertsen and Moehle Tests [13]

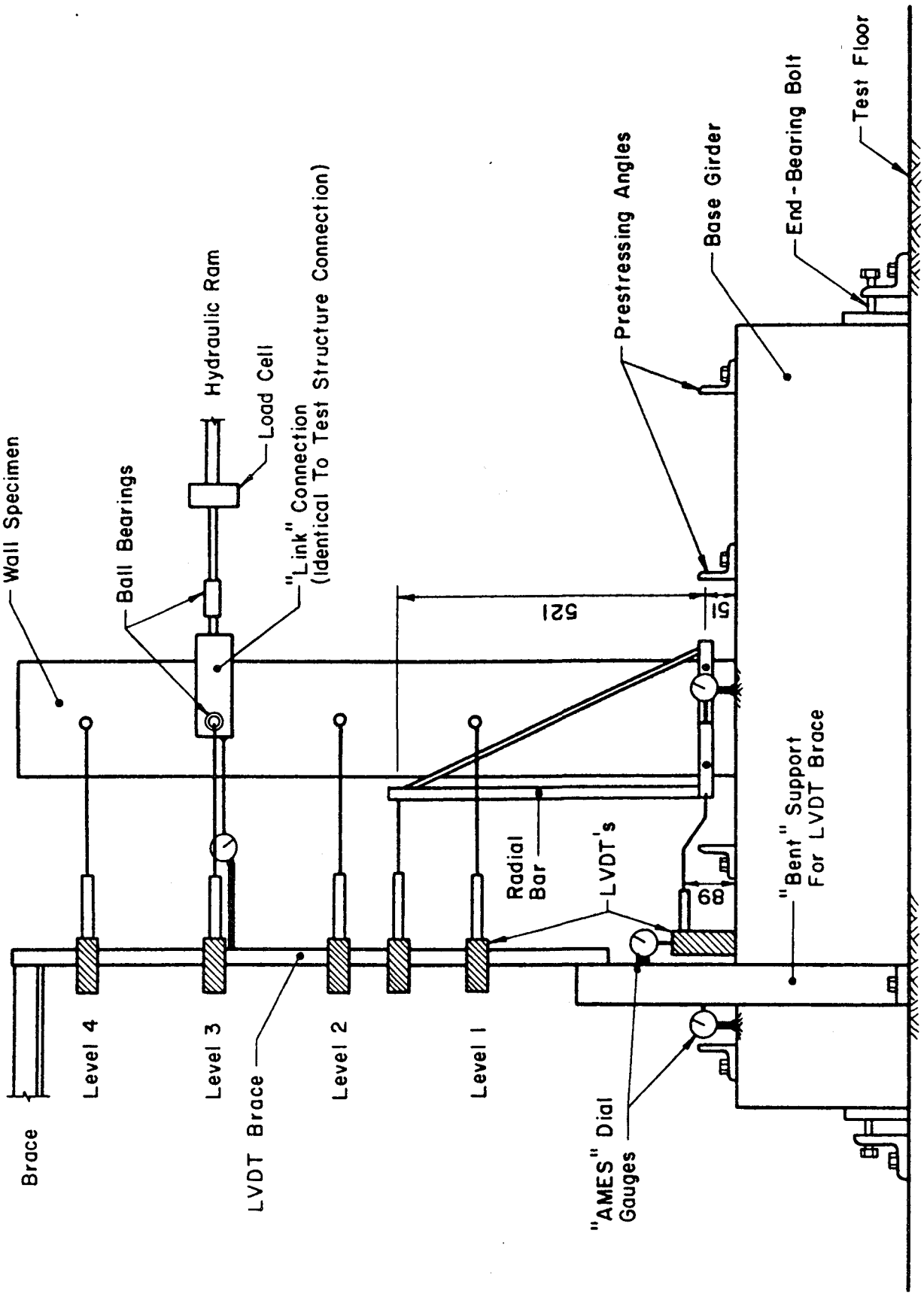

Fig. 7.9 Test Setup for Moehle Tests [24]

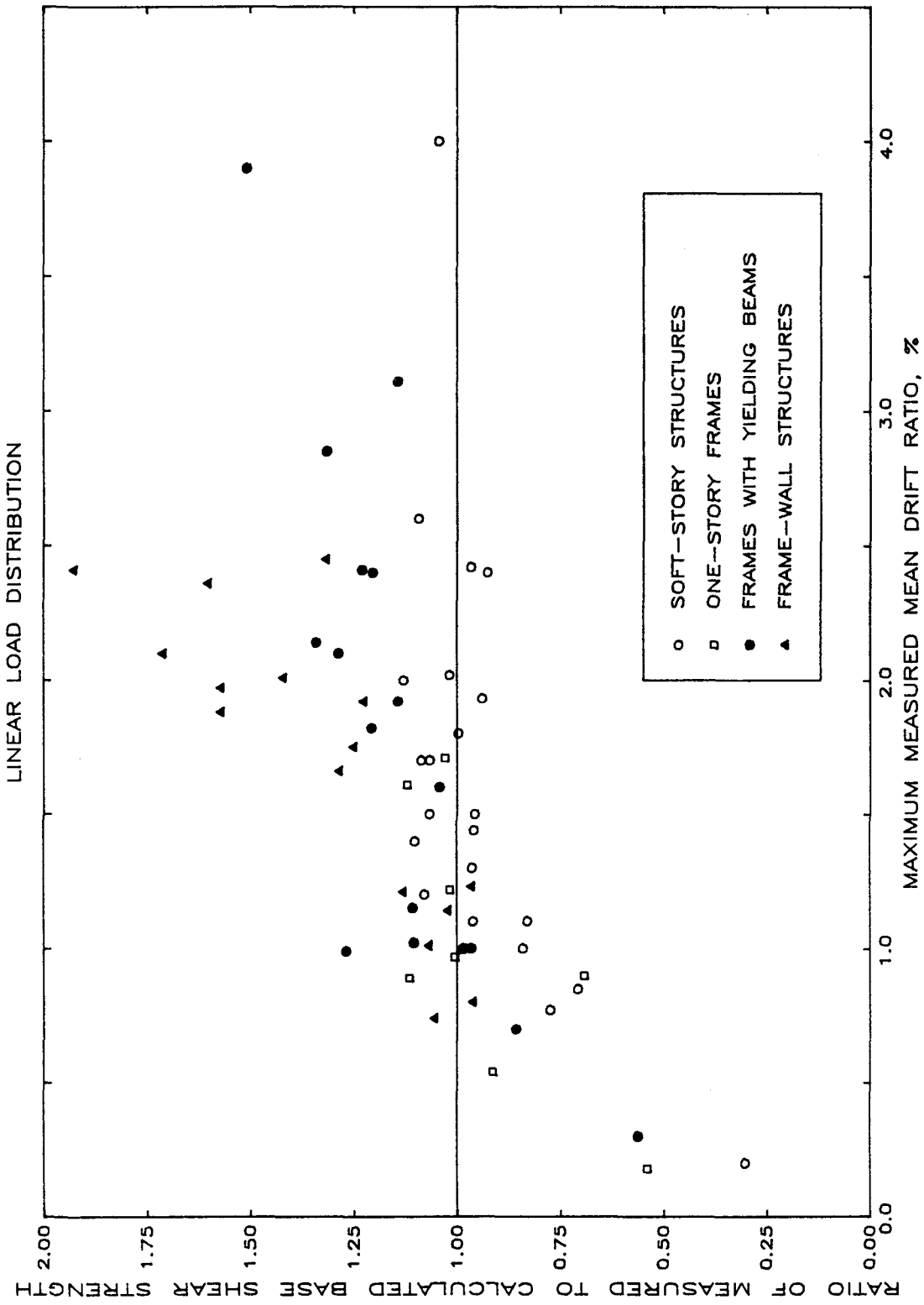

Fig. 7.10 Ratio of Measured Base Shear to Base-Shear Strength Calculated Assuming a Linear Load Distribution

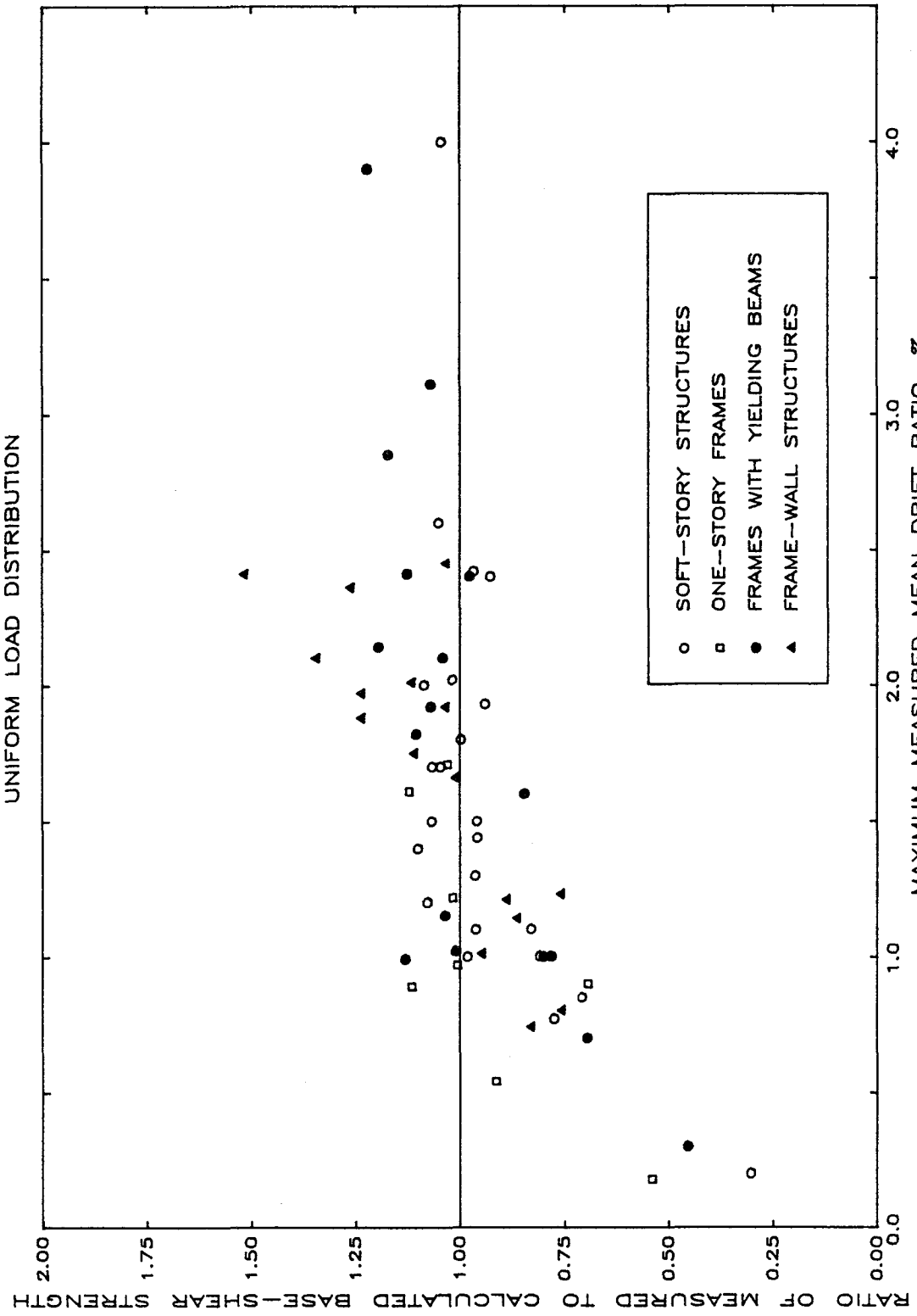

Fig. 7.11 Ratio of Measured Base Shear to Base-Shear Strength Calculated Assuming a Uniform Load Distribution

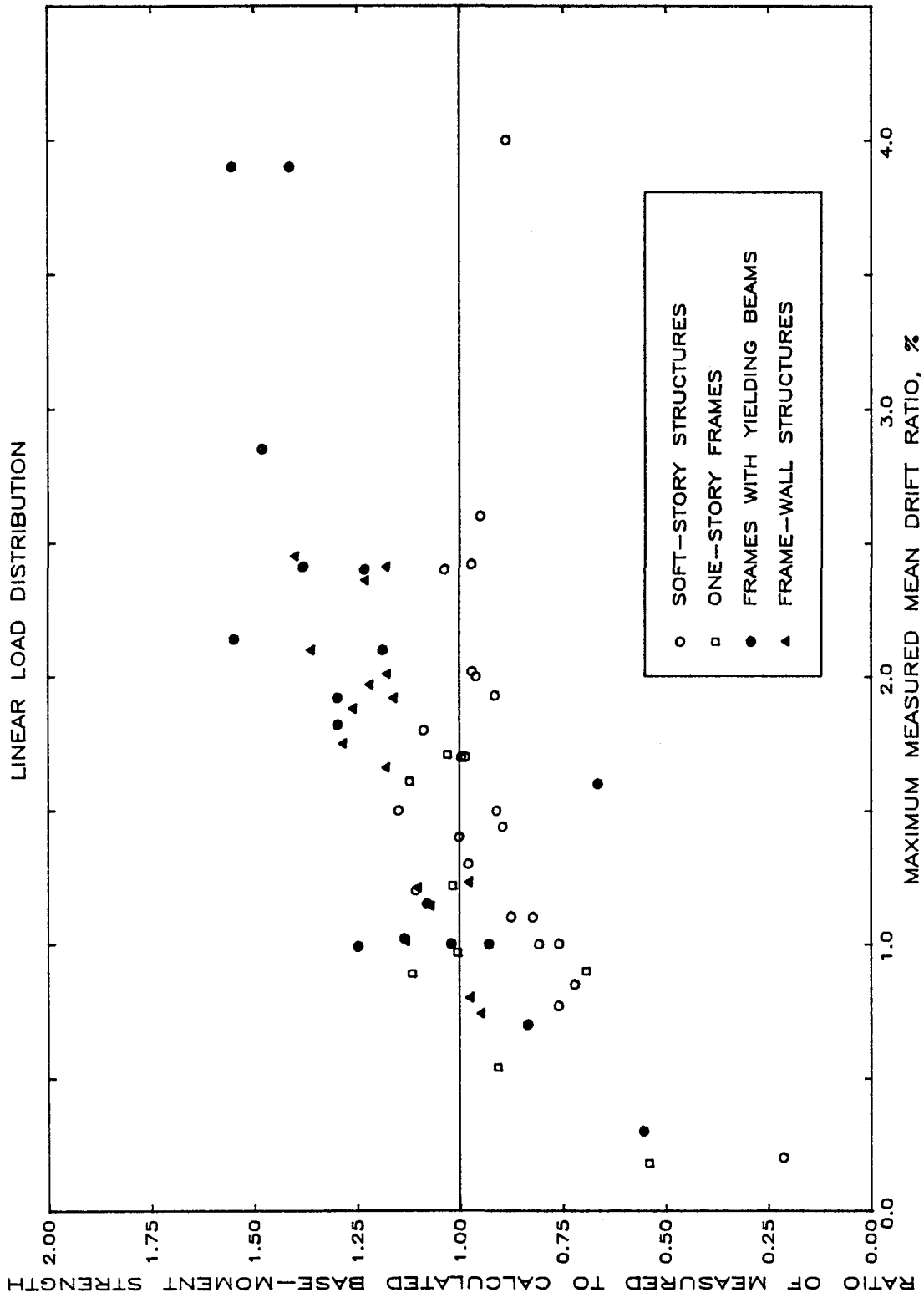

Fig. 7.12 Ratio of Measured Base Moment to Base-Moment Strength Calculated Assuming a Linear Load Distribution

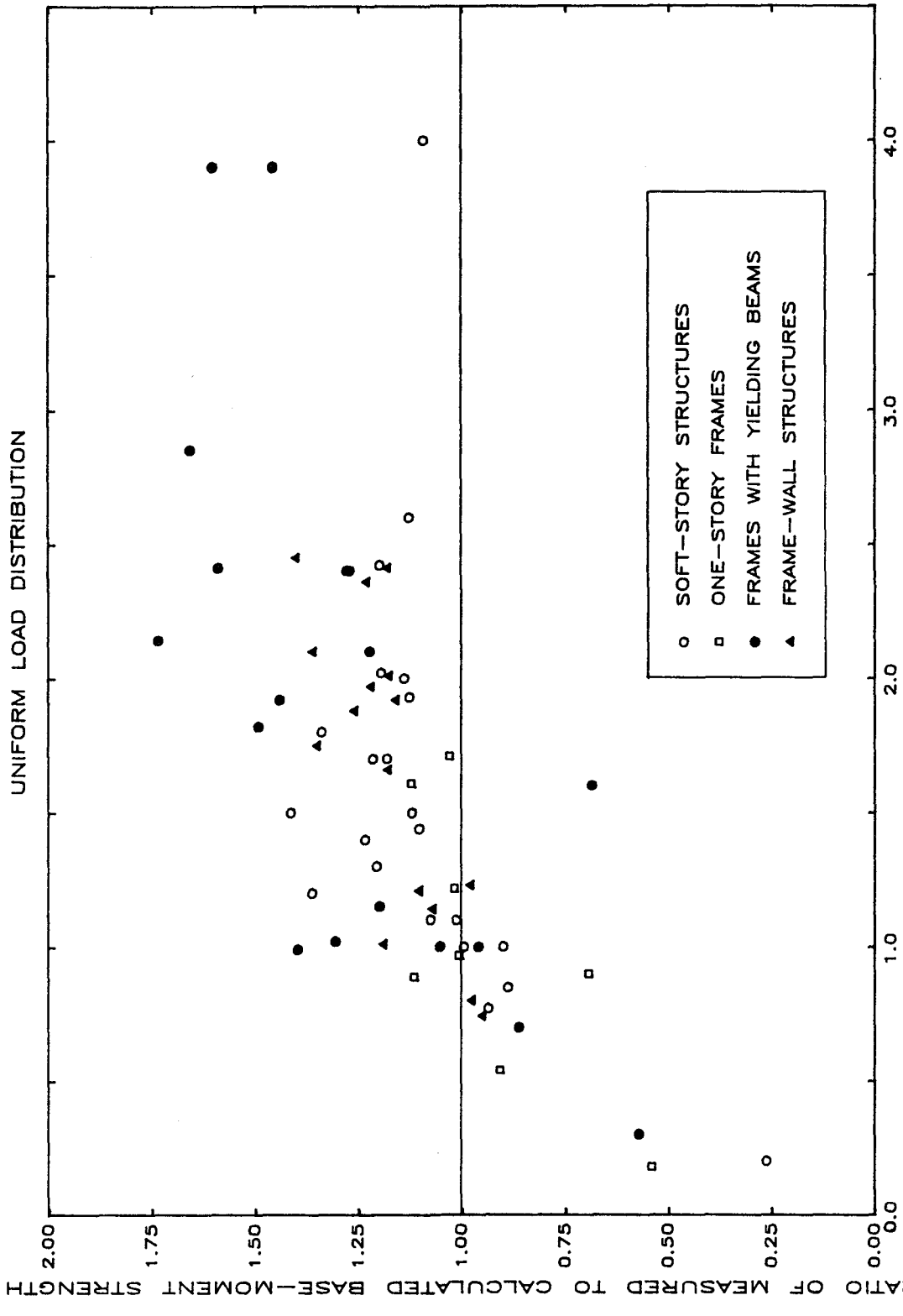

Fig. 7.13 Ratio of Measured Base Moment to Base-Moment Strength Calculated Assuming a Uniform Load Distribution

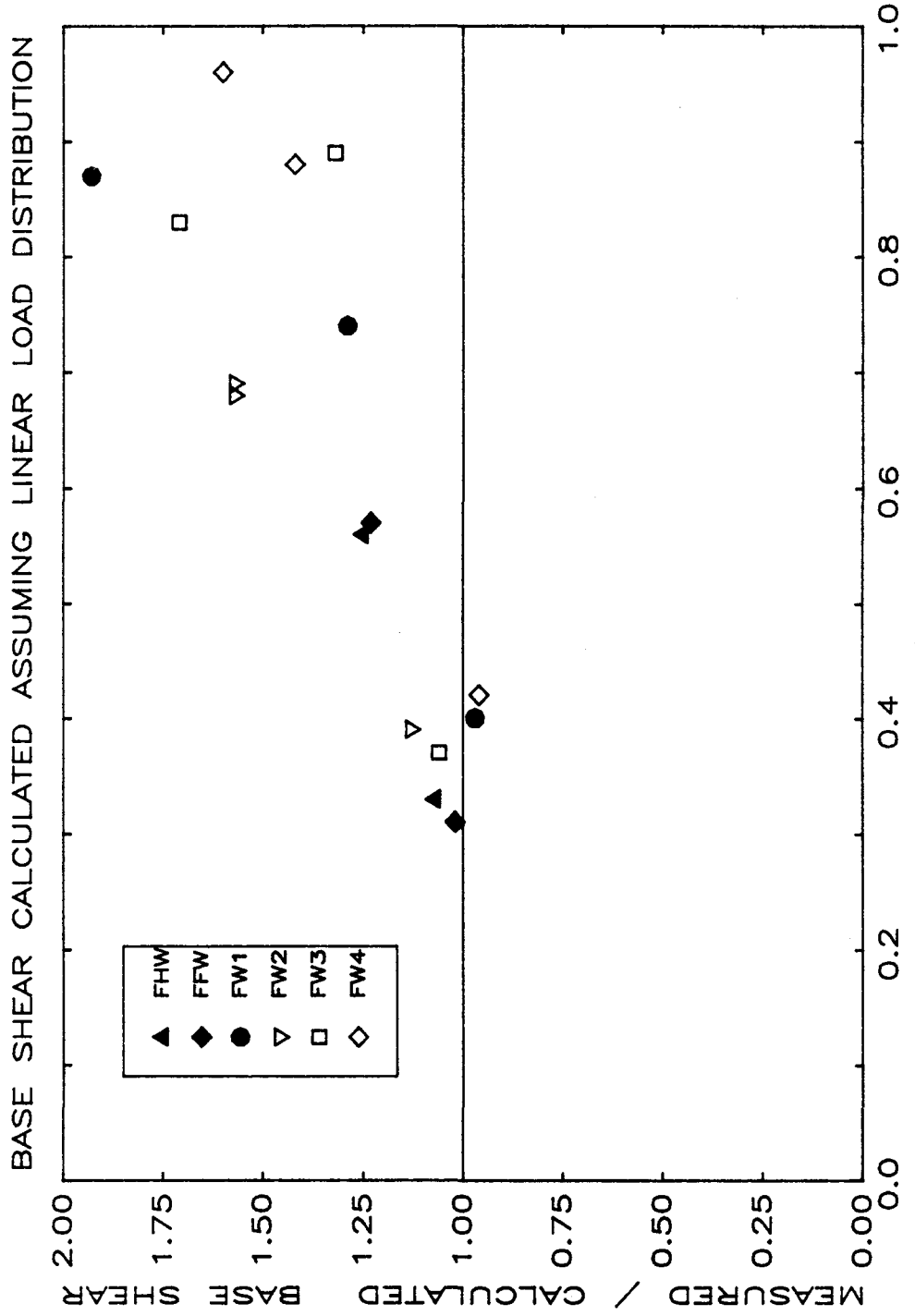

Fig. 8.1 Comparison of Measured Base Shear with Base-Shear Strength Calculated Assuming a Linear Force Distribution

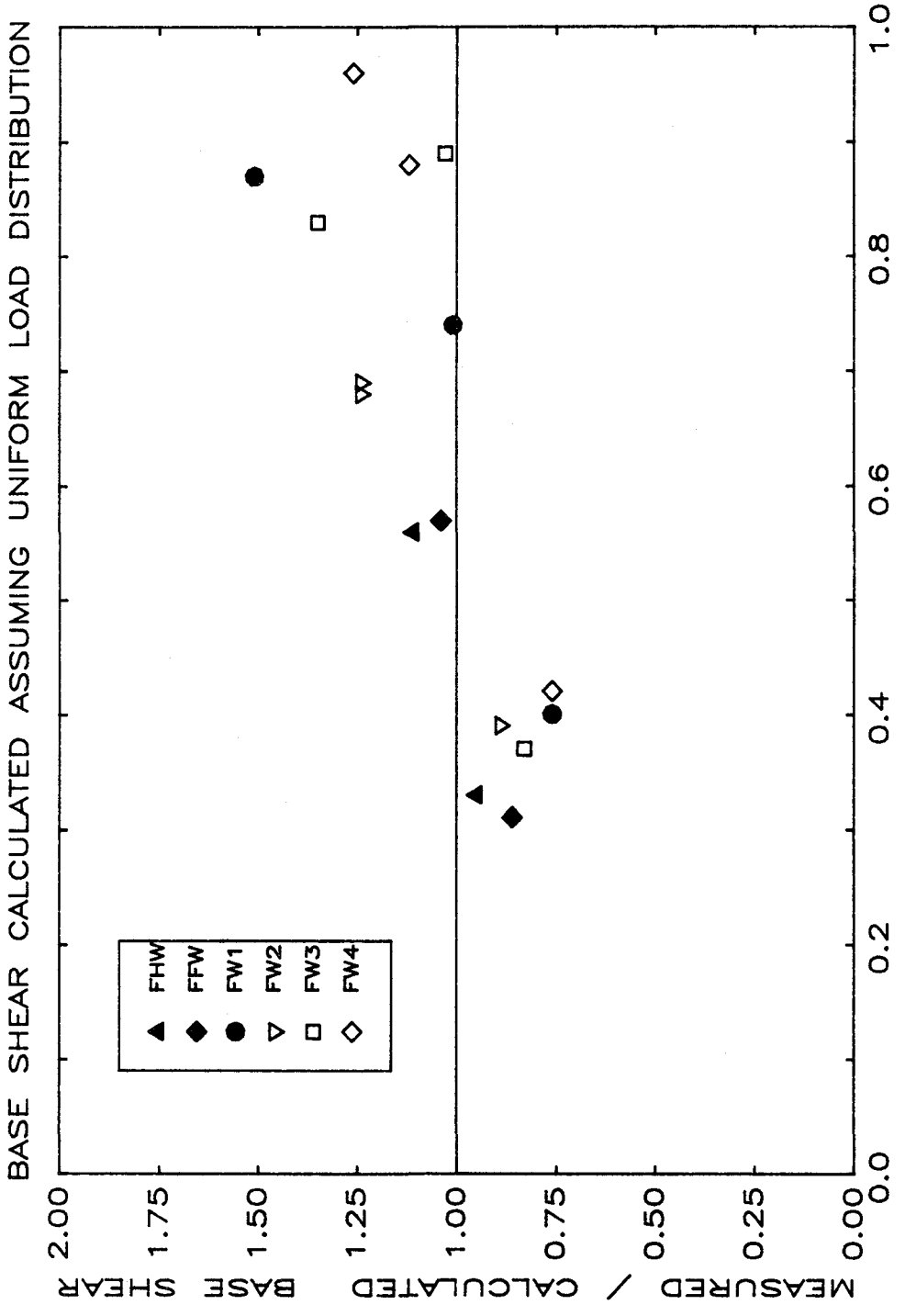

Fig. 8.2 Comparison of Measured Base Shear with Base-Shear Strength Calculated Assuming a Uniform Force Distribution

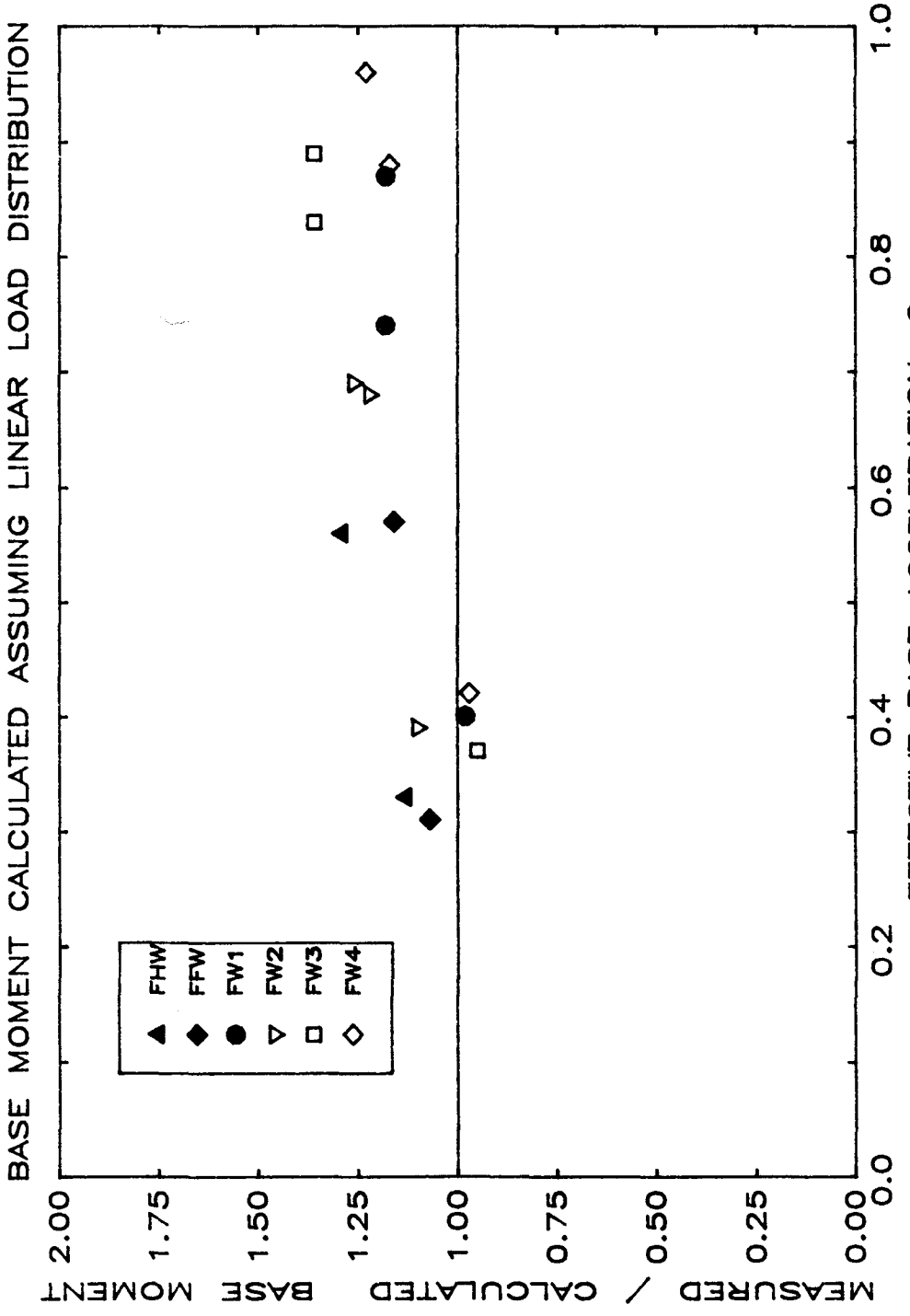

Fig. 8.3 Comparison of Measured Base Moment with Base-Moment Strength

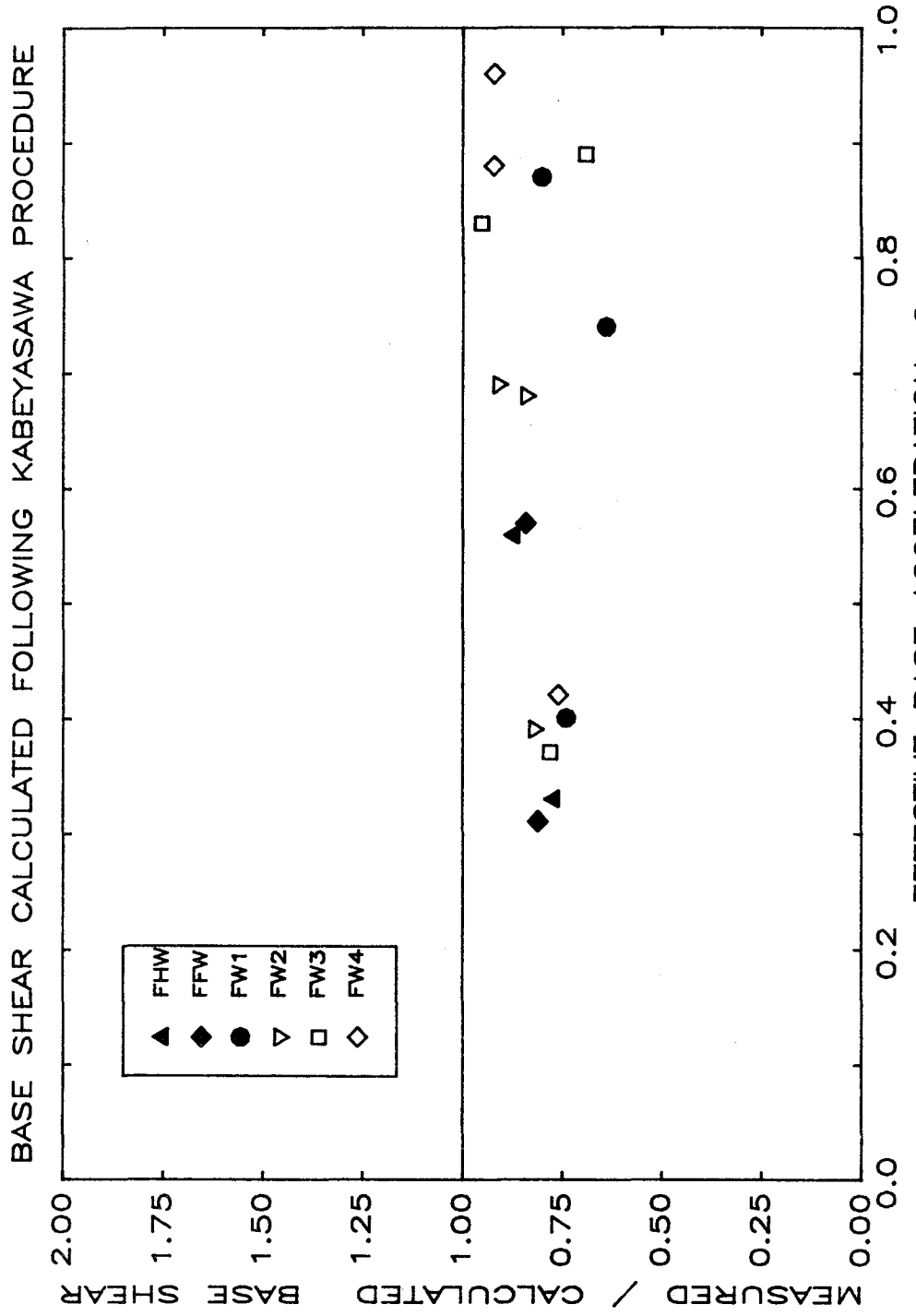

Fig. 8.4 Comparison of Measured Shear with the Base Shear Estimated Following the Kabeyasawa Procedure

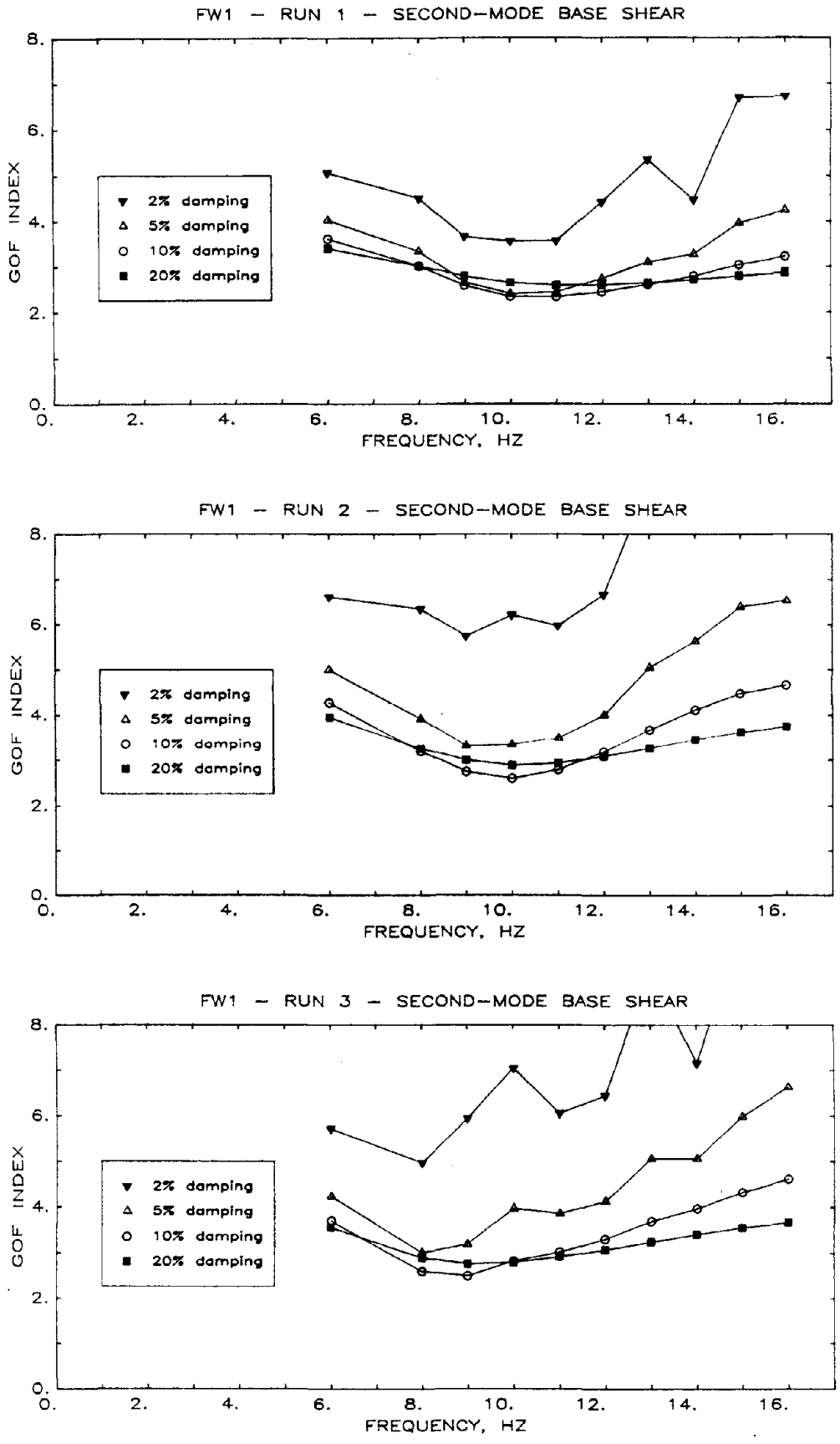

Fig. 8.5 Goodness-of-Fit Indices for Second-Mode Base Shear
(a) Structure FW1

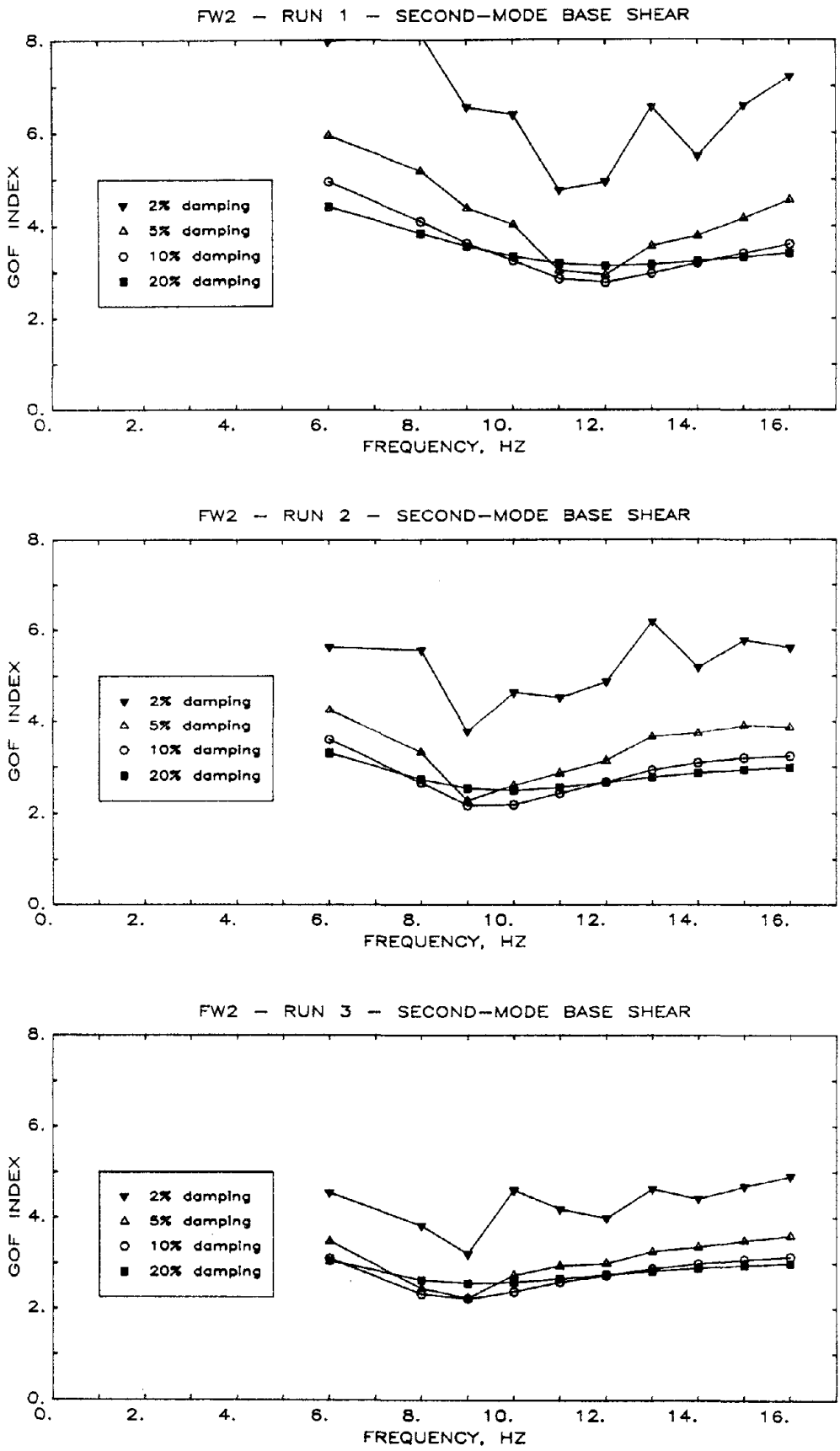

Fig. 8.5 Goodness-of-Fit Indices for Second-Mode Base Shear
(b) Structure FW2

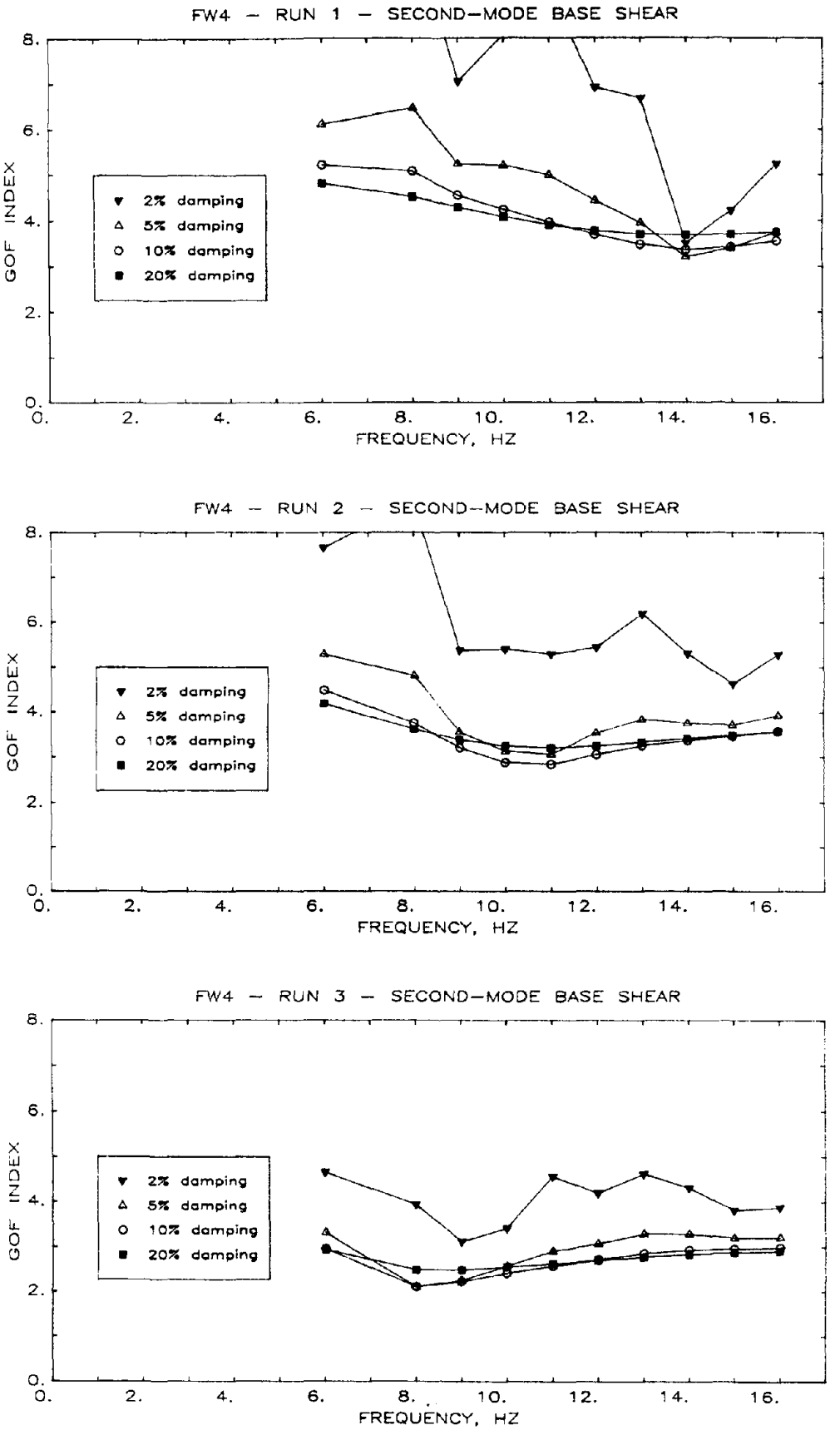

Fig. 8.5 Goodness-of-Fit Indices for Second-Mode Base Shear
(c) Structure FW4

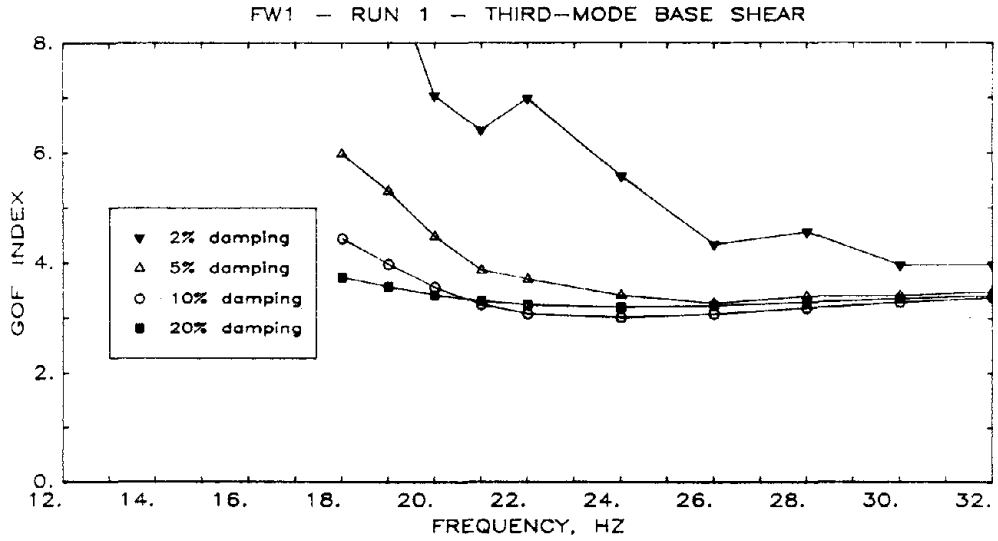

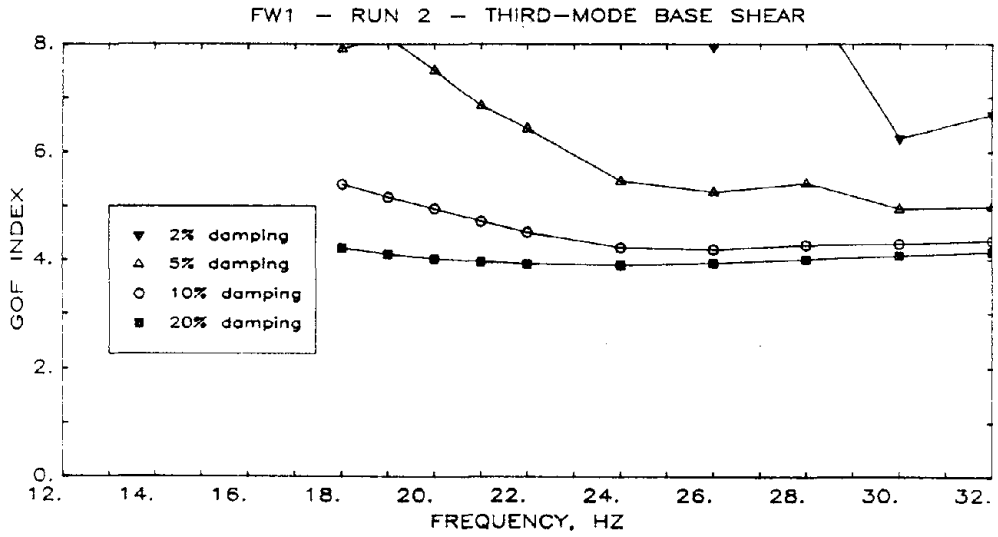

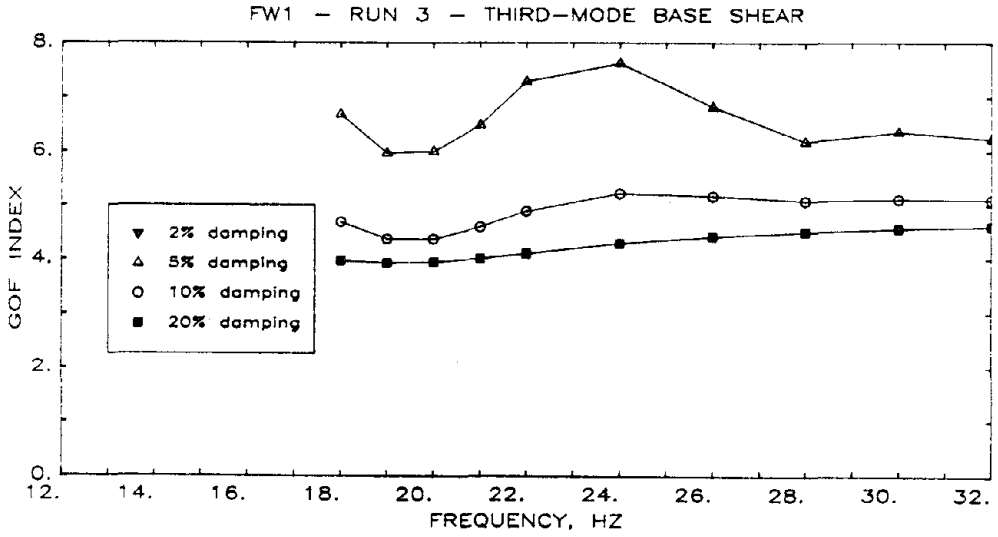

Fig. 8.6 Goodness-of-Fit Indices for Third-Mode Base Shear
(a) Structure FW1

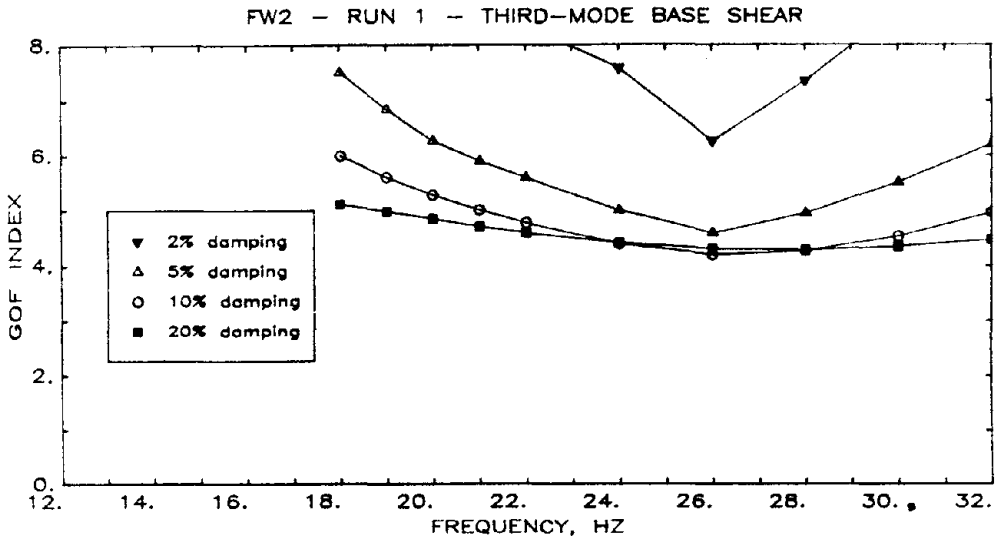

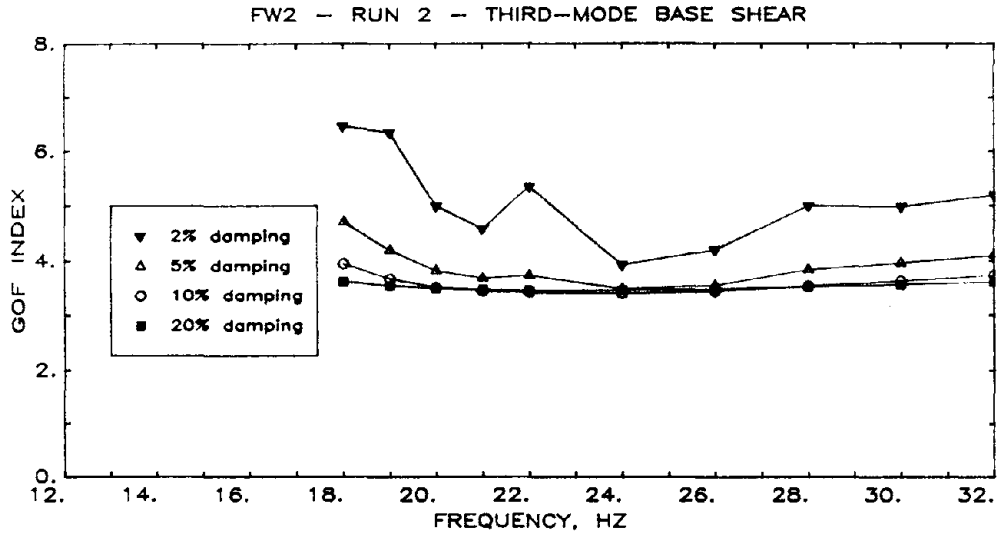

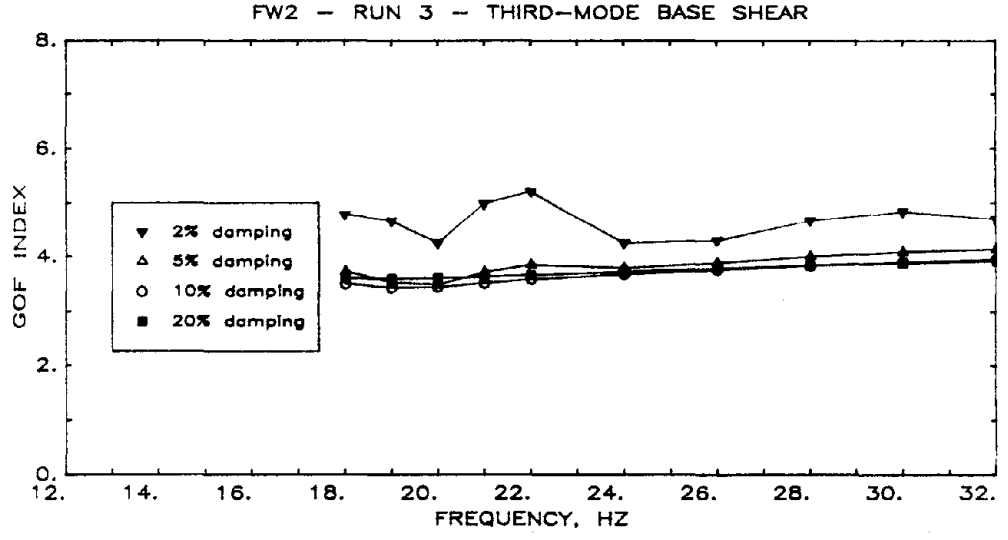

Fig. 8.6 Goodness-of-Fit Indices for Third-Mode Base Shear
(b) Structure FW2

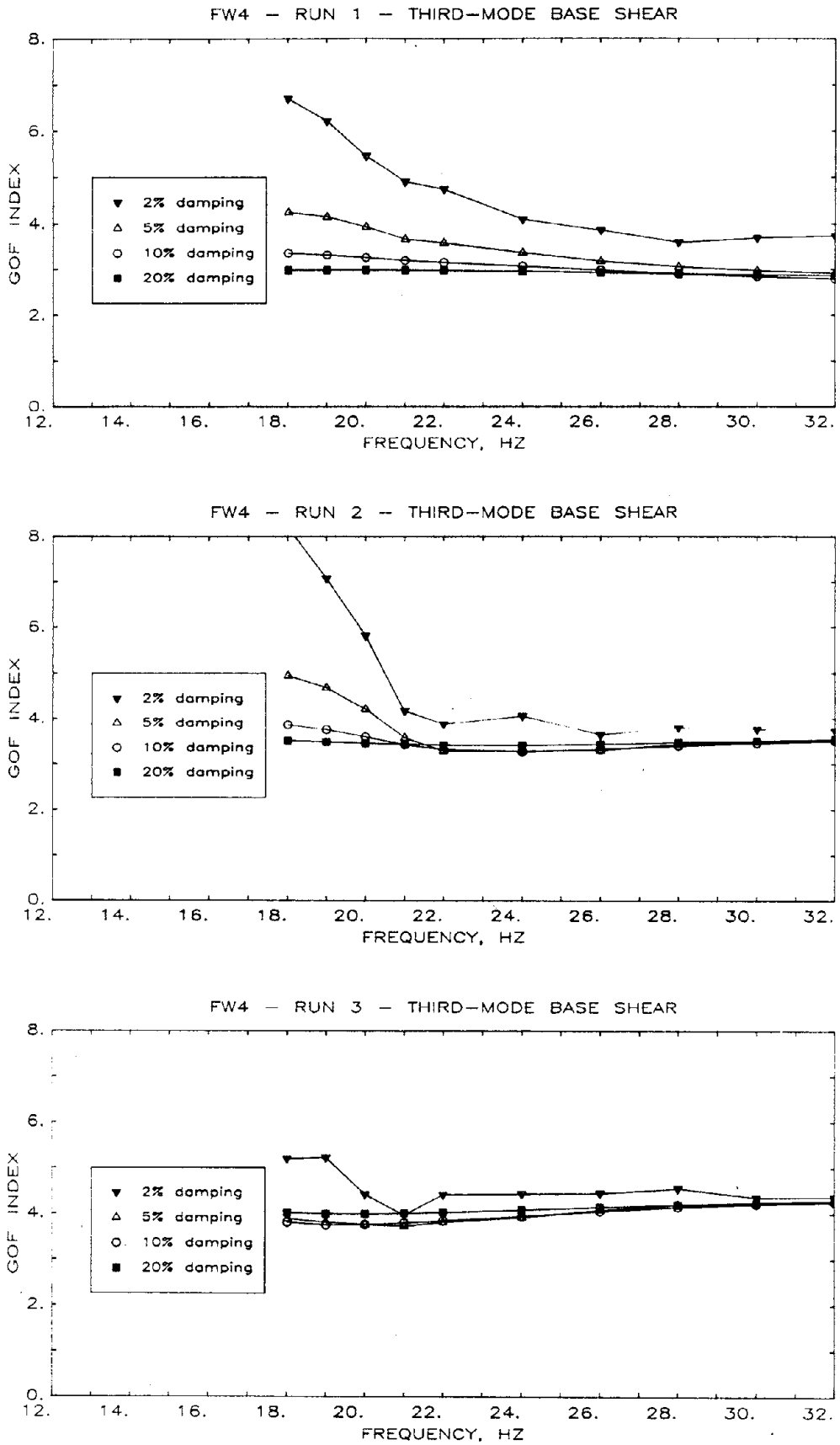

Fig. 8.6 Goodness-of-Fit Indices for Third-Mode Base Shear
(c) Structure FW4

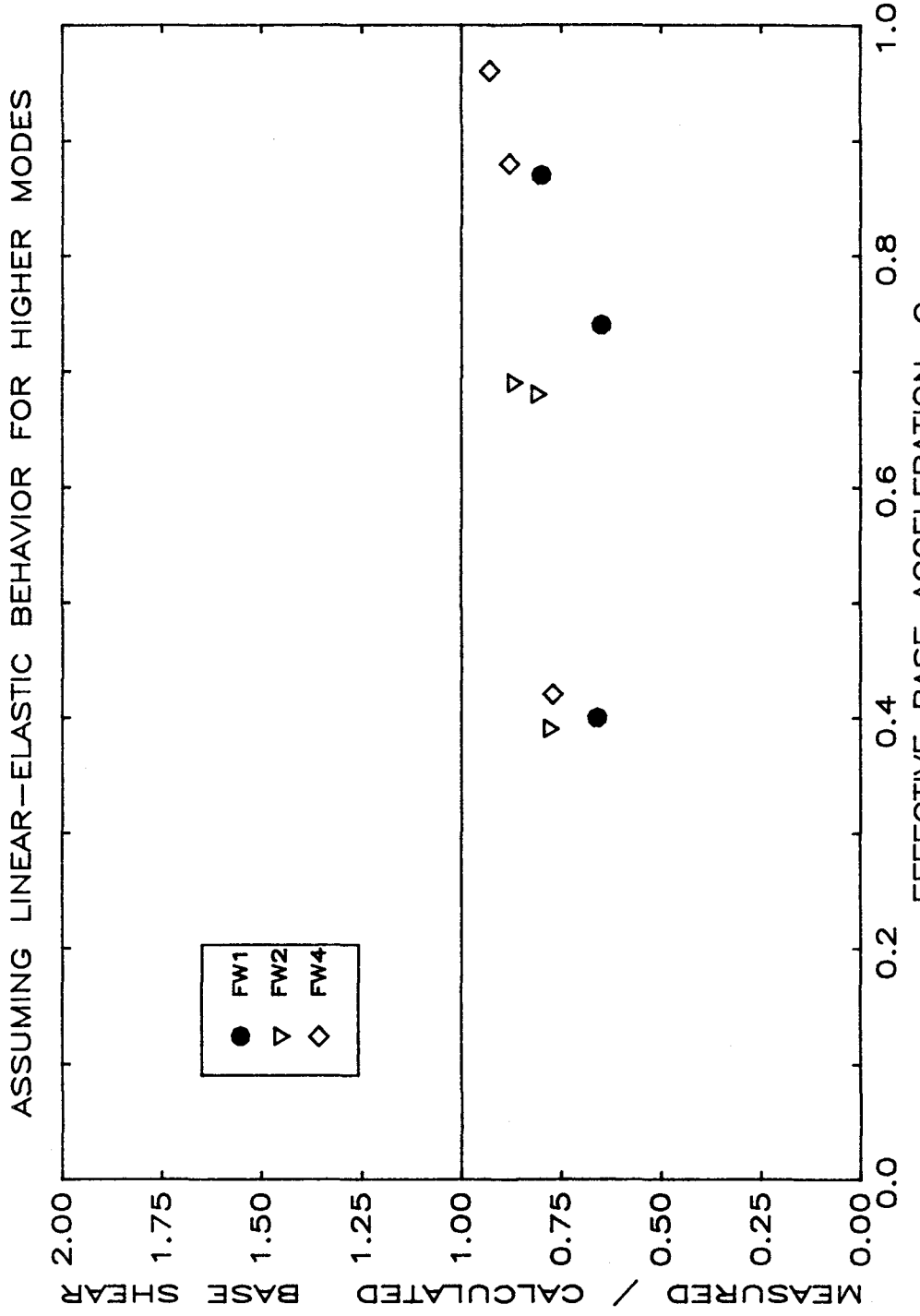

Fig. 8.7 Comparison of Measured Base Shear with the Base Shear Estimated Following the Response-Spectrum Procedure

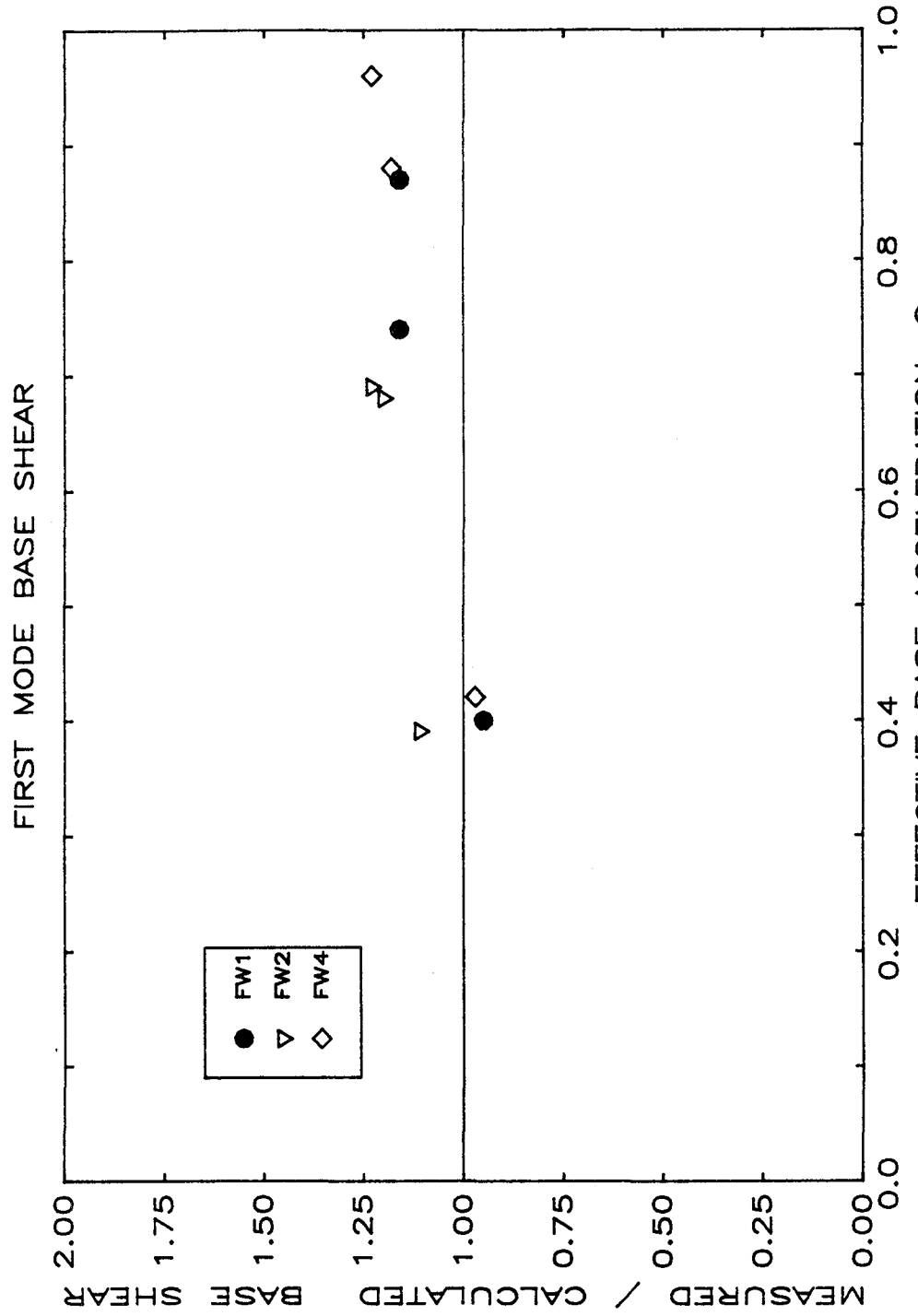

Fig. 8.8 Comparison of Measured and Estimated Maxima of First-Mode Base Shear

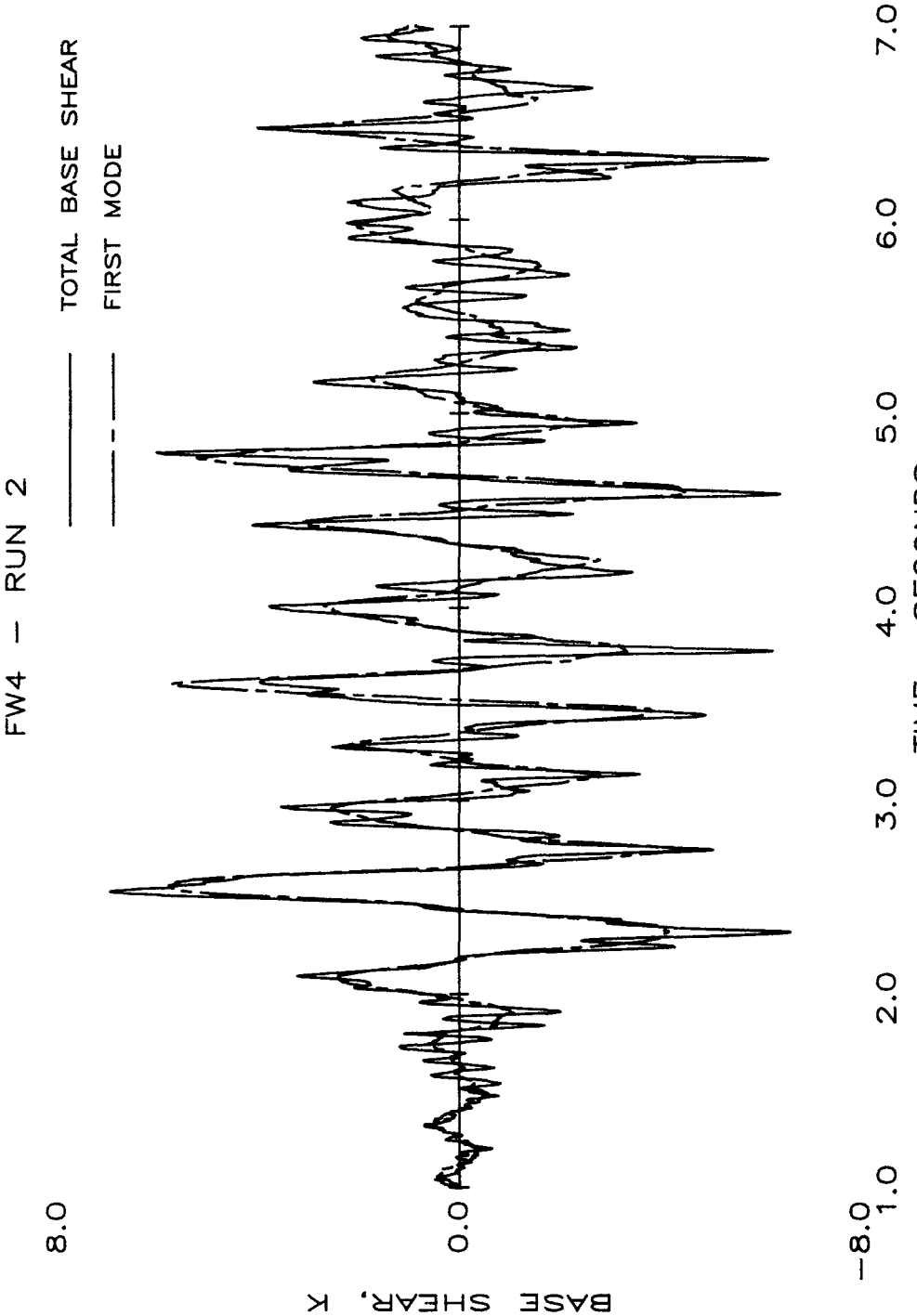

Fig. 8.9 Histories of Total Base Shear and First-Mode Base Shear

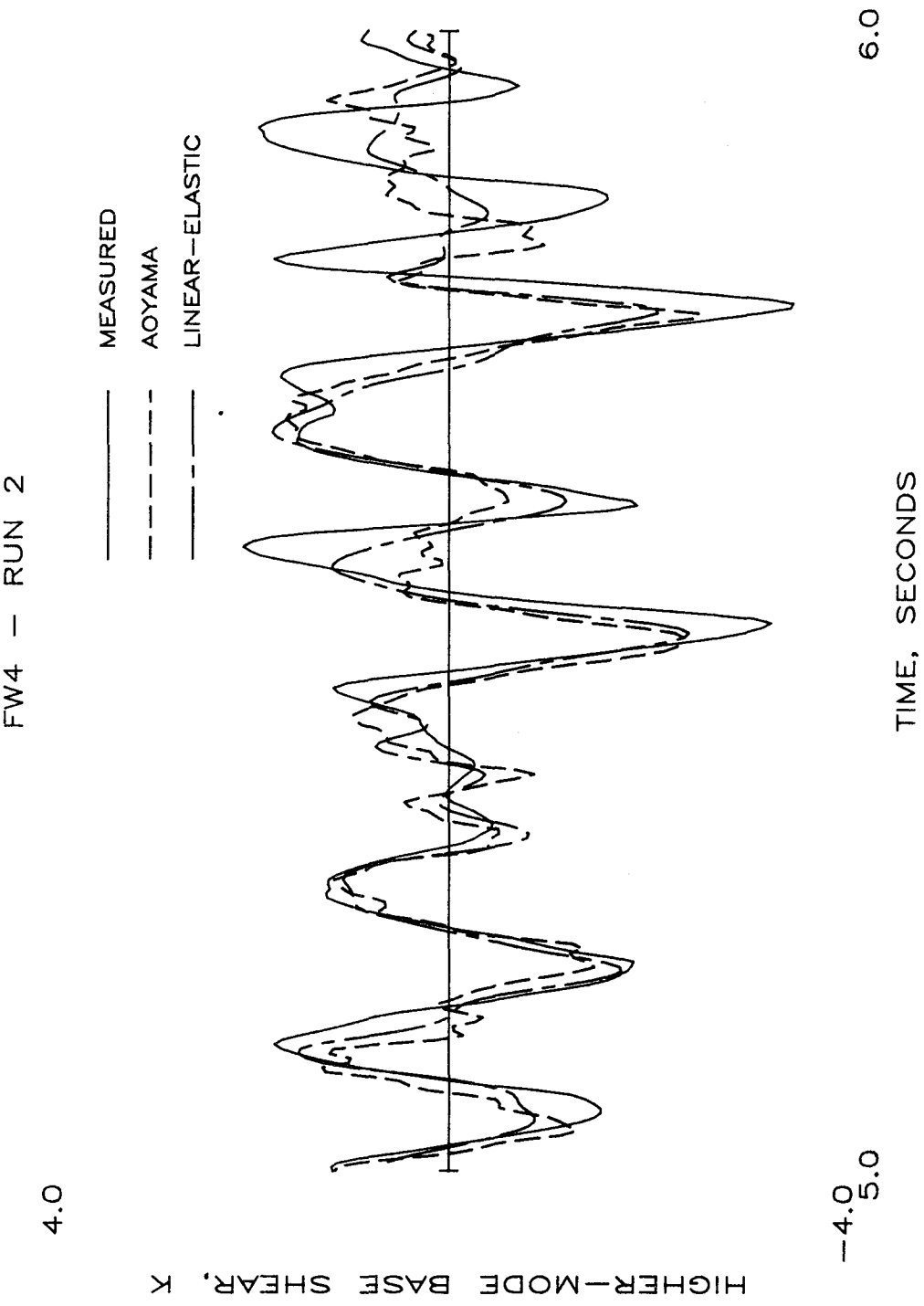

Fig. 8.10 Measured and Estimated Response Histories of Higher-Mode Base Shear

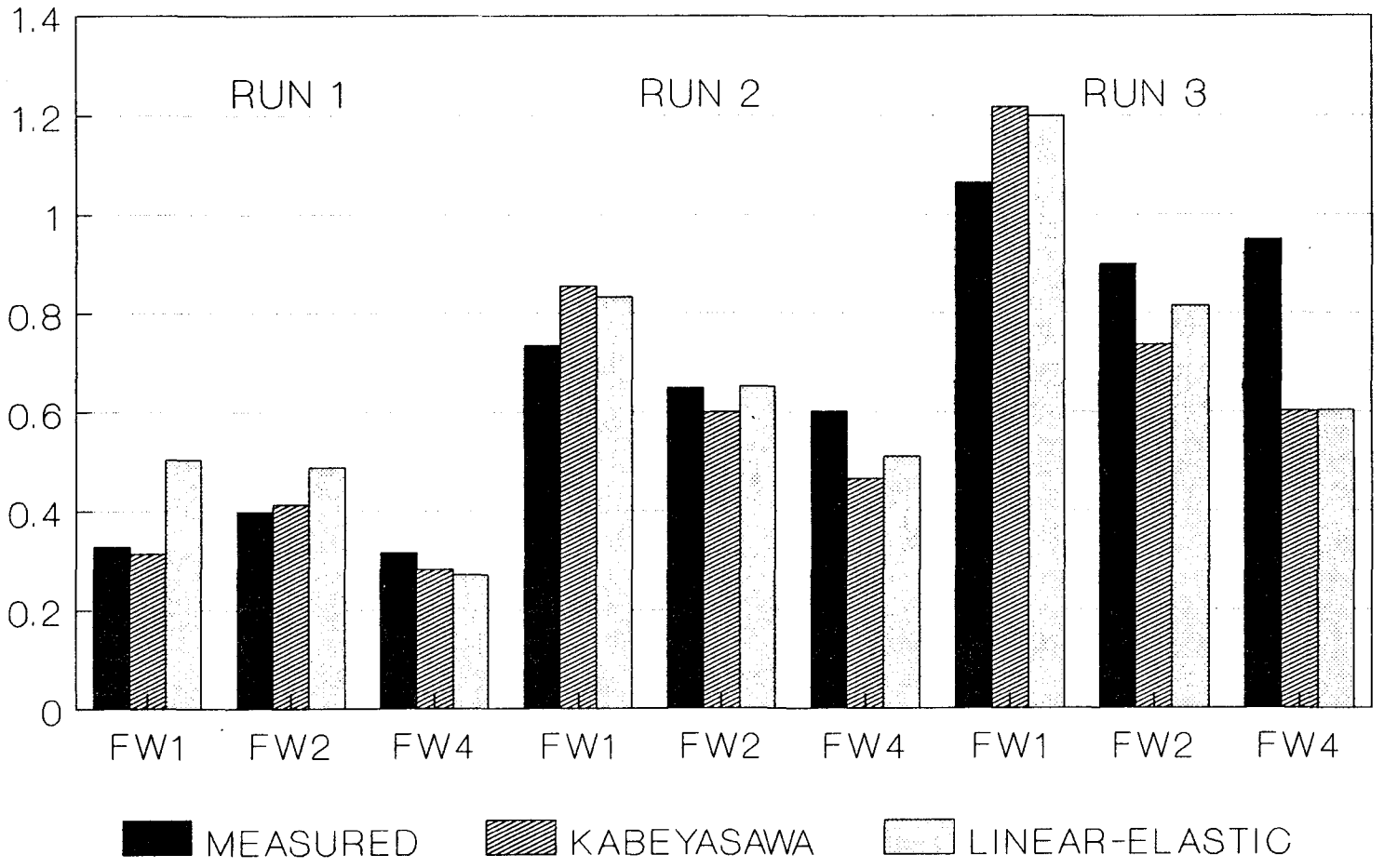

Fig. 8.11 Measured and Estimated Maxima of Higher-Mode Base Shear

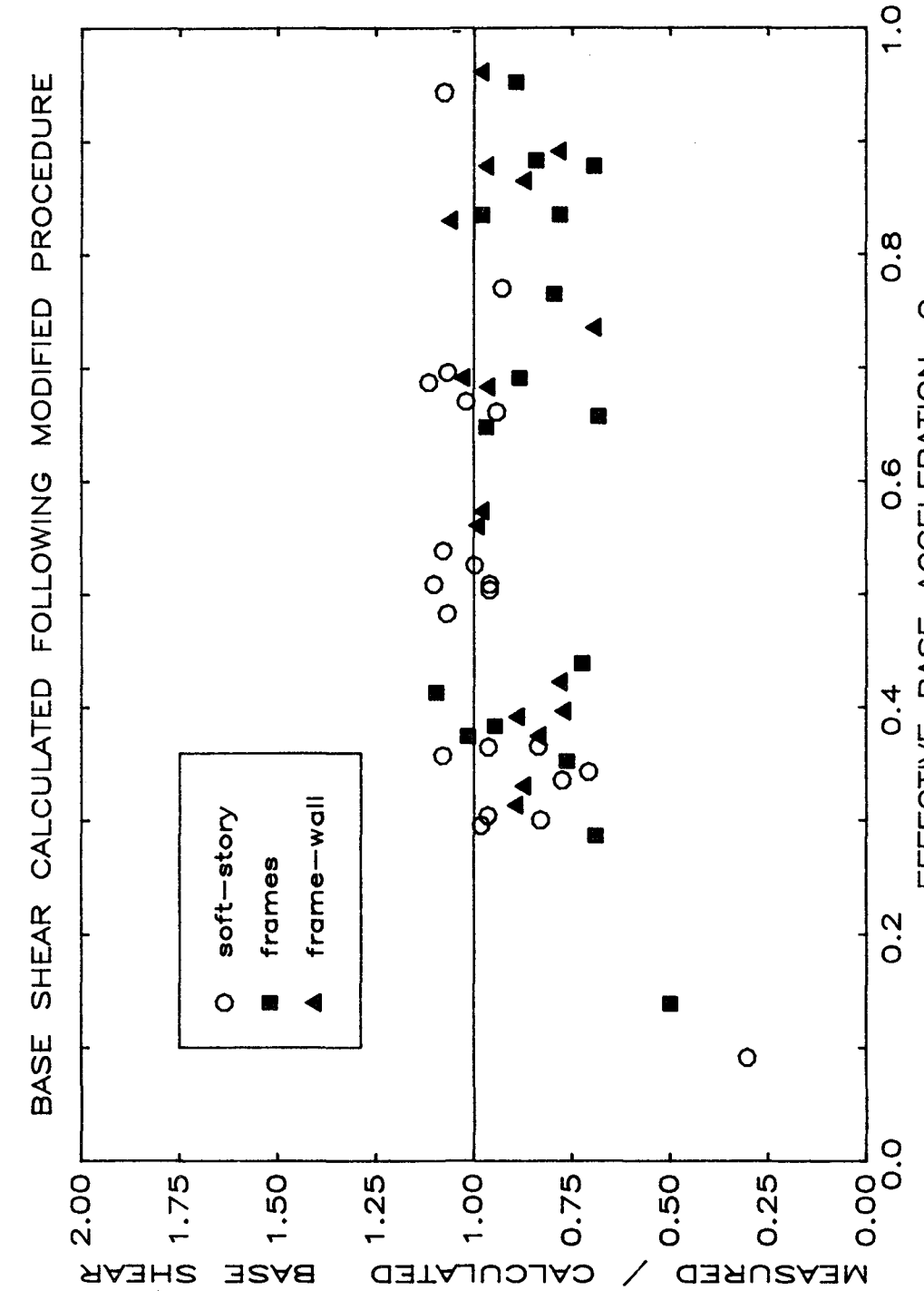

Fig. 8.12 Comparison of Measured Base Shear with the Base-Shear Estimated by the Modified Procedure

APPENDIX A

DESCRIPTION OF EXPERIMENTAL WORK

This appendix discusses construction procedures and physical characteristics of the test structures, as well as testing equipment, instrumentation, data acquisition and data processing.

A.1 Test Structure

A.1.1 Configuration

Test structures consisted of two, nine-story, three-bay, reinforced-concrete frames (Fig. A.1). The pairs of frames were mounted on the one-dimensional earthquake simulator parallel to the direction of simulator motion. Masses, connected at joints at each story, generated inertial and gravity forces. A connection system coupled the frames such that displacements of each frame at a given level would be equal. Stiff base girders were cast monolithically with the frames. Fixed-base conditions were obtained by prestressing base girders to the simulator platform.

A.1.2 Dimensions

Nominal dimensions of the test structure were presented in Chapter 2. Before testing, gross-section dimensions were measured at the ends of each member with a mechanical dial gage or a vernier caliper. Both instruments had a least count of 0.001 in. Because of surface irregularities, measurements were reproducible to within 0.01 in.. Measurements of cross-sectional dimensions are summarized in Table A.1.

The effective depth to reinforcement was obtained indirectly by measuring the thickness of concrete cover. After all dynamic and static tests were completed, concrete was chipped away at random locations of the frame. Concrete cover was then measured with a dial gage having a least count of 0.001 in.. Concrete cover measurements are summarized in Table A.2.

A.1.3 Story Masses

Masses, connected to each story, generated inertial and gravity loads, and were an integral part of the connection system that coupled the frames. Rectangular boxes fabricated from 1/2 in. steel plate were filled with concrete and reinforcing bars. Concrete was mixed from Type I cement, sand, and pea-sized gravel in dry weight proportions of 1.0:2.15:2.6. Masses were cast from a single batch of concrete with a 0.55 water to cement ratio. Channels (MC 3x7.1) were welded to the bottom of the masses. Measured weights of each story, including frame connections and frame self-weight, were 1.15 +/- .01 kips (mean +/- std. dev.). The masses are shown in Fig. A.2.

A.1.4 Connection System

A connection system was designed to force the two frames to displace equally at each story, apply vertical loads at joints without eccentricity, and allow rotation of joints with negligible restraint. Story masses spanned between the frames and were connected to joints by an assembly of 4-in. steel channels and 2 1/2 in. angles (Fig. A.3). The 4-in. channels, placed on both sides of the frames, spanned between adjacent joints. The channels were connected to joints by 7/16 in. diameter bolts that passed through 22-gage

1/2 in. diameter tubing that had been cast at the center of each joint. To reduce restraint of joint rotation, bolts were lubricated and pairs of greased washers were placed between the channels and the frames. The washers also separated the channels from the frames. The 4-in. channels, running along the beams, were connected to MC 3x7.1 channels, welded to the masses, by 2 1/2 in. angles.

To increase the transverse and rotational stiffness of the test structure, "bellows" were placed at the east and west ends of masses. Bellows consisted of pairs of 1/8 in. thick steel plates connected by hinges. The bellows were connected to two adjacent masses by three 1/4 in. diameter bolts. The bellows only negligibly affected longitudinal motion of the test structure.

To prevent motion of the base girders relative to the simulator platform, base girders were fastened to the platform by five 1-in. bolts with 1/2 in. threads. Three 3-in. steel angles connected the two base girders to two steel built-up sections, also bolted to the simulator. The built-up sections were fabricated from 12-in. channels and steel plate. Four-in. angles, placed at the east and west ends of the base girders, provided additional restraint to the base. Hydrocal was placed around the base girders and angles before testing began. The effectiveness of measures used to fix the base girder was verified by the absence of cracks in the hydrocal at the end of testing.

A.1.5 Construction of Test Structure

(a) Reinforcing Cage Fabrication

Reinforcement schedules and details were presented in Chapter 2. Measured properties, knurling, and rusting of the reinforcing steel are discussed in section A.1.6b. Frame longitudinal reinforcement consisted of No. 7-gage wire

in the beams and walls and No. 13-gage wire in the columns. Rectangular helices of No. 16-gage reinforcement were used as shear reinforcement and to increase confinement in the beam stubs. The helices were formed on a mandrel and straightened by hand. Circular spirals of No. 16-gage wire increased confinement of the joints. The No. 16-gage wire was neither knurled nor rusted. Typical frame reinforcement is shown in Fig. A.4.

All longitudinal reinforcement was continuous: no splicing was required. Bar cutoffs were made at mid-story height. To provide adequate development of reinforcement at exterior joints, longitudinal reinforcement was extended into the 4-in. stubs and terminated with a 90-degree hook. Vertical longitudinal reinforcement was anchored at the base by 2 x 2 x 1/8 in. steel plates welded to the wall and column reinforcement 6 in. below the base. Shear reinforcement was made continuous by overlapping at least three sides of a rectangular helix with an adjacent helix.

Wall longitudinal reinforcement consisted of a single No. 7-gage knurled and rusted wire at each corner of the No. 16-gage rectangular helix. At the base of the wall the No. 7-gage wire intersected at the center of the wall, making a 45-degree angle with the base girder. Four No. 13-gage wires, placed at each corner of the helix, extended from 6 in. within the base girder to 6 in. up the wall. Base reinforcing details are shown in Fig. A.5.

Reinforcement cage assembly began by tying longitudinal reinforcement to corners and sides of rectangular helices at 3 to 4 in. spacings. The longitudinal reinforcement straightened minor deviations in the helices and the helices maintained proper spacing of the longitudinal reinforcement. Beam cages were fabricated first. Sufficient clearance was left for the column and wall reinforcement. The complete cage was then fabricated on a platform, on

which the frame outline had been drawn. At joints, column and wall longitudinal reinforcement was placed outside beam reinforcing steel. Column and wall helices were continuous through joints. Ties holding the joints in-place on the bottom side of the reinforcement cage served as chairs to keep the reinforcement at the proper height once placed in the forms.

The base girder was reinforced with four No. 4 reinforcing bars and No. 7-gage wire stirrups spaced at 2 in.. Five vertical holes, required to permit the frame to be prestressed to the simulator, were blocked out using 11 7/8 in. lengths of 1 3/4 in. diameter galvanized steel tubing. Four horizontal holes, used to transport the frame, were blocked out using 8 7/8 in. lengths of 1-in. diameter galvanized steel tubing.

(b) Casting and Curing of Frames

Frames were cast horizontally on an 8 by 8 ft casting platform, with an extension for casting the base girder. Side forms for the frame were machined from cold-rolled steel bar. One 3/8 in. long, 1/2 in.-diameter, 22-gage joint tubes were attached to the 1/4 in. casting plate at the center of each joint. The tubes blocked-out an opening at the joint through which a bolt could pass to attach the frames to the steel channels described in Section A.1.4. The reinforcing cage was tied with wire to the joint tubes to restrain movement during casting. Figure A.6 shows a reinforcement cage placed within the forms.

Concrete was placed by hand and consolidated by two passes with a stud vibrator. All concrete was in place within 2 hours of mixing. After the concrete had set, it was covered with plastic. Frame, cylinder, and prism forms were removed approximately 8 hours after the concrete was finished. The north frame of ES1 was patched to fill voids found at the time of form

removal. Most of the patching was done at the time forms were removed, but some additional patching was done after the frame was removed from the casting platform. The frame, cylinders, and prisms were kept under wet burlap and plastic until the frames were removed from the casting platform. A chronology of the experimental work, including dates of casting and frame removal from the casting platform is given in Table A.3.

(c) Erection of Test Structures

Following construction of the frames, a pair of built-up steel sections was bolted to the simulator platform to serve as a base on which to stack the story masses. Masses were kept at the proper height by collapsible wooden blocks. Horizontal alignment of the masses was facilitated by placing two sheets of greased teflon between the wooden blocks and the masses. Each mass was placed and aligned before the next mass was added to the stack. An alignment frame, made of steel angle and cables, restrained movement of the lower masses during alignment of the mass at the top of the stack. To prevent movement of the masses in the transverse direction, bellows (described in Section A.1.4) were installed as soon as a mass was in place.

Once the masses were aligned, the frames were positioned and bolted to the simulator platform. Shims were placed under the base girder so that the frames were vertical. The connection system, also discussed in Section A.1.4, was then assembled. Channels were placed on both sides of the frames. The 2-in. angles were then placed and all bolts were tightened. During the day preceding the earthquake simulations, the steel alignment frame was removed and bolts were tightened again. Wooden blocks were removed on the day of testing.

A.1.6 Material Properties

(a) Concrete

A separate batch of concrete was mixed to cast each of the four frames. Each batch consisted of :

(i) Lone Star Brand Type III - high early strength cement	260 lbs
(ii) fine lake sand	234 lbs
(iii) coarse Wabash river sand (passing through a No. 4 sieve)	952 lbs
(iv) water	213 lbs

This mix corresponds to dry-weight proportions of 1.0:0.9:3.7 (cement:fine sand:coarse sand) and a water to cement ratio of 0.75 (after correction for absorption of water by sand). Voids in the north frame of ES1, discovered at the time forms were removed, were patched with a mix of 1 part cement, 1 part water, 1 part fine sand, and 1 part coarse sand, by weight.

Twenty-two 4 by 8-in. cylinders and twelve 2 by 2 by 8-in. beams were cast from each batch of concrete as control specimens. Ten cylinders were tested in compression (ANSI/ASTM C39-72) and six cylinders were used to establish the splitting tensile strength (ANSI/ASTM C496-71). The modulus of rupture was determined from loading the beams at the center of a 6-in. span (ANSI/ASTM C293-79).

Figure A.7 shows the stress-strain curves obtained from the cylinder compression tests. Compressive stress-strain behavior was calculated from the measured load, and deformation over a 5 in.-gage length. A parabola was fitted to the stress-strain data for each frame. The regression calculations gave extra weight to the zero-stress, zero-strain ordinate so that the parabolas would pass through the origin. The initial modulus was calculated from the

secant intersecting the curve at stresses of 0.4 and 0.8 ksi. Measured concrete properties are presented in Table A.4.

(b) Reinforcing Steel

Frame reinforcement was fabricated from straight wire purchased from Wire Sales Company and Central Steel and Wire, both of Chicago. No. 7-gage black-annealed wire was used as longitudinal reinforcement for the beams and walls. Column longitudinal reinforcement was fabricated from No. 13-gage, bright-basic wire. Rectangular helices of No. 16-gage bright-basic wire served as shear reinforcement and provided additional confinement in the beam stubs. Spirals of 16-gage wire increased confinement at joints.

Before reinforcement cages were fabricated, all reinforcement was cleaned with solvent and acetone to remove a layer of oil applied by the wire fabricator. No. 7-gage wire was knurled to indent the surface with a series of regularly spaced transverse notches. To accelerate rusting, longitudinal reinforcement was sprayed with a solution of 1 part 10M hydrochloric acid and 9 parts water. The reinforcement was then stored in a fog room for 4-5 days. Loose rust was removed with a wire brush and emery cloth. The reinforcement was cleaned again with solvent and acetone, revealing a pitted surface. The purpose of knurling and rusting longitudinal reinforcement was to roughen the wire surface and thereby, increase bond strength with surrounding concrete.

Five coupons of each type of wire were tested in tension at a strain rate of 0.005/sec. Measured steel properties are summarized in Table A.5. Stress-strain curves for the longitudinal reinforcement are shown in Fig. A.8. Tests on the No. 13-gage wire were performed after the wire had been rusted and cleaned. The No. 7-gage wire was tested after it had been knurled.

A.2 Test Equipment

A.2.1 Earthquake Simulator

All dynamic and static tests were conducted on the earthquake simulator at the University of Illinois. Figure A.9 shows the configuration of the ram, simulator platform, and test structure. Detailed descriptions of the simulator are given in references 36 and 37.

A 3/4 in. steel plate was bolted to the test platform before erection of the test structure. Displacements of the test structure were measured relative to a W 21 x 57 steel column bolted to the west end of the platform. One-quarter in. thick steel plates were welded across the flanges of the column to increase its frequency. Additional stiffness was obtained by bracing the column at 2/3 height with 4-in. structural tubes bolted to the simulator platform.

The command center included an MTS readout panel, 469 controller and 436 control panel, all installed in 1985. The closed loop provided by the servo-controller is shown in Fig A.10. Manufacturer ratings for the LVDT and accelerometer within the loop are listed in Tables 6 and 7, respectively. The reference generator, referred to in the figure derives acceleration, velocity, and displacement commands from a single drive signal. During testing of ES1 and ES2 the controller was operated in the direct displacement mode, effectively bypassing much of the reference generator. Feedback settings for acceleration, velocity, displacement, and force controls were 7.5, 8.0, 8.0, and 7.0.

The drive signal originated from virtual memory of an IBM PC. The digital record was converted to analog form by a Data Translation 2801A A/D D/A board

equipped with 2 D/A and 16 A/D channels with a 36 micro-second throughput (aperture + switching time).

A.2.2 Free-Vibration Test Setup

Free vibration tests were conducted before and after every earthquake simulation or sinusoidal motion. A 100-lb weight was used to impart a horizontal force to the ninth-level mass as shown in Fig A.11. Free-vibration of the structure after the cable was cut was monitored by the same instrumentation as used during other dynamic tests. Because of the small amplitude of motion, gains for ninth-story LVDT's and accelerometers were temporarily increased one step during free-vibration tests.

A.2.3 Static Test Setup

First-story static tests were performed on both structures after the completion of dynamic testing. A 10-ton, manually-operated, hydraulic jack applied a horizontal force to the centroid of the first-story mass. The jack was mounted on the instrument column as is shown in Fig A.12. The applied load was measured with a strain-gage load cell. Ball-bearings were placed on both sides of the load cell to minimize load eccentricity.

A.3 Instrumentation

A.3.1 Linear Variable Displacement Transformers (LVDT)

Location and orientation of LVDT's are shown in Fig. A.13. Story displacements relative to the instrument column, described in Section A.2.1, were measured by 19 LVDT's with ranges of +/- 1 in., +/- 2 in. or +/- 3 in.

The instrument column was considered to be sufficiently stiff (frequency = ~40 Hz) that displacement of the test structure relative to the column was considered to be the same as displacement relative to the simulator platform. Two LVDT's were mounted at each story on 2-in. angles bolted to the instrument column. Stainless-steel extension rods connected the LVDT cores to the mid-depth of the beam stubs. A third LVDT was placed 13 in. south of the ninth-level, north-frame LVDT to measure directly displacement of the ninth-level mass. Manufacturer ratings for the LVDT's are listed in Table A.7.

Six additional LVDT's were used to measure displacement of the walls 1 in. above the base girder. Instrumentation at the base of the wall is shown in Fig. A.14. A harness, machined from 1-in. aluminum block, was attached to the wall by means of 4 thumb screws. To increase the bearing area of the screws, 1/2 in. brass caps were placed between the screws and the walls. Mounting tape was placed between the brass caps and the wall.

One LVDT measured displacement of the harness in the direction of the frame. Two other LVDT's, spaced 5.25 in. apart, measured vertical displacement of the harness relative to the base girder. The harness was considered to be rigid. Wall rotation was calculated from the difference in signals from the two vertical LVDT's. Collins +/- 1G LVDT's were used at the base of the walls. LVDT's were calibrated using machinists' gage blocks.

A.3.2 Accelerometers

Longitudinal, transverse, and vertical accelerations were measured by twenty-five accelerometers. Table A.6 lists manufacturers' ratings for the accelerometers and Fig. A.13 shows their location and orientation. Eighteen piezoresistive accelerometers were mounted on the north and south sides of the

masses. These accelerometers were positioned at story center-lines and oriented parallel to the frame. Longitudinal base acceleration was measured at the top of both base girders. Only piezoresistive accelerometers were used at the base of structure ES1. During dynamic testing of ES2, Q-flex accelerometers replaced piezoresistive ones on the south base girder for all runs and on the north base girder for Run 4.

Vertical, transverse, and instrument-column accelerations were measured by five Q-flex accelerometers. Vertical accelerations were measured by accelerometers mounted of the east and west column stubs of the south frame. Transverse accelerations were measured by accelerometers on the east column stub of the north frame and the west column stub of the south frame. Acceleration of the instrument column in the longitudinal direction was measured at the height of the ninth-level mass.

Mechanical calibrations corresponding to accelerations of 0.0 G and +/- 1.0 G were obtained by rotating accelerometers with respect to the vertical.

A.3.3 Dial Gauges

Three dial gauges were used to measure residual displacements of the test structure following dynamic tests. A dial gauge with a least count of .001 in. was clamped to the instrument column at the center-line of the ninth-story mass. Dial gauges with least counts of .0001 in. were placed on the base girders to measure displacement of the wall 1 in. above the base. Unlike the LVDT's at the same level, dial gauges measured displacement of the wall directly, rather than displacement of the harness.

A.3.4 Static Tests

Displacements during the 1st-story static tests were measured with LVDT's at the first and second stories and at the base of the wall. Collins +/- 3 in. LVDT's used during dynamic tests to measure displacements of upper stories were moved to the first and second stories for the static test. Instrumentation at the base of the wall was identical to that of the dynamic tests.

A.4 Data Recording and Processing

A.4.1 LVDT and Accelerometer Signals

Analog signals from electronic instrumentation passed through conditioners and amplifiers before being recorded. The path followed by the signal is shown in Fig. A.15. Amplifier signals were chosen so that signals arriving at the A/D board did not exceed +/- 10 volts.

Data was acquired with an LSI 11/23 processor (Digital Equipment Corp.) equipped with a 64-channel, analog-to-digital convertor board (Data Translation DT 2769) and a real-time clock. The board has a 20 micro-second throughput (aperture + switching time). Fortran data acquisition and scaling programs relied on Data-Translation CPLIB software to control the A/D board and real time clock and, to unpack raw data.

A total of 59 channels were recorded during dynamic tests. Twenty channels were devoted to story accelerometers and 19 channels monitored story LVDT's. Five channels recorded other accelerometers. Twelve channels of data were acquired from instrumentation at the base of the walls. Each of the 3 LVDT's at the base of the each wall were recorded with two different gains

corresponding to maximum displacements of 0.25 in. and 0.50 in.. Remaining channels monitored the drive signal, ram LVDT, and a grounded circuit (to check for drift in the A/D board).

An IBM portable PC recorded 16 channels in parallel with the LSI 11/23 as a back-up measure. Analog-to-digital conversion for the PC was performed by the same Data Translation 2801 A/D, D/A board as was used to convert the drive signal (Sec. A.3.1).

Mechanical and electrical calibrations were performed the day preceding earthquake simulations. Electronic calibrations were repeated before each dynamic test. Electrical calibrations of the Q-flex accelerometers were not performed. Q-flex accelerometers were observed to be much more stable than the piezoresistive accelerometers.

A.4.2 Dial Gauges

Dial gauge readings at the base of the walls and at the ninth-level mass were recorded before and after every dynamic test. The ninth-level mass dial gauge was also read during the free-vibration test before and after the 100 lb horizontal force was applied to the ninth-level.

A.4.3 Observations

A visual survey of the structure was made after each test. The connection system prevented inspection of exterior beams and part of the wall/beam joints. To detect cracks, a fluorescent liquid (Partex P1-A Fluorescent, Magnaflux Co., Chicago) was sprayed on the frame. Fluorescent particles within the liquid collected in the cracks in the frame. The particles were then illuminated with a fluorescent light. Damage to the test structure, including crack locations

and widths were recorded on data sheets. Behavior of the structure during tests was recorded on 8-mm film and VCR videocassette.

A.4.4 Static Tests

During the static tests, data from LVDT's and the load cell were recorded with the same portable PC as used to backup dynamic tests. Dial gages at the first-level mass and at the base of the walls were read intermittently as a check of the electronic instrumentation and to keep track of the jack elongation.

Table A.1 Measured Cross-Sectional Dimensions[a]
(a) Structure ES1

Level/ Story	Beam Depth (in.)	Beam Width (in.)	Column Depth (in.)	Column Width (in.)	Wall Depth (in.)	Wall Width (in.)
9	2.23 ± .05	1.52 ± .02	1.48 ± .03	1.52 ± .01	4.51 ± .02	1.53 ± .01
8	2.22 ± .02	1.51 ± .02	1.48 ± .02	1.52 ± .01	4.51 ± .02	1.51 ± .01
7	2.21 ± .03	1.51 ± .02	1.50 ± .03	1.52 ± .01	4.47 ± .04	1.52 ± .02
6	2.22 ± .04	1.52 ± .01	1.49 ± .03	1.52 ± .01	4.49 ± .04	1.51 ± .02
5	2.22 ± .04	1.52 ± .02	1.49 ± .03	1.53 ± .01	4.50 ± .01	1.53 ± .01
4	2.22 ± .04	1.51 ± .02	1.48 ± .03	1.52 ± .02	4.46 ± .03	1.52 ± .01
3	2.20 ± .04	1.52 ± .01	1.47 ± .05	1.52 ± .01	4.46 ± .06	1.51 ± .01
2	2.21 ± .03	1.51 ± .01	1.48 ± .03	1.52 ± .01	4.51 ± .06	1.52 ± .01
1	2.22 ± .04	1.52 ± .01	1.49 ± .03	1.52 ± .01	4.48 ± .05	1.51 ± .02
All Levels	2.22 ± .04	1.52 ± .02	1.49 ± .03	1.52 ± .01	4.49 ± .04	1.52 ± .01

[a]Mean ± Standard Deviation

Table A.1 (cont.) Measured Cross-Sectional Dimensions[a]
(b) Structure ES2

Level/ Story	Beam Depth (in.)	Beam Width (in.)	Column Depth (in.)	Column Width (in.)	Wall Depth (in.)	Wall Width (in.)
9	2.24 ± .02	1.51 ± .02	1.49 ± .01	1.51 ± .02	4.51 ± .02	1.50 ± .02
8	2.23 ± .02	1.51 ± .02	1.50 ± .02	1.51 ± .01	4.48 ± .03	1.51 ± .01
7	2.25 ± .03	1.51 ± .02	1.49 ± .01	1.52 ± .01	4.49 ± .02	1.50 ± .02
6	2.23 ± .02	1.52 ± .01	1.50 ± .02	1.52 ± .01	4.48 ± .03	1.51 ± .02
5	2.24 ± .02	1.52 ± .01	1.50 ± .01	1.52 ± .01	4.49 ± .02	1.51 ± .02
4	2.24 ± .01	1.51 ± .02	1.49 ± .01	1.52 ± .02	4.49 ± .01	1.49 ± .02
3	2.24 ± .02	1.51 ± .01	1.50 ± .01	1.52 ± .01	4.51 ± .02	1.51 ± .02
2	2.23 ± .02	1.51 ± .01	1.49 ± .02	1.52 ± .02	4.49 ± .01	1.51 ± .01
1	2.24 ± .03	1.51 ± .01	1.49 ± .02	1.50 ± .02	4.51 ± .01	1.51 ± .01
All Levels	2.24 ± .02	1.51 ± .02	1.49 ± .02	1.52 ± .01	4.49 ± .02	1.51 ± .02

[a]Mean ± Standard Deviation

Table A.2 Measured Concrete Cover for Longitudinal Steel

	Number of Measurements	Measured Cover Depth (in.)	
		Mean	Std. Dev.
Tower Structure			
Columns	24	0.23	0.03
Beams	16	0.27	0.03
Stepped Structure			
Columns	50	0.23	0.04
Beams	30	0.29	0.04

Table A.3 Chronology of Experiments

Event		Structure ES1	Structure ES2
Cast Frame	(North)	18 Jul 86	9 Sep 86
	(South)	4 Aug 86	30 Sep 86
Remove Frame from Casting Platform	(North)	29 Jul 86	19 Sep 86
	(South)	15 Aug 86	10 Oct 86
Earthquake Simulation		17 Apr 87	8 Jun 87
Sinusoidal Motion Test		5 May 87	15 Jun 87
Static Test		8 May 87	17 Jun 87
Test Concrete Cylinders and Beams		17 Apr 87	8 Jun 87

Table A.4 Measured Concrete Properties

	Frame	Age at Testing (Days)	Initial[a,c] Modulus (psi x 10^6)	Secant[b,c] Modulus (psi x 10^6)	Compressive[c] Strength (psi)	Splitting[d] Strength (psi)	Modulus[e] of Rupture (psi)
Structure ES1	North	273	2.8 ± 0.3	2.7 ± 0.3	4270 ± 490	340 ± 40	900 ± 90
	South	256	2.8 ± 0.2	2.6 ± 0.2	4440 ± 660	390 ± 20	810 ± 100
Structure ES2	North	272	2.9 ± 0.2	2.6 ± 0.3	4460 ± 330	350 ± 50	780 ± 60
	South	251	2.6 ± 0.4	2.6 ± 0.2	5140 ± 270	390 ± 50	810 ± 50

[a]Calculated from strains measured at stresses of 400 and 800 psi

[b]Calculated at 0.5 * f_c'

[c]Ten 4 x 8-in. cylinders

[d]Six 4 x 8-in. cylinders

[e]Twelve 2 x 2 x 8-in. beams

Table A.5 Measured Steel Properties[a,b]

Location		Wire Gage	Nominal Diameter (in.)	Upper Yield Stress[d] (ksi)	Lower Yield Stress[d] (ksi)	Strength[d] (ksi)	Strain at Hardening
Beams and Walls		No. 7	.177	58.4 ± 0.5	57.6 ± 1.0	64.2 ± 0.6	.025
Columns		No. 13	.0915	55.5 ± 0.6	55.0 ± 0.2	59.9 ± 0.5	.010
Transverse Reinforcement	batch #1[c]	No. 16g	.0625	112.1 ± 4.8		117.9 ± 5.4	-
	batch #2					122.0 ± 5.2	

[a]Five samples

[b]Strain Rate - 0.005/sec

[c]Tested by A. Schultz [32]

[d]Mean ± Standard Deviation

Table A.6 Manufacturer's Ratings - Accelerometers

	Piezorestitive Accelerometers	Q-Flex Accelerometers
Manufacturer	Endevco	Endevco / Sunstrand
Model	2262C-25	QA-116-15 QA1000-AA01-011
Range	γ 25 g	γ 15 g
Linearity	1.0 %	0.03 %
Frequency Response (γ 5 %)	0-750 Hz	0-500 Hz
Natural Frequency	2500 Hz	1000 Hz
Fraction of Critical Damping	0.7	0.6

Table A.7 Manufacturer's Ratings - Linear Voltage Displacement Transformers

Manufacturer	Model	Working Range	Linearity
Collins	711T42	γ 1.0 in.	0.25 %
Pennsauken	2000 HR	γ 2.0 in.	0.25 %
Pennsauken	3000 HR	γ 3.0 in.	0.25 %
Collins[1]	LMT13048	γ 2.5 in.	1.00 %

(1) ram LVDT

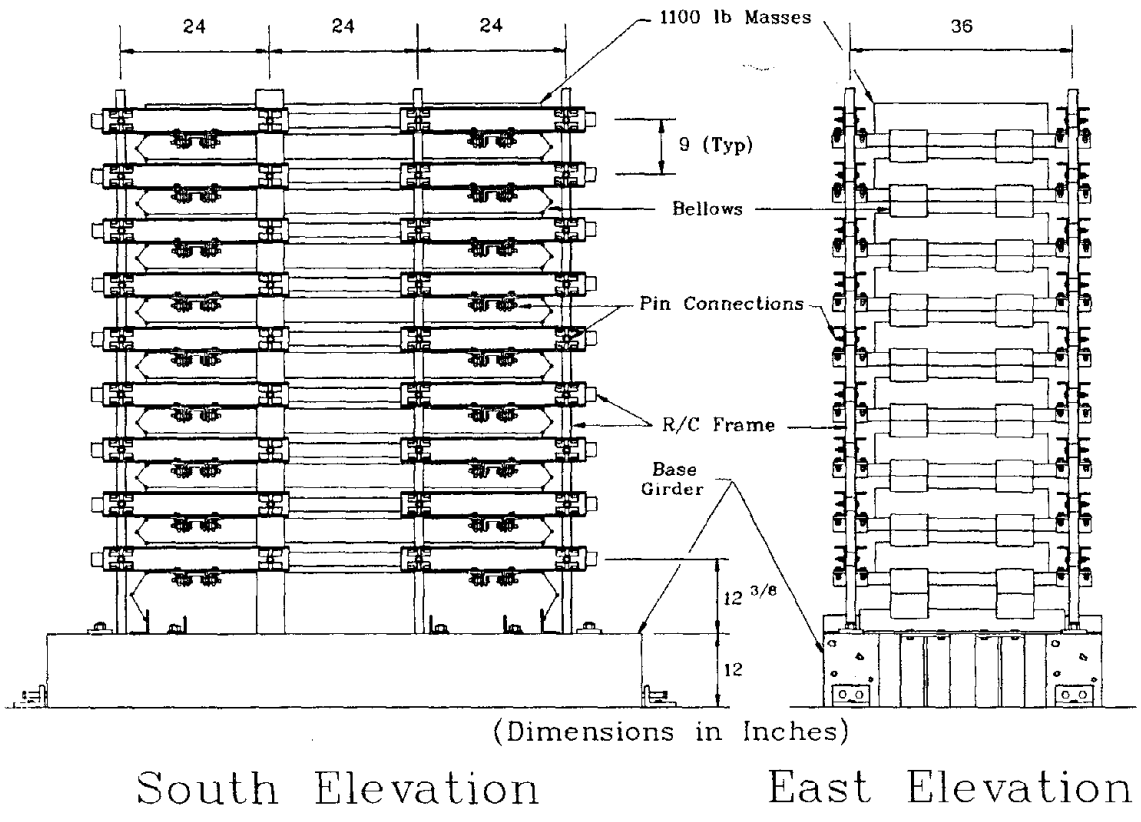

Fig. A.1 Test Structure

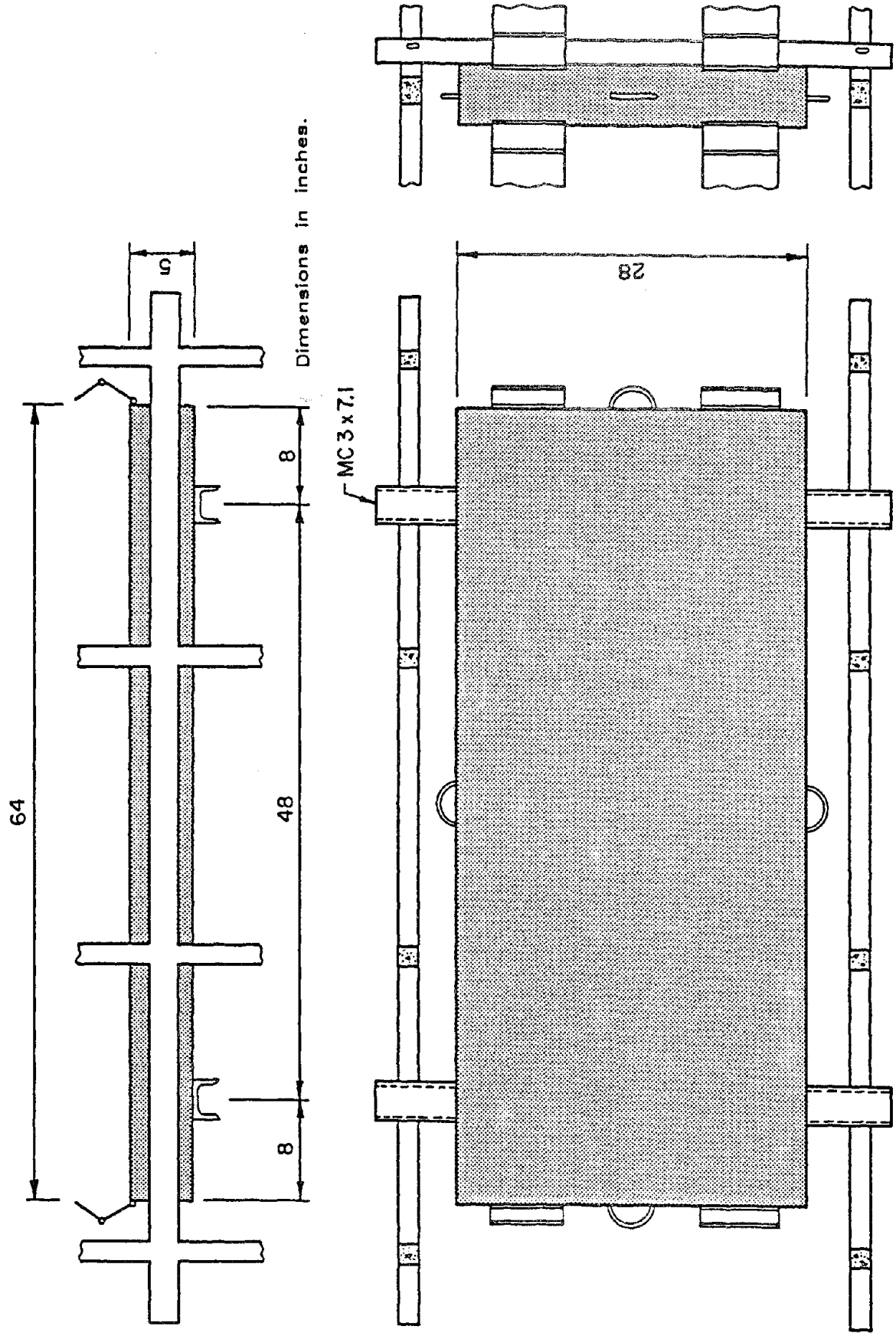

Fig. A.2 Story Masses

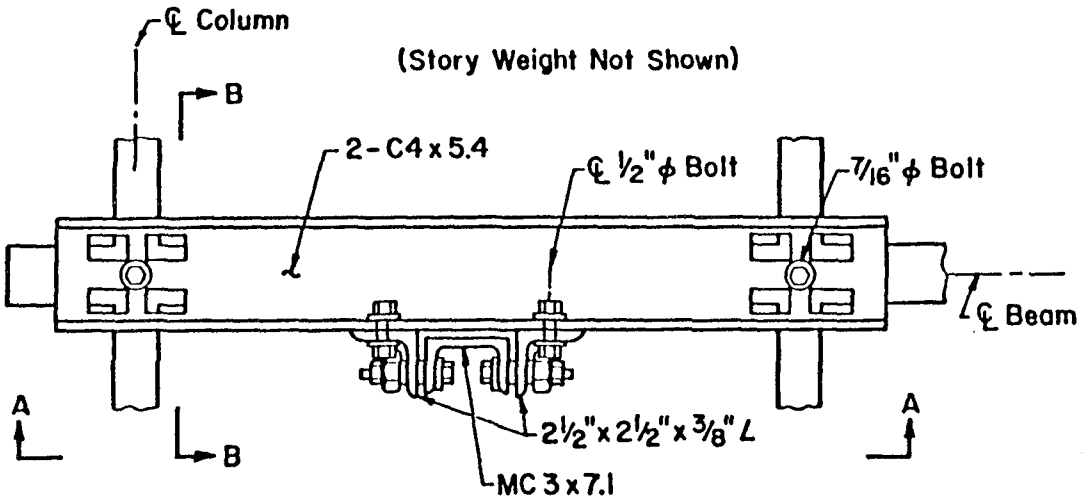

Elevation

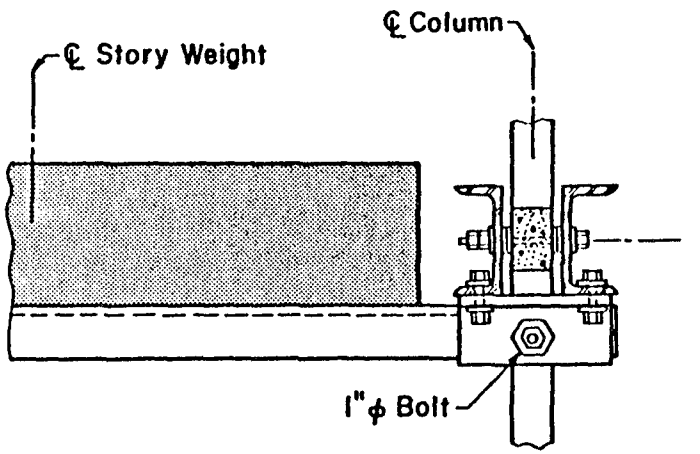

Section B-B

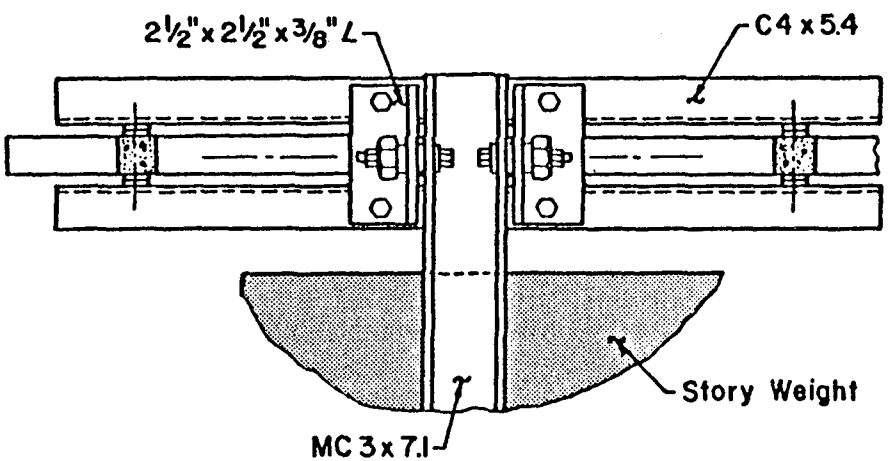

Section A-A

Dimensions in inches.

Fig. A.3 Connection System

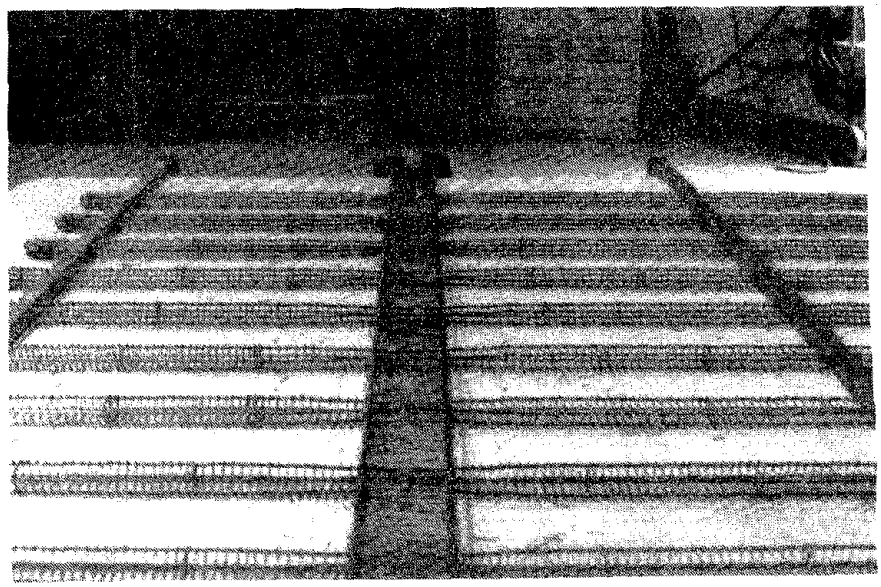

(a) Reinforcing Cage

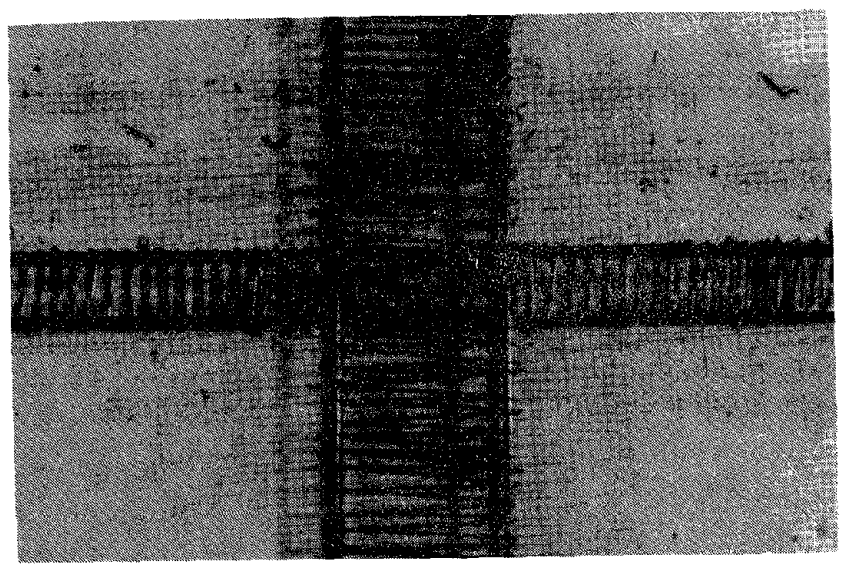

(b) Wall-Beam Joint

Fig. A.4 Frame Reinforcement

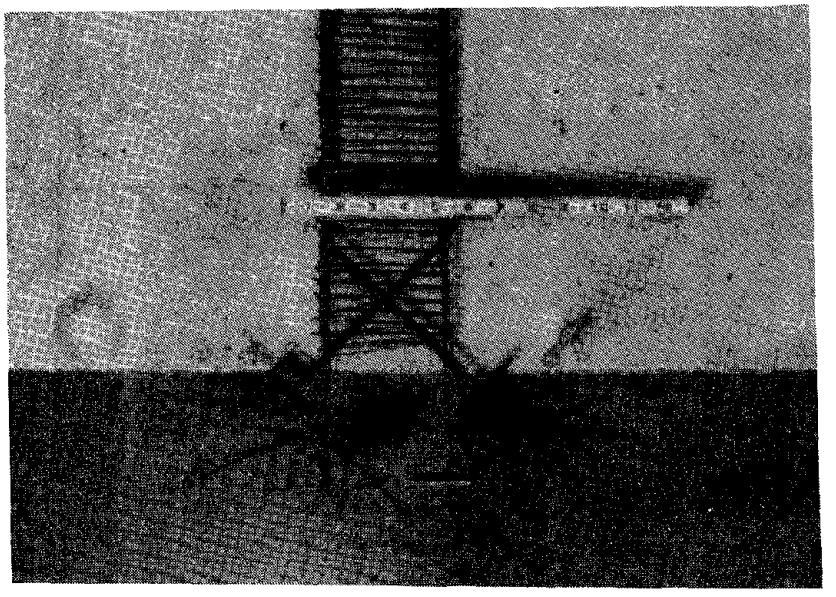

(a) Reinforcement During Fabriacation

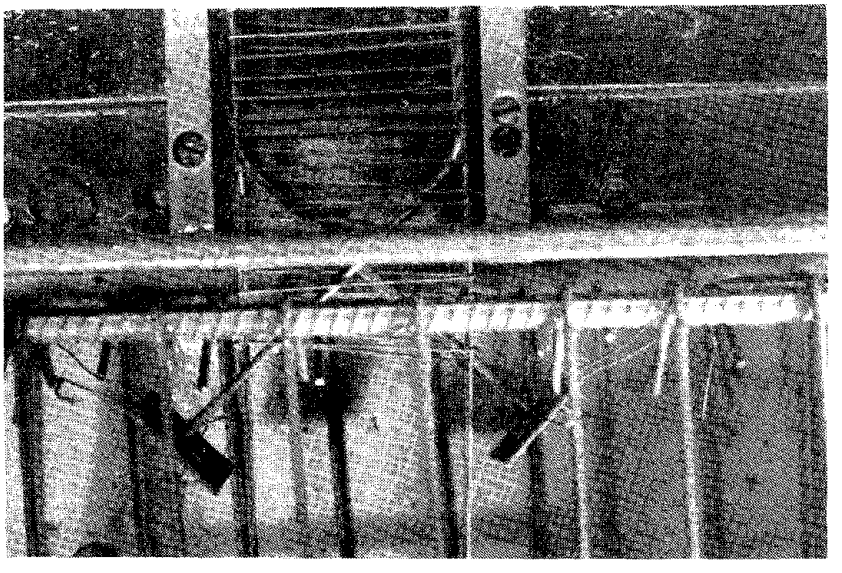

(b) Reinforcement in Forms

Fig. A.5 Reinforcement at Base of Wall

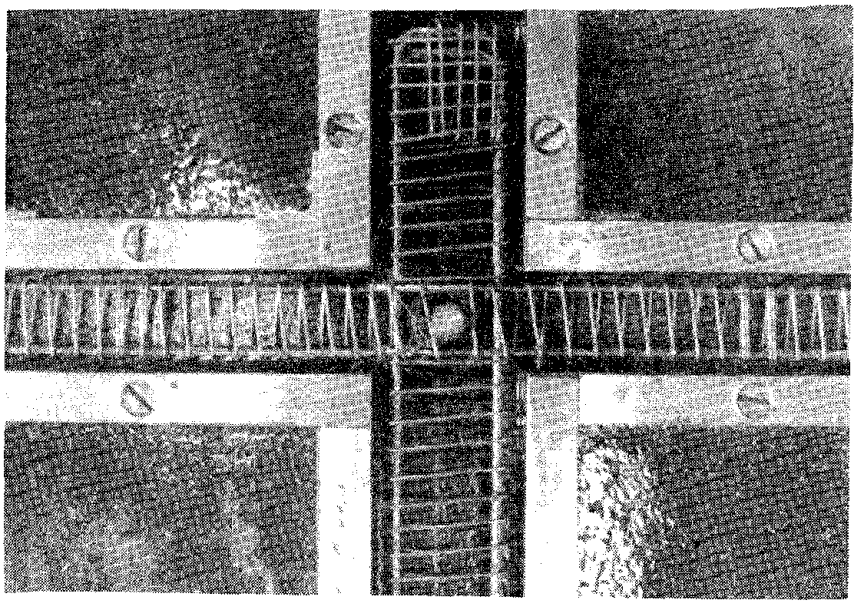

(a) Exterior Beam-Column Joint

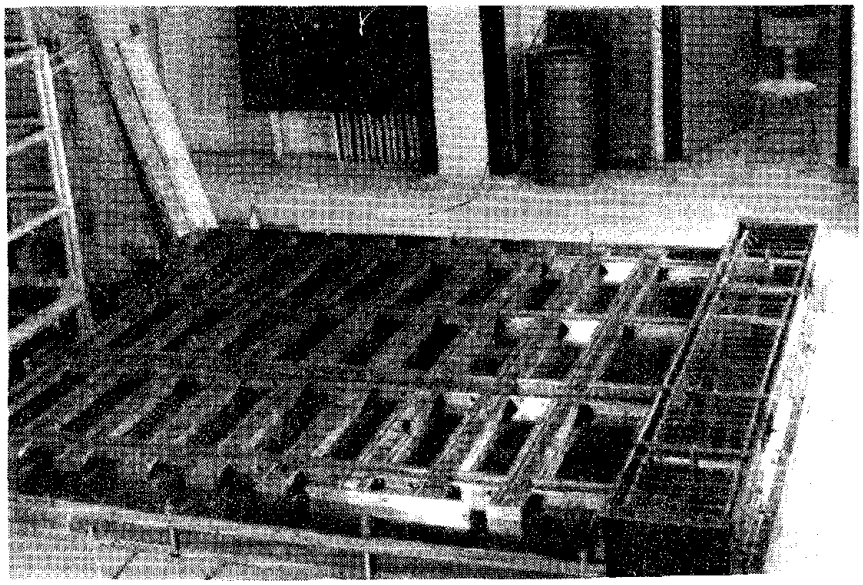

(b) Frame and Base Girder

Fig. A.6 Forms

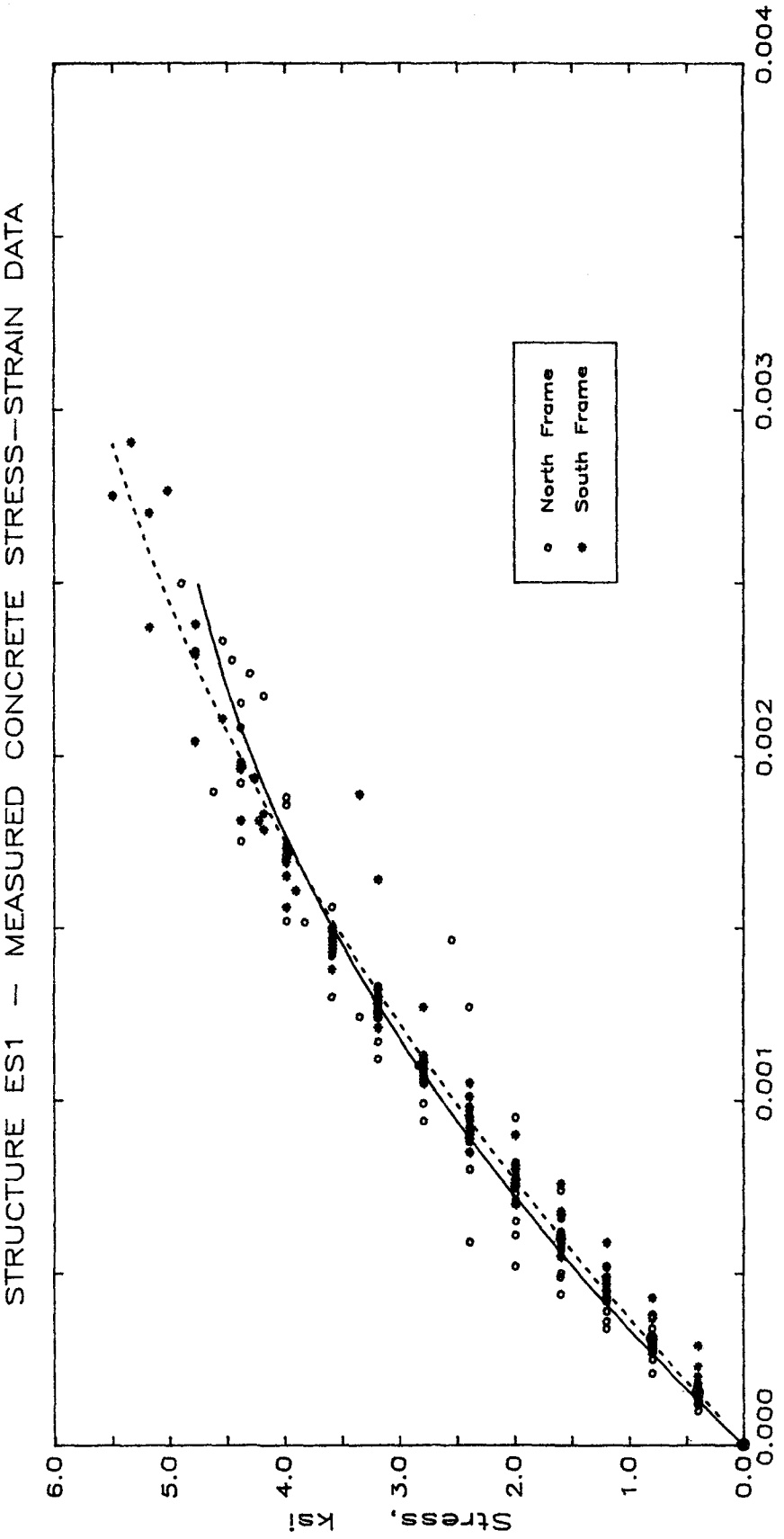

Fig. A.7 Stress-Strain Curves for Concrete
(a) Structure ES1

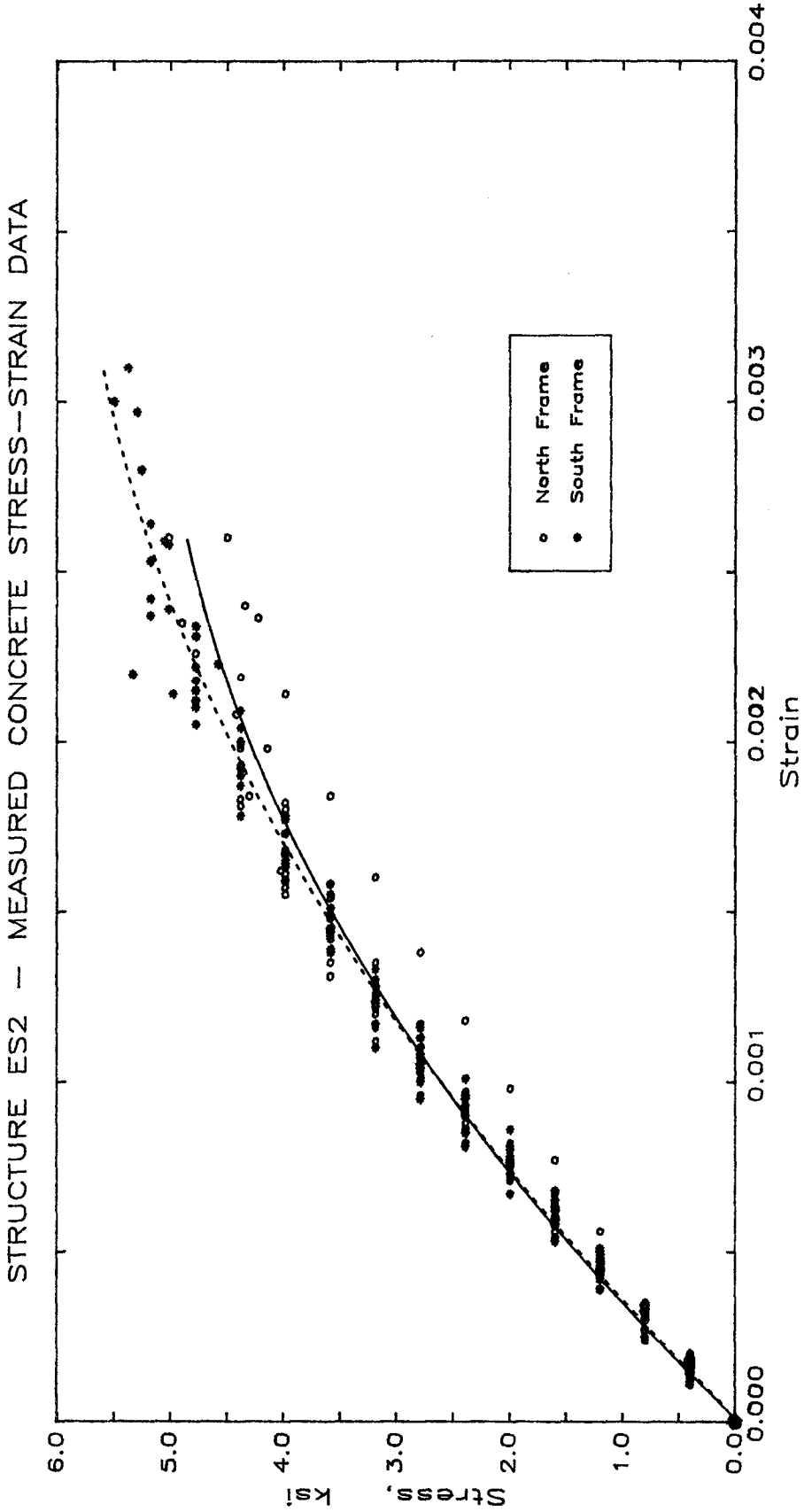

Fig. A.7 (cont.) Stress-Strain Curves for Concrete
(b) Structure ES2

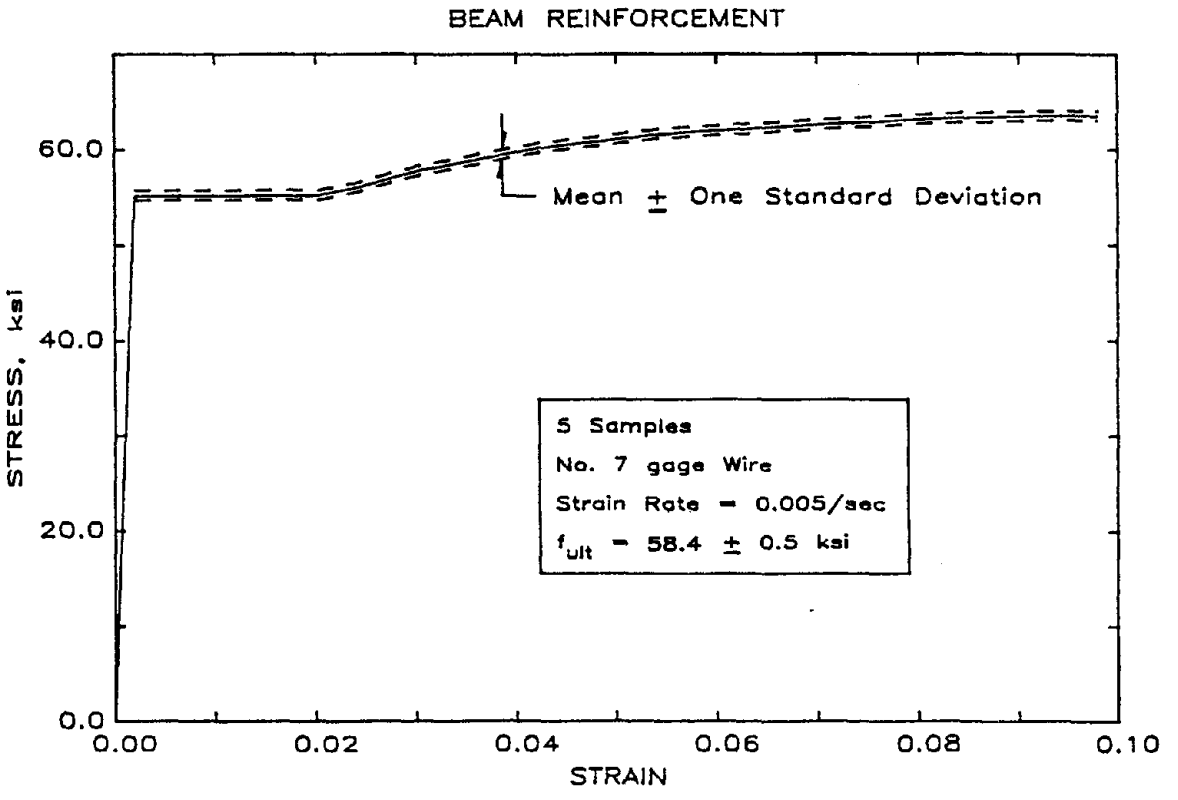

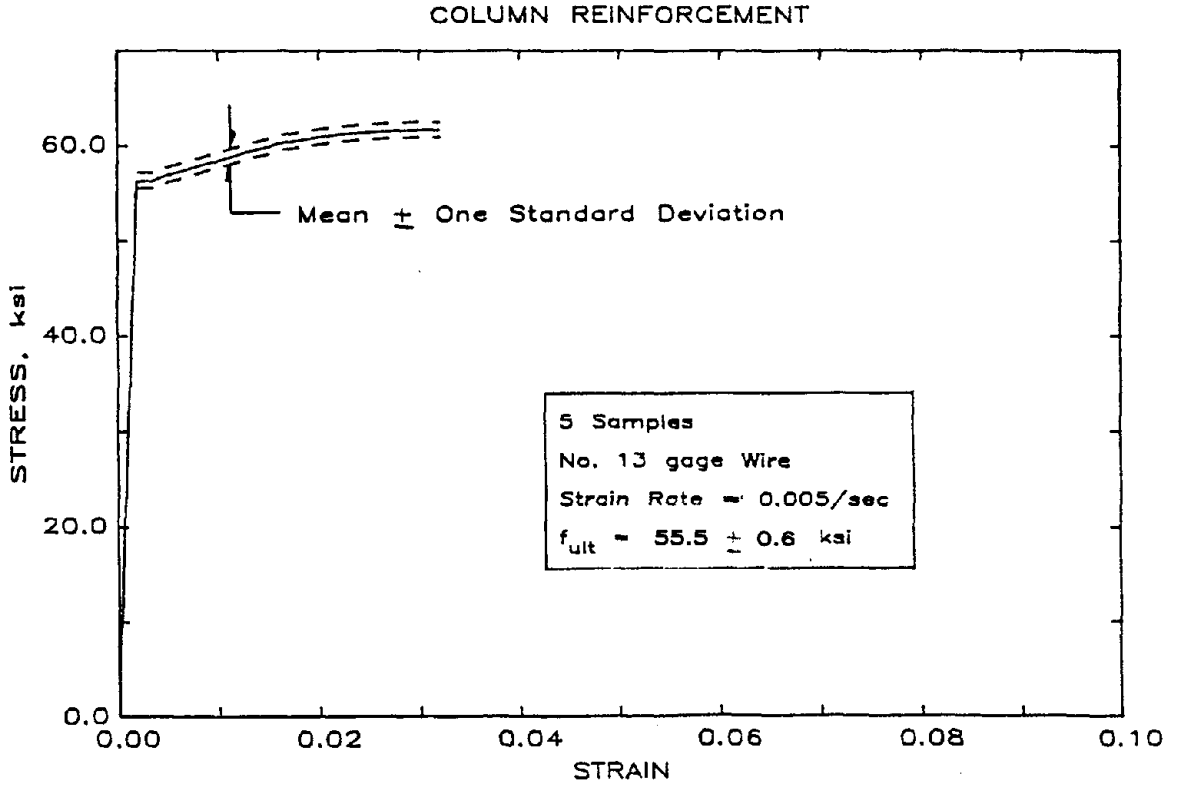

Fig. A.8 Stress-Strain Curves for Longitudinal Wire

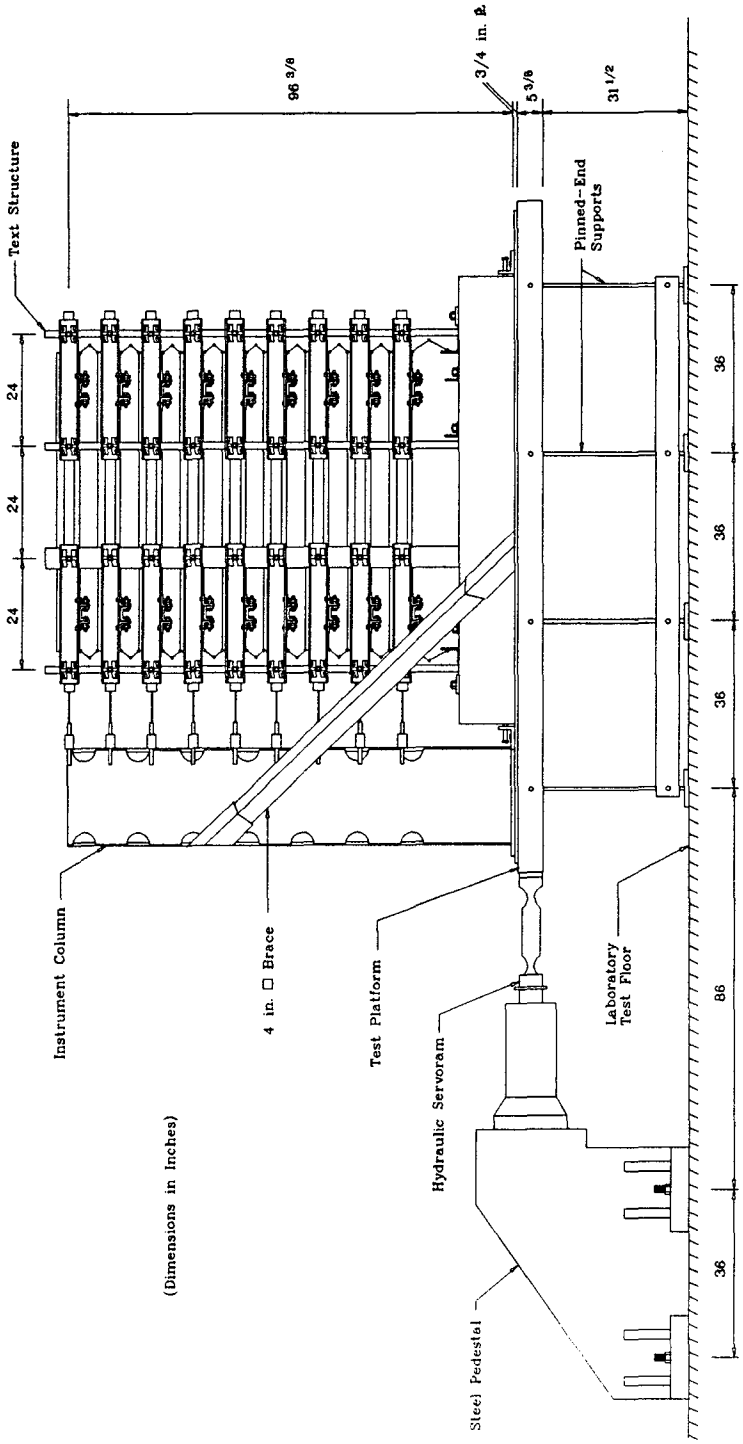

Fig. A.9 Earthquake Simulator

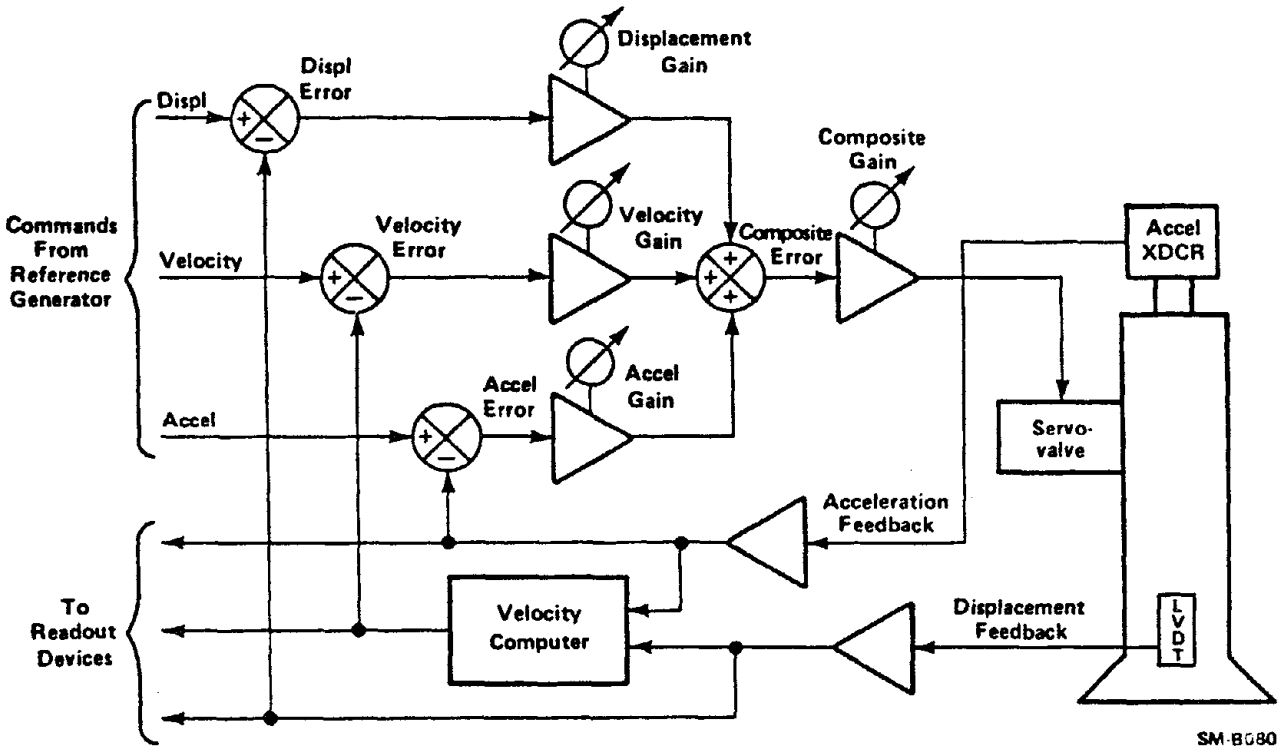

Fig. A.10 Three-Variable Servo Control

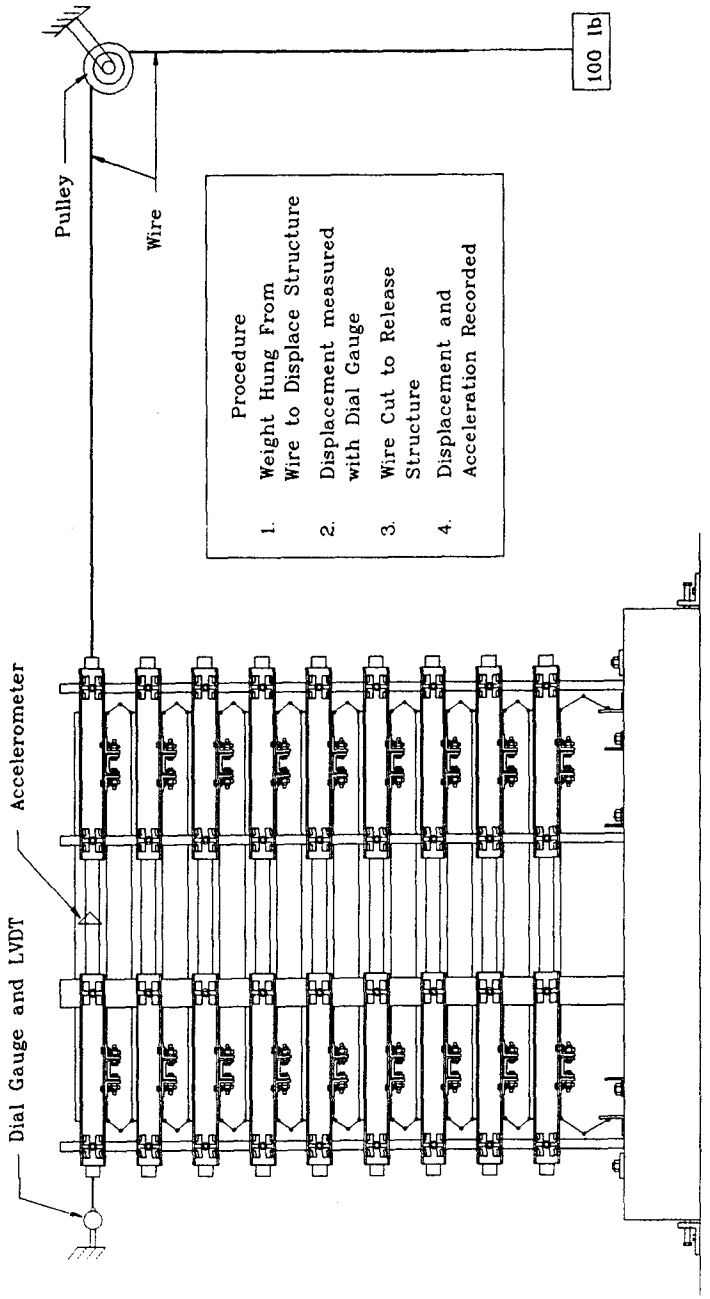

Fig. A.11 Setup for Free-Vibration Tests

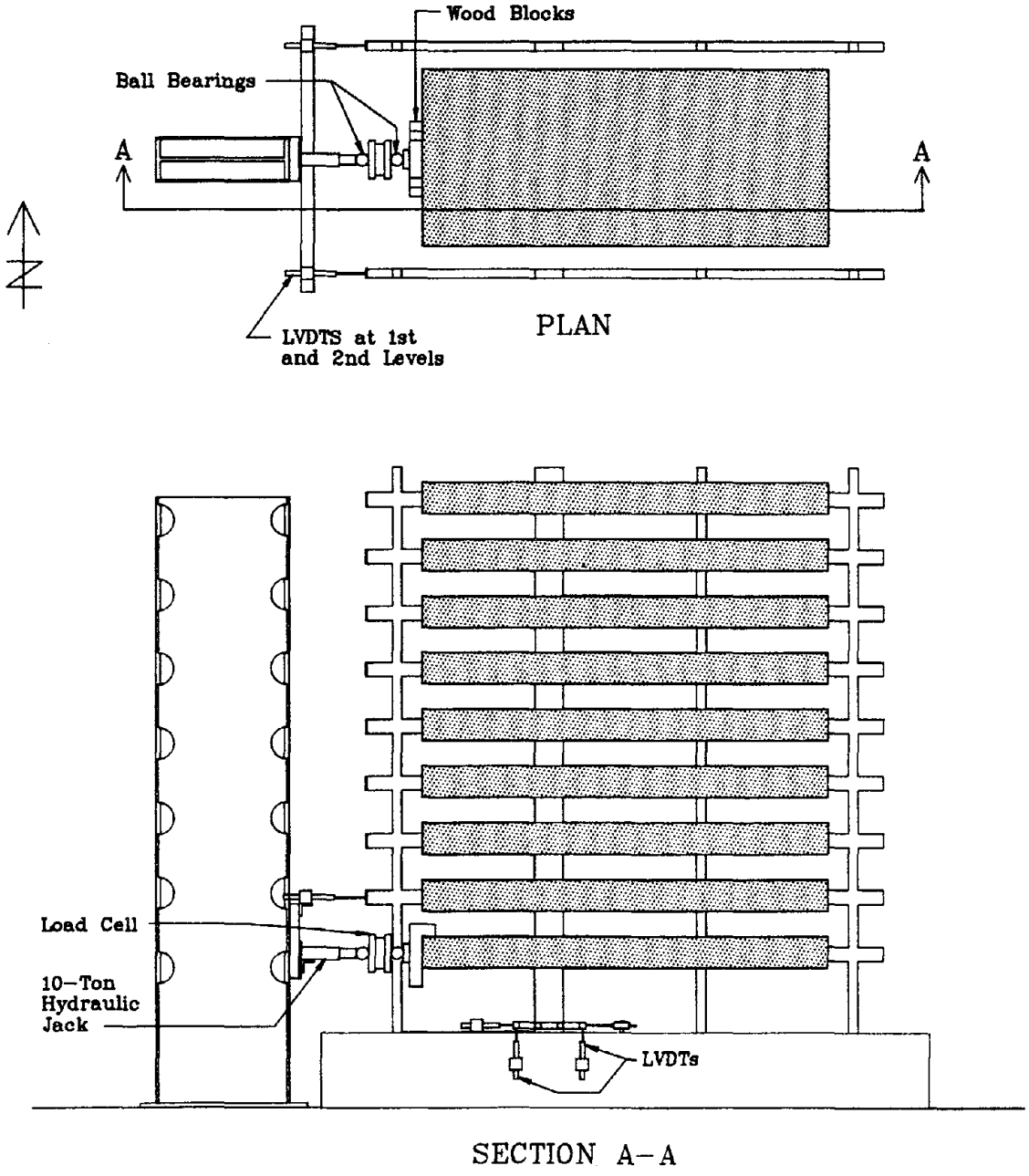

Fig. A.12 Setup for Static Tests

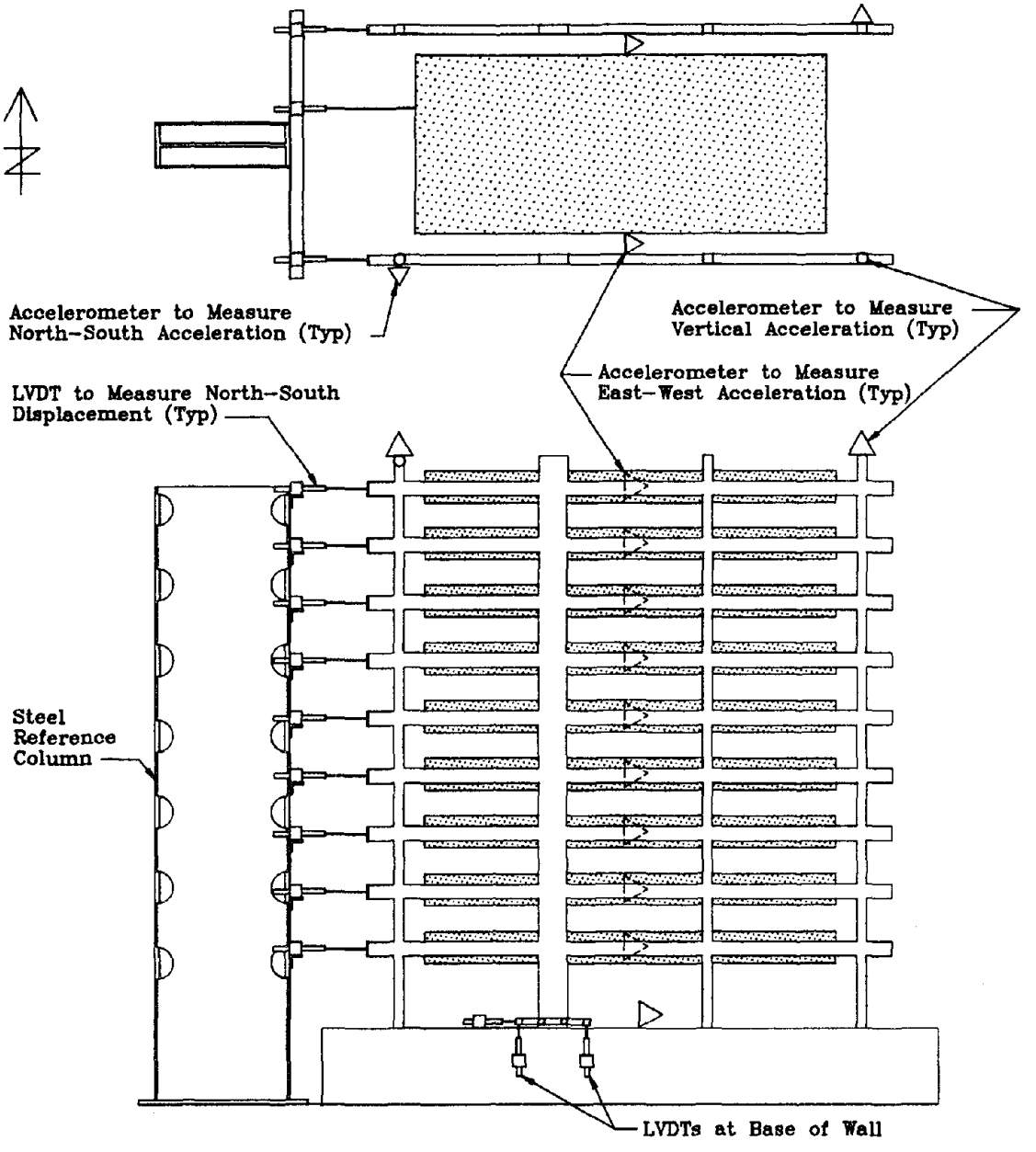

Fig. A.13 Location of Instrumentation

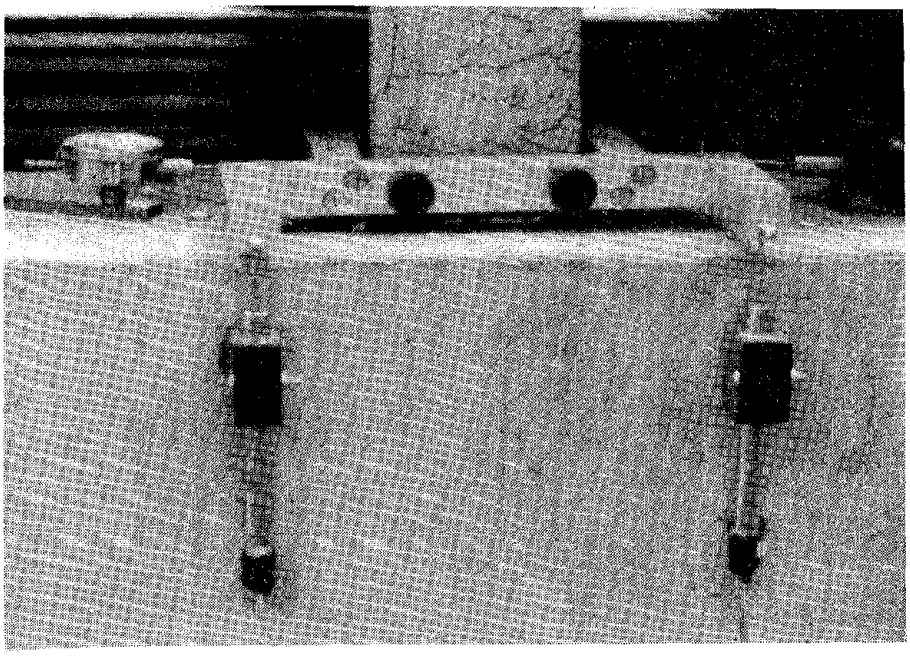

(a) Photograph of North Frame

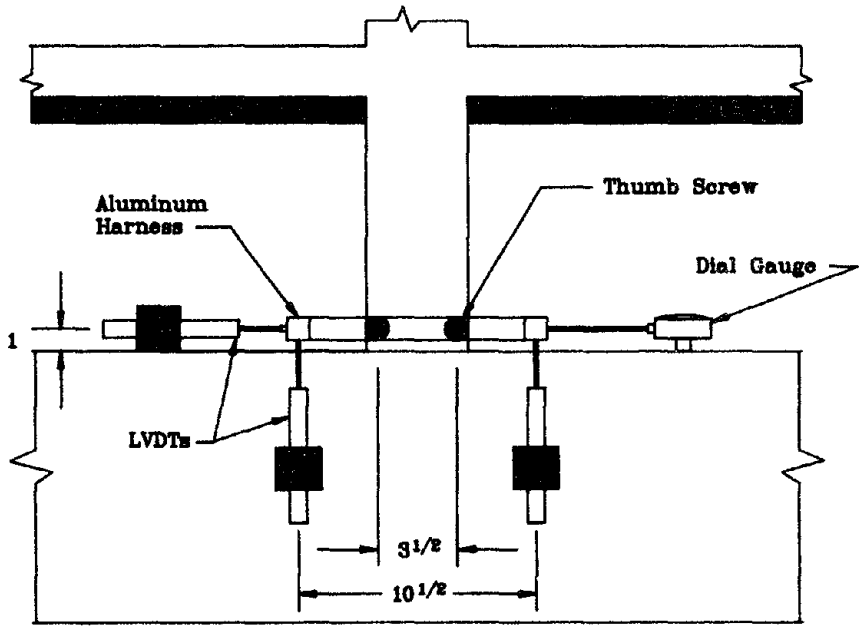

(Dimensions in Inches)

(b) Elevation of South Frame

Fig. A.14 Instrumentation at Base of Wall

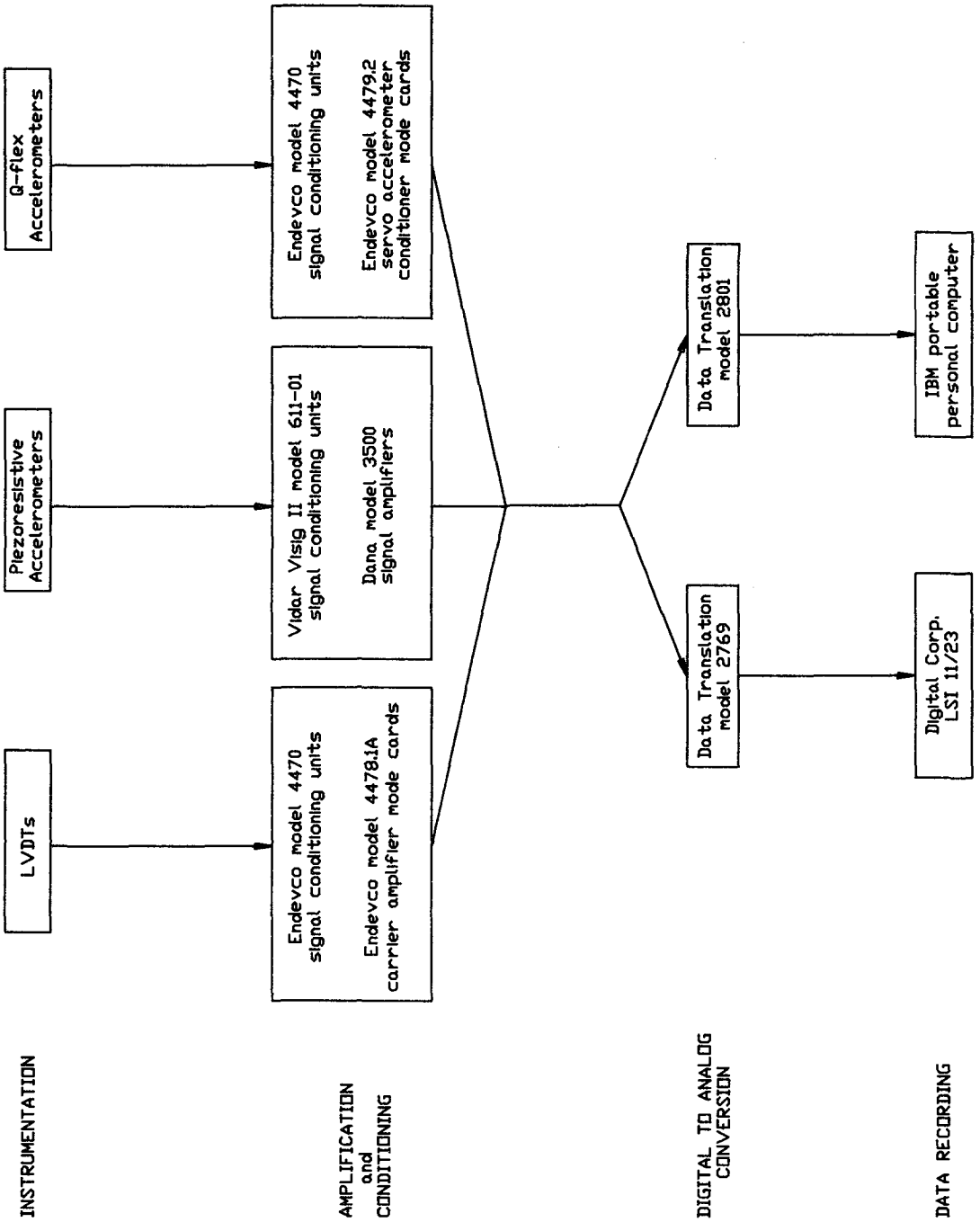

Fig A.15 Signal Path

APPENDIX B

DESCRIPTION OF TEST STRUCTURES

This appendix provides data used to calculate the lateral strength of the test structures considered in Chapter 5.

Measured material properties, measured dimensions and reinforcing schedules are given in Tables B.1-B.5. Nominal dimensions are listed for structures for which measured dimensions were not reported in the original reference.

Figures B.2-B.5 show the configuration of typical tests structures.

Table B.1 Configuration and Mass of Test Structures

	Reference	Structure	Level	Number of Bays	Wall Height (in.)	Weight per Level (lbs.)
Schultz	32	SS1	1-9	3		1140
		SS2	1-9	3		1140
Wood	46	Tower	1-2	3		1136
			3-7	1		392
		Stepped	1-3	3		1128
			4-6	2		756
			7-9	1		392
Eberhard		ES1	1-9	3	84.375	1150
		ES2	1-9	3	84.375	1150
Gulkan	14	HD1	1	1		690
		HD2	1	1		690
		HE1	1	1		690
		HE2	1	1		690
Healey	15	MF1	1-10	3		1000
Moehle	23	MF2[a]	1	3		667
			2-9	3		1000
Cecen	10	H1	1-10	3		1000
		H2	1-10	3		1000
Moehle	24	FNW	1-10	3		1013
		FHW	1-10	3	45.0	1020
		FFW	1-10	3	90.0	1020
Abrams	2	FW1	1-10	3	90.0	1020
		FW2	1-10	3	90.0	1020
		FW3	1-10	3	90.0	1020
		FW4	1-10	3	90.0	1020

[a]Structure MF2 was missing a beam in the first story.

Table B.2 Material Properties for Test Structures

Structure		Concrete Compressive Strength (psi)	Columns f_{su}[a] (ksi)	gage	Beams f_{su}[a] (ksi)	gage	Walls f_{su}[a] (ksi)	gage
Schultz	SS1	5590	59.9	13 G	64.2	7 G		
	SS2	5260	59.9	13 G	64.2	7 G		
Wood	Tower	6150	59.9	13 G	64.2	7 G		
	Stepped	5990	59.9	13 G	64.2	7 G		
Eberhard	ES1	4350	59.9	13 G	64.2	7 G	64.2	7 G
	ES2	4800	59.9	13 G	64.2	7 G	64.2	7 G
Gulkan	HD1	5620	49.5	7 G	49.5	7 G		
	HD2	6220	49.5	7 G	49.5	7 G		
	HE1	6130	49.5	7 G	49.5	7 G		
	HE2	5330	49.5	7 G	49.5	7 G		
Healey	MF1	5830	59.4	13 G	59.4	13 G		
Moehle	MF2	5510	58.0	13 G	58.0	13 G		
Cecen	H1	4660	70.3	7 G	72.4	13 G		
			72.5	8 G	68.3	16 G		
			71.5	10 G				
			72.4	13 G				
	H2	4100	70.3	7 G	72.4	13 G		
			72.5	8 G	68.3	16 G		
			71.5	10 G				
			72.4	13 G				
Moehle	FNW	5800	61.8	13 G	61.8	13 G		
	FHW	5220	61.8	13 G	61.8	13 G	56.8	2 G
	FFW	5360	61.8	13 G	61.8	13 G	56.8	2 G
Abrams	FW1	4790	54.1	13 G	54.1	13 G	53.1	2 G
	FW2	6100	54.1	13 G	54.1	13 G	53.1	2 G
	FW3	4660	54.1	13 G	54.1	13 G	53.1	2 G
	FW4	4900	54.1	13 G	54.1	13 G	53.1	2 G

[a]Tensile strength of reinforcement.

Table B.3 Reported Frame and Wall Dimensions

Structure		Story	Story Height (in.)	L (in.)	S (in.)	b (in.)	h (in.)	c (in.)	Wall Depth (in.)
Schultz	SS1	1	12.375	24.0	36.0	1.53	2.24	1.49	
		2-9	9.0						
	SS2	1	12.375	24.0	36.0	1.53	2.26	1.51	
		2-9	9.0						
Wood	Tower	1	12.375	24.0	36.0	1.53	2.25	1.50	
		2-9	9.0						
	Stepped	1	12.375	24.0	36.0	1.52	2.25	1.51	
		2-9	9.0						
Eberhard	ES1	1	12.375	24.0	36.0	1.52	2.22	1.49	4.49
		2-9	9.0						
	ES2	1	12.375	24.0	36.0	1.51	2.24	1.49	4.49
		2-9	9.0						
Gulkan	HD1	1	15.5	29.5	0.0	2.50	5.00	2.50	
	HD2	1	15.5	29.5	0.0	2.50	5.00	2.50	
	HE1	1	15.5	29.5	0.0	2.50	5.00	2.50	
	HE2	1	15.5	29.5	0.0	2.50	5.00	2.50	
Healey	MF1	1,10	11.0	12.0	36.0	1.53	1.50	2.00	
		2-9	9.0						
Moehle	MF2	1-10	11.0	12.0	36.0	1.53	1.50	1.99	
		2-9	9.0						
Cecen	H1	1-10	9.0	12.0	24.0	1.50	1.50	2.00	
	H2	1-10	9.0	12.0	24.0	1.50	1.50	2.00	
Moehle	FNW	1	18.0	12.0	36.0	1.53	1.51	2.01	
		2-9	9.0						
	FHW	1	18.0	12.0	36.0	1.53	1.51	2.01	8.03
		2-9	9.0						
	FFW	1	18.0	12.0	36.0	1.53	1.51	2.01	8.03
		2-9	9.0						
Abrams	FW1	1-10	9.0	12.0	36.0	1.54	1.50	2.00	8.00
	FW2	1-10	9.0	12.0	36.0	1.54	1.50	2.00	8.00
	FW3	1-10	9.0	12.0	36.0	1.54	1.50	2.00	8.00
	FW4	1-10	9.0	12.0	36.0	1.54	1.50	2.00	8.00

Note: See Fig. B.1 for definition of dimensions listed.

Table B.4 Beam and Wall Reinforcement Schedule

Structure		Beams			Wall		
		Level	Reinf.	ρ^a(%)	Story	Reinf.	ρ^b(%)
Schultz	SS1	1-2	3-7 g	2.60			
		3-9	2-7 g	1.73			
	SS2	1-3	3-7 g	2.60			
		4-9	2-7 g	1.73			
Wood	Tower	1-3	3-7 g	2.60			
		4-9	2-7 g	1.73			
	Stepped	1-2	3-7 g	2.60			
		3-9	2-7 g	1.73			
Eberhard	ES1	1-3	3-7 g	2.60	1-9	2-7 g	1.46
		4-9	2-7 g	1.73			
	ES2	1-3	3-7 g	2.60	1-9	2-7 g	1.46
		4-9	2-7 g	1.73			
Gulkan	HD1	1	2-7 g	0.44			
	HD2	1	2-7 g	0.44			
	HE1	1	2-7 g	0.44			
	HE2	1	2-7 g	0.44			
Healey	MF1	1-7	3-13 g	1.10			
		8-10	2-13 g	0.74			
Moehle	MF2	1-7	3-13 g	1.10			
		8-10	2-13 g	0.74			
Cecen	H1	1-4	2-13 g	0.74			
		5-10	3-16 g	0.50			
	H2	1-4	2-13 g	0.74			
		5-10	3-16 g	0.50			
		1-3	3-13 g	1.10			
Moehle	FNW	4-9	2-13 g	0.74			
	FHW	1-9	2-13 g	0.74	1-4	2-2 g	0.90
	FFW	1-9	2-13 g	0.74	1-9	2-2 g	0.90
Abrams	FW1	1-4	2-13 g	0.74	1-4	8-2 g	3.59
		5-9	3-13 g	1.10	5-6	4-2 g	1.80
		10	2-13 g	0.74	7-10	2-2 g	0.90
	FW2	1-2	2-13 g	0.74	1-9	2-2 g	0.90
		3-7	3-13 g	1.10			
		8-10	2-13 g	0.74			
	FW3	1-2	2-13 g	0.74	1-9	2-2 g	0.90
		3-7	3-13 g	1.10			
		8-10	2-13 g	0.74			
	FW4	1-4	2-13 g	0.74	1-4	8-2 g	3.59
		5-9	3-13 g	1.10	5-6	4-2 g	1.80
		10	2-13 g	0.74	7-10	2-2 g	0.90

[a]Ratio of tension reinforcement area to product of width and effective depth
[b]Ratio of total reinforcement area to cross-sectional area of wall

Table B.5 Column Reinforcement Schedule

Structure		Exterior Columns			Interior Columns		
		Story	Reinf.[a]	ρ[b](%)	Story	Reinf.[a]	ρ[b](%)
Schultz	SS1	1	5-13 g	2.92	1-2	5-13 g	2.92
		2-3	4-13 g	2.34	3-4	4-13 g	2.34
		4-9	2-13 g	1.17	5-9	2-13 g	1.17
	SS2	1	8-13 g	4.68	1-2	8-13 g	4.68
		2-3	5-13 g	2.92	3-4	5-13 g	2.92
		4-5	3-13 g	1.75	5-6	3-13 g	1.75
		6-9	2-13 g	1.17	7-9	2-13 g	1.17
Wood	Tower	1	4-13 g	2.34	1-3	6-13 g	3.51
		2	2-13 g	1.17	4-9	4-13 g	2.34
	Stepped	1-2	6-13 g	3.51	1	8-13 g	4.68
		3-9	4-13 g	2.34	2	6-13 g	3.51
					3-9	4-13 g	2.34
Eberhard	ES1[c]	1-2	3-13 g	1.75	1-2	6-13 g	3.51
		3-9	2-13 g	1.17	3-6	4-13 g	2.34
					7-9	2-13 g	1.17
	ES2	1-9	2-13 g	1.17	1-9	2-13 g	1.17
Gulkan	HD1	1	2-7 g	1.57	1	2-7 g	1.57
	HD2	1	2-7 g	1.57	1	2-7 g	1.57
	HE1	1	2-7 g	1.57	1	2-7 g	1.57
	HE2	1	2-7 g	1.57	1	2-7 g	1.57
Healey	MF1	1	3-13 g	1.32	1-2	3-13 g	1.32
		2-10	2-13 g	0.88	3-10	2-13 g	0.88
Moehle	MF2	1-2	4-13 g	1.75	1	4-13 g	1.75
		3-10	2-13 g	0.88	2-10	2-13 g	0.88
Cecen	H1	1-4	2-7 g	3.28	1-4	2-8 g	2.75
		5-10	2-10 g	1.91	5-10	2-13 g	0.88
	H2	1-4	2-7 g	3.28	1-4	2-8 g	2.75
		5-10	2-10 g	1.91	5-10	2-13 g	0.88
Moehle	FNW	1	4-13 g	1.75	1-2	4-13 g	1.75
		2-9	2-13 g	0.88	3-9	2-13 g	0.88
	FHW	1-9	2-13 g	0.88	1-9	2-13 g	0.88
	FFW	1-9	2-13 g	0.88	1-9	2-13 g	0.88
	FW1	1-10	2-13 g	0.88	1-8	2-13 g	0.88
					9-10	3-13 g	1.32
	FW2	1-3	3-13 g	1.32	1-10	2-13 g	0.88
		4-10	2-13 g	0.88			
	FW3	1-3	3-13 g	1.32	1-10	2-13 g	0.88
		4-10	2-13 g	0.88			
	FW4	1-10	2-13 g	0.88	1-8	2-13 g	0.88
					9-10	3-13 g	1.32

[a]Number of bars per tension face.
[b]Ratio of total reinforcement area to cross-sectional area of column.
[c]Exterior column near wall had same reinforcement as interior column.

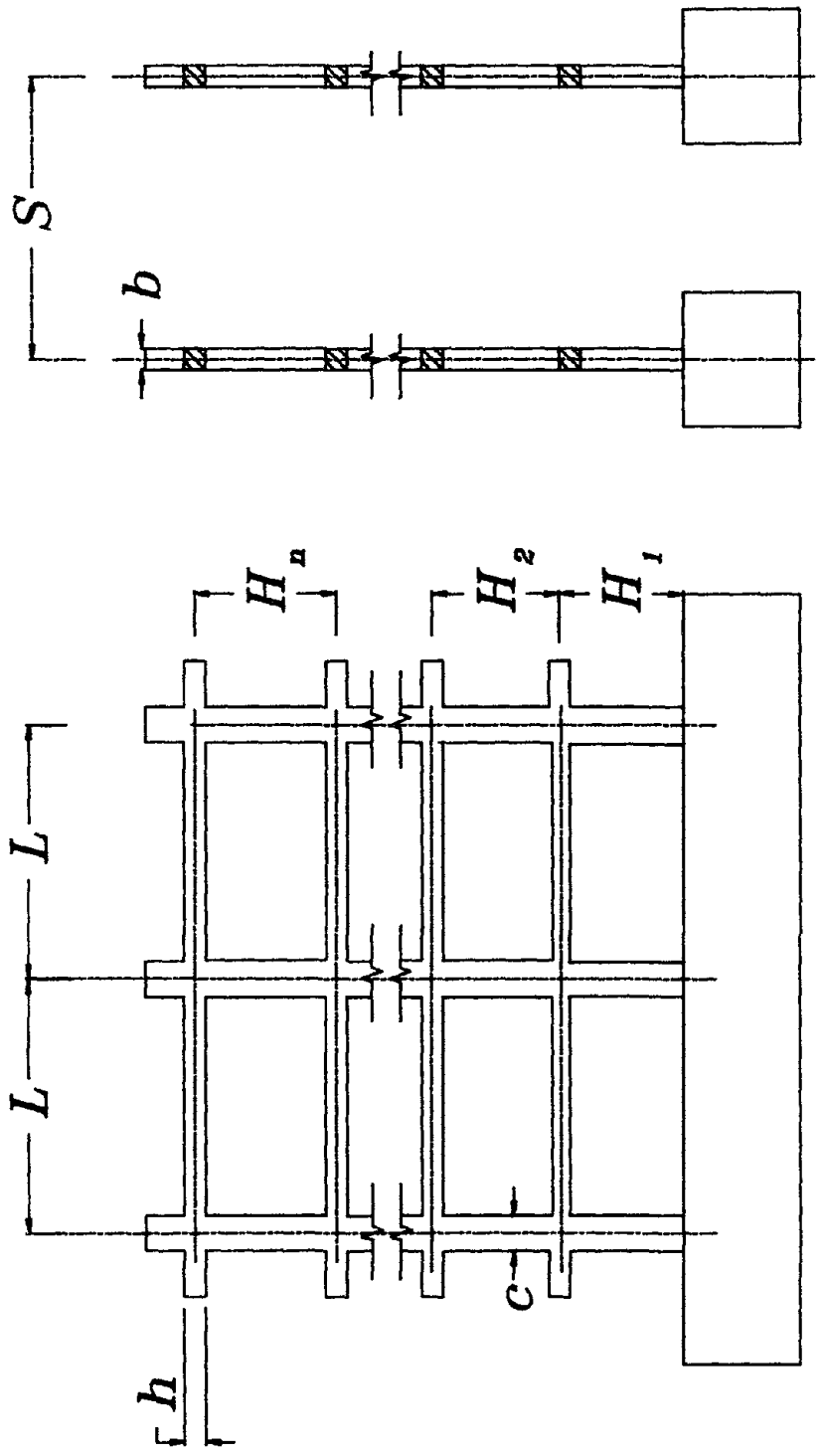

Fig. B.1 Definitions of Dimensions Listed in Table B.3

*Columns 1.5*1.5 in.*
*Girders 1.5*2.25 in.*
*Wall 1.5*4.5 in. (ES1 & ES2)*

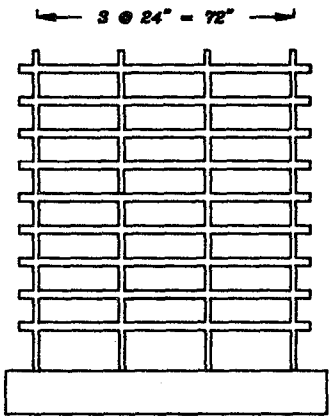

Structures SS1 and SS2

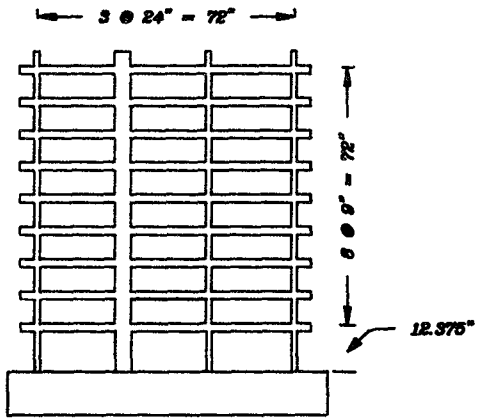

Structures ES1 and ES2

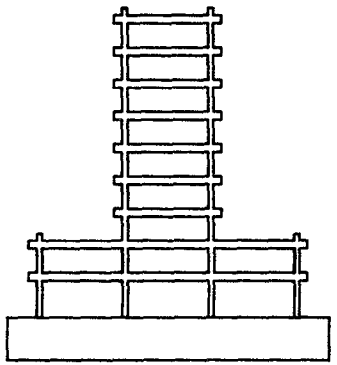

Tower Structure

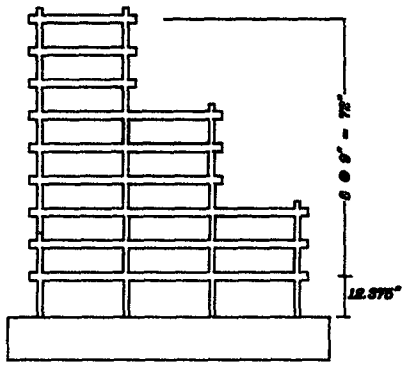

Stepped Structure

Fig. B.2 Profiles of Structures with Yielding Columns

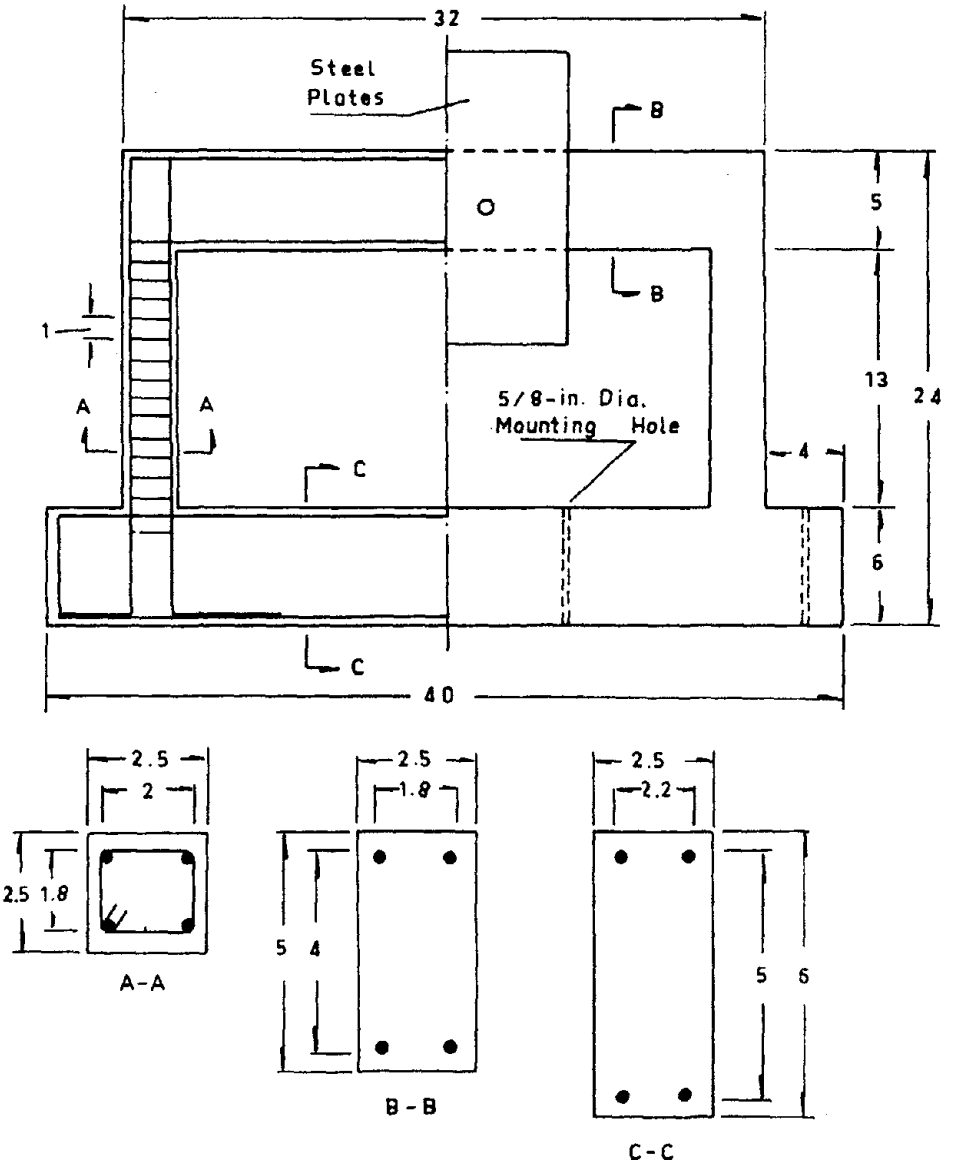

All dimensions in inches

Fig B.3 Structures Tested by Gulkan [14]

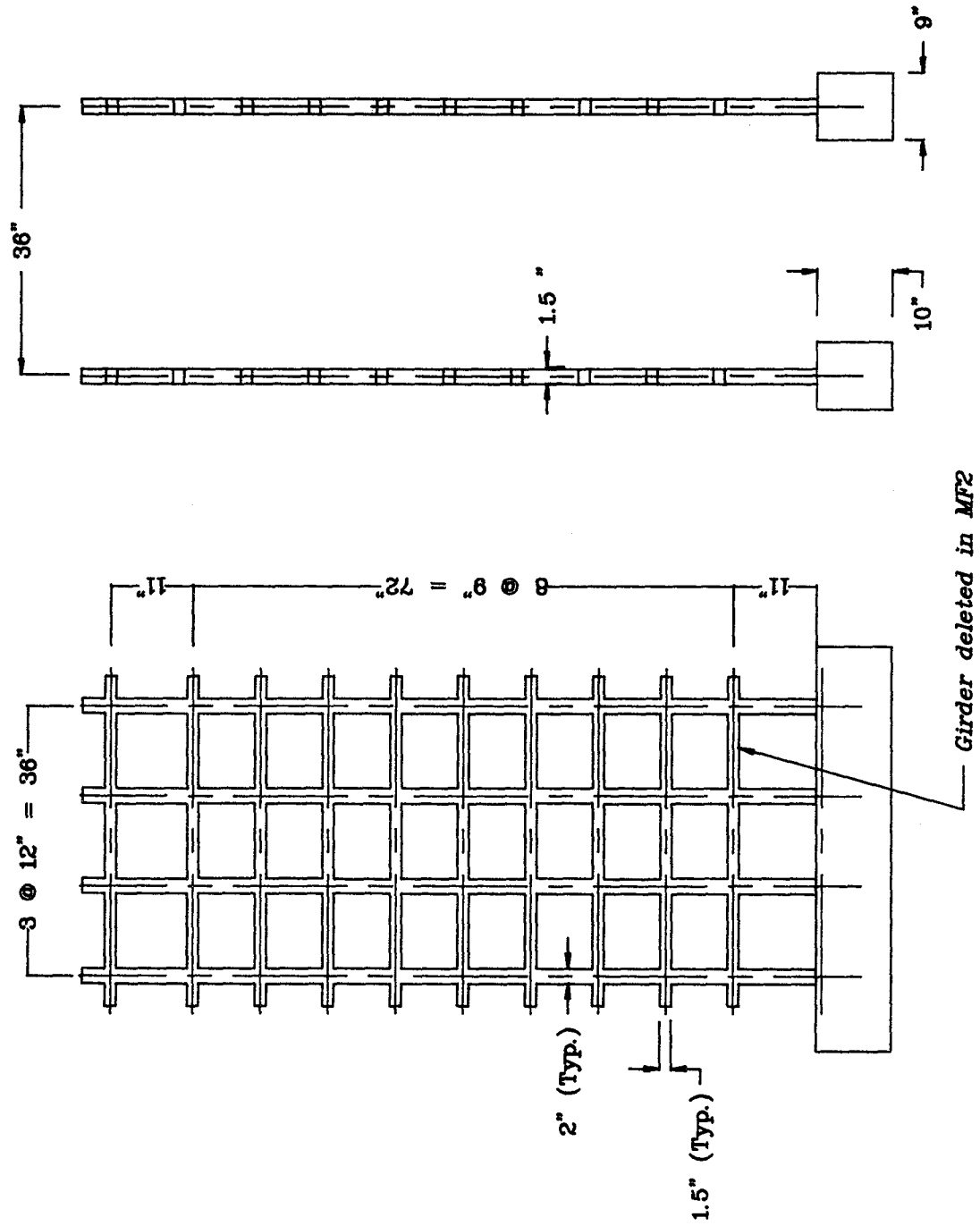

Fig. B.4 Frame Structures with Yielding Beams

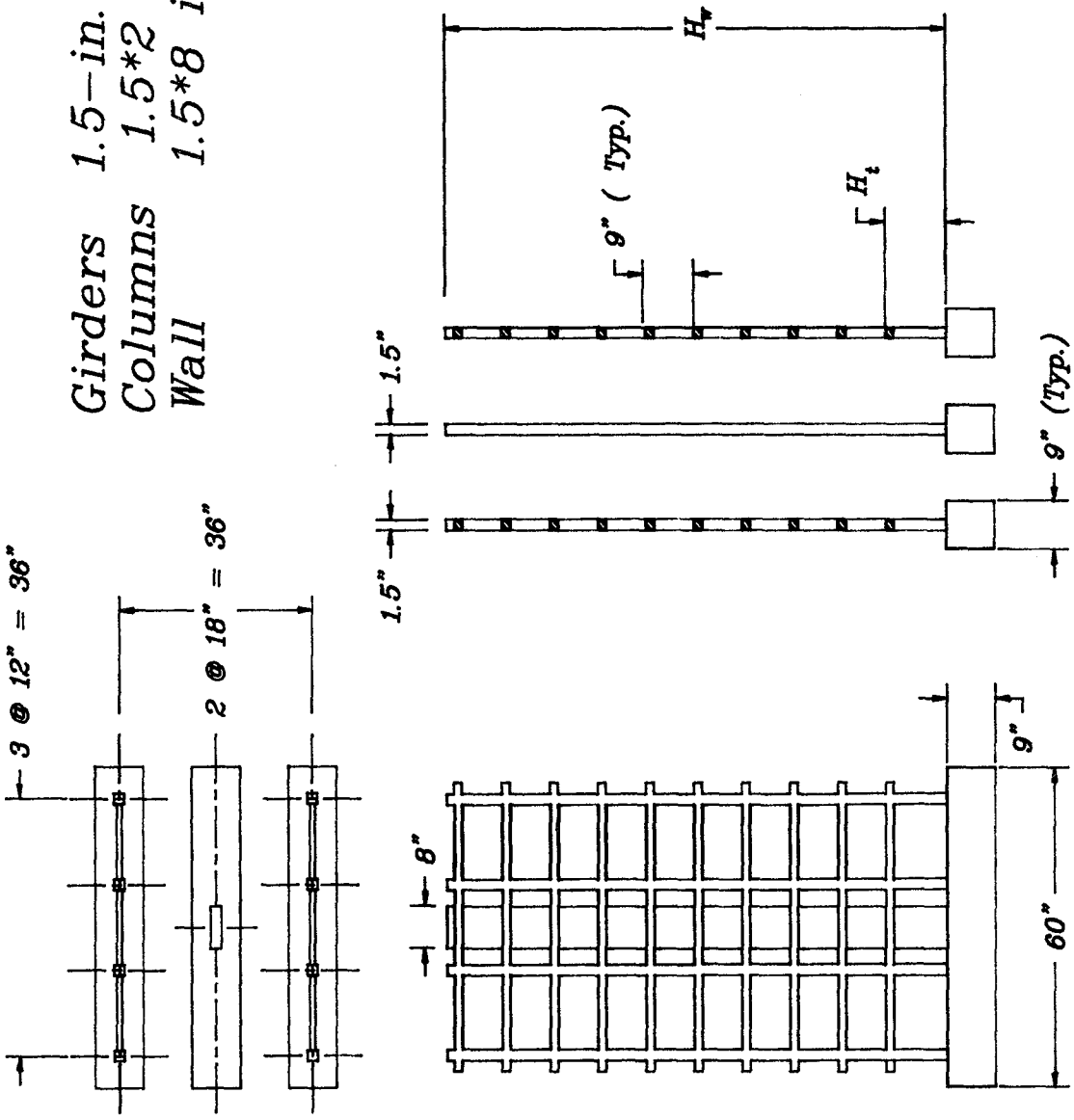

Fig. B.5 Frame-Wall Structures

APPENDIX C

INFLUENCE OF ASSUMED INERTIAL FORCE DISTRIBUTION ON CALCULATED BASE SHEAR AND BASE MOMENT

In general, the calculated base shear or base moment capacity varies with the assumed lateral force distribution. Two notable exceptions are stated and then derived below.

1. Calculated base shear strength is independent of assumed lateral force distribution if the base shear strength is limited by a first-story failure mechanism (Fig. 7.1(a)).

Proof:

By definition,

$$V = \sum_{i=1}^{N} F_i \tag{B.1}$$

where,

V = base shear

F_i = lateral force at level i

N = number of stories

The external work done by lateral forces while undergoing a virtual displacement is:

$$W_{ext} = \sum_{i=1}^{N} F_i * \delta_i \tag{B.2}$$

where,

δ_i = virtual displacement at level i

Assuming a first-story mechanism, and imposing a unit displacement at each story (Fig. 7.1(a)), Eq. B.2 becomes:

$$W_{ext} = 1 * \sum_{i=1}^{N} F_i$$

$$= 1 * V \qquad \text{(B.3)}$$

Applying the principle of virtual work and using Eq. B.3:

$$W_{ext} = W_{int}$$

$$1 * V_u = W_{int} \qquad \text{(B.4)}$$

Internal virtual work, W_{int}, does not depend on the assumed external force distribution. Noting Eq. B.4, the base shear strength, V_u, must also be independent of assumed force distribution.

2. Calculated base moment strength is independent of assumed lateral force distribution if the base moment strength is limited by a beam mechanism involving yielding at all stories (Fig. 7.1(d)).

Proof:

Assuming beams yield at all stories and imposing the linearly varying displacement pattern shown in Fig. 7.1(d), we get from Eq. B.2:

$$W_{ext} = \sum_{i=1}^{N} (F_i) \frac{h_i}{h_N} * 1$$

$$= \frac{1}{h_N} \sum_{i=1}^{N} (F_i * h_i)$$

$$= \frac{M}{h_N} * 1 \qquad \text{(B.5)}$$

where,

h_i = elevation of story i

$$M = \text{base moment} = \sum_{i=1}^{N} (F_i * h_i)$$

Applying the principle of virtual work together with Eq. B.5:

$$M * 1 = W_{int} * h_N \tag{B.6}$$

W_{int} and h_N do not depend on the assumed external force distribution. Noting Eq. B.6, the base moment strength, M_u, must also be independent of assumed force distribution.

REFERENCES

1. Abrams, D. P., "Measured Hysteresis Relationships for Small-Scale Beams," Civil Engineering Studies, Structural Research Series No. 432, University of Illinois, Urbana, November 1976.

2. Abrams, D. P. and M. A. Sozen, "Experimental Study of Frame-Wall Interaction in Reinforced Concrete Structures Subjected to Strong Earthquake Motions," Civil Engineering Studies, Structural Research Series No. 460, University of Illinois, Urbana, May 1979.

3. Algan, B. B. and M. A. Sozen, "Drift and Damage Considerations in Earthquake-Resistant Design of Reinforced Concrete Buildings," Ph.D. Dissertation submitted to the Graduate College of the University of Illinois, Urbana, March 1982.

4. American Concrete Institute Committee 318, "Building Code Requirements for Reinforced Concrete (ACI 318-83)," American Concrete Institute, Box 19150, Redford Station, Detroit, 1983.

5. Anton, H., Elementary Linear Algebra, John Wiley & Sons, Inc., New York, 1981.

6. Aoyama, H., "Earthquake Resistant Design of Reinforced Concrete Frame Buildings with 'Flexural Walls,' Journal of the Faculty of Engineering, the University of Tokyo, Vol. XXXIX, No. 2, 1987, pp. 87-109.

7. Applied Technology Council, Tentative Provisions for the Development of Seismic Regulations for Buildings, ATC 3-06, June 1978.

8. Bonacci, J., "Experiments to Study Seismic Drift of Reinforced Concrete Structures," Ph.D. Dissertation submitted to the Graduate College of the University of Illinois, Urbana, 1989.

9. California Institute of Technology, Earthquake Engineering Research Laboratory, "Strong Motion Earthquake Accelerograms, Digitized and Plotted Data," EERL Report No. 71-50, Pasadena, CA, 1971.

10. Cecen, H., "Response of Ten-Story Model Frames to Simulated Earthquakes," Ph.D. Dissertation submitted to the Graduate College of the University of Illinois, Urbana, October 1979.

11. Ernst, G. C., "Tests of Reinforced Concrete Hinges of the Mesnager Type," Proceedings, Highway Research Board, Vol. 17, 1937, pp. 187-201.

12. Gavlin, N. L., "Bond Characteristics of Model Reinforcement," Civil Engineering Studies, Structural Research Series No. 427, University of Illinois, Urbana, April 1976.

13. Gilbertsen, N. D. and J. P. Moehle, "Experimental Study of Small-Scale R/C Columns Subjected to Axial and Shear Force Reversals," Civil Engineering Studies, Structural Research Series No. 481, University of Illinois, Urbana, July 1980.

14. Gulkan, P. and M. A. Sozen, "Response and Energy Dissipation of Reinforced Concrete Frames Subjected to Strong Base Motions," Civil Engineering Studies, Structural Research Series No. 427, University of Illinois, Urbana, April 1976.

15. Healey, T. J. and M. A. Sozen, "Experimental Study of the Dynamic Response of a Ten-Story Reinforced Concrete Frame with a Tall First Story," Civil Engineering Studies, Structural Research Series No. 450, University of Illinois, Urbana, August 1978.

16. Housner, G. W., "Behavior of Structures During Earthquakes," Journal of the Engineering Mechanics Division, ASCE, Vol. 85, No. EM4, October 1959, pp. 109-130.

17. Joint Technical Coordinating Committee, "Interim Summary Report on Tests of 7-Story Reinforced Concrete Building," ASCE Journal of Structural Engineering, Vol. 110, No. 10, pp. 2393-2411, 1984.

18. Kabeysawa, T., "Ultimate-State Design of Reinforced Concrete Wall-Frame Structures," Proceedings, Pacific Conference on Earthquake Engineering," Wairakei, New Zealand, Vol. I, August 1987.

19. Kreger, M. E. and D. P. Abrams, "Measured Hysteresis Relationships for Small-Scale Beam-Column Joints," Civil Engineering Studies, Structural Research Series No. 453, University of Illinois, Urbana, August 1978.

20. Lopez, R. L., "A Numerical Model for Nonlinear Response of R/C Frame-Wall Structures," Ph.D. Dissertation submitted to the Graduate College of the University of Illinois, Urbana, 1988.

21. Mattock, A. H., L. B. Kriz, and E. Hognestad, "Rectangular Concrete Stress Distribution in Ultimate Strength Design," ACI Journal, Vol. 57, No. 8, February 1961, pp. 875-926.

22. Mesnager, M., "Experiences Sur Une Semi-Articulation Pour Voutes En Beton Arme," Annales des Ponts et Chaussees, Vol. II, 1907, pp. 180-199.

23. Moehle, J. P. and M. A. Sozen, "Earthquake-Simulation Tests of a Ten-Story Reinforced Concrete Frame with a Discontinued First-Level Beam," Civil Engineering Studies, Structural Research Series No. 451, University of Illinois, Urbana, August 1978.

24. Moehle, J. P. and M. A. Sozen, "Experiments to Study Earthquake Response of R/C Structures with Stiffness Interruptions," Civil Engineering Studies, Structural Research Series No. 482, University of Illinois, Urbana, August 1980.

25. Moncarz, P. D. and H. Krawinkler, "Theory and Application of Experimental Model Analysis in Earthquake Engineering," Report No. 50, Department of Civil Engineering, Stanford University, Stanford, June 1981.

26. Newmark, N. M., "A Method of Computational for Structural Dynamics," Journal of the Engineering Mechanics Division, ASCE, Vol. 85, EM3, July 1959, pp. 69-86.

27. Park, R. and T. Paulay, Reinforced Concrete Structures, John Wiley & Sons, Inc., New York, NY, 1975.

28. Price, W. H., "Factors Influencing Concrete Strength," ACI Journal, Vol. 47, No. 32, February 1951, pp. 417-431.

29. Riddell, R., S. L. Wood, and J. C. de la Llera, "The 1985 Chile Earthquake: Structural Characteristics and Damage Statistics for the Building Inventory in Vina del Mar," Civil Engineering Studies, Structural Research Series No. 534, University of Illinois, Urbana, April 1987.

30. Saiidi, M. and M. A. Sozen, "Simple and Complex Models for Nonlinear Seismic Response of R/C Structures," Civil Engineering Studies, Structural Research Series No. 465, University of Illinois, Urbana, August 1979.

31. Saiidi, M., "User's Manual for the LARZ Family: Computer Programs for Nonlinear Seismic Analysis of Reinforced Concrete Planar Structures," Civil Engineering Studies, Structural Research Series No. 466, University of Illinois, Urbana, November 1979.

32. Schultz, A. E., "An Experimental and Analytical Study of the Earthquake Response of R/C Frames with Yielding Columns," Ph.D. Dissertation submitted to the Graduate College of the University of Illinois, Urbana, 1985.

33. Shahrooz, B. M. and J. P. Moehle, "Experimental Study of Seismic Response of RC Setback Buildings," Report No. UCB/EERC-87/16, Earthquake Engineering Research Center, University of California, Berkeley, October 1987.

34. Shibata, A. and M. A. Sozen, "Substitute-Structure Method for Seismic Design in R/C," Journal of the Structural Division, ASCE, Vol. 102, ST1, January 1976, pp. 1-18.

35. Shimazaki, K. and Sozen, M. A., "Seismic Drift of Reinforced Concrete Structures," Research Reports, Hazama-Gumi, Tokyo, 1984, pp. 145-166.

36. Sozen, M. A., S. Otani and N. N. Nielsen, "The University of Illinois Earthquake Simulator," Proceedings, Fourth World Conference on Earthquake Engineering, Santiago, Chile, Vol. III, Session B5, January 1969, pp. 139-150.

37. Sozen, M. A. and S. Otani, "Performance of the University of Illinois Earthquake Simulator in Reproducing Scaled Earthquake Motions," Proceedings, U.S.-Japan Seminar on Earthquake Engineering with Emphasis on the Safety of School Buildings, Sandai, September 1970, pp. 278-302.

38. Sozen, M. A., "A Frame of Reference," Ralph B. Peck Symposium, University of Illinois, Urbana, April 1987.

39. Staffier, S. R. and M. A. Sozen, "Effect of Strain Rate on Yield Stress of Model Reinforcement," Civil Engineering Studies, Structural Research Series No. 415, University of Illinois, Urbana, February 1975.

40. Structural Engineers Association of California, Recommended Lateral Force Requirements, Draft, November 15, 1984.

41. Takeda, T., M. A. Sozen and N. N. Nielsen, "Reinforced Concrete Response to Simulated Earthquakes," Journal of the Structural Division, ASCE, Vol. 96, No. ST12, December 1970, pp. 2557-2573.

42. Thomas, K. and M. A. Sozen, "A Study of the Inelastic Rotation Mechanics of Reinforced Concrete Connections," Civil Engineering Studies, Structural Research Series No. 301, University of Illinois, Urbana, August 1965.

43. Thomson, W. T., Theory of Vibration with Applications, Prentice-Hall, Inc., Englewood Cliffs, New Jersey, 1981.

44. Uniform Building Code, International Conference of Building Officials, Los Angeles, Ca, 1988.

45. US-Japan Committee, "Earthquake Effects of R/C Structures," SP-84, American Concrete Institute, Detroit.

46. Wood, S. L., "Experiments to Study the Earthquake Response of Reinforced Concrete Frames with Setbacks," Civil Engineering Studies, Structural Research Series No. 544, University of Illinois, Urbana, December 1988.

47. Wood, S. L., J. K. Wight and J. P. Moehle, "The 1985 Chile Earthquake: Observations on Earthquake-Resistant Construction in Vina del Mar," Civil Engineering Studies, Structural Research Series No. 532, University of Illinois, February 1987.